

FAU Studies Mathematics & Physics 9

Benedikt Krüger

Simulating Triangulations: Graphs, Manifolds and (Quantum) Spacetime

FAU
UNIVERSITY
PRESS

Benedikt Krüger

Simulating Triangulations:
Graphs, Manifolds and (Quantum) Spacetime

FAU Studies Mathematics & Physics

Band 9

Herausgeber der Reihe:

Prof. Dr. Karl-Hermann Neeb und Prof. Dr. Klaus Mecke

Benedikt Krüger

**Simulating Triangulations:
Graphs, Manifolds and
(Quantum) Spacetime**

Erlangen
FAU University Press
2016

Bibliografische Information der Deutschen Nationalbibliothek:
Die Deutsche Nationalbibliothek verzeichnet diese Publikation in der
Deutschen Nationalbibliografie; detaillierte bibliografische Daten sind
im Internet über <http://dnb.d-nb.de> abrufbar.

Das Werk, einschließlich seiner Teile, ist urheberrechtlich geschützt.
Die Rechte an allen Inhalten liegen bei ihren jeweiligen Autoren.
Sie sind nutzbar unter der Creative Commons Lizenz BY-NC-ND.

Der vollständige Inhalt des Buchs ist als PDF über den OPUS Server
der Friedrich-Alexander-Universität Erlangen-Nürnberg abrufbar:
<https://opus4.kobv.de/opus4-fau/home>

Verlag und Auslieferung:

FAU University Press, Universitätsstraße 4, 91054 Erlangen

Druck: docupoint GmbH

ISBN: 978-3-944057-90-3 (Druckausgabe)
eISBN: 978-3-944057-91-0 (Online-Ausgabe)
ISSN: 2196-7482

Simulating Triangulations: Graphs, Manifolds and (Quantum) Spacetime

Triangulierungen auf dem Computer:
Graphen, Mannigfaltigkeiten und (quantisierte) Raumzeiten

Der NATURWISSENSCHAFTLICHEN FAKULTÄT
der FRIEDRICH-ALEXANDER-UNIVERSITÄT ERLANGEN-NÜRNBERG

zur Erlangung des

DOKTORGRADES DR. RER. NAT.

vorgelegt von

BENEDIKT KRÜGER

aus Kaider, Bad Staffelstein

Als Dissertation genehmigt
von der Naturwissenschaftlichen Fakultät
der Friedrich-Alexander-Universität Erlangen-Nürnberg

Tag der mündlichen Prüfung: 19. Juli 2016
Vorsitzender des Promotionsorgans: Prof. Dr. Jörn Wilms
Gutachter: Prof. Dr. Klaus Mecke
PD Dr. Frank H. Lutz (TU Berlin)

Abstract

Triangulations, which can intuitvly be described as a tessellation of space into simplicial building blocks, are structures that arise in various different branches of physics: They can be used for describing complicated and curved objects in a discretized way, e.g., in foams, gels or porous media, or they can be used for discretizing curved boundaries for fluid simulations or dissipative systems. Interpreting triangulations of graphs makes it possible to use them as networks in statistical physics, e.g., as networks of spins or in biological physics as actin networks. Since one can find an analogue of the Einstein-Hilbert action on triangulations, they can even be used for formulating theories of quantum gravity.

Triangulations have also important application in mathematics: They are maximal planar graphs in the sense that one cannot insert an interior edge without violating the planarity of the graph, so each planar graph is the subgraph of a triangulation. This means that triangulations can be used for getting an insight into general planar graphs. Furthermore, they are the simplest possibility for discretizing topological manifolds, which make them to an important topic in discrete topology. Additionally, triangulations are often used as a tool for describing curved boundaries, e.g., for finite element methods or for evaluating measures from integral geometry.

Despite their wide occurrence in different branches of physics and mathematics, there are still some fundamental open questions about triangulations in general. It is a prior unknown how many triangulations there are for a given set of points or a given manifold. For manifolds it is even unknown for three and more dimensions whether there are exponentially many triangulations of a given manifold or more, which is equivalent to the physical question whether the entropy of triangulations scales linearly in the system size. This becomes important if one uses triangulations as model for quantum geometry using a path integral formalism, which is only well defined if there are only exponentially many triangulations. Another major unknown question is whether elementary steps called Pachner moves, which transform triangulations into each other and are used for computer simulations on triangulations, are ergodic.

Beside this fundamental issues about triangulations themselves, also



within their physical applications there are questions that are unfinishedly discussed in literature or have not been answered at all. E.g., the behavior of graph observables on triangulations is known only for the random topological triangulations on surfaces, and not for triangulations of point sets or any ensemble that can weight order or disorder in triangulations, and the spectrum of the discrete Laplace operator, which is important for transport or diffusion problems on graphs, has not been studied for triangulations at all. Within the usage of triangulations as model for spacetime it is not clear whether there is a meaningful continuum limit that can be identified with the usual and well-tested theory of general relativity.

Within this thesis we will answer some of these fundamental questions about triangulations, mainly using the numerical method of Markov chain Monte Carlo (MCMC) simulations. These simulations use a Markov chain to generate states according to a given probability distribution, e.g., the Boltzmann distribution as the famous Metropolis algorithm. For the applications in this thesis mainly flat histogram MCMC simulations as the Wang-Landau algorithm are used, which sample according to a probability distribution that is flat in energy space. Within Sec. 2.3.3 we develop an algorithm for approximately counting states of arbitrary systems that utilizes such flat histogram methods. Furthermore the dependence of the runtime of a Wang-Landau algorithm on the number of energy bins and the flatness criterion (which is a measure of the quality of a simulation) is calculated (see Eqs. (2.93) and (2.96)).

Considering embedded triangulations, integer lattices as underlying point sets are an important subclass, because in general triangulations are maximal planar graphs in the sense that no further (interior) edge can be inserted without violating planarity, and every planar graph can be realized with rational coordinates, which by scaling leads to integer coordinates. We calculate the entropy density of two-dimensional triangulations on quadratic integer lattices and on stripes with a fixed width, which radically improves previously analytical bounds (see Eq. (3.16)). For three-dimensional integer lattices of different geometries, where there are no analytical calculations at all, we find similar results for the entropy density (see Eq. (3.50)). We will show in Sec. 3.4 results of the interpretation of lattice triangulations as planar graphs: While within a random ensemble there is a scaling behavior similar to common random graph models in terms of the system size (compare Fig. 3.37), in a canonical ensemble, where the inverse temperature measures order and disorder in the triangulation, we find a crossover behavior between an ordered, large-world and a disordered, small-world behavior (see Figs. 3.50



and 3.54). Calculating the spectrum of the associated Laplacian matrix enables us to calculate the inverse participation ratio, which results in the conclusion that the localization on random lattice triangulations is on average higher than in similar random graph models (Fig. 3.43).

The developed approximate counting algorithm allows to inspect important properties of triangulations of manifolds, which play an important role in discrete topology. While from direct enumeration techniques the number of triangulations is only known for small genus and a small number of vertices, we can approximatively count triangulations with a far larger number of vertices (as depicted in Fig. 4.13). It is even possible to find asymptotics of for the number of triangulations or the entropy density in terms of the number of triangles and the genus of the considered surface, both for orientable and non-orientable surfaces (see Eqs. (4.18) and 4.19). For triangulations of the 3-sphere we are able to extract results about the numerical ergodicity of Pachner moves (see Fig. 4.24 and Eq. (4.33)), where we consider the entropy density as measure for the ergodicity in terms of the number of maximal simplices and the size of the allowed detour. Furthermore we are able to improve existing results of the entropy density in the limit of infinite system size (compare Eq. (4.34a)), and show that probably there are in fact only exponentially many triangulations of the 3-sphere.

Considering triangulations as a spacetime model in the setup of causal dynamical triangulations, using the Wang-Landau algorithm we are able to calculate the one-slice propagator and develop a transfer matrix approach in Sec. 5.3.5 to derive the limit of infinite number of time slices. Applying this method to $(2 + 1)$ -dimensional causal dynamical triangulations we show that the fine-tune transition used to obtain a possible continuum limit is a discontinuous phase transition (see Fig. 5.31), and that the continuous phase transition at a certain coupling constant found in literature does occur only in one of the two phases of the fine-tune transition (see in Fig. 5.36). We furthermore list conceptional problems of the (causal) dynamical triangulation approach.

As an outlook on other discrete space(-time) models that can be considered numerically we present in Sec. 6.1 how to define equidistance in finite projective geometries, and in Sec. 6.2 how to calculate spin foam amplitudes for small quantum numbers.





Kurzzusammenfassung

Triangulierungen, die anschaulich als eine Überdeckung des Raums mit simplizialen Grundbausteinen beschrieben werden können, spielen in vielen Bereichen der Physik eine wichtige Rolle: Man verwendet sie, um komplizierte und gekrümmte Objekte zu diskretisieren, zum Beispiel in Schäumen, Gelen und anderen porösen Materialien, weiterhin werden sie zur Beschreibung gekrümmter Ränder in Fluidsimulationen oder in dissipativen Systemen verwendet. Triangulierungen, oder genauer ihre Interpretation als Graph, können auch als Netzwerke in der statistischen Physik eingesetzt werden, beispielsweise als Netzwerke aus Spins oder in der biologischen Physik als Aktinnetzwerke. Da man innerhalb von Triangulierungen ein Analogon der Einstein-Hilbert-Wirkung finden kann, ist es möglich, mit ihrer Hilfe Quantengravitation zu betreiben.

Auch in der Mathematik gibt es wichtige Anwendungsgebiete von Triangulierungen: Sie sind maximale planare Graphen (das heißt, man kann keine inneren Kanten einfügen, ohne die Planarität des Graphen zu zerstören), somit ist jeder planare Graph ein Untergraph einer Triangulierung. Diese Eigenschaft kann man nutzen, um Einblicke in die Eigenschaften von allgemeinen planaren Graphen zu gewinnen. Weiterhin stellen Triangulierungen die einfachste Möglichkeit da, topologische Mannigfaltigkeiten zu diskretisieren, was sie zu einem wichtigen Werkzeug in der diskreten Topologie macht. Auch werden Triangulierungen häufig eingesetzt, um Randwertprobleme mit Krümmung zu beschreiben, beispielsweise in der Methode der finiten Elemente, oder um integralgeometrische Maße zu berechnen.

Obwohl Triangulierungen in den verschiedensten Bereichen der Physik und der Mathematik eine wichtige Rolle spielen, gibt es einige wichtige, offene Fragen über Triangulierungen an sich. Es ist nicht ohne weiteres möglich, die Zahl der Triangulierungen einer bestimmten Punktconfiguration oder einer gegebenen Mannigfaltigkeit zu bestimmen. Für Mannigfaltigkeiten in drei oder mehr Dimensionen ist zudem nicht einmal bekannt, ob zu einer gegebenen Mannigfaltigkeit exponentiell viele oder mehr Triangulierungen existieren, in die Sprache der Physik übersetzt heißt das, dass nicht bekannt ist, ob die Entropie der Triangulierungen linear oder stärker mit der Systemgröße wächst. Diese Frage ist von besonderer Bedeutung für den Einsatz



von Triangulierungen als quantengeometrisches Modell, der entsprechende Pfadintegralformalismus ist nämlich nur wohldefiniert, falls nur exponentiell viele Triangulierungen existieren. Eine weitere wichtige, offene Frage ist, ob die elementaren Pachnerschritte, die Triangulierungen ineinander überführen und vor allem in numerischen Simulationen verwendet werden, ergodisch sind.

Neben diesen fundamentalen Fragen über Triangulierungen an sich gibt es auch innerhalb ihrer physikalischen Anwendung Fragen, die in der bestehenden Literatur nur unzureichend oder gar nicht beantwortet worden. Beispielsweise wurden Graphobservablen nur auf zufälligen, topologischen Triangulierungen von Oberflächen untersucht, nicht aber für Triangulierungen von Punktmengen oder für Ensembles, die Ordnung oder Unordnung von Triangulierungen gewichten können, weiterhin wurde das Spektrum des diskreten Laplace-Operators, das für Transport- oder Diffusionsprobleme auf Graphen relevant ist, noch überhaupt nicht auf Triangulierungen betrachtet. Bei der Nutzung von Triangulierungen als Raumzeitmodell es ist noch nicht klar, ob ein sinnvoller Kontinuumsgrenzwert existiert, der mit der normalen und experimentell bestätigten allgemeinen Relativitätstheorie übereinstimmt.

In dieser Arbeit werden einige dieser fundamentalen, offenen Fragen über Triangulierungen beantwortet, hauptsächlich durch die Anwendung von Markowketten Monte-Carlo-Simulationen. Diese Simulationen verwenden eine Markowkette, um Zustände entsprechend einer gegebenen Wahrscheinlichkeitsverteilung zu erzeugen, z.B. entsprechend der Boltzmann-Verteilung wie im bekannten Metropolisalgorithmus. Für die Zwecke dieser Arbeit werden hauptsächlich solche Simulationen verwendet, die Zustände gleichverteilt in einem Energieraum erzeugen, wie z.B. der Wang-Landau Algorithmus. In Kap. 2.3.3 wird eine Methode zum näherungsweise Zählen von Zuständen in beliebigen Systemen entwickelt, die auf solchen Algorithmen basiert, die Zustände gleichverteilt im Energieraum erzeugen. Weiterhin wird die Abhängigkeit der Laufzeit des Wang-Landau Algorithmus von der Anzahl der verwendeten Energieklassen und des verwendeten Flachheitskriteriums (das ein Maß für die Güte einer Simulation ist) berechnet (vgl. Gl. (2.93) und (2.96)).

Betrachtet man eingebettete Triangulierungen, so sind Gitter mit ganzzahligen Koordinaten ein wichtiger Spezialfall, da Triangulierungen in dem Sinne maximale planare Graphen sind, dass keine weitere innere Kante eingefügt werden kann, ohne die Planarität zu verletzen. Weiterhin kann jeder planare Graph mit rationalen Koordinaten realisiert werden, die durch



eine Skalierung auf ganzzahlige Koordinaten abgebildet werden können. In dieser Arbeit wird die Entropiedichte von zweidimensionalen Triangulierungen von quadratischen und rechteckigen Gittern mit konstanter Breite berechnet (vgl. Gl. (3.50)), dieser Ergebnisse verbessern die bisher bekannten analytischen Schranken deutlich. Für dreidimensionale Triangulierungen von Gittern unterschiedlicher Form kann man ähnliche Ergebnisse erhalten (vgl. Gl. (3.50)), hier gibt es leider keinerlei analytische Schranken. In Kap. 3.4 werden Ergebnisse gezeigt, die aus der Interpretation von Triangulierungen als planare Graphen entstehen: Während für zufällige Triangulierungen in Abhängigkeit der Systemgröße ein Skalenverhalten beobachtbar ist, dass den üblichen Zufallsgraphen entspricht (vgl. Abb. 3.37), findet man in einem kanonischen Ensemble, in dem die inverse Temperatur Ordnung und Unordnung der Triangulierung misst, einen Übergang zwischen einem geordneten, Große-Welt-Verhalten zu einem ungeordneten, Kleine-Welt-Verhalten (vgl. Abb. 3.50 und 3.54). Die Berechnung des Spektrums der zugehörigen Laplace-Matrizen ermöglicht es, die inverse Beteiligungsquote zu berechnen, aus der geschlossen werden kann, dass die Lokalisierung auf zufälligen Gittertriangulierungen im Durchschnitt höher als in vergleichbaren Zufallsgraphen ist (Abb. 3.43).

Die entwickelten Algorithmen zum näherungsweise Zählen erlauben es, wichtige Eigenschaften von Triangulierungen von Mannigfaltigkeiten zu untersuchen, die eine wichtige Rolle in der diskreten Topologie einnehmen. Während durch direktes Abzählen die Anzahl der Triangulierungen nur für einen kleinen Genus und eine kleine Anzahl von Vertices bekannt ist, kann durch das näherungsweise Zählen die Anzahl der Triangulierungen für eine viel größere Zahl an Vertices berechnet werden (wie in Abb. 4.13 dargestellt ist). Es ist sogar möglich, die Asymptotik der Zahl der Triangulierungen bzw. der Entropiedichte von orientierbaren und nicht-orientierbaren Oberflächen für unendlich viele Simplices in Abhängigkeit vom Genus zu bestimmen (vgl. Gl. 4.18 und 4.19). Für Triangulierungen der 3-Sphäre können mit diesem Algorithmus Schlussfolgerungen über die Ergodizität der Pachnerschritte gezogen werden, indem bei einer gewissen, festen Anzahl an maximalen Simplices die Abweichung der Entropiedichte in Abhängigkeit des erlaubten Umwegs als Maß für die Ergodizität betrachtet wird (vgl. Abb. 4.24 und Gl. (4.33)). Weiterhin können in diesem Fall bereits bekannte Ergebnisse über die Entropiedichte im Grenzwert unendlich großer Systeme verbessert werden (vgl. Abb. 4.34a), weiterhin wird gezeigt, dass es sehr wahrscheinlich nur exponentiell viele Triangulierungen der 3-Sphäre gibt.



Durch Anwendung von Wang-Landau Simulationen auf kausale dynamische Triangulierungen, die Triangulierungen als Raumzeitmodell interpretieren, kann der Ein-Schnitt-Propagator berechnet werden. Zusammen mit der Entwicklung eines Transfermatrix-Ansatzes in Kap. 5.3.5 erlaubt dies, den Grenzwert unendlich vieler zeitlicher Schnitte zu berechnen. Durch Anwendung auf $(2 + 1)$ -dimensionale kausale Triangulierungen kann gezeigt werden, dass der Feinabstimmungs-Phasenübergang, der genutzt wird, um den möglichen Kontinuums Grenzwert zu erhalten, ein diskontinuierlicher Phasenübergang ist (vgl. Abb. 5.31), und dass der bereits in der Literatur bei einer bestimmten Kopplungskonstante gefundene kontinuierliche Phasenübergang nur in einer der beiden Phasen des Feinabstimmungs-Phasenübergang auftritt (vgl. Abb. 5.36). Weiterhin werden einige konzeptionelle Probleme von (kausalen) dynamischen Triangulierungen herausgestellt.

Als Ausblick werden weitere diskrete Raumzeitmodelle vorgestellt, die numerischen Simulationen zugänglich sind. In Kap. 6.1 wird dargestellt, wie man Äquidistanz in endlichen projektiven Geometrien definieren kann, in Kap. 6.2 wird präsentiert, wie man Spinschaumamplituden für kleine Quantenzahlen berechnen kann.



Contents

Abstract	iii
Kurzzusammenfassung	vii
Contents	xi
1 Introduction	1
2 Markov chain Monte Carlo simulations	11
2.1 Statistical physics and phase transitions	13
2.1.1 Expectation values	13
2.1.2 Microcanonical ensemble	14
2.1.3 Thermodynamic equilibrium	15
2.1.4 Canonical ensemble	17
2.1.5 Grandcanonical ensemble	19
2.1.6 Phase transitions	20
2.1.7 Ising model	25
2.2 Markov chain Monte Carlo simulations	31
2.2.1 The Metropolis MCMC algorithm	31
2.2.2 The Wang-Landau algorithm	36
2.2.3 Other MCMC algorithms	41
2.2.4 Error analysis of Monte Carlo simulations	49
2.2.5 Phase transitions in Monte Carlo simulations	55
2.3 Details about Wang-Landau simulations	61
2.3.1 Optimal choice of parameters	61
2.3.2 Dependence of the runtime on bin-number and flatness criterion	67
2.3.3 Approximative counting with multicanonical Monte Carlo simulations	82
3 Embedded triangulations	87
3.1 Embedded triangulations and flips	90
3.1.1 Simplex, complex and triangulation	90



3.1.2	Special triangulations	93
3.1.3	Flips between triangulations	97
3.2	Entropy of two-dimensional unimodular lattice triangulations	109
3.2.1	Two-dimensional Lattice Triangulations	109
3.2.2	Approximate enumeration of triangulations	112
3.2.3	Results	116
3.2.4	Discussion	118
3.3	Counting three-dimensional lattice triangulations	120
3.3.1	Small three-dimensional lattice triangulations	121
3.3.2	Constructing three-dimensional lattice triangulations	129
3.3.3	A lower bound for the entropy density of three-dimensional lattice triangulations	130
3.3.4	Choosing the energy functional	132
3.3.5	Density of states and state space structure	136
3.3.6	Entropy density of three-dimensional lattice triangu- lations	141
3.4	Two-dimensional unimodular lattice triangulations as graphs	144
3.4.1	(Spectral) graph theory	147
3.4.2	Triangulations as random graphs	151
3.4.3	Analytical solution	153
3.4.4	Random triangulations	157
3.4.5	Microcanonical triangulations	174
3.4.6	Canonical triangulations	181
3.4.6.1	Ising critical temperature	188
3.4.7	Conclusion	191
4	Topological triangulations	195
4.1	Topological triangulations and Pachner moves	199
4.1.1	Abstract simplicial complexes and triangulations	199
4.1.2	Alexander and Pachner moves	214
4.1.3	Number of simplices in triangulations and their change due to Pachner moves	220
4.1.4	Selection probability of flips	227
4.2	Counting triangulations of two-dimensional manifolds	233
4.2.1	Setup and methods	235
4.2.2	Approximative counting of small surface triangulations	238
4.2.3	Asymptotics of the entropy density for $m \rightarrow \infty$	243
4.2.4	Conclusion and outlook	245



4.3	Ergodicity and extensivity of three-dimensional sphere triangulations	248
4.3.1	Calculating entropy density with the Metropolis algorithm	250
4.3.2	Calculations of the entropy density using multicanonical methods	254
4.3.3	Numerical ergodicity	259
4.3.4	Scaling of the entropy density	261
4.3.5	Conclusion	262
5	Triangulations as fluctuating space-(times)	265
5.1	General relativity without coordinates - The Regge formalism	270
5.1.1	Curvature assignment in simplicial complexes	270
5.1.2	The Riemann curvature tensor	277
5.1.3	Discrete Einstein equations	279
5.2	Fluctuating geometry - Dynamical triangulations	284
5.2.1	Definition of the dynamical triangulation model	284
5.2.2	The action of dynamical triangulations	287
5.2.3	Analytical solution for dynamical triangulations in two dimensions	289
5.2.4	Results of the dynamical triangulation approach	293
5.2.5	Problems of the dynamical triangulation approach	296
5.2.6	Multicanonical algorithms for dynamical triangulations	300
5.3	Fluctuating spacetimes - Causal Dynamical Triangulations	303
5.3.1	Causal dynamical triangulation setup	304
5.3.2	Important results in causal dynamical triangulations	307
5.3.3	Constructing causal triangulations - small triangulations and flips	310
5.3.4	The action of causal dynamical triangulations	316
5.3.5	Grandcanonical one-slice propagator approach to CDT	343
5.3.6	Numerical results of $(2 + 1)$ -dimensional CDT	356
5.3.7	Problems of the causal dynamical triangulation approach	384
6	Concluding remarks	387
6.1	Outlook: Equidistance in finite projective geometries through biquadrics	393
6.1.1	Affine and projective geometries	395
6.1.2	Quadrics and Biquadrics	399
6.1.3	Open questions and research directions	404



6.2	Outlook: Efficient calculations of $3nj$ -symbols for spin foam amplitudes	405
6.2.1	Spin foam models and amplitudes	407
6.2.2	Clebbsch-Gordan coefficients and $3nj$ -symbols	410
6.2.3	Calculation time of $3nj$ -symbols	412
6.2.4	Small angular momentum vertex amplitudes in the EPRL-model	415
6.3	Software developed within this thesis	418
6.3.1	The generic MCMC library <code>mocasinn</code> s	418
6.3.2	Triangulations on the computer with <code>mocatrind</code>	429
	Bibliography	433
	Acknowledgments	467
	Danksagung	469



1 Introduction

Triangulations are objects that occur in various different branches of physics. They are maximal planar graphs in the sense that no interior edge can be inserted without violating planarity. This means that every planar graph is a subgraph of a triangulation, so understanding the graph and spectral properties of triangulations can lead to more insight into planar graphs [47, 52, 259, 372, 433]. Triangulations are often used to discretize and describe curved boundaries, e.g., in finite element methods which solve partial differential equations on the computer. Triangulations can also be used for calculating several additive measures from integral geometry, the so-called Minkowski tensors [362], which can be used for characterizing various experimental data ranging from the structure of the atomic nucleus [363] to telescope images of astronomical objects [192]. Due to their inherent description of curvature they are predestined for an usage in one of the most famous physical theories incorporating the concept of curvature, namely general relativity. It was shown by Tullio Regge in 1961 [338] that triangulations can in fact describe general relativity without coordinates, which is often used for numerical classical general relativity [187]. Since triangulations are also discrete, they naturally can be used for formulating theories of quantum gravity, e.g., in the Ponzano-Regge model [330], simplicial gravity [204] and in (causal) dynamical triangulations [38, 280].

Triangulations are also an important subject of study in mathematics. There is a strong relation between triangulations and combinatorics, e.g., the number of triangulations of a convex polygon with n edges matches the number of binary trees with $n - 2$ nodes [132, Thm. 1.1.3], and a slight generalization of triangulations can also be used for examining linear optimization problems [132, Sec. 2.1]. Furthermore, triangulations are the way mainly used for describing manifolds in discrete topology, because they allow for a simple calculation of topological invariants.

Naturally the question arises why triangulations are so commonly used in the described contexts in mathematics and physics. In fact there are several reasons. The first is that triangulations are a more clever way for representing smooth structures on a digital computer (as the one you probably read this thesis on), where one has to use some discretization method to map the



continuous degrees of freedom to a countable set of parameter, which then can be stored in the finite memory of the computer. For this one usually uses lattices, which are a regular and repeating arrangement of points in \mathbb{R}^d , e.g., the points of \mathbb{Z}^d . Famous examples of such approximative discretizations are finite elements methods, which are used for numerically solving partial differential equations, or every image taken with a pixel detector, where smooth structures are mapped to discrete count numbers of single pixels (e.g., in a CCD or a particle detector). The usual discretization method using lattices reaches its limits if the underlying space to be discretized is not flat, but somehow curved. This happens e.g., if there are complicated boundary conditions in finite element methods (for modeling the flow through a complicated object), or if a curved structure should be described itself. To make the latter case clear, consider a ball B embedded into the \mathbb{R}^3 which is described by

$$B := \{x \in \mathbb{R}^3 \mid x_1^2 + x_2^2 + x_3^2 \leq 1\}. \quad (1.1)$$

If one uses a discretization of the whole space into cubes with constant edge length a , and calculates the volume by summing the volumes of the cubes that are completely contained in the ball B , then the discretized volume converges towards the actual value $4\pi/3$. But if one approximates the area of the boundary $A(\partial B) = 4\pi$ with the boundary area of the cubes, one gets

$$A_{\text{discretized}}(\partial B) = 6\pi,$$

since for every one of the six normal directions the boundary areas of the cubes approximates the area π of a circle. Using a triangulation of the surface, as depicted in Fig. 1.1, the surface area has the correct asymptotics.

In principle there are several other methods (e.g., quadrangulations that use quadrangles or polygons with more edges), but triangulation have the advantage that the geometry is determined solely by the edge lengths of the triangulation, and one needs no information about angles between edges. Furthermore, they allow for an easy calculation of topological invariants, e.g., the Euler characteristic χ . For an arbitrary surface S that is given implicitly, the Euler characteristic has to be calculated using the Gauss-Bonnet theorem as

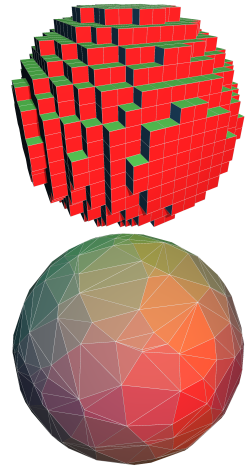
$$\chi = \frac{1}{2\pi} \int_S K dA,$$

where K is the Gaussian curvature and dA is an area element. If one can find a triangulation of the surface, one can calculate the Euler characteristic



Figure 1.1: Discretizing surfaces with lattices and triangulations.

(Top) Discretization of the ball Eq. (1.1) using a regular build from cubes. For decreasing edge length, the volume of the cubes converges towards the volume of the ball, but the surface converges towards 6π and not towards the actual value of 4π . (Bottom) Discretization of the ball Eq. (1.1) using a (Delaunay) triangulation of randomly distributed points on the sphere, both the volume and the surface converge towards the actual value. In both cases the color of a face encodes the direction of its normal vector.



using the much simpler equation

$$\chi = N_2 - N_1 + N_0,$$

where N_2 is the number of triangles, N_1 is the number of edges and N_0 is the number of vertices. Using triangulations of manifolds one can also address very fundamental questions of discrete topology, e.g., whether there is an exponential bound of the number of different (non-isomorphic) discretizations of a manifold in terms of the number of discrete objects used.

From a geometric point of view, triangulations can be defined as a tessellation of space with triangles or higher-dimensional simplices, alternatively within a graph theoretic approach triangulations are (maximal) planar graphs where each face is triangular (or their higher dimensional analogs). Mathematically there are different structures that are denoted as triangulations: One can consider triangulations of point sets embedded into an \mathbb{R}^d , or one can neglect the actual coordinates of the points and consider only the topological degrees of freedom for triangulations of manifolds. There are several methods for constructing triangulations, for the standard application in finite element methods one can use the cutting cube method [361] or the marching algorithm [213] for calculating triangulations of a surface. Due to their discreteness triangulations are a good candidate for numerical examinations on a computer. Within this thesis, we apply (flat histogram) Markov chain Monte Carlo simulations on the different types of triangulations. These algorithm are designed to calculate ensemble averages in statistical physics, but also allow to count the number of states in certain systems.



We do not go into greater detail about existing literature, application or importance of the considered systems in this part of the thesis. For those informations we refer to the respective introductory parts of the single chapters. The thesis is structured as following:

Markov chain Monte Carlo simulations The second chapter describes the numerical method of Markov chain Monte Carlo simulations, which are the main method for the calculations done throughout this thesis. In this chapter, we give first the necessary basic notations of statistical physics, furthermore we introduce phase transitions and the Ising model. Afterwards we present the general ideas of Markov chain Monte Carlo simulations before describing certain algorithms in detail, especially the Metropolis algorithm, which is the MCMC developed first and most accessible to the non-experts, and the Wang-Landau algorithm, which allows to calculate the density of states of a system and can be used for an approximate counting the number of states of arbitrary systems. We conclude by presenting our results about the Wang-Landau method in general, the most important results are the analytical approximation of the runtime of the algorithm in terms of the number of bins of the density of states in Eqs. (2.93) and (2.96), and the development of an approximative state counting algorithm for systems without any a prior information in Sec. 2.3.3.

Entropy and graph properties of lattice triangulations The third chapter is concerned with triangulations of point sets embedded into the Euclidean space \mathbb{R}^d , especially lattice triangulations in \mathbb{R}^2 and \mathbb{R}^3 . We start with a description of the definition of embedded triangulations in general, including some special triangulations used in mathematics and physics and the elementary steps that will be used within the MCMC simulations of such triangulations. Then we use the Wang-Landau algorithm for approximating the number of unimodular triangulations of a two-dimensional integer lattice, where we can improve analytical bounds of the entropy density in Eq. (3.16). The same methods are then applied to triangulations of three-dimensional integer lattices, after we examined triangulations of the three-dimensional unitcube to give the reader a more intuitive look on this higher dimensional triangulations.

A major part of this section is the interpretation of two-dimensional lattice triangulations as random graph models. In Fig. 1.2 a small random triangulation is displayed, and one can see that the inherent random structure can lead to shortcuts in the graph and to large clusters, which is a



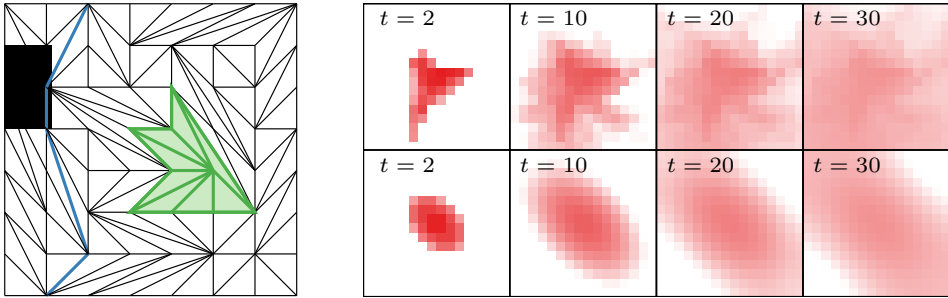


Figure 1.2: Random lattice triangulations as graphs.

(Left) Random triangulation on a 8×8 lattice. One can see that compared to an ordered lattice there shortcuts for traversing the lattice (blue path), and vertices with a high number of neighboring vertices (green), which are denoted as clusters. (Right) Random walk probability density (color code) evolved using the discrete Laplacian after a certain number of time steps for a random (top) and an ordered (bottom) 16×16 lattice triangulation. The initial condition is to set $p = 1$ on one center site. The shortcuts and the clusters lead to a faster spread for the random triangulation, due to the randomness the spread is also inhomogeneous.

key feature of real world networks. Furthermore, one can see that random triangulations exhibit interesting transport and diffusion properties.

Comparing random triangulations with usual random graph models as the Erdős-Rényi, the Newman-Watts and the Barabási-Albert random graph we find in Fig. 3.37 that graph observables like the clustering coefficient or the average shortest path length show a similar behavior in terms of the system size. Defining an energy that measures order and disorder of the triangulation, we find a transition behavior in the inverse temperature between an ordered, large-world behavior and an unordered, small-world behavior in Figs. 3.50 and 3.54. As an application of the calculated spectrum of the Laplacian matrix we calculate the inverse participation ratio of random and canonical triangulations, and show in Fig. 3.43 that this measure of localization is on average higher than in the comparable random graphs.

Entropy and ergodicity of topological triangulations The fourth chapter considers triangulations of topological manifolds, where in contrast to embedded triangulations only the topological degrees of freedom are taken into account, and not the actual coordinates of the vertices. Examples for topological triangulations of a two-dimensional torus can be found in Fig. 1.3 for various number of simplices. We first give the definition of topological manifolds, their triangulations as well as Alexander and Pachner moves,



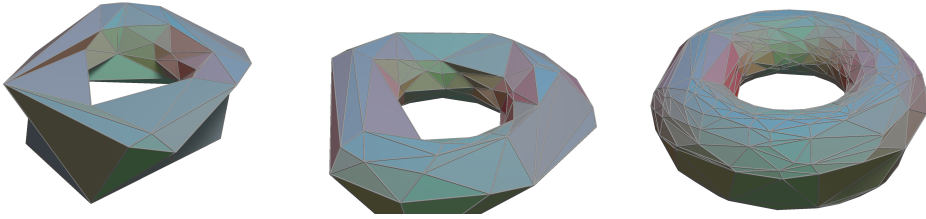


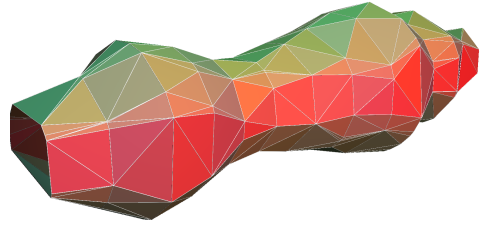
Figure 1.3: Topological triangulations of the torus surface with 50 (left), 100 (mid) and 500 (right) vertices, which were chosen randomly distributed on a torus surface. The color of the faces corresponds to their normal direction.

which can be used for transforming triangulations of the same manifold into each other and are the elementary steps used in the Markov chain simulations. Furthermore we present some interesting results and open problems from the mathematical literature.

In the following, we are interested in answering to main questions about manifold triangulations: Are they (computational) ergodic, which means whether it is possible to reach every triangulation of a given manifold with a finite number of Pachner moves, or whether there is restriction due to the limited system sizes we can consider on a computer, and are there exponentially many triangulations as for lattice triangulations (or perhaps more)? Both questions are important for the consideration of triangulations as spacetime models in the following chapter. For two-dimensional triangulations of surfaces, we consider both the limit of small and of large triangulations. Where in the former case exact results are only available for triangulations with very few vertices [379], we are able to find approximate numbers for far larger triangulations in Fig. 4.13. In the latter case we calculate in (4.19) next-to-leading order corrections for the entropy density that depend on the genus of the underlying (non-)oriented surface. We find that there is a qualitative change of the behavior for different genus in the orientable case: While for spheres the entropy density increases for increasing lattice size, it is approximately constant for a torus and decreases for surfaces with higher genus (compare Fig. 4.14). For triangulations of the 3-sphere we are able to give the deviation of the entropy density from its limiting value in terms of the size of the triangulation and the allowed range of Pachner moves in Eq. (4.33), which can be interpreted as a quantitative measure for the violation of ergodicity, and to verify and improve previous results about the scaling of the entropy density for 3-spheres in (4.34a).



Figure 1.4: Causal triangulation of $\mathbb{S} \times \mathcal{I}$ in $(1+1)$ dimensions. The time-direction goes from left to the right. Note that this is only a symbol picture not originating from an actual simulation.



(Causal) dynamical triangulations The fifth chapter describes the usage of triangulations as spacetime models. We introduce first the so-called Regge formalism, where one is able to find a discrete analogue of the Einstein equations using a discretization of space in terms of triangulations. This Regge formalism is the foundation for two models for quantum spacetime using triangulations, which we will consider afterwards. The first approach is denoted as dynamical triangulations and uses a path integral-like sum over all triangulations of a given manifold weighted with the Regge action, the second approach is the causal enhancement of this theory, where only triangulations that admit a causal structure contribute to the path integral. In contrast to other quantum theories based on Regge calculus, in (causal) dynamical triangulations the edge lengths are fixed, and the triangulations themselves are used as dynamical variables (a symbol picture of a causal triangulation in $(1+1)$ dimensions can be found in Fig. 1.4). For both cases we give a short literature review and list some major results as well as problems that still have to be addressed by these theories. We furthermore give a detailed derivation of the action of (causal) dynamical triangulations for two, three and four dimensions. Using the Wang-Landau algorithm we calculate the density of states for one time slice, which can then be used in a transfer matrix approach to calculate expectation values for an arbitrary number of time slices, and even to consider the limit of infinite time slices. For $(2+1)$ -dimensional triangulations we present in Fig. 5.31 that the fine-tuning phase transition is discontinuous (one has to choose the coupling constants so that the system is on the coexistence line of this transition in order to be able to get a continuum limit). We furthermore confirm that on the phase transition line there is a critical point where there is a continuous phase transition (which is needed for finding a discretization-scale invariant continuum limit), but we show that this phase transition does occur only in one of the two coexisting phases in Fig. 5.36.

Other discrete spacetime models The last chapter summarizes the main results of this thesis and gives an outlook about possible new research



directions that arise from the methods developed or the results obtained in this thesis. Furthermore we give an extended outlook about two alternative approaches that were tested during this thesis. The first is the usage of finite projective geometries as the underlying geometry of a physical theory, which requires the notion of distance or even weaker the notion of equidistance, which can be done with introducing a certain combination of two quadrics denoted as biquadric. The second are numerical calculations within the EPRL spin foam model for small quantum numbers. Both approaches were examined by students that were supervised by me during there thesis. The last part of the chapter gives a short overview about the software that was developed for this thesis.

General remarks Considering the outline of the thesis one can see that a large part of this thesis is concerned with mathematical foundations and applications of triangulations. Additionally, also in the physical part about triangulations as possible models for quantum gravity, experimental data is rare due to the high energy scales or small length scales where deviations from general relativity or quantum field theory are expected, scales that are not accessible by particle accelerators, also in the near futures. There are some proposals for experiments from phenomenological quantum gravity [219], and some very recent results from the BICEPS2 telescope [118], both are based on astronomical observations. This means that this thesis has almost no contact to present experiments, which can be seen already from the bibliography, where there are almost no experiments cited. The thesis on hand can be seen rather as *experimental mathematics*, because simulations that are inspired from physics are used for finding not rigorous proofs, but probable results or hints that can be very valuable for mathematicians to proof certain theorems.

Parts of this thesis have been published in the following papers (the numbers refer to their place in the bibliography)

[253] J. F. Knauf, B. Krüger, and K. Mecke, *Entropy of unimodular lattice triangulations*, EPL **109**(4), 40011 (2015)

[265] B. Krüger, E. M. Schmidt, and K. Mecke, *Unimodular lattice triangulations as small-world and scale-free random graphs*, New J. Phys. **17**(2), 023013 (2015)

[266] ———, *Sepectral properties of unimodular lattice triangulations*, J. Stat. Phys. **163**(3), 514–543 (2016)



[264] B. Krüger and K. Mecke, *Genus dependence of the number of (non-)orientable surface triangulations*, Phys. Rev. D **93**, 085018 (2016)

where Sec. 3.2 is based on Ref. [253], Sec. 3.4 is based on Refs. [265, 266], and Sec. 4.2 is based on Ref. [264]. In the respective sections the respective contributions to the numerical and analytical results as well as the text is stated in detail. Furthermore, there are several short term project reports and theses of students that were (co)supervised by me during my PhD-thesis

- [10] N. Alex, *Quadriken in endlichen projektiven Ebenen*, (2012), bachelor's thesis
- [62] W. Barfuss, *Quadratics in finite projective planes*, (2012), short term research project
- [94] W. Billenstein, *Monte Carlo simulations of the Ising model on triangulations*, (2013), bachelor's thesis
- [144] M. Düll, *Effiziente Berechnung von Wigner 3nj-Symbolen*, (2013), short term research project
- [145] ———, *Numerische Berechnung von Vertex-Amplituden im EPRL-Modell*, (2013), bachelor's thesis
- [271] ———, *Biquadric fields: Equipping finite projective spaces with metric structure*, (2014), master's thesis
- [360] E. M. Schmidt, *Spectrum of the discrete Laplace operator on two-dimensional lattice triangulations*, (2013), short term research project
- [411] T. Wasserka, *Critical phenomena of the Ising model on triangulations*, (2016), master's thesis
- [413] J. Wechs, *Lattice Laplacian on triangulations*, (2013), short term research project
- [425] F. Winterhalter, *Monte-Carlo-Simulationen mit Quadriken in endlichen projektiven Ebenen*, (2013), bachelor's thesis

where the number again corresponds to their place in the bibliography, and where the data of Ref. [360] is used in Sec. 3.4, results of Refs. [10, 271] are used in Sec. 6.1, and data and results of Refs. [144, 145] are used in Sec. 6.2. In all cases the exact contribution of the students is mentioned in the introductory parts of the respective sections.



1. Introduction

The pictures within the footer show some of the 852 triangulations of the 4×3 integer grid, so that there is a different triangulation on every page, and so that the triangulations on neighboring pages are connected by only one diagonal edge flip of the dashed edge. As an exercise, the interested reader can construct the remaining triangulations that are not displayed.



2 Markov chain Monte Carlo simulations

Markov chain Monte Carlo (MCMC) simulation are numerical approximation methods for calculating expectation values in statistical physics, or in general methods for evaluation high-dimensional integrals. The basic principle is to construct an ordered set of states which are connected by some elementary moves so that the probability to find a certain state (or in general a supporting point) in the Markov chain equals a given probability

MCMC methods are important in various branches of physics, especially in statistical and solid state physics [85, 269, 315]. Such methods are not restricted to physics, but are an important tool for many other branches of science: They are used to integrate over the probability distribution occurring in Bayesian statistics [185, 186, 384] (see [342, 348] for historical reviews) and therewith are an important tool in economics, political and social sciences as well as for medical science and psychology, where Bayesian statistics is often used. MCMC methods are also used directly in biology and medicine to understand e.g. the behavior of biological objects or the transport of drugs (see [298] for a collection of various applications in biology and medicine). Computational linguistic uses (mainly simple sampling) Monte Carlo results, too, e.g. for automatic language identification [332], comparing different languages for common roots [244] and for comparing the language usage of different social and ethnic groups [311]. Optimization problems can be solved using a special MCMC method called simulated annealing [250].

For all these problems there are various types of Monte-Carlo simulations available: The first invented method, which is also the commonly used Monte-Carlo simulations, is the *Metropolis(-Hasting) algorithm* sampling the Boltzmann distribution [214, 291]. Optimization problems are often used with a special Metropolis simulation called *simulated annealing*, where basically the temperature of the system is slowly decreased to find a ground state in the energy landscape [250]. A parallelization of the Metropolis algorithm calculation various inverse temperatures at once and allowing temperature interchanges is known as *Parallel Tempering* or



Replica Exchange Monte Carlo [223,382], which overcomes the problem with complicated energy landscapes that can occur in Metropolis simulations, but is known to have problems with first order phase transitions and large free energy barriers. *Multicanonical simulations* [84, 88] do not use the Boltzmann factor as weights for the certain states, but other more feasible weights. Concretizations are flat histogram methods like *Entropic sampling* [274], the *Wang-Landau algorithm* [406,407] and the *optimal ensemble sampling* [392,393] calculating the density of states, which is basically the number of states with given energy, using iterative approaches. Another method for determining the density of states of a system is *Transition Matrix Monte Carlo* [408]. For many MCMC algorithms there are *rejection-free* (also denoted as *continuous time* or *N-fold way*) versions [99,364], which do not reject steps but calculate the average time the system would stay in the state, which is the average number of rejected steps before the actual step will be accepted.

In this chapter we present first the basic notions of statistical physics, including phase transitions and the Ising model, which is commonly used for testing new MCMC algorithms. Afterwards we give an introduction into various types of MCMC algorithms, with a special emphasis on the Wang-Landau sampling, which is commonly used throughout this thesis. In the last part our results about MCMC algorithms in general are presented: We perform a numerical study to find optimal parameters of the Wang-Landau algorithm (see Fig. 2.14), in Eqs. (2.92) and (2.96) we present analytical approximations of the runtime of a Wang-Landau simulation in terms of the flatness criterion and the number of bins, which fit well with numerical results presented in Figs. 2.15 and 2.16, and we present an algorithm for counting the number of states of arbitrary systems using the extended energy function (2.98).



2.1 Statistical physics and phase transitions

For describing systems that consist of a huge number of similar, interacting objects, the usual methods of classical Lagrangian or Hamiltonian mechanics does not help. Due to the large number of degrees of freedom, on the one hand it is not possible to determine the initial state of the system, on the other hand integrating the equations of motions is practically impossible. However, it is possible to calculate average macroscopic quantities using methods of statistical physics.

In this section we will introduce the basic notions of statistical physics that we need in the course of this thesis, especially for introducing Markov chain Monte Carlo simulations. The considerations will be restricted to discretized systems, but can be generalized for continuous systems. In the latter case, instead of discrete sums one has to perform the integrals over small shells and add some factors for regularizing the phase space volume, which we will omit. Conceptionally we follow Ref. [317], but the considerations can be found in almost every other textbook about statistical physics. As an abbreviation we write $\int_{\Omega} d\omega$, which equals $\sum_{\omega \in \Omega}$ in the discrete and $\int_{\Omega} d\omega$ in the continuous case. Although we consider only discrete systems, we assume in the following that the considered systems are large enough to approximately make use of derivatives.

Consider now an arbitrary discrete system, e.g. a chain of N interacting spins. We denote by ω the *microstate* of the system, which can be the set of generalized coordinates and momenta in a Hamiltonian formulation, or some other configuration variables. So a microstate ω can be identified with a point in the phase space Ω . In our example $\omega \in \Omega = \{-1, 1\}^N$, so a state consists of all orientations of the spins, and Ω denotes the set of all possible states ω the system can have, so Ω is the whole phase space of the system. Furthermore, we denote by $H : \Omega \rightarrow \mathbb{R}$ the Hamilton function of the system, and by a *macrostate* of energy E all states with $H(\omega) = E$.

2.1.1 Expectation values

As the next step we calculate the average value of an observable $A(\omega)$ that depends on the microstate, therefor we follow Ref. [317, Sec. 1.2.1 and 1.2.2]. For every time t the system is in a certain microstate $\omega(t)$. Suppose that the system fluctuates so fast that we can in fact measure only the time average of the observable

$$\langle A \rangle_{t_0}(t) = \frac{1}{t} \int_{t_0}^{t_0+t} A(\omega(t')) dt', \quad (2.1)$$



where $\omega_0 = \omega(t_0)$ is the microstate of the system at the beginning of the measurement (initial conditions). In general the value of $\langle A \rangle_{t_0}(t)$ does depend on $\omega(t_0)$ for finite t , but we stipulate the limit

$$\langle A \rangle := \lim_{t \rightarrow \infty} \langle A \rangle_{t_0}(t) \quad (2.2)$$

exists and is independent of the initial conditions.

Now denote by $\rho(\omega, t_0, t)$ the (normalized) density distribution of the system, which is the probability to find the system in state ω between time t_0 and $t_0 + t$ in a discrete system¹. Using the density distribution ρ , the time average (2.1) can be formulated as

$$\langle A \rangle_{t_0}(t) = \int d\omega \rho(\omega, t_0, t) A(\omega).$$

As for expectation values of observables, we also assume that $\rho(\omega) := \lim_{t \rightarrow \infty} \rho(\omega, t_0, t)$ is independent of the initial conditions. So we take the limit $t \rightarrow \infty$ and get

$$\langle A \rangle = \lim_{t \rightarrow \infty} \langle A \rangle_{t_0}(t) = \lim_{t \rightarrow \infty} \int d\omega \rho(\omega, t_0, t) A(\omega).$$

Now we postulate that the limit and the integral commute (this is denoted as ergodic hypothesis), and get

$$\langle A \rangle = \int d\omega \rho(\omega) A(\omega), \quad (2.3)$$

which is the average of the observable A . This induces that we can replace the (infinite) time average (2.2) of an observable with the phase space or ensemble average (2.3), which is sometimes also denoted as ergodic hypothesis.

What is left is to determine the density distribution $\rho(\omega)$ of the system. This depends on the type of interaction of the system with the environment.

2.1.2 Microcanonical ensemble

For the presentation of this section we follow Ref. [317, Sec. 1.2.4]. Consider first a system that is completely isolated, so that neither particles nor energy can be transferred between system and environment. So if H is the Hamilton

¹ For continuous system, the density distribution is defined so that $\rho(\omega, t_0, t)d\omega$ is the probability to find a state in the phase space volume $d\omega$



function of the system and $H(\omega)$ is the energy of microstate ω , we have the constraint $H(\omega) = E$ in a discrete system².

We now have to determine the value of the density distribution $\rho(\mathbf{q}, \mathbf{p})$. The only reasonable choice is that the density is constant for every allowed microstate (*equal a priori probability postulate*, which is equivalent with the Gibbs entropy being maximal), so

$$\rho(\omega) = \rho_0 \delta(H(\omega), E) := \begin{cases} \rho_0 & H(\omega) = E \\ 0 & H(\omega) \neq E \end{cases}.$$

Because ρ is a normalized probability distribution, one gets

$$\begin{aligned} \int d\omega \rho_0 \delta(H(\omega), E) &\stackrel{!}{=} 1 \\ \Rightarrow \rho_0^{-1} &= \int d\omega \delta(H(\omega), E) =: g(E) \end{aligned} \quad (2.4)$$

where $g(E)$ is the density of states (DOS), which is the number of states with energy E . The logarithm

$$S(E) := \log g(E) \quad (2.5)$$

of the density of states is denoted as *microcanonical entropy* and is the thermodynamic potential of the microcanonical ensemble.

So the expectation value of an observable can be calculated using Eq. (2.3) as

$$\langle A \rangle(E) = \frac{\int d\omega A(\omega) \delta(H(\omega), E)}{\int d\omega \delta(H(\omega), E)} = \frac{1}{g(E)} \int d\omega A(\omega) \delta(H(\omega), E) \quad (2.6)$$

in the microcanonical ensemble.

2.1.3 Thermodynamic equilibrium

In this section some important properties of the microcanonical entropy $S(E) = \log g(E)$ are derived by considering two systems that are in thermodynamic equilibrium, following closely Ref. [317, Sec. 1.3.1, 1.3.2 and 1.3.4]. Consider a microcanonical system $\Omega = \Omega_1 \times \Omega_2$ that is composed of two

² In continuous systems one must replace this constraint with $E < H(\omega) < E + \delta E$ for a small δE that has to be introduced because it is not possible to suppress all energy transfer between system and environment. Additionally all distributions $\delta(H(\omega), E)$ in the following integrals have to be replaced with the step functions $\Theta(H(\omega) - E)\Theta(E + \delta E - H(\omega))$.



subsystems Ω_1 and Ω_2 which are in weak contact. The energy $E = E_1 + E_2$ and the total system size $N = N_1 + N_2$ of the whole system (where E_i and N_i are energy and system size of the two subsystems) are then constant³. The system is in thermal equilibrium, if the product $g_1(E_1, N_1) \cdot g_2(E_2, N_2)$ of the density of states of the single systems is maximal, due to the maximization of Gibbs entropy.

Consider now first the case which allows an exchange of energy between the systems, but keeps the system size of the two subsystems fixed. In this situation the total differential

$$d(g_1 g_2) = \left(\frac{\partial g_1}{\partial E_1} \right)_{N_1} g_2 dE_1 + \left(\frac{\partial g_2}{\partial E_2} \right)_{N_2} g_1 dE_2 \stackrel{!}{=} 0$$

vanishes if the two subsystems are in thermal equilibrium. Dividing this equation by $g_1 \cdot g_2$ and using $dE = dE_1 + dE_2 = 0$ gives the condition

$$\frac{1}{g_1} \left(\frac{\partial g_1}{\partial E_1} \right)_{N_1} = \frac{1}{g_2} \left(\frac{\partial g_2}{\partial E_2} \right)_{N_2} \Rightarrow \left(\frac{\partial S_1}{\partial E_1} \right)_{N_1} = \left(\frac{\partial S_2}{\partial E_2} \right)_{N_2},$$

where $S_i(E_i, N_i)$ is again the microcanonical entropy. If one defines the temperature T or the inverse temperature β using

$$\left(\frac{\partial S}{\partial E} \right)_N =: \frac{1}{T} =: \beta, \quad (2.7)$$

a necessary condition for the two systems to be in thermal equilibrium is $T_1 = T_2$ or $\beta_1 = \beta_2$.

As a second case consider the case where beside the exchange of energy also the exchange of system size of the two subsystems is allowed. Here the total differential becomes

$$d(g_1 g_2) = \left[\left(\frac{\partial g_1}{\partial E_1} \right)_{N_1} dE_1 + \left(\frac{\partial g_1}{\partial N_1} \right)_{E_1} dN_1 \right] g_2 + \left[\left(\frac{\partial g_2}{\partial E_2} \right)_{N_2} dE_2 + \left(\frac{\partial g_2}{\partial N_2} \right)_{E_2} dN_2 \right] g_1 \stackrel{!}{=} 0,$$

using $dE = dE_1 + dE_2 = 0$ and $dN = dN_1 + dN_2 = 0$ leads to the following to independent conditions

$$\begin{aligned} \left(\frac{\partial S_1}{\partial E_1} \right)_{N_1} &= \left(\frac{\partial S_2}{\partial E_2} \right)_{N_2} \\ \left(\frac{\partial S_1}{\partial N_1} \right)_{E_1} &= \left(\frac{\partial S_2}{\partial N_2} \right)_{E_2}, \end{aligned}$$

³ In this section we denote the variable N generalized as *system size*. In concrete systems this can be the number of particles, the number of spins or, as we will use later, the number of maximal simplices in a triangulation,



because dE_i and dE_j are independent in general. The first condition is fulfilled if both systems have the same temperature as defined in Eq. (2.7), the second definition is fulfilled for equal chemical potential $\mu_1 = \mu_2$ in both subsystems, where the chemical potential is defined as

$$\left(\frac{\partial S}{\partial N}\right)_E =: -\frac{\mu}{T} = -\beta\mu. \quad (2.8)$$

The intuitive meaning of the chemical potential is the energy a system gains if increasing the system size by 1.

2.1.4 Canonical ensemble

Until now only systems that do not allow an exchange of energy or particles with the environment were considered, they could be described using the microcanonical ensemble. If one allows for energy exchange with the environment, but still fixes the particle number, one gets systems that can be described with the *canonical ensemble*. These are often described as systems within a heat bath. In this section we follow Ref. [317, Sec. 1.4].

Consider now a (microcanonical) system with energy E and particle number N , which consists of two parts, a small system Ω_1 with energy $H_1(\omega_1) = E_1$ and particle number N_1 that is coupled to a large bath Ω_2 with energy $H_2(\omega_2) = E_2$ and particle number N_2 so that $E = E_1 + E_2$ and $N = N_1 + N_2$. Both systems are weakly coupled, so that the interaction energy $E_{12} = H_{12}(\omega_1, \omega_2)$ can be neglected compared to E_1 or E_2 . The density distribution of the whole system is

$$\rho(\omega_1, \omega_2) = \frac{1}{g(E)} \delta(H_1(\omega_1) + H_2(\omega_2), E),$$

and the density distribution of the first system can be obtained by integrating over the degrees of freedom of the second system:

$$\begin{aligned} \rho_1(\omega_1) &= \int d\omega_2 \rho(\omega_1, \omega_2) \\ &= \frac{1}{g(E)} \int d\omega_2 \delta(H_2(\omega_2), E - E_1) = \frac{g_2(E - E_1)}{g(E)} \end{aligned}$$

Since we postulated a small system Ω_1 in a large bath Ω_2 , we have $E_1 \ll E$, and we can use a Taylor expansion for the microcanonical entropy of the bath

$$\log g_2(E - E_1) = S_2(E - E_1) \approx S_2(E) - \left(\frac{\partial S_2}{\partial E_1}\right) E_1 = S_2(E) - \beta E_1,$$



where we denote by β the inverse temperature defined in Eq. (2.7). Since $E = \text{const.}$ for the whole system (which is still considered to be describable by a microcanonical observable, $g(E)$ and $g_2(E)$ are constants, and we get for the density distribution of the canonical ensemble

$$\rho_1(\omega) = \rho_0 \exp(-\beta H(\omega)).$$

Using that the density distribution is normalized, we get

$$\begin{aligned} \int d\omega \rho_0 \exp(-\beta H(\omega)) &\stackrel{!}{=} 1 \\ \Rightarrow \rho_0^{-1} &= \int d\omega \exp(-\beta H(\omega)) =: Z(\beta), \end{aligned} \quad (2.9)$$

where $Z(\beta)$ is the *canonical partition function*, that is sometimes also denoted as $Z(\beta, N)$ or $Z_N(\beta)$ to denote the implicit dependence of the partition function on the system size N .

So the expectation value of an observable can be calculated using Eq. (2.3) as

$$\langle A \rangle(\beta) = \frac{\int d\omega A(\omega) \exp(-\beta H(\omega))}{\int d\omega \exp(-\beta H(\omega))} = \frac{1}{Z(\beta)} \int d\omega A(\omega) \exp(-\beta H(\omega)) \quad (2.10)$$

in the canonical ensemble.

If considers an observable A that only depends on the energy of a microstate, and not on the microstate itself, one can calculate canonical expectation values also using the density of states

$$\begin{aligned} \langle A \rangle(\beta) &= \frac{1}{Z(\beta)} \int dE g(E) A(E) \exp(-\beta H(E)) \\ Z(\beta) &= \int dE g(E) \exp(-\beta E). \end{aligned} \quad (2.11)$$

This result implies that the canonical partition function $Z(\beta)$ is the Laplace transform of the density of states $g(E)$. A similar result can be found for observables A that do depend on the actual microstate, therefor all microcanonical expectation values $\langle A \rangle(E)$ of this observables must be known:

$$\langle A \rangle(\beta) = \frac{1}{Z(\beta)} \int dE \langle g(E) A \rangle(E) \exp(-\beta H(E)). \quad (2.12)$$

The thermodynamic potential of the canonical ensemble is the *free energy*

$$F(\beta, N) = -\frac{1}{\beta} \log Z(\beta, N), \quad (2.13)$$



which has the same role as the density of states in the microcanonical ensemble. The canonical entropy $S(\beta, N)$ can be defined as a derivative of the free energy by

$$S(\beta, N) := - \left(\frac{\partial F}{\partial T} \right)_N = - \left(\frac{\partial F}{\partial \beta} \frac{\partial \beta}{\partial T} \right)_N = \beta^2 \left(\frac{\partial F}{\partial \beta} \right)_N, \quad (2.14)$$

and every other thermodynamic quantity can be calculated in terms of derivatives of the free energy, e.g. the mean energy

$$\langle E \rangle(\beta, N) = - \frac{\partial}{\partial \beta} \log Z(\beta, N) = \frac{\partial}{\partial \beta} (\beta F(\beta, N)) \quad (2.15)$$

and the heat capacity

$$\begin{aligned} C(\beta, N) &:= \left(\frac{\partial \langle E \rangle}{\partial T} \right) = \beta^2 \left(\langle E^2 \rangle(\beta, N) - \langle E \rangle^2(\beta, N) \right) = \\ &= -\beta^2 \frac{\partial^2}{\partial \beta^2} \beta F(\beta, N). \end{aligned} \quad (2.16)$$

So knowledge of the partition function $Z(\beta, N)$ or the free energy $F(\beta, N)$ means knowledge about the thermodynamic properties of the system described by the canonical ensemble.

2.1.5 Grandcanonical ensemble

We can further generalize the canonical ensemble if we allow for the exchange of system size between the two subsystems, but keeping $N = N_1 + N_2$ constant, arriving at the grandcanonical ensemble, following Ref. [317, Sec. 1.5]. Denote by ω_{N_1} a state of the small system Ω_1 with system size N_1 , and by ω_{N_2} a state of the bath Ω_2 with large system size N_2 , the density distribution of the whole system is then $\rho(\omega_{N_1}, \omega_{N_2})$. As in the canonical distribution, the density distribution $\rho_1(\omega_{N_1})$ of the small system can be calculated by integrating over the states of the bath:

$$\begin{aligned} \rho_1(\omega_{N_1}) &= \sum_{N_2} \int \! \! \int d\omega_{N_2} \rho(\omega_{N_1}, \omega_{N_2}) \delta_{N_1, N_2} \\ &= \frac{1}{g(E, N)} \int \! \! \int d\omega_{N-N_2} \delta(H_2(\omega_2), E - E_1) = \frac{g_2(E - E_1, N - N_1)}{g(E, N)} \end{aligned}$$

The microcanonical entropy $S_2(E - E_1, N - N_1)$, which is now both a function of E and N , can be expanded to first order in N_1 and E_1 ,

$$\begin{aligned} S_2(E - E_1, N - N_1) &\approx S_2(E, N) - \left(\frac{\partial S_2}{\partial E_1} \right) E_1 - \left(\frac{\partial S_2}{\partial N_1} \right) N_1 = \\ &= S_2(E) - \beta(E_1 - \mu N_1), \end{aligned}$$



where we used the Definitions (2.7) and (2.8) for the inverse temperature β and the chemical potential μ as first derivatives of the microcanonical entropy. As in the canonical ensemble $S_2(E, N)$ as well as $g(E, N)$ are constants, so that $\rho_1(\omega_{N_1}) = \rho_0 \exp[-\beta(E_1 - \mu N_1)]$. Using the normalization condition and renaming the variable $N_1 \rightarrow N$ leads to

$$\rho_0 = \frac{1}{\sum_N \int d\omega_N \exp[-\beta(H(\omega_N) - \mu N)]} =: \frac{1}{\Xi(\beta, \mu)},$$

where $\Xi(\beta, \mu)$ is the *grandcanonical partition function*. Note that one can write the grandcanonical partition function in terms of the canonical partition function by

$$\Xi(\beta, \mu) = \sum_N \exp(\beta\mu N) Z_N(\beta) = \sum_N z^N Z_N(\beta),$$

where the quantity $z = \exp(\beta\mu)$ is denoted as *fugacity*.

So the expectation value of an observable can be calculated using Eq. (2.3) as

$$\begin{aligned} \langle A \rangle(\beta, \mu) &= \frac{\sum_N \int d\omega_N A(\omega_N) \exp[-\beta(H(\omega_N) - \mu N)]}{\sum_N \int d\omega_N \exp[-\beta(H(\omega_N) - \mu N)]} = \\ &= \frac{1}{\Xi(\beta, \mu)} \sum_N \int d\omega_N A(\omega_N) \exp[-\beta(H(\omega_N) - \mu N)] \end{aligned} \quad (2.17)$$

in the grandcanonical ensemble.

The thermodynamic potential $\Omega(\beta, \mu)$ of the grandcanonical ensemble is given by

$$\Omega(\beta, \mu) = -\frac{1}{\beta} \log \Xi(\beta, \mu). \quad (2.18)$$

As in the canonical ensemble, all expectation values can be expressed in terms of derivatives of this grandcanonical potential.

2.1.6 Phase transitions

A phase transition is the qualitative change of macroscopic equilibrium quantities within a thermodynamic or statistical system if changing some external parameters (generalized inverse temperature or coupling constants).

In this section we study phase transitions in more detail. We start by introducing the order of a phase transition by examining derivatives of the thermodynamic potential. For so-called continuous phase transitions, one can observe a power-law behavior for the relevant observables near



the critical point, where the (critical) exponents are universal in the sense that they do not depend on the microscopic details of the system. As a last part we present renormalization group theory, which can be used for understanding and deriving critical exponents and scaling relations between different critical exponents.

Order of phase transitions

Historically there are different characterizations of phase transitions [227]: The first categorization goes back to Ehrenfest and classifies a phase transition to be of n -th order, if all $(n - 1)$ -th partial derivatives of the thermodynamic potential (e.g., free energy (2.13) for the canonical ensemble, grand-potential (2.18) for the grandcanonical potential) with respect to one of the intensive parameter (inverse temperature, chemical potential or coupling constant) are continuous, and at least one n -th partial derivative is not continuous. There are two main problems if using this classification [227, 317]. On the one hand, no phase transition of third or higher order was found in nature, and discriminating between a second- and a higher-order phase transition is difficult in experiments as well as in simulations. On the other hand there are some transitions that do not fit into the classification scheme, e.g., the famous logarithmic divergence in the two-dimensional Ising model discovered by Onsager [320]. Therefore, today one discriminates between *discontinuous* phase transitions, which correspond to the first-order transitions in the Ehrenfest classification, and *continuous* phase transitions, which comprise all higher-order transition in terms of Ehrenfest and all divergent phase transitions. In Fig. 2.1 examples for the two different types of phase transitions are displayed.

Continuous phase transitions are additionally characterized by the existence of an order parameter. This is an observable of the system that takes values only at one side of the phase transition, but vanishes at the other. In a spin system often the magnetization per spin m can be used as an order parameter, which is 0 for $\beta < \beta_c$ ($T > T_c$), and has a non-vanishing value for $\beta > \beta_c$ ($T < T_c$).

Scaling and critical exponents

An important property of continuous phase transitions is the occurrence of critical exponents. One finds that near the critical temperature $T_c = \beta_c^{-1}$



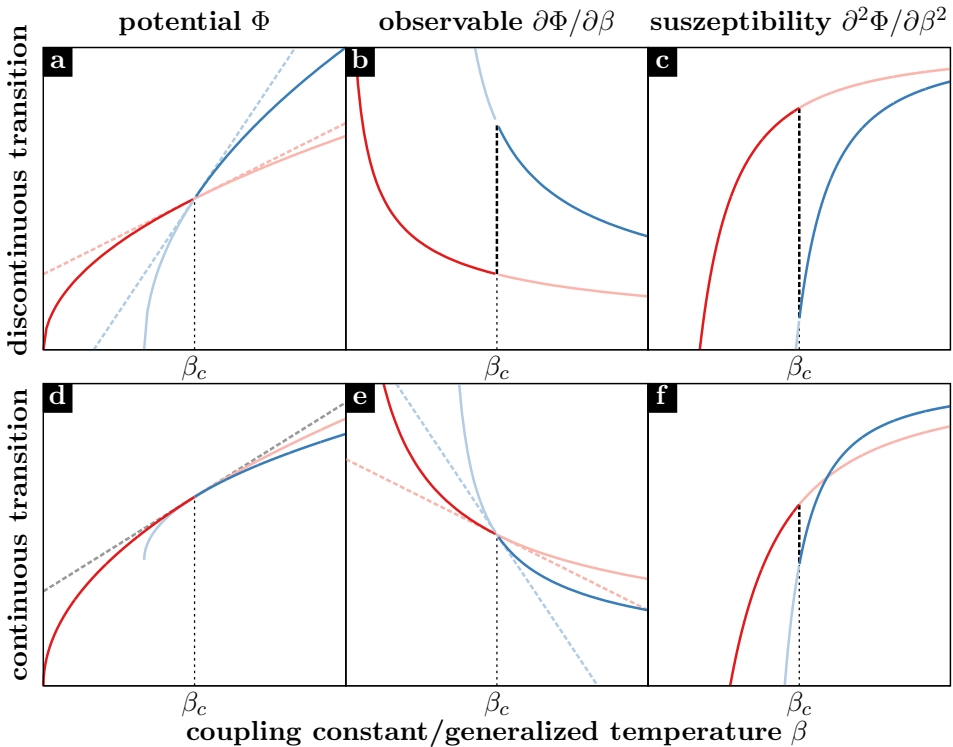


Figure 2.1: Discontinuous and continuous phase transitions.

Qualitative plot of the two different types of phase transitions at β_c , characterized by an arbitrary thermodynamic potential Φ in terms of a generalized inverse temperature or coupling constant β . The potential is section defined, where the red solid curves correspond to $\beta < \beta_c$, and the blue curves correspond to $\beta > \beta_c$. The dashed curves are the corresponding tangents at the critical point β_c . (a-c) Potential Φ , observable $\partial\Phi/\partial\beta$ and susceptibility $\partial^2\Phi/\partial\beta^2$ for a first-order or discontinuous phase transition. The thermodynamic potential Φ is continuous, but not differentiable at the critical point, the first derivative of the thermodynamic potential is discontinuous. (d-f) Potential, observable and susceptibility for a second-order or continuous phase transition. The thermodynamic potential Φ is simply differentiable at the critical point, the first derivative of the thermodynamic potential is continuous, the second derivative is discontinuous.



observables \mathcal{O} of the system behave as

$$\langle \mathcal{O} \rangle(t) \propto t^\phi (1 + c \cdot t^\epsilon + \dots) \quad \text{with } t := \frac{T - T_c}{T_c}, \epsilon > 0, \quad (2.19)$$

where t is denoted as *reduced temperature* [317]. Formally the critical exponent can be defined using the limit [317]

$$\phi_\pm := \lim_{t \rightarrow 0^\pm} \frac{\log |\langle \mathcal{O} \rangle(t)|}{\log |t|}, \quad (2.20)$$

which includes also logarithmic divergences at the critical points, where one gets $\phi = 0$.

The critical exponents of different observables are not independent, they can be related using the *scaling relation* (compare Ref. [317, Sec. 4.2.2]). This relation is based on the conjecture that the free energy density near the critical point is a generalized homogeneous function (GHF)

$$f(t, h) = \lambda^{-d} f(\lambda^{x_t} t, \lambda^{x_h} h), \quad (2.21)$$

where d is the dimensionality of the system, t is again the reduced temperature and h is the order parameter of the continuous phase transition. The parameter λ is an arbitrary scaling factor, and x_t and x_h are the scaling exponents of t and h . The scaling relation can be explicitly derived for some systems using renormalization group techniques (compare the following section), see Ref. [237] for one of the first derivations for the Ising model.

Since all expectation values can be calculated from derivatives of the thermodynamic potential, their critical exponents ϕ should be functions only of the dimensionality d and the scaling exponents x_t and x_h . In the usual Ising model one finds six observables with different critical exponents (for $\beta < \beta_c$, compare Ref. [317, Sec. 4.2.1]):

$$C_H := -\beta^2 \frac{\partial^2 \log Z}{\partial \beta^2} \xrightarrow{\beta \approx \beta_c} t^{-\alpha} \quad \text{heat capacity at } H = 0 \quad (2.22a)$$

$$M := \frac{1}{\beta} \frac{\partial \log Z}{\partial H} \xrightarrow{\beta \approx \beta_c} t^\beta \quad \text{order parameter at } H = 0 \quad (2.22b)$$

$$\chi := \frac{\partial M}{\partial H} \xrightarrow{\beta \approx \beta_c} t^{-\gamma} \quad \text{mag. susceptibility at } H = 0 \quad (2.22c)$$

$$M := \frac{1}{\beta} \frac{\partial \log Z}{\partial H} \xrightarrow{H \approx 0} H^{1/\delta} \quad \text{critical isotherm at } \beta = \beta_c \quad (2.22d)$$

$$\xi \xrightarrow{\beta \approx \beta_c} t^{-\nu} \quad \text{correlation length} \quad (2.22e)$$



Note that these quantities are defined for the whole system, one can define Eqs. (2.22a) to (2.22d) also per spin or per particle without changing the critical exponents. Furthermore one introduces the critical exponent η of the two-point correlation function as

$$g(r_1, r_2) \approx |r_1 - r_2|^{-d+2-\eta} \quad (2.22f)$$

near the critical point. Note that the correlation length (2.22e) and the two-point correlation function (2.22f) cannot be derived from the free energy as simple as the other quantities, but it is possible in principle.⁴

One can then use the scaling equation (2.21) to eliminate x_t and x_h and find connections between the different critical exponents [317, Sec. 4.2.1]

$$\alpha + 2\beta + \gamma = 2 \quad \text{Rushbrooke's identity} \quad (2.23a)$$

$$\delta - 1 = \frac{\gamma}{\beta} \quad \text{Widom's identity} \quad (2.23b)$$

$$2 - \alpha = d\nu \quad \text{Josephson's identity} \quad (2.23c)$$

$$\gamma = \nu(2 - \eta) \quad (2.23d)$$

Often also the Eqs. (2.23) are denoted as scaling equations.

Universality and the renormalization group

The critical exponents are conjectured to be universal, and depend only on the dimensionality, the symmetry and the spin-dimensionality of the system. This idea goes back to Fisher [171] (see also the work [196] by Griffiths for some similar ideas), who first observed that within a system with Hamiltonian $H(\omega) = H_0(\omega) + \lambda H_1(\omega)$, where H_1 breaks some symmetry that H_0 does possess, the critical exponents are not continuous in λ , but take one value for $\lambda = 0$ and another constant value for $\lambda \neq 0$. There are also experimental confirmations, one of the first can be found in Ref. [217], where critical exponents of xenon, sulfur hexafluoride and carbon dioxide are found to coincide with the critical exponents of the three-dimensional Ising model.

4 For the Ising model, one has to calculate the free energy $F(\beta, H_i)$, where H_i is the external field at spin i . Expectation values of the form $\langle \sigma_i \sigma_j \rangle$ can then be calculated using the mixed derivatives

$$\langle \sigma_i \sigma_j \rangle \propto \frac{\partial}{\partial H_i} \frac{\partial}{\partial H_j} \log Z \Big|_{H_0 = \dots = H_{N-1} = H}$$

at equal external fields.



A very valuable tool to understand both universality and the scaling relations is the renormalization group theory (see [172, 173, 424] for some reviews), that was developed mainly by Kadanoff [236] and Wilson [423] in the setup of statistical physics. The basic idea of the renormalization group is the following: Consider a Hamiltonian $H(\vec{\sigma}_0, \vec{J}_0)$ that depends on variables $\vec{\sigma}_0$ describing the state of the system and on coupling constants \vec{J}_0 that describe the interaction of the single states. Now reduce the number of variables describing the system as $\vec{\sigma}_0 \rightarrow \vec{\sigma}_1$, and find the coupling constants \vec{J}_1 so that the Hamiltonian $H(\vec{\sigma}_1, \vec{J}_1)$ still describes the system (e.g., using block-spins as in Ref. [236]). This step can be repeated arbitrarily often, which corresponds to a description of the system on larger and larger scales. If one denotes by $\beta(\vec{J}_n) = \vec{J}_{n+1}$ the Beta function that maps the coupling constants of one step to the coupling constants of the next step, a fixed point \vec{J}_f (with $\beta(\vec{J}_f) = \vec{J}_f$) of β corresponds to a critical point of the system.

2.1.7 Ising model

In this section we will present some basic features of the Ising model on integer lattices. This has three reasons: The first is that the Ising model is the simplest model where one can observe (in two dimensions) a second-order phase transition at finite temperature, which make it a prototype model of statistical physics. The second reason is that the solution of the one-dimensional Ising model using the transfer matrix method is very similar to our approach to solve causal dynamical triangulations in Sec. 5.3. The last reason is that we will later examine the Ising model coupled to lattice triangulations in Secs. 3.4.4 and Sec. 3.4.6.

The Ising model was first defined in the PhD-thesis of Ernst Ising (see Ref. [226] for a journal summary of the thesis) and solved analytically for the one-dimensional case, where no sign of a phase transition could be found. The analytical solution in two dimensions was found in 1944 by Lars Onsager [320] for vanishing external field, he showed that there is in fact a continuous phase transition at finite temperature. Neither the two-dimensional case with external field nor a higher-dimensional case could be solved analytically since then.

The usual definition of the lattice Ising model is the following: Consider a d -dimensional integer lattice with periodic boundary conditions, and assign to each lattice site i an integer spin $\sigma_i = \pm 1$, so that a state of the Ising model is given by specifying the orientation of all spins, denoted by $\vec{\sigma}$. The



Hamiltonian of the model is given by

$$H(\vec{\sigma}) = -J \sum_{\langle i,j \rangle} \sigma_i \sigma_j - H \sum_i \sigma_i \quad (2.24)$$

The scalar quantities J and H are coupling constants, and the first sum denotes the sum over all pairs $\langle i, j \rangle$ of next neighbors. Two sites of a lattice are considered as next neighbors if all but one integer coordinates are equal, and the remaining coordinate differs only by one, taking into account periodic boundary conditions. This implies that in a d -dimensional lattice every spin has $2 \cdot d$ neighbors.

Transfer matrix solution of the one-dimensional Ising model

The one-dimensional Ising model can be solved in terms of the transfer matrix method, for our solution we follow Sec. 2 in the nice book of Baxter [70]. Consider a chain of N spins σ_i , $i = 0, \dots, N - 1$ with periodic boundary conditions, and identify $\sigma_N := \sigma_0$. The Hamiltonian of the Ising model (2.24) can then be written as

$$E(\vec{\sigma}) = - \sum_{i=0}^{N-1} \left(J \sigma_i \sigma_{i+1} + \frac{H}{2} \sum_i (\sigma_i + \sigma_{i+1}) \right),$$

and the partition function $Z(\beta, H)$ is given by

$$Z(\beta, H) = \sum_{\sigma_0=\pm 1} \cdots \sum_{\sigma_{N-1}=\pm 1} \exp \left[\beta \sum_{i=0}^{N-1} \left(J \sigma_i \sigma_{i+1} + \frac{H}{2} \sum_i (\sigma_i + \sigma_{i+1}) \right) \right].$$

This can be rewritten as

$$Z(\beta, H) = \sum_{\sigma_0=\pm 1} \cdots \sum_{\sigma_{N-1}=\pm 1} \prod_{i=0}^{N-1} T(\sigma_i, \sigma_{i+1}),$$

with T defined as

$$T(\sigma_i, \sigma_{i+1}) := \exp \left[\beta \left(J \sigma_i \sigma_{i+1} + \frac{H}{2} \sum_i (\sigma_i + \sigma_{i+1}) \right) \right].$$

Since $\sigma_i = \pm 1$, the function T can be interpreted as a 2×2 *transfer matrix*

$$T(\beta, H) = \begin{pmatrix} T_{1,1}(\beta, H) & T_{1,-1}(\beta, H) \\ T_{-1,1}(\beta, H) & T_{-1,-1}(\beta, H) \end{pmatrix} = \begin{pmatrix} e^{\beta(J+H)} & e^{-\beta J} \\ e^{-\beta J} & e^{\beta(J+H)} \end{pmatrix},$$



and the partition function is given by

$$\begin{aligned} Z(\beta, H) &= \sum_{\sigma_0=\pm 1} \cdots \sum_{\sigma_{N-1}=\pm 1} T_{\sigma_0, \sigma_1}(\beta, H) \cdot T_{\sigma_1, \sigma_2}(\beta, H) \cdots T_{\sigma_{N-1}, \sigma_0}(\beta, H) \\ &= \text{Tr} \left[T(\beta, H)^N \right], \end{aligned}$$

the trace of the product of N copies of the transfer matrix.

Evaluating the trace in the diagonal basis of the transfer matrix results in

$$Z(\beta, H) = \lambda_1(\beta, H)^N + \lambda_2(\beta, H)^N,$$

where $\lambda_{1,2}(\beta, H)$ are the two eigenvalues of $T(\beta, H)$, w.l.o.g. we assume that $\lambda_1 > \lambda_2$. These eigenvalues are given by

$$\lambda_{1,2}(\beta, H) = \exp(\beta J) \cdot \left[\cosh(\beta H) \pm \left(\sinh^2(\beta H) + e^{-4\beta H} \right)^{1/2} \right]. \quad (2.25)$$

Since $\lambda_2 < \lambda_1$, for $N \rightarrow \infty$ the partition function becomes $Z(\beta, H) = \lambda_1(\beta, H)^N$, and we get for the free energy per spin

$$\beta f(\beta, H) = -\log Z(\beta, H) = \beta J + \log \left[\cosh(\beta H) + \sqrt{\sinh^2(\beta H) + e^{-4\beta H}} \right]. \quad (2.26)$$

One can see that the free energy is composed from analytic functions, which are smooth wherever there are defined. The argument of the logarithm is always bigger than 1, since $\cosh(\beta H) \geq 1$, and the argument of the square root is always greater or equal to 0. So the free energy or their derivatives have no discontinuities, and the one-dimensional Ising-model does not show a phase transition.

Furthermore, one can calculate the magnetization per spin

$$m(\beta, H) = \frac{\partial}{\partial H} f(\beta, H) = - \frac{\sinh(\beta H) + \frac{\sinh(\beta H) \cosh(\beta H)}{\sqrt{\sinh^2(\beta H) + e^{-4\beta H}}}}{\cosh(\beta H) + \sqrt{\sinh^2(\beta H) + e^{-4\beta H}}} \quad (2.27)$$

and see that $m(\beta, H = 0) = 0$ for finite temperature, so that there is no spontaneous magnetization in the one-dimensional model.

Onsager's solution of the two-dimensional Ising model

There are several possibilities to solve the two-dimensional Ising model, the first one was given by Lars Onsager in 1944 [320], which analytically



calculated the free energy of the two-dimensional Ising model in the absence of an external field ($H = 0$) to be

$$f(\beta, H = 0) = \frac{1}{2\pi} \int_0^\pi d\vartheta \log \left[2 \left(\cosh(2\beta J)^2 + \frac{1}{k} \sqrt{1 + k^2 - 2k \cos(2\vartheta)} \right) \right]$$

with $k = (\sinh \beta J)^2$,

(2.28)

where we used the formulation of Ref. [70, Sec. 7.12], which we will follow now closely to derive the value of the critical temperature.

One can find the singular part of the free energy [70, Eq. (7.12.7)]

$$\beta f_{\text{singular}} = \frac{(1+k)(1-k)^2}{2\pi k \cosh^2(2\beta J)} \log \left| \frac{1+k}{1-k} \right|,$$
(2.29)

which has a non-analytic point only at $k = 1$, which implies

$$J\beta_c = \frac{\log(1 + \sqrt{2})}{2} \approx 0.44069$$
(2.30)

for the critical temperature of the two-dimensional Ising model. Expanding the singular part (2.29) of the free energy (2.28) near the critical temperature $k \approx 1$, which is equivalent to the reduced temperature $t \approx 0$, yields

$$f_s(t) \propto t^2 \log |t| \Rightarrow c_s(t) \propto \log |t|$$
(2.31)

for the singular part of the heat capacity (2.22a) per spin, which implies the critical exponent $\alpha = 0$.

Note that the free energy (2.28) was calculated only for the case of $H = 0$ in Ref. [320]. Until now it was not possible to calculate the functional dependency of $f(\beta, H)$ for arbitrary H . But it is possible to calculate the spontaneous magnetization (which is the order parameter (2.22b)) given by the derivative of f with respect to the external field H at $H = 0$, yielding

$$m = (1 - k^2)^{1/8} \xrightarrow{k \approx 1} k^{1/4} \approx t^{1/8}$$

near the critical temperature for $\beta < \beta_c$, which implies the critical exponent $\beta = 1/8$. This result was given by Lars Onsager on a conference in 1949 [321], a complete proof was published by C. N. Yang in 1952 [429].



Mean-field solution of the Ising model

In the last section we saw that the Ising-model is hard to solve even in the two-dimensional case, and until now no analytical solution was found in three or more dimensions. So to derive properties of these higher-dimensional models, one has to use either approximate or numerical methods. In this section we present the mean field solution of the Ising model in arbitrary dimensions, following closely Ref. [70, Sec.2]. In the standard Ising model, each spin interacts with a number q of neighbors ($q = 2$ for the standard one-dimensional model, and $d = 4$ for the standard two-dimensional model). For the mean field model one assumes that the spins interact with all the other spins, but with a reduced interaction constant, so that the Hamiltonian becomes

$$E(\vec{\sigma}) := \frac{qJ}{2} \sum_i \sigma_i \frac{1}{N-1} \sum_{j \neq i} \sigma_j - H \sum_i \sigma_i, \quad (2.32)$$

where one can see that each spin interacts with the average field of all the other spins, hence the name mean field. One can re-express this Hamiltonian in terms of the total magnetization M of all the spins, yielding

$$E(\vec{\sigma}) = \frac{qJ}{2} \frac{M^2 - N}{N-1} - HM$$

This is a great simplification, because the magnetization itself depends only on the number of spins pointing in each direction, so one can derive the partition function and give the following self-consistent equation for the magnetization $m = M/N$ per particle,

$$m = \tanh(\beta q J m + \beta H), \quad (2.33)$$

which allows also to express the free energy $f(\beta, M)$ as a function of β and M , and therewith also as a function $f(\beta, M)$ of β and H .

One cannot solve (2.33) for m in terms of analytical functions. But it is possible to calculate

$$H(m) = -qJm + \frac{1}{\beta} \operatorname{artanh}(m),$$

which is invertible for $\beta q J \leq 1$, for $\beta q J > 1$ one finds spontaneous magnetization. So one can conclude that the critical temperature is given by

$$\beta_c = \frac{1}{qJ}, \quad (2.34)$$



2. Markov chain Monte Carlo simulations

and by expanding (2.33) or the free energy for $\beta \approx \beta_c$ one can find the critical exponents

$$\alpha = 0 \quad \beta = \frac{1}{2} \quad \gamma = 1 \quad \delta = 3 \quad (2.35)$$



2.2 Markov chain Monte Carlo simulations

The phrase Monte Carlo simulations is used widely in the area of computational physics. It is used as a buzzword for describing simulational setups where (pseudo-)random numbers or randomness in general are used. They can e.g., be used in experimental particle physics or in astrophysics for a better understanding of the used detectors. The name *Monte Carlo simulations* was mainly embossed by the 1949 paper of Nicholas Metropolis and Stanislaw Ulam [292]

In this thesis and in this section we restrict ourselves to Markov chain Monte Carlo (MCMC) simulations, which sample from a population of states according to some probability distribution by accepting or rejecting elementary moves that relate all states of the population. Important textbooks about MCMC simulations include [86, 269, 315]. We start by describing the Metropolis algorithm, which is the oldest and the most popular MCMC simulation, and afterwards present the Wang-Landau algorithm, which is the mainly used algorithm throughout the thesis. After presenting some other important algorithms, we describe how to analyse the statistical error of MCMC simulations, and conclude with some remarks about phase transitions in MCMC simulations.

2.2.1 The Metropolis MCMC algorithm

The Metropolis algorithm was proposed in the 1953 paper by Nicholas Metropolis and the married couples Arianna and Marshall Rosenbluth as well as Augusta and Edward Teller. It was originally used in the Los Alamos development of the Hydrogen bomb [216] and describes a method for sampling states according to a Boltzmann distribution. The idea was later generalized in 1970 by Hastings [214] for arbitrary target distributions, and the Metropolis algorithm is known as Metropolis-Hastings algorithm in mathematics, sometimes only as Hastings-algorithm.

In this section the basic principles of the Metropolis algorithm will be derived, following closely [315] with slight generalizations. These are also the foundations of all other Markov chain Monte Carlo algorithms covered in this book.

Simple and importance sampling

Let Ω be the phase space of an arbitrary system, and denote by $\omega \in \Omega$ the single possible states of the system. Consider a canonical ensemble at



inverse temperature β , so that the expectation value of an observable A can be calculated according to

$$\langle A \rangle(\beta) = \frac{\sum_{\omega \in \Omega} A(\omega) \exp(-\beta E(\omega))}{\sum_{\omega \in \Omega} \exp(-\beta E(\omega))},$$

where the denominator can be the partition function $Z(\beta)$ of the system. Since one usually deals with very large systems, and $|\Omega|$ normally scales exponentially with the system size, enumerating all microstates $\omega \in \Omega$ and evaluating the observable at each microstate is impossible. An approximation is to use not the whole set Ω of microstates to calculate the canonical expectation value, but only a subset $\{\omega_1, \dots, \omega_k\} \subset \Omega$ of k microstates ω_i , so that $p(\omega_i)$ is the probability of choosing the microstate ω_i from Ω . We then get

$$\langle A \rangle(\beta) \approx \frac{\sum_{i=1}^k A(\omega_i) p(\omega_i) \exp(-\beta E(\omega_i))}{\sum_{i=1}^k p(\omega_i) \exp(-\beta E(\omega_i))} \quad (2.36)$$

as an approximation for the actual expectation value.

The important question is how to select the test microstates ω_i from the huge set Ω , or precisely, which probabilities $p(\omega_i)$ to choose. The simplest possibility is to choose the ω_i uniformly distributed, so that $p(\omega_i) = |\Omega|^{-1}$, which simplifies the approximation (2.36) of the expectation values to

$$\langle A \rangle(\beta) \approx \frac{\sum_{i=1}^k A(\omega_i) \exp(-\beta E(\omega_i))}{\sum_{i=1}^k \exp(-\beta E(\omega_i))}. \quad (2.37)$$

Using this uniform distribution (denoted often as *simple sampling*) one expects that most chosen microstates have a very low Boltzmann weight $\exp(-\beta E(\omega_i))$ and do not contribute at all to the sums in the expectation values. This is bad, because either the approximation for the expectation value is poor, or one has to sample a number of microstates that is in the range of the total number of microstates, which will lead to the original problem.

A better choice is to use

$$p(\omega_i) = \frac{\exp(-\beta E(\omega_i))}{\sum_{\omega \in \Omega} \exp(-\beta E(\omega))} = \frac{\exp(-\beta E(\omega_i))}{Z(\beta)}, \quad (2.38)$$

where every state is selected with its Boltzmann weight, which is also denoted as *importance sampling*. Using the weights (2.38) in Eq. (2.36) leads to the simple formula

$$\langle A \rangle(\beta) = \frac{1}{k} \sum_{i=1}^k A(\omega_i).$$



So the expectation value of an observables just becomes the arithmetic mean of the observables evaluated at the chosen microstates, and in contrast to simple sampling, the states that are chosen are the states that contribute most to the expectation value. But the simplicity of this equation is a delusion: Until now we have no constructive algorithm for choosing the microstates according to Eq. (2.38), and even worse, we cannot calculate the weight of one certain microstate, because we would need to calculate the partition function therefor.

Markov chains

The idea to solve the problems brought up in the previous section is not to generate the states ω_i with probability $p(\omega_i)$ from scratch, but to create a sequence of states, where each one is constructed from the former one, so that the probability of a state ω_i to occur in this sequence is $p(\omega_i)$.

The mathematical tool that is used for this purpose is called Markov chain:

Definition 2.1 (Markov chain):

Let X_j with $j \in \mathbb{N}$ be a sequence of random variables that take values in a countable set of microstates Ω . The sequence X_j is called a *Markov chain* of order m , if

$$P\left(X_{j+1} = \omega_{i_{j+1}} \mid X_j = \omega_{i_j}, \dots, X_0 = \omega_{i_0}\right) \\ \stackrel{!}{=} P\left(X_{j+1} = \omega_{i_{j+1}} \mid X_j = \omega_{i_j}, \dots, X_{j-m+1} = \omega_{i_{j-m+1}}\right)$$

which means that the probability for the random variable X_{j+1} only depends on the values of the previous m random variables.

For $m = 1$, the *transition probabilities* for $\omega_k \rightarrow \omega_l$, $\omega_{k,l} \in \Omega$ are defined as

$$P(\omega_k \rightarrow \omega_l)^{(j)} := P(X_{j+1} = \omega_l \mid X_j = \omega_k),$$

they can be gathered in the *transition matrix* $(T)_{kl}^{(j)} = P(\omega_k \rightarrow \omega_l)^{(j)}$.

In the following we only deal with Markov chains of order 1 with stationary or time-independent transition probabilities, i.e., $P(\omega_k \rightarrow \omega_l)$ does not depend on the position j in the Markov chain (so we can omit the index (j) in the notation).

The transition probabilities must fulfill the normalization condition

$$\sum_{\omega_l \in \Omega} P(\omega_k \rightarrow \omega_l) = 1, \tag{2.39}$$



which intuitively means that being at state ω_k another state $\omega_l \in \Omega$ has to be reached in the next step. Note that $P(\omega_k \rightarrow \omega_k) \neq 0$ is a valid choice (which will be extensively made in the next sections), so it is possible to stay at the same state in one step of the Markov chain.

Another demand for the Markov chain is *ergodicity*, that means that every state $\omega \in \Omega$ can be reached by every other microstate in a finite number of steps. Mathematically such a Markov chain is denoted as irreducible:

Definition 2.2 (Irreducibility of Markov chains):

Let X_j with $j \in \mathbb{N}$ be a Markov chain that takes values Ω . The Markov chain is called *irreducible* if for every pair $\omega_k, \omega_l \in \Omega$ there is a j and $\omega_{i_1}, \dots, \omega_{i_j} \in \Omega$ so that

$$P(\omega_k \rightarrow \omega_{i_1}) \cdot P(\omega_{i_1} \rightarrow \omega_{i_2}) \cdot \dots \cdot P(\omega_{i_j} \rightarrow \omega_l) \neq 0$$

For the application for calculating statistical expectation values ergodicity is strictly necessary, otherwise regions of the phase space that cannot be accessed within the Markov chain would not be considered for the calculations of the expectation values.

Detailed balance

For applying the Markov chains to generate states for calculating the statistical expectation values, it is necessary to construct a Markov chain such that the probability $p(\omega)$ for a state occurring in the Markov chain equals a given probability distribution, e.g., the Boltzmann weight (2.38). This can only be achieved if the Markov chain is in equilibrium, i.e. the probability for going to a state ω must equal the probability for leaving this state:

$$\sum_{\omega_j \in \Omega} p(\omega_j) P(\omega_j \rightarrow \omega_i) = \sum_{\omega_j \in \Omega} p(\omega_i) P(\omega_i \rightarrow \omega_j) = p(\omega_i) \quad (2.40)$$

where in the second part we used the normalization condition (2.39) for the transition probabilities. This relation is often denoted as (*global balance* condition). Using a vectorized notation with $(\vec{p})_i = p(\omega_i)$, the balance condition can be formulated as $T^t \vec{p} = \vec{p}$. This means that T has to be chosen such that \vec{p} is an eigenvector of T^t .

Demanding only the global balance condition (2.40) on the one hand does not ensure a time-reversibility, and on the other hand can lead to non-trivial cycles in the Markov chain. So one usually introduces the *detailed balance* condition, which is stronger than the balance condition and demands



that probability for leaving a state ω to a specific state ω' must equal the probability for entering the microstate ω from ω'

$$p(\omega) \cdot P(\omega \rightarrow \omega') = p(\omega') \rightarrow P(\omega' \rightarrow \omega). \quad (2.41)$$

Note that the detailed balance conditions solves the mentioned problems of the global balance condition, especially the time reversal symmetry.

Selection and acceptance probabilities

A common choice is to split the transition probability $P(\omega_i \rightarrow \omega_j)$ into

$$P(\omega_i \rightarrow \omega_j) = S(\omega_i \rightarrow \omega_j) \cdot A(\omega_i \rightarrow \omega_j)$$

where $S(\omega_i \rightarrow \omega_j)$ is the probability for selecting a step $\omega_i \rightarrow \omega_j$ if being at state ω_i , and $A(\omega_i \rightarrow \omega_j)$ is the probability for accepting this step. This split is motivated due to the usual implementation of a MCMC simulation, where the possible steps are selected according to some distribution and accepted or rejected afterwards.

Using this split in the detailed balance condition (2.41) results in

$$\frac{S(\omega_i \rightarrow \omega_j) \cdot A(\omega_i \rightarrow \omega_j)}{S(\omega_j \rightarrow \omega_i) \cdot A(\omega_j \rightarrow \omega_i)} = \frac{p(\omega_j)}{p(\omega_i)}.$$

The selection probability $S(\omega_i \rightarrow \omega_j)$ depends on the considered system and the way possible steps are proposed. So the detailed balance condition fixes the ratio

$$\frac{A(\omega_i \rightarrow \omega_j)}{A(\omega_j \rightarrow \omega_i)} = \frac{p(\omega_j)}{p(\omega_i)} \cdot \frac{S(\omega_j \rightarrow \omega_i)}{S(\omega_i \rightarrow \omega_j)} \quad (2.42)$$

of the acceptance probabilities. Since only the ratio is determined by the detailed balance condition, there is some freedom for choosing the actual acceptance probability.

The following choice was proposed by Metropolis and coworkers in Ref. [291]

$$A(\omega_i \rightarrow \omega_j) = \min \left(1, \frac{p(\omega_j)}{p(\omega_i)} \cdot \frac{S(\omega_j \rightarrow \omega_i)}{S(\omega_i \rightarrow \omega_j)} \right). \quad (2.43)$$

It can be easily verified that this acceptance probability fulfills detailed balance, since if considering $A(\omega_j \rightarrow \omega_i)$, the fraction on the right hand side becomes it reciprocal, and either the fraction or its reciprocal are greater than one. In the special case $S(\omega_i \rightarrow \omega_j) = S(\omega_j \rightarrow \omega_i)$ and for Boltzmann



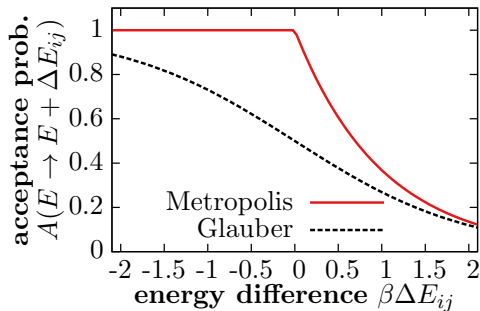


Figure 2.2: Comparison of Metropolis (2.44) (solid) and Glauber (2.46) (dashed) acceptance probabilities in terms of the energy difference ΔE .

weights one gets the actual form of the choice of the acceptance probability presented in Ref. [291],

$$A(\omega_i \rightarrow \omega_j) = \min(1, \exp(-\beta\Delta E_{ij})), \quad (2.44)$$

where $\Delta E_{ij} := E(\omega_j) - E(\omega_i)$ is the energy difference of the two states ω_i and ω_j .

Another possibility was proposed by R. J. Glauber 1963 in Ref. [188], where the acceptance probability is set to

$$\begin{aligned} A(\omega_i \rightarrow \omega_j) &= \frac{p(\omega_j)S(\omega_j \rightarrow \omega_i)}{p(\omega_i)S(\omega_i \rightarrow \omega_j) + p(\omega_j)S(\omega_j \rightarrow \omega_i)} \\ &= \frac{p(\omega_j)}{p(\omega_i)\frac{S(\omega_i \rightarrow \omega_j)}{S(\omega_j \rightarrow \omega_i)} + p(\omega_j)}. \end{aligned} \quad (2.45)$$

The original form in Ref. [188] was proposed for symmetric selection probabilities and Boltzmann weights, so that

$$A(\omega_i \rightarrow \omega_j) = \frac{\exp(-\beta E(\omega_j))}{\exp(-\beta E(\omega_i)) + \exp(-\beta E(\omega_j))} = \frac{1}{1 + \exp(-\beta\Delta E)}. \quad (2.46)$$

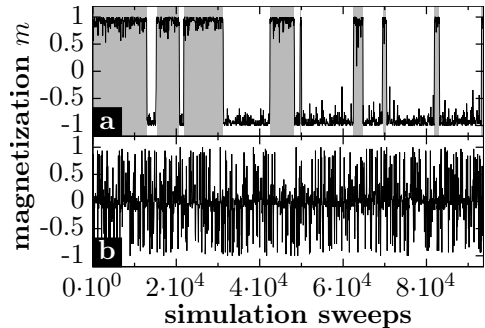
The Glauber acceptance probabilities (2.45) or (2.46) are often used for examining (quasi-)dynamics of the considered systems. In Fig. 2.2 one can find a comparison between the Metropolis (2.44) and the Glauber (2.46) acceptance probabilities in terms of the normalized energy difference $\beta\Delta E$. The Metropolis acceptance probability is always higher than the Glauber one, which means that the system is transversed more often, so one should prefer the former one for calculating equilibrium properties.

2.2.2 The Wang-Landau algorithm

Despite the Metropolis algorithm is the de facto standard algorithm for performing Markov chain Monte Carlo simulations, it comes with some



Figure 2.3: Metropolis (a) and Wang-Landau (b) algorithm for a two-dimensional 8×8 Ising model. The specific magnetization m is displayed in terms of the simulation sweeps that were done since the initial measurement. The Metropolis-data was recorded at inverse temperature $\beta = 0.5 > \beta_c$.



disadvantages. The acceptance probability (2.44) can be very low in cases of low temperature ($\beta \rightarrow \infty$) or high energy differences between the states ($\Delta E \gg 1$), so a lot of computation time is wasted rejecting those steps. There are modifications that can cure these problems, e.g. using a continuous time algorithm for the case of low temperatures or a replica exchange for the high energy barriers, both are described later. But also these modifications show problems near discontinuous phase transitions, because in general the states that constitute the two different phases are separated by states that are rarely sampled, so the system can be trapped effectively in one of the two phases for long time. Fig. 2.3a shows the specific magnetization for an 8×8 Ising ferromagnet at $\beta > \beta_c$ and $H = 0$, where a discontinuous transition occurs, in terms of the Metropolis simulation time. The specific magnetization of the system is near one of the extremal values for long simulation time, until it jumps to the other extremal value, while the jumps would be rarer if one increase the system sizes.

In contrast to this behavior, in Fig. 2.3 a similar measurement is done for the *Wang-Landau* algorithm, which will be described in this section, and shows that the system rapidly jumps between the different extremal magnetizations and traverses the whole phase space. For this section we follow the original papers [407, 407] by Fugao Wang and David Landau, first explaining flat histogram sampling in general, then proceeding to the actual calculation of the density of states (DOS) needed for flat sampling, and concluding with some remarks about the convergence behavior of the Wang-Landau algorithm.

Flat histogram sampling

A possibility to cure the problems of the Metropolis-like algorithms is called *flat histogram* sampling. Recall that the canonical partition function can be



formulated in terms of the density of states $g(E)$ as

$$Z(\beta) = \sum_E g(E) \exp(-\beta E),$$

and observables A that are only functions of the energy can be calculated by

$$\langle A \rangle(\beta) = \frac{1}{Z(\beta)} \sum_E A(E) g(E) \exp(-\beta E).$$

Even canonical expectation values of observables that do depend on the actual system can be calculated if the microcanonical expectation values are known, by

$$\langle A \rangle(\beta) = \frac{1}{Z} \sum_E \langle A \rangle_{\text{mc}}(E) g(E) \exp(-\beta E). \quad (2.47)$$

Flat histogram Monte Carlo algorithms introduce weights for the microstates that are no longer the Boltzmann factor, but

$$p(\omega) \propto \frac{1}{g[E(\omega)]}. \quad (2.48)$$

So the ratio of the acceptance probabilities (2.42) becomes

$$\frac{A(\omega_i \rightarrow \omega_j)}{A(\omega_j \rightarrow \omega_i)} = \frac{g[E(\omega_i)]}{g[E(\omega_j)]} \cdot \frac{S(\omega_j \rightarrow \omega_i)}{S(\omega_i \rightarrow \omega_j)},$$

which can be incorporated by the Metropolis-like choice

$$A(\omega_i \rightarrow \omega_j) = \min \left(1, \frac{g[E(\omega_i)]}{g[E(\omega_j)]} \cdot \frac{S(\omega_j \rightarrow \omega_i)}{S(\omega_i \rightarrow \omega_j)} \right). \quad (2.49)$$

Using this weights for the microstates respectively these acceptance probabilities the probability for being in a macrostate is

$$p(E) = g(E) \cdot p(\omega|E) \propto g(E) \cdot g(E)^{-1} = \text{const.},$$

therefore also the name flat histogram sampling, because a histogram that records the sampled macrostates (energies) is flat.

The calculation of microcanonical expectation values $\langle A \rangle_{\text{mc}}$ needed for the calculations in Eq. (2.47) can also be done in the setup of flat histogram sampling. During flat sampling one records the histogram $H(E, A)$, which counts the visits of the algorithm to states with energy E and observable



value A . The microcanonical expectation values can then be estimated using

$$\langle A \rangle_{mc}(E) = \frac{\sum_A A \cdot H(E, A)}{\sum_A H(E, A)}. \quad (2.50)$$

Another possibility for including canonical expectation values of general observables is to use an extended density of states $g(E, A)$ [267, 427].

Determining the density of states

Implementing the weights (2.48) or the acceptance probabilities (2.49) depends on the knowledge of the DOS, but in most physical systems the DOS is a priori unknown. So the actual problem is to numerically calculate the density of states. F. Wang and D. P. Landau proposed the following algorithm for calculating the DOS in Refs. [406, 407]: Start with an initial estimation of the density of states, which can be $g(E) = 1 \forall E$ if no information about the system is known or should be used in the simulation. Propose steps and accept or reject them with the multicanonical acceptance probability (2.49), and alter the DOS at the energy E after a step by

$$g'(E) = m \cdot g(E),$$

independent on whether the step was actually executed, where $0 < m < 1$ is denoted as *modification factor*. Additionally update an incidence histogram $H'(E) = H(E) + 1$ that is initialized with $H(E) = 0$ for all E and that counts the number of visits to the macrostate with energy E . After a certain number of steps check whether the incidence histogram is flat

$$\text{flat}H(E) := \frac{\min H(E)}{\text{avg}H(E)} \geq f \quad \text{with} \quad 0 < f < 1. \quad (2.51)$$

If this is the case, reset the incidence counter $H(E)$ and reduce the modification factor according to

$$m' = m^{\delta m} \quad \text{with} \quad 0 < \delta m < 1.$$

The choice used in Refs. [406, 407] and in many other applications is $f = 0.8$ and $\delta m = 0.9$. One starts with a modification factor of $m_{\text{initial}} = \exp(1)$ and stops at a modification factor between $m_{\text{final}} = \exp(10^{-6})$ and $m_{\text{final}} = \exp(10^{-12})$.

A small technical remark: The number of microstates in different macrostates can differ by several order of magnitudes, so due to limited accuracy



storing the DOS directly on a computer is difficult. One rather works with the microcanonical entropy $S(E) = \log g(E)$, which is the logarithm of the density of states, and performs the modification

$$\log g'(E) = \log g(E) + \log m$$

during the simulation.

Note that the Wang-Landau algorithm has two problems: On the one hand the sequence of generated states is not a Markov chain, because the acceptance probabilities depend on the DOS, which contains information about all states that were visited before. On the other hand, it does not fulfill detailed balance, because the density of states are altered in each step: Suppose that we have symmetric selection probabilities, and consider a step $\omega_i \rightarrow \omega_j$ with $g(E(\omega_i)) > g(E(\omega_j))$. The acceptance probability for the step is

$$A(\omega_i \rightarrow \omega_j) = \min \left(1, \frac{g(E(\omega_i))}{g(E(\omega_j))} \right) = 1,$$

so the step will be executed and the DOS will be multiplied with m at $E(\omega_j)$. Then the acceptance probability for the inverse step becomes

$$A(\omega_j \rightarrow \omega_i) = \min \left(1, \frac{m \cdot g(E(\omega_j))}{g(E(\omega_i))} \right) = \frac{m \cdot g(E(\omega_j))}{g(E(\omega_i))}.$$

So detailed balance is not fulfilled, but the modified detailed balance condition

$$p(\omega_i)P(\omega_i \rightarrow \omega_j) = \frac{1}{m}p(\omega_j)P(\omega_j \rightarrow \omega_i)$$

Especially at the end of the simulation $m \approx 1$, so the violation of detailed balance asymptotically vanishes. Despite these two problems the Wang-Landau algorithm is known to yield correct results for all tested simulational setups.

Saturation of error and the $1/t$ -algorithm

Although all simulation results of the Wang-Landau algorithm are consistent with known comparison data, one still has to answer whether the Wang-Landau algorithm converges towards the actual density of states in general. It can be shown analytical that also Markov chain Monte Carlo algorithms that fulfill detailed balance only asymptotically converge under some weak assumptions that the Wang-Landau algorithm fulfills, and that the obtained error scales as $\mathcal{O}(t^{-1})$ with t being the simulation time (proportional to the number of proposed steps) [149].



An important question about Wang-Landau simulation is to quantify the systematic and the statistical error. Consider e.g. Fig. 2.4, where the evolution of a Wang-Landau sampling in terms of the modification factor m for an Ising chain with 32 spins and periodic boundary conditions is displayed for different choices of the flatness f and the modification factor multiplier δm . In this Figure the systematic and the statistical error can be found: In the Subfigs. 2.4a-c the difference of the calculated microcanonical entropy $S(E_1)$ and its exact value are displayed for the first excited state. One can see that this difference, which is a measure for the systematic error, saturates for a small enough modification factor, and it decreases for larger f and δm . The same is true for the statistical error displayed in Subfigs. 2.4d-f, where we used the relative width of the obtained distribution for $S(E)$ as a measure for the relative error, simultaneously of course the simulation time increases.

There are also several proposals to alter the flatness criterion (2.51). The histogram $H(E)$ of visited energies can be considered flat if $H(E) \geq H_0$, which means that all energy bins have visited at least H_0 times. Under the condition that one can neglect the autocorrelation of adjacent Markov chain members (which can be done by doing a high enough number of steps that are not recorded in the histogram or the DOS), it can be shown analytically that the algorithm then converges, and that the statistical error scales as $(\log m)^{-1/2}$ [432]. A similar result was found numerically in Ref. [273], additionally it was shown that the obtained error is determined by the fluctuations of the energy histogram $H(E)$. Another alternation of the originally flatness criterion (2.51) was proposed in Refs. [72, 73]. Here the modification factor first scaled as in the original algorithm, but once $m_i < t^{-1}$ is valid for the modification factor, where t is the simulation time, one uses a modification factor $m(t) = t^{-1}$. Numerical simulations and analytical approximations performed in Refs. [72, 73] suggest that this can reduce the saturation of errors. In Fig. 2.5 one can see a visualization of the choice of the modification factor in this algorithm. Instead of using some of these proposed algorithm, in the course of this thesis we choose the parameter δm and the flatness criterion very carefully, so that we get small statistical and total errors. The effect of statistical error can be reduced furthermore by averaging over several independent simulation runs.

2.2.3 Other MCMC algorithms

In the previous section we discussed the Metropolis and the Wang-Landau algorithm, which are the two Markov chain Monte Carlo (MCMC) algorithms



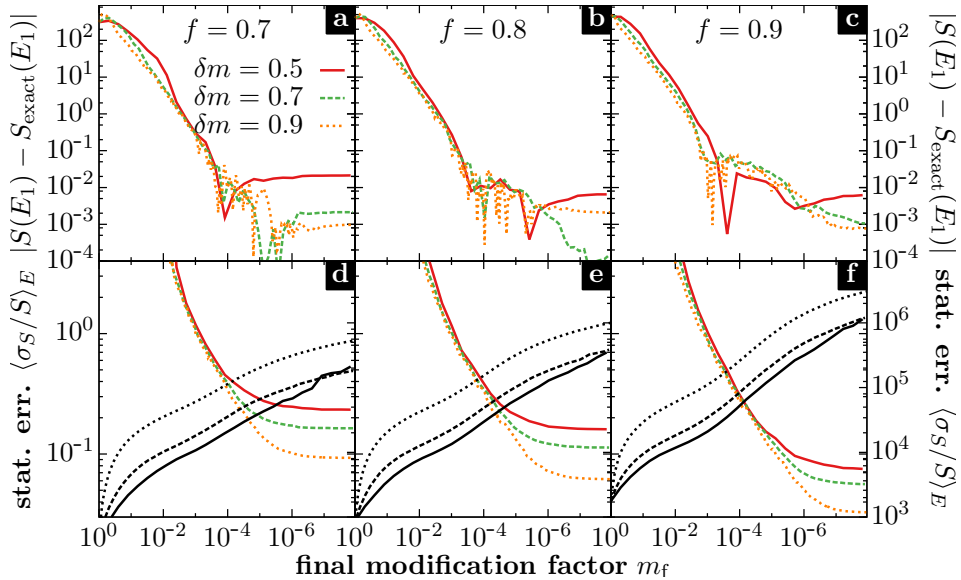


Figure 2.4: Total and statistical errors in Wang-Landau simulations.

Errors in Wang-Landau sampling of an Ising chain consisting of 32 spins for different values of the flatness f and for the modification factor multiplier δm in terms of the final modification factor m_f for initial modification factor $m_i = \exp(1)$. The obtained density of states was normalized with respect to the ground state bin, the presented results are averaged over 400 independent simulations. (a-c) Total error measured by the absolute difference of the calculated microcanonical entropy $S(E_1)$ and its exact value $S_{\text{exact}}(E_1) = (L - 1)L/2$ for the first excited state for $f = 0.7$ (a), $f = 0.8$ (b) and $f = 0.9$ (c) in terms of m_f . (d-f, left axis) Statistical error measured by the standard deviation σ the distributions obtained for $S(E)$ normalized with the mean value and averaged over all energy bins of the DOS. (d-f, right axis) Average of sweeps s necessary for reaching m_f .



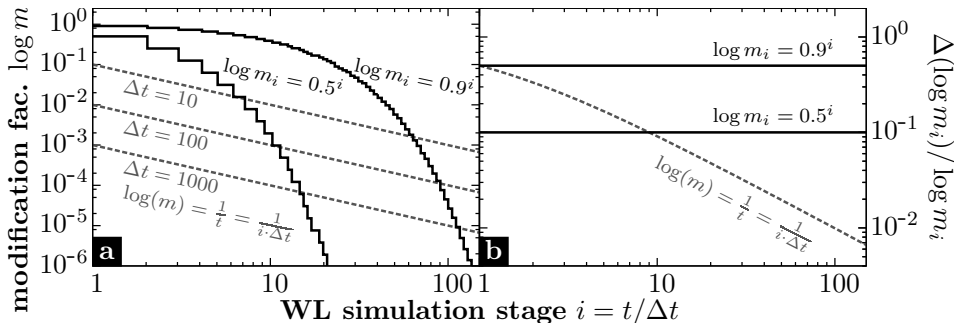


Figure 2.5: Modification factors in standard Wang-Landau sampling and $1/t$ -sampling.

Choice of the modification factor in the $1/t$ -version of Wang-Landau sampling introduced by Refs. [72, 73]. The logarithm $\log m$ of the modification factor is plotted with respect to the simulation stage i of the Wang-Landau simulation, where the i -th stage means the stage of the classical simulation where the modification factor $(\delta m)^i$ (solid lines) is used. For comparing the two modification factors, one assumes that in each stage of the simulation Δt sweeps are needed to reach flatness. The $1/t$ version of Wang-Landau sampling uses the standard modification factors $\log m_i = (\delta m)^i$ as long as $(\delta m)^i > t^{-1}$ (solid lines), afterwards it uses the modification factor $\log m = 1/t$ (dashed lines).

that will be used throughout this thesis. Of course a large number of other MCMC algorithms has been developed since the original paper of Metropolis and coworkers [291], many of them designed for dealing with only some special systems. For completeness we present in this section some other important all-purpose algorithms, which will also give some insight about the similarities and differences of Markov chain Monte Carlo algorithms that can be used for developing reusable software for doing Markov chain Monte Carlo simulations on the computer (compare Sec. 6.3.1).

Parallel Tempering

The standard Metropolis algorithm as presented in Sec. 2.2.1 has the disadvantage that energy barriers cannot be crossed in a suitable simulation time if the product $\beta \cdot \Delta E$ becomes large. So for large β , which corresponds to high temperature, ergodicity can effectively break, because the system cannot access all possible states in a limited computer time.

One possible solution to this problem is using a modification of the Metropolis algorithm which is known as *replica exchange* or *parallel tempering*, which was first presented in Ref. [382]. For its presentation we



follow Ref. [85, Sec.6.3] and Ref. [223]. The idea of the algorithm is to perform not one Metropolis simulation at one inverse temperature β , but n Metropolis simulations with different inverse temperatures β_i , $1 \leq i \leq n$. Additionally one allows for an exchange of the inverse temperatures between the different systems. Intuitively this solves the problem of high energy barriers at low temperatures by increasing the temperature of the system (which allows to overcome the barrier) and lowering it afterwards due to the possible exchange of temperatures.

By introducing this parallelization of the system, the detailed balance condition becomes technically slightly more complicated. Consider for example a simulation with two systems at different temperatures. The weight of the complete system

$$p(\omega_i^{(1)}, \omega_i^{(2)}) = p_1(\omega_i^{(1)})p_2(\omega_i^{(2)})$$

is decomposable into the weights of the single system, which are in general different for the two systems due to the different inverse temperature. The detailed balance condition now reads

$$\begin{aligned} p(\omega_i^{(1)}, \omega_i^{(2)})P(\omega_i^{(1)} \rightarrow \omega_j^{(1)}, \omega_i^{(2)} \rightarrow \omega_j^{(2)}) &= \\ = p(\omega_j^{(1)}, \omega_j^{(2)})P(\omega_j^{(1)} \rightarrow \omega_i^{(1)}, \omega_j^{(2)} \rightarrow \omega_i^{(2)}) &. \end{aligned} \quad (2.52)$$

For $\omega_i^{(1)} = \omega_j^{(1)}$ as well as for $\omega_i^{(2)} = \omega_j^{(2)}$, which are the steps in the single systems, using the standard acceptance probabilities for the respective inverse temperatures fulfills the two-system detailed balance condition (2.52) if the one-system detailed balance condition (2.41) is fulfilled. The remaining step is the interchange of the temperature between to replicas (which is equivalent with the interchange of two replicas), where the ratio of the transition probabilities has to fulfill

$$\frac{P(\omega^{(1)} \rightarrow \omega^{(2)}, \omega^{(2)} \rightarrow \omega^{(1)})}{P(\omega^{(2)} \rightarrow \omega^{(1)}, \omega^{(1)} \rightarrow \omega^{(2)})} = \frac{p(\omega^{(2)}, \omega^{(1)})}{p(\omega^{(1)}, \omega^{(2)})} = \frac{p_1(\omega^{(2)})p_2(\omega^{(1)})}{p_1(\omega^{(1)})p_2(\omega^{(2)})}$$

As for the standard steps we can split this probability into a selection and an acceptance probability. The selection probability for selecting two neighboring inverse temperatures to change is always $1/(n-1)$, so that the ratio of the selection probabilities is always 1. For the acceptance probabilities of the interchange step to fulfill detailed balance, one can use the standard Metropolis choice

$$A(\omega^{(1)} \rightarrow \omega^{(2)}, \omega^{(2)} \rightarrow \omega^{(1)}) = \min \left(1, \frac{p_1(\omega^{(2)})p_2(\omega^{(1)})}{p_1(\omega^{(1)})p_2(\omega^{(2)})} \right), \quad (2.53)$$



which for Boltzmann weights becomes

$$A(\omega^{(1)} \rightarrow \omega^{(2)}, \omega^{(2)} \rightarrow \omega^{(1)}) = \min \left(1, \frac{e^{-\beta_1 E(\omega^{(2)})} \cdot e^{-\beta_2 E(\omega^{(1)})}}{e^{-\beta_1 E(\omega^{(1)})} \cdot e^{-\beta_2 E(\omega^{(2)})}} \right) \quad (2.54)$$

$$= \min(1, \exp(\Delta\beta \cdot \Delta E)),$$

where $\Delta\beta := \beta_2 - \beta_1$ is the difference of the inverse temperatures, and $\Delta E = E(\omega^{(2)}) - E(\omega^{(1)})$ is the energy difference of the two replicas. Note that on average for $\beta_2 > \beta_1$ the energies are $E(\omega^{(2)}) < E(\omega^{(1)})$, so that $\Delta\beta \cdot \Delta E < 0$.

A possibility for optimization of a replica exchange is the choice of the different temperatures used. Suppose one is interested in the interval $[\beta_{\min}, \beta_{\max}]$ of inverse temperatures, and wants to perform k independent simulations? The first possibility is to choose the inverse temperatures such that the rates of temperature exchanges are equal for all neighboring pairs of temperatures. This ensures that there is no small or even vanishing exchange rate between two neighboring temperatures, which would imply that some replicas get stuck in one part of the temperature ranges. This can be done iteratively by measuring the exchange rates and adopting the set of inverse temperatures as described e.g. in Ref. [85].

The second possibility is to optimize the frequency of the replicas transversing the temperature range, as described in [241]. The time of a transverse of a replica is given by the time (measured e.g. in the number of replica exchanges tried) a certain replica of the system needs to go from one boundary of the energy range (e.g. β_{\min}) to the other boundary (e.g. β_{\max}).

Compared to the standard single Metropolis algorithm, parallel tempering can be used to overcome the problem of getting stuck in local minima for small temperatures. But as the Metropolis algorithm it has also a problems if simulating near discontinuous phase transitions. For this phase transitions the first derivatives of the partition function are discontinuous, so this is the case also for the energy. So the acceptance probability for the exchange of the replicas with temperatures slightly above and below the critical temperature then goes to zero, because there is a finite energy difference that grows with increasing system size. So one has either to increase the number of temperatures near the phase transition, or has to deal with very small acceptance probabilities for the replica exchanges, both increase the necessary simulation time.

The presented replica exchange generalization of the Metropolis algorithm can also be applied to other Monte Carlo algorithms, e.g., the Wang-Landau algorithm [404]. In this setup the desired energy range is split into n



overlapping pieces, and calculates within each of the parallel simulation the DOS for one of the energy ranges. The replica exchange step between systems in neighboring energy ranges can take place if the energy of both systems is in the overlap of both ranges.

Continuous time Monte Carlo

Even in the absence of large energy barriers, low temperatures can lead to problems in the standard Metropolis algorithm. This is due to the acceptance probabilities (2.44) becoming small, leading to the majority of steps being rejected.

A solution to this problem, the so-called *N-fold way* algorithm, was proposed in Ref. [99]. Alternative names are *continuous time* or *rejection free* Monte Carlo. The idea of this algorithm is to calculate the average number of steps a standard Metropolis algorithm would need to leave the present state of the system, in fact execute a step without the possibility of rejection, and then to book-keep the calculated time.

For calculating the average time the system would stay in a state ω_i , one has to calculate the self-transition probability $P(\omega_i \rightarrow \omega_i)$, which is the probability for staying at the microstate ω_i within one step. The probability to be still at state ω_i after t steps in then given by $P(\omega_i \rightarrow \omega_i)^t = \exp(t \cdot \log P(\omega_i \rightarrow \omega_i))$, which is an exponential decay. The average number of steps τ the algorithms stays in ω_i can then be simply read of the exponential and is

$$\tau = -\frac{1}{\log P(\omega_i \rightarrow \omega_i)} = -\frac{1}{\log \left(1 - \sum_{j \neq i} P(\omega_i \rightarrow \omega_j) \right)} \approx \frac{1}{\sum_{j \neq i} P(\omega_i \rightarrow \omega_j)}.$$

The step that actually will be executed can then be selected from the set of all possible steps $\omega_i \rightarrow \omega_j$, selected proportional to $P(\omega_i \rightarrow \omega_j)$.

This algorithm is suitable for low temperatures and low acceptance rates. For high temperatures the average time the algorithm stays in a certain state is small, and the bottleneck is to calculate all the transition probabilities, which dramatically slows down the algorithm.

As for the replica exchange method, one can also use the continuous time formulation in other algorithms, e.g., in Wang-Landau sampling [364]. Here also the average number τ of steps the algorithm stays in the actual state is calculated, one then uses $g'(E) = g(E) \cdot m^\tau$ for the DOS and $H'(E) = H(E) + \tau$ for the incidence histogram.



Transition matrix Monte Carlo

For the presentation of the transition matrix Monte Carlo algorithm we follow closely Ref. [408]. The idea of transition matrix Monte Carlo is to reformulate the transition probability $P(\omega_1 \rightarrow \omega_2)$ between two microstates ω_1 and ω_2 in terms of a transition matrix $T(E_1 \rightarrow E_2)$ which encodes the probability of a transition between two macrostates E_1 and E_2 . As a starting point, we sum the detailed balance condition (2.41) over the whole macrostates E_1 and E_2

$$\sum_{\omega_1 \in \Omega} \delta_{E(\omega_1), E_1} \sum_{\omega_2 \in \Omega} \delta_{E(\omega_2), E_2} [p(\omega_1)P(\omega_1 \rightarrow \omega_2) - p(\omega_2)P(\omega_2 \rightarrow \omega_1)] = 0$$

The next step is to define the stochastic transition matrix

$$T(E_1 \rightarrow E_2) := \frac{1}{g(E_1)} \sum_{\omega_1, \omega_2 \in \Omega} P(\omega_1 \rightarrow \omega_2) \delta_{E(\omega_1), E_1} \delta_{E(\omega_2), E_2}, \quad (2.55)$$

where the density of states (DOS) $g(E)$ is the number of microstates in the macrostate E . This leads to the macrostate detailed balance condition

$$\begin{aligned} g(E_1)p(E_1)T(E_1 \rightarrow E_2) &= g(E_2)p(E_2)T(E_2 \rightarrow E_1) \\ H(E_1)T(E_1 \rightarrow E_2) &= H(E_2)T(E_2 \rightarrow E_1), \end{aligned} \quad (2.56)$$

where by abuse of notation $p(E)$ is defined by $p(\omega(E)) =: p(E)$, and where $H(E) := p(E) \cdot g(E)$ is the probability to find a macrostate E in the simulation. Using the macrostate detailed balance condition (2.56) on three energy levels that are connected by elementary moves one gets the so-called TTT-rule

$$\begin{aligned} T(E_1 \rightarrow E_2)T(E_2 \rightarrow E_3)T(E_3 \rightarrow E_1) \\ = T(E_1 \rightarrow E_3)T(E_3 \rightarrow E_2)T(E_2 \rightarrow E_1), \end{aligned} \quad (2.57)$$

which can be used as a measure for reached convergence of the transfer matrix that was calculated numerically.

Due to $P(\omega_1 \rightarrow \omega_2)$ being a stochastic matrix, also $T(E_1 \rightarrow E_2)$ is a stochastic matrix and has an eigenvalue $\lambda = 1$, with corresponding eigenvector

$$\sum_{E_1} H(E_1)T(E_1 \rightarrow E_2) = H(E_2). \quad (2.58)$$

This can be used to extract $g(E)$ from the transition matrix (2.55) by diagonalization, but typically this is numerically unstable if the transition



matrix T is known only up to statistical errors. So in fact one uses the macrostate detailed balance condition (2.56) to calculate the DOS iteratively.

The remaining task is to numerically calculate the transition matrix (2.55). Therefor consider first a random ensemble with $p(\omega) = p(E) = \text{const.}$, which corresponds to a canonical ensemble at infinite temperature. We can then assume that the infinite temperature transition matrix T_∞ for constant selection probabilities and N steps originating from every state is

$$T_\infty(E_1 \rightarrow E_2) = \frac{\langle N(\omega, E_2 - E_1) \rangle(E_1)}{N} = \frac{p(E)}{N} \sum_{\omega \in \Omega} N(\omega, E_2 - E_1) \delta_{E(\omega), E_1}, \quad (2.59)$$

where $N(\omega, \Delta E)$ is the number of steps originating from ω that induce an energy difference ΔE . If the selection probabilities of the steps used are not constant, one has to use

$$T_\infty(E_1 \rightarrow E_2) = p(E) \sum_{\omega_1, \omega_2 \in \Omega} S(\omega_1 \rightarrow \omega_2) \delta_{E(\omega_1), E_1} \delta_{E(\omega_2), E_2} \quad (2.60)$$

(note that by definition $S(\omega_1 \rightarrow \omega_2) = 0$ for all states that are not connected by a step, so one only has to inspect all steps originating from the actual step). The actual transfer matrix for a different probability distribution can then be recovered by

$$T(E_1 \rightarrow E_2) = T_\infty(E_1 \rightarrow E_2) \cdot A(E_1 \rightarrow E_2),$$

where $A(E_1 \rightarrow E_2)$ is the chosen acceptance probability of the step that has to fulfill

$$\frac{A(E_1 \rightarrow E_2)}{A(E_2 \rightarrow E_1)} = \frac{p(E_2)}{p(E_1)}$$

in order to make the macrostate detailed balance condition (2.56) hold. One then can use a Metropolis-like choice for the acceptance probability

$$A(E_1 \rightarrow E_2) = \min \left(1, \frac{p(E_2)}{p(E_1)} \right),$$

or every other choice that fits into this equation (compare Ref. [408] for a comparison of different acceptance probabilities).

Note that one is also free in the choice of $p(E)$. It is possible to use the Boltzmann weights $p(E) \propto \exp(-\beta E)$ for a suitable β , similar to the Metropolis algorithm (in fact, in this situations one should use several simulations at different β , because $H(E)$ is normally peaked around a certain energy for a given β). Additionally one could use estimations for $g(E)$ from



the transition matrix to get a flat sampling probability $p(E) \propto 1/g(E)$. Since for calculating the transfer matrix according to Eqs. (2.59) and (2.60) one has to calculate all possible steps originating from the obtained states, continuous time algorithms can be used for free.

Other flat histogram methods

Beside the Wang-Landau algorithm described in detail in Sec. 2.2.2, there are other algorithms that calculate the density of states (DOS) using the flat histogram acceptance probability (2.49).

The first algorithm is called *entropic sampling* and was proposed in Ref. [274]. As in the Wang-Landau algorithm one starts with an initial estimation of DOS and records the incidence histogram $H(E)$ of visited macrostates, but one does not alter the DOS during these steps. After a number of steps (that is normally increased during the simulation), the estimation of the density of states is updated as

$$g'(E) = g(E) \cdot H(E) \quad \text{where} \quad H(E) \neq 0,$$

and the incidence histogram is reset. In contrast to the Wang-Landau algorithm, entropic sampling fulfills detailed balance except the one step before and after the adoption of the DOS.

Despite the fact that in entropic the DOS is not updated after every step and there is no decreasing modification factor, the main difference is that in entropic sampling the DOS the logarithm of the incidence counter is added to the microcanonical entropy, whereas in the Wang-Landau algorithm basically the actual incidence counter times the modification factor is added.

The second algorithm is *optimal ensemble sampling* proposed in Refs. [392, 393]. The idea is to iteratively adopt the weights $p(E) = p(E(\omega))$ of the macrostates so that the number of times the system traverses the energy range (travels from the highest to the lowest possible energy and vice versa) is optimized (so strictly speaking optimal ensemble sampling is no flat histogram algorithm, but it can be used for calculating the DOS).

2.2.4 Error analysis of Monte Carlo simulations

Markov chain Monte Carlo simulations are a probabilistic method for calculating expectation values, so naturally the results of the simulations are afflicted with statistical errors, sometimes even with systematic ones. In this section we shortly describe how to quantify the error obtained in Monte



Carlo simulations. For simplicity we assume that Markov chain Monte Carlo simulation produce results that are Gaussian distributed.

The error analysis of Monte Carlo simulations is a very large topic, in this section we will feature only two elements that are used within this thesis. The first aspect we cover is the problem of bias in the estimation of errorbars, the second aspect is the Markov chain autocorrelation time. For further information about the error analysis in Monte Carlo simulations, we refer to Ref. [85], which we also follow for the presentation of the considered two aspects.

Biased and unbiased estimators of the errorbar

The result of a Markov chain Monte Carlo simulation should be given in the form

$$\text{result} = \text{value} \pm \text{error},$$

where the value and the error have to be estimated from a set of samples of the Markov chain. If the result is denoted by y , we denote by $\hat{\mu}_y$ an estimator for the expectation value of y and by $\hat{\sigma}_y$ an estimator for the standard deviation of y . An estimator \hat{s} of a quantity s is called *unbiased*, if its expectation value $\langle \hat{s} \rangle = s$ coincides with the exact value s , otherwise the estimator is called *biased*.

In this section we use the following notation: Denote by x_i , $i = 1, \dots, N$ the different measurements taken in a Markov chain Monte Carlo simulation. This measurements can be numbers, e.g., the energy or another observable (magnetization in the Ising model), or more complicated objects, e.g., the logarithm of the density of states from a Wang-Landau simulation or the transition matrix from transition matrix Monte Carlo. We want to calculate estimators for the value and the error of a quantity $y = f(x)$ that can be calculated from the taken measurements by using some arbitrary function f , e.g., (2.11) for calculating the average energy in terms of the density of states at a certain temperature.

We first consider the situation that $y = f(x) = a \cdot x + c$ is a linear function, which includes the identity $f(x) = y = x$ by $a = 1$ and $c = 0$, implying that we want to calculate the average value and the error of a direct observable. Suppose that the samples x_i are drawn from a distribution with expectation value μ_x and standard deviation σ_x . If we use the sample mean

$$\hat{\mu}_y := \frac{1}{N} \sum_{i=1}^N f(x_i) = a \frac{1}{N} \sum_{i=1}^N x_i + c = a \hat{\mu}_x + c \rightarrow \mu_y \quad (2.61)$$



as estimator for μ_y , this estimator is unbiased due to the law of large numbers. Since this law predicts that the standard deviation of the sample mean is σ_x/\sqrt{N} , one could suppose that one can use

$$\hat{\sigma}'_y := \frac{1}{\sqrt{N}} \sqrt{\frac{1}{N} \sum_{i=1}^N (f(x_i) - \hat{\mu}_y)^2}$$

as an unbiased estimator for the standard deviation σ_y of y , but this naive estimator is in fact biased, because one would have to use μ_y instead of $\hat{\mu}_y$, which is in general unknown. But one can show that

$$\hat{\sigma}_y := \frac{1}{\sqrt{N-1}} \sqrt{\frac{1}{N} \sum_{i=1}^N (f(x_i) - \hat{\mu}_y)^2} \rightarrow \frac{\sigma_x}{\sqrt{N}} \quad (2.62)$$

is an unbiased estimator for the standard error.

The situation is more complicated if the function f is a non-linear function, because the naive estimator

$$\hat{\mu}'_y := \frac{1}{N} \sum_{i=1}^N f(x_i) \quad (2.63)$$

has a bias $\langle \hat{\mu}'_y \rangle - \mu_y \propto \mathcal{O}(1)$, so even for large sample size N the estimator does not converge towards the correct value. The correct estimator to use in this case is

$$\hat{\mu}_y := f(\mu_x) = f\left(\frac{1}{N} \sum_{i=1}^N x_i\right), \quad (2.64)$$

which coincides with the estimator (2.61) for the linear case and has a bias of $\mathcal{O}(N^{-1})$. Similarly one cannot use the estimator (2.62) for the standard deviation, because $f(x_i)$ is still a bad estimator for y_i . To find a correct estimator of the standard deviation, one mainly uses so-called *resampling* methods as the Jackknife or the Bootstrap resampling, which are described in more details in the following sections.

The Jackknife algorithm was originally presented in Refs. [333, 396], for a review see Ref. [153]. The idea is to create N estimators $\hat{x}_i^{(J)}$ by calculating the mean of the results x_j , leaving out x_i

$$\hat{x}_i^{(J)} := \frac{1}{N-1} \sum_{\substack{j=1 \\ j \neq i}}^N x_j.$$



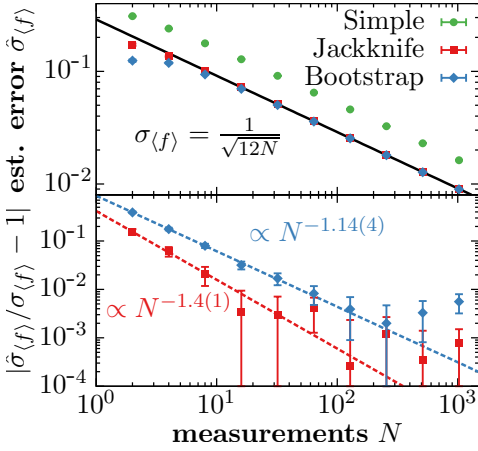


Figure 2.6: Jackknife and Bootstrap resampling methods.

Estimated errors of the non-linear function $f(x) = x^2$ used on samples taken from a uniform distribution between 0 and 1 in terms of the number N of measurements. The analytically calculated error (2.67) is displayed as a black solid line. The naive error estimator (2.63) (\bullet) overestimates the actual error, while the Jackknife estimator $\hat{\sigma}_{\langle f \rangle}^{(J)}$ (2.65) (\blacksquare) and the bootstrap estimator $\hat{\sigma}_{\langle f \rangle}^{(B)}$ (2.66) (\blacklozenge) agree with the actual error.

These can then be used for creating estimators of the mean and the error of the mean

$$\hat{\mu}_{\langle f \rangle}^{(J)} := \frac{1}{N} \sum_{i=1}^N f(x_i^{(J)})$$

$$\hat{\sigma}_{\langle f \rangle}^{(J)} := \sqrt{\frac{N-1}{N} \sum_{i=1}^N (f(x_i^{(J)}) - \hat{\mu}_y^{(J)})^2}, \tag{2.65}$$

where the estimator for the mean is the arithmetic average of the function evaluated at the N estimators $\hat{x}_i^{(J)}$, and the error of the mean is related to the standard deviation of this quantity. One sees that this calculations becomes slow if the number N of samples increases, because N averages of $N - 1$ quantities each have to be calculated.

The idea of the bootstrap approach, which was originally presented in Ref. [152], is to create an arbitrary number of b estimators $\hat{x}_i^{(B)}$ by

$$\hat{x}_i^{(B)} := \frac{1}{N} \sum_{j \in \phi_N} x_j,$$

where ϕ_N is a tuple with N elements, each element chosen uniformly distributed between 1 and N . This means that one draws N elements from



the N samples with replacement, so that every sample can be drawn several times. These estimators can again be used for creating estimators of the mean and for the error of the mean by

$$\begin{aligned}\hat{\mu}_y^{(B)} &:= \frac{1}{b} \sum_{i=1}^b f(x_i^{(B)}) \\ \hat{\sigma}_y^{(B)} &:= \sqrt{\frac{1}{b} \sum_{i=1}^b \left(f(x_i^{(B)}) - \hat{\mu}_y^{(B)} \right)^2}.\end{aligned}\tag{2.66}$$

In general the bootstrap method is better suited for large samples, because one can use a number b that is significantly smaller than N and calculate only b averages of N quantities.

In Fig. 2.6 we consider the naive estimator, the Jackknife estimator and the bootstrap estimator for the error of the mean of the function $f(x) = x^2$ if drawing N samples from a uniform distribution between 0 and 1. Clearly $\mu_{\langle x \rangle} = 0.5$ and $\sigma_{\langle x \rangle} = (12N)^{-1/2}$, which implies that $\mu_{\langle f \rangle} = f(\mu_{\langle x \rangle}) = 0.25$, and using the usual error propagation one finds that

$$\sigma_{\langle f \rangle} = \left| \frac{\partial f}{\partial x} \right|_{x=\mu_{\langle x \rangle}} = \frac{1}{\sqrt{12N}}\tag{2.67}$$

One can see that the naive estimator (2.63) clearly overestimates the actual error, whereas the Jackknife and the bootstrap estimators (2.65) and (2.66) estimate the error of the mean correctly.

Mixing and autocorrelation time

Another important source of errors for Markov chain Monte Carlo simulations is the mixing time into equilibrium and the autocorrelation between successive measurements. In order to get correct results from the simulation, one must know on the one hand how many steps one has to perform at the beginning of the simulation until the Markov chain can be considered to be in equilibrium (mixing time), and how many steps one has to perform between two successive measurements so that these measurements can be treated as independent (autocorrelation time). In Fig. 2.7 we show a sample simulation run for a one-dimensional Ising model at $\beta J = 1.0$ to demonstrate the two timescales.

Intuitively speaking, the mixing time is the number of steps that are needed until the Markov chain can be considered in equilibrium, or equivalently as the number of steps that has to be done in order to loose all



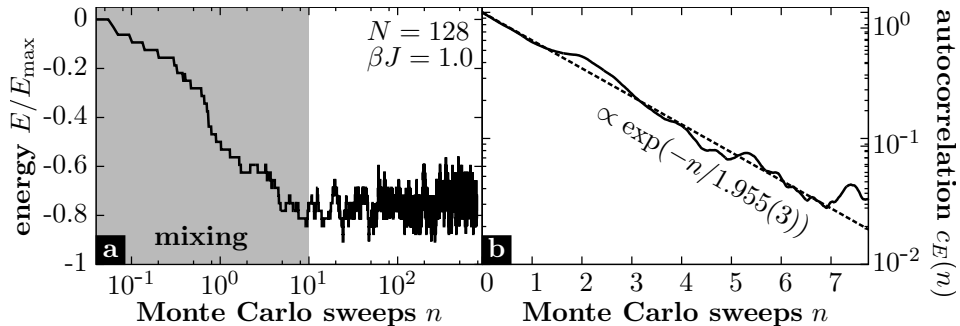


Figure 2.7: Mixing and autocorrelation time in Markov chains.

We consider a Metropolis Monte Carlo simulation for a one-dimensional ferromagnetic Ising model with $N = 128$ spins at temperature $\beta J = 1.0$ in terms of the number of sweeps n , which is the number of elementary spin flips divided by the system size N . In all cases we use only one independent simulation run starting from a random spin configuration. (a) Energy of the system in terms of the number of sweeps n . One sees that for $n < 10^2$ the energy of the system approaches the actual expectation value (mixing), and fluctuates around the expectation value only for $n > 10^2$. (b) Relative autocorrelation function (2.68) in terms of the number of sweeps n after relaxation. The dashed line is an exponential fit with autocorrelation time $\tau = 1.955 \pm 0.003$.

information of the initial state in the Markov chain. Taking measurements only makes sense after this mixing time, because otherwise the (arbitrary) initial state would influence the results of the simulations. Mathematically the mixing time is defined as the time after which the maximal deviation of the actual distribution from the stationary one is smaller than a certain threshold [279, Chap. 4]. Because the mixing time is difficult to measure within simulations, and because analytical calculations of the mixing times for general systems are rare, we restrict ourselves to inspecting plots like Fig. 2.7a to be sure to relax our systems longer than the mixing time.

The second possible source of problems is the autocorrelation, which is numerically much easier to calculate compared with the mixing time. For the rest of this section we follow Ref. [85, Sec. 4.1]. Suppose that we measure the observable x_i at times i . The autocorrelation function of the observable is then defined as

$$C_x(t) := (\langle x_i x_j \rangle - \langle x_i \rangle \langle x_j \rangle)_{j-i=t} = \langle x_0 x_t \rangle - \langle x \rangle^2, \quad (2.68)$$

one often uses the relative autocorrelation function $c_x(t) = C_x(t)/C_x(0)$, where $C_x(0) = \text{Var}(x)$. For large t the autocorrelation function shows an



exponential decay

$$C_x(t) \propto \exp\left(-\frac{t}{\tau}\right), \quad (2.69)$$

which defines the autocorrelation time τ . Note that in general the autocorrelation function $C_x(t)$ as well as the autocorrelation time τ does depend on the considered observable x (e.g., the relaxation time $\tau_{|m|}$ for the absolute value of magnetization in the 2d Ising model is much longer than the time τ_E for the energy).

In general one should take measurements in intervals that are much larger than the autocorrelation time. There can be situations where this is not possible within a reasonable simulation time, especially if the autocorrelation time is very large. In these situations one has to take the autocorrelation function into account for the calculation of the simulation errors. It can be shown that the autocorrelation time relates the error of correlated x_i and the error of totally uncorrelated measurements by

$$\sigma_{\langle x \rangle}^2 = \frac{\sigma^2}{N} \left[1 + 2 \sum_{t=1}^{N-1} \left(1 - \frac{t}{N} \right) c_x(t) \right], \quad (2.70)$$

where the fraction σ/\sqrt{N} is the error if one assumes uncorrelated outcomes. The quantity

$$\tau_{\text{int}} := 1 + 2 \sum_{t=1}^{N-1} \left(1 - \frac{t}{N} \right) \frac{C_x(t)}{C_x(0)} \xrightarrow{N \rightarrow \infty} 1 + 2 \sum_{t=1}^{\infty} c_x(t) \quad (2.71)$$

is also called integrated autocorrelation time and relates the uncorrelated error with the actual error taking into account the correlations. The measurement of the integrated autocorrelation time τ_{int} is difficult, because $c_x(t) \rightarrow 0$ for large t , but with non-vanishing error or noise. So one considers the cut integrated autocorrelation time $\tau_{\text{int}}(t')$ by introducing t' as upper bound for the summation in (2.71) and looks for a plateau at some t' , which is then used as integrated autocorrelation time.

2.2.5 Phase transitions in Monte Carlo simulations

Phase transitions are one of the most important and interesting topics in statistical physics, as already described in Sec. 2.1.6. Naturally one is also interested in phase transitions within systems that cannot be solved analytically, which are then often examined numerically using Markov chain Monte Carlo simulations. These examinations are restricted to finite system sizes,



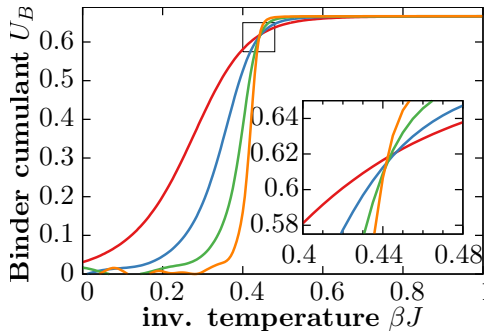


Figure 2.8: Binder cumulant (2.73) for the ferromagnetic 2d Ising model in terms of the inverse temperature β for system sizes 4×4 , 8×8 , 16×16 and 32×32 . The inset shows a zoom towards the intersection point of the curves.

less because of the finite memory of the computer, but because of the limited computation time. This is a fundamental problem for locating and examining phase transitions, because they only occur in the thermodynamic limit, i.e., for infinite system sizes, because for finite systems the thermodynamic potentials are always smooth functions of the relevant parameters.

In this section we describe several possibilities how to overcome these problems and how to find and analyse phase transitions using Monte Carlo simulations. One of the most important tasks is to discriminate between a continuous and a discontinuous phase transition, and how to calculate the critical exponents of the transition.

As an example system we use the two-dimensional ferromagnetic Ising model on an integer lattice. This system is known to exhibit a (temperature driven) continuous phase transition for $\beta_c J \approx 0.441$ and $H = 0$ and a discontinuous phase transition driven by the external field H for $\beta > \beta_c$ (compare Sec. 2.1.7). The calculations were done by first using the Wang-Landau algorithm for determining the density of states $g(E)$ and then perform a multicanonical sampling to calculate the microcanonical expectation values $\langle m^k \rangle_{\text{mc}}(E)$ of the moments of the specific magnetization m (compare Sec. 2.2.2).

Critical temperature and binder cumulant

Due to Monte Carlo simulations on a computer restricted to finite system sizes, the determination of the (inverse) critical temperature β_c is difficult because of the transition being smeared out. The simplest possibility is to define the location of the maxima of certain derivatives of thermodynamic observables as the quasi-critical temperature $\beta_c(L)$ for the considered linear system size L . For discontinuous phase transitions and for continuous phase transitions with divergences one considers the second derivatives of



the associated thermodynamic potential (e.g., the magnetic susceptibility or the heat capacity), for other continuous phase transitions one has to use the third derivatives of the potential. Empirically one finds that the quasi-critical temperatures calculated using this method scale like [269, Eq. (4.13b)]

$$\beta_c(L) = \beta_c + \lambda L^{-1/\nu}(1 + b \cdot L^{-w}), \quad (2.72)$$

where β_c is the true critical temperature, ν is the critical exponent of the correlation length, λ and b are parameters that depend on the observable used to determine the critical temperature and w is a parameter that depends only on the system [269, Sec. 4.2.3.2]. All these five parameters can be determined using a least-square fit in order to calculate β_c .

Another way to determine the critical temperature is using the Binder cumulant [95]

$$U_L := 1 - \frac{\langle \mathcal{O}^4 \rangle}{3\langle \mathcal{O}^2 \rangle^2}, \quad (2.73)$$

which measures the deviation of the probability distribution of the observable \mathcal{O} from a Gaussian shape. If the observable \mathcal{O} is an order parameter (e.g., the magnetization m in the usual Ising setup), the Binder cumulant vanishes for $\beta \rightarrow 0$, because here the order parameter is Gaussian distributed, so that $\langle m^4 \rangle = 3\langle m^2 \rangle^2$. For $\beta \rightarrow \infty$ the order parameter takes the value $m = 0$, so $\langle m^4 \rangle = \langle m^2 \rangle^2$ and $U_L \rightarrow 2/3$. For $L \rightarrow \infty$ these values are valid for all $\beta < \beta_c$ and $\beta > \beta_c$, respectively [95]. In Fig. 2.8 the temperature dependence of the Binder cumulant is displayed for different lattice sizes in a two-dimensional Ising system.

The advantage of using the Binder cumulant compared with the maxima of some susceptibilities is that for different L the Binder cumulants $U_L(\beta)$ intersect at the common point $U(\beta_c)$ which does not depend on L up to minor corrections, which are much smaller than the finite size corrections (2.72) of the observable maxima [269, Sec. 4.2.3.2]. In practice one calculates the Binder cumulant for different linear system sizes L and uses their intersection for neighboring L to get different values of β_c that can be extrapolated to the actual value.

The Binder cumulant can also be used for calculating the critical exponent ν of the correlation length in Eq. (2.22e) by [269, Eq. (4.14)]

$$\frac{\partial U_L}{\partial \beta} \propto L^{1/\nu} (1 + bL^{-w}), \quad (2.74)$$

which is essential for calculating other critical exponents using finite size scaling.



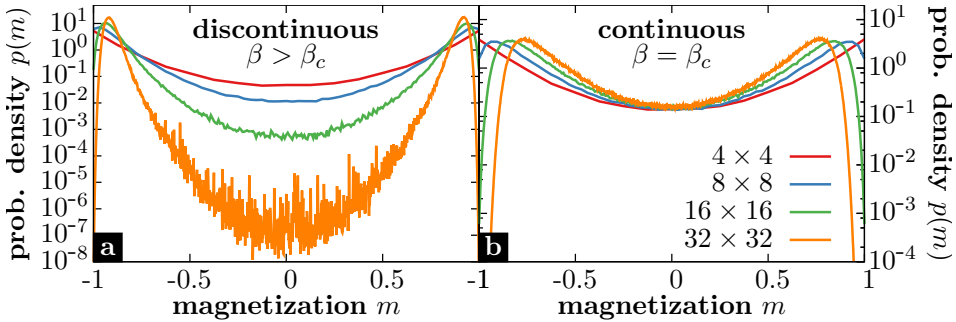


Figure 2.9: Probability density of observables for discontinuous and continuous phase transitions.

Probability density $p(m)$ for the occurrence of a relative magnetization m for different system sizes (4×4 , 8×8 , 16×16 and 32×32) for two different inverse temperatures, for vanishing external field in a 2d Ising model. (a) Probability distribution $p(m)$ of the magnetization m at a discontinuous phase transition ($\beta > \beta_c$), there is a two-peak structure where the probability for states inbetween vanishes for increasing system size. (b) Probability distribution $p(m)$ of the magnetization m at a continuous phase transition ($\beta = \beta_c$), there is a two-peak structure where the probability for states inbetween is approximately constant for increasing system size.

Probability distributions of observables

In the previous section we saw that the Binder cumulant (2.73) of the order parameter can be used for locating the quasi-critical temperature of continuous phase transitions for finite linear system size L . For discontinuous transitions this cumulant cannot be used, because there is usually no order parameter present. The method of choice for determining the quasi-critical temperature is to examine the distributions of the first derivatives of the thermodynamic potential that show a discontinuity at the critical point.

Consider e.g., the discontinuous transition in the two-dimensional Ising system with $\beta > \beta_c$ at $H = 0$. The probability distribution of the specific magnetization m at this transition point shows two peaks with equal height at $m = \pm m_0$, where m_0 depends on the actual inverse temperature β (compare Fig. 2.9a). For an external $H < 0$, the height of the peak at $m \approx -m_0$ increases, whereas the height of the peak at $m \approx +m_0$ decreases, and vice versa for $H > 0$.

If in contrast to the Ising model, where due to the invariance of the Hamiltonian (2.24) with respect to the transformation $H \rightarrow -H$ and $\sigma_i \rightarrow -\sigma_i$ the transition point can be located at $H = 0$, the critical value of



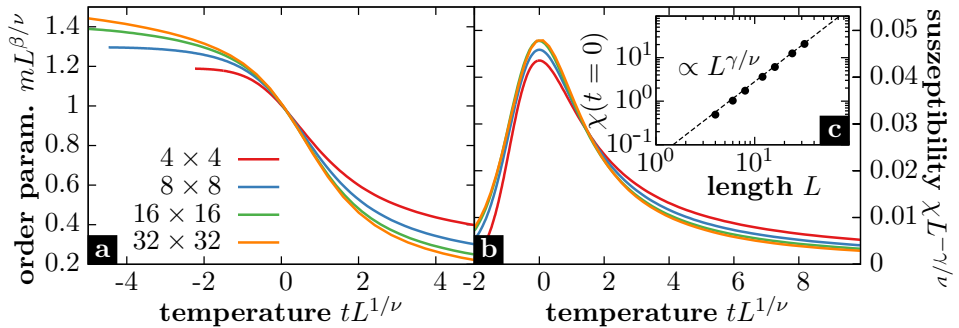


Figure 2.10: Finite size scaling and scaling functions.

(a) Order parameter m in terms of the relative temperature t in the two-dimensional Ising model for different lattice sizes (4×4 , 8×8 , 16×16 and 32×32), both quantities scaled according to Eq. (2.76b). (b) Magnetic susceptibility χ scaled according to (2.76c). In both cases the functions agree near $t \approx 0$, as predicted by the finite size scaling hypothesis. (c) Magnetic susceptibility χ at the quasi-critical point $t = 0$ in terms of the linear lattice size L , together with the prediction $\chi(t = 0) \propto L^{\gamma/\nu}$ from Eq. (2.76c).

the external parameter is unknown, the observable distribution can be used for its determination. The quasi-critical value at the corresponding system size can be found by tuning the two peaks to equal weight [98, Remark (vii)].

The distribution of the relevant observable can also be used for discriminating between discontinuous and continuous phase transitions. In fact one can find similar two-peak structures also at continuous transitions (compare Fig. 2.9b), but the probability density for the value between the two peaks is constant if increasing the system size for continuous transitions. In contrast, the probability decreases if increasing the system size for discontinuous phase transitions. Note that this is also the reason why Metropolis(-like) algorithms are difficult to use near discontinuous transitions, because the probability for intermediate states between the peaks effectively vanishes, which pins the simulation to one of the peaks.

Finite size scaling and critical exponents

It was already derived in Sec. 2.1.6, Eq. (2.22e) that the correlation length diverges as $\xi(t) = \xi_0 t^{-\nu}$ near the critical point for continuous transitions, where t is the reduced temperature and ν is the associated critical exponent. Let L be the linear length scale of the system, then it is obvious that $\xi(t) = L$ or equivalently $t_L := (L/\xi_0)^{-1/\nu}$ is an important point for the



behavior of the system. For reduced temperatures $t \gg t_L$ or $\chi(t) \ll L$ the finite system size does not influence the behavior of the system much, whereas for $t \ll t_L$ or $\chi(t) \gg L$ the finite system size becomes important, because the correlation length and therewith long-range correlations are bounded by the linear system size L .

This result, together with the observation that near for $\beta \approx \beta_c$ the correlation length is the only relevant length scale of the system, one can conclude that near the critical point the free energy $F(T, L)$ of the system should behave as [269, Eq. (4.9)]

$$F(T, L) \propto L^{-(2-\alpha)/\nu} f\left(\frac{L}{\xi(t)}\right) = L^{-(2-\alpha)/\nu} f\left(tL^{1/\nu}\right), \quad (2.75)$$

for vanishing external field, where $f(x)$ a scaling function, and α is the critical exponent of the heat capacity defined in (2.22a). Eq. (2.2.5) is also denoted as *finite size scaling hypothesis*. This implies for the other quantities (2.22) [269, Eq. (4.10)]

$$C_H = L^{\alpha/\nu} C_H^{(0)}\left(tL^{1/\nu}\right) \quad (2.76a)$$

$$M = L^{-\beta/\nu} M^{(0)}\left(tL^{1/\nu}\right) \quad (2.76b)$$

$$\chi = L^{\gamma/\nu} \chi^{(0)}\left(tL^{1/\nu}\right), \quad (2.76c)$$

where $C_H^{(0)}$, $M^{(0)}$ and $\chi^{(0)}$ denote the scaling functions of the respective quantities. Intuitively this means that if plotting $M \cdot L^{\beta/\nu}$ in terms of $tL^{1/\nu}$ the near $t = 0$ the curves collapse for all (sufficiently large) L , which is displayed in Fig. 2.10.

The finite size scaling approach can be used for determining the (relative) critical exponents α/ν , β/ν and γ/ν by plotting the maxima of the observables (2.76) in terms of L and fitting a power-law behavior (compare Fig. 2.10c), because at $t = 0$ Eqs. (2.76) become

$$C_H(t=0) \propto L^{\alpha/\nu} \quad M(t=0) \propto L^{-\beta/\nu} \quad \chi(t=0) \propto L^{\gamma/\nu}. \quad (2.77)$$

So for calculating the actual critical exponents, the exponent ν has to be calculated otherwise, e.g., using (2.74).

It is also possible to use finite size scaling for discontinuous phase transitions. In these cases not the linear length L of the system, but the volume L^d of the system is the relevant scaling parameter. For a more detailed discussion see Ref. [269, Sec. 4.2.3.3].



2.3 Details about Wang-Landau simulations

In this section we list the work done about the Wang-Landau algorithm in general. We first examine the optimal choice of the flatness criterion f and the modification factor multiplier δm in order to minimize the statistical error of the results and the simulation time needed. Second we derive an analytical approximation of the number of steps that are necessary within the Wang-Landau algorithm for the incidence histogram $H(E)$ to become flat, in terms of the number of bins b and the flatness criterion f . The last part of this section is the presentation of the approximate counting method that is based on the Wang-Landau algorithm and that one can use to estimate the number of states in arbitrary systems.

2.3.1 Optimal choice of parameters

In this subsection we examine the influence of the choice of the flatness criterion f and the modification factor multiplier δm on the statistical and the systematic error of Wang-Landau sampling as well as its influence on the simulation time. Therefor we consider a one-dimensional Ising chain with $L = 32$ spins and periodic boundary conditions without external magnetic field. The possible energy levels of such a system are $E = -L, -L + 4, \dots, L$, and the density of states is given by

$$g(E = -L + 4m) = \binom{L}{2m} = \binom{L}{(E+L)/2} \text{ with } m \in \mathbb{N}_0. \quad (2.78)$$

e performed 400 independent Wang-Landau simulations starting with modification factor $m_i = \exp(1)$ until the modification factor $m_f = \exp(10^{-8})$ was reached. The calculated DOS were normalized with the known value $g(E = -L) = 2$ for the ground state.

As a measure for the statistical error we use

$$\epsilon_{\text{stat}} := \left\langle \frac{\sigma_{S(E)}}{\mu_{S(E)}} \right\rangle_E, \quad (2.79)$$

where $\sigma_{S(E)}$ is the standard deviation of the distribution of the microcanonical entropy $S(E) = \log g(E)$ that was obtained from 400 independent runs, and $\mu_{S(E)}$ is its expectation value. The ratio is then averaged over all energy values E . Note that we explicitly used the standard deviation $\sigma_{S(E)}$ of the distribution, and not the standard error $\sigma_{\langle S(E) \rangle} = \sigma_{S(E)} / \sqrt{N - 1}$, where N is the number of independent simulation runs, because the relevant factor is



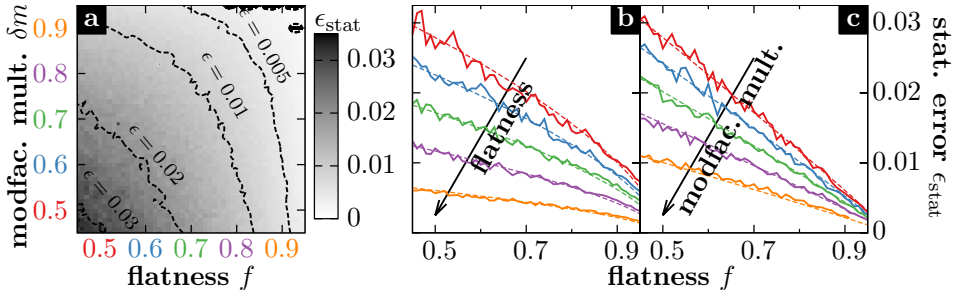


Figure 2.11: Parameter-dependence of the statistical error in WL simulations.

Statistical error ϵ_{stat} (2.79) of the Wang-Landau algorithm with respect to the flatness criterion f and the multiplier δm of the modification factor for a one-dimensional Ising chain with 32 spins. (a) Colorplot of the statistical error with respect to both f and δm , the dashed lines are (smoothed) isolines for the depicted values of the relative standard deviation. (b,c) Statistical error for different constant f (b) and constant δm (c), the constant values are in each plot from top to bottom $f, \delta m = 0.5, 0.6, 0.7, 0.8$ and 0.9 . The dashed lines are the fitted function (2.81).

the width of the result distribution, and not the error of the obtained mean (which furthermore would also depend on N).

The results of the calculations are depicted in Fig. 2.11 as a colorplot in terms of both f and δm and separately for both variables with the other quantity fixed. As expected, the statistical error grows for both smaller f and smaller δm , and the expected limits

$$\lim_{f \rightarrow 1} \epsilon_{\text{stat}}(f, \delta m) = \lim_{\delta m \rightarrow 1} \epsilon_{\text{stat.}}(f, \delta m) = 0$$

can be found. To quantify the results we construct a functional dependency that matches the expected limits and fit the free parameters. We have to choose a function that is 0 for $f = 1$, $\delta m = 1$ or both, so the most simple choice is

$$\epsilon_{\text{stat}}(f, \delta m) = a \cdot (1 - f)^b \cdot (1 - \delta m)^c. \quad (2.80)$$

Fitting this function with respect to the calculated data gives

$$\epsilon_{\text{stat}}(f, \delta m) \approx 0.0836(2) \cdot (1 - f)^{0.949(2)} \cdot (1 - \delta m)^{0.634(2)}, \quad (2.81)$$

comparing this result to the numerical data in Fig. 2.11 shows that this fit produces the correct qualitative behavior both for $f = \text{const.}$ and $\delta m = \text{const.}$



Beside the statistical error an important question is whether the systematic error of Wang-Landau sampling does alter the results significantly. As measure for the systematic error ϵ_{sys} , we use

$$\epsilon_{\text{sys}} := \left\langle \frac{|\mu_{S(E)} - S_{\text{exact}}(E)|}{\sigma_{S(E)}} \right\rangle_E, \quad (2.82)$$

which is the absolute difference of the calculated expectation and the exact value of the microcanonical entropy in units of the calculated standard deviation, averaged over all energy bins. The result in terms of the flatness condition f and the modification factor multiplier δm are depicted in Fig. 2.12. For high enough f and δm the systematic error is approximately 0.1, which the actual value lies within a $0.1\sigma_{S(E)}$ interval around the calculated value. On the first look this seems to be a very low systematic error, but remember that we measured the systematic error in units of the standard deviation $\sigma_{S(E)}$ and not in units of the standard error $\sigma_{\langle S(E) \rangle}$ of the mean. Since for these result 400 calculations were performed, the exact value lies only in the $2\sigma_{\langle S(E) \rangle}$ interval around the calculated value.

One can also measure the systematic error in units of the exact value

$$\epsilon'_{\text{sys}} := \left\langle \frac{|\mu_{S(E)} - S_{\text{exact}}(E)|}{S_{\text{exact}}(E)} \right\rangle_E, \quad (2.83)$$

so that it measures the relative error of the calculations. For $f = 0.8$ and $\delta m = 0.9$, a choice of parameters often used throughout this thesis, the relative error lies at approximately 10^{-4} , which is very good value. In contrast, for the choice $\delta m = 0.5$ as suggested in Refs. [406, 407] the relative error is around 8 times higher.

A fit of the systematic error measured in units of the standard deviation was not possible because of the noise in the data.

The other relevant factor in choosing the simulation parameters f and δm is the simulation time: the higher both parameters, the longer the simulation. The simulation time is measured in the number of sweeps, where one sweep consists of L proposed (not necessarily accepted) steps. There are two possibilities for measuring the simulation time t : On the one hand one can count the necessary sweeps for reaching the final modification factor m_f , resulting in the simulation time t_f . On the other hand one measure t_{sat} , which is the number of sweeps until the saturation of errors is reached. The former possibility is accessible rather simply, for the other one needs to determine when the saturation of error is reached. We define this as the point of time after which the statistical error is below 1.05 the statistical



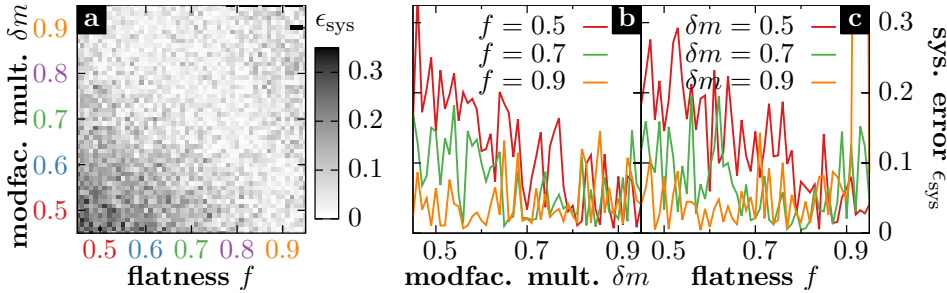


Figure 2.12: Parameter-dependence of the systematical error in WL simulations.

Systematic error ϵ_{sys} (2.82) of the Wang-Landau algorithm with respect to the flatness criterion f and the multiplier δm of the modification factor for a one-dimensional Ising chain with 32 spins. (a) Colorplot of the systematic error with respect to both f and δm . (b,c) Systematic error for different constant f (b) and constant δm (c), the constant values are in each plot from top to bottom $f, \delta m = 0.5, 0.7$ and 0.9 .

error at the final modification factor m_f . The results for both t_f and t_{sat} are displayed in Fig. 2.13.

As for the statistical error it is also possible to use a fit for describing the simulation time in terms of f and δm . In contrast to the error, one expects that $t \rightarrow \infty$ for $f \rightarrow 1$ or $\delta m \rightarrow 1$, because in the first case one would need a totally flat incidence histogram, which is almost impossible to get because of statistical fluctuation, and in the second case the modification factor will not be decreased. In principle one can imagine two simple functional dependencies

$$t(f, \delta m) = a \cdot (1 - f)^b \cdot (1 - \delta m)^c \quad (2.84a)$$

$$t(f, \delta m) = a \left[(1 - f)^b + (1 - \delta m)^c \right] \quad (2.84b)$$

(with $b < 0$ and $c < 0$) that match these limits, but comparing the respective fits with the obtained data shows that Eq. (2.84b) describes the data way better. Our fit results for both times are

$$t_f(f, \delta m) = 4.993(6) \left[(1 - f)^{-0.2272(9)} + (1 - \delta m)^{-0.116(1)} \right] \quad (2.85a)$$

$$t_{\text{sat}}(f, \delta m) = 4.435(4) \left[(1 - f)^{-0.2660(6)} + (1 - \delta m)^{-0.1695(8)} \right]. \quad (2.85b)$$

Until now we identified the dependence of the statistical and the systematic error as well as of the necessary simulation sweeps on the flatness



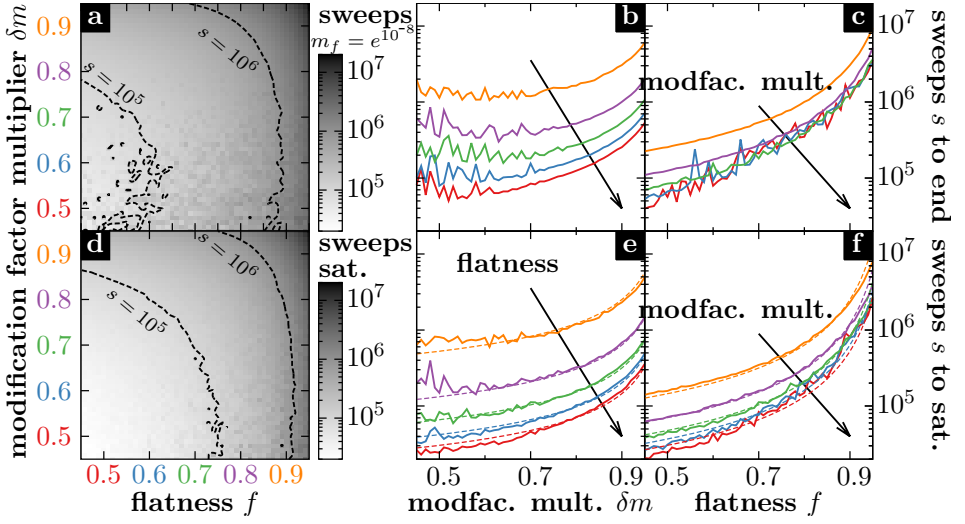


Figure 2.13: Parameter-dependence of the simulation time in Wang-Landau simulations.

Simulation time measured in units of system sweeps for Wang-Landau simulation of a 32 spin Ising chain in terms of the flatness and the modification factor multiplier. The upper row of plots (a-c) shows the simulation time necessary for reaching a final modification factor of $\log m_f = 10^{-8}$, the lower row of plots (d-f) shows the simulation time necessary to reach the saturation of error. (a,d) Colorplot of the simulation time in unit of system sweeps with respect to both f and δm . (b,c,e,f) Simulation time for different constant f (b,e) and constant δm (c,f), the constant values are in each plot from top to bottom $f, \delta m = 0.5, 0.6, 0.7, 0.8$ and 0.9 .



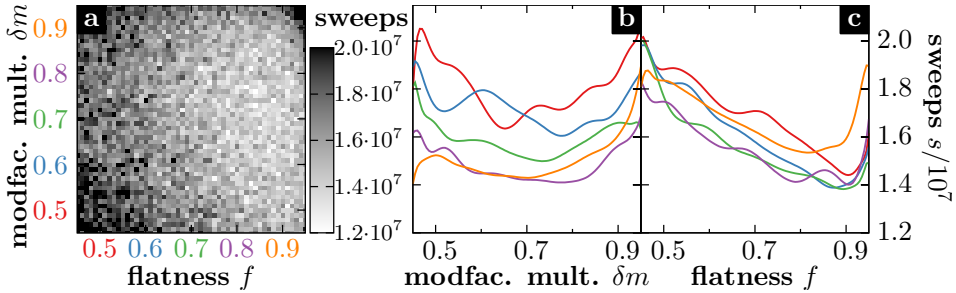


Figure 2.14: Optimal choice of parameters in WL simulations.

Minimal number of sweeps to reach a statistical standard error of $s < 10^{-3}$ for Wang-Landau sampling of a 32 spin Ising chain in terms of the flatness f and the modification factor modifier δm . For each pair of f and δm we already chose the optimal final modification factor m_f . (a) Colorplot of the number of minimal sweeps with respect to both f and δm . (b,c) Minimal number of sweeps for different constant f (b) and constant δm (c), the constant values are in each plot from top to bottom $f, \delta m = 0.5, 0.6, 0.7, 0.8$ and 0.9 . Here the curves are smoothed using Bezier curves to suppress the noise.

criterion f and the modification factor modifier δm . For efficient simulations, one wants both small errors and low simulation time, but these are two contrary goals. So one needs to introduce a measure for the efficiency of the simulation and search for combinations of the parameters f , δm and m_f so that this measure is optimal. We propose the quantity

$$T(s, f, \delta m, m_f) := t(f, \delta m, m_f) \cdot \left[1 + \left(\frac{\sigma_{\text{stat.}}(f, \delta m, m_f)}{s} \right)^2 \right]$$

as measure for (in)efficiency. It is the number of independent runs N_s that has to be performed to get a statistical error less than s , multiplied with the average number of sweeps $t(f, \delta m, m_f)$ necessary for one simulation. In Fig. 2.14 one can find $T(10^{-3}, f, \delta m)$, where for each pair of parameters the optimal final modification factor m_f was already chosen. For the considered system of a 32 spin Ising chain one can conclude that one should use a flatness $0.85 \leq f \leq 0.9$ for optimal performance, whereas the modification factor modifier has less influence on the performance of the simulation, its optimal value at the considered flatness is $0.6 \leq \delta m \leq 0.85$. Note that this choice of parameters is only a hint, and the optimal parameters can change if one considers other systems. If it is not possible to do a similar pretest for small system sizes as in this section, one should in general choose the parameters more conservative.



2.3.2 Dependence of the runtime on bin-number and flatness criterion

In the Wang-Landau simulations done within this thesis it was observed that the number of steps that is necessary until the histogram $H(E)$ becomes flat does depend strongly on the number b of energy bins used and the flatness criterion f applied. Unfortunately in the literature there is no estimation of the influence of the number of bins on the runtime of the algorithm. So in this section we want to give an estimation for this quantity.

In our considerations we neglect that the Wang-Landau simulation modifies the density of states (DOS) and therewith the acceptance probabilities. This approximation is valid especially in the last stages of the simulation with small modification factor. Consider now a simulation with b energy levels E_1, \dots, E_b . The probability to find the energy level E_i in the simulation is given by

$$p_i \propto \frac{g_{\text{exact}}(E_i)}{g_{\text{WL}}(E_i)}, \text{ with } \sum_i p_i = 1$$

where $g_{\text{exact}}(E_i)$ is the exact value of the DOS at energy bin E_i , and $g_{\text{WL}}(E_i)$ is the current value of the DOS in the Wang-Landau simulation. The histogram $H(E)$ of visited energies is considered as flat, if $\min H(E) > f \cdot \text{avg} H(E)$, with $0 < f < 1$. This means that after N steps the condition $H(E_i) > fN/b$ has to be fulfilled for every bin. In the following we estimate analytically the average number $\langle N \rangle$ of steps that are necessary to fulfill the flatness criterion, furthermore we present numerical data that supports our estimation.

We consider two different situations: First we examine the dependence of $\langle N \rangle$ for $p_i = p = 1/b$, i.e. that the algorithm samples with respect to the exact DOS. Later we consider sampling to a DOS with errors, which is similar to an actual DOS obtained in a simulation, so that we obtain a probability $p_i = (1 + \delta p_i)/b$.

The considered problem is related with the coupon collector problem or the double dixie cup problem. One can proof [313] that the waiting time for having visited every bin m times is

$$\langle N \rangle = b \log b + (m - 1) \cdot b \log \log b + C_m + \mathcal{O}(1)$$

But this cannot be applied to our problem directly, because m has to be a fixed number here, but in our case we have that m does depend on N because we choose $m = f \cdot N/b$.



Calculations for exact DOS

Denote by $p_f(N)$ the probability that the histogram of the Wang-Landau simulation is flat after doing N steps (that will be calculated in different ways later), and by $p_{\text{nf}}(N) = 1 - p_f(N)$ the probability that the histogram is not flat after doing N steps. Then the probability

$$P_{\text{ff}}(N) := \prod_{n=1}^{N-1} p_{\text{nf}}(n)p_f(N) \quad (2.86)$$

is the probability that the histogram is flat after N times for the first time (i.e. the histogram is flat after N steps, but is not flat at all other steps before). In this section we want to calculate the average number of steps that is necessary to make the histogram flat, which is defined as

$$\langle N \rangle = \sum_{N=1}^{\infty} N P_{\text{ff}}(N) = \sum_{N=1}^{\infty} N \prod_{n=1}^{N-1} p_{\text{nf}}(n)p_f(N) \quad (2.87)$$

Depending on the actual form of $p_f(N)$, calculating the average $\langle N \rangle$ can be difficult. In these situations it can be more easy to calculate the location N_{max} of the maximum of the probability distribution $P_{\text{ff}}(N)$ and use it as an estimate for $\langle N \rangle$. Note that N is a discrete variable, so one cannot simply derive the distribution $P_{\text{ff}}(N)$ with respect to N and calculate the roots to locate the maximum.

An alternative for locating the maximum of the distribution is to find the root of the discrete differential

$$\Delta P_{\text{ff}}(N) := P_{\text{ff}}(N + 1) - P_{\text{ff}}(N) \stackrel{!}{=} 0$$

and use them as approximative values for N_{max} . The discrete differential can be calculated as

$$\begin{aligned} \Delta P_{\text{ff}}(N) &= \prod_{n=1}^N p_{\text{nf}}(n)p_f(N + 1) - \prod_{n=1}^{N-1} p_{\text{nf}}(n)p_f(N) \\ &= \prod_{n=1}^{N-1} p_{\text{nf}}(n) [p_{\text{nf}}(N)p_f(N + 1) - p_f(N)] \end{aligned}$$

The first terms of the product do not have a root (because $p_{\text{nf}}(n) \neq 0$), so we have to find the solution to the equation

$$p_{\text{nf}}(N)p_f(N + 1) = p_f(N) \quad (2.88)$$



This equation can be written also only in terms of the probabilities p_f as

$$\frac{1}{p_f(N)} - \frac{1}{p_f(N+1)} = 1 \quad (2.89)$$

In the following we describe different approaches for actually calculating the probability $p_f(N)$ for the histogram to be flat after N steps:

- The multinomial probability distribution, which gives the exact description of the considered process
- The multivariate Gaussian distribution, which approximates the multinomial distribution with continuous, dependent random variables
- The Gaussian distribution, which neglects the covariance between the random variables of the multivariate distribution, so it approximates the multinomial distribution with continuous, independent random variables

Afterwards we compare these analytical estimations with numerically obtained data.

Multinomial flatness probability The multinomial distribution with probability density

$$P_{\text{mn}}(n_1, n_2, \dots, n_k) := \binom{N}{n_1, \dots, n_k} \cdot p_1 \cdot p_2 \cdot \dots \cdot p_k,$$

describes the probability that after $N = \sum_i n_i$ executions of a random experiments, that has k possible outcomes with probability p_i each (normalization $\sum_i p_i = 1$), n_i executions resulted in the i -th outcome [174, Chap. 30]. Here the multinomial is the generalization of the binomial and defined as

$$\binom{N}{n_1, \dots, n_k} := \frac{N!}{n_1! \cdot \dots \cdot n_k!} \delta_{N, \sum_i n_i}.$$

The probability that the histogram is flat after N steps is then given by

$$\begin{aligned} p_{f,\text{mn}}(N) &= \sum_{n_1 \geq f \cdot p \cdot N} \dots \sum_{n_b \geq f \cdot p \cdot N} P_{\text{mn}}(n_1, \dots, n_b) \\ &= P_{\text{mn}}(n_1 \leq f \cdot p \cdot N, \dots, n_b \leq f \cdot p \cdot N) \end{aligned}$$



This probability is not a cumulative distribution function (CDF)

$$F_{\text{mn}}(n_1, \dots, n_k) := \sum_{m_1 \leq n_1} \cdots \sum_{m_k \leq n_k} P_{\text{mn}}(m_1, \dots, m_k)$$

of the multinomial distribution, but it can be written in terms of the CDF. Using some basic formulas from statistic one can calculate

$$\begin{aligned} P_{\text{mn}}(m_1 \geq n_1, \dots, m_k \geq n_k) &= P_{\text{mn}}(m_1 \geq n_1 \cap \cdots \cap m_k \geq n_k) \\ &= 1 - P_{\text{mn}}(m_1 \leq n_1 \cup \cdots \cup m_k \leq n_k) = \\ &= 1 - \sum_{i_1} P_{\text{mn}}(m_{i_1} \leq n_{i_1}) + \sum_{i_1} \sum_{i_2 > i_1} P_{\text{mn}}(m_{i_1} \leq n_{i_1} \cup m_{i_2} \leq n_{i_2}) - \\ &\quad \cdots \pm \sum_{i_1} \cdots \sum_{i_k > i_1, \dots, i_{k-1}} P_{\text{mn}}(m_{i_1} \leq n_{i_1} \cup \cdots \cup m_{i_k} \leq n_{i_k}) \end{aligned}$$

Note that all the probabilities in the last step can be written in terms of the CDF, because the arguments that are not present can also be denoted as $m_j < N$. In our case (all n_i and all p are the same) this can be expressed in the following way:

$$P_{\text{mn}}(m_1 \geq fNp, \dots, m_b \geq fNp) = \sum_{i=0}^b \binom{b}{i} (-1)^i F_{\text{mn}}(n_1, \dots, n_k, N, \dots, N)$$

Calculating the CDFs of the multinomial distribution directly is possible, but does not lead to an analytical approximation of N_{max} . Furthermore even calculating the CDF numerically consumes too much computation time for large b . There is a representation of the multinomial CDF in terms of several CDFs of the (truncated) Poisson distribution [278], but also this representation does not lead to suitable analytical approximations of N_{max} , additionally it is numerically unstable.

Multivariate Gaussian flatness probability The exact form of the multinomial distribution is not suitable for an analytical estimation of the dependence of the runtime on the number of bins. One possibility is to approximate the multinomial distribution with the multivariate normal distribution, which describes a distribution of several normal distributed variables with covariance. As in the binomial distribution, the expectation value of H_i is $E(H_i) = Np$, the variance is $\text{Var}(H_i) = Np(1-p)$, and the covariance between two bins is $\text{Cov}(H_i, H_j) = -Np^2$ for $i \neq j$ [174, Chap. 30]. So let

$$\Sigma_{ij} := \begin{cases} Np(1-p) & i = j \\ -Np^2 & i \neq j \end{cases}$$



the $b \times b$ covariance matrix of the H_i with inverse matrix⁵

$$\Sigma_{ij}^{-1} = \begin{cases} \frac{(b-1)p-1}{Np(bp-1)} & i = j \\ -\frac{1}{N(bp-1)} & i \neq j \end{cases}$$

for $p \neq 1/b$. Note that we actually have the case $p = 1/b$, so our covariance matrix is not invertible, and we cannot use the standard formula

$$P_{\text{mv}}(x_1, \dots, x_b) = \frac{1}{\sqrt{(2\pi)^b \det(\Sigma)}} \exp \left(-\frac{1}{2} \sum_{i,j=1}^b (x_i - Np) \Sigma_{ij}^{-1} (x_j - Np) \right) \quad (2.90)$$

for the probability density function of the multivariate distribution.

To cure this problem, we need all eigenvalues and eigenvectors of the covariance matrix. The eigenvectors are⁶ $v_{1,i} = 1$ for the eigenvalue $\lambda_1 =$

⁵ Proof: One has to verify that

$$\sum_j \Sigma_{ij} \Sigma_{jk}^{-1} = \delta_{ik}$$

For the case $i \neq k$ it is

$$\begin{aligned} \sum_j \Sigma_{ij} \Sigma_{jk}^{-1} &= Np(1-p) \cdot \frac{-1}{N(bp-1)} - Np^2 \cdot \frac{(b-1)p-1}{Np(bp-1)} + (b-2)Np^2 \cdot \frac{1}{N(bp-1)} \\ &= \frac{-p^2 + p^3 - p^3(b-1) + p^2 + (b-2)p^3}{p(bp-1)} = 0, \end{aligned}$$

for the case $i = k$ it is

$$\begin{aligned} \sum_j \Sigma_{ij} \Sigma_{jk}^{-1} &= Np(1-p) \cdot \frac{(b-1)p-1}{Np(bp-1)} + (b-1) \cdot Np^2 \cdot \frac{1}{N(bp-1)} \\ &= \frac{bp-1 + p^2(1-b) - p^2(1-b)}{bp-1} = 1. \quad \square \end{aligned}$$

⁶ Proof: One has to show that $\sum_k \Sigma_{ik} v_{a,k} = \lambda_a v_{a,i}$. Consider first the case $a = 1$, there one has

$$\sum_k \Sigma_{ik} v_{1,k} = \sum_k \Sigma_{ik} = Np(1-p) - (b-1)Np^2 = (1-bp) \cdot Np = \lambda_1 v_{1,i}.$$

For the case $a \neq 1$ one performs a case by case analysis for i . Let first $i = 1$, then

$$\sum_k \Sigma_{1k} v_{a,k} = \Sigma_{11} v_{a,1} + \Sigma_{1a} v_{a,a} = -Np(1-p) - Np^2 = -Np = Np \cdot v_{a,1}$$

Let second $i = a$, then

$$\sum_k \Sigma_{ak} v_{a,k} = \Sigma_{a1} v_{a,1} + \Sigma_{aa} v_{a,a} = Np^2 + Np(1-p) = Np = Np \cdot v_{a,a}$$



$(1 - bp) \cdot Np$ and

$$v_{a,i} = \begin{cases} 1 & i = -1 \\ 1 & i = a \\ 0 & \text{otherwise} \end{cases}$$

with $a \neq 1$ for the eigenvalues $\lambda_a = Np$. We now calculate within the eigensystem of the covariance matrix and use only the linear independent degrees of freedom. This means that we only consider the space spanned by the eigenvectors \vec{v}_a with $a \neq 1$. One can understand this also intuitively: The first eigenvalue corresponds to the sum of all random variables H_i , which are constrained to be N . Outside of this hyperplane the probability density vanishes.

Let S be the orthonormal matrix of the eigenvectors of Σ^{-1} , so that $\Sigma^{-1} = SDS^{-1}$ with D being the diagonal matrix of the eigenvalues. The matrix and its inverse are given by

$$S = \frac{1}{\sqrt{b}} \begin{pmatrix} 1 & -\vec{1}^t \\ \vec{1} & \mathbb{1}_{b-1} \end{pmatrix} \quad S^{-1} = \frac{1}{\sqrt{b}} \begin{pmatrix} 1 & \vec{1}^t \\ -\vec{1} & \mathbb{1}_{b-1} \end{pmatrix},$$

where $\mathbb{1}_{b-1}$ is the $(b-1)$ -dimensional unit matrix and $\vec{1}$ is a vector consisting of $b-1$ entries 1. Using the Gram-Schmidt algorithm leads to the orthogonal eigenbasis

$$\bar{w}_{1,i} = 1 \quad \bar{w}_{a,i} = \begin{cases} -\frac{1}{a-1} & i < a \\ 1 & i = a \\ 0 & i > a \end{cases},$$

and normalizing yields

$$w_{1,i} = 1/\sqrt{b} \quad w_{a,i} = \begin{cases} -\frac{1}{\sqrt{a \cdot (a-1)}} & i < a \\ \sqrt{\frac{a-1}{a}} & i = a \\ 0 & i > a \end{cases}.$$

We denote by R the orthonormal matrix of this eigenbasis.

Let third $i \neq 1$ and $i \neq a$, then

$$\sum_k \Sigma_{ik} v_{a,k} = \Sigma_{i1} v_{a,1} + \Sigma_{ia} v_{a,a} = Np^2 - Np^2 = 0 = Np \cdot v_{a,i}$$



Now we can calculate the desired cumulative density function in the constrained subspace

$$\begin{aligned}
 P_{\text{mv}}(x_1 \geq fNp, \dots, x_b \geq fNp) &= \\
 &= \frac{1}{(\sqrt{2\pi Np})^{b-1}} \int_{-(1-f)Np}^{N(1-p)} dx_1 \dots \int_{-(1-f)Np}^{N(1-p)} dx_b \exp \left[-\frac{1}{2} (R^t \vec{x})^t D R^t \vec{x} \right]
 \end{aligned}$$

The next step is to substitute the integration variable $\vec{y} = R^t \vec{x}$, which leads to

$$\begin{aligned}
 y_2 &= \frac{1}{\sqrt{2}} x_2 \\
 y_3 &= -\frac{1}{\sqrt{6}} x_2 + \sqrt{\frac{2}{3}} x_3 \\
 &\vdots \\
 y_a &= -\frac{1}{\sqrt{a(a-1)}} \sum_{i=2}^{a-1} x_i + \sqrt{\frac{a}{a-1}} x_a
 \end{aligned}$$

in the single components. So the cumulative distribution function results in the following integral:

$$\begin{aligned}
 P_{\text{mv}}(H_1 \geq fNp, \dots, H_b \geq fNp) &= \\
 &= \frac{1}{\sqrt{2\pi Np}^{b-1}} \int dy_2 \dots \int dy_a \exp \left[-\frac{1}{2} (\vec{y}^t D \vec{y}) \right]
 \end{aligned}$$

The solution of this multiple integral cannot be given in a closed form, because the integral boundaries of the integration variable y_a depend on the other integration variables y_i with $i < a$, resulting in integrals mixing error functions and exponentials, which cannot be solved analytically. However, a numerical solution of this integral is possible, but we do not follow this direction because we want to give simple analytical approximations.

Gaussian flatness probability Suppose that we can approximate the multinomial distribution by the distribution of b independently distributed Gaussian random variables. This neglects the covariances between the variables, which is reasonable for a large number of bins: The variance of the multinomial distribution is $Np(1-p) \approx N/b$, and the covariance is $-Np^2 = -N/b^2$. The probability $p_{\text{f,g}}(N)$ for the histogram to be flat after N steps with bin sampling probability p and flatness criterion f is then

$$p_{\text{f,g}}(N) = \left(\int_{fNp}^{\infty} dx \frac{1}{\sqrt{2\pi p(1-p)}} \exp \left[-\frac{1}{2} \frac{(x - Np)^2}{Np(1-p)} \right] \right)^b$$



Switching the integration variable to $y = x - Np$ the integral can be calculated in terms of the error function

$$\begin{aligned} p_{f,g}(N) &= \left[\frac{1}{2} - \frac{1}{2} \operatorname{erf} \left((f-1) \sqrt{\frac{Np}{2(1-p)}} \right) \right]^b \\ &= \frac{1}{2^b} \operatorname{erfc}^b \left((f-1) \sqrt{\frac{Np}{2(1-p)}} \right), \end{aligned}$$

where $\operatorname{erfc}(x) = 1 - \operatorname{erf}(x)$ is the conjugated error function. Use the asymptotic expansion

$$\operatorname{erfc}(-x) \stackrel{x \rightarrow \infty}{\approx} 2 + \exp(-x^2) \cdot \left[-\frac{1}{\sqrt{\pi}x} + \mathcal{O}\left(\frac{1}{x^3}\right) \right]$$

which is in our case valid for big \sqrt{N} , to get

$$p_{f,g}(N) \approx \left[1 - \frac{1}{1-f} \sqrt{\frac{1-p}{2\pi Np}} \exp\left(-\frac{Np(f-1)^2}{2(1-p)}\right) \right]^b.$$

Approximating $(1-x)^b \approx 1 - b \cdot x$ for $x \ll 1$ gives then

$$p_{f,g}(N) \approx 1 - \frac{b}{1-f} \sqrt{\frac{1-p}{2\pi Np}} \exp\left(-\frac{Np(f-1)^2}{2(1-p)}\right)$$

Replace now the probability p for sampling one energy bin with the inverse number $1/b$ of bins, (so that $(1-p)/p = b-1$) and assume that $b \gg 1$ so that $b-1 \approx b$. This leads to the final version of the probability for being flat after N steps in the independent Gaussian approximation

$$p_{f,g}(N) \approx 1 - \frac{b^{3/2}}{\sqrt{2\pi N}(1-f)} \exp\left(-\frac{N(f-1)^2}{2b}\right) \quad (2.91)$$

Even with this simple Gaussian approximation the direct calculation of $\langle N \rangle$ using Eq. (2.87) and the calculation of asymptotics is not possible. Instead we use Eq. (2.88) to calculate the location N_{\max} of the maximum of the probability distribution $P_{\text{ff}}(N)$. This results in

$$\begin{aligned} &1 - 2 \frac{b^{3/2}}{\sqrt{2\pi N_{\max}}(1-f)} \exp\left(-\frac{N_{\max}(f-1)^2}{2b}\right) \\ &+ \left(\frac{b^{3/2}}{\sqrt{2\pi}(1-f)} \right) \frac{1}{\sqrt{N_{\max}(N_{\max}+1)}} \exp\left(-\frac{(2N_{\max}+1)(f-1)^2}{2b}\right) = 0. \end{aligned}$$



For large N_{\max} we can approximate $\sqrt{N_{\max}(N_{\max} + 1)} \approx N_{\max}$ and $2N_{\max} + 1 \approx 2N_{\max}$, so one has to solve

$$\left[1 - \frac{b^{3/2}}{\sqrt{2\pi N_{\max}}(1-f)} \exp\left(-\frac{N_{\max}(f-1)^2}{2b}\right) \right]^2 = 0.$$

Using the Lambert-W function $W(x)$, which is defined as the inverse of $W^{-1}(x) = x \exp(x)$, the solution of this equation is

$$N_{\max} = \frac{2b}{(1-f)^2} W\left(\frac{b^2}{2\pi}\right) \approx \frac{2b(\log(b) - \log(2\pi))}{(1-f)^2}. \quad (2.92)$$

This means that for an exact known DOS the time for the incidence histogram becoming flat in one stage of a Wang-Landau simulation grows approximately as $b \log(b)$ with the number b of bins and as $(1-f)^{-2}$ in the flatness criterion f .

Numerical results To verify the approximation (2.92) for the average number $\langle N \rangle$ of steps that need to be done until the histogram gets flat, we used a small simulation of one stage of the Wang-Landau algorithm. Therefor consider a histogram with b bins and increment the bins randomly by 1, where every bin is chosen with probability $1/b$. After each increment one checks whether the flatness criterion (2.51) is fulfilled, if this is the case, record the number N of increments done in this simulation run. For each considered value of b and f we performed more than 10^4 independent simulations to calculate $\langle N \rangle_{\text{flat}}$. The results of these simulations can be found in Fig. 2.15.

As predicted by the analytical estimation (2.92), for a constant flatness criterion f one finds in Fig. 2.15a that

$$\langle N \rangle_{\text{flat}} \propto b \cdot W\left(\frac{b^2}{2\pi}\right)$$

for a large enough number of bins $b \gtrsim 20$. For a constant number of bins Fig. 2.15b verifies that

$$\langle N \rangle_{\text{flat}} \propto (1-f)^{-2}.$$

In Fig. 2.15c one can see that the functional dependencies found lead to a collapse of the data points for large b .

In Tab. 2.1 the fitted proportionality constants c in

$$\langle N \rangle_{\text{flat}} = c \cdot \frac{2b}{(1-f)^2} \cdot W\left(\frac{b^2}{2\pi}\right) \quad (2.93)$$



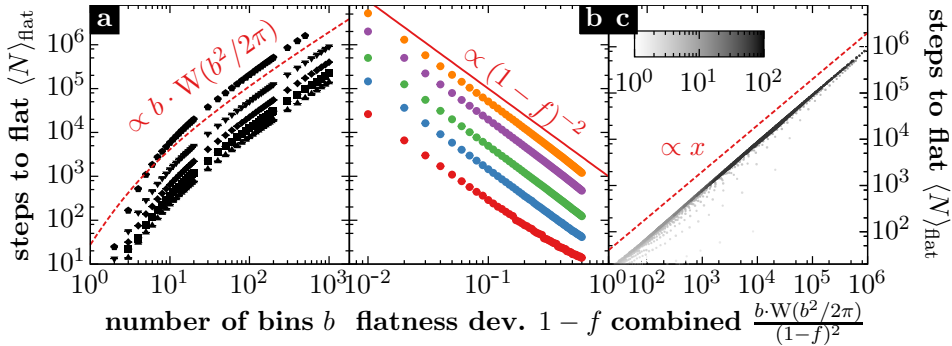


Figure 2.15: Average time $\langle N \rangle_{\text{flat}}$ until a Wang-Landau simulation becomes flat in terms of the number of bins b and the flatness criterion f . (a) $\langle N \rangle_{\text{flat}}$ in terms of the number of bins b for $f = 0.75$ (\blacktriangle), $f = 0.8$ (\blacksquare), $f = 0.85$ (\blacklozenge), $f = 0.9$ (\blacktriangledown) and $f = 0.95$ (\blacklozenge). The red, dashed line corresponds to the functional relation $b \cdot W(b^2/2\pi)$. (b) $\langle N \rangle_{\text{flat}}$ in terms of the flatness criterion f for $b = 5$ (\bullet), $b = 10$ (\circ), $b = 20$ (\odot), $b = 50$ (\odot) and $b = 100$ (\odot). The red, solid line corresponds to a power law $(1-f)^{-2}$. (c) Collapse of data points if using the analytical determined scaling behavior (2.92). The colorscale of the points corresponds to the logarithm $\log(b)$ of the number of used bins.

flatness f	fit parameter c
0.75	0.434 ± 0.003
0.8	0.440 ± 0.003
0.85	0.446 ± 0.004
0.9	0.452 ± 0.004
0.95	0.450 ± 0.005

Table 2.1: Fit parameters for the dependence of the Wang-Landau runtime on the number of bins and the flatness. The left column shows the flatness criterion f , the right column lists the fit parameter c in Eq. (2.93).

can be found for different values of the flatness f . Taking into account all obtained values of the simulation, a fit reveals the dependence

$$\langle N \rangle_{\text{flat}} = (0.4236 \pm 0.0006) \cdot \frac{2b}{(1-f)^2} \cdot W\left(\frac{b^2}{2\pi}\right). \quad (2.94)$$

Errors in the DOS

Until now we estimated the average number $\langle N \rangle$ that is necessary to reach a flat histogram using the assumption that we sample with respect to the exact density of states (DOS), so that the probability $p = 1/b$ to sample one of the b energy bins is independent of the bin. Of course, if doing actual



Wang-Landau simulations, the DOS is not known a priori, but gradually improved from an initial estimation.

In this section we calculate the influence of errors in the DOS on the average runtime $\langle N \rangle$ of one stage of a Wang-Landau algorithm. We assume that the probability for sampling the i -th energy bin is no longer given by $p = 1/b$ (independent of the energy bin), but by

$$q_i := p \cdot (1 + \delta p_i) = \frac{1 + \delta p_i}{b}$$

We consider first a global shift in the probabilities, second we take into account that the errors in each bins follow certain distributions. Note that we only use the Gaussian approximation here, and omit the respective index.

Global shift in the probability We first consider a global shift in the probabilities, i.e. that $\delta p_i = \delta p \neq 0$ is independent of the energy bin. This is of course only an approximation, because in this case the normalization of the probabilities of the single bins fails. However, the results can valuable hints for the behavior of the runtime for $\delta p < 0$, because the bins with to small probability determine the runtime of the algorithm. The probability that the algorithm is flat after N bins is then given by

$$p_f(N, q) = \left(\int_{fNp}^{\infty} dx \frac{1}{\sqrt{2\pi q(1-q)}} \exp \left[-\frac{1}{2} \frac{(x - Nq)^2}{Nq(1-q)} \right] \right)^b$$

Switching the integration variable to $y = x - Nq$ and evaluation the integral using the error function results in

$$\begin{aligned} p_f(N, q) &= \left[\frac{1}{2} - \frac{1}{2} \operatorname{erf} \left(\frac{\sqrt{N}(fp - q)}{\sqrt{2q(1-q)}} \right) \right]^b \\ &= \frac{1}{2^b} \operatorname{erfc}^b \left(\frac{\sqrt{N}(fp - q)}{\sqrt{2q(1-q)}} \right). \end{aligned}$$

Note that we have to choose $q > fp$, otherwise we would obtain a negative probability in this approximation. Intuitively this means that for $q \leq fp$ the flatness would on average never be reached. Using again the asymptotic expansion of the conjugated error function leads to

$$\begin{aligned} p_f(N, q) &= \left[1 - \sqrt{\frac{2}{\pi N}} \frac{\sqrt{q(1-q)}}{q - fp} \exp \left(-\frac{N(fp - q)^2}{2q(1-q)} \right) \right]^b \\ &= 1 - b \sqrt{\frac{2}{\pi N}} \frac{\sqrt{q(1-q)}}{q - fp} \exp \left(-\frac{N(fp - q)^2}{2q(1-q)} \right) \end{aligned}$$



We now formulate the probability in terms of the deviation δp . This means we have to replace

$$\frac{\sqrt{q(1-q)}}{q-fp} = \frac{\sqrt{1-p+\delta p(1-2p)}}{\sqrt{p}(1-f+\delta p)} = \frac{\sqrt{b-1+\delta p(b-2)}}{1-f+\delta p} \approx \frac{\sqrt{b(1+\delta p)}}{1-f+\delta p}$$

Inserting into the flatness probability yields

$$p_f(N, \delta p) = 1 - b \sqrt{\frac{2}{\pi N}} \frac{\sqrt{b(1+\delta p)}}{1-f+\delta p} \exp\left(-\frac{N}{2} \cdot \frac{(1-f+\delta p)^2}{b(1+\delta p)}\right),$$

and using Eq. (2.88) for N_{\max} can be used analogous to the case without error, resulting in

$$\left[1 - \frac{b^{3/2}\sqrt{1+\delta p}}{\sqrt{2\pi N_{\max}}(1-f+\delta p)} \exp\left(-\frac{N_{\max}(1-f+\delta p)^2}{2b(1+\delta p)}\right)\right]^2 = 0,$$

which has the solution

$$N_{\max}(\delta p) = \frac{2b(1+\delta p)}{(1-f+\delta p)^2} W\left(\frac{b^2}{2\pi}\right) \quad (2.95)$$

The relevant range of parameters is $\delta p < 0$, which means that the probability to reach the bins is smaller than the inverse of the actual density of states. These states are suppressed in the simulation, which means that the flatness criterion will probably fail there.

Distributed probability shifts Until now we only considered global shifts in the probability. It was already mentioned that this is not a good assumption, because the normalization of the probabilities is not fulfilled. In this section we suppose that the errors in the probabilities come from a probability distribution $P_{\text{error}}(\delta p, \sigma_{\delta p})$ with mean 0 and standard deviation $\sigma_{\delta p}$. The convenient choice motivated by the law of large number is a Gaussian distribution

$$P_{\text{error}}(\delta p, \sigma_{\delta p}) = \frac{1}{\sqrt{2\pi}\sigma_{\delta p}} \exp\left(-\frac{(\delta p)^2}{2\sigma_{\delta p}^2}\right).$$

There are now two possibilities one can calculate $N_{\max}(\sigma_{\delta p})$, the first is to average the result Eq. (2.95) for $N_{\max}(\delta p)$ over the probability distribution $P_{\text{error}}(\delta p, \sigma_{\delta p})$ by

$$N_{\max}(\sigma_{\delta p}) = \int_{-\infty}^{\infty} d(\delta p) P_{\text{error}}(\delta p, \sigma_{\delta p}) N_{\max}(\delta p),$$



the second possibility is to use $P_{\text{error}}(\delta p, \sigma_{\delta p})$ already in the calculation of p_f by

$$\begin{aligned} p_f(N, \sigma_{\delta p}) &= \prod_{i=1}^b \int_{-\infty}^{\infty} d(\delta p_i) P_{\text{error}}(\delta p_i, \sigma_{\delta p}) \left(\int_{f N p}^{\infty} dx \frac{e^{-\frac{1}{2} \frac{(x - N q_i)^2}{N q_i (1 - q_i)}}}{\sqrt{2\pi q_i (1 - q_i)}} \right) \\ &= \prod_{i=1}^b \int_{-\infty}^{\infty} d(\delta p_i) P_{\text{error}}(\delta p_i, \sigma_{\delta p}) \\ &\quad \cdot \left[1 - \sqrt{\frac{2}{\pi N}} \frac{\sqrt{q_i (1 - q_i)}}{q_i - f p} \exp\left(-\frac{N(f p - q_i)^2}{2 q_i (1 - q_i)}\right) \right] \end{aligned}$$

where $q_i = p(1 + \delta p_i)$.

In both cases there is a problem if $P_{\text{error}}(\delta p_i, \sigma_{\delta p}) \neq 0$ for δ_i in a small neighborhood of $1 - f$, because there is a pole of order 2 in the integrand, which makes the whole term not integrable. So instead of using a Gaussian $P_{\text{error}}(\delta p_i, \sigma_{\delta p})$, we use a uniform distribution

$$P_{\text{error}}(\delta p_i, \sigma_{\delta p}) = \frac{1}{2\sqrt{3}\sigma_{\delta p}} \mathbb{1}_{] -\sqrt{3}\sigma_{\delta p}, \sqrt{3}\sigma_{\delta p} [}$$

which has the same standard deviation as the Gaussian distribution. This implies that non-integrability only occurs for $1 - f \geq \sqrt{3}\sigma_{\delta p}$.

For the first case, averaging directly over $N_{\text{max}}(\delta p)$, we get

$$\begin{aligned} N_{\text{max}}(\sigma_{\delta p}) &= \int_{-\sqrt{3}\sigma_{\delta p}}^{\sqrt{3}\sigma_{\delta p}} \frac{d(\delta p)}{2\sqrt{3}\sigma_{\delta p}} \frac{2b(1 + \delta p)}{(1 - f + \delta p)^2} W\left(\frac{b^2}{2\pi}\right) \\ &= \frac{b \cdot W\left(\frac{b^2}{2\pi}\right)}{\sqrt{3}\sigma_{\delta p}} \left[\log\left(\frac{1 - f + \sqrt{3}\sigma_{\delta p}}{1 - f - \sqrt{3}\sigma_{\delta p}}\right) + \frac{2\sqrt{3}f\sigma_{\delta p}}{(1 - f)^2 - 3\sigma_{\delta p}^2} \right] \end{aligned} \quad (2.96)$$

For small $\sigma_{\delta p}$ this can be expanded as

$$N_{\text{max}}(\sigma_{\delta p}) = \frac{2b W\left(\frac{b^2}{2\pi}\right)}{(1 - f)^2} \left[1 + \frac{2f + 1}{(1 - f)^2} \sigma_{\delta p}^2 + \frac{9(4f + 1)}{5(1 - f)^4} \sigma_{\delta p}^4 + \mathcal{O}(\sigma_{\delta p}^6) \right]$$

The same result can be obtained by expanding Eq. (2.95) up to second or fourth order in δp (which then cancels the divergence) and integrating over a full Gaussian distributed δp .



The second case is more complicated. It is not possible to give a closed solution of the integral over δp because of the integration variable occurring in a rational function. A possible approximation is to replace

$$\operatorname{erf}\left(\frac{\sqrt{N}(fp - q_i)}{\sqrt{2q_i(1 - q_i)}}\right) \rightarrow \operatorname{erf}\left(\frac{\sqrt{N}(fp - q_i)}{\sqrt{2fp(1 - fp)}}\right)$$

which is a good approximation, because for $N \rightarrow \infty$ the error function is almost a step function around its root $q_i = fp$, where $q_i(1 - q_i)$ does not change much and can be approximated by its value at $q_i = fp$. This leaves us with calculating

$$\begin{aligned} p_f(N, \sigma_{\delta p}) &= \prod_{i=1}^b \int_{-\sqrt{3}\sigma_{\delta p}}^{\sqrt{3}\sigma_{\delta p}} \frac{d(\delta p_i)}{2\sqrt{3}\sigma_{\delta p}} \left[1 - \sqrt{\frac{2}{\pi N}} \frac{\sqrt{fp(1 - fp)}}{q_i - fp} \exp\left(-\frac{N(fp - q_i)^2}{2fp(1 - fp)}\right) \right] \\ &= \prod_{i=1}^b \int_{-\sqrt{3}\sigma_{\delta p}}^{\sqrt{3}\sigma_{\delta p}} \frac{d(\delta p_i)}{2\sqrt{3}\sigma_{\delta p}} \left[1 - \sqrt{\frac{2}{\pi N}} \frac{\sqrt{fb}}{1 - f + \delta p_i} \exp\left(-\frac{N(1 - f + \delta p_i)^2}{fb}\right) \right] \end{aligned}$$

With Ei denoting the exponential integral, the integral can be executed and yields

$$p_f(N, \sigma_{\delta p}) = \prod_{i=1}^b \left[1 - \frac{1}{2\sqrt{3}\sigma_{\delta p}} \sqrt{\frac{fb}{2\pi N}} \left[\operatorname{Ei}\left(-\frac{N(1 - f + \sqrt{3}\sigma_{\delta p})^2}{fb}\right) - \operatorname{Ei}\left(-\frac{N(1 - f - \sqrt{3}\sigma_{\delta p})^2}{fb}\right) \right] \right] \quad (2.97)$$

Using the exact form or the expansion $\operatorname{Ei}(-x) = -x^{-1} \exp(-x)$ for $x \rightarrow \infty$ leads to an equation for N_{\max} that cannot be solved analytically in terms of common functions if inserting the flatness probability into Eq. (2.88). However, a numerical solution of this equation is possible, but will not be used in the comparison with the data.

Numerical results Numerical simulations to check the analytical approximations were also done for the case of errors in the DOS. Therefore we chose the probability for choosing energy bin E_i not as $p = 1/b$ independent of i ,



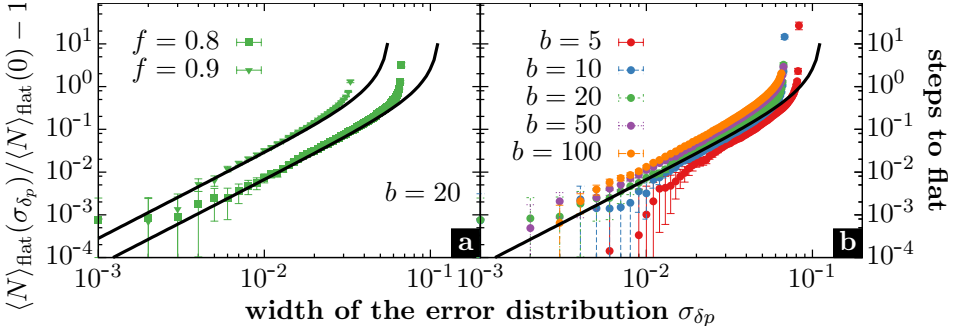


Figure 2.16: Average time $\langle N \rangle_{\text{flat}}$ until a Wang-Landau simulation becomes flat in terms of the standard deviation $\sigma_{\delta p}$ of the distribution of the errors for different flatness criteria f (a) and number of bins b (b). The black solid line corresponds to the analytical approximation (2.96).

but as $(1 + \delta p_i)/cb$ with δp_i being a Gaussian distributed random variable with mean 0 and standard deviation $\sigma_{\delta p}$, and c the normalization constant $c := \sum_i (1 + \delta p_i)/b$. As before we then calculated the average number $\langle N \rangle$ of steps that are necessary to obtain a flat distribution, in terms of the standard deviation $\sigma_{\delta p}$ of the errors, the flatness condition f and the number of bins b . The results of the numerical calculations are presented in Fig. 2.16

One can see that the analytical approximation describes the influence of the error almost perfectly for small $\sigma_{\delta p}$. Also the existence of a divergence can be explained, but its location is approximated wrong with $\sqrt{3}\sigma_{\delta p} = 1 - f$, the actual divergence occurs for smaller $\sigma_{\delta p}$ than predicted. This is because the bin with the smallest probability $q_i = p(1 + \delta p_i)$ (and therewith the smallest δp_i) does strongly dominate the number of necessary steps to reach flatness. The smallest number δp of b variables is not distributed with mean 0 and standard deviation $\sigma_{\delta p}$, but with mean $\mu < 0$. So the divergence occurs already at $\sqrt{3}\sigma_{\delta p} = 1 - f + \mu$.

So both the numerical data and the analytical approximation shows a divergence of the number of steps necessary to obtain a flat distribution. This does not imply that the Wang-Landau sampling gets stuck if the error of an intermediate estimation of the DOS is too high. Remember that the modification of the DOS by Wang-Landau sampling was neglected for both the analytical and the numerical calculations. These modifications are self-healing, i.e. they drive the DOS towards its actual value, i.e. if the error of the DOS is too large for the incidence histogram to become flat, the DOS will be gradually modified in such a way that the error becomes smaller.



2.3.3 Approximative counting with multicanonical Monte Carlo simulations

The result of a Wang-Landau simulation as described in Sec. 2.2.2 or other Markov chain Monte Carlo algorithms as entropic sampling or the transfer matrix method is the density of states (DOS) $g(E)$ of the system. The DOS $g(E)$ is the number of microstates $\omega \in \Omega$ with energy E , but can be calculated only up to a multiplicative normalization factor, which is irrelevant for calculating thermodynamic expectation values, with these numerical algorithms. The knowledge of the normalization factor would make it possible to numerically estimate the actual number of states with a certain energy, or even the total number of states within the system.

Markov chain Monte Carlo methods in general can be used for an approximate counting of states [230, 240, 242], and also the Wang-Landau algorithm was used in computer science to estimate number of solutions of certain problems [161, 162]. In this section we propose a method for estimating the number of states of an arbitrary system by using Wang-Landau simulations (or other flat histogram algorithms) that does not rely on any additional information about the system. In this thesis, this method will be used for estimating the number of triangulations, but it can have valuable applications in other fields of physics. It could be used for calculating the residual entropy of ice [87, 325], which is the degeneracy of the ground state and important for the low-temperature behavior of the system. Another possible field of application could be the calculation of the residual entropy of frustrated Ising anti-ferromagnets, or q -state Potts anti-ferromagnets without frustration [70, 116, 426].

There are three possibilities for determining the normalization factor of the calculated DOS. The first possibility is that from other considerations or calculations the degeneracy of a certain energy level (in most cases the ground state energy) is known. The DOS obtained from the Wang-Landau simulation can then be rescaled by the ratio of the known degeneracy and the calculated value of the DOS at this energy level. The second possibility is quite similar, if the total number of states is known (e.g., in almost all lattice systems), the DOS can be rescaled with the ratio of the known total number of states and the sum of the calculated DOS over all energy bins. The third possibility that neither the degeneracy of a single energy level nor the total number of states is known requires a slight alternation of the simulation setup. This situation can occur in complicated systems, e.g., the triangulations we consider in the course of this thesis, or if one artificially cuts the range of accessible energies to accelerate the simulations.



The idea of the generic counting algorithm is to extend the energy function of the system so that the degeneracy of a certain energy bin is known. Suppose that there is an energy function $E : \Omega \rightarrow \mathbb{R}$ that maps a state to its energy. We choose a reference state $\omega_r \in \Omega$ with reference energy $E(\omega_r)$ and define the extended energy

$$\begin{aligned} \tilde{E}[\omega_r] : \Omega &\rightarrow \mathbb{R} \times \{0, 1\} \\ \omega &\mapsto \begin{cases} (E(\omega), 0) & \omega \neq \omega_r \\ (E(\omega), 1) & \omega = \omega_r \end{cases} \end{aligned} \quad (2.98)$$

which is a pair consisting of the original energy $E(\omega)$ and an integer which is 1 if the state ω and the reference state ω_r are equal, otherwise it is 0.

So if we calculate the density of states with respect to the new extended energy function, the degeneracy of the extended energy bin $(E(\omega_r), 1)$ is known to be 1 and can be used for the normalization of the whole density of states.

The defined counting algorithm can be applied for each system where one is able to compare two states for equality and non-equality (to test whether the actual states match the reference state) and where the reference state does not have measure 0 in the set of all states (so there is only a finite number of states Ω). The second condition is no real restriction since counting states itself is restricted to problems with $\mathbb{N} \ni |\Omega| < \infty$.

For doing flat histogram Markov chain Monte Carlo simulations, the energy difference $\Delta\tilde{E}[\omega_r](\omega_1 \rightarrow \omega_2)$ induced by a step $\omega_1 \rightarrow \omega_2$ must be calculated:

$$\Delta\tilde{E}[\omega_r](\omega_1 \rightarrow \omega_2) = \begin{cases} (\Delta E(\omega_1 \rightarrow \omega_2), 0) & \omega_1 \neq \omega_r \wedge \omega_2 \neq \omega_r \\ (\Delta E(\omega_1 \rightarrow \omega_2), 1) & \omega_1 \neq \omega_r \wedge \omega_2 = \omega_r \\ (\Delta E(\omega_1 \rightarrow \omega_2), -1) & \omega_1 = \omega_r \wedge \omega_2 \neq \omega_r \\ (0, 0) & \omega_1 = \omega_r \wedge \omega_2 = \omega_r \end{cases} \quad (2.99)$$

Using this convention one can use the usual formula

$$\tilde{E}[\omega_r](\omega_2) = \tilde{E}[\omega_r](\omega_1) + \Delta\tilde{E}[\omega_r](\omega_1 \rightarrow \omega_2)$$

with an addition that is defined component-wise for each element of the extended energy pair.

One can also think about not choosing one single reference state ω_r , but a (small) set $\Omega_r \subset \Omega$ of reference states. The extended energy function can



then be defined as

$$\begin{aligned} \tilde{E}[\Omega_r] : \Omega &\rightarrow \mathbb{E} \times \{-1, 0, 1\} \\ \omega &\mapsto \begin{cases} (E(\omega), 0) & \omega \notin \Omega_r \\ (E(\omega), 1) & \omega \in \Omega_r \end{cases} \end{aligned} \quad (2.100)$$

The energy difference can also be calculated analogous to Eq. (2.99) as

$$\Delta \tilde{E}[\Omega_r](\omega_1 \rightarrow \omega_2) = \begin{cases} (\Delta E(\omega_1 \rightarrow \omega_2), 0) & \omega_1 \notin \Omega_r \wedge \omega_2 \notin \Omega_r \\ (\Delta E(\omega_1 \rightarrow \omega_2), 1) & \omega_1 \notin \Omega_r \wedge \omega_2 \in \Omega_r \\ (\Delta E(\omega_1 \rightarrow \omega_2), -1) & \omega_1 \in \Omega_r \wedge \omega_2 \notin \Omega_r \\ (\Delta E(\omega_1 \rightarrow \omega_2), 0) & \omega_1 \in \Omega_r \wedge \omega_2 \in \Omega_r \end{cases} \quad (2.101)$$

If the reference states Ω_r have different original energies, one can either consider extended energies of reference states with different energy as equal

$$\begin{aligned} (E_1, r_1) &=: \tilde{E}_1[\Omega_r] \stackrel{!}{=} \tilde{E}_2[\Omega_r] := (E_2, r_2) \\ \Leftrightarrow r_1 = r_2 = 1 \vee (r_1 = r_2 \wedge E_1 = E_2) \end{aligned}$$

so that the incidence histogram and the density of states only have one bin for the reference state, or as unequal

$$(E_1, r_1) =: \tilde{E}_1 \stackrel{!}{=} \tilde{E}_2 := (E_2, r_2) \quad \Leftrightarrow \quad r_1 = r_2 \wedge E_1 = E_2$$

so that the incidence histogram and the density of states have one reference bin for each possible energy of a reference state.

In general the performance of the algorithm compared with other counting methods depends on the ratio of the calculation time necessary for comparing to states and for calculating the energy difference of and possibly executing a step. Another important factor is the number of chosen reference states. If the number is too small, the entropy differences between the reference bin and bins that are connected via steps is large, which make the Wang-Landau simulation stay for a long time in the reference state. While this problem can be solved by using a continuous time version of the Wang-Landau algorithm only for the reference bin, for very large entropy differences it can be a problem to even reach the reference bin from a connected bin, because the probability for selecting such a step is small. On the other hand, if one chooses the number of reference states too high, one has to perform a lot of comparisons for steps towards the energy of the reference bin, which are expensive in computational time.



As a conclusion, note that the term *energy function* is motivated by the notions of statistical physics, which most of the Markov chain Monte Carlo simulations have been developed for. The proposed counting algorithm can be applied to a whole range of systems and objects, e.g., triangulations within this thesis. The energy function there is generalized to any function that quantifies the system, e.g., the number of maximal simplices in triangulations, and that can be calculated fast, especially its difference with respect to elementary steps.





3 Embedded triangulations

Embedded triangulations, which are tessellations of certain convex subspaces of \mathbb{R}^d using simplicial building blocks, are relevant for a broad range of physical phenomena. They serve as discretisation of all kinds of surfaces, hypersurfaces and volumes [132], yielding applications of computational geometry in physics, material science, medical image processing or even in computer graphics and visualization [151, 228, 257, 258, 261]. Many physical systems can be described by random surface models [178] – based on random triangulations. For instance, biological membranes and vesicles can be modeled using triangulated surfaces with curvature-dependent Hamiltonians [190, 191, 255, 256, 263, 289].

Triangulations are also used as a random graph model for real world networks: Random Apollonian networks [47, 372, 433] are basically triangulations and show both small-world and scale-free behavior, as many real world networks. Since each graph is a subgraph of a triangulation of a closed surface with certain topology, the properties of such triangulations arouse much interest [52, 259].

The (Causal) Dynamical Triangulation approach even tries to describe quantum gravity from scratch with an ensemble of random spacetime triangulations as their central entity [38]. Based on a discrete version of general relativity, where spacetime is approximated by triangles or higher-dimensional analogues, the curvatures become determined purely by the topological structure of the underlying triangulation, e.g. the number of triangles. The resulting action of the theory can be used to extract a phase diagram and observables - in a path-integral like sum over histories approach [26].

In this chapter we consider triangulations of embedded point sets, where the coordinates of the points are fixed and relevant. We mainly use the important subclass of lattice triangulations, so that the underlying point set can be controlled with only few integer parameters (the size of the lattice in every dimension), and different system sizes can be compared easily. Furthermore, lattice triangulations are widely studied in the mathematical literature [6, 109, 238, 374]. The considerations within these chapter can be easily transfered to non-lattice point sets.



Sec. 3.1 of this chapter contains the definition of triangulations of point sets in arbitrary dimensions. A general method for generating triangulations of point sets by lifting function is introduced, and the pulling, the pushing and the Delaunay liftings are defined. Furthermore elementary moves (denoted as flips) between different triangulations of the same point set are defined, that can be used to apply Markov chain Monte Carlo simulations on ensembles of triangulations. An important result is Eq. (3.11), which calculates the ratio of selection probabilities for a flip selected by a wall and its inverse flip, an important quantity that is necessary for ensuring detailed balance in Monte Carlo simulations.

Sec. 3.2 considers triangulations of two-dimensional integer lattices, the main goal is to estimate the number of possible triangulations using an approximative counting scheme based on the Wang Landau algorithm. As a basis for this algorithm an energy function on triangulations is defined in Eq. (3.13), and the scaling of the density of states with respect to these energies is calculated and presented in Fig. 3.17. To be able to simulate large system sizes, cuts on the density of states are introduced and rectified by inspecting the cumulative sum. Finally the entropy density (denoted sometimes as capacity in the mathematical literature) is calculated for lattices up to size 24×24 , and their limited is extrapolated for infinite system sizes in Fig. 3.19. These results replace the analytically known bounds on the entropy density by an estimation that is more accurate in several orders of magnitude. This Sec. 3.2 is based on the publication

[253] J. F. Knauf, B. Krüger, and K. Mecke, *Entropy of unimodular lattice triangulations*, EPL **109**(4), 40011 (2015)

The design and the implementation of the numerical simulation, recording the necessary data sets and first drafts of the text were done by the first author Johannes F. Knauf. I worked on the visual presentation of the figures, some of the placement of the work in the existent literature, and the final version of the text.

The following Sec. 3.3 applies the methods of Sec. 3.2 to three-dimensional lattices of different geometries (sticks, planes and cubes). We first consider the set on triangulations of the smallest three-dimensional integer lattice (unitcube consisting of eight vertices). Mainly for pedagogical reasons, the six different non-isomorphic triangulations of the unitcube are derived and displayed, and the number of different triangulations of the unitcube is then calculated to be 74 by symmetry arguments. Using the number and the geometry of the unitcell triangulations, bounds for the entropy density for triangulations of lattices with different geometry were derived in



Subsec. 3.3.3. The main result of this section, the scaling and the infinite system size limit of the entropy density, is displayed in Fig. 3.34.

Sec. 3.4 interprets two-dimensional lattice triangulations as maximal planar graphs, and calculates typical graph properties like clustering coefficient, average shortest path length and spectral properties of the adjacency and the Laplacian matrix. For the maximal ordered state of the lattice triangulations analytical calculations lead to the spectrum of the adjacency in Eq. (3.62) and the Laplacian matrix in Eq. (3.64). Considering expectation values in a random ensemble of triangulations in terms of the system size, a similar behavior to usual models of random graphs can be found. Microcanonical and canonical calculations showed that for certain choices of energy or inverse temperature triangulations show small-world and scale-free behavior as many real world networks. In the canonical ensemble a negative quasi-critical temperature can be found that coincides for all considered observables (displayed in Fig. 3.57), but an actual phase transition is not present, because the regime of negative temperatures is only well-defined for finite system sizes. This section is based on the two papers

[265] B. Krüger, E. M. Schmidt, and K. Mecke, *Unimodular lattice triangulations as small-world and scale-free random graphs*, *New J. Phys.* **17**(2), 023013 (2015)

[266] ———, *Spectral properties of unimodular lattice triangulations*, *J. Stat. Phys.* **163**(3), 514–543 (2016)

and on the project report

[360] E. M. Schmidt, *Spectrum of the discrete Laplace operator on two-dimensional lattice triangulations*, (2013), short term research project

of a short-term project of Ella Schmidt supervised by me, where she did simulational work on the Laplacian spectral properties of random and microcanonical triangulations.



3.1 Embedded triangulations and flips

In this section we will introduce the basic notations necessary to deal with embedded triangulations (also called triangulations of point sets) and flips between these triangulations. We give a method for constructing triangulations of arbitrary point sets and describe some special triangulations. Additionally we list some results about the ergodicity of the flips in the space of all triangulations.

For the presentation we follow mainly the nice book [132], but restrict to the very basic concepts that are necessary for understanding the work about embedded triangulations in this thesis. Readers that are interested in more details and some proofs of theorems we only give here without proof should refer to [132].

3.1.1 Simplex, complex and triangulation

First we need some very basic geometrical definitions to work with and to build our later considerations upon. We start with defining a point configuration:

Definition 3.1 (point configuration, index set [132, p. 47]):

A *point configuration* \mathbf{X} in d dimensions is a countable set of coordinate d -tuples that is not necessarily unique, i.e. there can be two points with the same coordinates. A set J together with a map $\phi : J \rightarrow \mathbf{X}; J \ni j \mapsto \mathbf{x}_j$ so that the inverse map $\phi^{-1} : A \rightarrow J; A \ni \mathbf{x}_j \mapsto j$ exists, is called the *index set* of the point configuration \mathbf{X} .

The allowance for duplicated points can simplify some propositions and proofs, but for our purposes we deal only with distinct points. So for our purposes a d -dimensional point configuration is always a set of points, which is a subset of the \mathbb{R}^d . For this reason we denote point configurations with curly brackets, as normal sets.

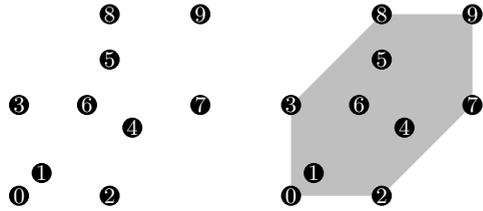
Triangulations are tessellation of space into elementary building objects, whose corners are defined by the points of the point configurations. So one needs to define the space spanned by points, this is done with the help of the convex hull:

Definition 3.2 (convex hull [132, p. 50]):

Let $\mathbf{X} = \{\vec{x}_j : j \in J\}$ be a point configuration with index set J . The



Figure 3.1: Convex hull.
 Two-dimensional point set (left) and its convex hull (right), which is the intersection of all convex sets that contain all of the points (compare Def. 3.1).



convex hull $\text{conv}(\mathbf{X})$ of X is the following set:

$$\text{conv}(\mathbf{X}) := \left\{ \vec{y} = \sum_{j \in J} \lambda_j \vec{x}_j : (\lambda_j \geq 0 \forall j \in J) \wedge \left(\sum_{j \in J} \lambda_j = 1 \right) \right\} \quad (3.1)$$

For two points the convex hull is the line segment between this points, for three points it is the triangle spanned by these points, for four points (in three dimensions) it is the tetrahedron spanned by this points.

The convex hull can alternatively be defined as the minimal convex set containing all points of the point set [132, p. 43]. In Fig. 3.1 an example for the convex hull of a point set is depicted.

The convex hull can be used to define whether a given set of points is dependent or independent, which is strongly connected with the linear (in)dependency of vectors.

Definition 3.3 (independence and dependence, general position [132, p.51]):

Let \mathbf{X} be a point configuration with $k := |\mathbf{X}|$ points. If $\dim(\text{conv}\mathbf{X}) = k - 1$ the point configuration is called *independent*, otherwise the point configuration is called *dependent*. A d -dimensional point set \mathbf{X} is called in *general position*, if every subset $\mathbf{Y} \subset \mathbf{X}$ with $|\mathbf{Y}| \leq d + 1$ is independent.

A point configuration is independent, if and only if the vectors connecting a certain point with all other points of the point configuration are linear independent.

Using the definitions of convex hull and independence of point configurations one can define simplices, which will be the elementary building blocks of triangulations:

Definition 3.4 (simplex [132, p.44]):

Let \mathbf{X} be an independent point configuration with $k := |\mathbf{X}|$ points and index set J . The convex hull $\text{conv}(X)$ of X is then called $(k - 1)$ -



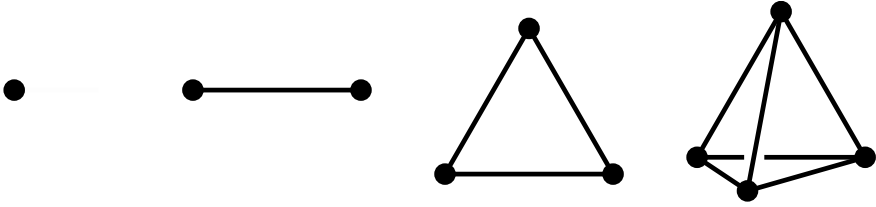


Figure 3.2: Different types of simplices.

(Left to right) 0-simplex consisting of 1 point, 1-simplex (line) spanned by two points, 2-simplex (triangle) spanned by 3 points and 3-simplex (tetrahedron) spanned by 4 points.

simplex. As an abbreviation a simplex is often identified with the underlying point configuration or its index set.

Examples for simplices are depicted in Fig. 3.2. For each k -simplex with $k \geq 1$ one can consider the simplices defined by proper subsets of the original simplex.

Definition 3.5 (subsimplex, supersimplex):

Let $\sigma = \{\vec{x}_1, \dots, \vec{x}_k\}$ be a k -simplex spanned by $k + 1$ points. A simplex $\bar{\sigma} \subset \sigma$ with $(\bar{k} + 1)$ points that are a proper subset of the points of the original simplex is called \bar{k} -*subsimplex* of σ . The original simplex σ is called *supersimplex* of $\bar{\sigma}$.

Using simplices we can define a simplicial complex, which can be seen as pre-triangulation, and finally a triangulation:

Definition 3.6 (simplicial complex of a point configuration [132, p.45f]):

Let \mathbf{X} be a point configuration with n points in d dimensions with index set J . A *simplicial complex* $\mathcal{S} \subset 2^J$ is a subset of the power set 2^J of J (a set of subsets $\sigma \subset J$), or equivalently a set of simplices σ spanned by the points of \mathbf{X} . fulfilling the following two properties:

1. Closure: For every simplex contained in the simplicial complex, all its subsimplices are also contained in the simplicial complex.

$$\sigma \in \mathcal{S}, \bar{\sigma} \subset \sigma \Rightarrow \bar{\sigma} \in \mathcal{S}$$

2. Intersection-freeness: The intersection of two simplices of the simplicial complex is either empty or a face/subsimplex of both simplices.

$$\sigma_1, \sigma_2 \in \mathcal{S} \Rightarrow \sigma_1 \cap \sigma_2 \subset \sigma_1 \wedge \sigma_1 \cap \sigma_2 \subset \sigma_2$$



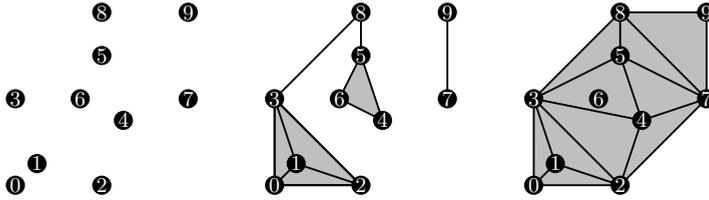


Figure 3.3: Simplicial complex and triangulation.

Point set (left), a simplicial complex of this point set (middle) and a triangulation of the point set (right). Note that the simplicial complex does not need to be connected, and that the triangulation does not need to include every point as underlying point of a simplex.

So a simplicial complex is a collection of simplices that do not overlap, even not necessarily connected, an example can be found in Fig. 3.3 But one wants to have additional structure that ensures that the whole space formed by the points is tessellated, which means that every point of the convex hull is part of at least one simplex.

Definition 3.7 (triangulation of a point configuration [132, p.54]):

Let \mathbf{X} be a point configuration and \mathcal{T} be a simplicial complex of \mathbf{X} . The simplicial complex \mathcal{T} is called *triangulation*, if it fulfils the following property:

- 3. Union: The union of all simplices of \mathcal{T} is the convex hull $\text{conv}(\mathbf{X})$ of the point configuration \mathbf{X} .

Note that it is not demanded by the definition of a triangulation that every point of a point set underlying a simplex of the triangulation. A triangulation where this property is fulfilled is called *full*. An example for a (non-full) triangulation can be found in Fig. 3.3. In the following we often denote only the maximal simplices of a triangulation, because the low-dimensional simplices can be easily deduced from the maximal ones.

3.1.2 Special triangulations

As a next step we present a method for constructing some special triangulations of a points set. Therefor we lift the point configuration to a higher dimension and look at the boundary of the higher dimensional hull.

Definition 3.8 (lifted point configuration [132, p.54f]):

Let $\mathbf{X} = (\vec{x}_1, \vec{x}_2, \dots, \vec{x}_k)$ a point configuration in d dimensions and



3. Embedded triangulations

$\omega : \mathbb{R}^d \rightarrow \mathbb{R}$ an arbitrary function. The point configuration

$$\mathbf{X}^\omega = \left\{ \left(\begin{array}{c} \vec{x}_1 \\ \omega(\vec{x}_1) \end{array} \right), \left(\begin{array}{c} \vec{x}_2 \\ \omega(\vec{x}_2) \end{array} \right), \dots, \left(\begin{array}{c} \vec{x}_k \\ \omega(\vec{x}_k) \end{array} \right) \right\} \quad (3.2)$$

is called *lifted point configuration* with respect to the *height function* ω .

A lifting of a point configuration can induce a triangulation as described in the following definition:

Definition 3.9 (lifting-induced triangulation [132, p.54f]):

Let $\mathbf{X} = (\vec{x}_1, \vec{x}_2, \dots, \vec{x}_k)$ a point configuration in d dimensions and $\omega : \mathbb{R}^d \rightarrow \mathbb{R}$ a lifting function. Let $\mathcal{P} = \text{conv}(\mathbf{X}^\omega)$ the convex hull polytope of the lifted triangulation. A face of \mathcal{P} is called *visible from below* if for every point $(\vec{x}, y)^t$ of the face $(\vec{x}, y + \epsilon)^t \in \mathcal{P}$ and $(\vec{x}, y - \epsilon)^t \notin \mathcal{P}$. If each face of \mathcal{P} visible from below is a d -simplex, there is a bijection from this faces to simplices in $\text{conv}(\mathbf{X})$ that form the triangulations of \mathcal{X} *lifting induced triangulation*. More precisely, a face that is visible from below and spanned by the points $(\vec{x}_{\pi(1)}, \omega(\vec{x}_{\pi(1)}))^t, \dots, (\vec{x}_{\pi(d+1)}, \omega(\vec{x}_{\pi(d+1)}))^t$ (with π being an arbitrary permutation) is mapped to the simplex $\sigma = \{\vec{x}_{\pi(1)} \dots \vec{x}_{\pi(d+1)}\}$.

Note that not every triangulation of a point configuration can be obtained by lifting the point configuration using a height function ω . A counterexample is the so-called mother of all examples [132, p. 56]. This gives rise to the following definition:

Definition 3.10 (regular triangulation [132, p. 55]):

A triangulation \mathcal{T} of a point configuration \mathbf{X} is called *regular*, if there exists a height function ω so that \mathcal{T} is the lifting-induced triangulation of the height function ω .

In the following we present three important lifting functions and describe the triangulations they lead to. Let $\mathbf{X} = (\vec{x}_1, \vec{x}_2, \dots, \vec{x}_k)$ be a point configuration. The height function

$$\omega_{\text{push}} : \mathbb{R}^d \rightarrow \mathbb{R}, \vec{x}_i \mapsto c \cdot i \quad (3.3)$$

with a sufficiently large constant c induces the *pushing* triangulation [132, p. 178ff], the height function

$$\omega_{\text{pull}} : \mathbb{R}^d \rightarrow \mathbb{R}, \vec{x}_i \mapsto -i \quad (3.4)$$



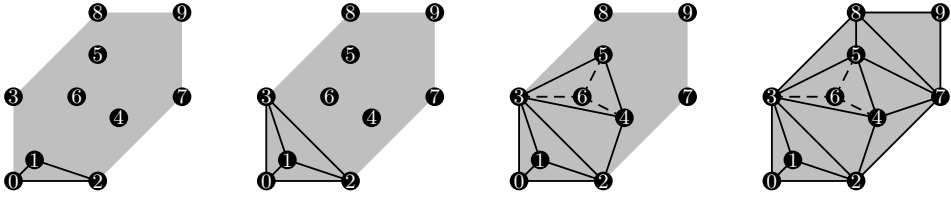


Figure 3.4: Pushing triangulation.

Construction of the (full) pushing triangulation of a point set. After starting with the first simplex $\{1, 2, 3\}$ the vertices are connected step by step to the faces or $(d - 1)$ -simplices of the already present triangulation that are visible to them. If choosing to create the full pushing triangulations, the additional edges (dashed lines) are inserted by connecting the vertices that are inside of the already obtained triangulation with the vertices of the maximal simplices they are contained in.

with a sufficiently large constant c induces the *pulling* triangulation [132, p. 181ff], and the height function

$$\omega_{\text{Delaunay}} : \mathbb{R}^d \rightarrow \mathbb{R}, \vec{x}_i \mapsto \vec{x}_i^t \cdot \vec{x}_i \quad (3.5)$$

induces the *Delaunay* triangulation [132, p. 57]. Note that the pushing and the pulling triangulation depend on the order of the points in the point configuration, where the Delaunay triangulation is independent of the order. If using the opposite ordering of the points, the pushing triangulation becomes the pulling triangulation and vice versa.

Pushing triangulation

Instead of directly considering the lifted point configuration, a pushing triangulation can also be constructed with the following algorithm (in two-dimensions, that can easily be generalized for higher dimensions) [132, p. 178ff]: Start with the vertices \vec{x}_1 , \vec{x}_2 and \vec{x}_3 and insert the triangle constituted by these vertices into the triangulation. Then consider the next vertex \vec{x}_i in the ordered list of points. If $\vec{x}_i \in \text{conv}(\vec{x}_1, \dots, \vec{x}_{i-1})$ (which means that the vertex is inside the convex hull of the vertices that were included before), then do not include the point into the triangulation. Otherwise (the vertex is outside of the convex hull) insert for each face of the convex hull which is visible from \vec{x}_i (each line from \vec{x}_i to a point of the face does not intersect the interior of the convex hull) the maximal simplex consisting of the visible face and \vec{x}_i . This algorithm is depicted in Fig. 3.4.

If one wants to construct a full triangulation, in the case where the new vertex is already contained in the convex hull of the previous vertices, the



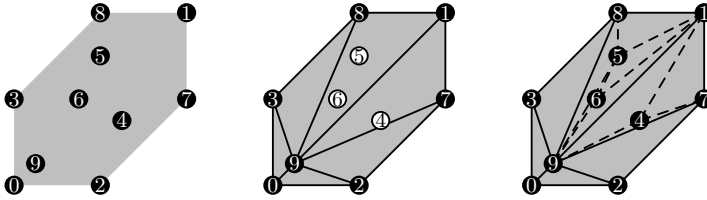


Figure 3.5: Pulling triangulation.

Construction of the pulling (middle) and full pulling (right) triangulation of a point set (left). The vertex with the lowest index not located on the boundary of the convex hull is connected with all $(d - 1)$ -simplices on the convex hull.

maximal simplex where \vec{x}_i is located can be divided into $d + 1$ smaller maximal simplices, each of them containing the vertex \vec{x}_i and a $(d - 1)$ -subsimplex.

Pulling triangulation

As for the pushing triangulations, there is also an algorithm for constructing the pulling triangulation without considering the actual lifting function [132, p. 181f]. Given a point configuration \mathbf{X} , choose the point $\vec{x}_i \in \mathbf{X}$ that is not located on the boundary of the convex hull $\partial\text{conv}(\mathbf{X})$ of the point configuration \mathbf{X} , so that i is minimal. For every $(d - 1)$ -simplex that is completely contained in the boundary of the convex hull, insert into the triangulation the d -simplex that is spanned by the $(d - 1)$ -simplex and the interior point \vec{x}_i .

To obtain a full pulling triangulation, all the other interior vertices can be included step by step by subdividing the maximal simplices they are located in. In Fig. 3.5 the construction of the (full) pulling triangulation is depicted.

Delaunay triangulation

The Delaunay triangulation is a very important triangulation in physics, because it has some important properties [132, p. 97f]. The dual graph of the Delaunay triangulation is the Voronoi tessellation, which consists of polygons that are the parts of the space which are nearest to vertices of the point configuration. Another property is that if two triangles share a common edge, the angles of the triangles which are located at the opposite of the common edge sum up to π or less. This means that the Delaunay triangulation is the most regular triangulation in the sense that it does not



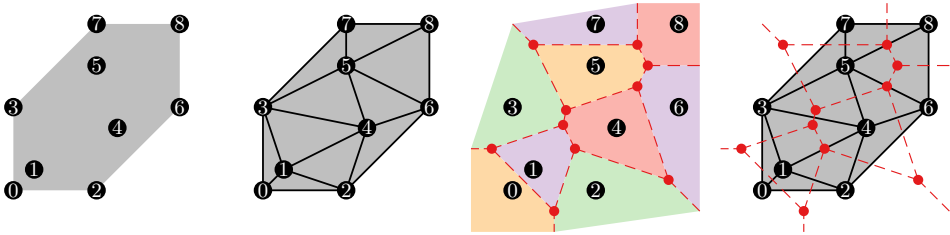


Figure 3.6: Delaunay triangulation.

From left to right: Planar point configuration with its convex hull, Delaunay triangulation of this point set, Voronoi tessellation of the point set and combined image with Voronoi tessellation and Delaunay triangulation.

posses very narrow or wide angles. This property is equivalent to saying that the circumspheres of every maximal simplex do not contain any other points of the given point set. An example for the Delaunay triangulation and the Voronoi tessellation of a point set is given in Fig. 3.6.

In two dimensions there is an easy way to obtain the Delaunay triangulation which will be presented in Sec. 3.1.3. This algorithm modifies the triangulation locally using the so-called flips and converges towards the Delaunay triangulation.

3.1.3 Flips between triangulations

Our goal is to learn something about all possible triangulations of a point set, e.g. the number of triangulations or other statistical properties using Markov chain Monte Carlo simulations. Therefore one needs a possibility to move from one triangulation of a given point set to another triangulation of the same point set. Such an elementary move will be called flip.

Definition - Minimal dependent sets, circuits and flips

Definition 3.11 (minimal dependent set [132, p. 72f]):

A set of points $\mathbf{X} = \{\vec{x}_1, \dots, \vec{x}_k\}$ in d dimensions is called a *minimal dependent set*, if it is a dependent set and each proper subset is an independent set.

Lemma 3.12. *If a set of points $\mathbf{X} = \{\vec{x}_1, \dots, \vec{x}_k\}$ is a minimal dependent set, there is a unique affine dependency relation*

$$\sum_{i=1}^k \lambda_i \vec{x}_i = 0 \quad \sum_{i=1}^k \lambda_i = 0$$



3. Embedded triangulations

Uniqueness means here up to a common multiplicative factor for each λ . Note that in d dimensions a minimal dependent set does not always consist of $(d + 2)$ points, this is only true if all points are in general position. If the points are restricted to an affine subspace, a minimal dependent set can consist of less points (consider e.g. three collinear points in two dimensions).

Definition 3.13 (oriented circuit [132, p. 72f]):

Let $\mathbf{X} = \{\vec{x}_1, \dots, \vec{x}_k\}$ be a minimal dependent set and λ_i as in the previous lemma. The pair (J_+, J_-) defined by the sets

$$\begin{aligned} J_+ &:= \{\vec{x}_i \in \mathbf{X} \mid \lambda_i > 0\} \\ J_- &:= \{\vec{x}_i \in \mathbf{X} \mid \lambda_i < 0\} \end{aligned} \tag{3.6}$$

is denoted as *oriented* or *signed circuit* of the minimal dependent set \mathbf{X} .

Note that $|J_+|, |J_-| \geq 1$, otherwise the sum of all λ_i could not be 0 as demanded in the definition of a minimal dependent set. Of course also the definition of a circuit depends on the choice of the sign of the λ_i , so that one has to identify the circuits

$$(J_+, J_-) \equiv (J_-, J_+)$$

A circuit of the minimal dependent set \mathbf{X} can also equivalently be defined in the following way [132, p. 73]: A circuit is a partition of \mathbf{X} into parts J_+ and J_- such that

$$\text{conv}(J_+) \cap \text{conv}(J_-) \neq \emptyset$$

Consider for example the following minimal dependent set in two dimension:

$$\mathbf{X} = \left\{ \vec{x}_1 = \begin{pmatrix} 0 \\ 0 \end{pmatrix}, \vec{x}_2 = \begin{pmatrix} 0 \\ 1 \end{pmatrix}, \vec{x}_3 = \begin{pmatrix} 1 \\ 0 \end{pmatrix}, \vec{x}_4 = \begin{pmatrix} 1 \\ 1 \end{pmatrix} \right\} \tag{3.7}$$

To calculate its oriented circuit, we have to find $\lambda_1, \lambda_2, \lambda_3$ and λ_4 so that

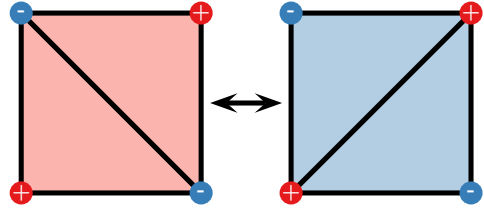
$$\begin{aligned} \lambda_1 \vec{x}_1 + \lambda_2 \vec{x}_2 + \lambda_3 \vec{x}_3 + \lambda_4 \vec{x}_4 &= 0 \\ \lambda_1 + \lambda_2 + \lambda_3 + \lambda_4 &= 0 \end{aligned}$$

This can be translated into the following matrix equation:

$$\begin{pmatrix} 0 & 0 & 1 & 1 \\ 0 & 1 & 0 & 1 \\ 1 & 1 & 1 & 1 \end{pmatrix} \cdot \begin{pmatrix} \lambda_1 \\ \lambda_2 \\ \lambda_3 \\ \lambda_4 \end{pmatrix} = \vec{0}$$



Figure 3.7: Minimal dependent point set (3.7) in two-dimensions, its oriented circuit (denoted by plus and minus) and its two possible triangulations \mathcal{T}_+ (left) and \mathcal{T}_- (right).



The solutions of this equation are the vectors of the kernel of the leading matrix:

$$\text{kern} \begin{pmatrix} 0 & 0 & 1 & 1 \\ 0 & 1 & 0 & 1 \\ 1 & 1 & 1 & 1 \end{pmatrix} = \text{kern} \begin{pmatrix} 1 & 0 & 0 & -1 \\ 0 & 1 & 0 & 1 \\ 0 & 0 & 1 & 1 \end{pmatrix} = \left\langle \begin{pmatrix} \lambda \\ -\lambda \\ -\lambda \\ \lambda \end{pmatrix} \right\rangle$$

So we find that $J_+ = \{\vec{x}_1, \vec{x}_4\}$ and $J_- = \{\vec{x}_2, \vec{x}_3\}$. The circuit points are sketched in Fig. 3.7.

One can show that there are exactly two triangulations for every oriented circuit. An interchange between these two triangulations will define our local flip.

Theorem 3.14 (triangulations of circuits [132, p. 73]). *Let $\mathbf{X} = \{\vec{x}_1, \dots, \vec{x}_k\}$ be a minimal dependent set and (J_+, J_-) its circuit. Then there are the following two triangulations of \mathbf{X} :*

$$\begin{aligned} \mathcal{T}_+ &:= \{\mathbf{Y} \subset \mathbf{X} : J_+ \not\subseteq \mathbf{Y}\} \\ \mathcal{T}_- &:= \{\mathbf{Y} \subset \mathbf{X} : J_- \not\subseteq \mathbf{Y}\} \end{aligned} \tag{3.8}$$

This is equivalent to saying that the triangulations are defined by the maximal simplices $\{\mathbf{X} \setminus \{j_+\} \mid j_+ \in J_+\}$ and $\{\mathbf{X} \setminus \{j_-\} \mid j_- \in J_-\}$ and their faces.

We consider again the oriented circuit of the minimal dependent set given in Eq. (3.7) and Fig. 3.7. The two triangulation are given by:

$$\begin{aligned} \mathcal{T}_+ &= \{\{x_1, x_2, x_3\}, \{x_2, x_3, x_4\}, \{x_1, x_2\}, \{x_1, x_3\}, \{x_2, x_3\}, \\ &\quad \{x_2, x_4\}, \{x_3, x_4\}, \{x_1\}, \{x_2\}, \{x_3\}, \{x_4\}\} \\ \mathcal{T}_- &= \{\{x_1, x_2, x_4\}, \{x_1, x_3, x_4\}, \{x_1, x_2\}, \{x_1, x_3\}, \{x_1, x_4\}, \\ &\quad \{x_2, x_4\}, \{x_3, x_4\}, \{x_1\}, \{x_2\}, \{x_3\}, \{x_4\}\} \end{aligned}$$

Principally we have everything that we need to define a flip. But we have to keep in mind that there are cases where the points of a minimal dependent set are not in general position, and the triangulations \mathcal{T}_+ and \mathcal{T}_- do not have full dimension.



Definition 3.15 (flip [132, p. 74f; p. 186f]):

Let \mathbf{X} a point set with triangulation \mathcal{T} . Let $\mathbf{Y} \subset \mathbf{X}$ be a minimal dependent set with circuit (J_+, J_-) so that (without loss of generality) $\mathcal{T}_+ \subset \mathcal{T}$. Let $\tilde{d} := |J_+| + |J_-| - 2$ be the effective dimension of the minimal dependent set.

If $\tilde{d} = d$, \mathcal{T}_+ is full-dimensional (the dimension of its maximal simplices equals the dimension of the triangulation \mathcal{T}) and the following operation is called a $(|J_+| \rightarrow |J_-|)$ -flip:

$$\mathcal{T} \rightarrow (\mathcal{T} \setminus \mathcal{T}_+) \cup \mathcal{T}_-$$

If $\tilde{d} < d$, \mathcal{T}_+ is not full-dimensional (the dimension of its maximal simplices is less than the dimension of the triangulation \mathcal{T}) and we use the following procedure: Let $\Sigma = \{\sigma \in \mathcal{T} \mid |\sigma| = d+1\}$ be the maximal simplices of the triangulation and let $S_+ = \{\sigma \in \mathcal{T}_+ \mid |\sigma| = \tilde{d} + 1\}$ be the maximal simplices of \mathcal{T}_+ . Denote by

$$\Sigma_+ := \{\sigma \in \Sigma \mid \exists \sigma' \in S_+ \text{ with } \sigma' \subset \sigma\}$$

the maximal simplices of the triangulation to which the maximal simplices of S_+ are subsets and by

$$\Sigma_{\text{reduced},+} := \{\sigma \setminus (J_+ \cup J_-) \mid \sigma \in \Sigma_+\}$$

the subsimplices of Σ_+ that consists of points not contained in the circuit. The following operation is called a $(|J_+|, |J_-|)$ -flip:

$$\mathcal{T} \rightarrow [\mathcal{T} \setminus (\mathcal{T}_+ \times (\Sigma_{\text{reduced},+}))] \cup [\mathcal{T}_- \times (\Sigma_{\text{reduced},+})]$$

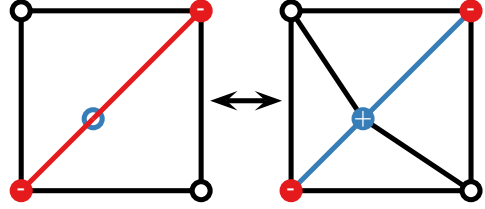
The degenerate formulation of flip intuitively means, that there is a non-degenerate flip in some lower dimension, and all the maximal simplices of the triangulations have to be adapted to the changes induced by the lower-dimensional flip. The notion $(|J_+| \rightarrow |J_-|)$ -flip indicates that $|J_+|$ \tilde{d} -simplices will be replaced by $|J_-|$ \tilde{d} -simplices by the flip.

Fig. 3.7 showed an example of a non-degenerate flip, in the following example (depicted in Fig. 3.8) we will consider a degenerate flip. Consider a triangulation \mathcal{T} of the following point set

$$\mathbf{X} = \left\{ \vec{x}_1 = \begin{pmatrix} 0 \\ 0 \end{pmatrix}, \vec{x}_2 = \begin{pmatrix} 0 \\ 1 \end{pmatrix}, \vec{x}_3 = \begin{pmatrix} 1 \\ 0 \end{pmatrix}, \vec{x}_4 = \begin{pmatrix} 1 \\ 1 \end{pmatrix}, \vec{x}_5 = \begin{pmatrix} \frac{1}{2} \\ \frac{1}{2} \end{pmatrix} \right\} \quad (3.9)$$



Figure 3.8: Degenerated minimal dependent point set (3.9) in two-dimensions, its oriented circuit (denoted by plus and minus) and its two possible triangulations \mathcal{T}_+ (left) and \mathcal{T}_- (right). Because the point set is degenerated, the maximal simplices of the triangulations the minimal dependent point set is embedded in must be updated, too.



given by the maximal simplices $\{\vec{x}_1, \vec{x}_2, \vec{x}_4\}$ and $\{\vec{x}_1, \vec{x}_3, \vec{x}_4\}$. Consider the minimal dependent set $\{\vec{x}_1, \vec{x}_4, \vec{x}_5\}$ and calculate its circuit using the matrix equation

$$\begin{pmatrix} 0 & \frac{1}{2} & 1 \\ 0 & \frac{1}{2} & 0 \\ 1 & 1 & 1 \end{pmatrix} \cdot \begin{pmatrix} \lambda_1 \\ \lambda_2 \\ \lambda_3 \end{pmatrix} = \vec{0}$$

with solution $\langle (-\lambda, 2\lambda, -\lambda)^t \rangle$. So we find that $J_+ = \{\vec{x}_5\}$ and $J_- = \{\vec{x}_1, \vec{x}_4\}$ and the triangulations \mathcal{T}_+ and \mathcal{T}_- are:

$$\begin{aligned} \mathcal{T}_+ &= \{\{x_1, x_4\}, \{x_1\}, \{x_4\}\} \\ \mathcal{T}_- &= \{\{x_1, x_5\}, \{x_4, x_5\}, \{x_1\}, \{x_4\}, \{x_5\}\} \end{aligned}$$

We can then calculate the sets Σ_+ and $\Sigma_{\text{reduced},+}$:

$$\begin{aligned} \Sigma_+ &= \{\{\vec{x}_1, \vec{x}_2, \vec{x}_4\}, \{\vec{x}_1, \vec{x}_3, \vec{x}_4\}\} \\ \Sigma_{\text{reduced},+} &= \{\{\vec{x}_2\}, \{\vec{x}_3\}\} \end{aligned}$$

The flip is then the following replacement of maximal simplices (and the respective subsimplices):

$$\begin{aligned} &\{\{\vec{x}_1, \vec{x}_2, \vec{x}_4\}, \{\vec{x}_1, \vec{x}_3, \vec{x}_4\}\} \\ \rightarrow &\{\{\vec{x}_1, \vec{x}_2, \vec{x}_5\}, \{\vec{x}_1, \vec{x}_3, \vec{x}_5\}, \{\vec{x}_2, \vec{x}_4, \vec{x}_5\}, \{\vec{x}_3, \vec{x}_4, \vec{x}_5\}\} \end{aligned}$$

Note that it is not sufficient to have a minimal dependent set of points to define and execute a step, one of the two possible triangulations of the minimal dependent set must be contained in actual triangulation of the whole point set. If none of the two triangulations is contained, no flip is



3. Embedded triangulations

associated with the chosen minimal dependent point set, or equivalently, one has to consider the flip as non-executable.

As the last part of this section we explicitly give a list of possible flips in d dimensions in general and present the possible flips up to three dimensions in detail. The largest minimal dependent set in d dimensions has $d + 2$ points, so that for the oriented circuit (J_+, J_-) the number of points is $|J_+| + |J_-| = d + 2$. So there are the $(1 \rightarrow d + 1)$ -flip, the $(2 \rightarrow d)$ flip and so forth, and the $(\lfloor d/2 \rfloor + 1 \rightarrow \lceil d/2 \rceil + 1)$ -flip, as well as their inverse flips. A minimal dependent set that has less than $d + 2$ points behaves like a lower-dimensional flip in the affine subspace, and the d -dimensional simplex structure has to be adapted to the lower-dimensional flip.

For $d = 1$ dimensions, the minimal dependent set of points have 3 points maximally. The only possible flips are the $(2 \rightarrow 1)$ -flip, which is the insertion of a vertex into an edge, and its inverse, the $(1 \rightarrow 2)$ -flip, which is the deletion of a vertex from an edge.

For $d = 2$ dimensions, minimal dependent set of points have 4 points maximally. So there are the $(1 \rightarrow 3)$ -flip and its inverse, the $(3 \rightarrow 1)$ -flip, which are the insertion/removal of a vertex into/from a triangle. Additionally there is the $(2 \rightarrow 2)$ -flip, denoted also as diagonal-edge flip, which replaces one diagonal of a quadrilateral with the other one. Supplementary to these non-degenerate flips there is the degenerate $(1 \rightarrow 2)$ -flip inherited from the one-dimensional case, where an edge is subdivided by inserting a vertex, and the two triangles incident with the edge are replaced with four triangles, two at a time incident with one of the new edges. In Fig. 3.9 these possible flips in two dimensions are displayed.

For $d = 3$ dimensions, minimal dependent set of points have 5 points maximally. So there are four non-degenerate flips, the $(1 \rightarrow 4)$ - and the $(4 \rightarrow 1)$ -flip, which are the insertion/removal of a vertex into/from a tetrahedron, and the $(2 \rightarrow 3)$ - and the $(3 \rightarrow 2)$ -flip, which flips to neighboring tetrahedra with common triangles into three neighboring tetrahedra with common edge and vice versa. Additionally there are the $(1 \rightarrow 3)$ -flip, the $(2 \rightarrow 2)$ -flip and the $(3 \rightarrow 1)$ -flip induced by the respective two-dimensional flips, and the $(1 \rightarrow 2)$ -flip as well as the $(2 \rightarrow 1)$ -flip induced by the one-dimensional flips. In Fig. 3.9 these possible flips in three dimensions are displayed. Note that degenerate flips look different if the circuit points are located at the boundary of the convex hull. In these cases there are maximal simplices present only on one side of the convex hull boundary.



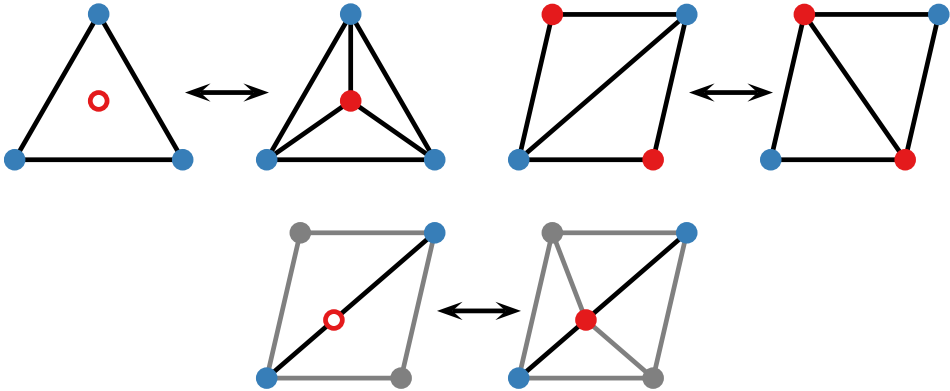


Figure 3.9: Possible flips in two dimensions.

If considering the flip from left to right, red points are the **positive circuit points**, blue points are the **negative circuit points**, and grey points and lines correspond to the two-dimensional extension of lower-dimensional flips. (First row, left) (1 → 3)-flip that divides a triangle into three triangles by inserting a point into the triangle. (First row, right) (2 → 3)-flip that interchanges the diagonals of a quadrilateral. (Second row) (1 → 2)-flip induced by the one-dimensional flip that subdivides an edge into two by inserting a vertex.

Selecting possible flips

In order to do Markov chain Monte Carlo simulations one needs a way to propose one of all possible steps with a known probability distribution. Finding all possible flips of a given embedded triangulation by the direct usage of Def. 3.15 can be very difficult, because one has to examine all subsets of $3, 4, \dots, d + 2$ points, check if they are minimal dependent, calculate the circuit and check whether one of the circuit triangulations is a subset of the triangulation. There is a way that allow us to propose the possible vertex-conserving steps more efficiently [132, p. 188f]:

Consider the *walls* of the triangulations, i.e. $(d - 1)$ -simplices that are subsimplices of two d -simplices. In fact every $(d - 1)$ -simplex that is not located at the boundary of the convex hull of the point configuration is a wall. To find the affine dependence relation as defined in Lemma 3.12 of the wall points and the two points that are not part of the wall, but of the two maximal simplices that are supersimplices of the wall. If these $d + 2$ points are more than minimal dependent, there will be factors $\lambda_i = 0$, the associated points do then not belong to the minimal dependent set and have to be removed from the considerations. With the obtained minimal dependent set one can then use the procedure as described before.



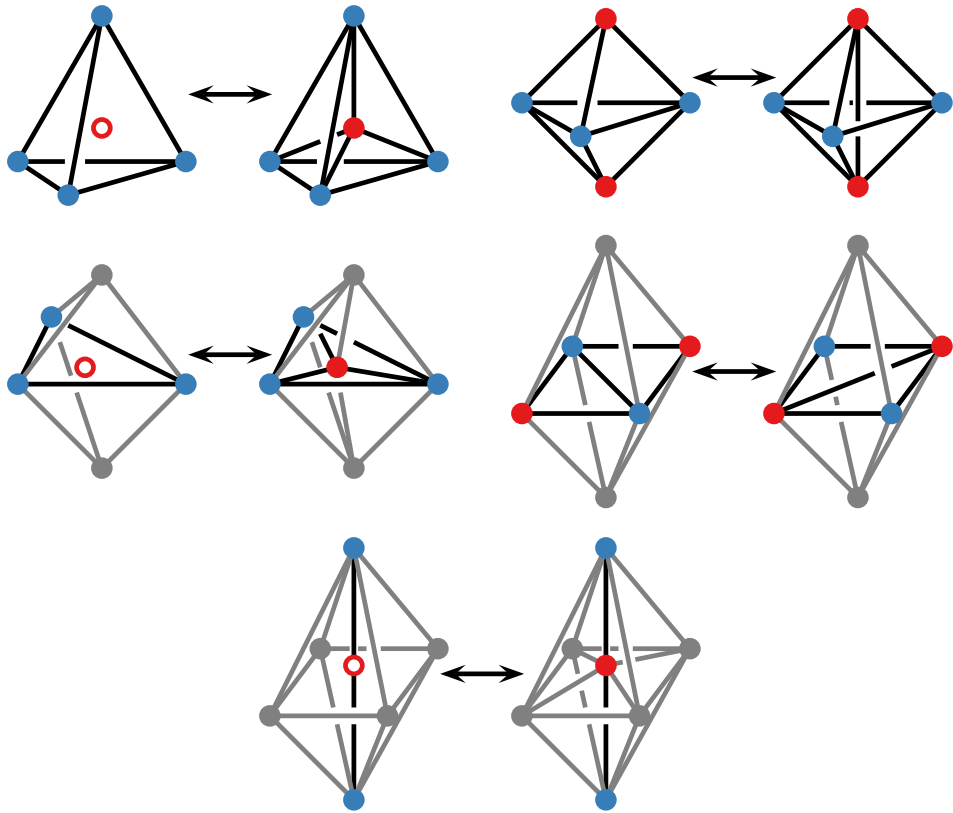


Figure 3.10: Possible flips in three dimensions.

If considering the flip from left to right, red points are the **positive circuit points**, blue points are the **negative circuit points**, and grey points and lines correspond to the three-dimensional extension of lower-dimensional flips. (First row, left) $(1 \rightarrow 4)$ -flip that divides a tetrahedron into four tetrahedra by inserting a point into the tetrahedron. (First row, right) $(2 \rightarrow 3)$ -flip that replaces a triangle shared by two tetrahedra by the edge joining the non-common points of the tetrahedra, effectively making three tetrahedra out of two. (Second row, left) $(1 \rightarrow 3)$ -flip induced by the two-dimensional flip that divides a triangle into three. (Second row, right) $(2 \rightarrow 2)$ -flip induced by the two-dimensional flip that interchanges the diagonal of a quadrilateral. (Third row) $(1 \rightarrow 1)$ -flip induced by the one-dimensional flip that divides one edge into two edges.



Inspecting the walls of the triangulation one can find all possible steps except the insertion steps. These can easily be included by considering all points that are not yet vertices of the triangulation and proposing the insertion step into the simplex the point is contained in (in fact one has to choose the smallest dimensional simplex the point is contained in). In this chapter we only consider fine triangulations and flips that conserve the number of vertices, so we do not need to look at these insertion and removal flips in detail.

For doing Markov chain Monte Carlo simulations it is important to know the probability to select a certain step, in order to calculate the ratio of this probability and the selection probability of the inverse step. This ratio is needed to correct the acceptance probability given by the Monte Carlo algorithm in order to fulfill the detailed balance condition, as mentioned in Eq. (2.42). Let $W(\mathcal{T})$ be the number of walls in triangulation \mathcal{T} . For calculating the ratio of the selection probabilities for a flip $\mathcal{T}_1 \rightarrow \mathcal{T}_2$, we need to calculate the change $\delta W(\mathcal{T}_1 \rightarrow \mathcal{T}_2) := W(\mathcal{T}_2) - W(\mathcal{T}_1)$ in the number of walls by executing the flip and the number of walls $W(\mathcal{T}_1 \rightarrow \mathcal{T}_2)$ and $W(\mathcal{T}_2 \rightarrow \mathcal{T}_1)$ that induce the certain flip and its inverse flip. The ratio of selection probabilities is then

$$\frac{S(\mathcal{T}_1 \rightarrow \mathcal{T}_2)}{S(\mathcal{T}_2 \rightarrow \mathcal{T}_1)} = \frac{W(\mathcal{T}_1 \rightarrow \mathcal{T}_2)}{W(\mathcal{T}_2 \rightarrow \mathcal{T}_1)} \cdot \frac{W(\mathcal{T}_1) + \Delta W(\mathcal{T}_1 \rightarrow \mathcal{T}_2)}{W(\mathcal{T}_1)}$$

Let the flip $\mathcal{T}_+ \rightarrow \mathcal{T}_-$ be induced by the oriented circuit (J_+, J_-) with $|J_+|$ positive and $|J_-|$ negative circuit points, and let Σ_{reduced} be the set of subsimplices of the maximal simplices containing \mathcal{T}_+ , that do not have J_+ or J_- as points. Let J_0 be the set of points in Σ_{reduced} . The number of walls that induce the flips and its inverse is then given by

$$\begin{aligned} W(\mathcal{T}_1 \rightarrow \mathcal{T}_2) &= |\Sigma_{\text{reduced}}| \binom{|J_+|}{|J_+| - 2} \\ W(\mathcal{T}_2 \rightarrow \mathcal{T}_1) &= |\Sigma_{\text{reduced}}| \binom{|J_-|}{|J_-| - 2} \end{aligned} \tag{3.10}$$

This relation holds because all walls that induce the flip $\mathcal{T}_+ \rightarrow \mathcal{T}_-$ are in the interior $\text{conv}(J_+ \cup J_- \cup J_0) \setminus \partial \text{conv}(J_+ \cup J_- \cup J_0)$. To be in this interior, a wall must either contain all points in J_+ and other points or contain all points in J_- and other points, and of course the wall must be part of \mathcal{T}_+ for the flip $\mathcal{T}_1 \rightarrow \mathcal{T}_2$ and vice versa, so only the second possibility can apply. So a wall consists of all points of J_- , one of the simplices of Σ_{reduced} and



for dimensional reasons all but two points of J_+ , which leads to the given number of walls inducing a flip.

So we have the following selection probability ratio for a flip:

$$\frac{S(\mathcal{T}_1 \rightarrow \mathcal{T}_2)}{S(\mathcal{T}_2 \rightarrow \mathcal{T}_1)} = \frac{\binom{|J_+|}{|J_+| - 2}}{\binom{|J_-|}{|J_-| - 2}} \cdot \frac{W(\mathcal{T}_1) + \binom{|J_+|}{|J_+| - 2}}{W(\mathcal{T}_1)} \quad (3.11)$$

Note that the wall formulation does not apply to insertion steps, so Eq. (3.11) does only apply to vertex-conserving steps. For non-conserving steps the selection probability depends on the choice how often to try an insertion step. Since we do only use vertex-conserving steps in this thesis, this selection probability ratio does need not to be calculated.

Ergodicity of flips

The elementary moves of triangulations, the flips defined in the previous section, will be used in Markov chain Monte Carlo simulations. In order to get correct results, these flips have to be ergodic, i.e. starting from an arbitrary triangulation, every other triangulation of the point set must be reachable by a finite number of these flips.

In two dimensions, it is proven for arbitrary point configurations that the flips are ergodic, even if one uses only diagonal-edge flips [272] (in this case one is of course restricted to fine triangulations of the point set).

In three and in four dimensions, the situation is a bit more difficult. Until now there is no proof for the ergodicity of the presented flips, but there are also no known counterexamples for a point set that possesses two triangulation which are not connected by a finite number of steps [132]. In this thesis we use the working hypothesis that at least in three dimensions the flips are ergodic.

In higher dimensions the situation becomes worse, because explicit counterexamples were found. For $d = 5$ it was shown that there exists a point configuration that has two triangulations that are not connected by a finite number of flips [358]. Earlier it was proven that for $d = 6$ there exists a point configuration and a triangulation which does not admit a single flip [357]. It is important to note that these two counterexamples are constructed in order to show that there are point configurations that are not ergodic. This does not exclude the existence of other point configurations which are ergodic, and it does of course not make a statement about whether



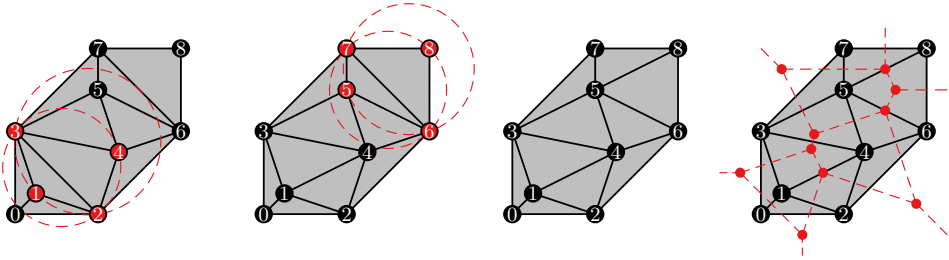


Figure 3.11: Flipping towards the Delaunay triangulation.

Find an interior edge so that the quadrilateral consisting of the two neighboring triangles is not locally Delaunay (the circumcircles of one of the triangles contains other points of the point set). Flipping this edge makes the quadrilateral locally Delaunay, if no non-locally Delaunay quadrilateral is present in the triangulation anymore, the whole triangulation is the Delaunay triangulation.

non-ergodic point configurations are many or few in the set of all possible point configurations.

The presented counterexamples disproving ergodicity are non-regular triangulations. One can show in arbitrary dimensions that the considered flips are ergodic if one restricts to regular triangulations (triangulations that are obtained using a height function) [132, p. 236f]. So we can apply our methods that will be presented in the next sections to arbitrary high triangulations, but have to restrict ourselves to regular triangulations to ensure ergodicity.

Flipping towards the Delaunay triangulation

In this small section we present an interesting application for flips in two dimensions: Diagonal edge flips can be used for creating the Delaunay triangulation of a point set \mathbf{X} step by step (denoted as *flipping towards the Delaunay triangulation*) [132, p. 238].

The algorithm is as follows: Start with an arbitrary triangulation \mathcal{T} of the point set \mathbf{X} . Now check every wall (edge that is subsimplex to two different triangles) of the triangulations. The quadrilateral consisting of the two incident triangles is called locally Delaunay if the two angles opposite to the common wall add up to π or less, or equivalently, if both circumcircles of the two triangles do not contain other points of the triangulation. If for all walls of the triangulation the quadrilateral is locally Delaunay, the whole triangulation is a Delaunay triangulation and the algorithm stops. Else, there is an edge with a non-locally-Delaunay quadrilateral, flip this edge



3. Embedded triangulations

using a diagonal edge flip into the other diagonal of the quadrilateral, so that it becomes locally Delaunay. Continue with checking the edges until every edge is locally Delaunay.

One can think about extending this algorithm to higher dimensions, but examples can be constructed where a higher-dimensional analog would get stuck in local minima. The algorithm is depicted in Fig. 3.11.



3.2 Entropy of two-dimensional unimodular lattice triangulations

In the last section we presented the definition of a triangulation of a point set and flips between these triangulations. In this section we consider triangulations of special two-dimensional point sets, namely of integer lattices.

For an exact evaluation of quantum gravity models based on triangulations, an enumeration of all possible triangulations would be necessary. However, efficient enumeration of triangulations is an open problem in combinatorics [5, 6, 335]. There is a comparably efficient enumeration algorithm for the special case of planar lattice triangulations at least for small system sizes [238]. Together with the known upper and lower bounds on the number of lattice triangulations this yields a perfect test case for the evaluation of new approximation methods.

In this section we demonstrate, that the Wang-Landau algorithm [407] that was described in detail in Sec. 2.2.2 can also be used for counting two-dimensional lattice triangulations approximately but accurately. Those flat histogram Monte Carlo methods [274, 407] have gained broad attention in statistical physics during the last years. As well as other Markov chain Monte Carlo methods they have already been applied also for approximate counting state spaces for problems in physics and informatics [162, 230, 242].

Using this approximate counting scheme we are able for the first time to calculate for large systems the entropy density of lattice triangulations and compare its scaling with analytical bounds obtained in [238]. The presented enumeration scheme can also be applied on other physical problems where the number of states of states with certain properties is important, e.g. calculating the degeneracy of the ground state (and thereby the residual entropy) plays an important role for checking the third law of thermodynamics [87, 116].

3.2.1 Two-dimensional Lattice Triangulations

Following the definitions of Sec. 3.1, our object of study are fine triangulations of the point set $P_{m,n} = \{0, \dots, m\} \times \{0, \dots, n\}$, which is a $(m+1) \times (n+1)$ integer grid. Note that according to this definition m and n do not count the number of vertices in each dimension, but the number of unitcells. These triangulations are unimodular, i. e. all triangles have constant area $A = 1/2$ [108, 238]. The number of vertices is $N_{\text{points}} = (m+1)(n+1)$, the number of triangles is $N_{\text{triangles}} = 2mn$ and the number of edges is



3. Embedded triangulations

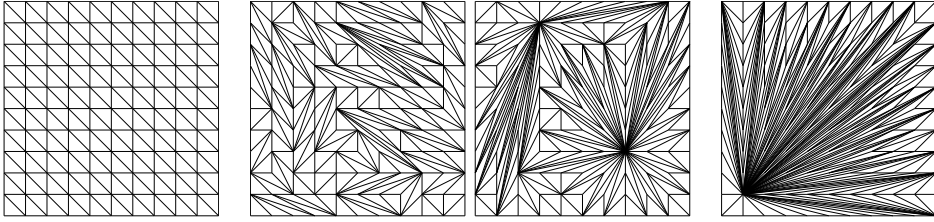


Figure 3.12: Examples for 10×10 lattice triangulations. From left to right: ordered, regular ground state of the lattice triangulations; random lattice triangulation; immobile lattice triangulation; lattice triangulation with high vertex degree E . The images are taken from Ref. [253].

$N_{\text{edges}} = 3mn + m + n$ [108, 238]. Fig. 3.12 show examples for 10×10 triangulation.

Due to the results presented in [272], we can restrict ourselves to the ergodic diagonal-edge flips between the different fine lattice triangulations. As noted in Sec. 3.1.3, one can find all possible flips by inspecting the walls (which are in two dimensions the edges) and the points of their two adjacent maximal simplices (which are triangles in two dimensions) as possible minimal dependent sets, and that for associated flip to be executable either \mathcal{T}_+ or \mathcal{T}_- has to be contained in the triangulation. One can show that for two-dimensional lattice triangulations this is equivalent to the two triangles sharing the common edge forming a parallelogram, or the quadrangle formed by the four points having diagonals intersecting in their respective mids, which reduces the calculation effort for flippability checks. Note that the case of a degenerate flip cannot occur if one considers only full triangulations, because a degenerate flip is induced by 3 circuit points on a common line, which would lead to an insertion or removal step. Several examples of (valid and invalid) flips are displayed in Fig. 3.13.

There are several possible choices of boundary conditions (BC), for instance free, periodic and fixed BC as shown in Fig. 3.14. For the latter case the different triangulations are embedded into a bigger lattice equipped with a fixed triangulation. For the numerical approximation we rely on a well behaved ground state degeneracy as depicted later, so for all simulations fixed boundary conditions are chosen. With periodic BC the ground state is highly degenerated, whereas with fixed BC the degeneracy of the ordered ground state is exactly 1. For free BC the ground state is not the maximum ordered state of a triangular lattice.

It was proven that the number $\Omega(m, n)$ of different unimodular lattice



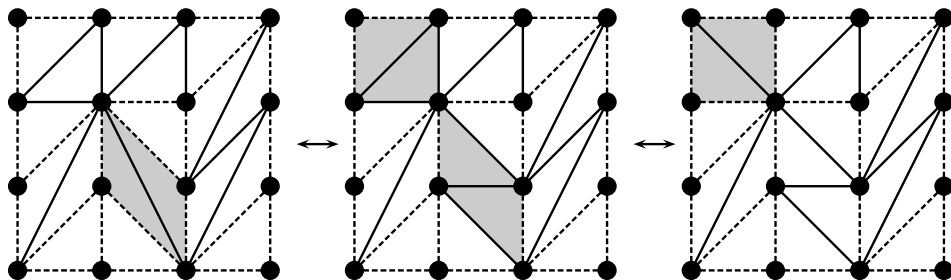


Figure 3.13: Diagonal edge flips in two-dimensional lattice triangulations. Solid edges correspond to valid flips, which for two-dimensional lattices mean that the adjacent lattices form a parallelogram. Dashed edges correspond to invalid flips. The three displayed triangulations differ by the flips that involve the gray parallelograms.

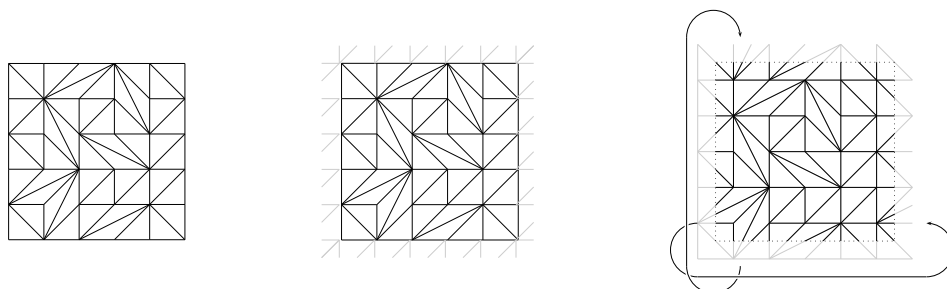


Figure 3.14: Different types of boundary conditions for lattice triangulations: open boundary conditions, fixed boundary conditions and periodic boundary conditions. The images are taken from Ref. [253].



triangulations on a grid $P_{m,n}$ grows exponentially with system size mn [238], hence, the entropy $S \propto \log \Omega$ is an extensive quantity. To compare with the exact results and the bounds given in Ref. [238], we use the entropy density (denoted by capacity in Ref. [238])

$$C(m, n) := \frac{\log_2 \Omega(m, n)}{mn}, \quad (3.12)$$

which is the entropy of the system divided by the system size¹

3.2.2 Approximate enumeration of triangulations

In this section we describe how the approximative counting procedure of Sec. 2.3.3 is applied for calculating the entropy density of two-dimensional lattice triangulations, and how the occurring problems were solved.

Topological Energy

We use the Wang-Landau algorithm [406, 407] to calculate the density of states of unimodular lattice triangulations. This method is originally designed to estimate densities of states in terms of the energy. To use it for counting arbitrary geometric configurations, one has to divide the configuration space into distinct classes by defining an energy functional as discrimination criterion. In principle this definition is arbitrary for this purpose, however, the choices differ in computational efficiency. A natural choice should be discrete valued, illustrative and cheap to calculate. Additionally the degeneracy of at least one energy class should be known exactly for normalization purposes and it should be calculated solely from topological parameters, so that the method can be easily generalized to triangulations of general point sets. The energy functional used here is the sum

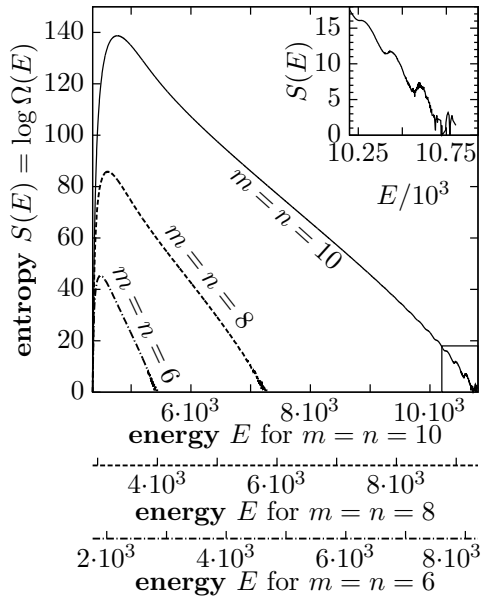
$$E = \sum_{\text{vertices } v} d_v^2 \quad (3.13)$$

over the squared vertex degrees, which are the number of incident edges at a vertex. The squaring is necessary as the sum over all vertex degrees is constant. Similar energy functions were already used for calculating mixing times of Glauber dynamic on lattice triangulations [108] and for calculating graph properties closed surface triangulations [52, 259]. The

¹ Note that we use the logarithm of basis 2 for the entropy density of lattice triangulations to agree with the conventions of Ref. [238]. For the entropy density of topological and causal triangulations later in this thesis we will use the natural logarithm.



Figure 3.15: Microcanonical entropy $S(E) = \log \Omega(E)$ of lattice triangulations, calculated using Wang-Landau sampling with the vertex-degree-energy (3.13): 6×6 (dash-dotted), 8×8 (dashed) and 10×10 (solid). The plot is taken from Ref. [253].



energy difference induced by flipping the diagonal x_1x_2 of a parallelogram $x_1x_2x_3x_4$ into the other diagonal x_3x_4 using the energy functional (3.13) is given by

$$\Delta E = (d_3 + d_4 - d_1 - d_2 + 2)^2,$$

where d_i is the number of incident edges at point x_i before the flip. Using the energy functional (3.13) and this energy difference the microcanonical entropy can be calculated using the Wang-Landau algorithm as displayed in Fig. 3.15.

Limits on system size

The entropy landscape shows a steep rise for small energies. Then, it reaches a maximum and declines smoothly towards high energies, as can be seen in Fig. 3.15. For the dense configuration space regions around the peak the common Wang-Landau approach is perfectly unproblematic, but difficulties for large systems arise in the low and high energy regions, where the simulation can get stuck for different reasons.

In the low energy regions there are huge entropy differences between neighboring states. The degeneracy of the first excited state $\Omega(E' =$



$E - E_{\text{gs}} = 4$) for $m \times n$ lattice triangulations can be calculated to be

$$\begin{aligned} \Omega(E' = 4) &= \sum_{i=1}^m \sum_{j=1}^n (m - i + 1)(n - j + 1) + \\ &+ \sum_{j=1}^n \sum_{i=1}^{m-j} (m - (i + j) + 1)(n - j + 1) + \\ &+ \sum_{i=1}^m \sum_{j=1}^{n-i} (n - (i + j) + 1)(m - i + 1) \approx n^4/2 \end{aligned} \quad (3.14)$$

So for example in a 10×10 system the number of first excited states is $\Omega(E' = 4) = 5665$ compared to $\Omega(E = 0) = 1$ for the single ground state. Now, imagine a simulation step where the system is in ground state. While all edges are flippable, the corresponding acceptance probability of any edge flip is then $P_{\text{acc}} = 1/5665$, the probability decreasing with system size $n \times n$ like n^{-4} . Certainly this limits the treatable system size severely – not only by means of runtime, but also by exceeding the numerical precision of common floating point arithmetics.

In high energy regions the immobility is caused by a lack of connection between states in the same energy region, i. e. in general no short flip paths exist between states with similar energy. Furthermore, most edges in high energy states are unflippable. A typical immobile high energy state is depicted in Fig. 3.12. As for the ground state the algorithm can get stuck for long time in a high energy state due to high rejection rates caused by huge entropy differences.

One common approach to fix high rejection rates in low temperature Metropolis simulations is to use a rejection-free algorithm, known as “the N -fold way” or continuous time algorithm [99], which can be combined with the Wang-Landau method [364]. The basic idea of the N -fold way is to accept every step and to correct for the average number of steps a normal algorithm would perform before leaving the state. The N -fold way was implemented for the lattice triangulations, but did not lead to improvements of the simulation times or the accessible system sizes.

The problem with high energy states can be overcome by defining an energy cut-off. Rejecting all steps beyond this energy leads to the correct estimate, as long as after each step – even a rejected one – the current state is correctly taken into account and added to the histogram of visits [365]. This cut-off leads to a systematic underestimation of the total number of triangulations, yet, if the cut-off is chosen correctly the error is small, as can be seen from the cumulative sum $\Omega_{\Sigma}(E) = \sum_{E' < E} e^{S(E')}$ and the relative



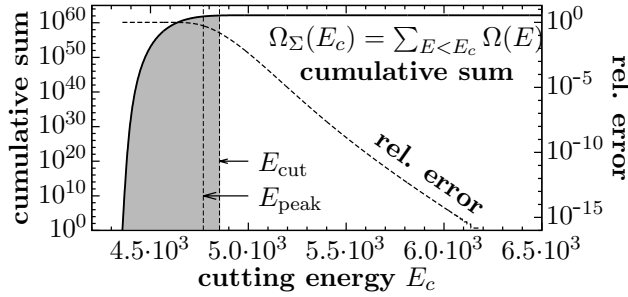


Figure 3.16: Cumulative sum $\Omega_{\Sigma}(E_c) = \sum_{E < E_c} \Omega(E)$ of the number of lattice triangulations $\Omega(E)$ in terms of the energy cutoff E_c for a 10×10 lattice (black, solid line). The relative error $\Omega_{\Sigma}(E_c)/\Omega_{\Sigma}(\infty) - 1$ (dashed line) decreases rapidly for $E_c > E_{\text{peak}}$, so that only the gray part of the energy range can be used for calculating the number of lattice triangulations. The plot is taken from [253].

error $\epsilon_{\text{cut}}(E) = (\Omega - \Omega_{\Sigma}(E))/\Omega$ in Fig. 3.16. Unfortunately the low energies cannot be cut, as those are needed for normalization. Furthermore, it is not known if ergodicity holds with a low energy cut-off. For high energy cut-offs ergodicity holds until a certain energy $E_{\text{erg}} < E_{\text{cut}}$, as the longest edge in a triangulations can always be shortened by a flip, and shorter edges correspond to lower energies. The energy E_{erg} is big enough to leave the results unchanged.

Energy cutoffs and initial estimates

The question of finding a reasonable cut-off E_{cut} remains. First the a-priori unknown energy range has to be estimated; while the energy E_{min} of the ground state can be calculated, we approximate the maximal energy by constructing a star-shaped state of nearly maximum energy E_{high} (cf. Fig. 3.12). As can be seen in Fig. 3.15, the entropy is peaked around an energy value of E_{peak} , that is easily accessible by simulating an unbiased random walk, i. e. a simulation where all proposed flips are accepted, and averaging over the sampled energies. These 3 energies suffice to set a sensible energy cut-off

$$\begin{aligned} E_{\text{cut}} &= E_{\text{min}} + \epsilon_{\text{high}}(E_{\text{high}} - E_{\text{min}}) \text{ or} \\ E_{\text{cut}} &= E_{\text{min}} + \epsilon_{\text{peak}}(E_{\text{peak}} - E_{\text{min}}) \end{aligned} \quad (3.15)$$

where $\epsilon_{\text{high}} < 1$ and $\epsilon_{\text{peak}} > 1$ are constants that have to be fixed empirically. Typical values can be $\epsilon_{\text{high}} = 1/4$ and $\epsilon_{\text{peak}} = 6/5$.



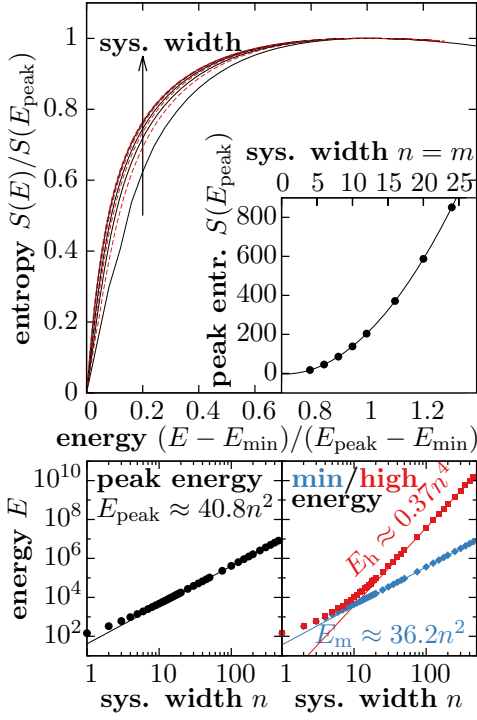


Figure 3.17: Scaling of the 2d lattice triangulation DOS.

(a) Rescaled densities of state for quadratic lattices up to $n = 25$. The densities converge, so that their extrapolation can be used as an initial estimation for simulations of larger lattices. (b) The peak and the minimal energy of triangulations as well as the peak energy entropy grow quadratically with the system width. The high energies, which are a lower bound for the maximal energy of triangulations, grow with the system width to the power of 4. The plot is taken from Ref. [253].

Extrapolating $S(E_{\text{peak}})$ from the Wang-Landau results for smaller systems an initial estimate for the entropy can be calculated for large systems. The precision of this extrapolation is not crucial. Anyhow, the error is small, as can be seen in Fig. 3.17. The 4 parameters $E_{\text{min}} = 6^2 \cdot (n+1)^2$, $S(E_{\text{min}}) = 0$ (by definition of boundary conditions), E_{peak} (measured or extrapolated) and $S(E_{\text{peak}})$ (extrapolated) characterize the entropy curve for quadratic lattices larger than 10×10 sufficiently well (cf. Fig. 3.17).

Using an initial estimate can speed up the relaxation process. For 15×15 triangulations the simulation with initial estimate extrapolated from 10×10 triangulations is by a factor of 3 faster than a simulation without one. For larger systems the speedup is even more drastically.

3.2.3 Results

We use Wang-Landau sampling for an approximate enumeration of lattice triangulations to calculate the entropy density for the different lattice sizes. For all system sizes 5 independent runs are performed. Beginning with modification factor $m_0 = \exp(10^{-2})$, it is reduced with the exponent $c = 0.9$ whenever flatness $f = 0.8$ is reached in the histogram of visits. The



simulation is stopped, when modification factor $m_f = \exp(10^{-12})$ is reached.

m	entr. dens. C	m	entr. dens. C	m	entr. dens. C
1	0.00000	9	2.04615	17	2.12374
2	1.39657	10	2.06343	18	2.12857
3	1.66927	11	2.07745	19	2.13263
4	1.81445	12	2.08887	20	2.13628
5	1.90071	13	2.09819	21	2.13858
6	1.95728	14	2.10617	22	2.14168
7	1.99535	15	2.11281	23	2.14352
8	2.02433	16	2.11917	24	2.14492

Table 3.1: Entropy density C as defined in Eq. (3.12) measured by the Wang Landau algorithm, taken from Ref. [253]

The validity of the method can be checked against the exact results of Kaibel and Ziegler [238] for small lattice sizes. The entity of interest is the entropy density defined by Eq. (3.12) which is equivalent to the capacity used in [238]. As the entropies for different energies vary over large ranges, summation is done using multiprecision arithmetics from Python `mpmath/gmp` [232]. In Fig. 3.18 simulation data for narrow lattice stripes are compared to the exact results. All measurements are averaged over 5 independent runs, for large lattices an energy cutoff (3.15) with the empirical $\epsilon_{\text{high}} = 0.75$ is used. While the accuracy of single Wang-Landau simulations is limited and the density of states does not change after reaching a certain modification factor (saturation of error) [72, 306] for almost all considered system sizes the relative error of the simulation data is below 10^{-3} , so a systematic error can be neglected.

The same is done for rectangular triangulations up to size 24×10 and quadratic triangulations up to size 24×24 , where the energy cutoff (3.15) with the empirical $\epsilon_{\text{peak}} = 1.2$ is used and an average over 3 independent runs was performed. The initial entropy estimations $S_0(E)$ for systems of size $m = n > 16$ are step-wise extrapolated from the relaxed result for smaller systems. Systems larger than including 20×20 did not reach their final modification factor $m = 10^{-12}$ in time. However, the results did not change any more during the last steps. This is an indication that saturation of error was already reached.

The entropy densities for the quadratic lattices are listed in Tab. 3.1. In Fig. 3.19 the capacity for the quadratic and rectangular triangulations is displayed. Using a fit the limit of the entropy density for infinite lattices



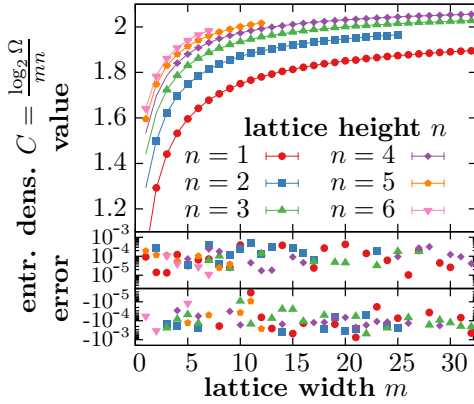


Figure 3.18: Comparison of exact and numerical entropy density.

(a) Entropy density $C(m, n) = (mn)^{-1} \log_2 \Omega(m, n)$ for triangulations of lattices with height $1 \leq n \leq 6$ (color code) in terms of the lattice width m , calculated using Wang-Landau sampling. (b) Relative error $C(m, n)/C_{\text{exact}} - 1$ compared to the exact enumeration results of [238]. The plot is taken from Ref. [253].

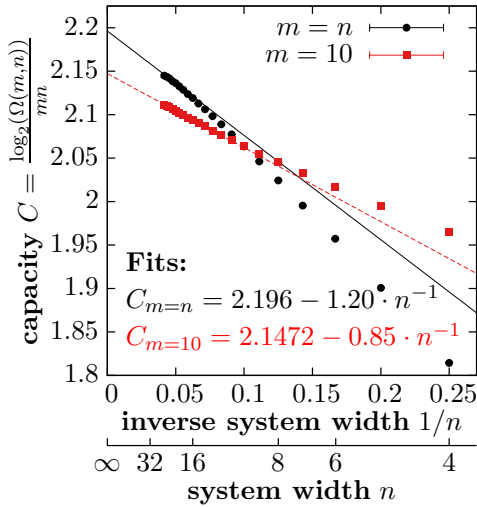


Figure 3.19: Extrapolation of the entropy density.

Measurements of the entropy density for systems up to size 24×24 . In the limit $n \rightarrow \infty$ the extrapolated values are $C_{10} = 2.1472(4)$ for stripes of width m and $C = 2.196(3)$ for quadratic lattices with $m = n$. The plot is taken from Ref. [253].

and the asymptotic behavior can be found to be

$$\begin{aligned} C_{m=10} &= (2.1472 \pm 0.0004) - (0.852 \pm 0.008) \cdot n^{-1} \\ C_{m=n} &= (2.196 \pm 0.003) - (1.20 \pm 0.07) \cdot n^{-1} . \end{aligned} \quad (3.16)$$

3.2.4 Discussion

It has been shown that approximate counting of lattice triangulations is possible and feasible up to an error of 10^{-3} by using a Wang-Landau Monte-Carlo scheme. Our results for the entropy density for lattice sizes below 24×24 improve the analytical bounds found in [238]. As exact numbers



are known for small systems, lattice triangulations provide a complement to the commonly used variants of the Ising model and other spin models.

One approach for optimizing the measurement efficiency and possible access bigger lattices could be a different choice of the energy functional. Thereby, the challenge of high entropy differences between flip-connected states could be tackled as well. As a different approach, optimized probability weights other than the flat histogram probabilities could help to improve the sampling of neuralgic configuration space areas. Different algorithmic approaches like the transition matrix Monte Carlo algorithm [408] should be tested against the problem as well.

A generalization of the estimation scheme could be interesting especially for mathematicians dealing with combinatorics. Scanning the energy landscape of a problem yields insight, it helps in winnowing dead ends from promising questions and generates a first estimate of what results to expect and quickly leads to interesting conjectures. Furthermore it can be applied to interesting counting problems in mathematics, informatics and physics.



3.3 Counting three-dimensional lattice triangulations

In the last section we counted triangulations of rectangular and quadratic two-dimensional lattices. In this section we increase the dimension by one and consider triangulations of three-dimensional lattices.

In comparison with the two-dimensional case, only few is known about three-dimensional lattice triangulations from the mathematical point of view. There are no proven exponential bounds as in [238] for the two-dimensional case, also the ergodicity of the flips is not proven yet, as explained in Sec. 3.1.3. Using the program TOPCOM [335] one can obtain some exact enumeration results, but only for the unitcube (where there are 74 triangulations, as depicted in Sec. 3.3.1) and for a $2 \times 1 \times 1$ lattice, where there are 10748 triangulations. For larger lattice sizes the program does not terminate in any reasonable time. So in this section we use the Wang-Landau algorithm to count the number of three-dimensional lattice triangulations with the same method as presented in Sec. 3.3.

We restrict ourselves to three special cases, which are displayed in Fig. 3.20: Triangulations of sticks, which are lattices with a linear size of n unitcubes in the x-direction and a linear size of 1 unitcube in the other two directions; triangulations of planes, which are lattices with a linear size of n unitcubes in the x-direction and the y-direction and a linear size of 1 unitcube in the third direction; and triangulations of cubes, which are lattices with a linear size of n unitcubes in all three directions. In all three cases we define the system size to be the number of unit cubes in the lattice.

Before using the Wang-Landau algorithm for counting the number of three-dimensional lattice triangulations, we present the 74 triangulations of the smallest possible lattice, the unitcube. On the one hand this is done for giving the reader an intuition about three-dimensional triangulations, which are far more difficult to visualize than two-dimensional ones. On the other hand this demonstrates that in three dimensions the structure of the triangulations can be more complicated than in two-dimensions (where there are only two triangulations of the unitcell and only one type of triangle used in these triangulations). Furthermore, the number and the structure of the unitcube triangulations can be used for calculating some rough estimates of the entropy density for three-dimensional lattice triangulations.

As for two-dimensional lattices we introduce a simple energy functional in order to calculate the density of states using a Wang-Landau simulation, and compare it to other energy functionals. Cuts on this energy have to be



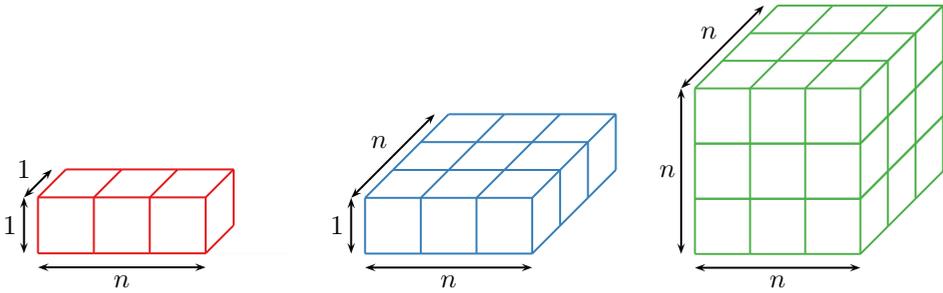


Figure 3.20: Different lattice shapes for counting three-dimensional lattice triangulations: (left, red) Stick consisting of $n \times 1 \times 1$ unitcells, (center, blue) plane consisting of $n \times n \times 1$ unitcells and (right, green) cube consisting of $n \times n \times n$ unitcells.

applied for large system sizes in order to get a convergence of the simulation in appropriate time.

3.3.1 Small three-dimensional lattice triangulations

In this section we present the six different types of triangulations of the unitcell, count the isomorphic realizations of each type and present the possible flips of each type. The six different types were already presented in [132, p. 21; p. 319ff]. The following points are used as the unitcube defining point set:

$$A = \begin{pmatrix} \mathbf{x}_0 & \mathbf{x}_1 & \mathbf{x}_2 & \mathbf{x}_3 & \mathbf{x}_4 & \mathbf{x}_5 & \mathbf{x}_6 & \mathbf{x}_7 \\ 0 & 1 & 1 & 0 & 0 & 1 & 1 & 0 \\ 0 & 0 & 1 & 1 & 0 & 0 & 1 & 1 \\ 0 & 0 & 0 & 0 & 1 & 1 & 1 & 1 \end{pmatrix}$$

In order to characterize the different triangulations we define different categories for the simplexes by looking at the length of the edges of the tetrahedrons (which can have edges with edge length a , an area-diagonal $\sqrt{2}a$ and a room-diagonal $\sqrt{3}a$), that can be seen in Fig. 3.21. The characterization and the names were introduced in [132, p. 319f].

- **Corner tetrahedron:** Tetrahedron with 3 edges and 3 area-diagonals. The points defining the tetrahedron are three points of a face of the cube (giving a rectangular triangle) and the counterpart of the point at the right angle in the opposite face.



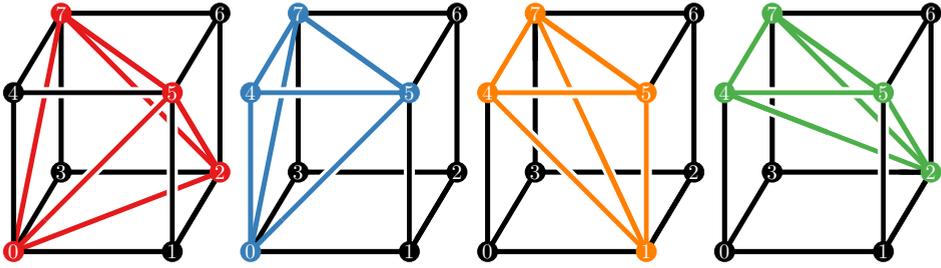


Figure 3.21: The four different simplices in the triangulation of one 3D unit cell: (red) **core tetrahedron**, (blue) **corner tetrahedron**, (orange) **staircase tetrahedron** and (green) **slanted tetrahedron**.

- **Staircase tetrahedron:** Tetrahedron with 3 edges, 2 area-diagonals and 1 room-diagonal. The points of this tetrahedron are three points of a face of the unit cell (giving a rectangular triangle) and the counterpart of one of the points not at the right angle in the opposite.
- **Slanted tetrahedron:** Tetrahedron with 2 edges, 3 area-diagonals and 1 room-diagonal. Build by three points of a face of the cell and the counterpart of the point being in the triangular plane, but not in the triangle.
- **Core tetrahedron:** Tetrahedron with 6 area diagonals. Defining points of the tetrahedron are two points of a diagonal of a face and the two points of the diagonal of the opposite face that is not parallel to the first one.

For determining the number of isomorphic triangulations of a certain type considering the permutation symmetry can be helpful:

Definition 3.16 (permutation of index set):

Let \mathbf{A} be a point configuration with index set J and with $|J| = n$ points. A bijective map $\pi : J \rightarrow J$ is called a *permutation* of the index set. We will use the notation $\pi = [j_1 j_2 \dots j_n]$ for the permutation that maps point i into point j_i , $\pi(i) = j_i$.

The points of the unitcube have a rich group of symmetries, all of them can be composed out of these three elementary ones:

1. A $\pi/2$ -rotation around an axis connecting the face centers of two opposite faces of the cube (4-axis)
2. A $2\pi/3$ -rotation around an axis on a volume-diagonal (3-axis)



3. A reflection symmetry with respect to the plane in the middle between the two faces defining the 4-axis (m-plane)

Because of this the cube symmetry is often referred to as 43m-symmetry-group (e.g. in crystallography). The index set permutations that correspond to these three symmetries are for example:

$$\begin{aligned}\pi_4 &:= [1, 2, 3, 0, 5, 6, 7, 4] \\ \pi_3 &:= [0, 3, 7, 4, 1, 2, 6, 5] \\ \pi_m &:= [4, 5, 6, 7, 0, 1, 2, 3]\end{aligned}\tag{3.17}$$

Composite symmetries can be displayed as a concatenation of these three permutations.

Until now we only considered the symmetry of the eight points that constitute the unit cube. As a next step one has to define the symmetries of the triangulation.

Definition 3.17 (permutation symmetry of triangulation):

A triangulation \mathcal{T} of a point configuration \mathbf{A} (index set J , number of points n) is said to be *symmetric under the permutation* π , if the image of every simplex of \mathcal{T} is element of the triangulation:

$$\pi(\sigma) \in \mathcal{T} \forall \sigma \in \mathcal{T}$$

In the following subsections we present the six different triangulations of the unit cube that cannot be mapped into each other by rotations and reflections, and list the possible flips in these triangulations. These six triangulations can be characterized mainly by the number of corner tetrahedra in the triangulation.

Corner-4-Triangulation (C4T)

We will start with a triangulation that has four corner tetrahedra and one core tetrahedron, this triangulation is denoted by Corner-4-Triangulation (short C4T). It can be obtained by connecting two area diagonals of two opposite faces of the cube that are not parallel. One example is the following triangulation:

$$\tau_{C4T} = \{\{0275\}, \{0125\}, \{0237\}, \{0457\}, \{2567\}\}\tag{3.18}$$

There are two triangulations of this type, because choosing one diagonal in one face fixes all the diagonals in the other faces; and there are two possibilities for choosing this diagonal.



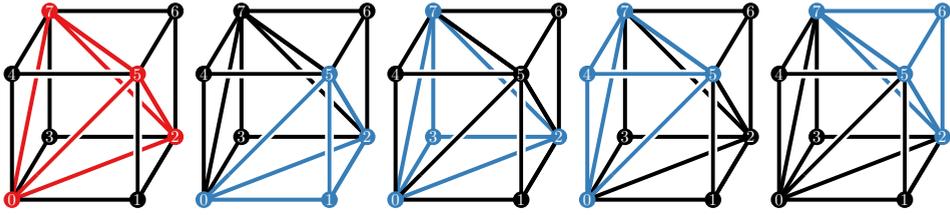


Figure 3.22: Corner-4-Triangulation (3.18) of the 3D unitcell with one **core tetrahedron** (red) and **four corner tetrahedra** (blue).

For each of the four corner tetrahedra there is a $2 \rightarrow 3$ flip together with the core tetrahedron, each of them flipping the triangulation to one of the Corner-3-Triangulations examined in the next section. For our example triangulation these flips are

$$\begin{aligned}
 \{\{0257\}, \{0125\}\} &\rightarrow \{\{0127\}, \{0157\}, \{1257\}\} \\
 \{\{0257\}, \{0237\}\} &\rightarrow \{\{0235\}, \{0357\}, \{2357\}\} \\
 \{\{0257\}, \{0457\}\} &\rightarrow \{\{0245\}, \{0247\}, \{2457\}\} \\
 \{\{0257\}, \{2567\}\} &\rightarrow \{\{0256\}, \{0267\}, \{0567\}\}
 \end{aligned} \tag{3.19}$$

Corner-3-Triangulation (C3T)

Flipping one corner and the core tetrahedron of a C4T as in Eq. (3.19) to three slanted tetrahedra leads to a Corner-3-Triangulation (C3T) consisting of three corner and three slanted tetrahedra, for instance to the following one:

$$\tau_{C3T} = \{\{0256\}, \{0267\}, \{0567\}, \{0125\}, \{0237\}, \{0457\}\} \tag{3.20}$$

There are 8 triangulations of this type, for each of the two C4Ts one can choose one of the corner tetrahedra to flip with the core tetrahedron. This can also be seen due to the fact that the triangulation is permutation symmetric with respect to 3-rotations around the $\{06\}$ -axis, so the remaining two symmetries generate $4 \cdot 2$ isomorphic C3-Triangulations.

In a C3-triangulation the following flips are possible:

- Each of the three slanted tetrahedra can be flipped with the neighboring corner tetrahedron using a $2 \rightarrow 2$ flip into two staircase tetrahedra.



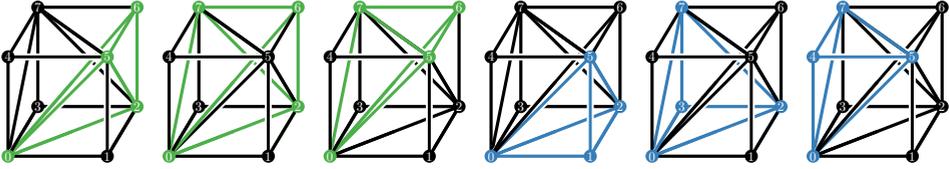


Figure 3.23: Corner-3-Triangulation (3.20) of the 3D unitcell with three slanted tetrahedron (green) and three corner tetrahedra (blue).

The three possible flips in our example (3.20) are:

$$\begin{aligned}
 \{\{0256\}, \{0125\}\} &\rightarrow \{\{0126\}, \{0156\}\} \\
 \{\{0267\}, \{0237\}\} &\rightarrow \{\{0236\}, \{0367\}\} \\
 \{\{0567\}, \{0457\}\} &\rightarrow \{\{0456\}, \{0467\}\}
 \end{aligned} \tag{3.21}$$

This results in a triangulation with two corner tetrahedra that are neighbors that will be examined in the next section. There are three of these flips.

- One $3 \rightarrow 2$ flip involving the three slanted tetrahedra that inverts the flip that led to the C3T.

Corner-2-Neighbor-Triangulation (C2NT)

Doing the flip (3.21) described in the section above for C3T leads to a triangulation with two slanted tetrahedra, two staircase tetrahedra and two corner tetrahedra that have a common edge, called the Corner-2-Neighbor-Triangulation (C2NT). The additional *neighbor* in the name will become clear later, because there is another triangulation with two corner tetrahedra that cannot be obtained by a flip out of a C3T. One example for such a C2N-triangulation is:

$$\tau_{C2NT} = \{\{0126\}, \{0267\}, \{0567\}, \{0156\}, \{0237\}, \{0457\}\} \tag{3.22}$$

There are 24 triangulations of this type: One can choose 8 edges for the first corner and then 3 edges for the second corner polytope, overcounting the number by a factor of 2 (because the order of choosing the corner tetrahedra does not matter), so there are 12 possibilities for choosing the two corner polytopes. For each of this one has two possibilities for choosing the room diagonal. This can also be checked by noticing that this triangulations is not symmetric under any symmetry transformation.



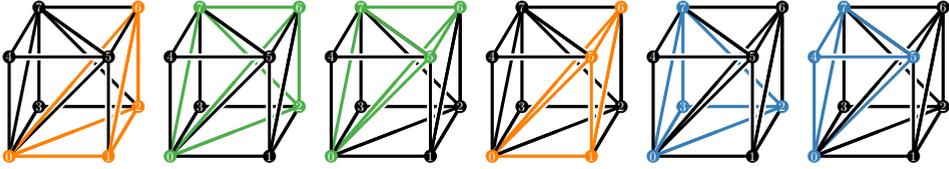


Figure 3.24: Corner-2-Neighbor-Triangulation (3.22) of the 3D unitcell with two slanted tetrahedra (green), two staircase tetrahedra (orange) and two corner tetrahedra (blue).

For the C2N-triangulation there are the following flips in our example (3.22):

- Each of the two remaining slanted tetrahedra can be flipped together with the neighboring corner tetrahedron in a $2 \rightarrow 2$ flip into two staircase tetrahedra, for our case:

$$\begin{aligned} \{\{0267\}, \{0237\}\} &\rightarrow \{\{0236\}, \{0367\}\} \\ \{\{0567\}, \{0457\}\} &\rightarrow \{\{0456\}, \{0467\}\} \end{aligned} \quad (3.23)$$

- There is a double $2 \rightarrow 2$ flip consisting of two $2 \rightarrow 2$ flips, each involving a staircase and a slanted tetrahedron. In our example triangulation this is the following flip:

$$\left. \begin{aligned} \{\{0156\}, \{0567\}\} \\ \{\{0126\}, \{0267\}\} \end{aligned} \right\} \rightarrow \left\{ \begin{aligned} \{\{1567\}, \{0157\}\} \\ \{\{1267\}, \{0127\}\} \end{aligned} \right\} \quad (3.24)$$

Each of the subflips produces again a staircase and a slanted tetrahedron. So this flip produces another C2N-Triangulation with another diagonal. One can see that this flip is equivalent with the $\pi = [6, 7, 2, 3, 4, 5, 0, 1]$ permutation, which is a reflection at the $\{2345\}$ -plane:

- There is one $2 \rightarrow 2$ flip involving the two staircase tetrahedra that produces one corner and one slanted tetrahedron and inverts the flip that we used to arrive at the C2NT.

Corner-1-Triangulation (C1T)

If one executes the flip (3.23) described in the section before, one arrives at a triangulation with four staircase tetrahedra, one slanted tetrahedron



and one corner tetrahedron, called the Corner-1-Triangulation (C1T). One example for this triangulation is:

$$\tau_{C1T} = \{\{0126\}, \{0267\}, \{0456\}, \{0156\}, \{0237\}, \{0467\}\} \quad (3.25)$$

There are also 24 triangulations of this type: There are 8 possibilities to choose one corner, and for each of this there are 3 possibilities for choosing the diagonal. One can obtain this result also by considering that this triangulation is not symmetric under one of the symmetry transformations.

There are the following flips for a C1-Triangulation:

- One can do a flip with the remaining corner and slanted tetrahedron, in the example triangulation this is the flip

$$\{\{0267\}, \{0237\}\} \rightarrow \{\{0236\}, \{0367\}\} \quad (3.26)$$

This leads to a triangulation consisting only of staircase tetrahedra considered in Sec. 3.3.1.

- There are two possibilities to flip two staircase tetrahedra to one corner and one slanted tetrahedron, so that the new corner tetrahedron and one that is already contained in the triangulation have a common edge. These two flips invert the flips that led us from the C2NT to the C1T:

$$\begin{aligned} \{\{0126\}, \{0156\}\} &\rightarrow \{\{0256\}, \{0125\}\} \\ \{\{0456\}, \{0467\}\} &\rightarrow \{\{0567\}, \{0457\}\} \end{aligned} \quad (3.27)$$

- Another possible flip is a $2 \rightarrow 2$ flip of two staircase tetrahedra, giving a triangulation with two opposite corner tetrahedra described in Sec. 3.3.1:

$$\{\{0156\}, \{0456\}\} \rightarrow \{\{0146\}, \{0467\}\} \quad (3.28)$$

Corner-2-Opposite-Triangulation (C2OT)

Doing the one special flip of the C2NT described in the section before that produces a triangulation with two corner tetrahedron at opposite edges one arrives at the Corner-2-Opposite-Triangulation (C2OT). One example of this triangulation is:

$$\tau_{C2OT} = \{\{0126\}, \{0267\}, \{0146\}, \{1456\}, \{0237\}, \{0467\}\} \quad (3.29)$$



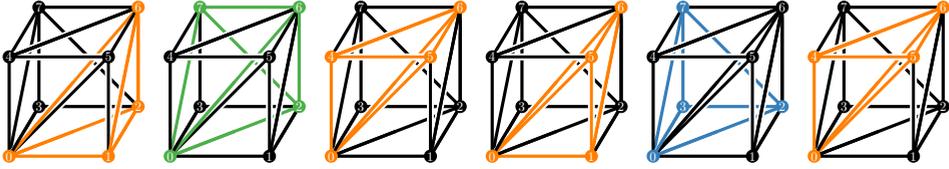


Figure 3.25: Corner-1-Triangulation (3.25) of the 3D unitcell with one **slanted tetrahedron** (green), four **staircase tetrahedra** (orange) and one **corner tetrahedron** (blue).

There are 12 of this triangulations, one has 3 possibilities to choose two opposite corner tetrahedra and 3 possibilities to choose a room diagonal. The triangulation is permutation symmetric with to the point reflection at the centre of the cube, which can be constructed by doing two times a 4-rotation and the corresponding mirror reflections.

We have the following flips for the C2O-Triangulation:

- There are two flips that lead back to a C1-Triangulations, each involving one of the corner and one of the staircase tetrahedra:

$$\begin{aligned} \{\{0237\}, \{0276\}\} &\rightarrow \{\{0236\}, \{0367\}\} \\ \{\{1456\}, \{0146\}\} &\rightarrow \{\{0156\}, \{0456\}\} \end{aligned} \quad (3.30)$$

- There are two double $2 \rightarrow 2$ flips that map the C2O-Triangulation to another C2OT having the same opposite corner tetrahedra, but different orientation of the diagonal:

$$\begin{aligned} \left. \begin{aligned} \{\{0126\}, \{0267\}\} \\ \{\{0467\}, \{0146\}\} \end{aligned} \right\} &\rightarrow \left\{ \begin{aligned} \{\{1267\}, \{0127\}\} \\ \{\{0147\}, \{1467\}\} \end{aligned} \right\} \\ \left. \begin{aligned} \{\{0467\}, \{0267\}\} \\ \{\{0126\}, \{0146\}\} \end{aligned} \right\} &\rightarrow \left\{ \begin{aligned} \{\{2467\}, \{0247\}\} \\ \{\{0124\}, \{1246\}\} \end{aligned} \right\} \end{aligned} \quad (3.31)$$

Corner-0-Triangulation (C0T)

If one does the flip listed first in the C1T described in Sec. 3.3.1, one arrives at a unitcell triangulation consisting only of staircase tetrahedra, for example at the following:

$$\tau_{C0T} = \{\{0126\}, \{0236\}, \{0456\}, \{0156\}, \{0367\}, \{0467\}\} \quad (3.32)$$



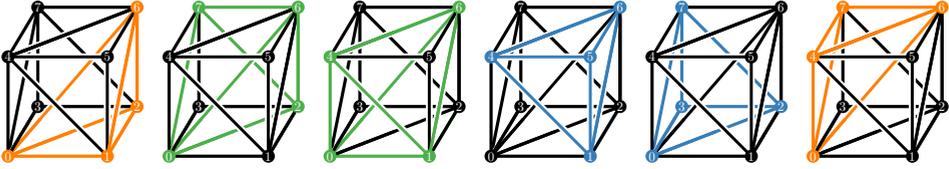


Figure 3.26: Corner-2-Opposite-Triangulation (3.29) of the 3D unitcell with two slanted tetrahedron (green), two staircase tetrahedra (orange) and two corner tetrahedra (blue) that are in opposite corners.

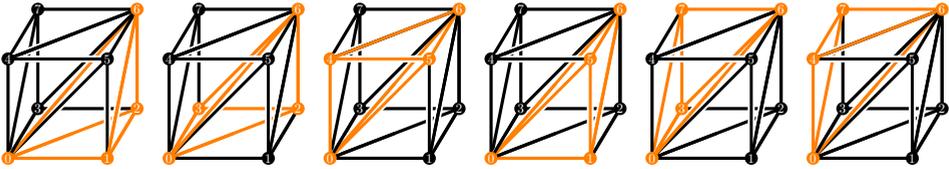


Figure 3.27: Corner-0-Triangulation (3.32) of the 3D unitcell six staircase tetrahedra (orange).

There are 4 of this triangulation, because the triangulation is determined already by the room diagonal where one has 4 possibilities to choose. It is invariant under a 3-rotation with respect to the chosen diagonal and with respect to point reflection at the body centre of the cube.

There are six $2 \rightarrow 2$ flips, each transforms two staircase tetrahedra into one corner and one slanted tetrahedron, so one arrives at a C1T again. Each of the flips can be interpreted as flipping one of the face diagonals:

$$\begin{aligned}
 \{\{0126\}, \{0156\}\} &\rightarrow \{\{0125\}, \{0256\}\} \\
 \{\{0156\}, \{0456\}\} &\rightarrow \{\{1456\}, \{0146\}\} \\
 \{\{0467\}, \{0367\}\} &\rightarrow \{\{3467\}, \{0346\}\} \\
 \{\{0367\}, \{0236\}\} &\rightarrow \{\{0237\}, \{0267\}\} \\
 \{\{0456\}, \{0467\}\} &\rightarrow \{\{0457\}, \{0567\}\} \\
 \{\{0126\}, \{0236\}\} &\rightarrow \{\{1236\}, \{0136\}\}
 \end{aligned} \tag{3.33}$$

3.3.2 Constructing three-dimensional lattice triangulations

The first step is to construct for a given size of the point lattice a triangulation that can be used as an initial state. Under the conjecture of ergodicity of the flips, all other lattice triangulations can then be constructed out of this initial state. As for the two-dimensional case, we construct the initial triangulation from triangulations of the elementary unitcube.



Therefore there are, e.g., the following two possibilities: Firstly, one can use the C4-triangulation presented in Sec. 3.3.1 in all unitcubes, which is the triangulation of the unitcube with the minimal number of tetrahedra and edges. One has to take in mind that we cannot use only one of the C4T, but both, because the diagonals in opposite faces of the unitcube are not parallel. So if one of the C4T is used in a unitcube, in all other unitcubes that are direct neighbors the other C4T has to be used.

Secondly one can use unitcubes with one of the C0-triangulation presented in Sec. 3.3.1 in all unitcubes. This has the advantage that the same triangulation can be used in all unitcubes, because the diagonals in opposite faces of the unitcube are parallel. The disadvantage is that the C0T is not the smallest triangulation of the unitcube.

3.3.3 A lower bound for the entropy density of three-dimensional lattice triangulations

As a first estimation we approximate a lower boundary for the entropy density by considering only triangulations that are composed of unitcell triangulations. These triangulations will be called atomic. This approximation will be very rough, because there are way more triangulations that mix the different unitcells than atomic ones, but it provides valuable insight about the influence of the lattice geometry (stick, plane, cube) on the entropy density.

We first start with the analog calculation for two-dimensional triangulations to present the method in a simplified way. For $d = 2$ there are two possible triangulations for a unitcell (square with one of the two possible diagonals). For each unitcell the triangulation can be chosen independently, because the boundary of the unitcell triangulation (the square) is the same for both possible triangulations. So the number of two-dimensional $n \times m$ lattice triangulations composed by unitcells is bounded by

$$N(m, n) \geq 2^{m \cdot n} \Rightarrow C(m, n) \geq \frac{\log_2 N_{\text{atomic}}}{m \cdot n} = 1. \quad (3.34)$$

In three dimensions there are 74 triangulations of the unitcube, but the boundaries of the triangulations are not equal. Therefore one has to take into account that the diagonals of the square faces of neighboring unitcells have to match. In the following we will estimate the lower boundary separately for sticks, planes and cubes.

Lower bound for sticks For calculating the number of atomic triangulations of $n \times 1 \times 1$ -lattices one has to calculate the number of triangulations of



the unitcube with one diagonal fixed. In section Sec. 3.3.1 the triangulation of the unitcubes were discussed in detail, one can see that if half of the triangulations have one diagonal of a given face, the other half has the other diagonal at the given face. So for a stick lattice with n unitcells there are

$$N_{\text{stick}}(n) \geq 74 \cdot 37^{n-1} = 2 \cdot 37^n \quad (3.35)$$

triangulations that do not mix between the single unitcubes. This leads to the lower bound

$$C_{\text{stick}}(n) = \frac{1}{n} \log_2 N_{\text{stick}}(n) \geq \log_2(37) + \frac{1}{n} \approx 5.21 + \frac{1}{n} \quad (3.36)$$

for the entropy density of sticks.

Lower bound for planes Estimating the lower bound for the entropy density of planes with the discussed method is much more difficult than for sticks. The reason is that for most of the unitcubes two diagonals are fixed and one has to inspect in detail the different unitcell triangulations to find the number of triangulations that match with the given diagonals. Since we are not interested in the actual numbers, but only in the qualitative behavior of the entropy density, we relinquish this detailed considerations and assume that only a quarter of the unitcube triangulations matches two given diagonals.

The number of plane triangulations is then bounded by

$$N_{\text{plane}}(n^2) \gtrsim (74 \cdot 37^{n-1}) \cdot \left(37 \cdot \left(\frac{37}{2} \right)^{n-1} \right)^{n-1} \quad (3.37)$$

The first contribution is the same as for a stick, for the other sticks one has to take into account that for the first unitcube one diagonal is fixed, for all other unitcubes in the additional sticks two diagonals are fixed. This leads to the lower bound

$$C_{\text{plane}}(n^2) = \frac{1}{n^2} \log_2 N_{\text{plane}}(n^2) \gtrsim 4.209 + \frac{2}{n} - \mathcal{O}(n^{-2}) \quad (3.38)$$

for the entropy density of planes.

Lower bound for cubes For calculating the lower bound for the entropy density of cubes we apply the same approximation as for the lower bound of planes, we assume that a quarter of the 74 triangulations match three



given diagonals. We find the following bound for the number of cube triangulations:

$$N_{\text{plane}}(n^2) \gtrsim 74 \cdot 39^{3(n-1)} \cdot \left(\frac{39}{2}\right)^{3(n-1)^2} \left(\frac{39}{4}\right)^{(n-1)^3} \quad (3.39)$$

because the triangulation of the first cube can be chosen arbitrarily, for the unitcubes at the three edges one diagonal is fixed, for the unitcubes at three faces two diagonals are fixed and for the remaining unitcubes three diagonals are fixed. This leads to the following lower bound

$$C_{\text{cube}}(n^3) = \frac{1}{n^3} \log_2 N_{\text{cube}}(n^3) \gtrsim 3.209 + \frac{3}{n} - \mathcal{O}(n^{-2}) \quad (3.40)$$

for the entropy density of cubes.

3.3.4 Choosing the energy functional

There are several possibilities to choose an energy functional for a triangulation. The flips that we are using in three dimensions are the $(2 \rightarrow 3)$ -flip and its inverse flip, which changes the number of tetrahedra, triangles and edges in the triangulation, but leaves the number of vertices invariant. So in general it would be possible to use one of these overall topological quantities as energy, but this would lead to technical difficulties in calculating the density of states. Consider for example the 74 triangulations of the unitcube. Only two of these triangulations consist of 5 tetrahedra, and 72 of these consist of 6 tetrahedra, so there are only two energy bins. Also for bigger triangulations the number of energy bins is small, and, which is much worse, the entropy difference of (flip-)neighboring energy bins becomes large, which drastically decreases the acceptance probability of the Wang-Landau algorithm. Since the sum of the linear number of edges, triangles or tetrahedra incident with a vertex is the overall number times an integer constant, the same problems occur using such local linear energy functions.

Due to this disadvantages of linear energy functions, as in the two-dimensional case we use local quadratic energy functions also for three-dimensional lattice triangulations. The simplest energy function

$$E_{\text{point}}(\mathcal{T}) = \sum_{v \in \mathcal{T}} d_v(\mathcal{T})^2, \quad (3.41)$$

where $d_v(\mathcal{T})$ is the degree of the vertex v in triangulation \mathcal{T} (the number of edges incident with v), has the disadvantage that the ground state and its degeneracy cannot be determined a priori. Additionally in Fig. 3.28 the



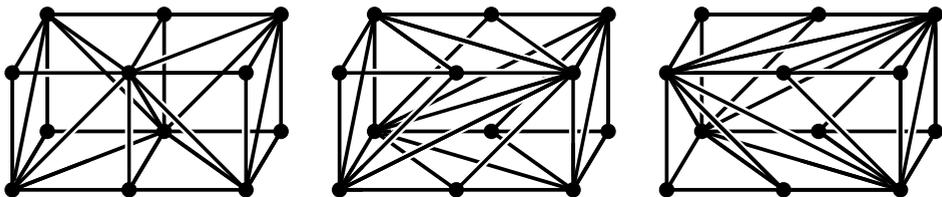


Figure 3.28: Ground state for the different energy functions on three-dimensional lattice triangulations. (Left) Ground state of the difference energy function Eq. (3.43) that is used throughout the counting, its point energy is $E_{\text{point}} = 374$ and its edge energy is $E_{\text{edge}} = 158$. (middle) Ground state of the quadratic edges-per-point energy function Eq. (3.41) with $E_{\text{point}} = 354$. (right) Ground state of the quadratic triangles-per-edge energy function Eq. (3.42) with $E_{\text{edge}} = 134$.

ground state of this energy function for a $2 \times 1 \times 1$ lattice triangulation is displayed, which is not composable by triangulations of the single unitcube. Using a similar function in the number of triangles per edge

$$E_{\text{edge}}(\mathcal{T}) = \sum_{e \in \mathcal{T}} t_e(\mathcal{T})^2 \quad (3.42)$$

(where $t_e(\mathcal{T})$ is the numbers of triangles incident with the edge e in the triangulation \mathcal{T}) leads to the same problems, the ground state of the $2 \times 1 \times 1$ lattice triangulation, which is also displayed in Fig. 3.28, is not composable into two triangulations of the unitcube.

So instead of using the simple energy Eq. (3.41), we use the energy function

$$E(\mathcal{T}) = \sum_{v \in \mathcal{T}} [d_v(\mathcal{T}) - d_v(\mathcal{T}_0)]^2, \quad (3.43)$$

which measures the local quadratic difference of the incident edges compared to an arbitrary reference triangulation \mathcal{T}_0 , which is then the ground state of the energy function. In this section we always use one of the two ordered states consisting of alternating C4T-triangulations as reference triangulation for the energy function Eq. (3.43). An equivalent formulation in terms of the number of triangles per edge is not possible, because in contrast to the vertices the edges and even their number can change during the simulation, so it is not possible to identify the edges of an arbitrary triangulation with the edges of a reference triangulation. In Tab. 3.2 the energies of the six different triangulations of the unitcube are presented with respect to the three possible energy functionals.

In principle there could exist triangulations which have for each vertex the same number of incident edges as the reference state \mathcal{T}_0 , but a different



3. Embedded triangulations

Table 3.2: Energy of the six different non-isomorphic triangulations of the unitcube ($1 \times 1 \times 1$) for the energy functionals E_{point} , E_{edge} and the actually used energy functional E which measures the quadratic difference of the vertex incidences to a given reference state. Here we use one of the C4-triangulations as ground state. The six different triangulations are presented in Sec. 3.3.1.

triang.	$E_{\text{point}} = \sum_v d_v^2$	$E_{\text{edge}} = \sum_e t_e^2$	$E = \sum_v (d_v - d_v(\mathcal{T}_0))^2$
C4T	180	66	0/72
C3T	200	90	2/74
C2NT	194	86	8/56
C2OT	190	84	28
C1T	192	86	18/42
C0T	194	90	32

topological structure (which vertex is connected with which other vertex), so the ground state of Eq. (3.43) would be degenerated. In our numerical simulations no such triangulation was found.

For applying Markov chain Monte Carlo algorithms to the triangulations with the energy functional (3.43), one has to calculate the energy difference induced by a flip. Therefor, consider a step $\mathcal{T}_+ \rightarrow \mathcal{T}_-$ that is induced by an oriented circuit (J_+, J_-) with the maximal simplices Σ_+ being involved into the step (compare Def. 3.15 for the details of the notion). Remember that the two possible (not necessarily full-dimensional) triangulations of the circuit are

$$\begin{aligned}\mathcal{T}_+ &:= \{\mathbf{Y} \subset \mathbf{J}_+ \cup J_- : J_+ \not\subset \mathbf{Y}\} \\ \mathcal{T}_- &:= \{\mathbf{Y} \subset \mathbf{J}_+ \cup J_- : J_- \not\subset \mathbf{Y}\}\end{aligned}$$

This means that the simplices in \mathcal{T}_\pm are constituted by the subsets of $J_+ \cup J_-$ that are not a proper superset of J_\pm . If the circuit is degenerated (not full dimensional), denote by J_0 the set of points that constitute the simplices in $\Sigma_{\text{reduced},+}$ (remember these are the subsimplices of Σ_+ without points in J_+ or J_-). In order to calculate the energy difference induced by the flip, one has to calculate for each point in $J := J_+ \cup J_- \cup J_0$ the change in the number of edges incident with the point, or equivalently, the number of edges incident with this point in the triangulations \mathcal{T}_+ and \mathcal{T}_- before and after the flip. In the following we denote by $e_o(p)$ the number of edges at point p where none of the two points is contained in $J \setminus J_0 = J_+ \cup J_-$, and by $e_\pm(p)$ the number of edges at point p in triangulation \mathcal{T}_\pm where at least one of the two points is contained in $J \setminus J_0 = J_+ \cup J_-$.



Consider for example a point $p_+ \in J_+$ that has $e_0(p_+)$ edges to points not contained in J , and $e_+(p_+)$ edges to points contained in J in the triangulation \mathcal{T}_+ . Edges that are contained in \mathcal{T}_+ must not be a proper superset of J_+ (must not contain all points of J_+). So if $|J_+| \geq 3$ every edge to another point of the circuit is present in \mathcal{T}_- because the two-element set of edge points cannot be a proper superset of a more than three-element set J_+ . So the number of edges $e_+(p_+) = |J| - 1$, because there is no edge from p_+ to itself. For $|J_+| = 2$ only edges between the positive point and a non-positive point are admissible, and for $|J_+| = 1$ no edge containing the positive point p_+ can be contained in \mathcal{T}_+ . Due to symmetry the numbers $e_-(p_-)$ can be calculated in the same way just by exchanging every sign in an index. So in triangulation \mathcal{T}_\pm , the number of additional edges $e_\pm(p_\pm)$ is given by

$$\begin{aligned} e_\pm(p_\pm) &= 0 & |J_\pm| &= 1 \\ e_\pm(p_\pm) &= |J_\mp| + |J_0| & |J_\pm| &= 2 \\ e_\pm(p_\pm) &= |J_\pm| + |J_\mp| + |J_0| - 1 & |J_\pm| &\geq 3 \end{aligned}$$

Using some similar arguments one can calculate the number $e_\mp(p_\pm)$ of additional edges at point p_\pm in the triangulation \mathcal{T}_\mp :

$$\begin{aligned} e_\mp(p_\pm) &= |J_\pm| + |J_0| - 1 & |J_\mp| &= 1 \\ e_\mp(p_\pm) &= |J_\pm| + |J_\mp| + |J_0| - 1 & |J_\mp| &\geq 2 \end{aligned}$$

For a point $p_o \in J_0$ we do not know alone from the circuit structure whether there are edges to other points in the component J_0 . But we know that the connections among points in J_0 do not change due to the flip. Due to our clever definition of $e_0(p)$ and $e_\pm(p)$, for $p_o \in J_0$ the number of edges can be calculated as

$$\begin{aligned} e_\pm(p_o) &= |J_\mp| & |J_\pm| &= 1 \\ e_\pm(p_o) &= |J_\pm| & |J_\pm| &\geq 2 \end{aligned}$$

As a next step we can calculate the energy difference locally for each point. Mind that one has to take into account the contributions of the reference triangulations, let $e_{\text{ref}}(p)$ be the number of edges incident with point p in the reference triangulation \mathcal{T}_0 . The local energy difference can



then be calculated using

$$\begin{aligned}\Delta E(p) &:= (d_p(\mathcal{T}_-) - d_p(\mathcal{T}_0))^2 - (d_p(\mathcal{T}_+) - d_p(\mathcal{T}_0))^2 \\ &= (e_-(p) - e_+(p)) \cdot (e_+(p) + e_-(p) + 2\delta e(p))\end{aligned}\quad (3.44)$$

for each point $p \in J$, where $\delta e(p) := e_0(p) - e_{\text{ref}}(p)$ is the difference of the number of edges at point p to points outside the circuit and the number of edges in the reference triangulation \mathcal{T}_0 . The total energy difference $\Delta E(\mathcal{T}_+ \rightarrow \mathcal{T}_-)$ is then the sum over the energy differences for each point. For a point p_{\pm} the local energy difference is

$$\Delta e(p_{\pm}) = \pm(|J_{\mp}| + |J_0| + 2\delta e(p_{\pm})) \cdot (|J_{\mp}| + |J_0|) \quad |J_{\pm}| = 1 \wedge |J_{\mp}| \geq 2 \quad (3.45a)$$

$$\Delta e(p_{\pm}) = 0 \quad |J_{\pm}| = 2 \wedge |J_{\mp}| = 1 \quad (3.45b)$$

$$\Delta e(p_{\pm}) = \pm 1 \mp 2(|J_{\mp}| + |J_0| + \delta e(p_{\pm})) \quad |J_{\pm}| = 2 \wedge |J_{\mp}| \geq 2 \quad (3.45c)$$

$$\Delta e(p_{\pm}) = \pm 1 \pm 2(|J_{\pm}| + |J_0| + \delta e(p_{\pm})) \quad |J_{\pm}| \geq 3 \wedge |J_{\mp}| = 1 \quad (3.45d)$$

$$\Delta e(p_{\pm}) = 0 \quad |J_{\pm}| \geq 3 \wedge |J_{\mp}| \geq 2 \quad (3.45e)$$

For a point p_0 the local energy difference is

$$\Delta e(p_0) = 1 + 2(|J_-| + \delta e(p_0)) \quad |J_+| = 1 \wedge |J_-| \geq 2 \quad (3.46a)$$

$$\Delta e(p_0) = -1 - 2(|J_+| + \delta e(p_0)) \quad |J_+| \geq 2 \wedge |J_-| = 1 \quad (3.46b)$$

$$\Delta e(p_0) = 0 \quad |J_+| \geq 2 \wedge |J_-| \geq 2 \quad (3.46c)$$

3.3.5 Density of states and state space structure

We calculate the density of states (DOS) of three-dimensional lattice triangulations with respect to the energy function (3.43) and a reference triangulation composed by C4-triangulations using the Wang-Landau algorithm. We use here the flatness criterion $\text{fl}[H(E)] > 0.8$ and alter the modification factor according to $m_{i+1} = m_i^{0.9}$. In Fig. 3.29 the simulation time dependence of Wang-Landau simulations is displayed, precisely the value of the DOS at selected energy bins, their distribution and standard deviations of these values obtained in independent simulation runs in terms of the final modification factor m_f . One can see that the standard deviation



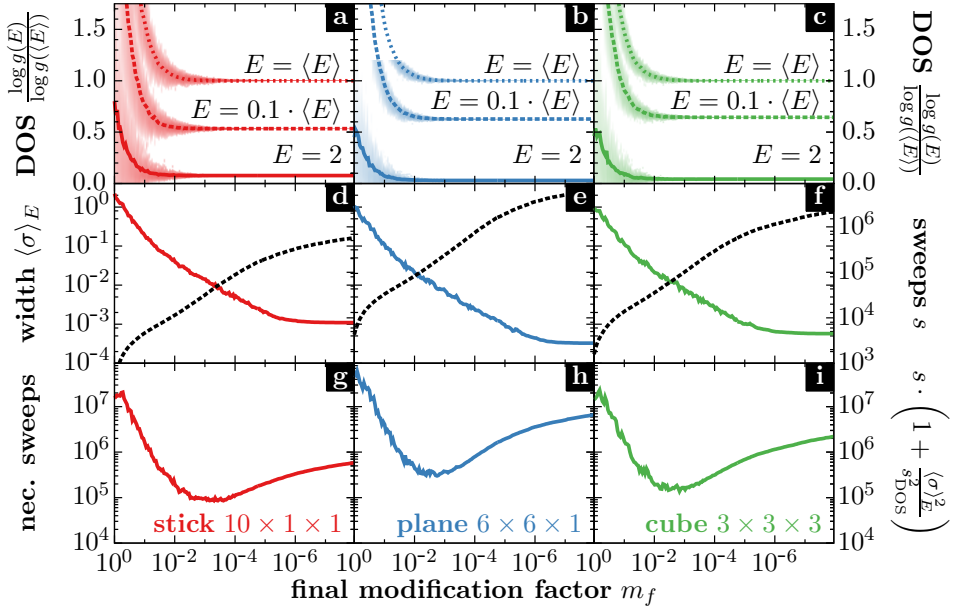


Figure 3.29: Wang-Landau simulations for lattice triangulations.

Characteristic plot of Wang-Landau simulations for $10 \times 1 \times 1$ sticks (left), $6 \times 6 \times 1$ cubes (middle), and $3 \times 3 \times 3$ cubes (right) for flatness $f = 0.8$ and $\delta m = 0.9$. Plots (a-c) show the behavior of single energy bins (first excited state, bin at $0.1 \cdot \langle E \rangle$ and bin at $\langle E \rangle$) of the density of states normalized with the bin at $\langle E \rangle$ for decreasing final modification factor, the colorplot indicates the distribution obtained by different independent Wang-Landau simulations. Plots (d-f) show the standard deviation $\langle \sigma \rangle_E$ obtained for the DOS in terms of the modification factor, averaged over all energy bins (solid, colored line), as well as the average number of sweeps s to do to get to this modification factor (dashed, black line). Finally, plots (g-i) show the number of necessary sweeps to obtain an average error $s_{\text{DOS}} = 0.01$ in the average bins, which is the product of the number of sweeps s for one run and the number of runs $n = 1 + \langle \sigma \rangle_E^2 / s_{\text{DOS}}^2$ (obtained from $s_{\text{DOS}} = \sigma / \sqrt{n-1}$).



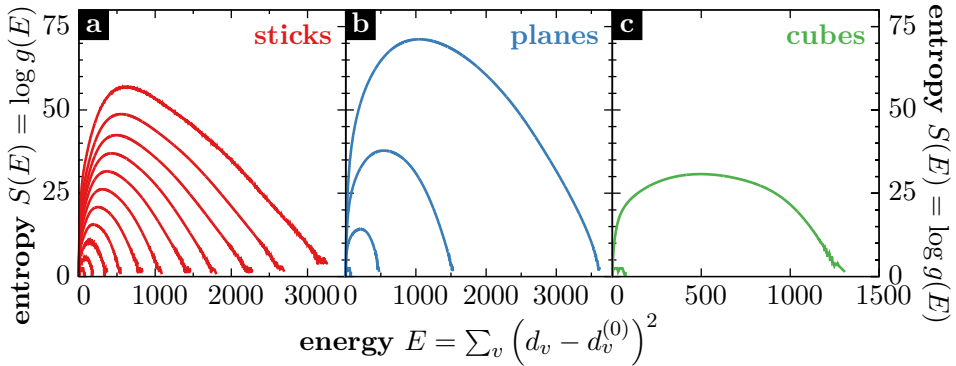


Figure 3.30: Microcanonical entropy $S(E) = \log g(E)$ of three-dimensional lattice triangulations, calculated using Wang-Landau sampling with the vertex-degree-energy (3.43). The three different lattice shapes are (a, red) stick lattices from $1 \times 1 \times 1$ to $11 \times 1 \times 1$ unitcubes, (b, blue) plane lattices $1 \times 1 \times 1$ to $6 \times 6 \times 1$ unitcubes and (c, green) cube lattices for $1 \times 1 \times 1$ and $2 \times 2 \times 2$ unitcubes.

decreases fast with decreasing modification factor, while the number of sweeps increases exponentially for $10^{-1} \gtrsim m_f \gtrsim 10^{-6}$. The saturation of error sets in for all cases at $m_f \approx 10^{-6}$. This leads to the observation that for most efficient usage of the computer resources the Wang-Landau simulations should be stopped at around $10^{-3} \gtrsim m_f \gtrsim 10^{-4}$. Despite possible inefficiencies we run every simulation beneath the saturation of error threshold in order to be very carefully about possible errors.

In Fig.3.30 the microcanonical entropy $S(E)$, which is the logarithm $\log g(E)$ of the density of states and which was calculated using the Wang Landau algorithm with the described parameters., is displayed for the different geometries of the underlying lattice. The microcanonical entropy has the same qualitative behavior as in the two-dimensional case, with a step ascent for low energies, a peak that is not symmetric in the range of possible energies, but shifted towards the ground state, and some complicated structure for high energies. There is no qualitative difference between stick, plane or cube geometries of the underlying lattice, but $S(E)$ for planes and even more pronounced $S(E)$ has a stronger curvature in the growth from the ground state to the peak energy, and a peak that is flatter.

As in the two-dimensional case one can also determine the scaling behavior of certain special points of the density of states, e.g. the average energy $\langle E \rangle$ of a random triangulation, the energy with the highest microcanonical entropy E_{peak} and the actual peak entropy $S(E_{\text{peak}})$, as well as the maximal energy E_{max} of the system. This can be useful for a general understanding



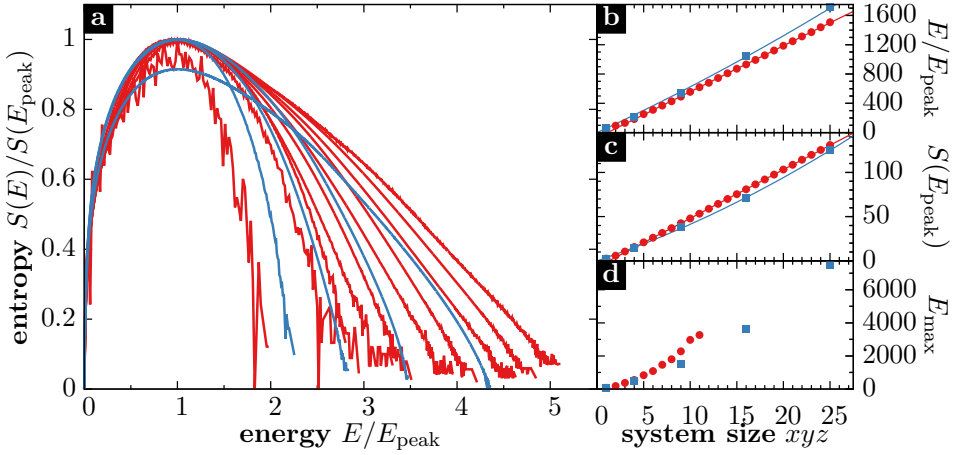


Figure 3.31: Density of states of three-dimensional lattice triangulations. (a) Scaling of the density of states for sticks (red), planes (blue) and cubes (green). The small plots show (b) the peak energy $E_{\text{peak}} \approx \langle E \rangle$, (c) the entropy at the peak energy $S(E_{\text{peak}})$ and (d) the maximal possible energy E_{peak} in terms of the system size.

of the structure of triangulation, for providing extrapolated initial estimates for the density of states of Wang Landau simulation for large systems and for determining cuts for the calculation of the total numbers. For sticks, one finds the following linear scaling behavior of the peak energy and the peak microcanonical entropy, where n is the system size (number of unitcubes):

$$\langle E \rangle(n) = (63.6 \pm 0.3) \cdot n - 54.2 \pm 3.7 \quad (3.47a)$$

$$E_{\text{peak}}(n) = (62.8 \pm 0.1) \cdot n - 69.7 \pm 2.1 \quad (3.47b)$$

$$[g(E_{\text{peak}})](n) = (5.508 \pm 0.007) \cdot n - 7.05 \pm 0.10 \quad (3.47c)$$

For planes, there is the following quadratic scaling behavior in terms of the system size $n^2 = n_x \cdot n_y$:

$$\langle E \rangle(n) = (0.41 \pm 0.05) \cdot n^2 - 59.3 \pm 1.2 \quad (3.48a)$$

$$E_{\text{peak}}(n^2) = (0.36 \pm 0.05) \cdot n^2 + (58.9 \pm 1.6) \cdot n \quad (3.48b)$$

$$[g(E_{\text{peak}})](n^2) = (0.058 \pm 0.006) \cdot n^2 + (3.6 \pm 0.1) \cdot n \quad (3.48c)$$

For cubes no scaling behavior can be given, because the system sizes that can be calculated using our Wang-Landau algorithm are too small. In all cases our assumption that $\langle E \rangle \approx E_{\text{peak}}$ (the average energy of random triangulations is approximately equal to the peak of the DOS) holds quite



3. Embedded triangulations

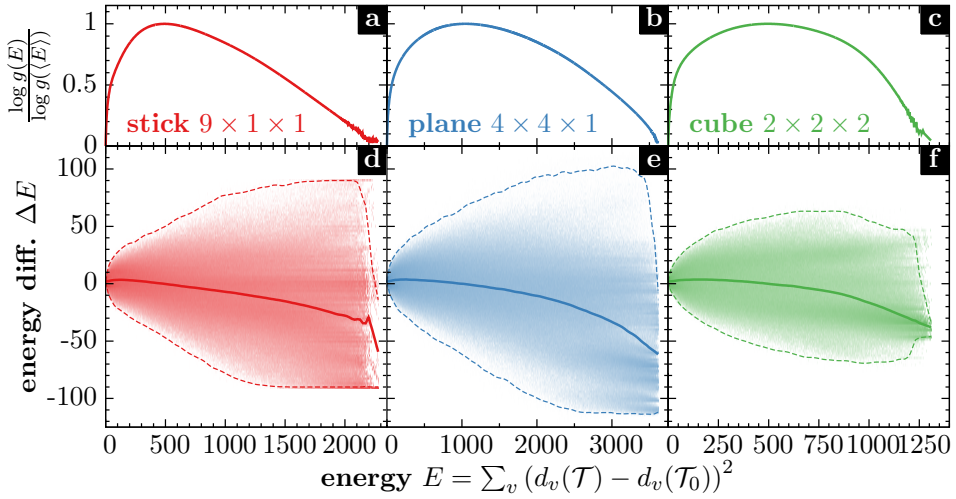


Figure 3.32: Typical ΔE for three-dimensional lattice triangulations. Energy-resolved distribution of the energy differences induced by steps for **sticks**, **planes** and **cubes**. (a-c) Microcanonical entropy $\log g(E)$ normalized to its peak value for $9 \times 1 \times 1$ sticks (a), $4 \times 4 \times 1$ planes (b) and $2 \times 2 \times 2$ cubes (c) for comparison. (d-f) The colorplot displays the distribution of the energy difference ΔE induced by steps in terms of the energy of the lattice triangulation. The solid line is the (smoothed) mean of the distribution, the dashed lines are the (smoothed) boundaries of the distribution.

well, so we can use $\langle E \rangle$ instead of E_{peak} for determining cutting values. This has the advantage that $\langle E \rangle$ can be calculated using a simple Metropolis Monte Carlo simulation at $\beta = 0$, whereas for the peak energy the DOS must be known.

Additional information about the structure of the state space of three-dimensional lattice triangulations can be obtained by inspecting the distribution of energy differences that can be induced by steps in terms of the energy of the triangulation. In Fig. 3.32 this distribution is displayed for sticks, planes and cubes of one system size each. The distribution was obtained by performing a flat sampling with respect to the density of states obtained by Wang Landau simulations. Between two measurements that recorded the current energy of the triangulation and the energy difference of a randomly selected step a certain number of steps were executed without measurements to avoid autocorrelation effects. After the simulation it was simply counted how often a certain energy difference ΔE was obtained at a certain triangulation energy E to obtain the distribution.

As expected the mean of this distribution is positive for energies $E < \langle E \rangle$



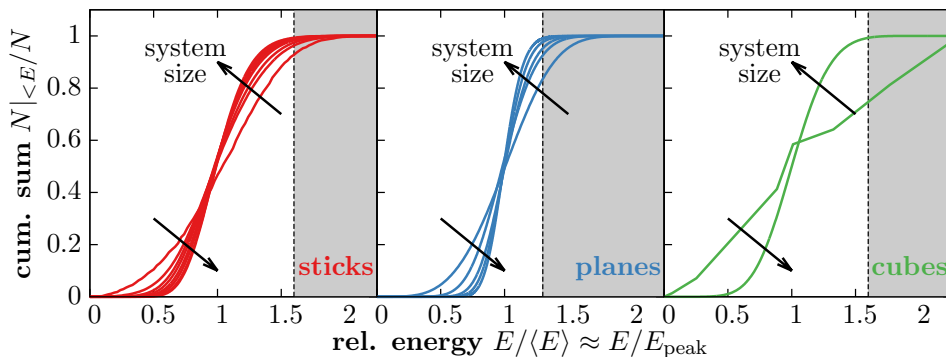


Figure 3.33: Relative cumulative sum $N_{<E}/N$ (where N is the total number of triangulations and $N_{<E}$ is the number of triangulations with energy $E(\mathcal{T}) < E$) for sticks (a, red), planes (b, blue) and cubes (c, green) for different system sizes in terms of the relative energy $E/\langle E \rangle$, where $\langle E \rangle$ is the average energy of the random triangulations. For larger system sizes the step function gets sharper. Considering the biggest system sizes where the full density of states is known, one can estimate that one can use $E_{\text{cut}} = 1.6\langle E \rangle$ for sticks, $E_{\text{cut}} = 1.3\langle E \rangle$ for planes and $E_{\text{cut}} = ?\langle E \rangle$ for cubes as cuts in the density of states resulting in an error of less than 0.01.

and negative for energies $E > \langle E \rangle$, driving the system to states with high microcanonical entropy. For small energies the distribution of energy differences is narrower than for higher energies, this can be understood because the energy function is quadratic in the number of incident edges, and for high energies there are vertices with high incidence number so that an insertion or a removal of only one edge at a vertex can lead to a high energy difference. Another observation is that for all energies the maximal energy difference $|\Delta E|_{\text{max}} < 0.05E_{\text{max}}$ is small compared to the actual range of possible energies. So the flips which are local changes in the triangulations lead to only small changes in the energy, which means that in that sense our energy function is a good choice.

3.3.6 Entropy density of three-dimensional lattice triangulations

In this section we calculate the limit of the entropy density (or capacity) for three-dimensional lattice triangulations of sticks, planes and cubes. We use the same definition

$$C(V) := \frac{\log_2(\Omega(V))}{V} \quad (3.49)$$



3. Embedded triangulations

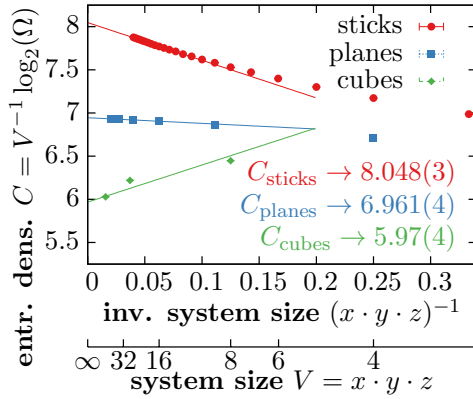


Figure 3.34: Measurements of the entropy density (3.49) for sticks up to $25 \times 1 \times 1$ (\bullet), for planes up to $7 \times 7 \times 1$ (\blacksquare) and for cubes up to $5 \times 5 \times 5$ (\blacklozenge) in terms of the inverse system size using the Wang-Landau algorithm. For the limit of infinite system sizes one finds $C_{\text{sticks}} \rightarrow 8.048(3)$, $C_{\text{planes}} \rightarrow 6.961(4)$ and $C_{\text{cubes}} \rightarrow 5.97(4)$. Measurements of the entropy density for systems up to size 24×24 .

as Eq. (3.12) in the two-dimensional case, where V is the system size ($V = x \cdot y \cdot z$ for lattices with $x \times y \times z$ unitcubes) and $\Omega(V)$ is the number of states at this system size. In order to get a sensitive limit, the entropy density has to be calculated for large system sizes, which cannot be accessed by the Wang-Landau algorithm if considering the whole density of states (DOS) of the system. So instead of calculating the whole DOS, we introduce a cutoff energy E_{cut} so that $\Omega(E < E_{\text{cut}}) \lesssim \Omega$ with an error less than 0.01. This cutoff can be found in terms of the average energy $\langle E \rangle$ of random three-dimensional lattice triangulations by inspecting the relative cumulative sum $\omega(E_{\text{cut}}) := \Omega(E < E_{\text{cut}})/\Omega$ in terms of $\langle E \rangle E$ as in Fig. 3.33. We find that the cumulative sum ω approaches a step function centered at $\langle E \rangle$ with growing system size. So choosing a cutoff energy $E_{\text{cut}} = c \cdot \langle E \rangle$ with $c > 1$ that produces a relative cumulative sum $\omega > 0.99$ for a certain system size V , the error even gets smaller for increasing system sizes. Considering Fig. 3.33 we choose the following cutoff energies for the different lattice shapes:

$$\begin{aligned} E_{\text{cut,sticks}} &= 1.6 \cdot \langle E \rangle \\ E_{\text{cut,planes}} &= 1.3 \cdot \langle E \rangle \\ E_{\text{cut,cubes}} &= 1.6 \cdot \langle E \rangle \end{aligned}$$

In Fig. 3.34 the entropy density for the different shapes of the lattices are plotted. Using least-square fits, one can find the following relations:

$$C_{\text{sticks}}(V) \rightarrow (8.048 \pm 0.003) - \frac{4.36 \pm 0.05}{V} \quad (3.50a)$$

$$C_{\text{planes}}(V) \rightarrow (6.961 \pm 0.004) - \frac{0.90 \pm 0.06}{V} \quad (3.50b)$$



$$C_{\text{cubes}}(V) \rightarrow (5.97 \pm 0.05) + \frac{4.3 \pm 1.6}{V} \quad (3.50c)$$

One sees that the limit of the entropy densities is highest for sticks and lowest for cubes, also the next-to-leading-order terms are strongest for sticks and weakest for cubes. This means for example that there are way more triangulations of $V \times 1 \times 1$ sticks than of $V^{1/2} \times V^{1/2} \times 1$ planes, and way more triangulations of these planes than of $V^{1/3} \times V^{1/3} \times V^{1/3}$ cubes.

These findings are different to the two-dimensional case, where the limit of the entropy density decreases if one confines the geometry of the lattice (for two-dimensional sticks $C \rightarrow 2$, for squares $C \rightarrow 2.196$, see Fig. 3.34). This difference can be understood already by considering the non-mixing unitcell triangulations. In the two-dimensional triangulations the one-dimensional boundary of the unitcells does not alter with the triangulations inside, so the number of non-mixing triangulations is given simply by $\Omega = 2^A$, where A is the system size, independent of the actual shape of the triangulation, so the limit of the entropy density would be 1 in all geometries of the lattice. In the three-dimensional case the two-dimensional boundary triangulations of the unitcube do depend on the triangulation within the unitcube, and one cannot combine the 74 unitcube triangulations arbitrarily. If extending a stick triangulation with another unitcube, only one side of the new unitcube is fixed. If extending a plane or cube triangulation, for most of the added unitcubes two or three sides are fixed, so there are much less triangulations of the unitcube that can be combined, which results in the decrease of the entropy density.



3.4 Two-dimensional unimodular lattice triangulations as graphs

Real world systems or networks that consist of many similar entities that are interacting can be described by graph theory (see [122, 314] for reviews). Examples are the world-wide-web, where single websites are modeled as vertices and links between websites are modeled as edges; the network of social interactions, where vertices represent single humans and edges imply an existing friendship between two humans and the scientific co-author network, where authors of scientific papers are vertices and an edge between two authors is existent if both are co-authors of a common paper.

Most of these real networks share three common properties [7, 122]:

1. The clustering coefficient, which is basically the probability that two neighbors of a common node are connected by a graph edge, is high and independent of the size of the network. In real networks this means for example that there is a high probability that if two persons know a common person, they know each other, too; if two scientific authors are co-authors of a common third author, also these two are very likely co-authors.
2. The length of the shortest path between two random vertices, measured by the number of edges the path consists of, is small even for huge graphs and scales like the logarithm of the system size for increasing system size. This behavior is commonly known for the network of social interactions, where every two random persons of the world should know each other over less then 10 middlemen, or in the world wide web, where each website can be reached from every other website within a few clicks.
3. The distribution of the number of edges incident with a vertex (its degree k) follows a power-law distribution ($P(k) \propto k^{-\gamma}$) with $2 < \gamma < 3$, which means that there are a lot of vertices with only a few neighbors, and only a minority highly connected vertices. For example in the co-author network there are few authors that worked together with a lot of different people, and there are a lot of authors that worked only with very few co-authors.

The appearance of the first two properties is often denoted as small-world behavior, networks with the third property are denoted as scale-free.

Another major tool in studying the physical properties of graphs is spectral graph theory, which examines the spectra of the adjacency and the



Laplacian matrices associated with the graph and some special eigenvalues of those, see e.g. [126]. The spectra of graphs are studied e.g. for quantum percolation [165] and Anderson transition on Bethe lattices [166, 167, 297] in terms of random matrices, as well as in biology [58] and chemistry [163, 394], for a review see [300] and the references therein. Special eigenvalues as the algebraic connectivity, the smallest non-zero eigenvalue of the Laplacian matrix, are important for characterizing the topology of graphs [235], for transport and dynamics on networks [12] and for optimization problems [302, 402], see [127, 301] for reviews. Additionally, spectral graph theory is well-connected with the common mathematical theory of random matrices used in quantum physics [199]. An important application of the spectrum of the Laplacian matrix are (quantum) random walks on networks [102, 305], where the Laplacian matrix corresponds to the discretization of the operator used in Poisson and Schrödinger equations. In both cases the spectrum can be used for calculating return probabilities and participation ratios.

To understand the structure and behavior of real world networks different random graphs are used as model systems [7]. Three widely used models are the Erdős-Rényi random graph [158–160], the Watts-Strogatz random graph [412] (and a slightly altered version denoted as Newman-Watts random graph [316]) and the Barabási-Albert random graph [60]. While all three models have a shortest path length scaling with the logarithm of the system size [180, 412], none exhibits both the other two properties of real-world networks: The Erdős-Rényi random graph has vanishing clustering coefficient and a binomial degree distribution; the Watts-Strogatz random graph exhibits a non-vanishing clustering coefficient for a special choice of parameters [412], but also a degree distribution that agrees quantitatively with the Erdős-Rényi graph [64]; the Barabási-Albert model creates a scale-free degree distribution with exponent $\gamma = 3$ [60, 140, 262], but leads also to a vanishing clustering coefficient for increasing system size [179]. Several more complicated models developed afterwards combine both small-world and scale-free behavior [218, 252, 383], there are also models that use graphs with vertices embedded in some geometric space that exhibit these two properties [74, 354, 428].

We present here a novel type of (embedded) random graphs by identifying triangulations of integer lattice point sets as graphs that shows a crossover from ordered, large-world to unordered, small-world and possible scale free behavior. Such triangulations are tessellations of the convex hull of the point set into non-intersecting simplicial building blocks (triangles in two dimensions, tetrahedrons in three dimensions) [132]. Triangulations are an



important tool in physics for describing curved space(-times), in quantum geometry (e.g. in the framework of Causal Dynamical Triangulations [38] and in spin foams [352]); they are also a major object of study in topology and geometry where one is for example interested in the number of distinct triangulations of a given topological manifold [380]. Triangulations are commonly used for describing foams [381], where often a special so-called Delaunay triangulation, which is the dual to the Voronoi tessellation, is used for foam construction. They can also be used for describing the topological properties of foams in terms of the neighboring cells [53, 143, 319]. Additionally glass-like dynamics near regular configurations can be found in dual graphs of topological triangulations [54]. The dual graphs of disordered triangulations as described in this paper can be used for the construction of poly-disperse foams, which exhibit a broad range of cell sizes, and for considering e.g. their transport and diffusion problems.

Triangulations have been used as random graph models before: Random Apollonian Networks [47, 372, 433] (randomized dual graphs of Apollonian packed granular matter) are triangulations constructed using a procedure similar to preferential attachment and show both small-world and scale-free behavior. Since each graph can be embedded into a closed surface with high enough genus, and triangulations are maximal planar graphs in the sense that each insertion of another edge will break planarity, triangulations of surfaces with arbitrary genus were studied in [52]. Canonical ensembles of triangulations of the sphere were used in [259] to consider a quench from the random triangulations to zero temperature.

In contrast to the triangulations considered in [47, 52, 259, 372, 433] before, which we denote as topological triangulations, we use embedded triangulations with vertices having fixed coordinates, precisely unimodular triangulations of two-dimensional integer point lattices. For topological triangulations only the topological degrees of freedoms (the way how vertices are connected) are important, contrary to embedded triangulations where additionally the actual coordinates of the vertices are fixed and specified. This causes complexities and numerical difficulties that do not have to be addressed in topological triangulations, e.g. to determine whether a Pachner flip leads to a valid triangulation.

In this section we measure the degree distribution, the clustering coefficient and the shortest path length as well as spectral observables of random lattice triangulation graphs using Metropolis Monte-Carlo simulations and find a high clustering coefficient and similarities to common network models. Introducing the notion of an energy of a triangulation that is well known



in literature and corresponds to the variance of the degree distribution we apply the usual notion of statistical physics and examine the canonical ensemble averages of these observables for different values of the inverse temperature. For the numerical calculation of the expectation values we use the Wang-Landau algorithm for calculating the density of states. This makes it possible to calculate equilibrium properties for all temperatures, in contrast to Metropolis or Glauber dynamics used in [52, 54, 259], where it is hard to access negative temperatures and low temperatures, but we lose the ability to consider dynamical behavior like quenches or glass-transitions studied in the literature before. In the canonical ensemble we find in all considered observables a transition from an ordered large-world behavior for positive temperatures to small-world and scale free behavior for negative temperatures. For the maximal ordered triangulations, which are the ground state of the energy functional used, analytical calculations are possible, as well as approximations for triangulations with low energies near the ground state. As an application of our results, we calculate the inverse participation ratio of certain eigenstates and show that random lattice triangulations on average exhibit stronger localization than comparable random graphs. Furthermore we consider the standard Ising model defined on this type of graph and calculate critical temperatures and phase transitions.

3.4.1 (Spectral) graph theory

An undirected simple graph $\mathcal{G} := (\mathbf{A}, E)$ is a pair consisting of a set \mathbf{A} (called vertices) with $n = |\mathbf{A}|$ elements and a set E (called edges) of two-element subsets of \mathbf{A} . A triangulation can be interpreted as a graph using the point set \mathbf{A} as vertices and the 1-simplices of the triangulation as edges E .

Important properties of graphs are related to global observables defined on graphs. The degree distribution

$$P(k) = \frac{1}{n} |\{v \in \mathbf{A} | d_v = k\}| \quad (3.51)$$

at incidence number k is the fraction of vertices that has k incident edges. The clustering coefficient

$$C := \frac{1}{n} \sum_{v \in \mathbf{A}} C_v \quad \text{with} \quad C_v := \frac{2N(v)}{d_v(d_v - 1)} \quad (3.52)$$

is the average over the local clustering coefficients C_v , where C_v is the ratio of the number $N(v)$ of edges between next neighbors of v in the graph and



the maximal possible number $d_v(d_v - 1)/2$ of edges between next neighbors of v . So a high clustering coefficient means a high probability that common neighbors of a vertex in the graph are neighbors themselves. The shortest path length $\ell_{v,w}$ between vertices v and w is the minimal number of edges of a path that connects v with w , and the average shortest path length

$$\ell := \frac{1}{n(n-1)} \sum_{v,w \in \mathbf{A}, v \neq w} \ell_{v,w} \quad (3.53)$$

is the average of the shortest path length between all pairs of vertices. A low average shortest path length means that the graph can be traversed in a small number of steps.

Important properties of graphs can also be found by examining spectral properties (the set of eigenvalues) of matrices associated with graphs. In the literature mostly the following three $n \times n$ -matrices (with n being the number of vertices) are considered for a graph \mathcal{G} [117]:

- The *adjacency matrix* $A(\mathcal{G})$ with

$$A(\mathcal{G})_{ij} := \begin{cases} 1 & \{v_i, v_j\} \in E \\ 0 & \{v_i, v_j\} \notin E \end{cases}$$

is a traceless, symmetric matrix that indicates whether two different vertices are connected. The matrix elements $A(\mathcal{G})_{ij}^k$ equal the number of paths from v_i to v_j containing exactly k edges. We will denote its sorted eigenvalues by $\alpha_0 \leq \alpha_1 \leq \dots \leq \alpha_{n-1}$.

- The *Laplacian matrix* $L(\mathcal{G}) := D(\mathcal{G}) - A(\mathcal{G})$ with degree matrix

$$D(\mathcal{G})_{ij} := \delta_{ij} k_{v_i}$$

is a discretization of the usual Laplace operator $\vec{\nabla}^2$. The Laplacian matrix is symmetric and positive-semidefinite, the smallest eigenvalue is always 0. We denote the sorted eigenvalues of the Laplacian matrix by $\lambda_0 \leq \lambda_1 \leq \dots \leq \lambda_{n-1}$. The multiplicity of the eigenvalue 0 is the number of connected components of the graph.

- The *normalized Laplacian matrix*

$$\mathcal{L}(\mathcal{G}) := \mathbb{1} - D(\mathcal{G})^{-1/2} A(\mathcal{G}) D(\mathcal{G})^{-1/2}$$

is useful for describing random walks on arbitrary geometries. This matrix is not considered in this paper, but our calculations can be extended simply to the normalized Laplacian.



The spectrum $\text{spec}_M(x)$ of a $n \times n$ -matrix M with eigenvalues μ_0, \dots, μ_{n-1} is given by the distribution

$$\text{spec}_M(x) := \frac{1}{n} \sum_{i=0}^{n-1} \delta(x - \mu_i)$$

For large graphs ($n \rightarrow \infty$) the spectrum can be approximated by a continuous function.

A well known result is that the spectrum of the Laplacian matrix can be used to calculate the number of spanning trees, which is $\lambda_1 \cdot \lambda_2 \cdot \dots \cdot \lambda_{n-1}/n$ [249]. The second-smallest eigenvalues λ_1 of the Laplacian spectrum is called *algebraic connectivity*, the largest eigenvalue λ_{MN-1} is called *spectral radius*. The algebraic connectivity is 0 if and only if the graph is not connected, it can be shown that it increases if one inserts additional vertices into a graph, so it is in fact a good measure for the connectedness of a graph. Additionally it can be used to bound other quantities of graphs that are more difficult to calculated, e.g., the isoperimetric number [299]. Fiedler [170] and Mohar [300] state that there are the following lower and upper bounds for the algebraic connectivity λ_1 of a graph \mathcal{G} :

$$2\eta(\mathcal{G}) \left[1 - \cos\left(\frac{\pi}{n}\right) \right] < \lambda_1(\mathcal{G}) < v(\mathcal{G}) \quad (3.54)$$

Here $\eta(\mathcal{G})$ is the edge connectivity and $v(\mathcal{G})$ is the vertex connectivity, the smallest number of edges or vertices (with incident edges) that must be removed from the graph to create at least two non-connected components. For the spectral radius λ_{MN-1} there are the following general bounds ([300, 430]) for a graph \mathcal{G} :

$$\frac{n}{n-1} \max \{k_i \mid v_i \in \mathbf{A}\} \leq \lambda_{n-1}(\mathcal{G}) \leq \max \{k_i + k_j \mid \{v_i, v_j\} \in \mathcal{G}\} \quad (3.55)$$

where k_i is the degree (number of incident edges) of vertex v_i .

One can show that the algebraic connectivity is proportional to the inverse of the synchronization time in consensus dynamics on networks [12]. Additionally, for the return probability it governs the large-time in classical and the small frequency behavior in quantum random walks on networks, whereas the spectral radius governs short-time respectively the large frequency behavior [307].

One can also find a bound for the sum of the j largest eigenvalues in terms of the j largest degrees $k_a \leq k_b$ for $a < b$ [198]

$$\sum_{i=1}^j \lambda_{n-j} \geq 1 + \sum_{i=1}^j k_{n-j}$$



The sum of the exponentiated eigenvalues of the adjacency and the Laplacian matrix is known as the (Laplacian) Estrada index and has many applications in the study of chemical molecules [142, 163, 164].

The eigenvectors of the Laplacian matrix can be used for examining localization on graphs in terms of the inverse participation ration (IPR) χ_m of the normalized eigenvector $|m\rangle$ corresponding to eigenvalue λ_m [96, 305], which is given by

$$\chi_m := \sum_k (|m\rangle_k)^4, \quad (3.56)$$

where $|m\rangle_k$ denotes the k -th component of the eigenvector. Since the normal basis corresponds to the vertices of the graph, these components are the overlap of the eigenvectors and the vertices, so large IPRs correspond to strong localization, whereas small IPRs correspond to delocalization of the corresponding eigenvector. To examine the localization properties for lattice triangulations, we consider the IPR χ_1 of the algebraic connectivity, the IPR χ_{MN-1} of the spectral radius and the average IPR $\bar{\chi} := (\sum_m \chi_m)/MN$.

An important use of random graphs in statistical physics are their use as underlying structures for Ising or other spin models. In the Ising case one assigns to every node a spin $\sigma \in \{-1, 1\}$ and defines the energy as

$$E_{\text{Ising}}(\vec{\sigma}) := J \sum_{\{n_1, n_2\} \in E} \sigma_{n_1} \sigma_{n_2} - H \sum_{n_1} \sigma_{n_1}, \quad (3.57)$$

where $\vec{\sigma} \in \{-1, 1\}^n$ denotes the configuration of all n spins, and where $\{n_1, n_2\} \in E$ is an edge that connects the nodes n_1 and n_2 . In the following we consider only the case of vanishing external field $H = 0$.

The Ising model has been solved analytically on one- and two-dimensional square lattices (see Sec. 2.1.7), for Cayley trees [154], which are generated iteratively by inserting $(q-1)$ nodes of the k -th generation connected to every node of the $(k-1)$ -th generation, and for Bethe lattices, which are Cayley-trees with $k \rightarrow \infty$ [70, Sec. 4.8]. Interestingly, in the thermodynamic limit the free energy for Cayley trees is still an analytic function [154], while for Bethe lattices there is a phase transition at $\coth(\beta_c) = q-1$ [70, Eq. (4.5.4)], because the limit $k \rightarrow \infty$ does not commute with the calculation of the free energy, and within a Cayley tree the surface lattice sites of the last generation dominate [154]. Furthermore one can calculate the critical temperature and critical exponents for uncorrelated graphs with a scale-free degree distribution $P(k) \propto k^{-\gamma}$, the critical temperature β_c depends on the average number of nearest and next-to-nearest neighbors, the critical exponents fall into different classes for $2 < \tau < 3$, $3 < \tau < 5$ and $\tau > 5$ [139, 277].



3.4.2 Triangulations as random graphs

We consider here full triangulations of the integer lattice

$$\mathbf{A} = \left\{ \binom{m}{n} \mid m \in \mathbb{Z}_M := \{0, 1, \dots, M-1\}, n \in \mathbb{Z}_N \right\}$$

which are unimodular, that is that all triangles have equal area $1/2$, and diagonal edge flips transforming those triangulations into each other ergodically. Examples of such triangulations can be found in Fig. 3.12. Note that we use a different convention to describe the lattice size than in Sec. 3.2, where $M \times N$ lattice referred to $M \cdot N$ unitcells and $(M+1) \cdot (N+1)$ vertices. Here an $M \times N$ lattices refers to $(M-1) \cdot (N-1)$ unitcells and $M \cdot N$ vertices.

There are analytical bounds [238] and numerical calculations [253] (compare Sec. 3.2) for the total number of triangulations on such integer lattices. Both the bounds and the numerical calculations show that number of triangulations scales exponentially with the system size of the underlying lattice, this extensivity makes it possible to apply tools from statistical physics to triangulations. A similar system was also considered in [108], where the convergence of a Metropolis-like Monte Carlo algorithm applied to lattice triangulations was analyzed for different parameter choices.

We interpret triangulations as graphs by identifying vertices as graph nodes and the triangulation edges as graph edges. Neglecting the boundary vertices triangulation graphs are maximal planar, i.e. no edge between an internal and another vertex can be inserted without violating the planarity of the graph.

To categorize triangulations of a point set according to their order and disorder, we define for a triangulation \mathcal{T} the energy function

$$E(\mathcal{T}) := \sum_{v \in \mathbf{A}} \left(k_v^{(\mathcal{T})} - k_v^{(\mathcal{T}_0)} \right)^2 \quad (3.58)$$

taking low values for ordered triangulations and high values for unordered triangulations. Here $k_v^{(\mathcal{T})}$ is the number of edges that are incident with the vertex v in triangulation \mathcal{T} and \mathcal{T}_0 is a reference triangulation that will be the ground-state of the energy function (in this paper we choose the maximal ordered triangulation displayed in Fig. 3.12 as the reference triangulation). The additional term $k_v^{(\mathcal{T}_0)}$ with \mathcal{T}_0 being the maximal ordered triangulation can be seen as an implementation of fixed boundary conditions. Periodic boundary conditions, which yield toroidal topology, cannot be used



for lattice triangulations, because on closed surfaces without boundaries there are several possibilities to connect two vertices with an edge (e.g. with different winding number) and therewith it depends on the choice of the connection whether the considered object is a valid triangulation. In contrast, for the considered topology, the edge between two vertices is always the line segment.

Since the number of edges of full lattice triangulations is constant, sums over linear vertex degrees vanish and the chosen energy function (3.58) is the simplest possible polynomial energy function in the number of vertices, edges and triangles. It can be related to the square of the local curvature usually used in dynamical triangulations [38] (which is basically the deficit angle given by the number of triangles around a vertex minus six). Similar energy functions were already applied to graphs in [168]; in [108] the total length of all edges was used as energy function in lattice triangulations, which qualitatively agrees with our choice since high energy leads to long edges in the triangulations; previous works [52, 54, 259] considering topological triangulations as graphs also use the energy function (3.58) with the mean vertex degree $\langle k \rangle$ instead of $k_v^{(\mathcal{T}_0)}$.

Interpreting the triangulation vertices as graph nodes and the 1-simplices as graph edges, we compare the graph properties of the triangulations with Erdős-Rényi [158–160], Newman-Watts [316] and Barabási-Albert [60] random graphs. In all three cases we choose the model parameters so that the number n of the random graph nodes matches the number MN of the lattice triangulation vertices and the average number of random graph edges matches the number $e = 3MN - 2(M + N) + 1$ of the lattice triangulation edges.

In the Erdős-Rényi random graph there are n vertices, each pair of vertices is connected by an edge with probability p [158–160]. They have a small world behavior for the shortest path length, but vanishing clustering coefficient and a binomial degree distribution. To compare the Erdős-Rényi random graph with triangulations we choose its parameters to be $n = MN$ and $p = 2e/n(n - 1) \rightarrow 6/n$.

The Newman-Watts random graph [316] is a modification of the Watts-Strogatz graph [412]. Starting with a regular graph of n vertices and connections to the next L neighbors, for each present edge an additional edge is inserted between two random vertices with probability q . This model can be seen as the periodic regular graph superimposed with a random graph. The random rewiring leads to shortcuts and a short average path length, the basic regular graph leads to a high clustering coefficient. To



obtain a comparable random graph we use the parameters $n = MN$, $L = 4$ and $q = -1 + e/2MN$

The Barabási-Albert random graph [60] is constructed as following: Start with m isolated vertices and iteratively insert t vertices, each with m edges to already present vertices, such that the probability for connecting to a present vertex is proportional to its degree (preferential attachment). This random graph has vanishing clustering coefficient, but a power-law degree distribution and a small-world shortest path length. We choose the model parameters $m = 3$ and $t = MN - 3$ to compare with $M \times N$ lattice triangulations.

3.4.3 Analytical solution

In this section we calculate analytical solutions for the clustering coefficient of the maximal ordered ground state of a lattice triangulation, and the effect of flips on the clustering coefficient. If one extends the ground state to periodic boundaries (resulting in a periodic, triangular lattice), also analytical solutions for the eigenvalues of the adjacency and the Laplacian matrix can be found. It is even possible to use perturbation theory to calculate the effect of flips on the spectrum and therewith to approximate the spectral properties of low-energy triangulations.

Clustering coefficient

Since for the periodic extension of the ground state every vertex has $d_i = 6$ neighbors, the average clustering coefficient is $C = 2/5$ due to (3.52). For calculating the clustering coefficient of the ground state with boundary on a $M \times N$ -lattice one has to take into account the deviating contribution of the boundary vertices:

$$\begin{aligned} C &= \frac{1}{MN} \left[\frac{2}{5}(M-2)(N-2) + \frac{2}{4}(2(M-2) + 2(N-2)) + \frac{2}{3} \cdot 2 + \frac{2}{2} \cdot 2 \right] \\ &= \frac{2}{5} + \frac{1}{5} \cdot \frac{M+N}{MN} + \frac{14}{15} \cdot \frac{1}{MN} \end{aligned} \tag{3.59}$$

A flip originating from the ground state that does not involve boundary vertices increases the number of incident edges for two vertices from 6 to 7 and decreases it for two other vertices from 6 to 5. So the change in the clustering coefficient is

$$\Delta C = \frac{1}{15} \cdot \frac{1}{MN} \tag{3.60}$$



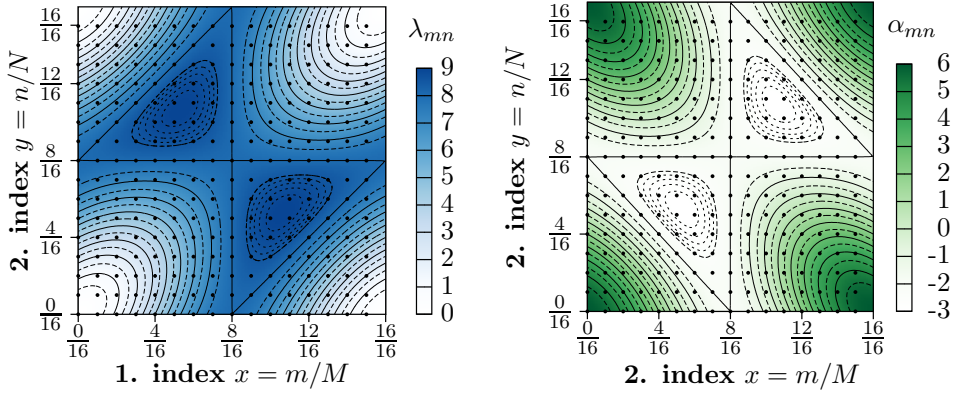


Figure 3.35: Analytical solutions of the ground state spectra.

Analytical calculated eigenvalues of the Laplacian matrix (left, Eq. (3.64)) and of the adjacency matrix (right, Eq. (3.62)) for the periodic ground state of a triangulation in terms of m/M and n/N . The solid lines are the isocurves for the integer values, the dashed lines are the isocurves for the half-integers and the dots represent the realized values for $M = N = 16$. For larger triangulations the dots become denser.

Adjacency and Laplacian spectrum (ground state)

In this section we calculate the spectrum of the adjacency and the Laplacian matrix for a triangular $M \times N$ -lattice graph with periodic boundary conditions. This is an approximation for the maximal ordered ground state of a triangulation. The components $A_{(i_1 j_1)(i_2 j_2)} := A_{i_1, N+j_1, i_2, N+j_2}$ (with $i_k \in \mathbb{Z}_M, j_k \in \mathbb{Z}_N$) of the adjacency matrix are given by

$$\begin{aligned}
 A_{(i_1 j_1)(i_2 j_2)} &= \delta_{i_1 i_2}^{(M)} B_{j_1 j_2} + \delta_{i_1(i_2+1)}^{(M)} C_{j_1 j_2} + \delta_{(i_1+1)i_2}^{(M)} C_{j_2 j_1} \\
 B_{j_1 j_2} &= \delta_{j_1(j_2+1)}^{(N)} + \delta_{(j_1+1)j_2}^{(N)} \\
 C_{j_1 j_2} &= \delta_{j_1 j_2}^{(N)} + \delta_{(j_1+1)j_2}^{(N)}
 \end{aligned} \tag{3.61}$$

The matrix B describes the connections between vertices in a common row, the matrix C describes the connections between the different rows. $\delta_{i_1 i_2}^{(M)}$ is the M -periodic Kronecker delta (1 for $i_1 = i_2 + k \cdot M$ with $k \in \mathbb{Z}$, 0 otherwise). The Laplacian matrix L is then given by

$$L_{(i_1 j_1)(i_2 j_2)} := 6\delta_{j_1 j_2}^{(N)}\delta_{i_1 i_2}^{(M)} - A_{(i_1 j_1)(i_2 j_2)}$$

Using a decomposition into Fourier components one can show that $\alpha_{mn} \in$



\mathbb{R} and $|m, n\rangle \in \mathbb{C}^{MN}$ solve the eigenvalue equation

$$A|m, n\rangle = \alpha_{mn}|m, n\rangle$$

with eigenvalues

$$\alpha_{m,n} = 2 \left[\cos\left(2\pi \frac{n}{N}\right) + \cos\left(2\pi \frac{m}{M}\right) + \cos\left(2\pi \left(\frac{m}{M} + \frac{n}{N}\right)\right) \right] \quad (3.62)$$

and the corresponding components of the eigenvectors

$$|m, n\rangle_{kl} = \frac{1}{\sqrt{MN}} \exp\left(2\pi i \frac{k \cdot m}{M}\right) \exp\left(2\pi i \frac{l \cdot n}{N}\right). \quad (3.63)$$

The eigenvalues and (up to a scaling factor) the eigenvectors depend only on the relative indices m/M and n/N . So the spectrum as visualized in Fig. 3.35 is independent of the system size in terms of the relative indices, but the actual system size becomes important to determine which relative indices m/M and n/N with $m \in \mathbb{Z}_M, n \in \mathbb{Z}_N$ are possible. The two-fold degenerated smallest eigenvalues of the adjacency matrix are

$$\alpha_0 = \alpha_1 = \alpha_{\frac{M}{3}, \frac{N}{3}} = \alpha_{\frac{M}{3}, \frac{N}{3}} = -3$$

the largest eigenvalue is $\alpha_{MN-1} = \alpha_{0,0} = 6$.

The eigenvectors of the adjacency matrix (3.62) also solve the eigenvalue equation for the Laplacian matrix

$$L|m, n\rangle = \lambda_{mn}|m, n\rangle$$

with eigenvalues

$$\lambda_{m,n} = 6 - 2 \left[\cos\left(2\pi \frac{n}{N}\right) + \cos\left(2\pi \frac{m}{M}\right) + \cos\left(2\pi \left(\frac{m}{M} - \frac{n}{N}\right)\right) \right] \quad (3.64)$$

which are visualized in Fig. 3.35. These Laplacian eigenvalues of a periodic triangular lattice were also found in [400]. The lowest eigenvector $\lambda_0 = \lambda_{00}$ is zero since the triangulation is connected. The algebraic connectivity λ_1 is

$$\lambda_1 = \begin{cases} \lambda_{1,0} = \lambda_{N-1,0} = 6 - 6 \cos\left(\frac{2\pi}{N}\right) & N \geq M \\ \lambda_{0,1} = \lambda_{0,M-1} = 6 - 6 \cos\left(\frac{2\pi}{M}\right) & N < M \end{cases} \quad (3.65)$$

and for $M, N \in 3 \cdot \mathbb{N}$ the spectral radius λ_{MN-1} is

$$\lambda_{MN-1} = \lambda_{\frac{N}{3}, \frac{2N}{3}} = \lambda_{\frac{2N}{3}, \frac{N}{3}} = 9 \quad (3.66)$$



Adjacency and Laplacian spectrum (low energy states)

As a next step we use the usual quantum mechanical perturbation theory to calculate analytically the influence of a single and multiple flips on the eigenvalues of the Laplacian operator. Consider a flip of the edge $\{(a, b)(a - 1, b + 1)\}$ into the new edge $\{(a - 1, b)(a, b + 1)\}$. The Laplacian operator $L' = L + V$ of the flipped state can be calculated using the Laplacian operator L of the ground state and a perturbation matrix V with the following non-vanishing components:

$$\begin{aligned} V_{ab,ab} &= V_{(a-1)(b+1),(a-1)(b+1)} = -1 \\ V_{(a-1)b,(a-1)b} &= V_{a(b+1),a(b+1)} = 1 \\ V_{ab,(a-1)(b+1)} &= V_{(a-1)(b+1),ab} = 1 \\ V_{(a-1)b,a(b+1)} &= V_{a(b+1),(a-1)b} = -1 \end{aligned}$$

The expectation value for the perturbation V is then :

$$\begin{aligned} \langle m, n | \hat{V} | m', n' \rangle &= \frac{1}{MN} e^{2\pi i \frac{(m'-m)\mu}{M}} e^{2\pi i \frac{(n'-n)\nu}{N}} \\ &\cdot \left[4e^{\pi i \frac{m-m'}{M}} e^{\pi i \frac{n'-n}{N}} \sin\left(\pi \frac{m-m'}{M}\right) \sin\left(\pi \frac{n'-n}{N}\right) + \right. \\ &\left. + \left(e^{2\pi i \frac{n'}{N}} - e^{-2\pi i \frac{n}{N}} \right) \left(e^{-2\pi i \frac{m'}{M}} - e^{2\pi i \frac{m}{M}} \right) \right] \end{aligned}$$

In the following we consider only quadratic lattices $M = N$, the rectangular case can be treated in an analogue fashion. For calculating the first order correction for the spectral radius one has to take into account that $\lambda_{N/3,2N/3} = \lambda_{2N/3,N/3}$ is two fold degenerate, so one has to calculate the perturbation matrix and to diagonalize it. The relevant terms of the perturbation matrix are the diagonal element

$$\left\langle \frac{N}{3}, \frac{2N}{3} \left| \hat{V} \right| \frac{N}{3}, \frac{2N}{3} \right\rangle = \frac{3}{N^2}$$

and the complex off-diagonal element

$$\left\langle \frac{N}{3}, \frac{2N}{3} \left| \hat{V} \right| \frac{2N}{3}, \frac{N}{3} \right\rangle = \frac{3}{N^2} e^{\frac{2\pi i}{3}(a-b-1)}$$

The eigenvalues of the resulting hermitian 2×2 -matrix are 0 and $6/N^2$, so in first order perturbation theory the spectral radius becomes

$$\lambda_{N^2-1} \approx 9 + \frac{6}{N^2} \tag{3.67}$$



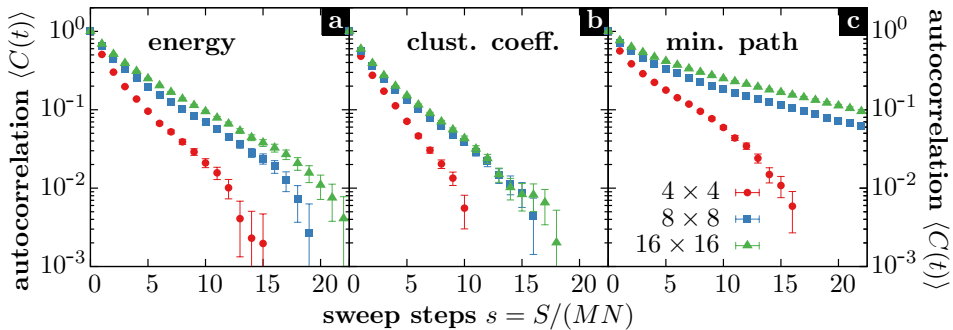


Figure 3.36: Autocorrelation function $\langle c \rangle(t)$ in units of steps per system size of the (a) average mean energy, (b) the clustering coefficient and (c) the average shortest path length for random triangulations of size 4×4 (\bullet), 8×8 (\blacksquare) and 16×16 (\blacktriangle).

with the second being the important contribution since the spectral radius needs to be the biggest eigenvalue. This relation will be used later on to estimate the energy dependence of the spectral radius for small energies.

The perturbation theory unfortunately fails if one considers the algebraic connectivity. For the case $M = N$ the corresponding eigenvalue is six-fold degenerated and the perturbation matrix has to be diagonalized numerically. This leads for all M, N to a decrease in the algebraic connectivity, which is consistent with a direct diagonalization of the new Laplacian $L + V$ for the periodic case. In contrast to that, if one diagonalizes $L + V$ directly for the non-periodic case, the algebraic connectivity increases. So for the small eigenvalues the difference between a regular and a periodic triangulation leads to a qualitative change in the behavior of the algebraic connectivity, which is quite comprehensible since the algebraic connectivity is dominated by the vertices with low degree (two for non-periodic and six for periodic triangulations), which can be seen already in the bounds (3.54). The spectral radius is determined by the vertices with high degree, which is six for both periodic and non-periodic triangulations, also apparent in the bounds (3.55).

3.4.4 Random triangulations

In this section we calculate the scaling behavior of the vertex degree distribution, the mean energy, the average clustering coefficient and the average shortest path length in terms of the system size of random triangulations and compare it with random graphs. With random triangulations we denote the ensemble with each possible triangulation having the same constant



3. Embedded triangulations

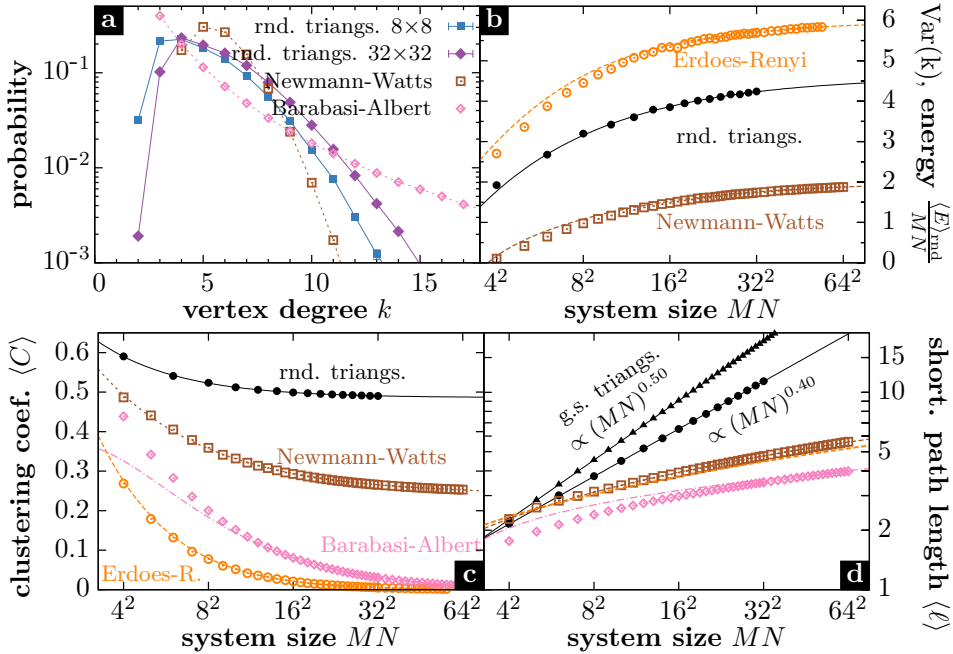


Figure 3.37: Graph observables of random lattice triangulations.

Scaling behavior of random lattice triangulations and comparable random graphs. a) Degree distribution for random triangulations of 8×8 (■) and 32×32 (◆) lattices compared to the average degree distribution of a Newman-Watts (□) and a Barabási-Albert (◇) random graph with $n = 32^2$ vertices. b) Specific mean energy, variance of the degree distribution, c) clustering coefficient and d) shortest path length for maximal ordered (▲) and random (●) triangulations, the Erdős-Rényi (○) and the other random graphs in terms of the number of vertices MN . For the random triangulations and the Newman-Watts graph the lines were determined by a power-law fit, all other lines are analytical results. The asymptotic behavior is listed in Tab. 3.3.



weight and contributes equally in the calculation of expectation values. The results are especially interesting, because due to the constant ensemble weights (that are in particular independent of the triangulation energies) they do not depend on the actual choice of the energy function.

We calculate these observables in the random ensemble using the Metropolis algorithm [291] taking into account at least 1000 different random triangulations per considered system size. The behavior of the autocorrelation for different observables is displayed in Fig. 3.36. The autocorrelation time of all considered observables is smaller than $10MN$ Pachner moves, to avoid errors due to the autocorrelation, we execute $1000MN$ flips before the first and between two successive measurements to calculate the observable averages.

Random triangulations were considered up to a system size of 64×64 , which seems to be small if comparing with topological triangulations [52,259]. For lattice triangulations one has to check the convexity of quadrangles to decide whether a step is permissible, which increases the computation time needed for one Metropolis step and which decreases the step acceptance ratio, because some steps have to be rejected.

In this section we restrict to quadratic integer lattices for clarity reasons, actually also simulations for non-quadratic lattices were performed. Except of the average shortest path length (which grows with $|M - N|$) all observables only depend on the actual system size $M \cdot N$ for $M \cdot N \gtrsim 10^2$ and $M, N \gtrsim 4$ and not on the two linear sizes.

For comparing the random triangulation averages with the results in the Erdős-Rényi, the Newman-Watts and the Barabási-Albert random graphs of the same size that are not known analytically, we use averages over 500 randomly generated instances of the respective random graphs. The generation of these random graphs was done using the NetworkX framework [201].

Vertex degree distribution

The vertex degree distribution of the considered random graphs is known analytically: for the Erdős-Rényi and Newman-Watts it follows a binomial distribution, for the Barabási-Albert random graph it is a power-law distribution [140,262].

In Fig. 3.37a) the degree distribution of random triangulations is displayed for different lattice sizes and compared with the different random graphs. In contrast to the random graphs the values $k = 0$ and $k = 1$ are not encountered for triangulations since these vertex degrees are forbidden for



the graph to form a valid triangulation. The degree $k = 2$ can only be realised on the boundary of the triangulation, so the probability decreases for increasing lattice size and decreasing importance of the boundary.

The calculations for our random triangulations agree for $k \geq 4$ with the results for the degree distribution of a topological triangulation of a torus in [259]. In contrast to our results, where $P(k)$ is peaked at $k = 4$, in [259] a monotonically decreasing $P(k)$ with maximal value at $k = 3$ was found. This is because the vertex degree $k = 3$ is difficult to realise due to the non-general coordinates of the vertices in lattice triangulations (there are many collinear points), so even by constructing one cannot realise more than one out of four vertices having degree $k = 3$. In topological triangulations one can realise Apollonian-like networks [47, 372, 433], where every second vertex can have degree $k = 3$.

To compare a Newman-Watts random graph we used a ring with each vertex connected to its $L = 4$ nearest neighbors and added edges, so for this graph the degrees $k < 4$ are not present. As a result one can see that the degree distribution of random triangulations is comparable with the Erdős-Rényi and Newman-Watts random graph for $k \geq 5$, whereas the Barabási-Albert model shows a scale free power law behavior $\propto k^{-3}$.

Mean energy

To quantify the disorder of a triangulation we use an energy function which is, up to boundary terms, the variance of the degree distribution multiplied with the lattice size. In Fig. 3.37b) we compare the specific average energy of random triangulations with the degree variance of the random graphs, which can be calculated from the vertex degree distributions. For the random triangulations a fit to the numerical calculated data yields a convergence of the specific average energy to 4.62 ± 0.05 , the Erdős-Rényi and Newman-Watts random graphs show a similar behavior (see Tab. 3.3 for the detailed values). For the Barabási-Albert random graph the second moment of the degree distribution diverges.

For random topological triangulations the energy per vertex can be calculated analytically to be $E/n = (\langle k \rangle - 3)^2 = 9$ for $\langle k \rangle = 6$ in topological triangulations [52], which agrees with our finding that E/MN converges for $MN \rightarrow \infty$. The absolute value of the specific energy in lattice triangulations is smaller, because the degree distribution has a peak located nearer at the mean value as discussed in Sec. 3.4.4.



Clustering coefficient

The clustering coefficient $C_i = 2K/k_i(k_i - 1)$ of a vertex i with degree k_i is the ratio of the number of connections K between the k_i neighbors and number of possible connections. For a non-boundary vertex of a triangulation holds $K = k_i$ and $C_i = 2/(k_i - 1)$, for a boundary vertex $K = k_i - 1$ and $C_i = 2/k_i$. The clustering coefficient C of the whole graph is the average of the vertex clustering coefficients.

The clustering coefficient for the Erdős-Rényi random graph equals the edge connection probability p ($\approx 6/MN$ to ensure equal edge number), for the Barabási-Albert model it can be calculated using a mean-field approach [179]. In both cases the clustering coefficient vanishes for increasing lattice sizes for our choice of parameters.

The numerical results for the random triangulations and the Newman-Watts graph can be seen in Fig. 3.37c), both are converging to a constant value for increasing lattice sizes. For random triangulations the limit is 0.4859 ± 0.0005 , which is higher than for all considered random graphs (see Tab. 3.3 for the detailed values). Intuitively this means that almost every second possible edge between neighbors of a common vertex is present in the random triangulation.

For topological triangulations the clustering coefficient is $C \approx 0.6$ [52]. This is higher than for our lattice triangulations, mainly due to the fact that the degree $k = 3$ is much more probable for topological than for random triangulations.

Shortest path length

As for the clustering coefficient the shortest path length is analytically known for both the Erdős-Rényi and the Barabási-Albert random graphs [180] and has to be calculated numerically for the Newman-Watts graph. For all random graphs the shortest path length shows small-world behavior and increases approximately with the logarithm of the vertex number.

These values are compared with the shortest path length of random triangulations in Fig. 3.37d). In contrast to the random graphs, for random triangulations there is a power law behavior of the shortest path length $\propto (MN)^{0.400 \pm 0.001}$. Also for random topological triangulations a power law scaling of the average shortest path length can be found [52].



3. Embedded triangulations

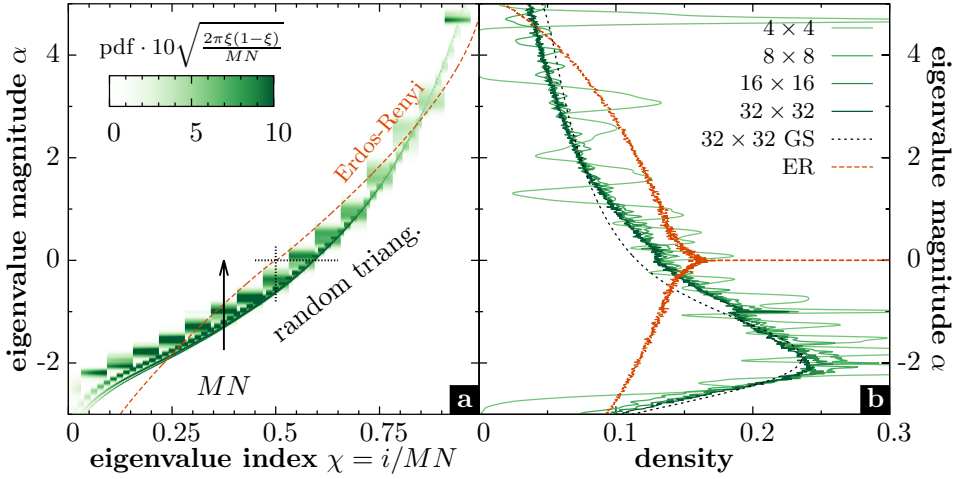


Figure 3.38: Average adjacency spectrum of random triangulations for different system sizes. The color scale (a) shows the probability density function (PDF) for every normalized index of the eigenvalues scaled with the maximum value expected from order statistics (3.68). The orange, dashed line is the spectrum of the Erdős-Rényi random graph with 32^2 vertices. One sees a convergence of the spectrum for increasing system size. The indexed-summed PDF (b) is compared with the Erdős-Rényi random graph and the spectrum of the maximal ordered ground state of the triangulation (dashed black line). The dotted lines in the indexed-summed spectrum show the cuts that are displayed in Fig. 3.39



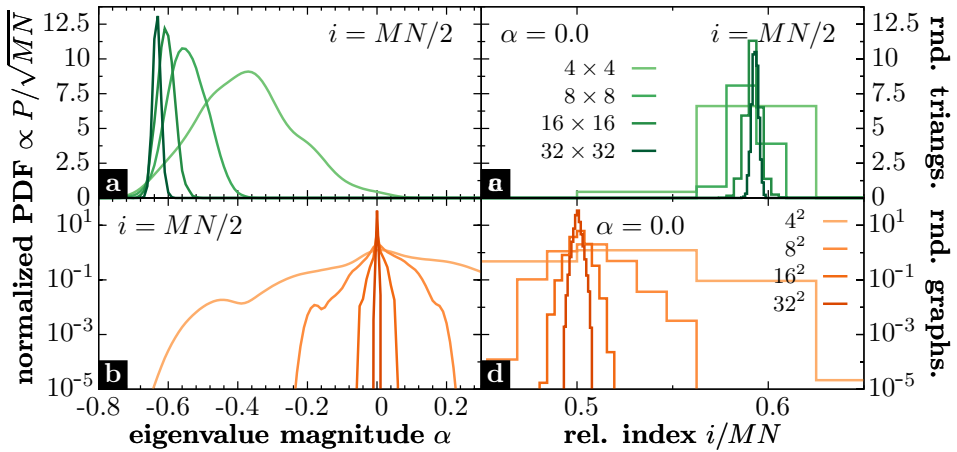


Figure 3.39: Adjacency spectrum of random lattice triangulations, cuts. Cuts through the probability density function (PDF) of the adjacency spectrum of random triangulations (a,c) and Erdős-Rényi random graphs (b,d). The cut through index $i = MN/2$ (a,b) displays the probability distribution of the eigenvalues for this index, the cut through $\alpha = 0$ (c,d) shows the probability for an index to have this eigenvalue magnitude.

Spectrum of the adjacency matrix

For the Erdős-Rényi random graph there are some analytical results for the spectrum of the adjacency matrix. The random graph adjacency spectra are strongly related with the spectra of random matrices, which follows in most cases a semi-circle distribution [233, 420, 421].

Numerical investigations showed that for constant edge probability $p \neq 0, 1$ the adjacency spectrum of the Erdős-Rényi model converges to the semi-circle distribution up to the largest eigenvalue, but there are additional peaks for $p \propto n^{-1}$, which we actually choose to compare with random triangulations (see [166, 167] for investigations on the level of random matrices and [69, 169] for investigations on random graphs).

In Fig. 3.38 the probability density function (PDF) for the spectrum of the adjacency matrix of random triangulations is displayed in an index-resolved and an index-summed way for different lattice sizes. The spectrum is compared with the spectra of the ground state triangulations and the Erdős-Rényi random graph. Fig. 3.39 displays cuts through the random triangulation and the Erdős-Rényi adjacency PDF for the eigenvalue index $i = MN/2$ and the eigenvalue magnitude $\alpha = 0$. The displayed PDFs are created using a kernel density estimation [323, 350] with Gaussian kernel



and Silverman's rule [369] for the width of the Gaussian.

The adjacency spectra of random and ground state triangulations both have a main peak around the eigenvalue magnitude of -2. The only difference is that at $\alpha \approx 0$ the random PDF has a higher value than the ground state one, and vice versa at $\alpha \approx 4.5$.

In contrast to the random triangulations the numerically calculated adjacency spectrum of the Erdős-Rényi random graph is symmetric with respect to $\alpha \approx 0$ and behaves like Wigner's semicircle law with an additional peak at $\alpha = 0$. The peak is due to the eigenvalue $\alpha_{MN/2} = 0$ occurring in all random graphs that were calculated numerically and can also be seen as a small horizontal piece in the index-resolved adjacency PDF.

Considering the values of the index-resolved PDF one can see for each eigenvalue index a peaked distribution of the eigenvalue magnitudes with increasing height and decreasing width for growing system size. One can assume that this is due to the number of eigenvalues MN growing with the lattice sizes, but all having values in a fixed interval $\approx [-4, 6]$. This behavior can be quantified using order statistics: Assume that one draws n random variables X_i from a uniform distribution on the fixed interval $[a, b]$ and sorts them so that $X_i \leq X_j$ for $i < j$. Then the probability density function (PDF) for the X_k is given by the beta distribution

$$P(X_k = x) = \frac{1}{b-a} \frac{n!}{k!(n-k-1)!} x^k (1-x)^{n-k-1}$$

The PDF takes its maximal value at $x_{\max} = a + (b-a)k/(n-1)$, the maximal value is

$$P(X_k = x_{\max}) \xrightarrow{n \rightarrow \infty} \frac{1}{b-a} \sqrt{\frac{n}{2\pi\xi(1-\xi)}} \quad (3.68)$$

where $\xi = k/(n-1)$ denotes the relative index and Stirling's formula was used for calculating the asymptotics of the factorials. So one expects that the maximal value of the PDF scales $\propto (MN)^{0.5}$ independently for each relative index $\xi = k/(n-1)$. This is in fact the scaling behavior that can be found in the Fig. 3.38 and Fig. 3.39 for the adjacency spectrum.

Spectrum of the Laplacian matrix

The same considerations as for the adjacency spectrum can also be done for the Laplacian spectrum of random triangulations and graphs. In Fig. 3.40 the index-resolved and index-summed probability density function (PDF) for



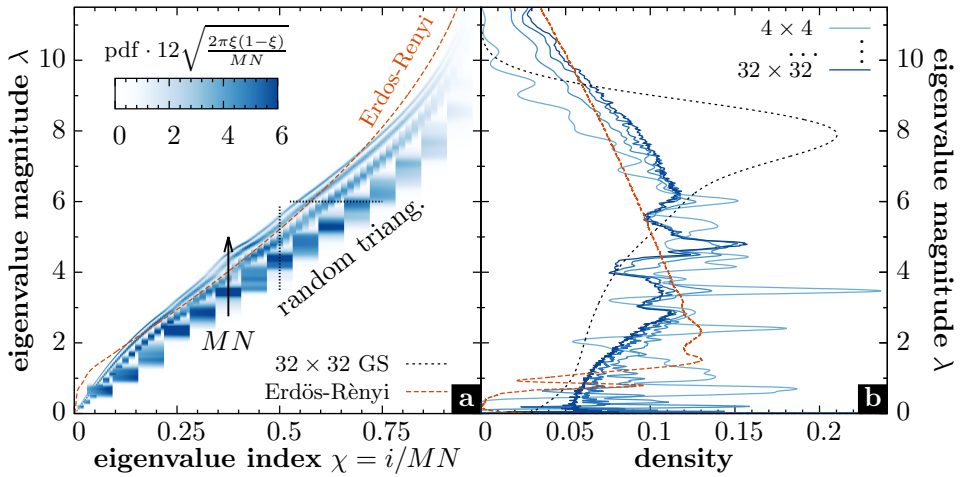


Figure 3.40: Average Laplacian spectrum of random lattice triangulations for different system sizes. The color scale (a) shows the probability density function (PDF) for every normalized index of the eigenvalues scaled with the maximum value expected from order statistics (3.68). The orange, dashed line is the spectrum of the Erdős-Rényi random graph with 32^2 vertices. One sees a convergence of the spectrum for increasing system size. The indexed-summed PDF (b) is compared with the Erdős-Rényi random graph and the spectrum of the maximal ordered ground state of the triangulation (dashed black line). The dotted lines in the indexed-summed spectrum show the cuts that are displayed in Fig. 3.41



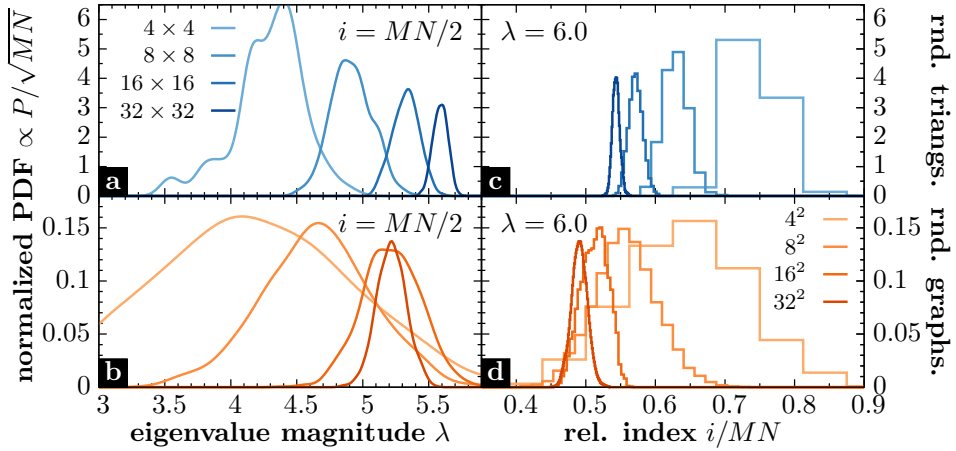


Figure 3.41: Laplacian spectrum of random lattice triangulations, cuts. Cuts through the probability density function (PDF) of the Laplacian spectrum of random triangulations (a,c) and Erdős-Rényi random graphs (b,d). The cut through index $i = MN/2$ (a,b) displays the probability distribution of the eigenvalues for this index, the cut through $\lambda = 6$ (c,d) shows the probability for an index to have this eigenvalue magnitude.

the spectrum of the Laplacian matrix of random triangulations is displayed. For comparison also the Laplacian spectra of the ground state triangulation and an Erdős-Rényi random graph with the same number of vertices are plotted. Fig. 3.41 displays cuts through the PDF for a given eigenvalue index and a given eigenvalue magnitude. As for the spectra of the adjacency matrix, the PDFs are calculated using a Gaussian kernel density estimation and normalized with the order statistics expected maximal values (3.68).

If one compares the Laplacian random spectrum with the spectrum of the ground state two main things differ: For the ground state triangulation the largest possible eigenvalue is 9 (as shown analytically for the periodic ground state), whereas the largest eigenvalues of the random triangulations are much higher for increasing lattices sizes. The index-summed PDF is peaked around an eigenvalue magnitude of 8 for the ground state, for the random triangulation (of lattices with size bigger than 10×10) there is a peak around an eigenvalue magnitude of 5 which is less dominant than the peak of the ground state.

For the considered parameter set of Erdős-Rényi random graphs there are approximative analytical calculations [133] for the spectrum of the Laplacian that coincide with earlier numerical calculations [96]. Ding and Jiang [136] showed that the spectrum of the adjacency matrix of a random (Erdős-



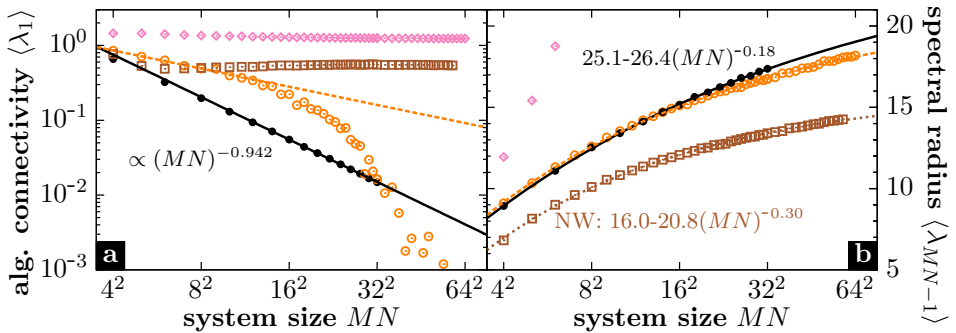


Figure 3.42: Spectrum observables of random lattice triangulations.

Algebraic connectivity λ_1 (a) and spectral radius λ_{MN-1} (b) of random triangulations (\bullet), Erdős-Rényi (\circ), Newman-Watts (\square) and Barabási-Albert (\diamond) random graphs for different number of vertices MN . The displayed lines are power law fits for the numerical data.

Rényi) graph converges to the semi-circle distribution, and the spectrum of the Laplacian matrix converges to a free convolution of the semi-circle distribution and a normal distribution.

The Laplacian spectrum of the Erdős-Rényi random graph looks similar to the spectrum of the triangulations for eigenvalue magnitudes bigger than 6, both exhibit a linear density decrease for increasing eigenvalue magnitudes. For eigenvalue magnitudes between 2 and 6 there are several peaks in the spectrum of the random triangulation which also survive if one considers the limit $MN \rightarrow \infty$, whereas the random graph spectrum in this interval is nearly linear. Between eigenvalue magnitudes 0 and 2 the laplacian spectrum of the random graph shows two peaks and three dips, while the spectrum of the random triangulation is smooth at most for large lattice sizes.

Comparing the Laplacian spectra cuts of the random triangulations and the Erdős-Rényi random graphs with the expectations from the order statistics in Fig. 3.41, one can find similar results as in the case of the adjacency spectra.

Algebraic connectivity and spectral radius

In this section we examine the dependence of the smallest Laplacian eigenvalue λ_1 (algebraic connectivity) and the biggest Laplacian eigenvalue λ_{MN-1} (spectral radius) of random triangulations on the lattice size. The results of the Monte-Carlo simulations for random triangulations can be



found in Fig. 3.42, as well as the values of the algebraic connectivity and the spectral radius for the different considered models of random graphs.

Using a power law fit for the algebraic connectivity of random triangulations one finds that

$$\langle \lambda_1 \rangle \approx (10.7 \pm 0.2)(MN)^{-0.949 \pm 0.003} \quad (3.69)$$

This compares well with the analytical result for the periodic ground state (3.65)

$$\lambda_1^{(\text{p.gs})} = 4 - 4 \left[1 - \frac{4\pi^2}{N^2} + \mathcal{O}\left(\frac{1}{N^4}\right) \right] \propto (M \cdot N)^{-1}$$

For the algebraic connectivity of the Erdős-Rényi random graph one finds a different behavior: For $MN \lesssim 200$ there is a power law behavior $\propto x^{-0.44}$, but for $MN \gtrsim 200$ there is a power law behavior with exponent ≈ -2 . The change in the power law exponent corresponds to the fact that for large number of vertices MN and $p \rightarrow 6/MN$ some of the random graphs become disconnected as described in Sec. 3.4.2 and have an algebraic connectivity $\lambda_1 = 0$. So the fraction of disconnected random graphs increases with MN which influences the averaging of the algebraic connectivity. The algebraic connectivities of the Newman-Watts model and the Barabási-Albert model converge to the finite values $\lambda_{1,NW} = 0.553 \pm 0.003$ and $\lambda_{1,BA} = 1.238 \pm 0.001$.

For the spectral radius of the random triangulation the power law fit yields

$$\langle \lambda_{MN-1} \rangle = (27.4 \pm 0.5) - (27.6 \pm 0.3) \cdot (MN)^{-0.147 \pm 0.006} \quad (3.70)$$

For the Erdős-Rényi model one gets a limit of 21.1 ± 0.2 and power law exponent -0.259 ± 0.006 , for the Newman-Watts model the limit is 15.46 ± 0.09 with power law exponent -0.337 ± 0.007 . For the Barabási-Albert model the spectral radius grows much more quickly, because the preferential attachment and the resulting power law degree distribution lead to nodes with much higher degrees than in random triangulations and the other random graphs. Since in Eq. (3.55) the maximal vertex degree is a lower bound for the spectral radius this implies a higher spectral radius for the Barabási-Albert model.

The parameters obtained by the fits of the spectral radius and the algebraic connectivity are summarised in Tab. 3.4.



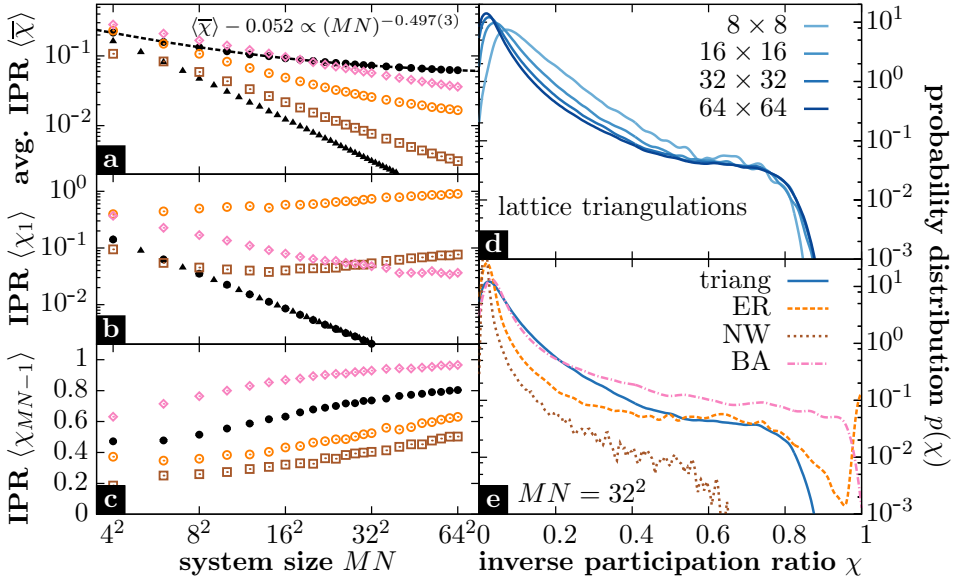


Figure 3.43: Inverse participation ratio for random lattice triangulations.

Scaling of the inverse participation ratio (IPR) of the Laplacian spectrum of random triangulations. Expectation values of the average IPR $\langle \bar{\chi} \rangle$ (a), the IPR $\langle \chi_1 \rangle$ of the algebraic connectivity λ_1 (b) and the IPR of $\langle \chi_{MN-1} \rangle$ of the spectral radius λ_{MN-1} of random triangulations (\bullet), maximal ordered triangulations (\blacktriangle), Erdős-Rényi (\triangle), Newman-Watts (\circ) and Barabási-Albert (\diamond) random graphs for different number of vertices MN . The displayed lines are power law fits for the numerical data. Probability density function $p(\chi)$ of the IPR for random triangulations for different system sizes (d) and for the different random graphs for 32^2 vertices (e).



Inverse participation ratio and localization

In this section the inverse participation ratio (IPR) (3.56) of the Laplacian spectrum of random triangulations is examined in terms of the system size. In Fig. 3.43 the average IPR $\langle \bar{\chi} \rangle$, as well as the IPR of the algebraic connectivity $\langle \chi_1 \rangle$ and the spectral radius $\langle \chi_{MN-1} \rangle$ are displayed and compared with the common random graph models.

For random triangulations the average IPR $\langle \bar{\chi} \rangle$ decreases with a power law

$$\langle \bar{\chi} \rangle \approx (0.671 \pm 0.008) \cdot (MN)^{-0.512 \pm 0.004} + (0.05334 \pm 0.0005) \quad (3.71)$$

for increasing system size (similar to the other considered random graph models), the exponent -0.512 ± 0.004 being smaller than the analytical calculated exponent -1 for periodic maximal ordered triangulations. Since the data obtained for random lattice triangulations does not allow for a power-law fit without constant offset, one can conclude that for random triangulations there is a non-vanishing limit (0.05334 ± 0.0005) for infinite system sizes, in contrast to Newman-Watts and Barabási-Albert random graphs (compare Tab. 3.4, for Erdős-Rényi the situation is ambiguous, both possible fits are done there). This implies that on average the localization of eigenvectors for random triangulations is higher than for comparable random graphs.

The IPR $\langle \chi_1 \rangle$ of the algebraic connectivity random lattice triangulations is approximately equal to that of the maximal ordered triangulation and decreases with a power law $\propto x^{-0.896 \pm 0.006}$, since the algebraic connectivity is determined by the vertices with low degree (which are the vertices at the corner of the lattice), and the degree is likely to be unchanged for the random triangulations. One can find a similar decrease for Barabási-Albert, but not for Erdős-Rényi or Newman-Watts random graphs (which converge towards a finite value for increasing system size). The IPR of the spectral radius converges to a value above 0.8, with a similar functional dependency as the other random graph models.

The probability distribution function of the IPRs for random triangulations is comparable to the one of random graphs, there are differences only in the probability of the largest IPRs, which correspond to the strongest localization.





Table 3.3: Scaling of graph observables on random lattice triangulations in terms of system size.

Scaling and functional dependence obtained by a least-square fit of the mean energy (or the degree distribution variance), the clustering coefficient and the shortest path length in terms of the system size for ground state (maximal ordered) and random triangulations as well as for comparable size Erdős-Rényi , Newman-Watts and Barabási-Albert graphs. If there are no error bars, the results are taken from analytical calculations.

quantity	graph	scaling behavior
$\langle E \rangle / MN$	per. triangular lat.	0
	random triang.	$(4.62 \pm 0.02) - (10.80 \pm 0.043) \cdot (MN)^{-0.47 \pm 0.02}$
Var(k)	Erdős-Rényi	$6 - 4 \cdot (MN)^{0.5}$
	Newman-Watts	$2 - 4 \cdot (MN)^{0.5}$
	Barabási-Albert	$\rightarrow \infty$
$\langle C \rangle$	per. triangular lat.	0.4
	random triang.	$(0.4849 \pm 0.0003) - (0.78 \pm 0.02) \cdot (MN)^{-0.73 \pm 0.01}$
	Erdős-Rényi	$6 \cdot (MN)^{-1}$
	Newman-Watts	$(0.241 \pm 0.001) - (1.18 \pm 0.02) \cdot (MN)^{-0.557 \pm 0.007}$
	Barabási-Albert	$0.678 \cdot (MN)^{-1} \log(MN)^2$
$\langle \ell \rangle$	per. triangular lat.	$(0.5677 \pm 0.0002) \cdot (MN)^{0.49978 \pm 0.00005}$
	random triang.	$(0.673 \pm 0.006) \cdot (MN)^{0.409 \pm 0.001}$
	Erdős-Rényi	$\log(MN)/6$
	Newman-Watts	$(0.063 \pm 0.001) \cdot \log[(0.595 \pm 0.002)MN]$
	Barabási-Albert	$\log(MN)/\log(\log(MN))$

Table 3.4: Scaling of spectral observables on random lattice triangulations in terms of system size.

Scaling and functional dependence obtained by a least-square fit of the algebraic connectivity, the spectral radius and the average inverse participation ratio in terms of the system size for ground state (maximal ordered) and random triangulations as well as for comparable size Erdős-Rényi , Newman-Watts and Barabási-Albert graphs. If there are no error bars, the results are taken from analytical calculations.

quantity	graph	scaling behavior
$\langle \lambda_1 \rangle$	per. triangular lat.	$12\pi(MN)^{-1}$
	rnd. triang.	$0 + (10.7 \pm 0.2) \cdot (MN)^{-0.949 \pm 0.003}$
	Erdős-Rényi	$\rightarrow 0$
	Newman-Watts	0.541 ± 0.003
	Barabási-Albert	1.235 ± 0.001
$\langle \lambda_{MN-1} \rangle$	per. triangular lat.	9
	rnd. triang.	$(27.4 \pm 0.5) - (27.6 \pm 0.3) \cdot (MN)^{-0.147 \pm 0.006}$
	Erdős-Rényi	$(21.4 \pm 0.2) - (23.6 \pm 0.2) \cdot (MN)^{-0.236 \pm 0.006}$
	Newman-Watts	$(16.01 \pm 0.08) - (20.8 \pm 0.2) \cdot (MN)^{-0.301 \pm 0.006}$
	Barabási-Albert	$\rightarrow \infty$
$\langle \bar{\chi} \rangle$	per. triangular lat.	$(MN)^{-1}$
	rnd. triang.	$(0.643 \pm 0.009) \cdot (MN)^{-0.497 \pm 0.004} + (0.0522 \pm 0.0002)$
	Erdős-Rényi	$(1.19 \pm 0.03) \cdot (MN)^{-0.601 \pm 0.007} + (0.0074 \pm 0.0007)$ $(1.02 \pm 0.03) \cdot (MN)^{-0.539 \pm 0.007}$
	Newman-Watts	$(0.59 \pm 0.05) \cdot (MN)^{-0.58 \pm 0.02}$
	Barabási-Albert	$(0.820 \pm 0.006) \cdot (MN)^{-0.383 \pm 0.002}$



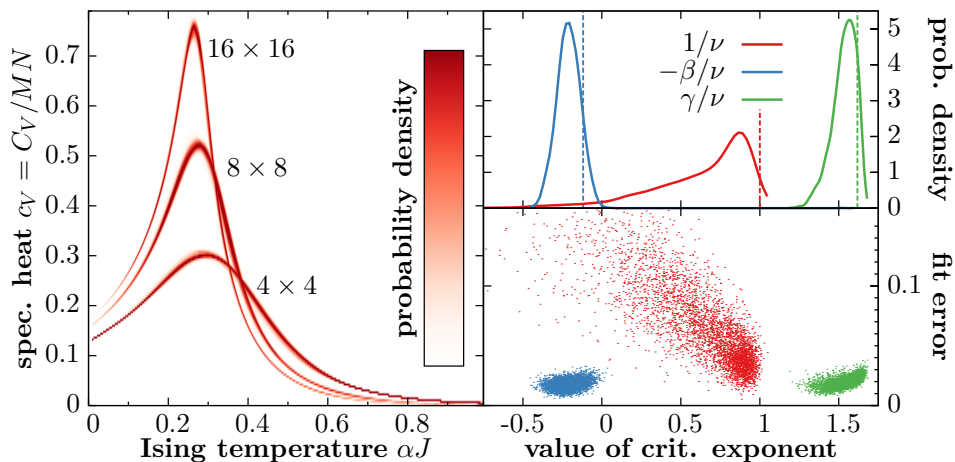


Figure 3.44: Ising model on random lattice triangulations.

(a) Probability distribution of the specific heat c_V for in terms of the Ising temperature α for 4×4 , 8×8 and 16×16 random lattice triangulations. (b) Probability distribution of the critical exponents ν , $-\beta/\nu$ and γ/ν obtained by finite size scaling for different random triangulations of the 16×16 lattice. The dashed lines correspond to the value of the critical exponent for the maximal ordered triangulation. (c) Fit errors of the critical exponents. Every dot corresponds to one independent calculation of the critical exponent using a tuple of triangulations with different system size and correlates the value of the critical exponent with the error of the fit.

Ising model on random triangulations

In Fig. 3.44 the results for calculations of the Ising model on the ensemble of random triangulations are displayed. Despite the fact that there can be very diverse triangulations, if one considers Ising observables as the specific heat² $c_V(\alpha)$ they show a narrow distribution with respect to the underlying random triangulation ensemble, and agree qualitatively with the results for the Ising model of square lattices.

The fact that we do not consider the Ising model on a fixed lattice, but on an ensemble of underlying lattices, does lead to a problem if trying to determine critical exponents using the Binder cumulant or finite size scaling as described in Sec. 2.2.5. For calculating e.g., the critical exponent ν of the correlation length using Eq. (2.74) one has to calculate the slope of the Binder

² To avoid mixing up the inverse temperature of the Ising model and the inverse temperature of the canonical ensemble of triangulations, we denote already here the inverse Ising temperature by α , whereas we denote the inverse triangulation temperature by β .



cumulant at the quasi-critical point, but for random triangulations, for a fixed system size there is no single quasi-critical point, but a distribution. To circumvent this problem, to calculate critical exponents we generate tuples of triangulations by choosing one out of the ensemble for every system size, which are then used to calculate the quasi-critical temperatures and the critical exponents using the methods of Sec. 2.2.5.

Note that due to the finite system size the critical exponents, that are determined by a functional fit, are not universal, but are distributed with a finite width, which can be seen in Fig. 3.44. In contrast to the other critical exponents, the distribution of the critical exponent ν of the correlation length seems to be not Gaussian distributed. If one considers the errors of the respective fits in Fig. 3.44c, one can see that the regions that deviate from a Gaussian distribution all have a large fit error, so it is probable that also this distribution in fact has a Gaussian shape. We also tried an alternative approach by using averaged of the Binder cumulant over the random triangulation ensemble to calculate the critical inverse temperature and exponents, which basically leads to the same average results as the tuple method, but one loses the information about the distribution of the critical exponents.

3.4.5 Microcanonical triangulations

In this section we consider triangulations with a fixed energy which corresponds to a microcanonical ensemble and examine the Laplacian spectrum, the algebraic connectivity λ_1 and the spectral radius λ_{MN-1} in terms of the energy for different system sizes. For each lattice size we measure the energy in units of the average energy $\langle E \rangle_{\text{rnd}}$ of random triangulations on an equal sized lattice to make the results for different lattice sizes comparable. We will use $\epsilon = E/E_{\text{rnd}}$ to denote this rescaled energy.

Since in general the Pachner moves are not ergodic if restricting to the subset of triangulations with energy E , we use the following algorithm for generating sample triangulations with given energy E :

- Start with a random triangulation with arbitrary energy, generated as described in Sec. 3.4.4.
- Perform Metropolis Monte Carlo steps [291] with the acceptance probability

$$A_{\text{Metropolis}}(\mathcal{T}_1 \rightarrow \mathcal{T}_2) := \min \left(1, \frac{\exp[-\beta E(\mathcal{T}_2)]}{\exp[-\beta E(\mathcal{T}_1)]} \right) \quad (3.72)$$



and check after each step whether the obtained triangulation has the desired energy, then stop (the inverse temperature β can be tuned to find the desired energy more quickly). Note that the actual number of steps necessary to find a suitable triangulation depends on the given energy and cannot be predicted.

- If the desired energy was reached, take the triangulation for measuring the observables and perform $1000MN$ steps at $\beta = 0$ to randomise the triangulation and avoid autocorrelations between successive measurements. Note that the autocorrelation time is always below $10MN$ as explained in Sec. 3.4.4.

These steps are repeated until the desired number of sample triangulations with the correct energy are found. In this section we use 1000 samples for each energy and system size.

For relative energies $\epsilon \gtrsim 2$ one must use negative inverse temperatures in Eq. (3.72), but there are many local minima where the simulation can get stuck in, which make searching specific energies difficult. In these situations we use the acceptance probability

$$A_{\text{flat}}(\mathcal{T}_1 \rightarrow \mathcal{T}_2) := \min(1, \exp(H[E(\mathcal{T}_1)] - H[E(\mathcal{T}_2)])), \quad (3.73)$$

for locating triangulations with the proper energy. This acceptance probability weights every energy level E with the inverse exponential of the number $H(E)$ the simulation has visited the energy level before. Intuitively this means the longer the system stays at a certain energy, the larger is the probability for leaving it, which avoids getting stuck in local energy minima. Basically this procedure is the Wang-Landau algorithm [406, 407] that was explained in detail in Sec. 2.2.2, using only a single modification factor.

The performed algorithms for searching triangulations with suitable energy are much slower for relative energies $\epsilon > 2$ than for lower relative energies. The problems increase since the maximal specific energy (and with it the maximal relative energy) does not converge to a finite value for infinite system size, but is unbounded from above as one can see in some easily constructable examples. Consider $N \times N$ lattice triangulations that are constructed as in Fig. 3.45, which have energy

$$E = 4N^3 - 8N^2 + 4N - 2 \quad \Rightarrow \quad \epsilon = 4N - 8 + \mathcal{O}(N^{-1}).$$

So for $N = 4$ there is a lower bound for the maximal relative energy of $\epsilon_{\text{max}} > 4.4$ from this construction, for $N = 32$ the same construction leads to



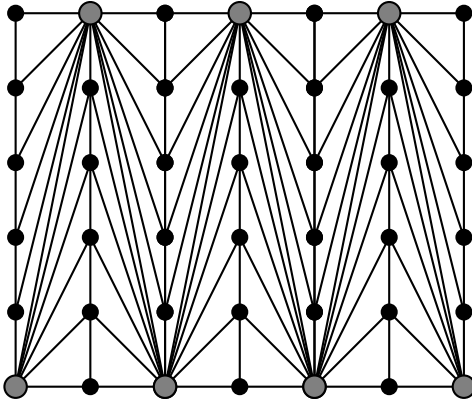


Figure 3.45: Construction for triangulations with unbounded specific energy. The energy of this quadratic $N \times N$ triangulation is $E \approx 4N^3 - 8N^2$ (due to the contribution of the large gray vertices). This means that the specific energy $E/N^2 \approx 4N - 8$ is not bounded.

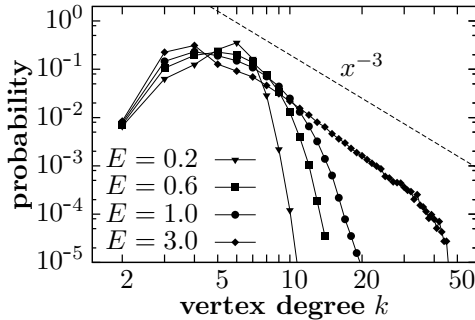


Figure 3.46: Double logarithmic plot of the **microcanonical averaged degree distribution** of lattice triangulations of 16×16 lattices at different energies. For comparison the dashed line shows a power law $\propto k^{-3}$.

the lower bound $\epsilon_{\max} > 34.3$. Using the methods applied here for calculating the microcanonical average this relative energies cannot be reached due to the fastly increasing calculation time.

Degree distribution

In Fig. 3.46 the degree distribution for different relative energies is displayed. For relative energies $\epsilon < 1$ the distribution agrees qualitatively with the degree distribution of random triangulations. For the relative energy $\epsilon = 3$ there is a qualitative change in the behavior: While for $k \leq 4$ the degree distribution behavior does not change if compared to the other relative energies, for degrees $4 \leq k \leq 40$ there is a power law behavior $P(k) \propto k^{-3}$ with the same exponent as the Barabási-Albert random graph, which is a hint for small-world behavior. For $k > 40$ the degree distribution decreases faster than the power law, probably because finite size effects become important.



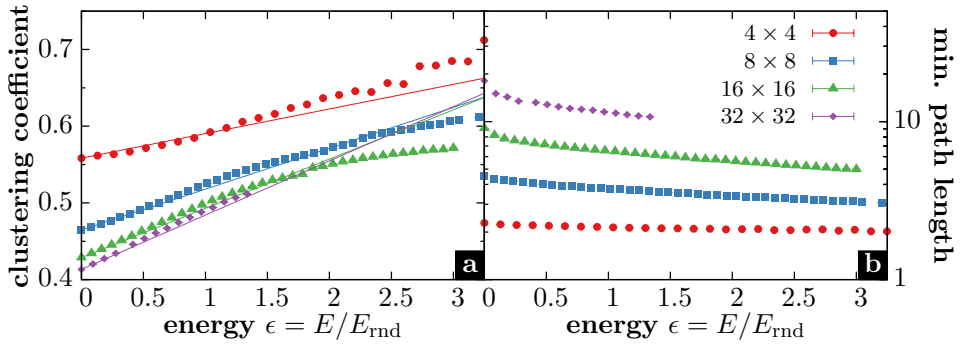


Figure 3.47: Graph observables of microcanonical lattice triangulations. Clustering coefficient (a) and shortest path length (b) of microcanonical lattice triangulations in terms of the normalized energy $\epsilon = E/E_{\text{rnd}}$ for different lattice sizes. The solid lines are the approximative predictions (3.74) for the clustering coefficients at low energy.

Clustering coefficient

The clustering coefficient of the maximal ordered ground state ($E = 0$) as well as its change due to a Pachner flip originating at the ground state were calculated in Eqs. (3.59) and (3.60) and can be used for estimating the average clustering coefficient for small energies in the microcanonical ensemble. The energy of a ground state triangulation increases from $E = 0$ to $E = 4$ if executing a Pachner flip that is not located at the boundary. Extrapolating both the clustering coefficient and the energy linearly leads to

$$\langle C \rangle_{\text{mc}}(E) \approx C_{\text{gs}} + \frac{1}{60} \cdot \frac{E}{MN} = C_{\text{gs}} + \frac{\epsilon}{60} \cdot \frac{E_{\text{rnd}}}{MN}. \quad (3.74)$$

The Monte-Carlo results for the clustering coefficient as well as the approximation (3.74) are plotted in Fig. 3.47. One can see an a good agreement for $\epsilon = E/E_{\text{rnd}} < 0.5$, for an intermediate energy range the actual clustering coefficient grows more than linear with the relative energy, and for high energy it saturates at nearly constant value.

Shortest path length

The Monte-Carlo results for the average shortest path length are plotted in Fig. 3.47. The shortest path length decreases with increasing energy since for high energies there are more long edges in the triangulations that decrease the path length between two arbitrary vertices, but as for random



triangulations for all calculated relative energies the shortest path length grows with a power law in the system size.

In contrast to the power law behavior for the considered energy ranges, for triangulations with nearly maximal energy, where one vertex is connected with all possible other vertices as displayed in Fig. 3.12, the diameter, which is the maximal shortest path length between any two vertices, is 4 independent of the lattice size. Since the diameter is an upper bound for the average path length also $\ell \leq 4$ for these triangulations. So for microcanonical triangulations there is an energy with crossover from the power law behavior of the shortest path length found in Fig. 3.47 to a constant shortest path length.

Laplacian spectrum

The microcanonical average of the Laplacian spectrum probability distribution function (PDF) for different values of the relative energy $\epsilon = E/\langle E \rangle_{\text{rnd}}$ is plotted in Fig. 3.48. With increasing energy the eigenvalues λ_i become smaller for relative index $i/MN \lesssim 0.75$ and bigger for relative index $i/MN \gtrsim 0.75$, at index $i/MN \approx 0.75$ the eigenvalues do not change in a significant way. As expected the index-summed PDF looks similar to the ground state for $\epsilon \gtrsim 0$ with a broad and dominating peak around the eigenvalue magnitude of $\lambda \approx 8$ and a smooth decrease for $\lambda < 6$, and for $\epsilon \approx 1$ it is comparable with the spectrum of the random triangulation with small and narrow peaks emerging. For relative energies $\epsilon > 2.0$ narrow peaks emerge in the eigenvalue range $2 < \lambda < 6$, which can be seen as nearly horizontal lines in the index-resolved PDF.

Algebraic connectivity and spectral radius

Fig. 3.49 shows the algebraic connectivity λ_1 , which is the second-smallest Laplacian eigenvalue, and the spectral radius λ_{MN-1} , which is the biggest Laplacian eigenvalue, for microcanonical triangulations in terms of the normalized energy for different lattice sizes. For energies around the average random energy and smaller ($\epsilon = E/\langle E_{\text{rnd}} \rangle \leq 1.5$) both eigenvalues depend linearly on the energy of the triangulation

$$\frac{\lambda(E)}{\lambda(0)} \approx m(M, N) \cdot \frac{E}{\langle E \rangle_{\text{rnd}}} + t(M, N)$$

where slope $m(M, N)$ increases with growing system size M, N . The linear dependence of the eigenvalues is more clearly for the spectral radius than for the algebraic connectivity, and so the fits have smaller errors.



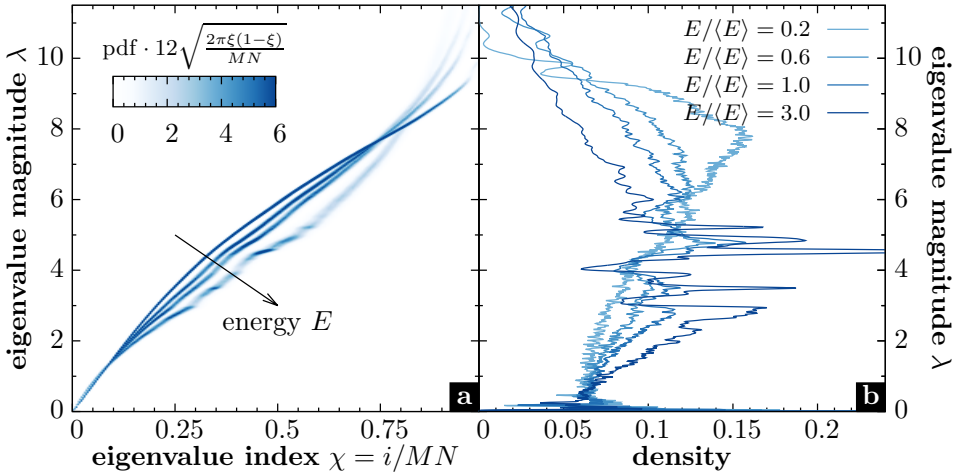


Figure 3.48: Laplacian spectrum of a microcanonical ensemble of 16×16 triangulations. The color code (a) left shows the index-resolved probability density function (PDF) in terms of the index of the eigenvalue and the magnitude of the eigenvalues for normalized energies $E/\langle E \rangle_{\text{rnd}} = 0.2, 0.6, 1.0, 1.4$, with $\langle E \rangle_{\text{rnd}} \approx 1000$. The index-summed PDF (b) is also displayed for the different energies.

The slope $m(M, N)$ can be fitted for the algebraic connectivity and the spectral radius by

$$m_{\text{ac}}(M, N) = (0.28 \pm 0.02) - (1.21 \pm 0.26) \cdot (MN)^{-0.51 \pm 0.09} \quad (3.75)$$

$$m_{\text{sr}}(M, N) = (2.22 \pm 0.32) - (2.84 \pm 0.27) \cdot (MN)^{-0.11 \pm 0.02} \quad (3.76)$$

From Eq. (3.67) one knows how the spectral radius increases in first order perturbation theory if one performs one step. One can derive an approximation for the change of the spectral radius in terms of the relative energy $\epsilon = E/\langle E \rangle_{\text{rnd}}$ by assuming that doing several steps at diagonals that are well separated the spectral radius is linear in the number of steps f :

$$\lambda_{N^2-1} \approx 9 + \frac{6f}{N^2} = 9 + \frac{6E}{4N^2} = 9 + \frac{6\langle E \rangle_{\text{rnd}}}{4N^2} \cdot \frac{E}{\langle E \rangle_{\text{rnd}}}$$

Here we used that each step increases the energy by 4 and so $E = 4f$. So by using the results for $\langle E \rangle_{\text{rnd}}/N^2$ from [265], we can find the following relation for the spectral radius:

$$\frac{\lambda_{MN-1}(\epsilon)}{\lambda_{MN-1}(0)} = 1 + \frac{1}{6} \cdot \frac{\langle E \rangle_{\text{rnd}}}{MN} \cdot \epsilon \quad (3.77)$$

Comparing Eq. (3.77) with the fitted values in Fig. 3.49d one finds a good agreement of the two values for the slope.



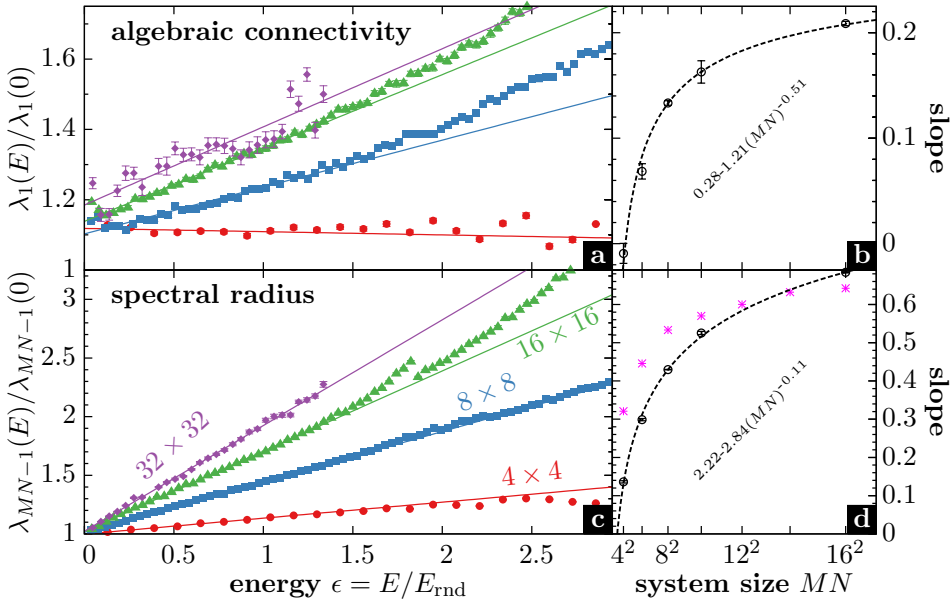


Figure 3.49: Spectral observables of microcanonical lattice triangulations.

Dependence of the algebraic connectivity (a) and the spectral radius (c) on the energy of the triangulation normalized by the energy of the random triangulation for 4×4 -triangulations (\bullet), 8×8 -triangulations (\blacksquare), 16×16 -triangulations (\blacktriangle) and 32×32 -triangulations (\blacklozenge). The solid lines are fits for $E/\langle E_{\text{rnd}} \rangle \in [0, 1.5]$. The eigenvalues are normalized by their values at ground states of the respective system size. (b,d): Gradients of the fits are plotted against the lattice size of the triangulations, the purple points are the approximation for the spectral radius using first order perturbation theory with periodic ground state from Eq. (3.77).



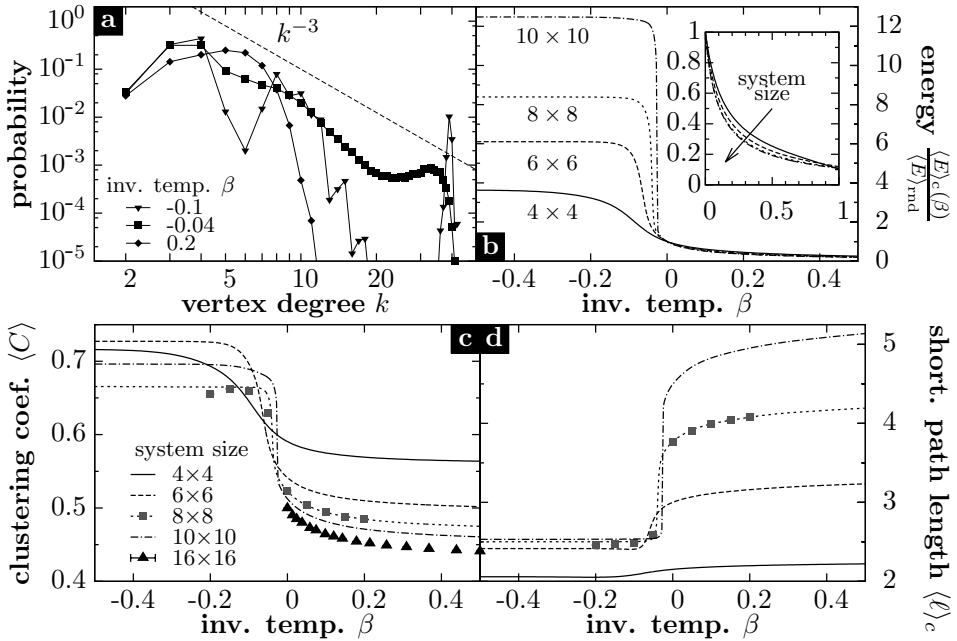


Figure 3.50: Graph observables of canonical lattice triangulations.

a) Canonical averaged degree distribution of 8×8 triangulations for different inverse temperatures β . The dashed line is a power law $\propto k^{-3}$. b) Mean energy in units of the energy of a random triangulation (with inset for positive temperatures), c) clustering coefficient and d) shortest path length in terms of the inverse temperature β for triangulations of different lattice sizes. The degree distribution and the lines in b)-d) were calculated using a Wang-Landau simulation, the data points in c)-d) are taken from a parallel tempering simulation.

3.4.6 Canonical triangulations

In this section we consider canonical averages of the degree distribution, the mean energy, the clustering coefficient and the shortest path length of lattice triangulations in terms of the inverse temperature with respect to the energy defined in (3.58). These calculations extend the results obtained in the previous section which correspond to the special case of vanishing inverse temperature $\beta = 0$. The numerical simulations are not restricted to the usually considered case $\beta \geq 0$, but can be extended to the case of negative inverse temperatures $\beta < 0$. These negative temperatures can also be interpreted as positive inverse temperatures with a negative coupling constant included in the definition (3.58) of the energy, which makes most disordered triangulations the ground state of the energy function.



It is difficult to use Metropolis Monte-Carlo simulations [291] to perform canonical averages for triangulations, especially if one wants to explore the regime of negative temperatures/coupling. There exist triangulations that are local minima in the energy landscape [253], and due to the small Metropolis acceptance probabilities ($\propto \exp(-\beta\Delta E)$, where ΔE is the energy difference induced by the flip) the algorithm gets stuck in one of these local minima. Other states outside of the local minimum that contribute to the ensemble average are reached only after many steps or not at all, so the autocorrelation times and therewith the simulation errors become large, or the possibility arises that the system is not even computationally ergodic anymore. This problem was also treated analytically in [108], where the mixing time (which is related to the autocorrelation time) of Glauber dynamics on lattice triangulations is shown to scale exponentially with the system size for a small enough $\beta < 0$.

Using a parallel tempering approach [150], which is basically the parallel calculation of multiple Metropolis simulations at different inverse temperatures with the possibility of interchanging the inverse temperatures, can help to overcome the problem of these local minima in the energy landscape. But parallel tempering is known to fail in situations with a large free energy barrier, e.g. in first order phase transitions.

Flat histogram algorithms as the Wang-Landau algorithm [406, 407] are used to calculate the density of states (DOS) $g(E)$ (which is the normalized number of states with energy E) of systems and can help to overcome both the local minima and the free energy barrier problem. This algorithm samples the single states according to their inverse DOS $g(E)^{-1}$ based on an initial estimation of $g(E)$ and simultaneously improves the estimation until it converges to the actual DOS of the system. The two main advantages of this algorithm is that with the knowledge of the DOS the observables can be calculated for all inverse temperatures β based on only one simulation, whereas for the Metropolis algorithm a new simulation for each β has to be used. The second one is that the algorithm does not get stuck anymore in local minima and the problems of large autocorrelation times described before and in [108] do not occur.

In Fig. 3.51 one can see a comparison of Metropolis sampling and a sampling based on the DOS calculated with Wang-Landau in terms of the acceptance ratios and the autocorrelation time of the energy observable. For negative temperatures the Metropolis algorithm basically gets stuck in high-energy states, which leads to low acceptance ratios and long autocorrelation times. Using the Wang-Landau algorithm this problem does not occur,



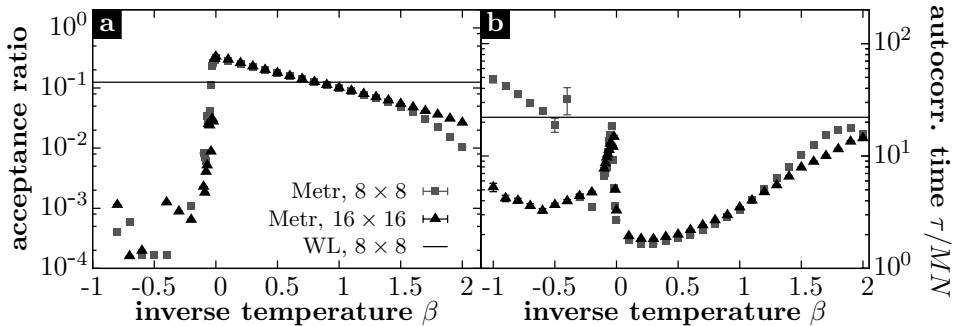


Figure 3.51: Comparison of Metropolis and Wang-Landau simulation for canonical lattice triangulations.

Acceptance ratio of a Monte Carlo step (a) and autocorrelation time of the energy observable (b) in terms of the inverse temperature for the Metropolis algorithm for 8×8 (\blacksquare) and 16×16 (\blacktriangle) lattices. The solid line is the temperature independent value obtained by a multicanonical simulation. Note that for the simulations based on the density of states the acceptance ratio is lower and the autocorrelation time is higher than in the Metropolis case for certain temperatures ranges, but the Wang-Landau algorithm has on the one hand the advantage that only one simulation has to be performed for the whole temperature range, on the other hand it makes negative temperatures accessible at all.

because steps are weighted according to their entropy difference, and not their energy difference.

The DOS of two-dimensional lattice triangulations can only be calculated up to 11×11 triangulations for all energies, introducing an energy cutoff makes it possible to calculate the density of states up to 25×25 triangulations that can be used only for positive inverse temperatures $\beta > 0$. For bigger lattice sizes the Wang-Landau algorithm does not converge anymore in a reasonable amount of time, since on the one hand the entropy between neighboring states differs by orders of magnitude, on the other hand the high energy states are only connected among themselves by paths involving low energy states, which makes flat histogram sampling difficult (see Sec. 3.2 for a detailed discussion).

For our simulations we use an initial modification factor of $f_{\text{initial}} = \exp(1)$ and decrease it to $f_{\text{final}} = \exp(10^{-8})$ using $f_{i+1} = 0.9 \cdot f_i$. The decrease of the modification factor is chosen carefully compared to $f_{i+1} = 0.5 \cdot f_i$ proposed in [406, 407] to reduce possible statistical errors. The incidence histogram $H(E)$ is considered to be flat if $\min H(E) \geq 0.8 \cdot \text{avg} H(E)$. One simulation for the largest considered system size, 10×10 lattice triangulations, took around 4 to 5 days of computing time on a single core, and a total of $8.1 \cdot 10^{10}$



attempted steps, which correspond to $3.4 \cdot 10^8$ attempted steps per flippable edge in the triangulation. We performed 10 independent Wang-Landau simulations for system sizes smaller or equal than 8×8 , and 5 independent simulations for the larger system sizes. The relative statistical error of $g(E)$ is below 0.02 in the former and below 0.03 in the latter case for all energies E .

Degree distribution

The canonical averaged distribution $P(k)$ of the vertex degrees of 8×8 lattice triangulations is plotted for different temperatures in Fig. 3.50a). For the positive inverse temperature $\beta = 0.2$ one finds a similar behavior as for the random triangulations $\beta = 0$ with the maximum of the degree distribution shifted towards degrees $k = 5$ and $k = 6$, because this degrees are preferred at low temperatures due to the energy function (3.58). For negative inverse temperatures $\beta = -0.1$ there is an additional peak at vertex degree $k \approx 40$, because for this inverse temperature the triangulation with maximal energy contributes most to the ensemble average. An interesting behavior can be found for the inverse temperature $\beta = -0.04$ (here the probability distribution of the triangulation energies has two peaks, which is a hint for a phase transition). For this inverse temperature the degree distribution behaves similar to a power law k^{-3} for vertex degrees in the range $5 < k < 25$, which matches the degree distribution of the Barabási-Albert model qualitatively. One has to admit that due to the small system size the range of vertex degrees found spans less than one magnitude and that there are deviations from a pure power law behavior even in this range. Nevertheless the qualitative change of the degree distribution compared to random triangulations is remarkable. Additionally we suspect that for bigger system sizes there is a clearer power law behavior for larger ranges of degrees.

Similar results for the canonical averaged triangulation degree distribution can be found in [259] for positive temperatures.

Mean energy, clustering coefficient and shortest path length

To compare the temperature dependence of the mean energy for different lattice sizes, we consider the expectation value of the mean energy $\epsilon = \langle E \rangle_c(\beta) / \langle E \rangle_{\text{rnd}}$ in terms of the energy of a random triangulation. The results of the numerical calculations for the relative mean energy, the clustering coefficient and the shortest path length can be found in Fig. 3.50b) - d).



The temperature dependence of all considered observables shows the characteristic behavior of a first-order phase transition, with quasi-critical inverse temperature $\beta_c \rightarrow 0$ for increasing system size, but this is not a real phase transition. For the maximal energy of a quadratic $N \times N$ lattice triangulation there is a lower bound that scales with N^4 [253], so that the maximal specific energy scales at least with N^2 . For $\beta < 0$ (which is equivalent to using negative coupling) these maximal energy states are the ground states, which are then not bounded by below for the limit of infinite system size. For negative temperatures only finite systems can be considered and the thermodynamic limit of infinite system size cannot be obtained, so the behavior found at $\beta \rightarrow 0$ is then no actual phase transition in sense of statistical physics.

For negative inverse temperatures one finds a high clustering coefficient (approximately 0.7 independent of the system size), and small average path length between 2 and 3 independent of the system size. The latter can be understood in terms of the graph theoretical diameter of the highest energy triangulations, which can be shown to be 4 independent of the lattice size. So for a small enough negative inverse temperature one can find a small-world behavior for the triangulation graphs.

For positive temperatures the average energy per vertex and the clustering coefficient can be approximated analytically. The first possibility is to use the mean-field approach suggested in [52], where the topological and entropic properties of the triangulations are neglected. This results in

$$\frac{\langle E \rangle}{MN} \approx \frac{2}{2 + e^\beta} \quad (3.78a)$$

$$\langle C \rangle \approx \frac{5e^{-\beta}/6 + 2/5}{2e^{-\beta} + 1}. \quad (3.78b)$$

The second possibility is to use the known degeneracy $\Omega(E = 4)$ and $\Omega(E = 0)$ of the ground state and the first excited state [253] to calculate the expectation values neglecting all other states, resulting in

$$\frac{\langle E \rangle}{MN} \approx \frac{\Omega(E = 4)}{MN} \frac{4}{e^{4\beta} + \Omega(E = 4)} \approx \frac{4MN}{2e^{4\beta} + M^2N^2} \quad (3.79a)$$

$$\langle C \rangle \approx C_{\text{gs}} \frac{1 + (15MN)^{-1}\Omega(E = 4)e^{-4\beta}}{1 + \Omega(E = 4)e^{-4\beta}}. \quad (3.79b)$$

Both approximations are compared with the numerical results in Fig. 3.52. For both the specific energy and the clustering coefficient the mean field approximation is correct for $0 < \beta < 1.5$, the two-niveau low-temperature approximation is correct for $\beta > 3$.



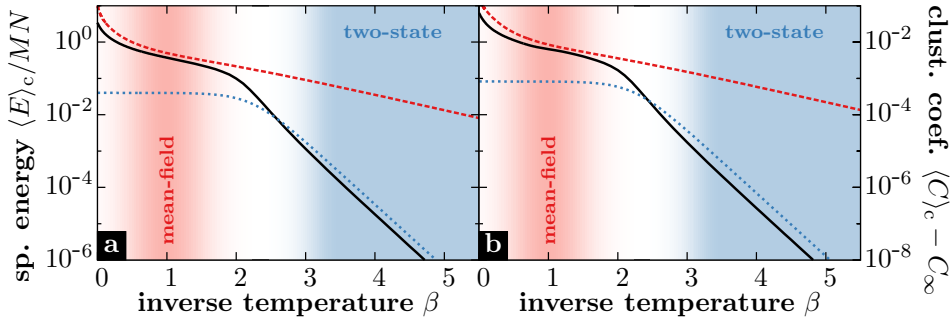


Figure 3.52: Analytical approximations for canonical lattice triangulations.

Analytical approximations for the specific energy (a) and the clustering coefficient (b) in two different regimes compared with the actual data obtained numerically. The mean-field approach (red, dashed line, see Eq. (3.78)), which is valid for an intermediate regime of positive inverse temperatures, neglects the entropic properties of the triangulations, the two-state approximation (blue, dotted line, see Eq. (3.79)), which is valid for $\beta \rightarrow \infty$, just considers the ground state and the first excited state of the lattice triangulations.

Laplacian spectrum

In Fig. 3.53 the results for the canonical averages of the Laplacian spectrum of 8×8 -triangulations are displayed. The indexed-resolved spectrum shows similar behavior as for the different energies in the microcanonical ensemble. For finite positive temperatures ($\beta = 0.1$) the spectrum approaches the Laplacian spectrum of the ground state. For finite negative temperatures/couplings ($\beta = -0.04$) the spectrum gets more irregular, which can be seen in the rich peak structure of the summed probability density functions. This means that the peaked eigenvalues occur very often in the triangulations that contribute to the ensemble average at these temperature with height weight.

Algebraic connectivity and spectral radius

The results for the canonical expectation values of algebraic connectivity λ_1 and the spectral radius λ_{MN-1} are displayed in Fig. 3.54 for lattice size 8×8 .

Both eigenvalues show the same step-like behavior as the energy, the clustering coefficient and the shortest path length at a negative quasi-critical temperature [265]. The algebraic connectivity is almost independent of



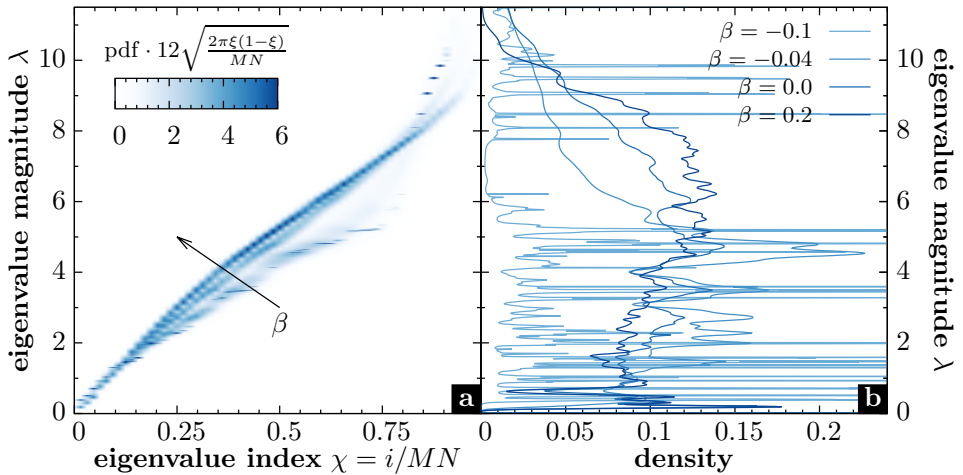


Figure 3.53: Laplacian spectrum of a canonical ensemble of 8×8 triangulations. The color code (a) left shows the index-resolved probability density function (PDF) in terms of the index of the eigenvalue and the magnitude of the eigenvalues for inverse temperatures $\beta = -0.1, -0.04, 0, 0.2$. The index-summed PDF (b) is also displayed for the different inverse temperatures.

the lattice size for $\beta \rightarrow -\infty$ and decreases for larger lattices in the limit $\beta \rightarrow \infty$, while the spectral radius is approximately independent of the lattice size in the limit $\beta \rightarrow \infty$ and increases for larger lattices in the limit $\beta \rightarrow -\infty$. The latter behavior can be understood completely by considering the bounds (3.55) of the spectral radius. For $\beta \rightarrow \infty$ the triangulation with the biggest weight are the triangulations near the ground state, where most vertex degrees are 6 independently of the size, which bounds the spectral radius between 6 and 12. For $\beta \rightarrow -\infty$ the ensemble average is dominated by the triangulation with high energy, which are the triangulations where one edge is connected with almost all possible edges. Since the degree of this maximal connected vertex, which is the lower bound for the spectral radius, is increasing with the size of the lattice, also the spectral radius must increase.

For a possible application of the canonical ensemble of lattice triangulations one can consider the relation of the algebraic connectivity and the spectral radius with the synchronization time and the return probability [12, 307]. Here the canonical ensemble with the inverse temperature as control parameter can be used for continuously fine-tuning these quantities on lattice triangulation networks. For negative inverse temperatures (small-world behavior of the triangulation graph ensemble) with high algebraic



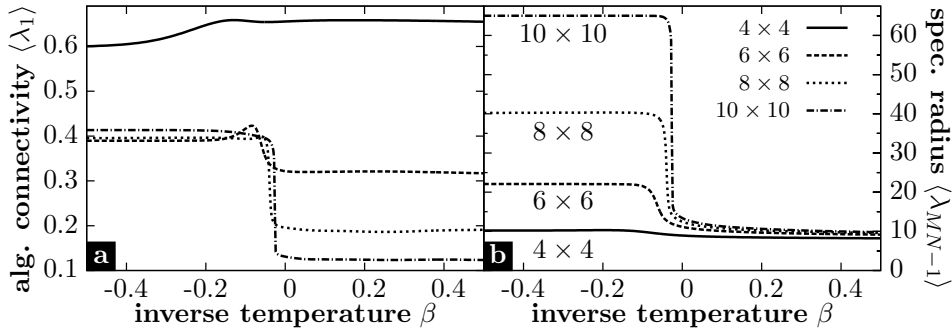


Figure 3.54: Spectral observables for canonical lattice triangulations. Canonical averages of the algebraic connectivity (a) and spectral radius (b) in terms of the inverse temperature β for different lattice sizes, calculated using the Wang-Landau algorithm. The algebraic connectivity is independent of the system size for negative temperatures, whereas the spectral radius is independent of the system size for positive temperatures.

connectivity and spectral radius one finds a short synchronization time and a fast decrease of the return probability, which implies a fast delocalization. For growing inverse temperatures (approaching the large-world behavior of the triangulation graph ensemble) the synchronization time decreases and the delocalization is slower than in the previous region.

Inverse participation ratio

In Fig. 3.55 the average inverse participation ration (IPR) and the IPRs of the algebraic connectivity and the spectral radius are plotted in terms of the inverse temperatures. As expected, all considered IPRs and therewith the localization increases for increasing disorder in the triangulations. Near the quasi-critical inverse temperature β_{qc} on observes that the IPRs scale with the logarithm $\log |\beta - \beta_{qc}|$ of the reduced inverse temperature.

3.4.6.1 Ising critical temperature

In Fig. 3.56 the dependence of the critical inverse temperature α_c of an Ising model defined on lattice triangulations on the inverse temperature β of an underlying canonical ensemble of triangulations is displayed. As for the other observables in the canonical ensemble for each possible energy we used the calculated density of states of the triangulations to do a flat histogram sampling in order to calculate microcanonical averages of the observables. In contrast to the other observables, the critical Ising temperature on a



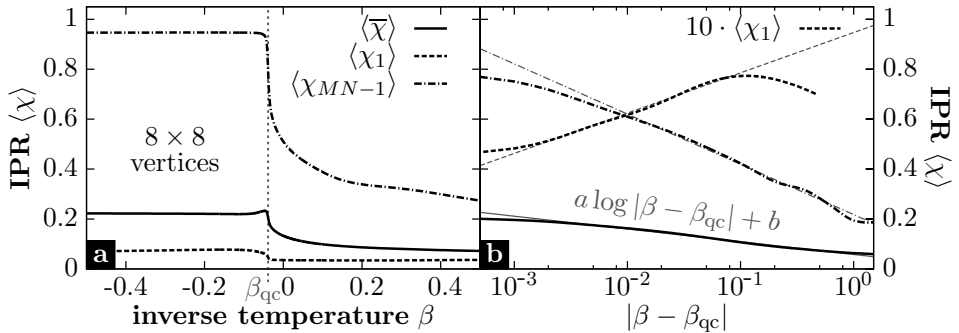
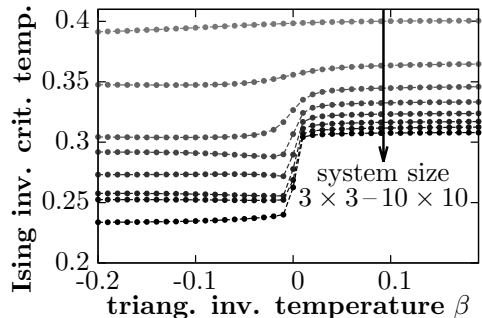


Figure 3.55: Canonical averages of the inverse participation ratio for 8×8 lattices. (a) Expectation values of the average IPR (solid line), the IPR of the algebraic radius (dashed line) and of the spectral radius (dash-dotted line) in terms of the inverse temperature. (b) The same expectation values in terms of the (logarithmically plotted) distance from a quasi-critical temperature β_{qc} , for $\beta > \beta_{qc}$ ($\langle \bar{\chi} \rangle$, $\langle \chi_{MN-1} \rangle$) and for $\beta < \beta_{qc}$ ($\langle \chi_1 \rangle$). The thinner, red lines are linear fits with respect to $\log |\beta - \beta_{qc}|$. Note that the value of $\langle \chi_1 \rangle$ is stretched by a factor 10.

Figure 3.56: Ising model on canonical lattice triangulations.

Dependence of the critical inverse temperature α of the Ising model on the inverse temperature β of the underlying canonical ensemble of triangulations for different lattices sizes (from 3×3 to 10×10). The data for this plot is taken from Ref. [411].



certain triangulation has to be calculated numerically doing a Markov chain Monte Carlo simulation. We used a Wang-Landau simulation to calculate for every triangulation the Ising density of states $g_{\text{Ising}}(E)$, which then can be used to find the Ising critical temperature of the respective triangulation by locating the maximum of the specific heat $c_V(\alpha)$. Using the Binder cumulant is not constructive in this situation, because there is not only one underlying triangulation for each system size, so that there is no well defined intersection between the Binder cumulants of different system sizes, but a distribution of intersections that is usually broader than the distribution of the critical temperatures obtained from locating the maximum of the heat capacity.

As for the other observables we find a transition behavior near the random lattice triangulations. For $\beta \rightarrow \infty$ the underlying triangulation is basically the ordered ground state, so that the Ising inverse critical temperature converges towards the value for triangular lattices. For $\beta \rightarrow -\infty$ the triangulations contributing to the partition function are stars as displayed in Fig. 3.12, where one that is connected with almost all other spins dominates the partition function. One can compare this situation with the mean-field solution of the Ising model (since this solution describes the behavior of one spin in the average field of its neighbors), where the inverse critical temperature equals the inverse average number of neighbors, which converges towards $1/6$ within integer lattice triangulations with increasing system size.

Quasi-critical temperature

As described in Sec. 3.4.5, the specific energy of lattice triangulations is not bounded by below, i.e. the regime of negative temperatures is not well-defined in the thermodynamic limit, it is only valid for finite systems. So the search for a possible phase transition, which can be found only for infinite systems and thus within the thermodynamic limit, can only take place at positive temperatures.

In Fig. 3.57 the quasi-critical temperatures are plotted in terms of the system size for the different observables. The inverse quasi-critical temperatures were found by searching the maximum of the susceptibilities of the respective observable. All inverse quasi-critical temperatures are all in the regime of negative temperatures for the considered range of system sizes, they seem to converge to $\beta_c = 0$ for infinite system size. So one can conclude that there is no phase transition in two-dimensional lattice triangulations, if using the energy functional considered in this section.



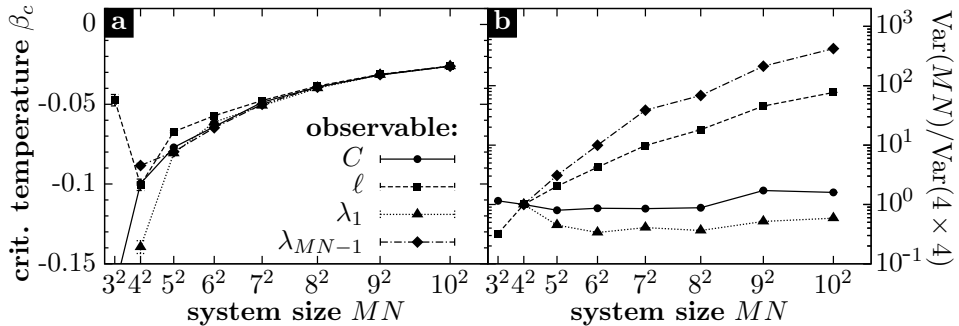


Figure 3.57: Quasi-transition for canonical lattice triangulations.

(a) Quasi-critical temperatures $\beta_c(MN)$ in terms of the system size MN for the clustering coefficient C (\blacktriangle), the average shortest path length ℓ (\blacksquare), the algebraic connectivity λ_1 (\blacktriangle) and the spectral radius λ_{MN-1} (\blacklozenge). (b) Normalized variance per vertex of the observables at the quasi-critical temperature for the same observables.

3.4.7 Conclusion

In this section we proposed a new model for real-world graphs or networks by interpreting unimodular triangulations of two-dimensional integer lattice as graphs. Considering averages of random triangulations we found that they show a higher clustering coefficient than common random graph models, but also a power law growing shortest path length in terms of the system size, where one would expect a logarithmic scaling for small world behavior. The degree distribution behaves similar as in the Erdős-Rényi and Newman-Watts random graph.

Introducing an energy function that measures the order and disorder of a triangulation, canonical averages of graph observables in triangulations can be calculated using the Wang-Landau algorithm. This Monte Carlo method made it possible for the first time to calculate expectation values for the whole temperature range, albeit only for small system sizes. Using the Wang-Landau algorithm it is possible to access equilibrium properties of both high energy triangulations, which are poorly connected with other similar triangulations, and low energy triangulations, where dynamically a glass-like phase was found in the literature before, both phenomena making it difficult to use the Metropolis algorithm. Considering the temperature dependence of the clustering coefficient, the average shortest path length and the degree distribution we found small-world behavior for negative temperatures $\beta < \beta_c$ below a negative, quasi-critical temperature and hints for scale-free behavior for temperatures near the quasi-critical temperature. All considered



observables show a cross-over behavior going from negative temperatures, where the partition function dominated by disordered triangulations, to positive temperatures, where it is dominated by ordered triangulations.

In contrast to the topological the lattice or in general embedded triangulations are useful if one deals with networks and graphs where the actual coordinates of the vertices become important. Despite the introduction of vertex coordinates which induce non-executable flips, our results show qualitative agreement with the graph properties of topological triangulations of surfaces with suitable genus that were estimated analytically and calculated numerically in the literature.

An extension to the grandcanonical ensemble, where the number of vertices is not fixed any more, is possible by considering also insertion and removal Pachner moves. Additionally one can apply the methods described in this paper also to triangulations of arbitrary point sets in two and more dimensions.



Table 3.5: Table summarizing the results of the interpretation of lattice triangulations as graphs for the various ensembles and observables. The observables are the degree distribution $P(k)$ (see Eq. (3.51)), the triangulation energy E (see (3.58)), the clustering coefficient C (see Eq. (3.52)), the average shortest path length ℓ (see Eq. (3.53)), the spectra $\text{spec}_A(x)$ and $\text{spec}_L(x)$ of the adjacency and the Laplacian matrix, the algebraic connectivity λ_1 , the spectral radius λ_{MN-1} , the inverse participation ratio χ (see Eq. (3.56)) and the results of coupling of the Ising model with the lattice triangulations. Note that in Tabs. 3.3 and 3.4 the scaling behavior of these observables in terms of the system size is listed for random triangulations and common random graphs.

observable	max. ordered	random	microcan.	can.
$P(k)$		Fig. 3.37a	Fig. 3.46	Fig. 3.50a
E		Fig. 3.37b		Fig. 3.50b Fig. 3.52a Eq. (3.78a) Eq. (3.79a)
C	Eq. (3.59)	Fig. 3.37c	Fig. 3.47a Eq. (3.74)	Fig. 3.50c Fig. 3.52b Eq. (3.78b) Eq. (3.79b)
ℓ		Fig. 3.37d	Fig. 3.47b	Fig. 3.50d
$\text{spec}_A(x)$	Fig. 3.35	Fig. 3.38 Fig. 3.39		
$\text{spec}_L(x)$	Fig. 3.35	Fig. 3.40 Fig. 3.41	Fig. 3.48	Fig. 3.53
λ_1	Eq. (3.65)	Fig. 3.42a Eq. (3.69)	Fig. 3.49a Eq. (3.75)	Fig. 3.54a
λ_{MN-1}	Eq. (3.66)	Fig. 3.42b	Fig. 3.49b Eq. (3.76)	Fig. 3.54b
IPR χ		Fig. 3.43		Fig. 3.55
Ising	see Ref. [411]	Fig. 3.44		Fig. 3.56





4 Topological triangulations

Until now we only considered triangulations of point sets embedded into the Euclidean space \mathbb{R}^d . In this chapter we move on to triangulations of more general spaces, namely topological spaces or manifolds, thus these triangulations are also called topological triangulations. The main difference with respect to embedded triangulations is that the actual coordinates of the points or vertices of the triangulations are neglected in the topological case, and only topological degrees of freedom (which vertex is part of which maximal simplex etc.) are considered.

Topological triangulations have been used as random graph models [47, 52, 259, 372, 433], because every graph is embeddable into a surface with high enough genus. They can also be used for describing the topology of foams in terms of neighboring cells [53, 143, 319, 381].

Since topological manifolds can be used for discretizing curved spaces, they are an important tool for calculations in general relativity. Historically the first use of triangulations in discrete general relativity is the Regge formalism [338], where instead of coordinates only the topological and geometric quantities of a fixed triangulation are considered. The edge lengths of the triangulation are used as generalized coordinates in a Lagrangian formalism. Based on the Regge formalism, but fixing the edge lengths and using the triangulation itself as dynamical variable in a path-integral like formalism, the quantum gravity approaches of dynamical triangulations (DT) [29] or causal dynamical triangulations (CDT) [38] try to solve the puzzle of unifying quantum mechanics and general relativity. The Regge formalism as well as DT and CDT are presented in detail in Chap. 5 later.

For mathematicians, as well as for the described quantum spacetime models based in triangulations there are three important questions. The first question is: Are triangulations *ergodic*? Strictly speaking this question means whether it is possible to define a set of local moves, so that each triangulation of a topological space can be transformed into each other triangulation using a finite number of these moves. In fact one can define two such sets, the so-called *Alexander* [11] and the *Pachner* moves [322], where the latter ones are a certain subset of the first ones that are easier to handle conceptually and on the computer. From the mathematical point



of view ergodicity of topological triangulations with respect to these moves is only proven in two and three dimensions [303, 334] (there are explicit counterexamples for higher dimensions, compare Ref. [337]), and for a certain subclass of (so-called piecewise linear) manifolds [322] (see Sec. 4.1.2 for more detailed explanations). In this context, there is also the question whether triangulations are *computationally ergodic*, i.e. whether the moves are ergodic in a certain simulational setup. This notion is stronger than ergodicity, there can be situations where the latter holds, but the former is violated. Computational ergodicity can break if the number of moves that connects two triangulations is higher than the number of total steps done in the simulation, or if for the connection a detour is needed that leads to triangulations outside of a certain observation window (which can be given by cuts or by sampled probability distributions that assign nearly zero weight to certain regions of the phase space).

The second question is: Are triangulations *exponentially many*? This means, is there a number κ_c^∞ so that there are less than $\exp(\kappa_c^\infty \cdot m)$ triangulations with m maximal simplices? In the notion of statistical physics this implies that the entropy (which is up to a constant the logarithm of the number of states) is a linear function in terms of the system size (denoted as *extensive*), or that the entropy density is a constant, at least in the limit of infinite system sizes. Only systems that have an extensive entropy can be treated with the methods of statistical physics, and only if there are exponentially many triangulations the partition functions of the DT and CDT quantum gravity models are well defined. Additionally, the entropy density κ_c^∞ in the infinite system limit determines the value of the coupling constant to obtain a phase transition necessary for results independent of the introduced discretization scale in those models [13, 38]. As for the ergodicity, there is a strict mathematical proof only for two-dimensional triangulations [399], and the question for three and higher dimensions is an unsolved puzzle [197].

The third and last question is: How do the properties of triangulations depend on the *topology* (in the sense of topological invariants) of the underlying space? Since coordinates and other geometric quantities are neglected if considering topological triangulations, the only remaining controllable parameter is the topology of the underlying space. For two-dimensional closed manifolds this is fully determined by specifying whether a surface is orientable and how many holes are in the surface [101], in three and more dimensions the classification of manifolds is much more complicated (see e.g. Refs. [366, 390]). The question arising is how certain properties defined on



ensembles of triangulations (e.g. their number in terms of the number m of maximal simplices) depend on the type of the manifold, and whether such observables can be used to determine the topological type of the underlying manifold. In appreciation of the famous question "Can you hear the shape of a drum?", one can ask "Can you count the topology of a triangulation?"

In this chapter we apply the methods that were used for counting the number of embedded lattice triangulations on the topological case. We use the Wang-Landau algorithm to calculate the density of states of triangulations for different underlying spaces, which will be the number of triangulations in terms of the number of maximal simplices. This allows us to numerically give answers to the three questions (ergodicity, extensivity and topology dependence) of topological triangulations.

This chapter is organized as follows: In Sec. 4.1 first different types of topological spaces and manifolds that can be triangulated are examined, and triangulations are defined as homeomorphisms between realizations of abstract simplicial complexes and the space to be triangulated. Afterwards Alexander and Pachner moves are introduced and the mathematical exact results about their ergodicity are presented. An important result of this section is the proof of Thm. 4.22 that one can formulate Pachner in terms of oriented circuits, which can be used for easily calculating the change of the number of simplices induced by a Pachner move and for treating embedded and topological triangulations unified in an object-oriented computer code for simulations. The last part treats the ratio of selection probabilities of Pachner moves and explains why isomorphisms of triangulations are a computational challenge for calculating this ratio and therewith for the whole simulation.

Sec. 4.2 examines the entropy density of triangulations of two-dimensional orientable and non-orientable surfaces and its dependence on the genus of the underlying surface. The first important result depicted in Fig. 4.10 is that one can neglect symmetries in large enough triangulations. This means that one can use a simplified version of the selection probability ratio, which allows us to access very large system sizes with our Monte Carlo methods. Using an approximative counting algorithm based on Wang-Landau simulations and comparing to some exact results known from counting rooted graphs [182, 398], the asymptotic number of surface triangulations is conjectured in Eq. (4.18) to be

$$N(m, h) \rightarrow (170.4 \pm 15.1)^h m^{-2(h-1)/5} \left(\frac{256}{27} \right)^{m/2}$$

where m is the number of triangles and h is the type of the surface, which



is the genus for orientable and the half of the genus for non-orientable surfaces. Our result is the first to present the leading order behavior for non-sphere triangulations and differs from the asymptotics of ordinary graphs on surfaces. This section is based on the paper

[264] B. Krüger and K. Mecke, *Genus dependence of the number of (non-)orientable surface triangulations*, Phys. Rev. D **93**, 085018 (2016)

In Sec. 4.3 we apply a similar algorithm on triangulations of the 3-sphere to obtain results about their numerical ergodicity and the numerical value of a possibly existing exponential bound of their number in terms of the system size. (Note that due to a recent (unpublished) statement of Karim Adiprasito using a certain number of steps only exponentially many triangulations in terms of the number of executed flips can be reached [286]. So it is not possible to make a statement about the existence of an upper bound, but only about its value if it exists.) We present the methods of Metropolis Monte Carlo simulations that were used in a dynamical triangulation setup to numerically calculate the entropy density of 3-sphere triangulations and give some drawbacks of this method compared to our methods. For triangulations with m tetrahedra we consider the difference between the entropy density $\kappa_c(m)$ and the entropy density $\kappa_c(m, \Delta m)$ with a finite window $[m - \Delta m, m + \Delta m]$ of allowed numbers of maximal simplices as a measure for the violation of the numerical ergodicity of the Pachner moves, and show in Fig. 4.24 and Eq. (4.33) that this measure scales as

$$\kappa_c(m) - \kappa_c(m, \Delta m) \propto \frac{m^{0.68 \pm 0.03}}{(\Delta m)^2}.$$

Furthermore we can improve in Fig. 4.25 the asymptotics of the number of triangulations of the 3-sphere in terms of number of maximal simplices.



4.1 Topological triangulations and Pachner moves

In this section we present step by step the definition of triangulations of topological spaces. We proceed by introducing elementary steps (stellar and bistellar exchanges, also called Alexander and Pachner moves), that can be used to transform triangulations of a given topological space into other triangulations of the same space. For the Pachner moves we present the changes in the number of simplices they induce, calculate the selection probability ratio that has to be used in Markov chain Monte Carlo algorithms and present the difficulties that arise due to the fact that topological triangulations are only defined up to isomorphism.

4.1.1 Abstract simplicial complexes and triangulations

As a first step in the development of the mathematical foundations of topological triangulations, we develop the definition of a triangulation of a topological space. Therefore we introduce first the notions of topological spaces and manifolds. Afterwards we present two different types of simplicial complexes, abstract and Euclidean ones, where the first class is defined purely set-theoretically and the members of the second one can be embedded into an \mathbb{R}^n . On both types certain operations can be defined, and we introduce an algebraic notion that can sometimes simplify notation and proofs. Last we define a triangulation of a topological space as an abstract simplicial complex that is associated with an Euclidean simplicial complex homeomorphic to the space to be triangulated, together with this homeomorphism.

Topological spaces and manifolds

Despite of topology and manifolds are topics that can fill several textbooks, in this section we try to give a very short introduction to the basic concepts we need to consider topological triangulations. Nice introductions to these topics can be found in the textbooks [275] (topology and topological manifolds), [351] (piecewise-linear structures and manifolds) and [276] (differentiable and smooth manifolds).

Recall that in the case of embedded triangulations we constructed a tessellation of the convex hull of a set of points in an \mathbb{R}^d using triangles or higher dimensional simplices. Topological triangulations can be seen as tessellations of much more general spaces, namely topological ones:

Definition 4.1 (topological space, [275, p. 18]):

Let X be a set and let T be a set of subsets of X , which elements



are called *open sets*. (X, T) is a *topological space* (often abbreviated simply by X), if

1. The set X and the empty set are open, i.e. they are contained in T : $\emptyset, X \in T$
2. Any union $\bigcup_i t_i$ of open sets $t_i \in T$ is open: $\bigcup_i t_i \in T$
3. Any finite intersection $\bigcap_i t_i$ of open sets $t_i \in T$ is open: $\bigcap_i t_i \in T$

The next step is to define so-called continuous maps between topological spaces that preserve their defined structure, i.e., that inverse images of open sets are open sets.

Definition 4.2 (continuous function, [275, p. 20]):

Let (X_1, T_1) and (X_2, T_2) be two topological spaces. A function $f : X_1 \rightarrow X_2$ is called *continuous*, if for every open set $V \in T_2$ the inverse image $f^{-1}(V) := \{x \in X_1 | f(x) \in V\} \in T_1$ is an open set in T_1 .

To define equivalence of topological spaces, one needs continuous bijections with continuous inverse.

Definition 4.3 (homeomorphism, homeomorphic, [275, p. 20]):

Let (X_1, T_1) and (X_2, T_2) be two topological spaces. A function $f : X_1 \rightarrow X_2$ is called *homeomorphism*, if f is a bijection and f and its inverse f^{-1} are continuous. Two topological spaces (X_1, T_1) and (X_2, T_2) are called *homeomorphic*, if there exist a homeomorphism $f : X_1 \rightarrow X_2$.

Clearly homeomorphisms are an equivalence relation on topological spaces, because they are reflexive with $f = \text{id}$, symmetric and transitive.

In this thesis we use as underlying space of triangulations mainly objects that have more structure than a topological space, namely manifolds, which are topological spaces that are locally equivalent to an \mathbb{R}^d .

Definition 4.4 ((topological) manifold, chart, atlas, [275, p. 30-34]):

A topological space M is called *(topological) d -manifold*, if the following axioms hold:

1. M is a Hausdorff-space (i.e., for two distinct points $x, y \in M$ there are open sets $U_x \subset M$ and $U_y \subset M$ with $x \in U_x$, $y \in U_y$ so that $U_x \cap U_y = \emptyset$)
2. There is a countable basis for the open sets $U \subset M$.



3. For every point $x \in M$ there is an open set U_x that is homeomorphic to an open subset of \mathbb{R}^d .

The homeomorphism $\phi : U_x \rightarrow \mathbb{R}^d$ is often denoted as a *chart*, the set of all charts is denoted as *atlas*.

Manifolds can be equipped with additional structure by specifying how the charts of different intersecting neighborhoods are related. This is done by stipulating the type of the transition maps:

Definition 4.5 (transition maps; piecewise linear, differentiable and smooth manifolds, [276, p. 12-15, 32-35], [351, p. 7]):

Let M be a topological d -manifold and let $U_x, U_y \subset M$ be two open sets on M with $U_x \cap U_y \neq \emptyset$ and charts ϕ_x, ϕ_y . The homeomorphism

$$\tau_{x,y} := \phi_y \circ \phi_x^{-1} : \phi_x(U_x \cap U_y) \rightarrow \phi_y(U_x \cap U_y),$$

introduces a commutative diagram and is called *transition map*.

If all transition maps are piecewise linear¹, the topological manifold is called *piecewise linear (PL)* manifold. If all transition maps are k -differentiable (i.e. k -differentiable in every component), the topological manifold is called *k -differentiable* manifold. For $k = 1$ the manifold is simply called *differentiable*, for $k = \infty$ the manifold is called *smooth* manifold.

The three presented structures, in the given order, become stronger, i.e. every smooth manifold is also a differentiable manifold, and every differentiable manifold is also a PL manifold.

For all these types of manifolds there are structure preserving maps that can be used for defining equivalence, which are special homeomorphisms²:

Definition 4.6 (maps between manifolds, [275, p. 22], [276, p. 38-39], [351, p. 6]):

Let M and N be two topological (piecewise-linear, smooth) d -manifolds with charts (U_x, ϕ_x) and (V_y, ψ_y) . A map $F : M \rightarrow N$ is called *continuous (piecewise linear, smooth)*, if for each pair of charts ϕ of M and ψ of N there exists a continuous (piecewise linear, ∞ -differentiable) map $f : \phi_x(U_x) \rightarrow \psi_y(U_y)$ with $F = \psi_y^{-1} \circ f \circ \phi_x$.

¹ A map $f : P \supset \mathbb{R}^m \rightarrow \mathbb{R}^n$ is *piecewise-linear*, if $(x, f(x)) \in \mathbb{R}^{m+n} | x \in P$ is a polyhedron, see [351, p. 6]

² Note that for continuous maps between topological manifolds this is just an application of the respective maps between topological spaces on manifolds. Nevertheless we included these maps because they show the nice parallel between the definitions.



If there is a bijective continuous (piecewise linear, smooth) map $F : M \rightarrow N$ with continuous (piecewise linear, smooth) inverse $F^{-1} : N \rightarrow M$, the manifolds M and N are called *homeomorphic* (*PL homeomorphic, diffeomorphic*), and the map F is called *homeomorphism* (*PL homeomorphism, diffeomorphism*). One abbreviates $M \simeq N$ ($M \stackrel{\text{PL}}{\simeq} N$, $M \stackrel{\text{diff.}}{\simeq} N$).

As the continuous maps between topological spaces, these maps also define an equivalence relation.

There are some very interesting results about the different structures of triangulations³: First, every two diffeomorphic manifolds are also PL homeomorphic (by the work of Cairns in 1935 [107] and Whitehead in 1940 [419]), and every two PL homeomorphic manifolds are also homeomorphic (by definition). This can be summarized as

$$\text{DIFF} \rightarrow \text{PL} \rightarrow \text{TOP},$$

in the categorial sense that there are morphisms that map every differentiable manifold to a PL manifold, and every PL manifold to a topological manifold. There are several important results about this morphisms for manifolds in general:

- $\text{PL} \rightarrow \text{TOP}$ is *not injective*, i.e., there are topological manifolds which can be equipped with several (non-PL homeomorphic) PL structures. E.g., there are uncountably many different PL structures of the topological manifold \mathbb{R}^4 [189].
- $\text{PL} \rightarrow \text{TOP}$ is *not surjective*, i.e., not every topological manifold admits a PL structure. Only topological manifolds with vanishing Kirby-Siebenmann class can be piecewise linear manifolds [248], so there are topological manifolds that do not admit a PL structure (in [248] it was shown that this happens for all dimensions $d \geq 5$, in Ref. [175] it was shown that the topological E_8 4-manifold does not admit a PL structure).
- The original conjecture that $\text{PL} \rightarrow \text{TOP}$ is bijective was posed by Steinitz [376] and Tietze [391] in 1908, and was denoted as *Hauptvermutung der algebraischen Topologie*⁴. The Hauptvermutung was proven

³ The following paragraphs are inspired by the MathOverflow answer <http://mathoverflow.net/questions/96670/classification-of-surfaces-and-the-top-diff-and-pl-categories-for-manifolds/97019#97019>

⁴ Main conjecture of algebraic topology



in 1925 by Radó [334] for 2-manifolds and in 1952 by Moise [303] for 3-manifolds, and there was hope that the conjecture is true in arbitrary dimensions. But in 1961 Milnor [295] gave a first counterexample in six dimensions (but for a simplicial complex that is not a manifold), for a general overview see Ref. [337].

- An important difference can be found for topological d -spheres, which can be equipped with a unique PL structure for $d \leq 3$ [304] and for $d \geq 5$ [370]. Whether this is true also for $d = 4$ is still unsolved.
- $\text{DIFF} \rightarrow \text{PL}$ is *not injective* in general, i.e., there are PL manifolds which can be equipped with several (non-diffeomorphic) differentiable structures. There is a manifold (called Milnor's sphere) that is homeomorphic (and therewith PL homeomorphic) to the S^7 , but not diffeomorphic to it [294]. For dimensions less or equal 6 $\text{DIFF} \rightarrow \text{PL}$ is in fact injective [296, Thm. 2].
- $\text{DIFF} \rightarrow \text{PL}$ is *not surjective* in general, i.e., not every PL manifold admits a differentiable structure [243]. For dimensions less or equal 7 $\text{DIFF} \rightarrow \text{PL}$ is in fact surjective [296, Thm. 2].

For the dimensions $d \leq 4$ that are important for this thesis (and in general for most physical applications), one can summarize that for $d \leq 3$ the morphisms between the categories are bijective, so every topological manifold has a unique PL structure, and every PL manifold has a unique differentiable structure. For $d = 4$ this is only true for the relation between PL and DIFF, there are topological 4-manifolds without any or several PL structures.

Abstract simplicial complexes

Remember that the key ingredients of the definition of an embedded triangulation were simplices grouped together to a simplicial complex. For triangulations of manifolds we need an object that is slightly more general than a simplicial complex in the embedded case.

Definition 4.7 (abstract simplicial complex, [318, Def. 2.7]):

Let A be an arbitrary set⁵. An *abstract simplicial complex* \mathcal{K} on A is a set of subsets $\sigma \subset A$ called *faces* or *simplices* of \mathcal{K} , that is closed

⁵ In this thesis we are restricting ourselves to complexes over finite sets, and therewith finite triangulations. Extensions can be made for infinite sets and complexes, but this leads to complications we do not want to deal with



under the formation of subsets, formally

$$\sigma \in \mathcal{K} \wedge \sigma' \subset \sigma \quad \Rightarrow \quad \sigma' \in \mathcal{K}$$

The *vertex set* $V(\mathcal{K}) := \bigcup \mathcal{K} \subset A$ is the union of all faces and consists of the elements of A that are used in the subsets \mathcal{K} . A simplex $\sigma' \subset \sigma$ is called *subsimplex* of σ , σ is called *supersimplex* of σ' .

The faces with the maximal cardinality in the complex are called *facets* or *maximal simplices*. The dimension $d = \max\{|\sigma| - 1 \mid \sigma \in \mathcal{K}\}$ of the abstract simplicial complex is the maximal cardinality of the facets minus 1. Note that every abstract simplicial complex contains the empty set by definition.

So the notion of an abstract simplicial complex encapsulates the concept of closure. For example, consider the set $A = \{0, 1, 2, 3, 4, 5\}$. The following set of subsets of A is an abstract simplicial complex

$$\begin{aligned} \mathcal{K}_1 = & \{\{0, 1, 4\}, \{1, 2, 4\}, \{2, 3, 4\}, \{0, 3, 4\}, \\ & \{0, 1, 5\}, \{1, 2, 5\}, \{2, 3, 5\}, \{0, 3, 5\}\} \\ & \cup \{\{0, 1\}, \{1, 2\}, \{2, 3\}, \{0, 3\}, \{0, 4\}, \{1, 4\}, \\ & \{2, 4\}, \{3, 4\}, \{0, 5\}, \{1, 5\}, \{2, 5\}, \{3, 5\}\} \\ & \cup \{\{0\}, \{1\}, \{2\}, \{3\}, \{4\}, \{5\}, \emptyset\} \end{aligned} \tag{4.1}$$

but the set of subsets

$$\mathcal{K}_2 = \{\{0, 1, 2\}, \{0, 1\}, \{0, 2\}, \{0\}, \{1\}, \{2\}, \emptyset\}$$

is not an abstract simplicial complex, since $\{1, 2\} \subset \{0, 1, 2\}$, but $\{1, 2\} \notin \mathcal{K}_2$.

One can define maps between abstract simplicial complexes that conserve their structural properties:

Definition 4.8 (simplicial map, [275]):

Let \mathcal{K}_1 and \mathcal{K}_2 be abstract simplicial complexes. A map $f : V(\mathcal{K}_1) \rightarrow V(\mathcal{K}_2)$ which fulfills

$$\sigma_1 \subset \sigma_2 \in \mathcal{K}_1 \quad \Rightarrow \quad f(\sigma_1) \subset f(\sigma_2) \in \mathcal{K}_2$$

is called *simplicial map* between \mathcal{K}_1 and \mathcal{K}_2 , and the abstract simplicial complexes are called *isomorphic*. If $\mathcal{K}_1 = \mathcal{K}_2$ a simplicial map $f : V(\mathcal{K}_1) \rightarrow V(\mathcal{K}_1)$ is called *simplicial automorphism*.



Clearly simplicial automorphisms form an equivalence relation amongst abstract simplicial complexes. Consider e.g. the simplicial complex (4.1). The permutations

$$\begin{aligned}\pi_1 &: [0, 1, 2, 3, 4, 5] \mapsto [0, 1, 2, 3, 5, 4] \\ \pi_2 &: [0, 1, 2, 3, 4, 5] \mapsto [2, 1, 0, 3, 4, 5]\end{aligned}$$

are simplicial automorphisms of \mathcal{K}_1 , whereas the permutation

$$\pi_3 : [0, 1, 2, 3, 4, 5] \mapsto [0, 1, 2, 4, 3, 5]$$

is not a simplicial automorphism, because $\pi_3(\{2, 3, 5\}) = \{2, 4, 5\}$, which is not a simplex of \mathcal{K}_1 .

Euclidean simplicial complexes

The idea for defining a topological triangulation is to construct an object embedded into an \mathbb{R}^n that can be related to an abstract simplicial complex that consists of elementary building blocks (vertices, lines, triangles, tetrahedra etc.) and that is homeomorphic to the topological space that should be triangulated. This object is denoted as Euclidean simplicial complex and will be defined in this section.

First we have to define the elementary building blocks, which are very similar to the simplices in embedded triangulations.

Definition 4.9 (simplex, [318, Def. 2.1]):

Let $x := \{x_0, x_1, \dots, x_k\}$ be a set of $k + 1$ linearly independent points in \mathbb{R}^n ($k \leq n$). An *open k -simplex* supported by the point set x is a subset of \mathbb{R}^n and defined as

$$\sigma^{(k)} := \left\{ \sum_{i=0}^k \lambda_i x_i \mid 0 < \lambda_i < 1, \sum_{i=0}^k \lambda_i = 1 \right\} \subset \mathbb{R}^n$$

A *closed k -simplex* supported by the point set x is defined as

$$\bar{\sigma}^{(k)} := \left\{ \sum_{i=0}^k \lambda_i x_i \mid 0 \leq \lambda_i \leq 1, \sum_{i=0}^k \lambda_i = 1 \right\} \subset \mathbb{R}^n$$

The point set x is called *support* of the open or closed simplex. The *boundary* $\partial\sigma^{(k)}$ of an open or closed simplex for $k > 0$ is the union of all simplices that arise from proper and non-empty subsets of its support $\{x_0, x_1, \dots, x_n\}$, for $k = 0$ and for the empty simplex the boundary is the empty simplex.



So a closed simplex is again the convex hull of the defining points, and the open simplex is the interior of the convex hull. Note that there is an ambiguity in the notion *simplex*: On the one hand it denotes an element of an abstract simplicial complex, on the other hand it is the (interior of) the convex hull of a set of points. We will see later that these concepts are strongly related, and in most cases the term *simplex* can refer to both objects, especially since we often use simplex as a synonym for its support.

Using simplices one can define Euclidean simplicial complexes, which are equivalent to the simplicial complexes defined in Sec. 3.1 for embedded triangulations:

Definition 4.10 (Euclidean simplicial complex, underlying polyhedron, [318, Definitions 2.3 and 2.5]):

Let K be a finite set of open simplices $\subset \mathbb{R}^n$. K is called *Euclidean simplicial complex* if

1. The intersection of two distinct simplices is empty

$$\sigma_1^{(k_1)}, \sigma_2^{(k_2)} \in K, \sigma_1^{(k_1)} \neq \sigma_2^{(k_2)} \Rightarrow \sigma_1^{(k_1)} \cap \sigma_2^{(k_2)} = \emptyset$$

2. For each simplex of K also its boundary simplices are contained in K :

$$\sigma^{(k)} \in K \Rightarrow \partial\sigma^{(k)} \subset K$$

The set $|K| := \bigcup\{\sigma \mid \sigma \in K\}$ is called the *underlying polyhedron* of K . The set $V(K)$ is the set of all points defining the simplices of the simplicial complex and is called *vertex set* of K .

Consider for example the points

$$\begin{aligned} \vec{x}_0 &= \begin{pmatrix} 1 \\ 0 \\ 0 \end{pmatrix}, \vec{x}_1 = \begin{pmatrix} 0 \\ 1 \\ 0 \end{pmatrix}, \vec{x}_2 = \begin{pmatrix} -1 \\ 0 \\ 0 \end{pmatrix}, \\ \vec{x}_3 &= \begin{pmatrix} 0 \\ -1 \\ 0 \end{pmatrix}, \vec{x}_4 = \begin{pmatrix} 0 \\ 0 \\ 1 \end{pmatrix}, \vec{x}_5 = \begin{pmatrix} 0 \\ 0 \\ -1 \end{pmatrix} \end{aligned} \tag{4.2}$$

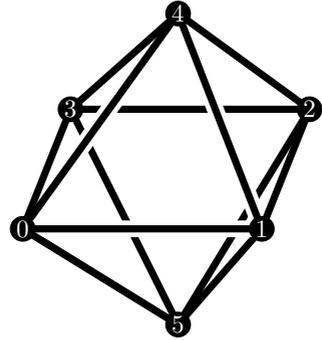
in \mathbb{R}^3 and the set of simplices supported by the sets

$$\begin{aligned} K = \{ \{ \vec{x}_0, \vec{x}_1, \vec{x}_4 \}, \{ \vec{x}_1, \vec{x}_2, \vec{x}_4 \}, \{ \vec{x}_2, \vec{x}_3, \vec{x}_4 \}, \{ \vec{x}_0, \vec{x}_3, \vec{x}_4 \}, \\ \{ \vec{x}_0, \vec{x}_1, \vec{x}_5 \}, \{ \vec{x}_1, \vec{x}_2, \vec{x}_5 \}, \{ \vec{x}_2, \vec{x}_3, \vec{x}_5 \}, \{ \vec{x}_0, \vec{x}_3, \vec{x}_5 \} \} \cup \dots \end{aligned} \tag{4.3}$$

with the respective subsimplices, as depicted in Fig. 4.1. Then K is an Euclidean simplicial complex, and its underlying polyhedron $|K|$ is homeomorphic to the 2-sphere.



Figure 4.1: Two-dimensional Euclidean simplicial complex (4.3) with vertex set (4.2), consisting of 8 2-simplices, 12 1-simplices and 6 0-simplices (and the trivial empty face \emptyset). This complex is homeomorphic to the 2-sphere S^2 and a geometric realization of the abstract simplicial complex (4.1).



Triangulations of topological spaces

The following definition shows that there is a natural relation between Euclidean and abstract simplicial complexes:

Definition 4.11 (geometric realization, [318, Def. 2.8]):

Let K be an Euclidean simplicial complex with vertex set $V(K)$. Let \mathcal{K} be the following set of supports of simplices in K (which are subsets of $V(K)$):

$$\{x \subset V(K) \mid \exists \sigma^{(n)} \in K \text{ supported by } x\}$$

Then \mathcal{K} is an abstract simplicial complex, and K or sometimes $|K|$ is called a *geometric realization* of the abstract simplicial complex \mathcal{K} .

One can show that there is a geometric realization for each abstract simplicial complex [318, Prop. 2.9], but the dimension of the space the Euclidean simplex is embedded in is in general larger than the dimension of the abstract simplicial complex.

Now we have all ingredients to define the triangulation of a topological space:

Definition 4.12 ((combinatorial) triangulation of a topological space [318, Def. 2.12].):

Let (X, T) be a topological space, and let \mathcal{K} be a d -dimensional abstract simplicial complex. If there is a geometric realization $|K|$ of \mathcal{K} that admits a homeomorphism $\mathcal{T} : |K| \rightarrow (X, T)$, the homeomorphism is called *triangulation* of the topological space (X, T) .

A triangulation is denoted as *combinatorial*, if the link of every vertex is PL homeomorphic to the boundary of the d -simplex.



Often *triangulation* is also used to denote the pair consisting of the abstract simplicial complex \mathcal{K} and the homeomorphism \mathcal{T} . There are also *pseudo-simplicial* triangulations, which are tessellations of manifolds into simplices not forming a valid simplicial complex (e.g., the triangulation of the 1-sphere with two vertices and two edges), which are not considered in this thesis.

Throughout this thesis we only use combinatorial triangulations and denote them simply as triangulations. There is a slightly more general definition, which also includes non-combinatorial triangulations, where simplices cannot be embedded locally flat into an \mathbb{R}^n (even with arbitrarily large n), so they are not homeomorphic to an Euclidean simplicial complex, or equivalently, where there are vertices that have a link (as defined in the next section) that is not homeomorphic to the $(d - 1)$ -sphere. An example for a non-combinatorial triangulation is the triangulation of the S^1 with two edges and two vertices.

As an example we give here the homeomorphism that maps the geometric realization (4.3) (depicted in Fig. 4.1) of the abstract simplicial complex (4.1) onto the 2-sphere S^2 and triangulates it. This is not its smallest triangulation of the 2-sphere, but it allows a simple construction of the homeomorphism between the geometric realization and the manifold. Therefor we note that S^2 can be coordinatized by the polar coordinates

$$[0, 2\pi] \times [0, \pi] \rightarrow S^2 \quad (\phi, \vartheta) \mapsto \begin{pmatrix} \cos \phi \sin \vartheta \\ \sin \phi \sin \vartheta \\ \cos \vartheta \end{pmatrix}$$

As a homeomorphism we construct the function that maps a point of the geometric realization onto the intersection of the line through the origin and this point with the sphere given by this coordinatization. If both the octahedron and the sphere points are given in spherical coordinates, this is the map $(r, \phi, \vartheta) \rightarrow (1, \phi, \vartheta)$. A point on the closed simplex $\{\vec{x}_0, \vec{x}_1, \vec{x}_4\}$ is given by

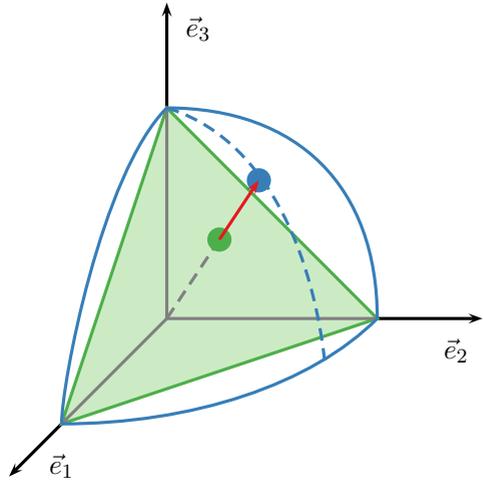
$$\vec{x} = \vec{x}_0 + \lambda_1(\vec{x}_1 - \vec{x}_0) + \lambda_2(\vec{x}_4 - \vec{x}_0) = \begin{pmatrix} 1 - \lambda_1 - \lambda_2 \\ \lambda_1 \\ \lambda_2 \end{pmatrix}$$

in Cartesian coordinates, with $0 \leq \lambda_1 \leq 1$ and $0 \leq \lambda_2 \leq 1$. So the homeomorphism can be constructed by the transformation of Cartesian coordinates into polar coordinates, for the considered simplex this is

$$\mathcal{T} : |K| \rightarrow \mathbb{S}^2 \quad \begin{pmatrix} \lambda_1 \\ \lambda_2 \end{pmatrix} \mapsto \begin{pmatrix} \phi \\ \vartheta \end{pmatrix} = \begin{pmatrix} \arctan\left(\frac{\lambda_1}{1 - \lambda_1 - \lambda_2}\right) \\ \arccos\left(\frac{\lambda_2}{1 + 2\lambda_1^2 + 2\lambda_2^2 - \lambda_1 - \lambda_2 - \lambda_1\lambda_2}\right) \end{pmatrix} \quad (4.4)$$



Figure 4.2: Closed simplex $\{\vec{x}_0, \vec{x}_1, \vec{x}_4\}$ of the Euclidean simplicial complex (4.3) (green) and standard coordinization of the sphere (blue) in the same sector. The vectors \vec{e}_i are the coordinate vectors. The red arrow depicts the homeomorphism (4.4) that maps points of the Euclidean simplicial complex onto the sphere, which is a triangulation of a sphere.



The procedure is displayed in Fig. 4.2. For the other simplices the homeomorphisms can be constructed similarly.

We now introduce a name for topological manifolds that can be triangulated and have to fit this subclass into the hierarchy of manifolds introduced in Sec. 4.1.1.

Definition 4.13 (triangulable, triangulated and combinatorial manifold, [318, Def. 2.12], [97, Sec. 2].):

Let M be a topological manifold. If there is a triangulation \mathcal{T} of M , the manifold is called *triangulable*.

A simplicial complex with geometric realization that is homeomorphic to a topological manifold is denoted as *triangulated* (sometimes also *simplicial*) manifold. A *combinatorial* manifold is a triangulated manifold where the link of every vertex is PL homeomorphic to the boundary of a simplex.

So by definition each triangulated or combinatorial manifold is also a topological manifold, and one can show easily that each combinatorial manifold has a PL structure, and every PL manifold is combinatorially triangulable [222], which can be summarized a bit sloppy as

$$(\text{triangulated} \supseteq \text{combinatorial} = \text{PL}) \text{ manifolds}$$

Due to the equivalence of the TOP and the PL category for $d \leq 3$, in these dimensions every topological manifold is triangulable, and every triangulation is a combinatorial one. Due to the proof of the Poincaré conjecture by Perelman also in $d = 4$ every triangulation is combinatorial [78]



(but remember that in $d = 4$ there are topological manifolds with different PL structures [189]). For four and more dimensions there are topological manifolds that cannot be triangulated, and for $d \geq 5$ there are, e.g., non-combinatorial triangulations of the d -sphere that are not PL homeomorphic to the boundary of the $(d + 1)$ -simplex [286].

As a last step we have to define under which circumstances triangulations are considered to be equal:

Definition 4.14 (isomorphic triangulations [318, Def. 2.13]):

Let X be a topological space, let \mathcal{K} and \mathcal{L} be two abstract simplicial complexes with geometric realizations $|K|$ and $|L|$. Let $\mathcal{T}_{\mathcal{K}} : |K| \rightarrow X$ and $\mathcal{T}_{\mathcal{L}} : |L| \rightarrow X$ be two triangulations of the topological space X . If the map $\tau_{\mathcal{L}}^{-1} \circ \tau_{\mathcal{K}} : |K| \rightarrow |L|$ is a homeomorphism consistent with the simplicial structure (i.e. maps simplices of the geometric realization into simplices), then the two triangulations are called *isomorphic*.

So two triangulations are isomorphic if the geometric realizations $|K|$ and $|L|$ are homeomorphic and the underlying abstract simplicial complexes \mathcal{K} and \mathcal{L} are isomorphic.

Operations on simplicial complexes

In this section we describe some elementary unary and binary operations that can be applied to simplicial complexes. The definitions of these operations are formulated in terms of abstract simplicial complexes, but they can be formulated for Euclidean simplicial complexes or combinatorial triangulations as well.

First we define the closed and the open star, which is intuitively the simplicial neighborhood of a simplex, the link, which is the boundary of the closed star, and the deletion of a simplex.

Definition 4.15 (((open) star, deletion and link [260, Sec. 2.1.2]):

Let \mathcal{K} be an abstract simplicial complex, and let $\sigma \in \mathcal{K}$ be one of its simplices. The (*closed*) *star* $\overline{\text{st}}_{\mathcal{K}}(\sigma)$ and the *open star* $\text{st}_{\mathcal{K}}(\sigma)$ of the simplex σ are the subsets

$$\begin{aligned}\overline{\text{st}}_{\mathcal{K}}(\sigma) &:= \{\tilde{\sigma} \in \mathcal{K} \mid \tilde{\sigma} \cup \sigma \in \mathcal{K}\} \\ \text{st}_{\mathcal{K}}(\sigma) &:= \{\tilde{\sigma} \in \mathcal{K} \mid \tilde{\sigma} \supseteq \sigma\}.\end{aligned}$$

The *deletion* $\text{dl}(\sigma)$ and the *link* $\text{lk}(\sigma)$ of the simplex σ are defined as:

$$\begin{aligned}\text{dl}_{\mathcal{K}}(\sigma) &:= \{\tilde{\sigma} \in \mathcal{K} \mid \tilde{\sigma} \not\supseteq \sigma\} \\ \text{lk}_{\mathcal{K}}(\sigma) &:= \{\tilde{\sigma} \in \mathcal{K} \mid \sigma \cap \tilde{\sigma} = \emptyset \wedge \sigma \cup \tilde{\sigma} \in \mathcal{K}\}\end{aligned}$$



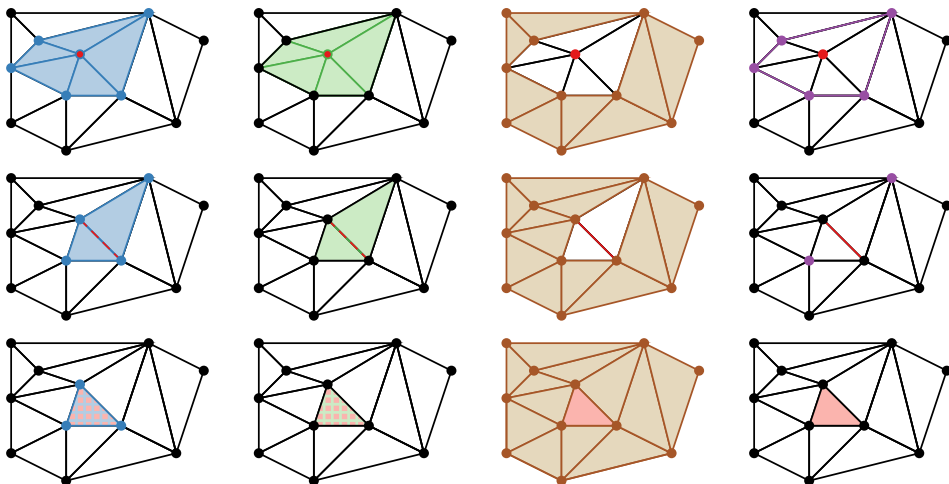


Figure 4.3: Different parts of a simplicial complex \mathcal{K} in two-dimensions. (From left to right) **star** $\overline{\text{st}}_{\mathcal{K}}(\sigma)$, **open star** $\text{st}_{\mathcal{K}}(\sigma)$, **deletion** $\text{dl}_{\mathcal{K}}(\sigma)$ and **link** $\text{lk}_{\mathcal{K}}(\sigma)$ of a (from top to down) **0-simplex**, **1-simplex** and **2-simplex** σ . The **open star** consists of all simplices that contain the given simplex sigma, the **deletion** is the complementary set of the **open star**. The **star** is the closure of the **open star**, and the **link**.

Note that the (closed) star, the link and the deletion are itself abstract simplicial complexes, but the open star is not an abstract simplicial complex. Consider e.g. the abstract simplicial complex (4.1) denoted by \mathcal{K} . There we have for the 0-simplex $\{0\}$ the operations

$$\begin{aligned} \text{st}_{\mathcal{K}}(\{0\}) &= \{\{0, 1, 4\}, \{0, 3, 4\}, \{0, 1, 5\}, \{0, 3, 5\}, \\ &\quad \{0, 1\}, \{0, 3\}, \{0, 4\}, \{0, 5\}, \{0\}\} \\ \overline{\text{st}}_{\mathcal{K}}(\{0\}) &= \text{st}_{\mathcal{K}}(\{0\}) \cup \{\{1,4\}, \{1,5\}, \{3,4\}, \{3,5\}, \{0\}, \{1\}, \{3\}, \{4\}, \{5\}, \emptyset\} \\ \text{lk}_{\mathcal{K}}(\{0\}) &= \overline{\text{st}}_{\mathcal{K}}(\{0\}) \setminus \text{st}_{\mathcal{K}}(\{0\}), \end{aligned}$$

and for the 1-simplex $\{0, 1\}$ we have the operations

$$\begin{aligned} \text{st}_{\mathcal{K}}(\{0, 1\}) &= \{\{0, 1, 4\}, \{0, 1, 5\}, \{0, 1\}\} \\ \overline{\text{st}}_{\mathcal{K}}(\{0, 1\}) &= \text{st}_{\mathcal{K}}(\{0,1\}) \cup \{\{0,4\}, \{0,5\}, \{1,4\}, \{1,5\}, \{0\}, \{1\}, \{4\}, \{5\}, \emptyset\} \\ \text{lk}_{\mathcal{K}}(\{0, 1\}) &= \{\{4\}, \{5\}, \emptyset\}. \end{aligned}$$

In Fig. 4.3 stars, links and deletions for all types of simplices in a two-dimensional simplicial complex are depicted.

In addition to the functions that act on one simplicial complex we introduce a binary function that combines two simplicial complexes into a new one.



Definition 4.16 (join of complexes [260, Sec. 2.1.3]):

Let \mathcal{K} and \mathcal{L} be abstract simplicial complexes with disjoint vertex sets $V(\mathcal{K})$ and $V(\mathcal{L})$. The *join* $\mathcal{K} \star \mathcal{L}$ of \mathcal{K} and \mathcal{L} is defined as:

$$\mathcal{K} \star \mathcal{L} := \{\sigma \subseteq (V(\mathcal{K}) \cup V(\mathcal{L})) \mid \sigma \cap V(\mathcal{K}) \in \mathcal{K}, \sigma \cap V(\mathcal{L}) \in \mathcal{L}\}$$

The join $\sigma \star \mathcal{K}$ of a simplex σ and a simplicial complex \mathcal{K} is the join of the simplicial complex consisting of σ and all of its subsimplices with \mathcal{K} .

Consider for example the abstract simplicial complexes $\mathcal{K} = \{\{0\}, \emptyset\}$ and $\mathcal{L} = \{\{1, 2\}, \{2, 3\}, \{1, 3\}, \{1\}, \{2\}, \{3\}, \emptyset\}$. The join of \mathcal{K} and \mathcal{L} is

$$\begin{aligned} \mathcal{K} \star \mathcal{L} = \{ & \{0, 1, 2\}, \{0, 2, 3\}, \{0, 1, 3\}, \{0, 1\}, \{0, 2\}, \{0, 3\}, \\ & \{1, 2\}, \{2, 3\}, \{1, 3\}, \{0\}, \{1\}, \{2\}, \{3\}, \emptyset \} \end{aligned}$$

Algebraic representation of simplicial complexes

There is an interesting algebraic formulation of (abstract or Euclidean) simplicial complexes, compare e.g. Ref. [11]. We give this formulation here for two reasons, first because of its elegance and second because it allows a very simple definition of the boundary operator and the link (without the necessity of defining stars and deletions). Let \mathcal{K} be a simplicial complex over the set \mathcal{I} and let $\sigma = \{i_0, \dots, i_{k+1}\} \subset \mathcal{I}$ be a k -simplex. The simplex is now represented by the monomial

$$\sigma = \{i_0, \dots, i_{k+1}\} \rightarrow x_{i_0} x_{i_1} \dots x_{i_k}$$

The whole simplicial complex \mathcal{K} is then represented by a polynomial with coefficients in \mathbb{Z}_2 (so that $1 + 1 = 0$). The example of the abstract simplicial complex (4.1) can be formulated as the polynomial

$$\begin{aligned} \mathcal{K} = & x_0 x_1 x_4 + x_1 x_2 x_4 + x_2 x_3 x_4 + x_0 x_3 x_4 + \\ & + x_0 x_1 x_5 + x_1 x_2 x_5 + x_2 x_3 x_5 + x_0 x_3 x_5 + \\ & + x_0 x_1 + x_1 x_2 + x_2 x_3 + x_0 x_3 + x_0 x_4 + x_1 x_4 + x_2 x_4 + x_3 x_4 + \\ & + x_0 x_5 + x_1 x_5 + x_2 x_5 + x_3 x_5 + x_0 + x_1 + x_2 + x_3 + x_4 + x_5 + 1. \end{aligned}$$

The presence of the term 1 corresponds to the empty set which is part of every simplicial complex. Sometimes this term has to be added after operations manually in order to get again a correct representation.



The algebraic representation can be used for easily calculating the join, which is then simply the product of the two associated polynomials: The join of the simplicial complexes $\mathcal{K} = \{\{0\}, \emptyset\} \rightarrow x_0 + 1$ and

$$\begin{aligned} \mathcal{L} &= \{\{1, 2\}, \{2, 3\}, \{1, 3\}, \{1\}, \{2\}, \{3\}, \emptyset\} \\ &\rightarrow x_1x_2 + x_2x_3 + x_1x_3 + x_1 + x_2 + x_3 + 1 \end{aligned}$$

is given by the product

$$\begin{aligned} \mathcal{K} \star \mathcal{L} &= (x_0 + 1) \cdot (x_1x_2 + x_2x_3 + x_1x_3 + x_1 + x_2 + x_3 + 1) \\ &= x_0x_1x_2 + x_0x_2x_3 + x_0x_1x_3 + \\ &\quad + x_1x_2 + x_2x_3 + x_1x_3 + x_0x_1 + x_0x_2 + x_0x_3 \\ &\quad + x_0 + x_1 + x_2 + x_3 + 1 \end{aligned}$$

We can now use the usual differential operators $\partial_i := \partial/\partial x_i$ to define the boundary operator

$$\partial := \sum_{i \in \mathcal{I}} \partial_i$$

Since the monomials are linear in each term x_i , as always $\partial\partial \equiv 0$. Consider for example the simplicial complex

$$\mathcal{K} = x_0x_1x_2 + x_0x_1 + x_0x_2 + x_1x_2 + x_0 + x_1 + x_2 + 1,$$

which has the boundary

$$\begin{aligned} \partial\mathcal{K} &= (\partial_0 + \partial_1 + \partial_2)(x_0x_1x_2 + x_0x_1 + x_0x_2 + x_1x_2 + x_0 + x_1 + x_2 + 1) = \\ &= x_1x_2 + x_0x_2 + x_0x_1 + x_1 + x_0 + x_2 + x_0 + x_2 + x_1 + 1 + 1 + 1 = \\ &= x_1x_2 + x_0x_2 + x_0x_1 \end{aligned}$$

Note that due to the coefficients of the polynomial being in \mathbb{Z}_2 all double terms cancel.

The differential operators ∂_i and the boundary operator ∂ allow us to formulate the operations on simplicial complexes in the algebraic representation:

$$\begin{aligned} \text{lk}_{\mathcal{K}}(\{i_0, \dots, i_k\}) &= \partial_{i_0} \dots \partial_{i_k} \mathcal{K} \\ \text{st}_{\mathcal{K}}(\{i_0, \dots, i_k\}) &= x_{i_0} \dots x_{i_k} \cdot \text{lk}_{\mathcal{K}}(\{i_0, \dots, i_k\}) = x_{i_0} \dots x_{i_k} \cdot \partial_{i_0} \dots \partial_{i_k} \mathcal{K} \\ \overline{\text{st}}_{\mathcal{K}}(\{i_0, \dots, i_k\}) &= (x_{i_0} \dots x_{i_k} + \partial x_{i_0} \dots x_{i_k}) \cdot \text{lk}_{\mathcal{K}}(\{i_0, \dots, i_k\}) \\ &= (x_{i_0} \dots x_{i_k} + \partial x_{i_0} \dots x_{i_k}) \cdot \partial_{i_0} \dots \partial_{i_k} \mathcal{K} \end{aligned}$$

Note the easy formulation of the link compared to Def. 4.15.



4.1.2 Alexander and Pachner moves

In the previous section we gave the definition of the triangulation of a topological space, and the definitions of certain classes of manifolds. Here we present the two different types of moves that can be used to transform triangulations of the same manifold into each other. The first one are stellar exchanges or Alexander moves, the second are bistellar exchanges or Pachner moves. The latter ones are deduced from the former ones and are used later in our simulations.

Stellar exchanges (Alexander moves)

We first state the definition of stellar exchanges, which will not be used in our simulations, but are the foundations of the flips used later on.

Definition 4.17 (Stellar exchange, stellar subdivision, stellar equivalence [11, 322]):

Let M be a triangulated d -manifold with boundary ∂M , and let $A \in M \setminus \partial M$ be a simplex in the interior of M with $\text{lk}_M(A) = \partial B \star \mathcal{L}$ for a simplex $B \notin M$ and a subset $\mathcal{L} \subset M$ ($\dim(A), \dim(B) \geq 0$). Then the operation $\kappa_{A,B}$ that transforms M into

$$\kappa_{A,B}M := (M \setminus A \star \partial B \star \mathcal{L}) \cup \partial A \star B \star \mathcal{L}$$

is called *stellar exchange* of simplices A and B . The stellar exchange $\kappa_{A,B}^{-1} := \kappa_{B,A}$ is called *inverse* of the stellar exchange $\kappa_{A,B}$ (one can easily show that $\kappa_{A,B}^{-1}\kappa_{A,B} = \text{id}$).

If $\dim(B) = 0$ (i.e. B is a point), then the stellar exchange $\kappa_{A,B} =: \kappa_A$ is called *stellar subdivision*.

Let M and M' be two triangulated manifolds. M and M' are called *stellarly equivalent* (denoted by $M \stackrel{\text{st}}{\sim} M'$), if there is a finite number of stellar exchanges κ_{A_i,B_i} so that

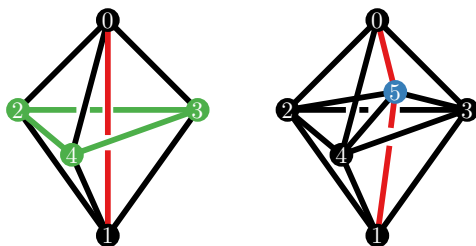
$$M' = \kappa_{A_1,B_1} \kappa_{A_2,B_2} \dots \kappa_{A_k,B_k} M$$

The stellar subdivisions and their inverses are also called *Alexander moves* due to the following theorem of J. W. Alexander in 1930:

Theorem 4.18 (Stellar equivalence of triangulated manifolds [11]). *Let $M_1 \stackrel{\text{PL}}{\cong} M_2$ be two PL homeomorphic, triangulated manifolds. Then $M_1 \stackrel{\text{st}}{\sim} M_2$ are stellarly equivalent, even if one restricts to stellar subdivisions and their inverses, and vice versa: $M_1 \stackrel{\text{PL}}{\cong} M_2 \Leftrightarrow M_1 \stackrel{\text{st}}{\sim} M_2$.*



Figure 4.4: Stellar subdivision (Alexander move) $\kappa_{A,B}$ of a three-dimensional simplicial complex. The simplices that induce the flip are $A = \{0, 1\}$ and $B = \{5\}$, the link $\text{lk}(A)$ and the observing complex \mathcal{L} coincide and are displayed in green.



This theorem implies that Alexander moves can be used to transform triangulations of PL manifolds ergodically into each other.

In Fig. 4.4 an example for a stellar subdivision (Alexander move) is depicted. Starting point is the simplicial complex

$$\mathcal{K} = \{\{0, 1, 2, 3\}, \{0, 1, 2, 4\}, \{0, 1, 3, 4\}\} \cup \text{subsimplices},$$

and we consider the stellar subdivision $\kappa_{A,B}$ given by the simplices $A = \{0, 1\}$ and $B = \{5\}$, where $B \notin \mathcal{K}$. The boundary $\partial B = \{\emptyset\}$ is empty, the link of A is given by

$$\text{lk}_{\mathcal{K}}(A) = \{\{2, 3\}, \{2, 4\}, \{3, 4\}, \{2\}, \{3\}, \{4\}, \emptyset\},$$

so $\mathcal{L} = \partial B \star \text{lk}_{\mathcal{K}}(A) = \text{lk}_{\mathcal{K}}(A)$. So the simplices removed by the stellar subdivision are

$$\begin{aligned} A \star \partial B \star \mathcal{L} &= \{\{0, 1\}, \{0\}, \{1\}, \emptyset\} \star \{\emptyset\} \\ &\star \{\{2, 3\}, \{2, 4\}, \{3, 4\}, \{2\}, \{3\}, \{4\}, \emptyset\} = \\ &= \{\{0, 1, 2, 3\}, \{0, 1, 2, 4\}, \{0, 1, 3, 4\}\} \cup \text{subsimplices} \end{aligned}$$

the simplices inserted by the stellar subdivision are

$$\begin{aligned} \partial A \star B \star \mathcal{L} &= \{\{0\}, \{1\}\} \star \{\{5\}\} \star \{\{2, 3\}, \{2, 4\}, \{3, 4\}, \{2\}, \{3\}, \{4\}, \emptyset\} = \\ &= \{\{0, 2, 3, 5\}, \{0, 2, 4, 5\}, \{0, 3, 4, 5\}, \\ &\quad \{1, 2, 3, 5\}, \{1, 2, 4, 5\}, \{1, 3, 4, 5\}\} \cup \text{subsimplices}, \end{aligned}$$

so every 3-simplex is replaced by two 3-simplices containing the new vertex 5.

Bistellar exchanges (Pachner moves)

Alexander moves have the disadvantage that there are (countable) infinitely many of them if one considers all possible triangulations of a manifold, so



there cannot be a complete list of all possible Alexander moves. (Note that of course in a fixed triangulations there is only a finite number of Alexander moves). E.g., consider the stellar subdivision of an edge in a three-dimensional triangulated manifold. There is no limit on the number of tetrahedra incident with this edge, and for every number k of incident tetrahedra there is an Alexander move that transforms the k incident tetrahedra into $2k$ tetrahedra incident with the newly inserted vertex. In fact one can define another finite set of flips that can be used to transform two triangulations of PL homeomorphic manifolds into each other:

Definition 4.19 (Bistellar exchange, bistellar equivalence [322]):

Let M be a triangulated d -manifold and let $\kappa_{A,B}$ be a stellar exchange. If $\dim(A) + \dim(B) = d$, then $\chi_A := \kappa_{A,B} = \kappa_B^{-1}\kappa_A$ is called a $(d+1-\dim(A) \rightarrow 1+\dim(A))$ -*bistellar exchange* (because it transforms $d+1-\dim(A)$ into $1+\dim(A)$ maximal simplices).

Let M and M' be two triangulated manifolds. M and M' are called *bistellarly equivalent*, denoted by $M \stackrel{\text{bst}}{\sim} M'$, if there is a finite number of bistellar exchanges χ_{A_i} so that

$$M' = \chi_{A_1}\chi_{A_2} \cdots \chi_{A_k}M$$

These exchanges are denoted as bistellar because a bistellar exchange $\chi_A = \kappa_B^{-1}\kappa_A$ can be composed into a stellar subdivision κ_A and an inverse stellar subdivision κ_B [322]. Bistellar exchanges are also called *Pachner moves*, referring to the following theorem of Udo Pachner:

Theorem 4.20 (Bistellar equivalence of triangulated manifolds [322]). *Let $M_1 \stackrel{\text{PL}}{\simeq} M_2$ be two PL homeomorphic triangulated manifolds. Then $M_1 \stackrel{\text{bst}}{\sim} M_2$ are bistellarly equivalent and vice versa: $M_1 \stackrel{\text{PL}}{\simeq} M_2 \Leftrightarrow M_1 \stackrel{\text{bst}}{\sim} M_2$.*

For d -manifolds there are $d+1$ different Pachner moves, namely the moves $(1 \rightarrow d+1), (2 \rightarrow d), \dots, (d+1 \rightarrow 1)$. They are displayed in the first rows of Figs. 3.9 (on page 103) for $d=2$ and 3.10 (on page 104) for $d=3$, since there is a one-to-one correspondence between the non-degenerated flips used in embedded triangulations and Pachner moves, which will be proven later.

Note that not every simplex A of a triangulation generates a valid Pachner move χ_A . First a k -simplex A must be incident with $d-k+1$ maximal simplices in order to find a suitable simplex B . Furthermore the simplex B that will be inserted into the triangulation must not be contained in the triangulation before.

There are two alternate ways of defining Pachner moves, the first one is by considering the different partitionings of the facets of the boundary



of a $(d + 1)$ -simplex, the second one uses the notion of circuits as in the embedded case. We give a sketch for the proof of the former alternative, and a complete proof of the latter one, because we did not find a similar proof in the literature and the alternative definition is important for the unified algorithmic implementation of triangulations in computer code.

Theorem 4.21 (Pachner move by boundary of $(d + 1)$ -simplex [318, Numbs. 2.16, 2.17, 2.18]). *Let M be a triangulated d -manifold with underlying abstract simplicial complex \mathcal{K} and triangulation $\mathcal{T}_{\mathcal{K}} : |\mathcal{K}| \rightarrow M$, and let $\sigma^{(d+1)}$ be a $(d + 1)$ -simplex with boundary d -simplices $\sigma_1^{(d)}, \dots, \sigma_{d+1}^{(d)}$. Let $0 < k \leq d$ and define the two Euclidean simplicial complexes*

$$A := \bigcup_{i=1}^k \{ \sigma \mid \sigma \subseteq \sigma_k^{(d)} \} \quad B := \bigcup_{i=k+1}^{d+1} \{ \sigma \mid \sigma \subseteq \sigma_k^{(d)} \},$$

and their associated abstract simplicial complexes \mathcal{A} and \mathcal{B} , where $\partial\mathcal{A} = \partial\mathcal{B}$. Let $\Psi_A : \mathcal{A} \rightarrow \mathcal{K}$ be an injective simplicial map. Then there exists an abstract simplicial complex \mathcal{L} and a triangulation $\mathcal{T}_{\mathcal{L}} : |\mathcal{L}| \rightarrow M$ so that

- the map $\mathcal{T}_{\mathcal{L}} \circ \mathcal{T}_{\mathcal{K}}^{-1}$ is simplicial outside of $|\Psi_A(\mathcal{A} \setminus \partial\mathcal{A})|$, and
- there exists a injective simplicial map $\Psi_B : \mathcal{B} \rightarrow \mathcal{L}$ with

$$\begin{aligned} \mathcal{T}_{\mathcal{L}}(|\Psi_B(\mathcal{B})|) &= \mathcal{T}_{\mathcal{K}}(|\Psi_A(\mathcal{A})|) \\ \mathcal{T}_{\mathcal{L}}(|\Psi_B(x)|) &= \mathcal{T}_{\mathcal{K}}(|\Psi_A(x)|) \text{ for } x \in \partial\mathcal{A} = \partial\mathcal{B}. \end{aligned}$$

The replacement of $\mathcal{T}_{\mathcal{K}}$ with $\mathcal{T}_{\mathcal{L}}$ is then a $(k, d - k)$ Pachner move.

Proof. (sketch) The simplex A of the original definition Def. 4.19 is the largest simplex which is a subsimplex of all maximal simplices in \mathcal{A} . Identify then \mathcal{A} with $A \star \partial B$ of the original definition and \mathcal{B} with $\partial A \star B$ of the original definition. \square

So consider, e.g., a triangulated manifold M in two dimensions and a 3-simplex. There are two possibilities to subdivide the boundary of the 3-simplex into two non-empty groups, first using two triangles each in \mathcal{A} and in \mathcal{B} , secondly using three triangles in one component and one triangle in the other component. The first case leads to the $(2 \rightarrow 2)$ -flip (depicted in Fig. 4.5), and the second case leads to the $(3 \rightarrow 1)$ -flip and its inverse, the $(1 \rightarrow 3)$ -flip (depicted in Fig. 4.6).

The next theorem states the equivalence of the original Pachner move formulation and the formulation of oriented circuits. This formulation will



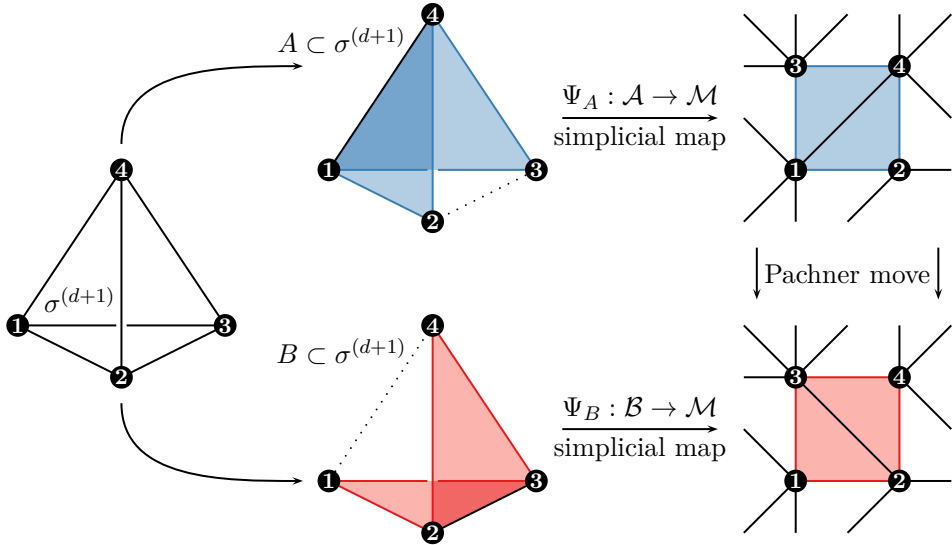


Figure 4.5: Visualization of the $(2, 2)$ -bistellar Pachner move, compare Thm. 4.21. From a 3-simplex $\sigma^{(4)}$ two boundary simplices are chosen for the **complex A**, the two other boundary simplices are chosen for **complex B**. Note that Ψ_A and Ψ_B map simplicial complexes, the geometric realizations are only displayed for visualization.

be very useful later for calculating the change in the number of simplices induced by a flip, and for a unified treatment of several types of triangulations in a numerical setup.

Theorem 4.22 (Pachner move by oriented circuit). *Let M be a triangulated d -manifold, and let $\sigma \in M \setminus \partial M$ be a k -simplex in the interior of M with $d + 1 - k$ maximal supersimplices $\sigma_1, \dots, \sigma_{d+1-k}$. Denote by $Z := V(\sigma_1 \cup \dots \cup \sigma_{d+1-k})$ the set of vertices of the maximal simplices, by $Z_- := V(\sigma)$ the set of vertices of σ , and by $Z_+ := Z \setminus Z_-$. Then the following operation is the bistellar move χ_σ :*

$$\chi_\sigma M = (M \setminus \{\sigma' \subset Z \mid Z_+ \not\subset \sigma'\}) \cup \{\sigma' \subset Z \mid Z_- \not\subset \sigma'\}$$

Proof. We identify σ with A in Def. 4.17 and have to define a simplex $B \notin M$ so that

$$\{\sigma' \subset Z \mid Z_+ \not\subset \sigma'\} = \sigma \star \partial B \text{ and } \{\sigma' \subset Z \mid Z_- \not\subset \sigma'\} = \partial \sigma \star B$$

In the following we choose B to be the simplex composed of the points of Z_+ . We can restrict to the case that $|Z_+| = d + 1 - k$, because otherwise



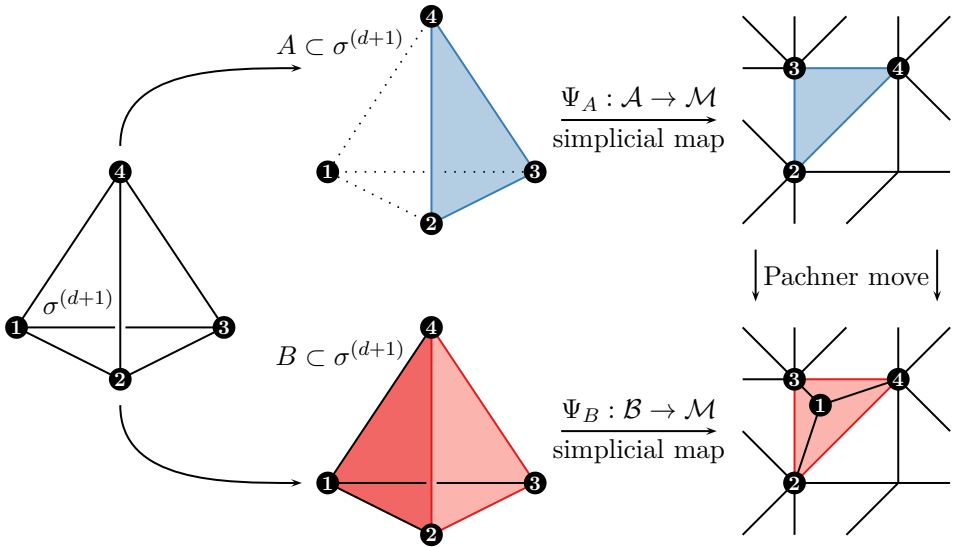


Figure 4.6: Visualization of the (1,3)-bistellar Pachner move, compare Thm. 4.21. From a 3-simplex $\sigma^{(4)}$ one boundary simplex is chosen for the complex **complex A**, the three other boundary simplices are chosen for **complex B**. Note that Ψ_A and Ψ_B map simplicial complexes, the geometric realizations are only displayed for visualization.



the considered move would not be bistellar, and also in the alternative formulation we would discard this move. We use the description of simplicial complexes in terms of polynomials and use the following monomials for the considered simplices

$$\sigma \rightarrow x_{i_0^-} \dots x_{i_k^-} \text{ and } B \rightarrow x_{i_0^+} \dots x_{i_l^+}$$

with $l = d - k$, $\{i_0^+, \dots, i_l^+\} := Z_+$ and $\{i_0^-, \dots, i_k^-\} := Z_-$.

The first part of the proof is to show that

$$\{\sigma' \subset Z \mid Z_+ \not\subseteq \sigma'\} \supset \sigma \star \partial B.$$

For a simplex $\tilde{\sigma} \in \sigma \star \partial B$ it is true that $\tilde{\sigma} \subset Z$, because $\sigma \subset Z$ and $B \subset Z \Rightarrow \partial B \subset 2^Z$. However, for a simplex $\tilde{\sigma} \in \sigma \star \partial B$ it is also true that $\tilde{\sigma} \not\subseteq Z_+$, because supersets of Z_+ can only be generated by multiplying a monomial in σ and its subsimplices with $x_{i_0^+} \dots x_{i_l^+}$, but the latter is not contained in ∂B because of the boundary operator.

The second part of the proof is to show that

$$\{\sigma' \subset Z \mid Z_+ \not\subseteq \sigma'\} \subset \sigma \star \partial B.$$

A simplex $Z_+ \not\subseteq \tilde{\sigma} \rightarrow x_{j_0^+} \dots x_{j_{l'}^+} x_{j_0^-} \dots x_{j_{k'}^-}$ with $\{j_0^+, \dots, j_{l'}^+\} \subsetneq Z_+$ and $\{j_0^-, \dots, j_{k'}^-\} \subseteq Z_-$ is constructed from the product of the monomial $x_{j_0^+} \dots x_{j_{l'}^+}$ in ∂B and the monomial $x_{j_0^-} \dots x_{j_{k'}^-}$ in σ , so $\tilde{\sigma} \in \sigma \star \partial B$.

So we proved that the two sets are equivalent, the proof for $\{\sigma' \subset Z \mid Z_- \not\subseteq \sigma'\} = \partial \sigma \star B$ is analogue. \square

4.1.3 Number of simplices in triangulations and their change due to Pachner moves

Our aim is to approximately count the number of triangulations of a given manifold using the Wang-Landau algorithm similar to Secs. 3.2 and 3.3. The therefor necessary ergodic steps (Pachner moves) were defined in the previous section. Another necessary ingredient will be an energy function that classifies the microstates of triangulations into macrostates. A canonical quantity for this classification are the number of k -simplices of the respective triangulation. So in this section we present some general relation between the number of simplices in a triangulation and calculate the change in these numbers induced by Pachner moves.

The numbers of k -simplices are not independent, in fact their are the following relations:



Theorem 4.23 (Dehn-Sommerville relations for triangulated manifolds, see Refs. [134, 251, 371]). *Let M be a d -dimensional manifold with triangulation, let K be a simplicial complex and let $\tau_K : |\mathcal{K}| \rightarrow M$ be a triangulation of M . Let N_k be the number of k -simplices in the simplicial complex K . Then there are the following (not necessarily independent) relations between the simplex numbers:*

$$N_k = \sum_{i=k}^d (-1)^{d+i} \binom{i+1}{k+1} N_i, \quad k \in \{0, \dots, d\} \quad (4.5)$$

If one defines $N_{-1} := \chi/2$ for the Euler characteristic χ the relation for $k = -1$ is also valid.

We specify these relations for $2 \leq d \leq 4$, which will be the dimension that are considered within this thesis. For 2-dimensional triangulated manifolds there are the following independent Dehn-Sommerville relations:

$$k = -1 : \quad \chi = N_0 - N_1 + N_2 \quad (4.6a)$$

$$k = 0, k = 1 : \quad 2N_1 = 3N_2 \quad (4.6b)$$

Eq. (4.6a) is simply Euler's formula for surfaces relating the number of vertices, edges and faces, and Eq. (4.6b) encodes the fact that there are three edges per triangle, and each edge is incident with two triangles.

For 3-dimensional triangulated manifolds there are the following independent Dehn-Sommerville relations:

$$k = -1 : \quad 0 = N_0 - N_1 + N_2 - N_3 \quad (4.7a)$$

$$k = 0 : \quad 2N_0 = 2N_1 - 3N_2 + 4N_3 \quad (4.7b)$$

$$k = 1, k = 2 : \quad N_2 = 2N_3 \quad (4.7c)$$

Note that Eqs. (4.7a) and (4.7c) imply⁶ Eq. (4.7b). Eq. (4.7a) intuitively means that every 3-manifold has a vanishing Euler characteristic, and Eq. (4.7c) encodes the fact that there are four triangles per tetrahedron, and every triangle is incident with two tetrahedra.

For 4-dimensional triangulated manifolds there are the following independent Dehn-Sommerville relations:

$$k = -1 : \quad \chi = N_0 - N_1 + N_2 - N_3 + N_4 \quad (4.8a)$$

$$k = 0, k = 1 : \quad 2N_1 = 3N_2 - 4N_3 + 5N_4 \quad (4.8b)$$

$$k = 2, k = 3 : \quad 2N_3 = 5N_4 \quad (4.8c)$$

⁶ By calculating $2 \cdot (4.7a) + (4.7c)$



The Eqs. (4.8b) for $k = 0$ and $k = 1$ are equivalent if one uses $2N_3 = 5N_4$ from Eqs. (4.8c) for $k = 2$ or $k = 3$. The implications are similar to the two- or three-dimensional cases.

As the next step we calculate the change in the simplex numbers induced by a Pachner move in the oriented circuit notion. Remember that we denote by Z_- the set of points of simplex A , by Z_+ the set of points of simplex B , and by $Z = Z_+ \cup Z_-$ the union of these disjoint sets. We begin by giving the number of different k -simplices that can be constructed from points in Z , and the number of those that contain Z_{\pm} as a subset:

Lemma 4.24. *Let $Z = (Z_+, Z_-)$ be an oriented circuit in d dimensions, and let $|Z_{\pm}|$ be the number of points in Z_{\pm} . Then the following assertions hold:*

1. *The total number N_k of k -simplices that can be constructed using the points of Z is:*

$$N_k = \binom{|Z|}{k+1}$$

2. *The total number N_k^{\pm} of k -simplices that can be constructed using all the points of Z_{\pm} (and possible other points of Z) is:*

$$N_k^{\pm} = \binom{|Z| - |Z_{\pm}|}{k+1 - |Z_{\pm}|} = \binom{|Z_{\mp}|}{k+1 - |Z_{\pm}|}$$

Proof. 1. A k -simplex consists of $k+1$ points. The number of possibilities for choosing a subset with $k+1$ elements out of a set with $|Z|$ elements is given by the stated binomial coefficient.

2. To obtain the possibilities for constructing the k -simplex containing all the points of Z_{\pm} one has to multiply the number of possibilities to choose all elements out of $|Z_{\pm}|$ elements and to choose the remaining $k+1 - |Z_{\pm}|$ elements out of the remaining $|Z| - |Z_{\pm}|$ points. This is given by

$$N_k^{\pm} = \binom{|Z_{\pm}|}{|Z_{\pm}|} \binom{|Z| - |Z_{\pm}|}{k+1 - |Z_{\pm}|} = \binom{|Z| - |Z_{\pm}|}{k+1 - |Z_{\pm}|} = \binom{|Z_{\mp}|}{k+1 - |Z_{\pm}|}.$$

□

Using this lemma we can calculate the change ΔN_k in the total number N_k of k -simplices induced by a Pachner move.



Proposition 4.25 (simplex number change in flips). *Let $Z = (Z_+, Z_-)$ be an oriented circuit in a d -dimensional triangulation \mathcal{T} that induces a flip $\mathcal{T}_+ \rightarrow \mathcal{T}_-$. Then the change in the number of k -simplices $\Delta N_k(\mathcal{T}_+ \rightarrow \mathcal{T}_-) := N_k(\mathcal{T}_-) - N_k(\mathcal{T}_+)$ can be calculated as following:*

$$\begin{aligned} \Delta N_k &= \binom{|Z| - |Z_+|}{k+1 - |Z_+|} - \binom{|Z| - |Z_-|}{k+1 - |Z_-|} = \\ &= \binom{|Z_-|}{k+1 - |Z_+|} - \binom{|Z_+|}{k+1 - |Z_-|} \end{aligned} \tag{4.9}$$

Proof. The simplices of \mathcal{T} that are not subsets of Z are not affected by the flip, so it is enough to consider the change in the number of simplices that are subsets of Z . The number $N_k(\mathcal{T}_\pm)$ of k -simplices in the \mathcal{T}_\pm triangulation is the number of k -simplices that can be constructed using points out of Z minus the number of simplices that contain all the points of Z_\pm . Using the proceeding lemma this number can be calculated as:

$$N_k(\mathcal{T}_\pm) = \binom{|Z|}{k+1} - \binom{|Z| - |Z_\pm|}{k+1 - |Z_\pm|}$$

So the change in the number of k -simplices is:

$$\begin{aligned} \Delta N_k &= \binom{|Z|}{k+1} - \binom{|Z| - |Z_-|}{k+1 - |Z_-|} - \binom{|Z|}{k+1} + \binom{|Z| - |Z_+|}{k+1 - |Z_+|} \\ &= \binom{|Z| - |Z_+|}{k+1 - |Z_+|} - \binom{|Z| - |Z_-|}{k+1 - |Z_-|} \end{aligned}$$

□

In Tab. 4.1 the total change in the number of simplices is listed for the small dimensions $d = 2$, $d = 3$ and $d = 4$, which are the dimensions that are considered in this thesis.

After calculating the change $\Delta N_k = N_k(\mathcal{T}_-) - N_k(\mathcal{T}_+)$ of the total number of simplices in the triangulation, we proceed calculating the local per-vertex change $\Delta N_k^{(\pm)}$ of k -simplices for points $\in Z_\pm$, which can be useful in certain applications.

Proposition 4.26 (change of number of incident simplices at points in flips). *Let $Z = (Z_+, Z_-)$ be an oriented circuit in the d -dimensional triangulation \mathcal{T} that induces a flip $\mathcal{T}_+ \rightarrow \mathcal{T}_-$. Then the change in the number of k -simplices*



dim	step	ΔN_0	ΔN_1	ΔN_2	ΔN_3	ΔN_4
$d = 2$	$1 \rightarrow 3$	1	3	2		
	$2 \rightarrow 2$	0	0	0		
	$3 \rightarrow 1$	-1	-3	-2		
$d = 3$	$1 \rightarrow 4$	1	4	6	3	
	$2 \rightarrow 3$	0	1	2	1	
	$3 \rightarrow 2$	0	-1	-2	-1	
	$4 \rightarrow 1$	-1	-4	-6	-3	
$d = 4$	$1 \rightarrow 5$	1	5	10	10	4
	$2 \rightarrow 4$	0	1	4	5	2
	$3 \rightarrow 3$	0	0	0	0	0
	$4 \rightarrow 2$	0	-1	-4	-5	-2
	$5 \rightarrow 1$	-1	-5	-10	-10	-4

Table 4.1: Change ΔN_k in the number N_k of k -simplices induced by a $(l \rightarrow d+2-l)$ Pachner move in $d = 2$ (top), $d = 3$ (middle) and $d = 4$ (bottom) dimensions. Note that $\Delta N_k = 0$ if $l = (d + 2)/2$, so the number of non-maximal simplices does not change in a move that conserves the number of maximal simplices. Additionally note that $\Delta N_k(l \rightarrow d + 2 - l) = -\Delta N_k(d + 2 - l \rightarrow l)$, because these moves are their inverses.

$\Delta f_k^{(\pm)}(\mathcal{T}_+ \rightarrow \mathcal{T}_-) := f_k^{(\pm)}(\mathcal{T}_-) - f_k^{(\pm)}(\mathcal{T}_+)$ that are incident with a point $P \in Z_{\pm}$ can be calculated as following:

$$\begin{aligned} \Delta N_k^{(\pm)} &:= N_k^{(\pm)}(\mathcal{T}_-) - N_k^{(\pm)}(\mathcal{T}_+) = \\ &= \pm \binom{|Z_{\mp}|}{k - |Z_{\pm}| + 1} \mp \sum_{i=0}^{k-|Z_{\mp}|} \binom{|Z_{\pm}| - 1}{i} \cdot \binom{|Z_{\mp}|}{k - i} \end{aligned}$$

Proof. The number $N_k^{(+)}(\mathcal{T}_{\pm})$ of k -simplices incident with a point $p \in Z_+$ of the positive circuit in triangulation \mathcal{T}_{\pm} that consist only of circuit is

$$\begin{aligned} N_k^{(+)}(\mathcal{T}_+) &= \sum_{i=0}^{|Z_+|-2} \binom{|Z_+| - 1}{i} \cdot \binom{|Z_-|}{(k + 1) - 1 - i} \\ N_k^{(+)}(\mathcal{T}_-) &= \sum_{i=k-|Z_-|+1}^{|Z_+|-1} \binom{|Z_+| - 1}{i} \cdot \binom{|Z_-|}{(k + 1) - 1 - i}. \end{aligned}$$

For calculating $N_k^{(+)}(\mathcal{T}_+)$, one has to calculate the number of possibilities to construct a k -simplex with $k + 1$ points from Z , so that Z_+ is not a subset



of the chosen points. This can be done by choosing at most $|Z_+| - 2$ points out of $|Z_+ - 1|$ points (positive points without the point where the change should be calculated), and the remaining points from Z_- . The difference in the bounds of the summations for $N_k^{(+)}(\mathcal{T}_+)$ and $N_k^{(+)}(\mathcal{T}_-)$ comes from the fact that for \mathcal{T}_- the set Z_- may not be a subset of the chosen points. Using the same arguments one can calculate the number of simplices incident with a negative point:

$$N_k^{(-)}(\mathcal{T}_+) = \sum_{i=k-|Z_+|+1}^{|Z_-|-1} \binom{|Z_-|-1}{i} \cdot \binom{|Z_+|}{(k+1)-1-i}$$

$$N_k^{(-)}(\mathcal{T}_-) = \sum_{i=0}^{|Z_-|-2} \binom{|Z_-|-1}{i} \cdot \binom{|Z_+|}{(k+1)-1-i}$$

Empty sums (from $i = 0$ to $i = -1$) in both equations are considered as zero, which agrees with the intuitive fact that inserted points or removed points do not have any simplex before or after the flip.

We can now very easily calculate the difference in the numbers induced by a flip:

$$\begin{aligned} \Delta N_k^{(+)} &:= N_k^{(+)}(\mathcal{T}_-) - N_k^{(+)}(\mathcal{T}_+) = \\ &= \binom{|Z_+|-1}{|Z_+|-1} \cdot \binom{|Z_-|}{k-|Z_+|+1} - \sum_{i=0}^{k-|Z_-|} \binom{|Z_+|-1}{i} \cdot \binom{|Z_-|}{k-i} = \\ &= \binom{|Z_-|}{k-|Z_+|+1} - \sum_{i=0}^{k-|Z_-|} \binom{|Z_+|-1}{i} \cdot \binom{|Z_-|}{k-i} \\ \Delta N_k^{(-)} &:= N_k^{(-)}(\mathcal{T}_-) - N_k^{(-)}(\mathcal{T}_+) = \\ &= -\binom{|Z_-|-1}{|Z_-|-1} \cdot \binom{|Z_+|}{k-|Z_-|+1} + \sum_{i=0}^{k-|Z_+|} \binom{|Z_-|-1}{i} \cdot \binom{|Z_+|}{k-i} = \\ &= -\binom{|Z_+|}{k-|Z_-|+1} + \sum_{i=0}^{k-|Z_+|} \binom{|Z_-|-1}{i} \cdot \binom{|Z_+|}{k-i} \end{aligned}$$

□

The calculations for the change of the total number of simplices in arbitrary dimensions can be used to proof that the usual Euler characteristic in two



dimensions and a generalization of the Euler characteristic in three and more dimensions is invariant under all flips.

Definition 4.27 (Euler characteristic for simplicial complexes):

Let \mathcal{K} be a simplicial complex and N_k its number of k -simplices. The Euler-characteristic $\chi(\mathcal{K})$ of the simplicial complex is defined as:

$$\chi(\mathcal{K}) := \sum_{k=0}^d (-1)^k N_k = N_0 - N_1 + N_2 - + \dots$$

Theorem 4.28 (Invariance of the Euler-characteristic w.r.t. Pachner moves).
The Euler-characteristic of a simplicial complex is invariant under performing Pachner moves

Proof. Consider an oriented circuit $Z = Z_+ \cup Z_-$ in d -dimensions, and denote by $\Delta\chi$ the change in the Euler-characteristic induced by the step. Clearly

$$\begin{aligned} \Delta\chi &= \sum_{k=0}^d (-1)^k \Delta N_k \\ &= \sum_{k=0}^d (-1)^k \left[\binom{|Z| - |Z_+|}{k+1 - |Z_+|} - \binom{|Z| - |Z_-|}{k+1 - |Z_-|} \right] \\ &= \sum_{k=0}^d (-1)^k \left[\binom{d+2 - |Z_+|}{k+1 - |Z_+|} - \binom{d+2 - |Z_-|}{k+1 - |Z_-|} \right] \end{aligned}$$

Now switch the summation variable from k to $k' = k + 1 - |Z_{\pm}|$:

$$\begin{aligned} &= \sum_{k'=1-|Z_+|}^{d+1-|Z_+|} (-1)^{k'-1+|Z_+|} \binom{d+2 - |Z_+|}{k'} - \\ &\quad - \sum_{k'=1-|Z_-|}^{d+1-|Z_-|} (-1)^{k'-1+|Z_-|} \binom{d+2 - |Z_-|}{k'} \end{aligned}$$

The lower bound of the sums is always 0 or smaller, since $|Z_{\pm}| \geq 1$. Using the identity

$$\sum_{k=0}^n (-1)^k \binom{n}{k} = 0 \Rightarrow 1 = \binom{n}{n} = (-1)^{n+1} \sum_{k=0}^{n-1} \binom{n}{k}$$



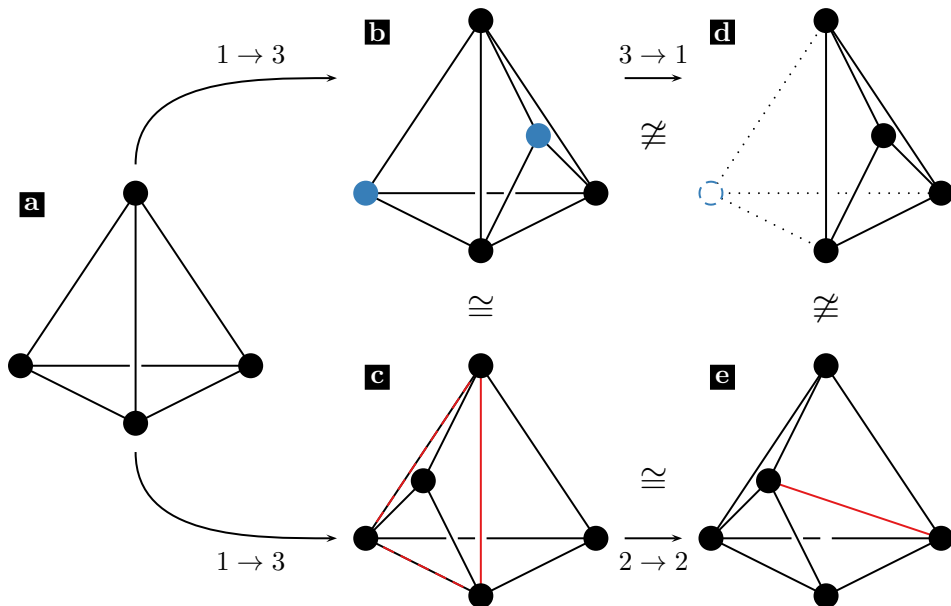


Figure 4.7: Possible flips of the smallest triangulation of a two-dimensional sphere S^2 . The two $(1 \rightarrow 3)$ -flips $a \mapsto b$ and $a \mapsto c$ are treated as different flips, but lead to topologically equivalent configurations b and c . The $(2 \rightarrow 2)$ -flip $c \mapsto e$ does not lead to a different triangulation from the topological point of view. Starting from configuration b , there are two $(3 \rightarrow 1)$ -steps leading to a configuration that is equivalent to a , namely steps $b \mapsto a$ and $b \mapsto d$.

for alternating sums of binomials one can simplify both sums in the upper calculation:

$$\begin{aligned} \Delta\chi &= (-1)^{|Z_+|-1}(-1)^{d+2-|Z_+|} - (-1)^{|Z_-|-1}(-1)^{d+2-|Z_-|} \\ &= (-1)^{d+1} - (-1)^{d+1} = 0 \end{aligned}$$

□

4.1.4 Selection probability of flips

For applying Markov chain Monte Carlo simulations to topological triangulations, the ratio of the selection probability of a flip and of its inverse flip has to be calculated. We will see in this section that this can lead to difficulties, because the actual coordinates of the vertices are not important, and so two triangulations have to be treated as equal if their simplicial structure is equal. Therefore we introduce in this section first a simple and later an exact way to calculate the selection probability, and compare both.



For both the simple and the exact selection probability the algorithm of choosing a certain step is important. Throughout this thesis we use the following one:

1. Choose which type of simplex to flip by selecting $k \in \{0, \dots, d\}$ equally distributed.
2. Choose the k -simplex that will be considered equally distributed in the set of all N_k k -simplices.

If there is no Pachner move associated with this k -simplex (see Sec. 4.1.2 for a discussion which simplices are associated with a Pachner move), we treat the step as rejected step. This means that we do sample from all simplices, and not from the simplices associated with valid flips, because the latter complicates the calculation of the selection probability.

Naively one could now calculate the selection probability of a certain k -simplex inducing a $(d - k + 1 \rightarrow k + 1)$ -step if following the stated selection algorithm:

$$S_{\text{simple}}(d - k + 1 \rightarrow k + 1) = \frac{1}{d + 1} \cdot \frac{1}{N_k}$$

Analogously the selection probability for the simplex inducing the inverse $(k + 1 \rightarrow d - k + 1)$ -Pachner move selected by a $(d - k)$ -simplex can be calculated, denoting by N_{d-k} the number of $(d - k)$ -simplices before the original Pachner move and ΔN_{d-k} is the change of this number induced by the original Pachner move.

$$S_{\text{simple}}(k + 1 \rightarrow d - k + 1) = \frac{1}{d + 1} \cdot \frac{1}{N_{d-k} + \Delta N_{d-k}}$$

By using Equation (4.9) for ΔN_{d-k} , the ratio of the simplified selection probability of a flip and its inverse flip can be calculated as

$$\frac{S_{\text{simple}}(d - k + 1 \rightarrow k + 1)}{S_{\text{simple}}(k + 1 \rightarrow d - k + 1)} = \frac{1}{N_k} \cdot \left(N_{d-k} + 1 - \binom{d - k + 1}{k + 1} \right) \quad (4.10)$$

As the name suggests, $S_{\text{simple}}(d - k + 1 \rightarrow k + 1)$ is not the correct selection probability for the Pachner move. The way it is defined calculates the probability for selecting a simplex that induces a certain Pachner move, but not the selection probability for the move itself. There is a difference between these two selection probabilities because there can be several different simplices that induce flips that lead to the same triangulation, since isomorphic triangulations are considered as equal.



Consider e.g. the situation in Fig. 4.7 where we restrict to triangulations of the two-dimensional sphere \mathbb{S}^2 with four or five vertices. One can check easily that for both vertex numbers there is only one triangulation up to permutation of the vertices, two possible embeddings into \mathbb{R}^3 are displayed in Figs. 4.7a and 4.7b. If using a Markov chain Monte Carlo algorithm for counting triangulations using the selection probability ratio (4.10) one gets that there are twice as much triangulations with five vertices than triangulations with four vertices. This can be understood by considering all possible flips of the two triangulations. For the triangulation with four vertices (displayed in Fig. 4.7a) there are the following flips:

- For each of the four 2-simplices a $(1 \rightarrow 3)$ -flip is proposed and can be executed. Each step leads to the five-vertex triangulation.
- For each of the six 1-simplices a $(2 \rightarrow 2)$ -flip is proposed, but all of these flips are not executable, because they would introduce a new simplex that is already contained in the triangulation
- For each of the four 0-simplices (vertices) a $(3 \rightarrow 1)$ -flip is proposed, but all of these flips are not executable, because they would introduce a new triangle that is already contained in the triangulation.

For the triangulation with five vertices (displayed in Figure Fig. 4.7b) there are the following flips:

- For each of the five 2-simplices a $(1 \rightarrow 3)$ -flip is proposed, but we do not consider them here, because they lead to triangulations with six vertices being outside of our bounds on the number of vertices.
- For three of the nine 1-simplices there is an executable $(2 \rightarrow 2)$ -flip which leads to a triangulation that is equivalent to the original triangulation before the step.
- For two of the five 0-simplices there is an executable $(3 \rightarrow 1)$ -flip which leads to the triangulation with four vertices, the other three 0-simplices do not have the right number of maximal simplices.

In order to fulfill detailed balance, the following equations has to be fulfilled in the case of Wang-Landau sampling

$$\frac{S_{\text{exact}}(\mathcal{T}_1 \rightarrow \mathcal{T}_2)}{S_{\text{exact}}(\mathcal{T}_2 \rightarrow \mathcal{T}_1)} \cdot \frac{A_{\text{exact}}(\mathcal{T}_1 \rightarrow \mathcal{T}_2)}{A_{\text{exact}}(\mathcal{T}_2 \rightarrow \mathcal{T}_1)} = \frac{g(E(\mathcal{T}_1))}{g(E(\mathcal{T}_2))},$$



4. Topological triangulations

where S_{exact} is the exact selection probability, A is the acceptance probability, \mathcal{T}_1 and \mathcal{T}_2 are the unique triangulations with four and five vertices, and E is the energy function used to map microstates to macrostates. Here we assume that E yields different results for the two triangulations, so $g(E(\mathcal{T}_{1,2})) = 1$. By inserting the ratio of the simple selection probabilities on both sides, we get

$$\begin{aligned} & \frac{S_{\text{simple}}(\mathcal{T}_1 \rightarrow \mathcal{T}_2)}{S_{\text{simple}}(\mathcal{T}_2 \rightarrow \mathcal{T}_1)} \cdot \frac{A_{\text{exact}}(\mathcal{T}_1 \rightarrow \mathcal{T}_2)}{A_{\text{exact}}(\mathcal{T}_2 \rightarrow \mathcal{T}_1)} = \\ & = \frac{g(E(\mathcal{T}_1))}{g(E(\mathcal{T}_2))} \cdot \frac{S_{\text{simple}}(\mathcal{T}_1 \rightarrow \mathcal{T}_2)}{S_{\text{simple}}(\mathcal{T}_2 \rightarrow \mathcal{T}_1)} \cdot \left[\frac{S_{\text{exact}}(\mathcal{T}_1 \rightarrow \mathcal{T}_2)}{S_{\text{exact}}(\mathcal{T}_2 \rightarrow \mathcal{T}_1)} \right]^{-1}. \end{aligned}$$

The different selection probabilities are

$$\begin{aligned} S_{\text{simple}}(\mathcal{T}_1 \rightarrow \mathcal{T}_2) &= \frac{1}{3} \cdot \frac{1}{4} & S_{\text{exact}}(\mathcal{T}_1 \rightarrow \mathcal{T}_2) &= \frac{1}{3} \cdot 1 \\ S_{\text{simple}}(\mathcal{T}_2 \rightarrow \mathcal{T}_1) &= \frac{1}{3} \cdot \frac{1}{5} & S_{\text{exact}}(\mathcal{T}_2 \rightarrow \mathcal{T}_1) &= \frac{1}{3} \cdot \frac{2}{5}, \end{aligned}$$

so that we get the following modified detailed balance equation

$$\frac{S_{\text{simple}}(\mathcal{T}_1 \rightarrow \mathcal{T}_2)}{S_{\text{simple}}(\mathcal{T}_2 \rightarrow \mathcal{T}_1)} \cdot \frac{A_{\text{exact}}(\mathcal{T}_1 \rightarrow \mathcal{T}_2)}{A_{\text{exact}}(\mathcal{T}_2 \rightarrow \mathcal{T}_1)} = \frac{g(E(\mathcal{T}_1))}{2 \cdot g(E(\mathcal{T}_2))}.$$

This induces that by using the simple selection probability we wrongly conclude that there are twice as many triangulations with five vertices as there are in reality.

As next step we give the general formula for calculating the exact selection probability:

$$S_{\text{exact}}(\mathcal{T}_1 \xrightarrow{d-k+1 \rightarrow k+1} \mathcal{T}_2) = \frac{1}{d+1} \cdot \frac{|\{\sigma_k \in \mathcal{T}_1 \mid \sigma_k \text{ induces } \mathcal{T}_1 \rightarrow \mathcal{T}_2\}|}{N_k} \quad (4.11)$$

Calculating this selection probability has two disadvantages compared to (4.10): On the one hand, this exact selection probability depends not only on the type of the flip, but also on the actual flip. On the other hand and even worse, for calculating this selection probability for every k -simplex of the triangulation it has to be checked whether the induced flip leads to a triangulation isomorph to \mathcal{T}_2 , which scales with the squared system size (for every simplex the whole triangulation has to be compared).

The difference between exact and simple selection probability does not only occur in small triangulations, and the error resulting if using simple



selection probability is not bounded. Consider for example the abstract simplicial complex

$$\mathcal{K} = \{\{0\}, \{1\}, \emptyset\} \star \{\{2, 3\}, \{3, 4\}, \dots, \{n+1, 2\}, \{2\}, \{3\}, \dots, \{n+1\}, \emptyset\}$$

which is a ring consisting of n vertices, where every vertex of the ring is additionally connected with two external vertices, so there are in total $n+2$ vertices and $3n$ edges. \mathcal{K} has a geometric realization that is homeomorphic to \mathbb{S}^2 , so it can be used for a triangulation \mathcal{T} of \mathbb{S}^2 . The simple probability for selecting a certain $\mathcal{T} \xrightarrow{2 \rightarrow 2} \mathcal{T}'$ Pachner move is

$$S_{\text{simple}}(\mathcal{T} \xrightarrow{2 \rightarrow 2} \mathcal{T}') = \frac{1}{3} \cdot \frac{1}{3n} \Rightarrow \frac{S_{\text{simple}}(\mathcal{T} \xrightarrow{2 \rightarrow 2} \mathcal{T}')}{S_{\text{simple}}(\mathcal{T}' \xrightarrow{2 \rightarrow 2} \mathcal{T})} = 1,$$

independent of the actual move. But in fact there are only two triangulations that can be reached from \mathcal{T} doing a $(2 \rightarrow 2)$ -Pachner move: Triangulation \mathcal{T}_1 originates from a flip of one of the $2n$ edges $\{0, i\}$ or $\{1, i\}$ (with $2 \leq i \leq n+1$), and triangulation \mathcal{T}_2 originates from a flip of one of the n edges $\{i, i+1\}$ (with $2 \leq i \leq n+1$ and $2 \equiv n+2$). The respective inverse flips are generated only by one edge, so the ratios of the selection probabilities are

$$\begin{aligned} S_{\text{exact}}(\mathcal{T} \xrightarrow{2 \rightarrow 2} \mathcal{T}_1) &= \frac{1}{3} \cdot \frac{2n}{3n} & S_{\text{exact}}(\mathcal{T}_1 \xrightarrow{2 \rightarrow 2} \mathcal{T}) &= \frac{1}{3} \cdot \frac{1}{3n} \\ \Rightarrow \frac{S_{\text{exact}}(\mathcal{T} \xrightarrow{2 \rightarrow 2} \mathcal{T}_1)}{S_{\text{exact}}(\mathcal{T}_1 \xrightarrow{2 \rightarrow 2} \mathcal{T})} &= 2n \\ S_{\text{exact}}(\mathcal{T} \xrightarrow{2 \rightarrow 2} \mathcal{T}_2) &= \frac{1}{3} \cdot \frac{n}{3n} & S_{\text{exact}}(\mathcal{T}_2 \xrightarrow{2 \rightarrow 2} \mathcal{T}) &= \frac{1}{3} \cdot \frac{1}{3n} \\ \Rightarrow \frac{S_{\text{exact}}(\mathcal{T} \xrightarrow{2 \rightarrow 2} \mathcal{T}_2)}{S_{\text{exact}}(\mathcal{T}_2 \xrightarrow{2 \rightarrow 2} \mathcal{T})} &= n \end{aligned}$$

so the errors in the ratios obtained by using simple selection probability are $2n$ for $\mathcal{T} \rightarrow \mathcal{T}_1$ and n for $\mathcal{T} \rightarrow \mathcal{T}_2$.

There are two strategies for handling the difficulties introduced by calculating the exact selection probability. The first one is to examine the phase space and find regions where triangulations with symmetries (which produce deviations between simple and exact selection probability) are rare compared to unsymmetrical ones. We will see later that in all considered cases the ratio of symmetric triangulations with respect to all triangulations approaches 0 if one increases the number of maximal simplices, so the error if using simple selecting probability vanishes for large triangulations. The



calculation of the density of states can then be split into two parts, one part is limited only to small triangulations and uses the exact selection probability, the other ranges over all triangulations and uses the simple selection probability. These two density of states can than be glued together using a suitable normalization.

The second strategy to handle the problems occurring if using the exact selection probability is to accelerate its calculation by efficiently testing triangulations for isomorphisms. Naively, for two triangulation $\mathcal{T}_{1,2}$ that are based on simplicial complexes $\mathcal{K}_{1,2}$ w.l.o.g. on the set $\{1, 2, \dots, n\}$, one has to check for every of the $n!$ permutations $\pi \in S_n$ whether it is a simplicial map. Because one can find invariants of vertices which have to be conserved by the permutation, for example the number of maximal simplices incident with each vertex, most permutations can be excluded before, So on the one hand one can exclude an isomorphism between triangulations if the set of vertex invariants does not match, one the other hand we can reduce the number of permutations that needed to be checked. Consider, e.g., the simplicial complexes

$$\begin{aligned} \mathcal{K}_1 &= \{\{0, 1, 3\}, \{0, 1, 4\}, \{0, 2, 4\}, \{0, 2, 3\}, \{1, 2, 3\}, \{1, 2, 4\}\} \cup \text{subsimpl.} \\ \mathcal{K}_2 &= \{\{0, 2, 3\}, \{0, 2, 4\}, \{0, 3, 4\}, \{1, 2, 3\}, \{1, 2, 4\}, \{1, 3, 4\}\} \cup \text{subsimpl.} \end{aligned}$$

For \mathcal{K}_1 , the vertices 3 and 4 are incident with three maximal simplices, whereas the vertices 0, 1 and 2 are incident with 4 maximal simplices. The vertex invariants match, because for \mathcal{K}_2 , the vertices 0 and 1 are incident with three maximal simplices, whereas the vertices 2, 3 and 4 are incident with 4 maximal simplices. But one has to check not all $5! = 120$ permutations of S_5 , but only the $2! \cdot 3! = 12$ permutations π with $\pi(\{3, 4\}) = \{0, 1\}$ and $\pi(\{0, 1, 2\}) = \{2, 3, 4\}$. In this thesis we use even more complicated vertex invariants, namely the number of incident maximal simplices together with the set of numbers of incident maximal simplices of the nearest neighbors of the vertices, so the size of the permutations that need to be checked reduces drastically.

In fact, throughout this thesis we use both strategies at the same time, since they can be used independently.



4.2 Counting triangulations of two-dimensional manifolds

As already mentioned in the introduction of this chapter, triangulations of manifolds provide a standard method of discretizing them and a possibility to quantize spacetime. They are used in the simplicial quantum gravity models of dynamical triangulations [13], the causal version thereof [38], as well as in spin-foams [352]. For the simplicial quantum geometry models it is crucial to know the scaling of the number of triangulations in terms of the system size, because on the one hand the statistical models are only well-defined if there exists an exponential scaling, and on the other hand the scaling constant determines the value of the coupling constant to obtain a phase transition necessary for results independent of the introduced discretization scale [13, 38].

For rooted triangulations of the 2-sphere it is well-known that the number scales $\propto \sqrt{256/27^m}$, with m being the number of triangles [398]. A triangulation is rooted by marking some vertex as well as some adjacent edge and face as special in order to break symmetry and to simplify the counting procedure. For standard triangulations the same result was obtained later by proving that the ratio of triangulations possessing any non-trivial symmetry vanishes for large triangulations [399]. For other surfaces with different genus or orientability, like the torus or the projective plane, no asymptotic numbers are known, neither for the rooted nor for the default, unrooted case.

For simplicial quantum gravity, triangulations of arbitrary surfaces are important, because the models are not restricted to a certain topology of the underlying manifold, but they are also an object of study in other branches of physics: Since every graph is embeddable into a surface with arbitrary high genus, and triangulations are the maximal embeddable graphs for the respective surfaces (every insertion of an edge would violate the embeddability into the respective surface), they are an important tool in graph and network theory [47, 52, 259]. Furthermore, critical properties of statistical systems defined on quantum surfaces or triangulated manifolds are sometimes easier to solve than on Euclidean lattices, but can be related to these using the KPZ-formula [146, 184, 254].

Using lexicographic enumeration it is possible to exactly count triangulations of orientable and non-orientable surfaces for small genus $g \leq 6$ and small number of vertices $v \leq 23$ [103, 379, 380]. For bigger genera or larger triangulations this method does not give results in any reasonable



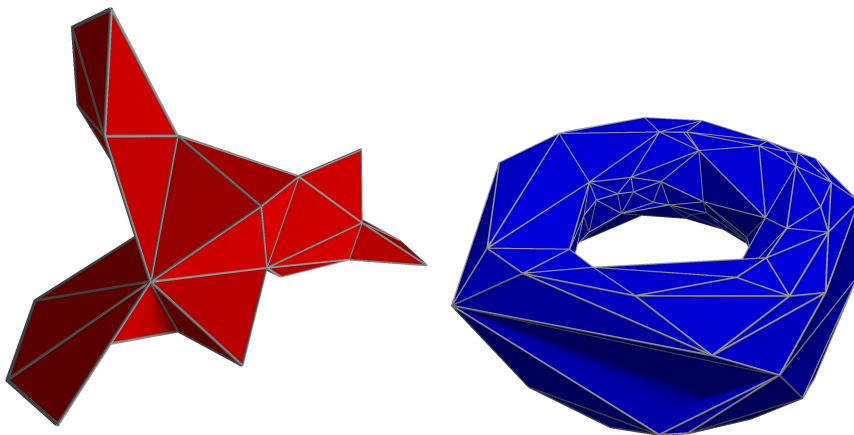


Figure 4.8: Examples for triangulations of surfaces with low genus. (Left, red) Triangulation of the 2-sphere with $m = 50$ maximal simplices. (Right, blue) Triangulation of the torus (orientable surface with genus $g = 1$ with $m = 200$ maximal simplices).

computation time.

In contrast to triangulations, the asymptotic behavior of (triangular) maps on surfaces is far better understood. A triangular map is a graph drawn on a surface so that each face is a triangle, the main difference to triangulations is that triangular maps allow for digons, multiple edges or loops (depending on the exact definition). One can show that the asymptotic number $T(k, h)$ (orientable) and $P(k, h)$ (non-orientable) of certain classes of maps on arbitrary surfaces has the form [182]

$$\begin{bmatrix} T(k, h) \\ P(k, h) \end{bmatrix} = \alpha \begin{bmatrix} t_h \\ p_h \end{bmatrix} (\beta k)^{5(h-1)/2} \cdot \gamma^k \quad (4.12)$$

where k is the number of edges and $h = g$ (orientable) respectively $h = g/2$ (non-orientable) is the type of the surface. The constants t_h and p_h do only depend on h and not on the class of maps that are counted, they were calculated in [76] using a recursion relation obtained in [194]. The numbers α , β and γ depend on the class of maps, one finds e.g. $\gamma = 12$ for all maps [75] or $\gamma = 2^{2/3}\sqrt{3}$ for triangular maps [183].

In this section we numerically approximate the number of surfaces triangulation in terms of the genus g and the number of triangles m using the Wang-Landau algorithm [406, 407] for several orders of magnitude in g and m . A similar version of this method was used in Secs. 3.2 and 3.2 to



approximate the number of lattice triangulations. We are able to extract the asymptotics for the number of triangulations of arbitrary surfaces for the first time in literature and find an exponential growth that coincides with the one found for spheres in [399]. Additionally, we determine the sub-exponential corrections similar to Eq. (4.12), which are a valuable hint for mathematicians proving the exact asymptotics for the number of surface triangulations. The presented calculations are not limited to estimating the total number of surface triangulations, but could also be used for estimating the asymptotics of the cardinality for certain subclasses of these triangulations. A possible application can be estimating the asymptotic number of irreducible triangulations, which are triangulations without contractible edges (see Ref. [63] for detailed definition, and Ref. [379] for enumerations of small irreducible triangulations). Furthermore, our method can also be applied to k -equivelar or k -covered triangulations, where in the former every vertex has degree k and in the latter there is at least one vertex with degree k (see Refs. [287,310] for detailed discussion and numbers for few vertices), and to much more different subclasses of triangulations.

4.2.1 Setup and methods

The topology of surfaces is characterized only by their Euler characteristic (integrated curvature) and whether they are orientable [101], so we have to construct surface triangulations with given genus and orientability and given number of triangles as initial configurations for the Monte Carlo algorithm. A triangulation of the sphere is given by the boundary of a 3-simplex. To create triangulations of orientable and non-orientable surfaces of arbitrary genus one needs triangulations of torus \mathbb{T} (orientable surface with $g = 1$), of the projective plane \mathbb{P} (non-orientable surface with $g = 1$) and the connected sum $\#$. A (non-)orientable surface with genus g can then be constructed by taking the g -fold connected sum $\mathbb{T}\#\mathbb{T}\#\dots\#\mathbb{T}$ ($\mathbb{P}\#\mathbb{P}\#\dots\#\mathbb{P}$) of the torus (projective plane). The connected sum of two triangulated surfaces can be constructed easily by removing a triangle from each triangulation and gluing the boundary together.

To create then a triangulation with the correct number of maximal simplices, we then use the three Pachner moves in two dimensions (insertion, removal and diagonal edge flip, compare Sec. 4.1.2. Note that there is a lower bound on the number of vertices or triangles necessary to triangulate a surface with given genus [215,234,346], so it is not possible to create arbitrary small triangulations for a given g . If one has obtained a triangulation with the desired topology and number of triangles, for the Wang-Landau



algorithm (see Sec. 2.2.2) one can restrict to the diagonal edge flips, because are ergodic for the subset of triangulations with same number of vertices v , if choosing v high enough [247, 309].

There are two different questions that should be addressed in this section, each requiring different methods. The first one is to estimate numerically the number of small triangulations, i.e., triangulations with few vertices or triangles. Therefore one needs to know or to calculate the normalization factor to scale the DOS that was calculated by the Wang-Landau algorithm. Without any further analysis it is only possible to give the exact number for sphere (orientable surface with genus $g = 0$), there is only the triangulation with four vertices having four triangles that is the boundary of the 3-simplex, thus for other genera we extend the energy and introduce a reference bin as described in Sec. 2.3.3.

The second question address in this section is to estimate the asymptotics of large triangulations, i.e., triangulations with lots of vertices or triangles. Here, instead of using the number $N(m, g)$ of triangulations, we instead calculate the entropy density $\kappa_c(m, g)$ defined by

$$\kappa_c(m, g) := m^{-1} \log N(m, g). \quad (4.13)$$

By using the entropy density we can use directly the output of the WL-algorithm, which is the logarithmic DOS, and cancel the normalization factor. It is also a common quantity discussed in literature [112, 238, 253] and corresponds to the value of the DT and CDT coupling constant for obtaining scale invariance [13, 38]. In Fig. 4.9 a comparison between our calculations and results obtained by lexicographic enumeration for small triangulations [380] shows excellent agreement and justifies our method.

Due to the diagonal-edge flips being ergodic for large enough surface triangulations it is enough to calculate the density of states in an interval $[m - 2, m + 2]$ to obtain the entropy density κ_c by

$$\kappa_c(m) = \frac{1}{8} \cdot \log \frac{g(m + 2)}{g(m - 2)}, \quad (4.14)$$

using the assumption that $\kappa_c(m \pm 2) \approx \kappa_c(m)$, which is valid for large m . Choosing this small interval of calculations, the calculation speeds up drastically compared to calculating the whole DOS using the Wang-Landau algorithm, because calculation time scales with the number of bins, as derived in Sec. 2.3.2.

As already described in Sec. 4.1.4, for fulfilling the detailed balance condition in the Wang-Landau algorithm and to correctly calculate the transition



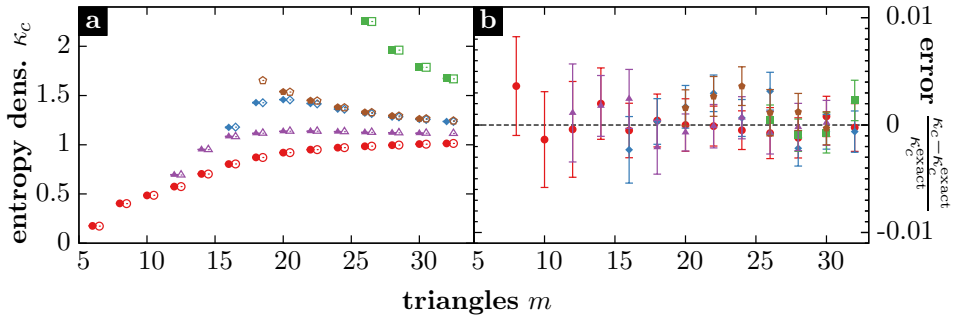


Figure 4.9: Comparison of the exact entropy density from [380] and our numerical calculations. (a) Entropy density $\kappa_c(m, g)$ in terms of the number of triangles m for orientable surfaces ($g = 0$ ●, $g = 1$ ◆, $g = 2$ ■) and non-orientable surfaces ($g = 1$ ▲, $g = 2$ ●). Our numerical data is plotted with filled symbols, the exact values are plotted with empty symbols and are shifted slightly to the right to resolve these points. (b) Relative error $\kappa_c(m, g)/\kappa_c^{(\text{exact})}(m, g) - 1$ of numerical data with respect to the exact values.

probabilities, one has to calculate for each flip the ratio of selection probabilities of the flip and the inverse flip. Assuming that the triangulation has no special symmetries, the selection probabilities can be calculated in terms of the current simplex numbers and their change induced by the flip using Eq. (4.10). However, there are symmetric triangulations which make it necessary to check whether there are other flips leading to an isomorphic triangulation (these flips are then equivalent), the same for the inverse flip, in order to calculate the exact ratio of selection probabilities using Eq. (4.11). These isomorphism checks increase the computation time needed for one step drastically. But fortunately, as depicted in Fig. 4.10, the deviations of the exact (with isomorphisms) calculated and the simplified calculations are negligible for triangulations with $m > 30$. These results are comparable with these of [343] on the level of maps, where it was shown that almost all maps do not possess intrinsic symmetries, which implies in our notion that simplified and exact selection probability match. Note that for approximately counting the number of small triangulations we in fact have to use the slow but exact selection probability Eq. (4.11) in order to get correct results.

Throughout our Wang-Landau simulations we start with the modification factor $m_0 = \exp(1)$ and decrease it by $m_{i+1} = m_i^{0.9}$ till the final modification factor $m_f = \exp(10^{-8})$. This choice of the modification factor is more careful than the original choice proposed in Refs. [406, 407], but it ensures a small



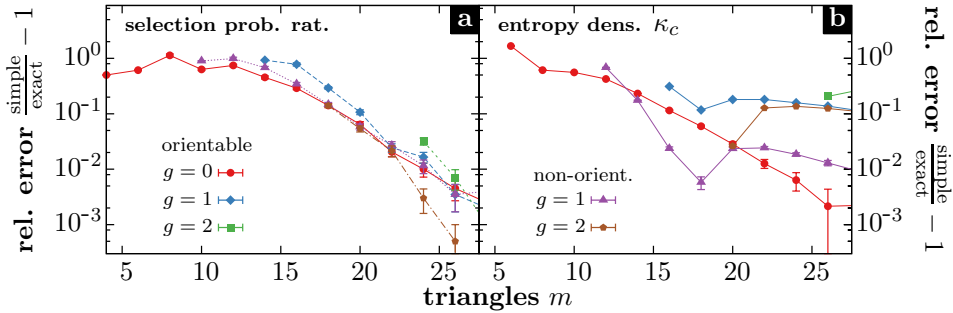


Figure 4.10: Influence of using the simplified selection probability not taking into account isomorphy. (a) Relative error of the selection probability factors for orientable ($g = 0$ ●, $g = 1$ ◆, $g = 2$ ■) and non-orientable ($g = 1$ ▲, $g = 2$ ★) surfaces in terms of the number of triangles. (b) Relative error of the entropy density.

statistical error and better simulational results.

In Fig. 4.11 the course of a Wang-Landau simulation in terms of the modification factor is displayed for estimating the asymptotic number of triangulations of the 2-sphere. We will see in Sec. 4.3.2 that using the standard flatness criterion $\text{flat}H(m) \leq 0.8$ as requirement for decreasing the modification factor can lead to wrong results, so we will propose an alternative flatness criterion (4.30) that starts tightly and will be relaxed towards the end of the simulation. We checked also for the counting of triangulations of 2-manifolds whether there is a similar problem and did calculations with the alternative flatness criterion (4.30) also displayed in Fig. 4.11, but no similar problems were found. In fact the resulting error using the alternative flatness criterion is a bit smaller than using the standard, constant flatness criterion, but the necessary simulation time grows. Since we are not limited by the simulation time but merely by the memory usable, we used the alternative flatness criterion in our calculations to be absolutely sure to eliminate this possible error.

4.2.2 Approximative counting of small surface triangulations

In this section the number of triangulations of surfaces with arbitrary orientability and genus is numerically estimated for small number v of vertices, which can bijectively mapped to the number m of maximal simplices using the Euler characteristic or the genus of the surface. (In fact we use here the number v of vertices to easily compare with existing results). Calculating the exact number is possible using lexicographic enumeration as presented



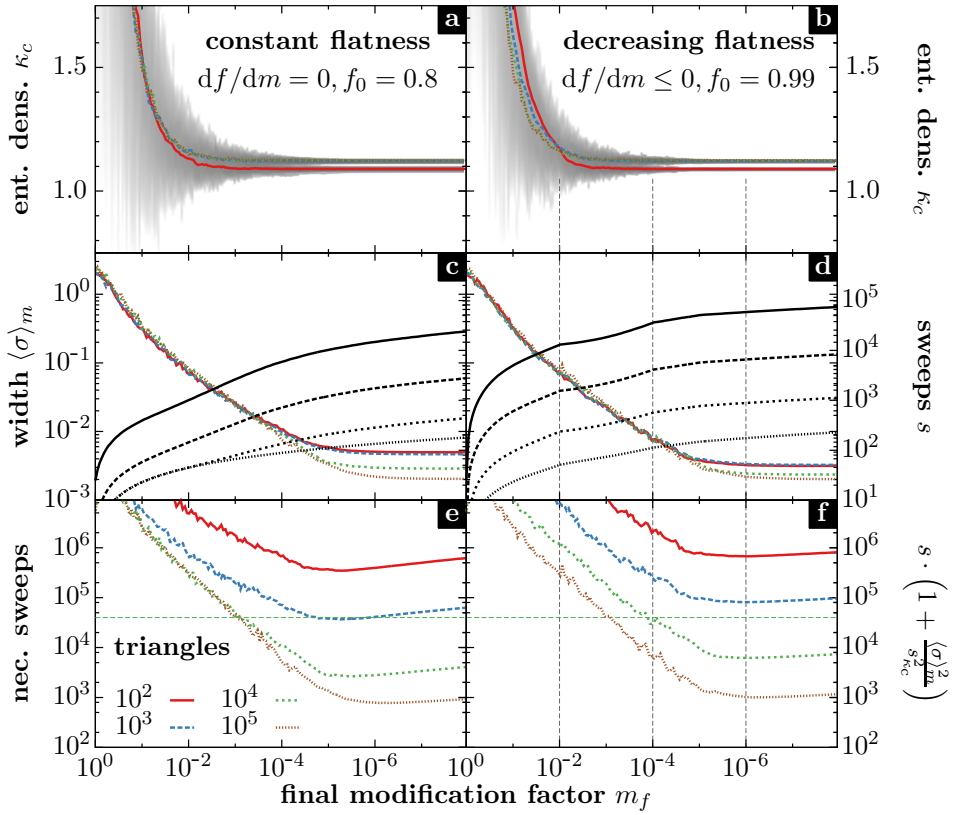


Figure 4.11: Alternative flatness criterion (4.30) for WL-simulations on triangulated surfaces.

Characteristic plot of Wang Landau simulations for two-dimensional topological triangulations of the sphere for 10^2 (red), 10^3 (blue), 10^4 (green) and 10^5 (brown) triangles. The left column (a, c, e) shows the standard Wang-Landau simulation with the decrease $f_{i+1} = f_i^{0.9}$ of the modification factor and the flatness criterion $\text{flat}(H) \geq 0.8$. The right column (b, d, f) shows a modified Wang-Landau simulation with the same decrease of the modification factor, but an alternative flatness criterion (4.30) which is very rigorous for large modification factors and more relaxed for small ones. (a,b) Average value and distribution of the entropy density κ_c in terms of the decreasing modification factor. (c,d) Standard deviation of the distribution of κ_c (color, left axis) and mean number of sweeps (black, right axis) in terms of the modification factor. (e,f) Necessary number of sweeps to calculate κ_c with an error of less than 10^{-3} .



in [379], but this method is limited to a rather small triangulations and genera. Using our approximative counting scheme allows to increase the accessible system size by several order of magnitudes, but unfortunately it is not possible to access higher genera than using the lexicographic enumeration.

As explained already in Sec. 2.3.3, multicanonical algorithms as the Wang-Landau algorithm estimate the density of states (DOS) only up to a common normalization factor. This normalization factor can be determined by a known number of states in a certain macrostate. For counting triangulations of surfaces this is the case for the triangulations of the sphere (orientable surface of genus $g = 0$), because there is only one triangulation with $m = 4$ triangles, which is the boundary of a 3-simplex. For surfaces with different genus or orientability a similar result is not available a priori, only the lexicographic enumeration in [379] can provide the number of triangulations with minimal number of triangles for the different genera. In order to check the approximate counting algorithm proposed in Sec. 2.3.3, we did not use these numbers of minimal triangulations in our calculations, but used an extended an extended energy to be able to compare these numbers with the exact calculations.

The relative error $N(v)/N_{\text{exact}}(v) - 1$ of the number of triangulations $N(v)$ calculated using our approximative counting scheme with respect to the exact number $N_{\text{exact}}(v)$ in terms of the number v of vertices is displayed in Fig. 4.12. One can see in almost all cases a deviation from the exact result less than 0.01.

In Fig. 4.13 the parameters of triangulations accessible with our algorithm are displayed and compared to the set of parameters where results from lexicographic enumeration are known. We can outperform the lexicographic enumeration especially with respect to the number of vertices of the triangulation. In principle we can obtain the number of triangulations for surfaces with up to at least up to $m = 10^5$ without any problems on a standard desktop computer (by merging results with exact selection probability ratio (4.11) for small triangulations with results for simple selection probability (4.10) for larger triangulations, as used for calculating the asymptotics in the next Sec. 4.2.3). For larger number of triangles we can access the number of triangulations with higher computational effort. In fact we are at present not limited by the computing time, but by the size of the memory needed for storing the single triangulation.

The lower boundary of accessible vertex numbers v is given by the Hea-



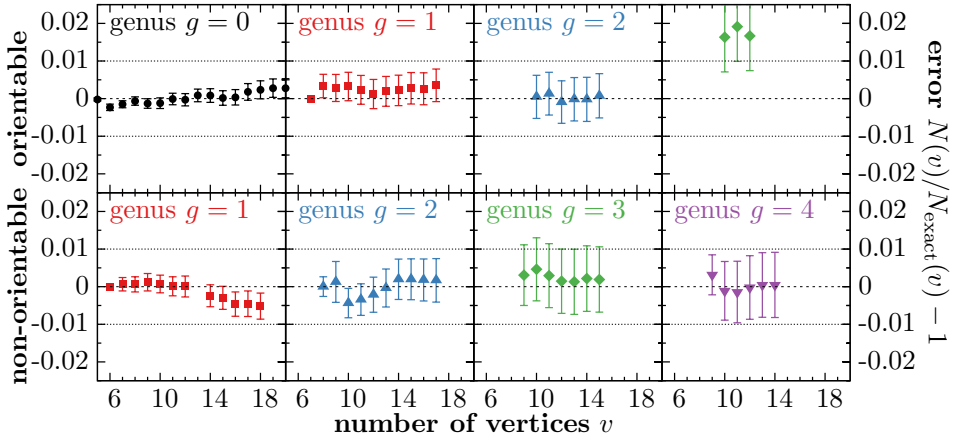
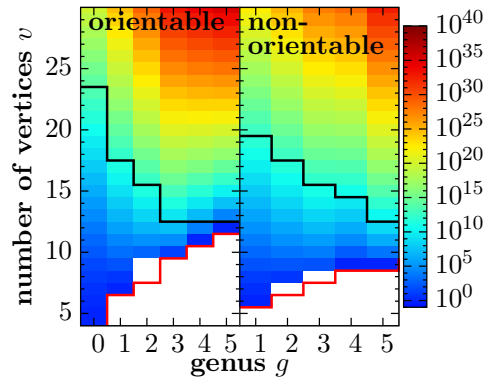


Figure 4.12: Comparison of the number of small surface triangulations $N(v)$ calculated using the approximative counting algorithm with the exact results $N_{\text{exact}}(v)$ obtained by lexicographic enumeration in [379] in terms of the number v of vertices of the triangulation for genera $g = 0$ (\blacksquare), $g = 1$ (\blacksquare), $g = 2$ (\blacktriangle), $g = 3$ (\blacklozenge) and $g = 4$ (\blacktriangledown). The upper row displays the errors for orientable surfaces, the lower row for non-orientable surfaces.

Figure 4.13: Number of surface triangulations with respect to the number of vertices and the genus of the surface for orientable (left) and non-orientable (right) surfaces displayed as a logarithmic colorplot. The red lines corresponds to Heawoods bound (4.15), which specifies the minimal number of vertices necessary to triangulate a surface of given genus. The black lines is the upper bound of the region where the number of triangulations is accessible using lexicographic enumeration [379].



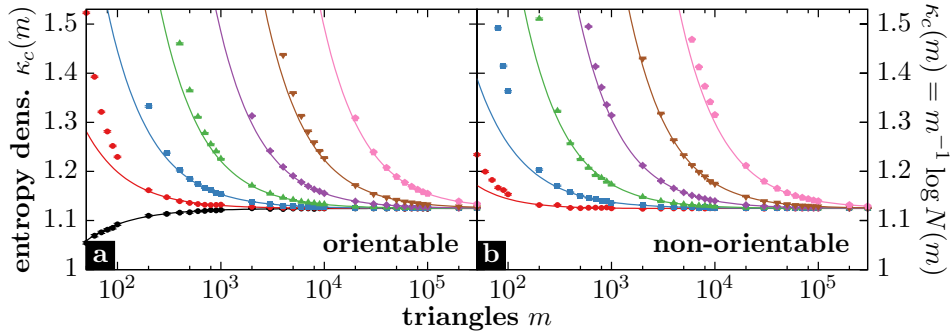


Figure 4.14: Entropy density in terms of the number of triangles. Entropy density for triangulations of orientable (a) and non-orientable (b) surfaces in terms of the number of triangles m for genus $g = 0$ (\circ) (only orientable), $g = 3$ (\bullet), $g = 10$ (\blacksquare), $g = 30$ (\blacktriangle), $g = 100$ (\blacklozenge), $g = 300$ (\blacktriangledown) and $g = 1000$ (\blacklozenge). The lines are fits of (4.17) with respect to $a(g)$ and $b(g)$.

wood bound [215]

$$v \geq \frac{1}{2} \left(7 + \sqrt{49 - 24\chi} \right), \quad (4.15)$$

where χ is the Euler characteristic. This bound is proven to be tight for orientable surfaces with genus $g \neq 2$ [346], and for non-orientable surfaces with genus $g \neq 2, 3$ [234].

Unfortunately it is not possible to approximately count triangulations with higher genera than it is possible with lexicographic enumeration. This is because of the Wang-Landau algorithm getting stuck already in the first modification factor, or a few modification factors later. We conjecture that this is because the number of triangulations with minimal vertices grows fast, which make it difficult to sample the minimal energy bin correctly. If using only a few reference triangulations, the entropy difference between the reference and the non-reference triangulations gets large, and it is unlikely to find reference triangulations at all in the simulation. If using more reference triangulation, in each step going to the macrostate with minimal vertices the resulting triangulation has to be compared with a huge number of reference triangulations, which increases the necessary computation time for one step. Even worse, the system size of the minimal triangulations grows as \sqrt{g} with the genus, and the time for calculating the exact ratio of the selection probabilities (4.11) grows with the factorial of the system size.



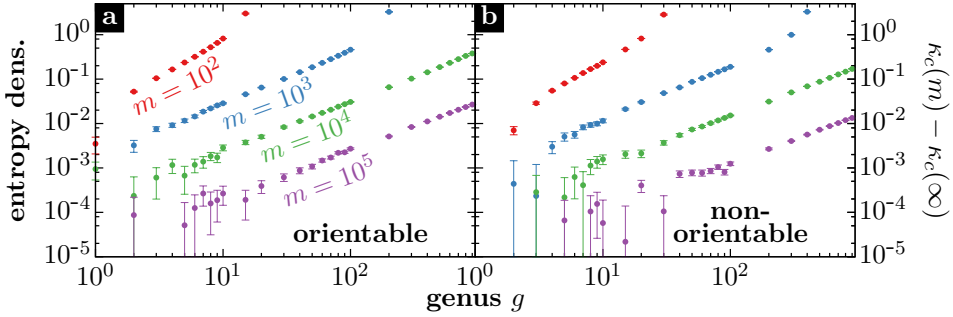


Figure 4.15: Entropy density in terms of the genus of the surface.

Deviation of the entropy density from the limiting value $\kappa_c^{(\infty)}$ for triangulations of orientable (a) and non-orientable (b) surfaces in terms of the genus g for $m = 10^2$ (\bullet), $m = 10^3$ (\circ), $m = 10^4$ (\circ), and $m = 10^5$ (\circ) triangles.

4.2.3 Asymptotics of the entropy density for $m \rightarrow \infty$

As explained previously, for calculating the entropy density (4.14) $\kappa_c(m, g)$ it is not necessary to calculate the common normalization factor of the density of states. So the energy has not to be extended with a reference bin, and we can limit the interval of accessible energies for the algorithm to shorten the computation time.

We calculated the entropy density (4.14) $\kappa_c(m, g)$ for orientable and non-orientable surface triangulations up to genus $g_{\max} = 1000$ and up to $m_{\max} = 10^7$ triangles using 400 independent Wang-Landau simulations each. In Figs. 4.14 and 4.15 $\kappa_c(m, g)$ is displayed for fixed genus and for fixed number of triangles in terms of the other variable.

Inspired by the asymptotic enumeration results for triangulations of the 2-sphere and for maps on arbitrary surfaces we assume that the number of triangulations behaves as

$$N(m, g) = \bar{a}(g) \cdot \bar{b}(g)^m \cdot m^{\kappa_c^\infty(g)}, \quad (4.16)$$

which implies the following relation for the entropy density (4.14)

$$\kappa_c(m, g) = a(g) \cdot \frac{1}{m} + b(g) \cdot \frac{\log(m)}{m} + \kappa_c^\infty(g). \quad (4.17)$$

Considering Fig. 4.14 we find that the constant term $\kappa_c^\infty(g)$ in (4.17) does not depend on the genus g and on whether the surfaces is orientable, furthermore we find excellent agreement with the theoretical value of $\log(\sqrt{256/27}) \approx 1.1247$ obtained for triangulations of the sphere [399].



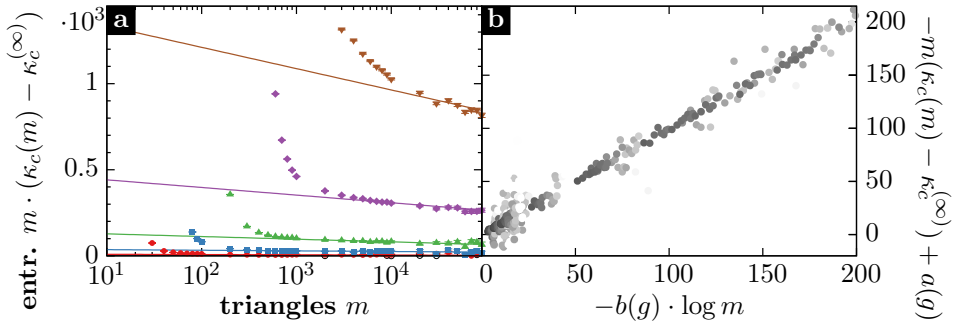


Figure 4.16: Scaling of the entropy density.

(a) Plot of the entropy $m \cdot \kappa_c(m)$ in terms of the logarithm of the number m of triangles used to extract the constants $a(g)$ and $b(g)$ by fitting a straight line. The data points are the same as used in Fig. 4.14(b) Collapse of the data points, the points are darker for smaller error, only points with $\kappa_c(m)/\kappa_c^\infty < 1.05$ are plotted.

By inspecting $\kappa_c(m, g = 1)$ one finds that for $g = 1$ the entropy density is approximately constant in terms of m , which implies the conjecture that $b(g) \propto b_1 \cdot (g - 1)$ without any constant term, in agreement to [399] and [76], where $b_1 = 7/2$ for triangulations of the 2-sphere and $b_1 = 5/2$ for triangular maps on surfaces.

To obtain the constants $a(g)$ and $b(g)$ we rescale the entropy density (4.17) so that

$$m \cdot [\kappa_c(m, g) - \kappa_c^\infty(g)] = a(g) + b(g) \log m.$$

For every genus g both constants can then be determined by a linear fit of the rescaled entropy density in terms of $\log m$. In Fig. 4.16a the rescaled entropy density is plotted for orientable surfaces of different genera, one can see an excellent agreement with the proposed linear dependency in terms of $\log m$ for sufficient triangles. Using the fitted constants all obtained data points can be brought to a collapse as depicted in Fig. 4.16b.

Having fitted $a(g)$ and $b(g)$ for all considered genera of orientable and non-orientable surfaces, one can access numerically the scaling relation of both for triangulations as depicted in Fig. 4.17. The leading order $b(g) = b_1 \cdot (g - 1)$ does differ from the results for triangular maps qualitatively, we find $b_1 = -0.197 \pm 0.006$ for orientable and $b_1 = -0.102 \pm 0.004$ for non-orientable triangulations, while for triangular maps the theoretical value $b_1 = 5/2$ was found [76]. We conjecture that $b_1 = -2/5$ for orientable and $b_1 = -1/5$ for non-orientable surface triangulations, since these small integer fractions are in the 1σ bounds of the numerically obtained values.



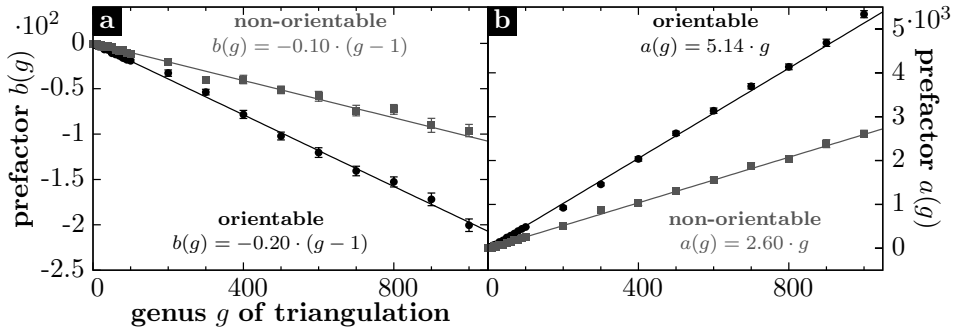


Figure 4.17: Values of the asymptotic constants a and b in terms of the genus g for orientable (\bullet) and non-orientable (\blacksquare) triangulations. The corresponding lines are linear fits.

The next-to-leading order $a(g) = (5.14 \pm 0.09) \cdot g$ (orientable) respectively $a(g) = (2.60 \pm 0.03) \cdot g$ (non-orientable) has a linear dependency on g for the considered range of genera (implying $\bar{a} \propto \exp(g)$ in (4.16)), no logarithmic correction as proposed in [76] for triangular maps is present. For both $a(g)$ and $b(g)$ one can deduce that the results for orientable and non-orientable triangulations coincide, if one does not consider the genus, but the type of the surface (which is half the genus for non-orientable surfaces).

4.2.4 Conclusion and outlook

In this section the number of triangulations of (orientable and non-orientable) surface triangulations with arbitrary genus was calculated using the Wang-Landau Markov chain Monte Carlo algorithm. Based on our results, we conjecture the following relation for the asymptotic number of surface triangulations

$$N(m, h) \rightarrow (170.4 \pm 15.1)^h m^{-2(h-1)/5} \left(\frac{256}{27}\right)^{m/2} \quad (4.18)$$

in terms of the type h of the surface, which can be concluded from the entropy density

$$\kappa_c(m, h) \rightarrow (5.14 \pm 0.09) \cdot g \frac{1}{m} - \frac{2(h-1) \log(m)}{5} \frac{1}{m} + \frac{1}{2} \log\left(\frac{256}{27}\right) \quad (4.19)$$

These quantitative results for the leading and next-to-leading order terms can be a valuable hint for mathematicians proving the exact asymptotics of the number of surface triangulations. Additionally, the numerical method



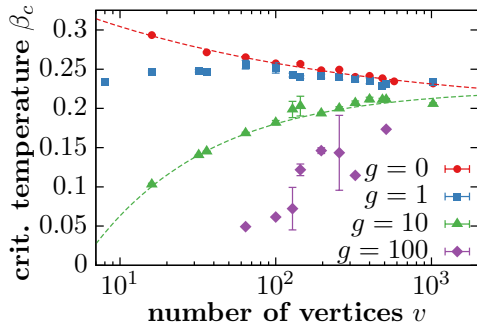


Figure 4.18: Critical inverse temperature β_c for the Ising model defined on random surface triangulations in terms of the number v of vertices for different value g of the genus of the underlying orientable surface. One finds a similar dependence of the curve on the genus of the surface as for the number of triangulations in Fig. 4.14. The dashed lines are the fits (4.21) that are inspired from the mean field solution (4.20).

presented in this paper can be directly applied to estimate the number and its asymptotics of special types of triangulations, e.g. irreducible, k -equivelar or k -covered triangulations.

Our methods and results can also be used for solving simplicial quantum gravity models like (causal) dynamical triangulations on surfaces with arbitrary genus, where the leading order term gives the value of the coupling constant necessary for obtaining scale-independent limits. Furthermore, the next-to-leading order terms can provide insights into their finite size scaling, which is important since these models are solved mainly using Monte Carlo simulations.

As a possible application we give a short outlook on the Ising model defined on such surface triangulations, as considered in Ref. [411]. As for the embedded triangulations, we assign an Ising spin to each of the vertices, and define the neighboring vertices as those that are connected with the original vertex by an edge. One of the quantities of interest is the critical inverse temperature β_c , which is displayed for orientable triangulation in Fig. 4.18. The critical inverse temperature β_c shows unexpectedly a similar behavior as the entropy density displayed in Fig. 4.14⁷.

We already calculated in Eq. (2.34) that using a mean-field solution the critical inverse temperature β_c on an arbitrary network is given by the inverse average number q of neighbors. For topological triangulations, this

⁷ Note that in Fig. 4.14 the entropy density is plotted in terms of the number m of triangles, and not in terms of the number v of vertices as in Fig. 4.18. At fixed genus g these quantities can be converted easily.



quantity is given by

$$\beta_c J = \frac{1}{q} = \frac{v}{2e} = \frac{v}{12(g-1) + 6v} \stackrel{v \rightarrow \infty}{\approx} \frac{1}{6} - \frac{12(g-1)}{v}, \quad (4.20)$$

where e is the number of edges, because every edge is common to two vertices. Since the mean-field solution breaks down near the critical point due to the correlations becoming important, as expected the numerically calculated data in Fig. 4.18 does not match Eq. (4.20). But it can be used as a hint for the actual functional dependency of the critical temperature on the genus g and on the number v of vertices. Using a least-square fit resulted in

$$\beta_c J \approx 0.20(2) - 0.190(8) \cdot (g-1)v^{-0.25(8)} \quad g = 0 \quad (4.21a)$$

$$\beta_c J \approx 0.225(5) - 0.065(9) \cdot (g-1)v^{-0.56(6)} \quad g = 10 \quad (4.21b)$$

For $g = 1$ (torus), the function is constant up to the first order in v^{-1} as predicted, for $g = 100$ there are too few data points and too large errors to get a suitable fit.



4.3 Ergodicity and extensivity of three-dimensional sphere triangulations

As already stated in the introduction of this chapter, it is crucial for simplicial quantum gravity models like dynamical triangulations (DT) [29] or causal dynamical triangulations (CDT) [38] that the number of triangulations grows at most exponentially with the number of maximal simplices (triangles in 2d, tetrahedra in 3d and 4-simplices in 4d). Faster growth implies that the partition function of these models does not possess a valid thermodynamic limit, so that the model is not well-defined. In this section we focus on the number of triangulations of the 3-sphere, which is important for 3-dimensional DT and $(3 + 1)$ -dimensional CDT. Also for other models of quantum gravity like spin-foams triangulations are an important tool for constructing discrete structures [328].

Deciding whether the number of triangulations of the 3-sphere grows exponentially or faster has also been an important and open problem in mathematics for long time [197]. For 2-spheres, already in 1980 Tutte showed that the number N of triangulations scales as $N \propto (256/27)^{m/2}$ with the number m of triangles [399], and we considered the case of arbitrary genus in the previous Sec. 4.2. For 3-spheres, neither asymptotics nor explicit bounds are known. It can be shown that there are only exponentially many of a special group, so called locally constructable (LC), of 3-sphere triangulations [147], but there are triangulations that are not LC [80]. Nevertheless, one can give the exponential bound $2^{d^2 \cdot n}$ for the number of LC triangulations of any d -manifold [80]. There are also exponential bounds for further subclasses of 3-sphere triangulations (e.g., locally constructable triangulations [80, 147], geometric triangulations [2], triangulations with a Morse function with a fixed number of critical cells [79], or melonic triangulations, which are the dominant contribution to the $1/N$ expansion in group field theory [200]).

Recent results show that N scales like $c^{v^{5/4}}$ in terms of the number v of vertices for 3-spheres [329] and for d -spheres with $d \geq 4$ [239], very recently this asymptotics were improved to be $c^{v^{(d+1)/2}}$ for odd dimensions [312]. Furthermore, there are some consideration about triangulations of the homology sphere [347] and reformulations of the problem in terms of so-called nuclei triangulations [120].

Beside the analytical treatments there are also numerical calculations searching for an exponential bound for 3- and 4-spheres [28, 44, 45, 100, 104, 111, 112], all using standard Metropolis Monte Carlo simulations [291]



4.3. Ergodicity and extensivity of three-dimensional sphere triangulations

calculating the local growth rate of the number of triangulations in the vicinity of triangulations with m_0 maximal simplices. Due to technical details of the Metropolis algorithm the action has to be modified by lowering (increasing) the external chemical potential by a constant for being above (below) the desired value of m_0 as in [44, 45, 104], or by introducing an artificial term $\propto |m(t) - m_0|^c$ as in [28, 111, 112]. These calculations claim to find that the number of simplicial 3-spheres grows exponentially with the number of simplices [44, 112], but there are diverging results for 4-spheres (Ref. [111] argues for a faster than exponential growth, Ref. [28] for exponential growth). Due to a recent (unpublished) statement by Karim Adiprasito there are only exponentially many triangulations in terms of the number of executed bistellar Pachner moves [286], so simulations using a finite number of Pachner moves can in principle make no statement about the existence of exponential bounds.

Another important question in simplicial quantum gravity addressed in this section is the ergodicity of the Pachner moves [322] that are used as elementary steps in the Markov chain Monte Carlo simulations (compare Sec. 4.1.2). Pachner moves are ergodic for partially linear (PL) manifolds [322], and for $d = 3$ every topological manifold has a unique PL structure [303], so Pachner moves are also ergodic for topological manifolds in this dimensions. (Not that this is in general not true for higher dimensional manifolds, where not every topological manifold is a PL manifold, so the Pachner moves may be not ergodic). This ergodicity results is only valid if one allows for triangulations with arbitrary many vertices or maximal simplices, but in all numerical simulations one must apply a cut on these numbers due to limited computation time or limited memory. For triangulations of the 4-sphere it was shown analytically that they are not computationally ergodic [308], i.e. that there is no recursive function that bounds the number of Pachner moves necessary for transforming one triangulation into another one. Numerical experiments showed that there is no hint for computational non-ergodicity for the 4-sphere [29], but these experiments relied on constructing triangulations from the smallest one (boundary of a 5-simplex) in terms of Pachner moves, so it is possible that this result was obtained because the simulations were near enough to this simplest triangulation.

Ergodicity of Pachner moves in S^3 has also been discussed in the mathematics before, but for a slightly more general version of triangulations, where one allows for a tetrahedron to be its own neighbor. It was shown that the number of steps for reaching the smallest possible triangulation of



S^3 is exponentially bounded [293]. Numerical experiments suggest that it is enough to increase the number of tetrahedra by two using Pachner moves to reach this ground state [106]. In this section we want to take another perspective and ask the question, whether two triangulations with m tetrahedra are connected by Pachner moves that include only triangulations with their number of tetrahedra between $m - \Delta m$ and $m + \Delta m$, so we bound the accessible range of tetrahedra numbers symmetrically from both sides.

We use the Wang Landau algorithm [406, 407] to calculate directly the number of triangulations of the 3-sphere in terms of the number v of vertices and m of tetrahedra. These calculations also give the critical coupling constant of 3d DT that has to be used for getting a reasonable continuum limit (see Sec. 5.2.1). By introducing cutoffs in m one can predict how big the interval of allowed tetrahedra must be to ensure ergodicity of the calculations. For our purposes this algorithm has the main advantage that one can calculate the density of states directly, which is basically the normalized number of states. As energy function grouping the microstates into macrostates for calculating the density of states we use either the v or m . Compared with usual methods in literature our method has the advantage that one does not need to introduce a certain physically motivated action, or even to modify this action unphysically to cancel the entropic force driving the simulation to triangulations with more vertices, since the algorithm ensures that each v or m is hit equally often. Despite the mentioned (unpublished) results of Adiprasito about the recognizability of non-exponential growth using simulations, our results about the scaling of the entropy density provide valuable hints for mathematicians proving such an exponential bound. Additionally, using our methods we see also an almost perfect match with other enumeration techniques for small 3-spheres, as well in the previous section with asymptotic results about 2-spheres, so there is hope that after a thorough inspection of our methods and the (unpublished) proof by Adiprasito one can yet make statements about the existence of an exponential bound, e.g., by inspecting the scaling of the entropy density in terms of the number of executed steps.

4.3.1 Calculating entropy density with the Metropolis algorithm

The entropy density of three- and four-dimensional spheres was calculated in the literature before using the Metropolis algorithm in the context of dynamical triangulations, which will be described in detail in Sec. 5.2. The



4.3. Ergodicity and extensivity of three-dimensional sphere triangulations

common procedure used e.g. in [28, 111, 112] is to extend the action

$$S_{\text{DT}}(\kappa_d, \kappa_{d-2}, \mathcal{T}) = \kappa_d N_d(\mathcal{T}) - \kappa_{d-2} N_{d-2}(\mathcal{T})$$

(that will be derived in detail in Sec. 5.2.2) within the partition function

$$Z_{\text{DT}}(\kappa_d, \kappa_{d-2}) = \sum_{\mathcal{T}} e^{-S_{\text{DT}}(\kappa_d, \kappa_{d-2}, \mathcal{T})} = \sum_{\mathcal{T}} \exp[-\kappa_d N_d(\mathcal{T}) + \kappa_{d-2} N_{d-2}(\mathcal{T})]$$

of dynamical triangulations (where the sum is over all possible triangulations of a given d -manifold, N_i are the number of i -simplices in the triangulation and κ_i is a coupling constant or generalized inverse temperature) with an additional term $-\gamma(N_d(\mathcal{T}) - V)^2$. Here V is the number of maximal simplices of the triangulations (volume of the triangulation) where the entropy density $\kappa_{d,c}(V)$ should be calculated, γ is an additional coupling constant and the whole term drives the system near triangulations with $N_d \approx V$. So that the modified action becomes

$$S_{\text{DT,mod}}(\kappa_d, \kappa_{d-2}, \gamma, V, \mathcal{T}) = \kappa_d N_d(\mathcal{T}) - \kappa_{d-2} N_{d-2}(\mathcal{T}) + \gamma(N_d(\mathcal{T}) - V)^2. \quad (4.22)$$

In the following we set the inverse temperature $\kappa_{d-2} = 0$ and omit the index at the inverse temperature κ_d . The number of maximal simplices will be denoted by m instead of N_d . Note that one can do these calculations and the resulting simulations also for $\kappa_{d-2} \neq 0$, which leads to similar interesting results, but not the actual entropy density or number of triangulations. For comparing with our method we only need the calculations for $\kappa_d = 0$.

Introduce the entropy density as the exponential growth rate of the number $N(m)$ of triangulations with m maximal vertices in terms of the number of maximal vertices

$$N(m) = \exp[\kappa_c(m) \cdot m] \Leftrightarrow \kappa_c(m) := \frac{\log N(m)}{m},$$

and rewrite the partition function using the density of states $g(m) \propto N(m)$, which is the (normalized) number of triangulations with m maximal simplices:

$$\begin{aligned} Z_{\text{DT,mod}}(\kappa, \gamma, V) &= \sum_{m=d+2}^{\infty} g(m) \exp[-\kappa m - \gamma(m - V)^2] \\ &= \sum_{m=d+2}^{\infty} \exp\left[(\kappa_c(m) - \kappa)m - \gamma(m - V)^2\right] \end{aligned}$$



The index c (for *critical*) in κ_c comes from the fact that naturally there is a phase transition at $\kappa = \kappa_c$, where the physical phase does only exist for $\kappa \geq \kappa_c$. For $\kappa < \kappa_c$ the system would be driven entropically to an infinite number m of maximal simplices.

Now assume that the entropy density $\kappa_c(m)$ is slowly varying with m , so that one can approximate $\kappa_c(m) \approx \kappa_c$ for $m \approx V$. Assume additionally that one can replace the infinite sum in the partition function with an integral, and complete the square to get

$$Z_{\text{DT,mod}}(\kappa, \gamma, V) = \int_{d+2}^{\infty} dm \exp \left[-\gamma \left(m - \frac{\kappa_c - \kappa + 2\gamma V}{2\gamma} \right)^2 \right] \cdot \exp \left[-\gamma V^2 + \frac{(\kappa_c - \kappa + 2\gamma V)^2}{4\gamma} \right]$$

Assuming that we can extend the lower boundary of the integral to ∞ , which is justified because the integral kernel is zero outside a certain region around $m \approx V \gg d + 2$, the integral becomes a simple Gaussian integral, resulting in the partition function

$$Z_{\text{DT,mod}}(\kappa, \gamma, V) = \sqrt{\frac{\pi}{\gamma}} \exp \left[\frac{1}{4\gamma} (\kappa_c - \kappa + 2\gamma V)^2 - \gamma V^2 \right] \quad (4.23)$$

A similar calculation can be done now for the average number $\langle m \rangle(\kappa, \gamma, V)$ of maximal simplices, resulting in

$$\langle m \rangle_{\text{mod}} = \frac{1}{Z} \int_{-\infty}^{\infty} dm' \left(m' + \frac{\kappa_c - \kappa + 2\gamma V}{2\gamma} \right) \cdot \exp^{-\gamma m'^2} \exp \left[-\gamma V^2 + \frac{(\kappa_c - \kappa + 2\gamma V)^2}{4\gamma} \right].$$

Using the expression for the partition function (4.23) one arrives at

$$\langle m \rangle_{\text{mod}}(\kappa, \gamma, V) = \frac{\kappa_c - \kappa + 2\gamma V}{2\gamma}, \quad (4.24)$$

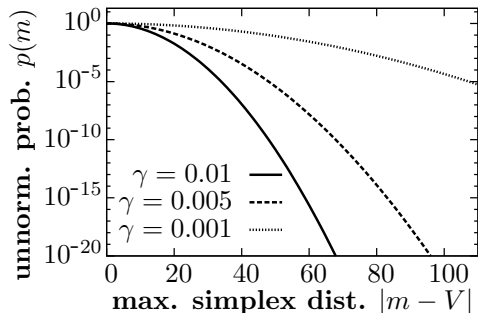
which can be used for calculating the entropy density by

$$\kappa_c = \kappa + 2\gamma (\langle m \rangle_{\text{mod}}(\kappa, \gamma, V) - V), \quad (4.25)$$

where the average number of maximal simplices $\langle m \rangle_{\text{mod}}(\kappa, \gamma, V)$ can be determined using a Metropolis simulation.



Figure 4.19: Influence of the artificially included term $-\gamma(m - V)^2$ in the action (4.22) on the probability for finding a state with $m = V \pm \Delta m$ maximal simplices. The approximate probability $\propto \exp(-\gamma(m - V)^2)$ is plotted in terms of $\Delta m = m - V$ for different values of the constant γ .



We identified that there are some problems if using this approach to determine the entropy density of topological triangulations. The first problem is that the additional term $-\gamma(m - V)^2$ in the action restricts the simulation to values of m that are in the proximity of V , as can be seen in Fig. 4.19. For the common choice of $\gamma = 0.005$ in [111, 112] and assuming that $\kappa = \kappa_c$ the probability for encountering a triangulation \mathcal{T} with $|m(\mathcal{T}) - V| > 50$ is smaller than 10^{-10} . This can lead to problems with ergodicity, because it could be possible that in order to transform two triangulations with $m \approx V$ into each other it is necessary to use Pachner moves that lead to intermediate triangulations with the number of maximal simplices far away from V . These paths would be rejected because of the additional penalty for triangulations far away from V .

The second problem is that there are a lot of assumptions and approximations for calculating the analytical correspondence between κ_c and $\langle m \rangle$. Especially the assumption $\kappa_c(m) \approx \kappa_c$ near V can cause problems. The error of this approximation can be quantified by not using a constant approximation, but a linear Taylor expansion

$$\kappa_c(m) = \kappa_c^{(0)} + \kappa_c^{(1)} \cdot (m - V) + \mathcal{O}[(m - V)^2]$$

Doing the same calculations as above leads to the expectation value

$$\langle m \rangle_{\text{mod}} = \frac{\kappa_c^{(0)} - \kappa_c^{(1)}V - \kappa + 2\gamma V}{2(\gamma - \kappa_c^{(1)})}, \quad (4.26)$$

which can be used for calculating the entropy density

$$\kappa_c(V) = \kappa_c^{(0)} = \kappa + 2\gamma(\langle m \rangle_{\text{mod}} - V) + \kappa_c^{(1)}(V - 2\langle m \rangle_{\text{mod}}). \quad (4.27)$$

Using $\langle m \rangle_{\text{mod}} \approx V$ one can deduce that for $\kappa_c^{(1)} > 0$ (which is found in the calculations of the considered paper, and also later in our calculations) the



entropy density calculated using the constant approximation overestimates the actual value by approximately $\approx \kappa_c^{(1)}V$. The first order term $\kappa_c^{(1)}$ could even be calculated using Metropolis simulations by measuring the variance $\text{Var}(m)$ of the number of maximal simplices, which can also be determined using the Gaussian integrals as above to be $\text{Var}(m) = 1/2(\gamma - \kappa_c^{(1)})$, so the entropy density can be calculated as

$$\kappa_c(V) = \kappa_c(0) = \kappa + 2\gamma(\langle m \rangle - V) + \left(\gamma - \frac{1}{2\text{Var}(m)} \right) \cdot (V - 2\langle m \rangle). \quad (4.28)$$

If one uses the constant approximation $\kappa_c^{(1)} \approx 0$, the variance in this approximation is $\text{Var}(m) = 1/2\gamma$. This could be checked in the Metropolis simulation done in the papers [28, 111, 112] to verify the validity of the method, but was inattentively not done.

Using the new method developed in this thesis we can on the one hand calculate the full functional form (including derivatives as $\kappa_c^{(1)}$) of the entropy density from scratch, because the density of states $g(m)$ can be calculated directly. On the other hand we can estimate the error of the Metropolis method with modified action used in Refs. [28, 111, 112].

4.3.2 Calculations of the entropy density using multicanonical methods

In the previous section it was discussed which problems can occur if estimating the entropy density of triangulations using the Metropolis algorithm. To overcome this problem, we use the same approximative counting algorithm based on Wang Landau simulations [406, 407] as for lattice triangulations in Secs. 3.2 and 3.3, and for two-dimensional topological triangulations in Sec. 4.2. For details about the Wang-Landau simulation refer to Sec. 2.2.2.

The annealing procedure towards the direct density of states can take a lot of computation time, especially if the number of energy bins is high. So we do not simulate the whole DOS at once, but within certain intervals $[m - \Delta m, m + \Delta m]$ and combine the DOS of these intervals to obtain the DOS of the whole range of maximal simplices. For this procedure it is of course necessary that the system is ergodic within the single intervals $[m - \Delta m, m + \Delta m]$, otherwise not all configurations can be reached from every other triangulations using steps within the intervals. This ergodicity will be examined in this section.

Having calculated the DOS using the Wang-Landau algorithm, $\kappa_c(m)$ can



be calculated using the density of states $g(m)$ by

$$\kappa_c(m) \approx \frac{1}{2} [\log(g(m+1)) - \log(g(m-1))]. \quad (4.29)$$

This is good since the actual quantity considered in the Wang-Landau algorithm is the logarithm of the density of states, and due to the subtraction (which is a division on the level of the density of states) the unknown normalization constant cancels.

For using Markov chain Monte Carlo simulations the ratio of the selection probabilities of a step and its inverse step (4.11) must be known. As explained in Sec. 4.1.4 this can be difficult for topological triangulations, because we count triangulations up to isomorphisms. So in principle several steps originating from one triangulation can result in the same other triangulation, which leads to the necessity for checking all results of possible steps whether they are isomorphic to the result of the considered step. One can also use the simplified version (4.10) of the ratio of the selection probabilities which is computable much faster especially for large system sizes, because it only depends on the f -vector of triangulations and its change due to the flip, but can lead to errors in the obtained results.

In Fig. 4.20 the influence of using the simple selection probability on the results is depicted. In Fig. 4.20a one can see that the relative error of the simple ratio (4.10) with respect to the exact ratio (4.11) vanishes $\propto 2^{-m/2}$, where m is the number of maximal simplices. Intuitively that means that increasing the number of tetrahedra or the system size by 2, the average relative error of the simple selection probability is halved. Another feature that can be seen is that for a fixed number m of tetrahedra the average error introduced by a $(d-k+2 \rightarrow k)$ -flip decreases with increasing k , which is clear because a high k means that the target triangulation is larger than the original one, and symmetries are less likely in larger triangulations. In Fig. 4.20b the relative error of the entropy density (4.29) is displayed. As for the error of the selection probabilities one can see an exponential decrease $\propto 2^{-m/3}$, which is slower than for the selection probabilities. For $m \approx 40$ triangles the error in the entropy density is $\approx 10^{-3}$, so one can neglect the error for all bigger triangulations.

For verifying the correctness of our methods and numerical implementations we calculated the number of triangulations of the 3-sphere with $5 \leq v \leq 11$ vertices (using the exact selection probability) and compared with the results obtained by lexicographic enumeration of triangulations in [380], as displayed in Fig. 4.21. The relative error of our approximative results compared with the exact enumeration is always below 0.003 with



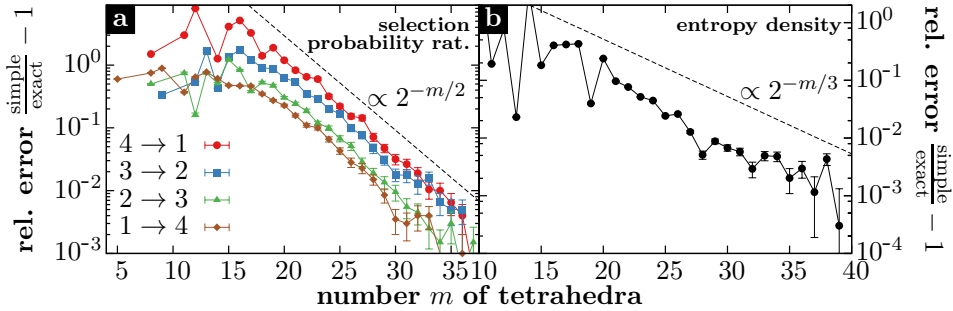


Figure 4.20: Error of the simple selection probability for 3-spheres.

(a) Relative error of the simple ratio $S_{\text{simple}}(\mathcal{T}_1 \rightarrow \mathcal{T}_2)/S_{\text{simple}}(\mathcal{T}_2 \rightarrow \mathcal{T}_1)$ of selection probabilities (4.10) with respect to the exact ratio $S_{\text{exact}}(\mathcal{T}_1 \rightarrow \mathcal{T}_2)/S_{\text{exact}}(\mathcal{T}_2 \rightarrow \mathcal{T}_1)$ calculated in Eq. (4.11) in terms of the number m of tetrahedra for triangulations of the 3-sphere. The different colors correspond to the different type of flips: ($4 \rightarrow 1$)-flip (\bullet), ($3 \rightarrow 2$)-flip (\blacksquare), ($2 \rightarrow 3$)-flip (\blacktriangle) and ($1 \rightarrow 4$)-flip (\blacklozenge). The dashed black line is an exponential $\propto 2^{-m/2}$ drawn for comparison. (b) Relative error of the entropy density $\kappa_c(m) = m^{-1} \log g(m)$ calculated using simple selection probability with respect to the entropy density calculated using the exact selection probability. The dashed black line is an exponential $\propto 2^{-m/3}$ drawn for comparison.

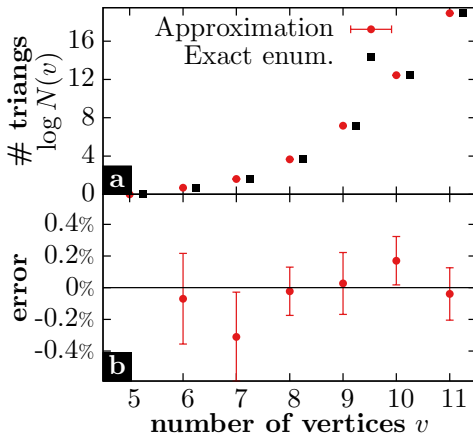


Figure 4.21: Comparison of the approximate enumeration of 3-spheres (\bullet) with the exact lexicographic enumeration results [380] (\blacksquare) in terms of the number v of vertices. (a) Direct comparison of the logarithms of approximate and exact enumeration. The exact enumeration data is shifted to the right to distinguish both data sets on this scale. (b) Relative error $N_{\text{approx}}/N_{\text{exact}} - 1$ of the approximative enumeration.

the exact values always being in the $2 \cdot \sigma$ interval of the approximative data. This implies that our numerical method in fact produces correct results.

In Fig. 4.22 the course of a Wang-Landau simulation in terms of the modification factor is displayed for the approximative counting of three-dimensional triangulations of the sphere. In our first standard simulations that used the flatness criterion $\text{flat}(H(m)) \geq 0.8$ we observed that the recorded density of states (DOS) is very inaccurate at the beginning of



the simulations, which leads to the histogram not becoming flat and the simulations getting stuck for large system sizes. This is traceable to the flatness criterion being very relaxed, it can be reached sometimes just by coincidence and not because the DOS is accurate enough. So a flatness criterion that depends on the current modification factor and that is very strict for low and more relaxed for high ones was tested:

$$\text{flat}(H(m)) \geq \begin{cases} 0.99 & 10^{-2} < f_i \leq 10^0 \\ 0.95 & 10^{-4} < f_i \leq 10^{-2} \\ 0.90 & 10^{-6} < f_i \leq 10^{-4} \\ 0.85 & 10^{-8} < f_i \leq 10^{-6} \end{cases} \quad (4.30)$$

The standard and the adapted procedures are compared for small m in Fig. 4.22. In both cases one can see in the standard deviation of the distributions of κ_c the onset of the saturation of error at modification factor $f \approx 10^{-6}$, for smaller modification factors the standard deviation is approximately constant and independent of the system size. As expected, the value of the relative standard deviation $\sigma/\kappa_c \approx 3.8 \cdot 10^{-3}$ for the standard flatness criterion depicted in Fig. 4.22c is higher than $\sigma/\kappa_c \approx 2.7 \cdot 10^{-3}$ for the alternative flatness criterion depicted in Fig. 4.22d at the smallest modification factor used, because the annealing is done more cautiously in the latter case. For the same reason more sweeps are necessary to reach a given modification factor (depicted in the same subfigures). Considering the necessary sweeps for reaching a relative error of 10^{-3} in Fig. 4.22e and f one sees that the standard procedure is faster for the small system sizes ($m = 10^2$ and $m = 10^3$), for $m = 10^4$ the speed is almost equivalent.

But one can find a relevant difference between the two different flatness criteria if one considers the average value of κ_c ($m = 10^4$) in terms of the modification factor. Using the standard flatness criterion the entropy density is underestimated for a long time during the simulation and approaches the correct value only for relative small modification factors, while for smaller system sizes ($m = 10^2$ and $m = 10^3$) the deviation from the actual value vanishes much earlier. For even larger system sizes the convergence to the actual value is shifted to small modifications factors even more, and there is the danger that the convergence sets in after the last modification factor used in the simulations. For the alternative flatness criterion the underestimation is damped, the convergence to the actual value sets in much faster. So we use in all cases the alternative flatness criterion (4.30) in order to assure a convergence to the actual value before the end of the simulation.



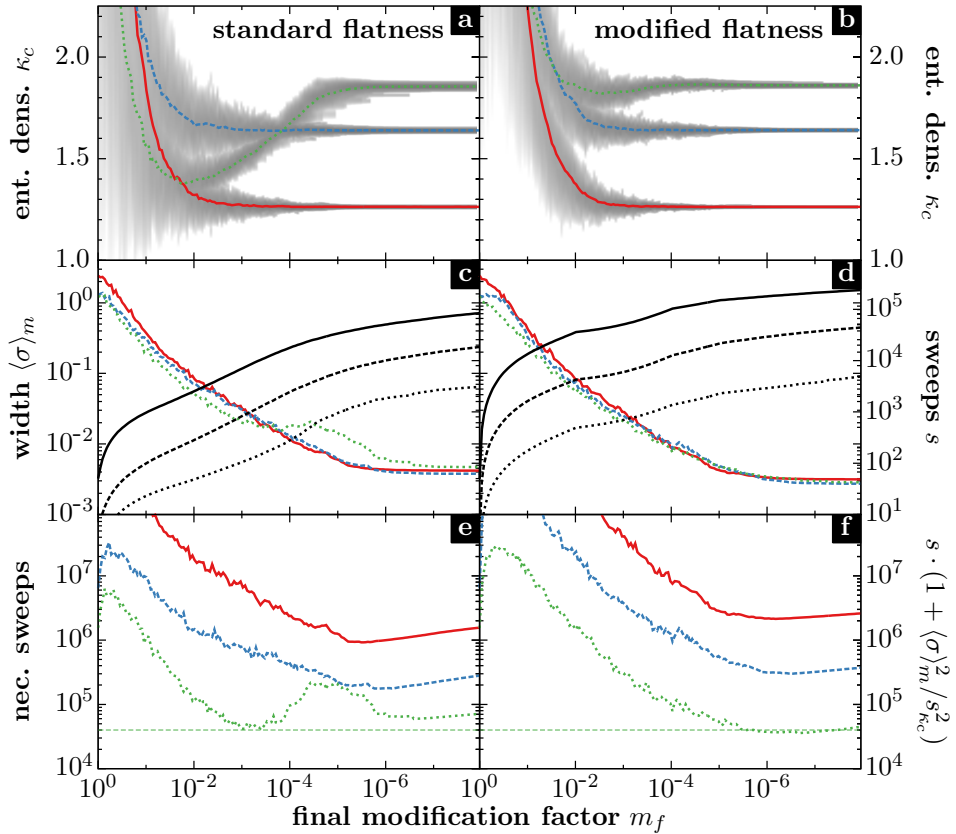


Figure 4.22: Modified flatness criterion for Wang-Landau simulations of the 3-sphere.

Characteristic plot of Wang Landau simulations for three-dimensional topological triangulations of the sphere for 10^2 (red), 10^3 (blue) and 10^4 (green) maximal simplices, and $\Delta m = 10$. The left column (a, c, e) shows the standard Wang-Landau simulation with the decrease $f_{i+1} = f_i^{0.9}$ of the modification factor and the flatness criterion $\text{flat}(H) \geq 0.8$. The right column (b, d, f) shows a modified Wang-Landau simulation with the same decrease of the modification factor, but an alternative flatness criterion (4.30) which is very rigorous for large modification factors and more relaxed for small ones. (a,b) Average value and distribution of the entropy density κ_c in terms of the decreasing modification factor. (c,d) Standard deviation of the distribution of κ_c (color, left axis) and mean number of sweeps (black, right axis) in terms of the modification factor. (e,f) Necessary number of sweeps to calculate κ_c with an error of less than 10^{-3} .



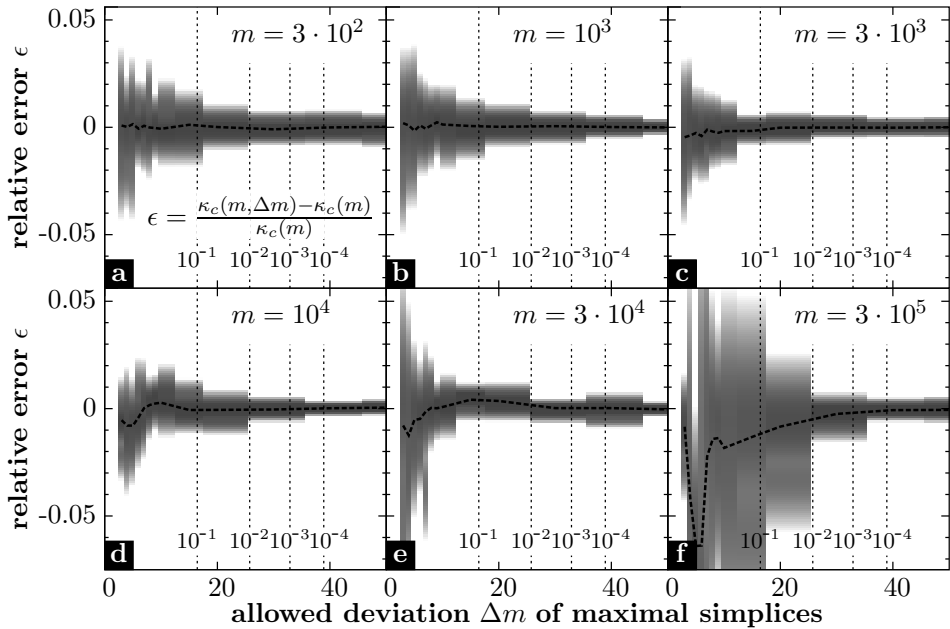


Figure 4.23: Ergodicity of Pachner moves in terms of the accessible tetrahedra range.

The grayscales show the probability distribution of the relative deviation ϵ (4.31) of the finite bin-number entropy density $\kappa_c(m, \Delta m)$ from the actual entropy density $\kappa_c(m)$ in terms of Δm of simplicial 3-spheres for $m = 3 \cdot 10^2$ (a), $m = 10^3$ (b), $m = 3 \cdot 10^3$ (c), $m = 10^4$ (d), $m = 3 \cdot 10^4$ (e) and $m = 3 \cdot 10^5$ (f). The black, dashed line is the mean error of the distribution. The black, dotted lines show the probability for accessing a state at $m \pm \Delta m$ if using the modified action (4.22) with $\gamma = 0.005$ as in Refs. [28, 111, 112]. The labels of the lines are the probabilities of finding a state right of the line.

For the following results we performed at least 5 independent simulations for every data point, and changed the modification factor according to $f_{i+1} = f_i^{0.9}$ after reaching flatness. Within a typical simulation we performed 10^3 to 10^5 sweeps of Pachner moves, where one sweep consists $\approx m$ proposed Pachner moves.

4.3.3 Numerical ergodicity

For testing the numerical ergodicity of simplicial 3-spheres we calculated the entropy density $\kappa_c(m, \Delta m)$ for m maximal simplices using the interval $[m - \Delta m, m + \Delta m]$ of accessible number of maximal simplices within the Wang-Landau algorithm. As a measure for the ergodicity we use the relative



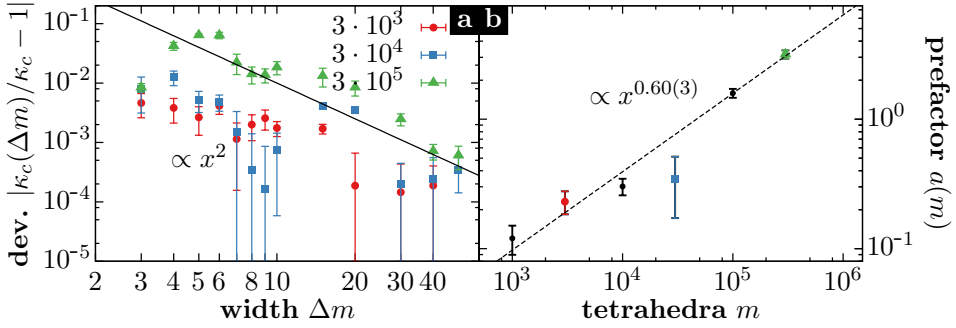


Figure 4.24: Scaling of the ergodicity violation in 3-spheres.

(a) Scaling of the error ϵ (4.31) of the entropy density in terms of Δm of simplicial 3-spheres for $m = 3 \cdot 10^3$ (\bullet), $m = 3 \cdot 10^4$ (\blacksquare) and $m = 3 \cdot 10^5$ (\blacktriangle) tetrahedra. Especially for a low range Δm one finds that $|\epsilon| = a(m) \cdot (\Delta m)^{-2}$. (b) Scaling behavior of the power law prefactor $a(m)$ in terms of the number of tetrahedra m .

error

$$\epsilon := \frac{\kappa_c(m, \Delta m) - \kappa_c(m)}{\kappa_c(m)}, \quad (4.31)$$

where $\kappa_c(m)$ is either given by $\kappa_c(m, \Delta m)$ with the largest Δm , or by fitting to the model (4.32) for ϵ that will be discussed later in this section. For fixed $m > 5$ the entropy density $\kappa_c(m, \Delta m)$ and the relative error ϵ are monotonous increasing functions converging to the actual value $\kappa_c(m)$ (see Fig. 4.23). For low Δm there is a broad distribution of κ_c obtained in independent numerical simulations that narrows for increasing Δm . For increasing m the convergence to κ_c is slower, the distribution broader, and determined mainly by the statistical error of the Wang-Landau algorithm.

Additionally, in Fig. 4.23 the influence of using the modified action (4.22) for $\gamma = 0.005$ is depicted (which is the value used in Refs. [28, 111, 112]). Using $\kappa = \kappa_c$, the probability of finding a state in the Metropolis Markov chain that has a difference of Δm or more in the number of tetrahedra is given by $1 - \text{erf}(\sqrt{\gamma} \cdot \Delta m)$, which is below 10^{-3} for $\Delta m = 33$. This shows that using the method described in Sec. 4.3.1 can lead to errors for larger system sizes.

Using a double-logarithmic plot as in Fig. 4.24a for the ergodicity deviation ϵ in terms of the width Δm of accessible bins, one can see that it follows a power law

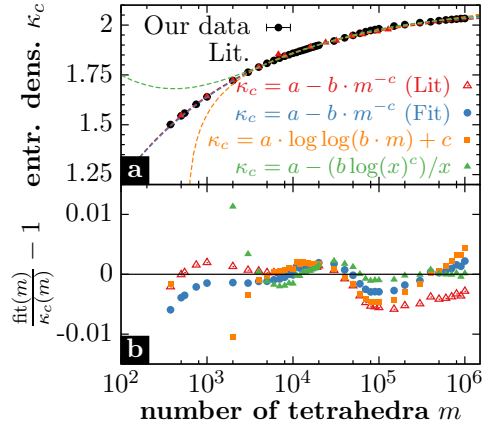
$$|\epsilon| := \left| \frac{\kappa_c(m, \Delta m) - \kappa_c(m)}{\kappa_c(m)} \right| = \frac{a(m)}{(\Delta m)^2} \quad (4.32)$$

with prefactor $a(m)$ growing with the system size m , which can be deter-



Figure 4.25: Scaling of the entropy density of 3-spheres.

(a) Entropy density $\kappa_c(m)$ in terms of the number of tetrahedra m calculated using Wang-Landau simulations (\bullet), and the literature values [112] (\blacktriangle), together with the listed fits. (b) Error $(\text{fit}(m) - \kappa_c(m))/\kappa_c(m)$ of the fit functions with respect to the Wang-Landau results, for the power law fit of Ref. [112] (red, \blacktriangle) and our fits (4.34) of a power law (blue, \bullet), the logarithm of a logarithm (orange, \blacksquare) and a function inspired by the enumeration results for 2-manifolds (orange, \blacktriangle).



mined using a fit in terms of Δm for constant m . For large Δm the exponent -2 changes slightly, because of $\kappa_c(m, \Delta m) - \kappa_c(m)$ becoming small and there is some uncertainty in $\kappa_c(m)$. By fitting the prefactor functional dependency of $a(m)$ in terms of m as in Fig. 4.24b one finds that

$$|\epsilon| := \left| \frac{\kappa_c(m, \Delta m) - \kappa_c(m)}{\kappa_c(m)} \right| \propto \frac{m^{0.60 \pm 0.03}}{(\Delta m)^2}. \quad (4.33)$$

This result can be used for extrapolating the necessary width Δm of accessible bins for large systems without the need for simulations for different Δm .

4.3.4 Scaling of the entropy density

The entropy density $\kappa_c(m)$ was calculated and plotted in Fig. 4.25 for up to $m = 10^6$ vertices and compared to the already existing calculations in Ref. [112]. We find a good agreement for $m \neq 1.28 \cdot 10^5$, but for this value Ref. [112] claims a result lower than our calculations. We think that this is the first sign of ergodicity breaking introduced by the γ -term into the action to be able to measure $\kappa_c(m)$ using the Metropolis algorithm.

We use our data to compare three possible fits: On the one hand we use a power law fit $\kappa_c(m) = \kappa_c^{(\infty)} - a \cdot m^{-c}$ (which suggests that there is an exponential bound $N(m) \leq e^{\kappa_c^{(\infty)} m}$ for the number of 3-spheres in



terms of the number of tetrahedra) and a fit $\kappa_c(m) = \kappa_c^{(\infty)} - a \cdot \log^b(m)/m$ inspired by the enumeration results for 2-manifolds (which also suggests an exponential bound), On the other hand we use a double-logarithmic fit $\kappa_c(m) = a \cdot \log(\log(b \cdot m)) + c$ (suggesting an over-exponential growth $N(m) \propto m^{\log m}$ of the triangulation number). These fits that were done for $m \geq 3000$ result in

$$\kappa_c(m) = 2.107(6) - 3.16(20) \cdot m^{-0.276(9)} \quad (4.34a)$$

$$\kappa_c(m) = 2.056(1) - 0.0031(3) \cdot \frac{\log^{6.03(4)}(m)}{m} \quad (4.34b)$$

$$\kappa_c(m) = 0.189(9) \cdot \log \log(0.0017(3)m) + 1.66(2) \quad (4.34c)$$

A logarithmic fit $\kappa_c(m) = a \cdot \log(b \cdot m)$, implying $N(m) \propto m^m$ is not compatible with our data.

Considering the relative error of $\kappa_c(m)$ calculated with the respective models and the numerical results depicted in Fig. 4.25b shows that the power law fit (4.34a) matches better if one considers all values of m , and that the fit (4.34b) inspired by the two-dimensional results fits better for large m . So for the considered values of m an exponential bound for the number of triangulations (that can be reached with the number of Pachner moves done in the simulation) of the 3-sphere is preferred among the considered models.

4.3.5 Conclusion

The number of triangulations and their scaling in terms of the number of vertices and maximal simplices is an unsolved question in topology and has important applications in simplicial quantum gravity, where exponential scaling is crucial for the models being well-defined. We calculated the effective scaling function $\kappa_c(m)$ of simplicial 3-spheres using the Wang-Landau algorithm for up to $m = 10^6$ tetrahedra and found that an exponential bound of the number N of triangulations (that can be reached with the number of Pachner moves done in the simulation) in terms of m is more favorable than even a very slow increasing function. The same simulational setup can be used to calculate the effective scaling function $\kappa_c(m, \Delta m)$ only considering triangulations with tetrahedra in the interval $[m - \Delta m, m + \Delta m]$. We found that $|\kappa_c(m, \Delta m) - \kappa_c(m)| \propto m^{0.60(3)} (\Delta m)^{-2}$. This result is important for estimating the width of the interval of maximal simplices one needs to allow in order to get correct results in numerical simulations in simplicial quantum geometry.

Since for larger triangulations the number of bins that have to be taken into account for ergodicity increases, and so does the simulation time. This



4.3. Ergodicity and extensivity of three-dimensional sphere triangulations

is why our simulations cannot be performed for larger system sizes. In the future one can use a replica-exchange Wang-Landau simulation with several overlapping energy windows, in order to decrease the simulation time without violating the ergodicity of the system.





5 Triangulations as fluctuating space-(times)

One of the most challenging questions of physics today is the search for a theory of quantum gravity that contains both general relativity and quantum field theory as asymptotic theories, or in a simpler setup to quantize gravity without matter. Both theories are very successful on their own and are the basis of most of modern physics. In fact there are also no observations that contradict any of the theories, the search for a unified theory is driven only by speculations about energy ranges or length scales that cannot be accessed by today's experiments. However, they may have importance in the early universe or in the context of black holes.

The quantization of three of the four elementary forces, the electromagnetic, the weak and the strong one, involves a procedure called perturbative renormalization. This very successful approach (that led to the standard model of particle physics) cannot be applied to general relativity, because one would have to include an infinite number of coupling constants that are undetermined by the theory (comparable to integration constants) Thus perturbatively renormalized gravity is not predictive [204, Sec. 1.5]. There are several alternative approaches that try to find a quantum theory of gravitation (compare also the list given in Ref. [388, pp. 15-21]), of which we present only a selection in the following list:

- *Loop quantum gravity* [388]: Loop quantum gravity (LQG) is an attempt to canonically quantize general relativity using a Hamiltonian formulation of gravity given by ADM or Ashtekar variables, following the quantization methods proposed by Paul Dirac [137]. When applying this formalism to general relativity one finds canonical momenta that cannot be solved for the associated velocities, which leads to the necessity to introduce new variables as Legendre multipliers of constraints in order to obtain the Hamiltonian from the Lagrangian formulation (which is usually and for the invertible momenta done by a Legendre transformation). After the quantization, which leads first to a kinematic Hilbert space, these constraints have to be implemented on the quantum level, which leads to the dynamic Hilbert



space (which contains only the states of the kinematic Hilbert space that fulfill the constraints). The resulting states (of both Hilbert spaces) can be described in terms of spin-networks (see Sec. 6.2 for a closer look on spin networks). Although not all of the constraints can be implemented at present, there are several interesting results within LQG, e.g., that the area operator has a minimal non-vanishing eigenvalue near ℓ_{P}^2 (where ℓ_{P} is the Planck-length), which implies some discreteness of space at short scales [51, 353, 387].

- *String theory* [71, 434]: The basic idea of string theory is to use one-dimensional strings instead of zero-dimensional point particles as basic building blocks of the theory, that cannot be distinguished on the usual observation scales. Different elementary particles can then emerge from the vibration modes of these strings. A famous extension that claims to unify gravity, supersymmetry and string theory is the so-called M-theory, but to formulate it in a consistent way, one has to consider an eleven-dimensional spacetime instead of the usual four-dimensional spacetime.
- *Causal sets* [141]: Causal sets are finite sets of points in Lorentzian spacetime together with an order $x \prec y$ if x is in the past of y . If these points are sprinkled into a small part of a Lorentzian manifold with a probability that is proportional to the volume of the part, the causal set can be shown to be Lorentz invariant. One of the most promising results is that the causal structure alone determines the geometry or equivalently the metric on a manifold up to a conformal factor.
- *Spin foams*: Roughly speaking, spin foams can be seen as describing spacetime as the time-evolution of spin-networks, which are the states of LQG and describe time. Since we consider spin foams in more detail in Sec. 6.2, we refer the reader to the more detailed description there.

In general one has to discriminate between two types of approaches to quantum gravity: On the one hand there are approaches that start from a continuum theory and try to quantize it, as LQG or string theory. This approach is comparable with the usual approach of quantum mechanics or quantum field theory. On the other hand there are approaches that start from some discretized system and try to obtain a continuum limit, as causal sets, spin foams or different models using triangulations. This approach is comparable with the usual setup of statistical physics, or with lattice quantum field theory.



In this chapter we consider the use of triangulations as models for Euclidean or Lorentzian spacetime described by Einsteins theory of general relativity. There are three reasons why to use such discretized spaces for this purpose [339]: The continuous Einstein equations can analytically only be solved in situations with a lot of symmetries (e.g. the Schwarzschild solution for isotropic space). Additionally, it is difficult to describe spaces with complicated topological structure within the Einstein equations. Furthermore, it is discussed in various quantum gravity setups that spacetime is discrete on the smallest length- and time-scales, so discrete manifolds are the actual description of spacetime, and using continuous variables is the approximation.

First approaches in this direction can be found already in 1840 by Jakob Steiner [375], who defined *Flächenkrümmung* (curvature of area) and *Eckenkrümmung* (curvature at corners) on simplicial manifolds. The starting point of almost all results using triangulations as models for (quantum) spacetime is the paper *General relativity without coordinates* by Tullio Regge from 1961 [338]. In this paper the author shows how to obtain an analogue of the Einstein-Hilbert action for simplicial manifolds, and derives the corresponding classical Einstein equation of motions by considering the edge lengths of the triangulation as the dynamic variables of the theory. The derivation of Regge will be described in detail in Sec. 5.1. Note that in the original paper [338] the Riemann tensor on simplicial manifolds was calculated only for a certain limit case, and that it is a conjecture that this is valid in all setups. In 1984 a strict proof was given that the Regge method for simplicial manifolds approximates smooth space, by showing that the curvature defined in the discrete and in the continuous approach are close in the sense of measures [115]. In the same year the Regge action was derived from the Einstein-Hilbert action by discretizing it [177]. More information about the usage of the Regge formalism and its application of quantizing gravity can be found in the reviews [280, 339, 422].

A popular method for quantum gravity using triangulations was first proposed by Berg [83] and is still developed in the ongoing work of Hamber and Williams (e.g., Refs. [202, 203, 205–211], see the book [204] for an exhausting review). The idea is to start with a triangulation of a flat Euclidean space and let the edge lengths evolve using Monte Carlo simulations, using the standard Regge action.

There are further applications of triangulations as spacetime models in the spin-foam setup, which we consider in detail in Sec. 6.2. Note that there are several models assigning different amplitudes to a spin foam, the



earliest model was the Ponzano-Regge model [330] in 1968, a more recent development is the Turaev-Viro model [397] or the EPRL model [155] which we will consider in Sec. 6.2.

In this chapter we are mainly concerned with the approaches of dynamical and causal dynamical triangulations, explained in great detail in Secs. 5.2 and 5.3. In contrast to the other approaches that go back to the Regge approach, the dynamical variables are not the edge lengths (which are fixed in this approach), but the triangulation itself. First approaches into this direction go back to Don Weingarten in 1982 [417], who calculated transition amplitudes between different three-geometries by summing over possible four-geometries that connect these three geometries, and to J. Römer and M. Zähringer in 1986 [349], who fixed the edge length in the simplicial complex and for the first time write the Regge action in terms of the number of simplices. Another origin of the model lies in the study of random surfaces by Jan Ambjørn [17], that was used as a model for quantum gravity later on. The extension to three and four dimensions was then done at the beginning of the 1990s [18, 27, 45]. An important modification was done by using Lorentzian instead of Euclidean spacetime, or imposing causality on the level of the single triangulations [42]. The history and the different models used in the approaches of (causal) dynamical triangulations will be explained in detail in Secs. 5.2 and 5.3.

This chapter consists of three different parts. The first part, Sec. 5.1, explains how to reformulate the Einstein-Hilbert action and the resulting Einstein equations of motion with edge lengths of a triangulation as dynamical variable. This is basically a didactic expansion of the historic paper [338] by Tullio Regge. The first part is to explain that curvature on d -dimensional triangulations is located on the $(d - 2)$ -dimensional simplices, the interior of the higher dimensional simplices can be considered as flat. As a next step we express the Riemann curvature tensor in terms of the discrete curvature, which then can be used for deriving equations of motion in the last part of this section.

The second part, Sec. 5.2, considers the model of dynamical triangulations (DT). The path-integral formulation as well as the expression of the action in terms of the number of simplices and the analytical solution of the 2-dimensional model are reconsidered. The main result of this part is Subsec. 5.2.5, which is a synopsis of the problems of the DT approach. Some of the problems were already given by the authors of the original papers about DT in their later work about the more sophisticated model of causal dynamical triangulations (CDT). But there are also more severe problems



that remain in the CDT approach, mainly concerning the mathematical foundation of discrete topology (e.g., ergodicity and extensivity as explained in Chap. 4).

The last part of this chapter, Sec. 5.3, considers the model of causal dynamical triangulations. After explaining details about the construction of causal triangulations, we develop a transfer matrix method for calculating expectation values using the one-slice density of states that can be calculated with the Wang-Landau algorithm (see Eqs. (5.70) to (5.84)). This method allows for taking the thermodynamic limit of infinite time slices $T \rightarrow \infty$ exactly. The main result of this part is the application of this transfer matrix method to $(2 + 1)$ -dimensional causal dynamical triangulations and the finding in Fig. 5.37 that the second-order phase transition that was found in the literature takes only place in one of the coexisting phases of the first-order transition that is used for fine-tuning the cosmological constant.



5.1 General relativity without coordinates - The Regge formalism

As already stated in the introduction, the foundation for using topological triangulations as spacetime models were laid by Tullio Regge in 1961 [338], where general relativity was formulated without coordinates using edge lengths of a fixed triangulation as dynamic variables. Because of the great importance of this work for all successive formulations of simplicial quantum geometry, we explain in detail how to obtain an action in terms of the geometric quantities of a triangulation and the corresponding equations of motions from the usual continuum theory of general relativity. Therefore we follow closely the original paper of Regge [338], although it presents no rigorous proofs, but it is very suited for getting an intuitive picture of the discrete approach to general relativity. For a detailed proof of the Regge formalism we refer the reader to Ref. [115], where it is rigorously proven that the curvature defined by Regge approximates a smooth space, by showing that discrete and smooth curvature are close in a measure sense, and to Ref. [177], where the opposite way was taken and the Regge equations were derived by discretizing the continuum version of general relativity.

In this section we first present how curvature can be described in triangulations or simplicial complexes. Afterwards we express the Riemann curvature tensor in terms of this discrete curvature. As a last step the Regge action is introduced, which is a discrete version of the Einstein-Hilbert action, and the equations of motion are derived from this discrete action.

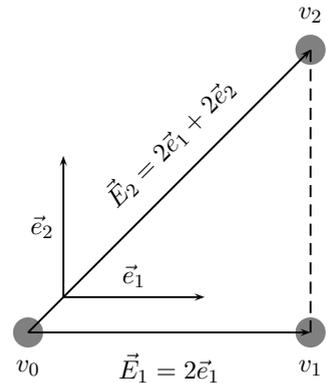
5.1.1 Curvature assignment in simplicial complexes

In this section it will be explained how curvature arises if gluing flat simplices together at the boundaries. We will see that for a d -dimensional triangulation the curvature is located at the $(d - 2)$ -dimensional simplices, which will be denoted as bones.

We first describe how to use the metric tensor for calculations within flat simplices. Then we consider how the metric can be continued if gluing two flat simplices at their boundary. Last we make plausible by considering closed paths around bones that the curvature of the simplicial manifold is located at the $(d - 2)$ -dimensional bones.



Figure 5.1: Orthonormal basis \vec{e}_i and non-orthonormal edge basis \vec{E}_μ in a two-dimensional simplex.



Geometry within flat simplices

We first explain how geometric quantities within a simplex can be calculated using the metric tensor, if using the edges of the simplices as a basis. The interior of a d -simplex (as defined in Def. 4.9) is flat, since it is a subset of \mathbb{R}^d . So the metric tensor $g_{ij} = \delta_{ij}$ for Euclidean signature and $g_{ij} = \eta_{ij}$ for Lorentzian signature. Note that we use the convention $\eta_{00} = -1$ and $\eta_{ii} = 1$ for $i \neq 0$. In this section we restrict ourselves to Euclidean signature.

Suppose that we have an orthonormal basis \vec{e}_i (with $0 \leq i \leq d-1$) inside of the simplex. Choose now an arbitrary vertex of the simplex and define as \vec{E}_μ (with $0 \leq \mu \leq d-1$) the vectors that point from this chosen vertex to the other vertices of the simplex. The vectors \vec{E}_μ are a non-orthonormal basis of the \mathbb{R}^d , and there exists a transformation matrix relating the edge vectors and the orthonormal basis:

$$\vec{E}_\mu = T_\mu^i \vec{e}_i \quad (5.1)$$

(here and in the remaining section we will use Einstein's sum convention where there are sums over double indices).

Consider for example the case $d = 2$ and the two basis vectors $\vec{E}_0 = 2\vec{e}_0$ and $\vec{E}_1 = 2\vec{e}_0 + 2\vec{e}_1$, displayed in Fig. 5.1. The transformation matrix is then given by

$$T = \begin{pmatrix} 2 & 0 \\ 2 & 2 \end{pmatrix}$$

If one has a vector v_μ given in coordinates of the basis \vec{E}_μ , for calculation of lengths, distances and angles one needs the metric tensor $g_{\mu\nu}$. This tensor is a constant (its entries does not depend on the actual point), but in general it is not a diagonal matrix, because the edge basis \vec{E}_μ in general is no



orthonormal basis. The components of the metric tensor can be computed by scalar product of the basis vectors:

$$\begin{aligned} g_{\mu\nu} &= \vec{E}_\mu \cdot \vec{E}_\nu = (T_\mu^i \vec{e}_i) \cdot (T_\nu^j \vec{e}_j) = \\ &= T_\mu^i T_\nu^j (\vec{e}_i \cdot \vec{e}_j) = T_\mu^i T_\nu^j \delta_{ij} = T_\mu^i T_\nu^i = (TT^t)_{\mu\nu} \end{aligned} \quad (5.2)$$

In our example the metric tensor is given by the matrix

$$g = (TT^t) = \begin{pmatrix} 2 & 0 \\ 2 & 2 \end{pmatrix} \begin{pmatrix} 2 & 2 \\ 0 & 2 \end{pmatrix} = \begin{pmatrix} 4 & 4 \\ 4 & 8 \end{pmatrix}$$

Using the metric tensor one can, e.g., calculate the distance between two points given by their vectors v_μ and w_μ in coordinates of the edge vectors:

$$\text{dist}(v, w) = \sqrt{v^\mu w_\mu} = \sqrt{g^{\mu\nu} v_\mu w_\nu}$$

In our example, the distance between vertices v_1 and v_2 , which is the length of the vector \vec{E}_{12} given by coordinates $(-1, 1)$ in the edge basis, can be calculated by

$$\text{dist}(v_1, v_2) = |\vec{E}_{12}| = \sqrt{\begin{pmatrix} -1 & 1 \end{pmatrix} \begin{pmatrix} 4 & 4 \\ 4 & 8 \end{pmatrix} \begin{pmatrix} -1 \\ 1 \end{pmatrix}} = 2$$

Geometry on neighboring simplices

In this section we show how geodesics and thus distances between points in different simplices can be calculated. First we consider two neighboring simplices, then we generalize this to two points in arbitrary simplices. We use $\vec{E}_\mu(\sigma_n)$ and $g_{\mu\nu}(\sigma_n)$ to denote the edge basis vectors and the metric tensor in terms of these edge basis vectors in the d -simplex σ_n .

Let σ_1 and σ_2 be two neighboring simplices and let $p_\mu \in \sigma_1$ and $q_\mu \in \sigma_2$ be two points coordinatized with respect to the edge vectors. The geodesic distance $\text{dist}(p, q)$ between these two points is defined as

$$\begin{aligned} \text{dist}(p, q) &= \min_{r \in \sigma_1 \cap \sigma_2} \{ \text{dist}(p, r) + \text{dist}(r, q) \} = \\ &= \min_{r \in \sigma_1 \cap \sigma_2} \left\{ \sqrt{g^{\mu\nu}(\sigma_1) p_\mu r_\nu} + \sqrt{g^{\mu\nu}(\sigma_2) r_\mu q_\nu} \right\} \end{aligned}$$

Intuitively that means that the distance between two points in neighboring simplices is the minimum of the length of the two sub-paths from each point to the respective boundary of the simplex. Note that the coordinates



of r must be given in terms of $\vec{E}_\mu(\sigma_1)$ for the first and in terms of $\vec{E}_\mu(\sigma_2)$ for the second term.

In the following we give an example shown in Fig. 5.2, with edge basis coordinates

$$\begin{aligned}\vec{E}_1(\sigma_1) &= 2\vec{e}_1 & \vec{E}_2(\sigma_1) &= 2\vec{e}_1 + 2\vec{e}_2 \\ \vec{E}_1(\sigma_2) &= -2\vec{e}_1 - 2\vec{e}_2 & \vec{E}_2(\sigma_2) &= -2\vec{e}_1.\end{aligned}$$

The aim is to calculate the distance between the points $\sigma_1 \ni p = (p_0, p_1)$ with respect to basis $\vec{E}_\mu(\sigma_1)$ and $\sigma_2 \ni q = (q_0, q_1)$ with respect to basis $\vec{E}_\mu(\sigma_2)$. The transformation matrices in the two different simplices are given by

$$T(\sigma_1) = \begin{pmatrix} 2 & 0 \\ 2 & 2 \end{pmatrix} \quad T(\sigma_2) = \begin{pmatrix} -2 & -2 \\ -2 & 0 \end{pmatrix},$$

resulting in the metric tensors

$$g(\sigma_1) = \begin{pmatrix} 4 & 4 \\ 4 & 8 \end{pmatrix} \quad g(\sigma_2) = \begin{pmatrix} 8 & 4 \\ 4 & 4 \end{pmatrix}.$$

A point r on the common boundary of $\bar{\sigma}_1$ and $\bar{\sigma}_2$ has coordinates $(\lambda, 1 - \lambda)^t$ with $0 \leq \lambda \leq 1$ in both bases. The distances $d(p, r)$ and $d(r, q)$ are then given by

$$\begin{aligned}d(p, r) &= \sqrt{(p_0 \ p_1) \begin{pmatrix} 4 & 4 \\ 4 & 8 \end{pmatrix} \begin{pmatrix} \lambda \\ 1 - \lambda \end{pmatrix}} = 2\sqrt{p_0 + p_1(2 - \lambda)} \\ d(r, q) &= \sqrt{(\lambda \ 1 - \lambda) \begin{pmatrix} 8 & 4 \\ 4 & 4 \end{pmatrix} \begin{pmatrix} q_0 \\ q_1 \end{pmatrix}} = 2\sqrt{q_0(\lambda + 1) + q_1}\end{aligned}$$

Minimizing the sum of both distances with respect to λ yields

$$\lambda_{\min} = \frac{(p_0 + 2p_1)q_0^2 - p_1^2(q_0 + q_1)}{p_1q_0(p_1 + q_0)}$$

and the minimal distance

$$\begin{aligned}d(p, q) &= 2\sqrt{p_0 + 2p_1 - \frac{(p_0 + 2p_1)q_0^2 - p_1^2(q_0 + q_1)}{q_0(p_1 + q_0)}} + \\ &+ 2\sqrt{\frac{(p_0 + 2p_1)q_0^2 - p_1^2(q_0 + q_1)}{p_1(p_1 + q_0)} + q_0 + q_1}\end{aligned}$$



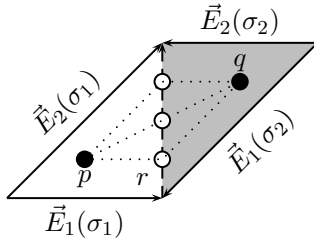


Figure 5.2: Calculating the distance between points in neighboring simplices.

For the special case $p_0 = p_1, q_0 = q_1$ we have $\lambda_{\min} = 0.5$ and $d(p, q) = \sqrt{10}(p_0 + q_0)$.

This procedure can be generalized for two points in arbitrary simplices σ and σ' . Therefor one first has to find all possible paths $\sigma \rightarrow \sigma_1 \rightarrow \dots \rightarrow \sigma_k \rightarrow \sigma'$ of neighboring simplices that connect simplex σ and σ' . Pathes with simplices occurring more than once can be neglected (because they will always be longer as the path leaving out the detour). Then one calculates for every path the length by introducing additional points in the $(d - 1)$ -dimensional boundaries, and minimizes the length with respect to the position of the additional points. The geodesic distance is then the minimum of these minimal lengths with respect to the possible pathes.

As a last point we want to calculate how the coordinates of a vector $v_\mu(\sigma_1)$ with respect to the edge basis of simplex σ_1 transform to the coordinates of the vector $v_\nu(\sigma_2)$ with respect to the edge basis of simplex σ_2 . Suppose first that the edge basis vectors have coordinates in terms of the same orthonormal basis $\vec{e}_i(\sigma_1) = \vec{e}_i(\sigma_2)$ and suppose that the considered vector has the coordinates v_i with respect to \vec{e}_i .

$$\begin{aligned} v_\mu(\sigma_1) = T(\sigma_1)_\mu^i v_i &\Rightarrow v_i = T^{-1}(\sigma_1)^\mu_i v_\mu(\sigma_1) \\ v_\nu(\sigma_2) = T(\sigma_2)_\nu^i v_i &\Rightarrow v_\nu(\sigma_2) = T(\sigma_2)_\nu^i T^{-1}(\sigma_1)^\mu_i v_\mu(\sigma_1) \end{aligned}$$

In general the orthonormal basis vectors of the neighboring simplices need not to be parallel, but can be transformed into each other by a rotation. Suppose that $\vec{e}_i(\sigma_2) = S(\sigma_1 \rightarrow \sigma_2)_i^j \vec{e}_j(\sigma_1)$ with $\det(S) = 1$, then we have the following relation between the coordinates of the same vector:

$$\begin{aligned} v_\mu(\sigma_1) &= T(\sigma_1)_\mu^i v_i \\ &\Rightarrow v_i = T^{-1}(\sigma_1)^\mu_i v_\mu(\sigma_1) \\ v_\nu(\sigma_2) &= T(\sigma_2)_\nu^i S(\sigma_1 \rightarrow \sigma_2)_i^j v_j \\ &\Rightarrow v_\nu(\sigma_2) = T(\sigma_2)_\nu^i S(\sigma_1 \rightarrow \sigma_2)_i^j T^{-1}(\sigma_1)^\mu_j v_\mu(\sigma_1) \end{aligned}$$



The resulting transformation matrix is

$$V(\sigma_1 \rightarrow \sigma_2)_{\nu}^{\mu} := T(\sigma_2)_{\nu}^i S(\sigma_1 \rightarrow \sigma_2)_i^j T^{-1}(\sigma_1)^{\mu}_j \quad (5.3)$$

This can be again generalized to points in non-neighboring simplices by simply transporting stepwise through the simplices along the path of the transport.

Closed pathes in simplicial complexes

In this section we will show that there is a deficit angle if transporting a vector along a path encircling a $(d - 2)$ -dimensional simplex. First we start with a simple example in $d = 2$ dimensions and then we generalize it to arbitrary dimensions and geometries.

Suppose that there is a vertex with incident triangles $\sigma_1, \dots, \sigma_k$, and that triangle σ_i has an interior angle of ϕ_i at the considered vertex. We choose the edge basis so that $\vec{E}_2(\sigma_i)$ and $\vec{E}_1(\sigma_{i+1})$ are the basis vectors at the common edge of the triangles σ_i and σ_{i+1} (with $\sigma_{k+1} := \sigma_1$). In each triangle we choose the orthonormal basis so that $\vec{e}_1(\sigma_i) \parallel \vec{E}_1(\sigma_i)$ and so that $\vec{e}_1(\sigma_i)$ and $\vec{e}_2(\sigma_i)$ form a right-hand system.

Let $v_{\mu}(\sigma_1)$ be an arbitrary vector given in the edge basis coordinates of σ_1 . We transport the vector along a path

$$\sigma_1 \rightarrow \sigma_2 \rightarrow \dots \rightarrow \sigma_k \rightarrow \sigma_1$$

Applying multiple times Eq. (5.3) for the parallel transport of a vector between neighboring simplices we get:

$$\begin{aligned} v'_{\mu}(\sigma_1) &= T(\sigma_1)_{\mu}^{a_1} S(\sigma_k \rightarrow \sigma_1)_{a_1}^{b_1} T^{-1}(\sigma_k)_{b_1}^{\nu_1} \\ &\quad T(\sigma_k)_{\nu_1}^{a_2} S(\sigma_{k-1} \rightarrow \sigma_k)_{a_2}^{b_2} T^{-1}(\sigma_{k-1})_{b_2}^{\nu_2} \\ &\quad \dots \\ &\quad T(\sigma_2)_{\nu_{k-1}}^{a_k} S(\sigma_1 \rightarrow \sigma_2)_{a_k}^{b_k} T^{-1}(\sigma_1)_{b_k}^{\nu_k} v_{\nu_k} \end{aligned}$$

Note that all transformation matrices T cancel with their inverses, except for the first and the last transformation matrix. The orthonormal basis transformation matrices $S(\sigma_i \rightarrow \sigma_{i+1}) = S(\phi_i)$ are rotations that depend only on the interior angle ϕ_i and not on the simplex itself. Since for rotations $S(\phi_i)S(\phi_j) = S(\phi_i + \phi_j)$, the equation becomes

$$\begin{aligned} v'_{\mu}(\sigma_1) &= T(\sigma_1)_{\mu}^{a_1} S(\phi_k)_{a_1}^{a_2} S(\phi_{k-1})_{a_2}^{a_3} \dots S(\phi_1)_{a_k}^b T^{-1}(\sigma_1)_b^{\nu_k} v_{\nu_k} \\ &= T(\sigma_1)_{\mu}^a S(\phi_1 + \phi_2 + \dots + \phi_k)_a^b T^{-1}(\sigma_1)_b^{\nu_k} v_{\nu_k} \\ &= T(\sigma_1)_{\mu}^a S(2\pi - \epsilon)_a^b T^{-1}(\sigma_1)_b^{\nu_k} v_{\nu_k} \end{aligned}$$



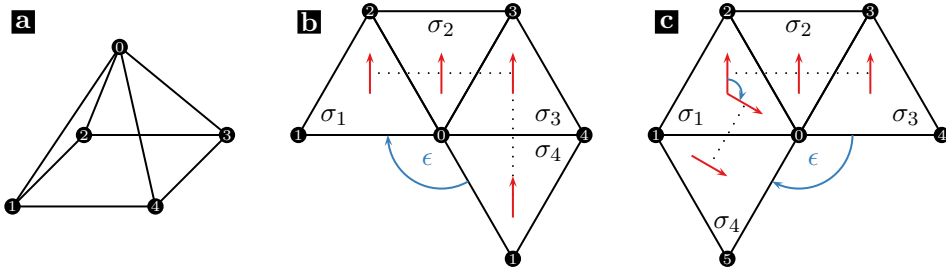


Figure 5.3: Example for the deficit angle in a two-dimensional triangulation. (a) Part of a two-dimensional triangulation consisting of the maximal simplices $\sigma_1 = \{012\}, \sigma_2 = \{023\}, \sigma_3 = \{034\}$ and $\sigma_4 = \{014\}$, each edge having length 1. (b) Cutting along one edge the four maximal simplices can be drawn into a flat plane and a vector (red) can be parallel transported along a path $\sigma_1 \rightarrow \sigma_2 \rightarrow \sigma_3 \rightarrow \sigma_4$ without changing the direction in the plane. (c) To transport the vector parallel along a path $\sigma_4 \rightarrow \sigma_1$, one has to cut along another edge. Redrawing the simplex σ_4 rotates also the contained vector. Altogether the vector is rotated by an angle of ϵ , which is exactly the deficit angle of the triangulation at vertex 0.

In this equation

$$\epsilon := 2\pi - \sum_i \phi_i \tag{5.4}$$

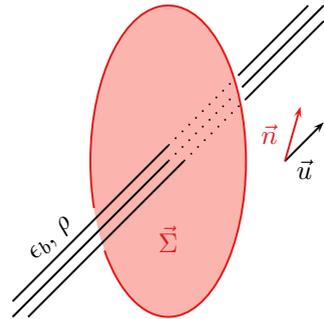
is the *deficit angle* of the revolved vertex, which is the difference between the full angle and the sum of the incident angles of the incident triangles. So we get $v'_a(\sigma_1) = S(2\pi - \epsilon)_a^b v_b(\sigma_1)$, which means that the vector is rotated with the deficit angle if transported around the edge. An example for this behavior can be found in Fig. 5.3.

From differential geometry it is known that curvature is related with changes of the angle of vectors within closed parallel transports. One can show that all closed parallel transports that do not revolve a vertex do not alter the angle of a vector. (Intuitively, one can always draw the simplices in a common plane, so that one has again the geometry of \mathbb{R}^2 .) This means that the curvature of a two-dimensional triangulation is located only at the vertices, and not on the edges or the triangles. Thus the curvature is a distribution with support of the vertices.

For higher dimensions one has a similar situation. One can always glue two d -simplices using a common $(d - 1)$ -simplex so that the resulting object can be embedded into the \mathbb{R}^d . This is not possible if gluing several d -simplices sharing a common $(d - 2)$ -simplex, in general there will be again a deficit angle associated with every $(d - 2)$ -simplex. Parallel transports along closed curves around such $(d - 2)$ -simplices will then lead to a rotation



Figure 5.4: Setup for identifying the Riemann tensor with the quantities of a three-dimensional triangulation. We consider a closed path revolving an area $\vec{\Sigma} = \Sigma \vec{n}$ with normal vector \vec{n} . Within the area we have bones with density ρ and deficit angle ϵ_b for each bone. The bones have a direction \vec{u} .



of the transported vector, and one can conclude that the curvature in d -triangulations is a distribution with support on the $(d - 2)$ -simplices. These $(d - 2)$ -simplices are then often denoted as *bones*.

5.1.2 The Riemann curvature tensor

In the last section we concluded that the curvature in a d -dimensional simplicial manifold is located at the $(d - 2)$ simplices. Using this information we will compute in this section an expression for the Riemann curvature tensor in a certain limit, following Ref. [338]. This limit will be compared later on with the Einstein-Hilbert action on the simplicial complex to get the discretized Regge action of general relativity.

For simplicity we will restrict first to the 3d case. Consider a bunch of N parallel bones (edges) with deficit angle ϵ_b and a direction given by the normal vector \vec{u} . We want to transport a vector \vec{A} around a loop $\vec{\Sigma} = \Sigma \vec{n}$ with area Σ and normal vector \vec{n} surrounding the parallel bones. Let ρ be the density of bones in space, and assume ϵ_b and ρ can be treated as constants. An image of the situation can be found in Fig. 5.4.

After the transport the vector \vec{A} is rotated by

$$\delta \vec{A} = \vec{A}' - \vec{A} = N \cdot \epsilon_b (\vec{u} \times \vec{A})$$

The cross product originates from the fact that only the components of the vector that are orthogonal to the bones have a non-vanishing rotation when performing a parallel transport around the bones. The number N of revolved bones can be calculated using the density and the area of the loop by

$$N = \rho (\vec{u} \cdot \vec{\Sigma}),$$

taking into account the angle between the normal vectors of the loop and the bones. So in index notation the rotation of the vector can be calculated



as

$$\delta A_\mu = \rho \epsilon_b \epsilon_{\mu\alpha\nu} u^\alpha A^\nu u^\sigma \Sigma_\sigma. \quad (5.5)$$

From differential geometry we know that the same quantity can be calculated using the Riemann curvature tensor R :¹

$$\delta A_\mu = R_{\mu\alpha\beta}^\nu \Sigma^{\alpha\beta} A_\nu = R_{\nu\mu\alpha\beta} |g|^{-1/2} \epsilon^{\alpha\beta\sigma} \Sigma_\sigma A^\nu \quad (5.9)$$

Comparing the sides of the Eqs. (5.5) and (5.9) leads to

$$\epsilon^{\alpha\beta\sigma} |g|^{-1/2} R_{\nu\mu\alpha\beta} \stackrel{!}{=} \rho \epsilon_b \epsilon_{\mu\alpha\nu} u^\alpha u^\sigma.$$

Use Eq. (5.6a) on the right side to get

$$\epsilon^{\alpha\beta\sigma} |g|^{-1/2} R_{\nu\mu\alpha\beta} = |g|^{-1/2} \rho \epsilon_b u_{\nu\mu} u^\sigma.$$

Rewriting u^σ using Eq. (5.7a) yields

$$\epsilon^{\alpha\beta\sigma} R_{\nu\mu\alpha\beta} = |g|^{-1/2} \rho \epsilon_b u_{\nu\mu} \epsilon^{\alpha\beta\sigma} u_{\alpha\beta}.$$

From $T_{\alpha\beta} \epsilon^{\alpha\beta\sigma} = S_{\alpha\beta} \epsilon^{\alpha\beta\sigma}$ it follows that $T_{\alpha\beta} = S_{\alpha\beta}$ for two arbitrary antisymmetric tensors T and S (which can be seen by expanding both sides with $\epsilon_{\mu\nu\sigma}$ and using Eq. (5.8a)). Using this fact together with $R_{\nu\mu\alpha\beta}$ being

1 Here and in the following we use the definition

$$B_{\alpha\beta} := |g|^{1/2} \epsilon_{\alpha\beta\gamma} B^\gamma = -B_{\beta\alpha} \quad (5.6a)$$

for a vector B , where $|g|^{1/2}$ is the square root of the determinant of the metric. Note that the Levi-Civita symbol $\epsilon_{\alpha\beta\gamma}$ is not a tensor, but a tensor density, and so is $B_{\alpha\beta}$, and thus the transformation law for a covector is

$$B^{\alpha\beta} := |g|^{-1/2} \epsilon^{\alpha\beta\gamma} B_\gamma. \quad (5.6b)$$

Considering these two equations component-wise yields the inverse transformations

$$B^\gamma = |g|^{-1/2} \epsilon^{\alpha\beta\gamma} B_{\alpha\beta} \quad (5.7a)$$

$$B_\gamma = |g|^{1/2} \epsilon_{\alpha\beta\gamma} B^{\alpha\beta}. \quad (5.7b)$$

Note that the well known formulas for contracting indices of the Levi-Civita remain unchanged

$$\epsilon_{\alpha\beta\gamma} \epsilon^{\alpha\beta\sigma} = 2\delta_\gamma^\sigma \quad (5.8a)$$

$$\epsilon_{\alpha\beta\gamma} \epsilon^{\alpha\mu\nu} = (\delta_\beta^\mu \gamma_\beta^\nu - \delta_\beta^\nu \gamma_\beta^\mu). \quad (5.8b)$$



antisymmetric in the last two indices, as well as $u_{\alpha\beta}$ by its definition (5.6a), it follows for the Riemann curvature tensor that

$$\sqrt{|g|}R_{\mu\nu\alpha\beta} = \rho\epsilon_b u_{\mu\nu} u_{\alpha\beta}. \quad (5.10)$$

The Ricci tensor can be derived by contracting the Riemann tensor with the metric tensor by

$$\sqrt{|g|}R_{\mu\nu} := \sqrt{|g|}g^{\alpha\beta}R_{\alpha\mu\beta\nu} = \rho\epsilon_b g^{\alpha\beta}u_{\alpha\mu}u_{\beta\nu},$$

and the Ricci scalar can be calculated by contracting the Ricci tensor again with the metric tensor by

$$\sqrt{|g|}R := \sqrt{|g|}g^{\mu\nu}R_{\mu\nu} = \rho\epsilon_b g^{\alpha\beta}g^{\mu\nu}u_{\alpha\mu}u_{\beta\nu} = \rho\epsilon_b u_{\alpha\beta}u^{\alpha\beta}.$$

Insert here the definitions (5.6) to get

$$\sqrt{|g|}R = \rho\epsilon_b \epsilon_{\alpha\beta\gamma} u^\gamma \epsilon^{\alpha\beta\sigma} u_\sigma,$$

and use (5.8a) as well as $u^\gamma u_\gamma = 1$ due to u_γ being a unit vector to obtain

$$\sqrt{|g|}R = 2\rho\epsilon_b. \quad (5.11)$$

for the Ricci scalar in the considered limit. This will be the basic ingredient for formulating the discretized version of the Einstein-Hilbert action.

Friedberg and Lee [177] showed explicitly in 1984 that for a bone b that the Ricci scalar is given by the distribution

$$\sqrt{|g|}R = 2\epsilon_b \delta(x_1)\delta(x_2),$$

if transforming the coordinate system such that x_1 and x_2 are perpendicular to the bone b , and b is located in the origin.

5.1.3 Discrete Einstein equations

The Einstein-Hilbert action S_{EH} of (continuous) general relativity for space-time without matter is given by

$$S_{\text{EH}} = \frac{1}{16\pi G} \int_M d^d x \sqrt{|\det g|} (R - 2\Lambda),$$

where Λ denotes the cosmological constant (which corresponds to an energy density that is assigned to empty space). For simplicity we restrict to the



case $\Lambda = 0$ first. Because the Ricci scalar (5.11) was only derived in a certain limit, one cannot directly insert it into the action. Instead one has to derive a discrete version of the action from first principle and compare it with the usual Einstein-Hilbert action in the considered limit.

Since the curvature vanishes outside of the $(d-2)$ -simplices $\sigma^{(d-2)}$ (bones), so the action should be an additive function of the bones:

$$S = \sum_{b \in \mathcal{B}} F \left(\sigma_b^{(d-2)} \right)$$

where F is the same function for all bones, and \mathcal{B} denotes the set of all bones in the triangulation. One can assume that the curvature has a constant density over the bone, so the function F should be proportional to the hyperlength $V \left(\sigma_b^{(d-2)} \right) = V_b^{(d-2)}$ of the bone,

$$F \left(\sigma_b^{(d-2)} \right) = V \left(\sigma_b^{(d-2)} \right) \cdot f \left(\epsilon_b \right),$$

and depend furthermore only on the deficit angle ϵ_b of the bone b , because no other quantity influences the curvature induced by the bone. If there are two bones with identical shape and identical location the deficit angle is additive, so $\epsilon = \epsilon^{(1)} + \epsilon^{(2)}$, and so it is reasonable to assume that $f \left(\epsilon^{(1)} + \epsilon^{(2)} \right) = f \left(\epsilon^{(1)} \right) + f \left(\epsilon^{(2)} \right)$. So f is linear and one can write $f(\epsilon) = C\epsilon$ with C being a constant that needs yet to be calculated. The total action is then

$$S = C \sum_{b \in \mathcal{B}} V_b^{(d-2)} \epsilon_b.$$

By comparing this action with the Einstein-Hilbert action in the previously considered limit $\sqrt{|g|}R = 2\epsilon_b\rho$ one gets $C = 1/8\pi G$. So the resulting action is

$$S_{\text{Regge}} = \frac{1}{8\pi G} \sum_{b \in \mathcal{B}} V_b^{(d-2)} \epsilon_b, \tag{5.12}$$

yet for vanishing cosmological constant $\Lambda = 0$.

For completeness we include now a non-vanishing cosmological constant $\Lambda \neq 0$. Since the curvature is located at the $(d-2)$ -dimensional simplices, but the integration for the action is over the complete d -dimensional manifold, the metric and therewith its determinant is constant except on the bones, which a set of measure 0 with respect to M . One can always choose the length of the basis vectors in each maximal simplex such that the absolute value of the determinant of the metric is 1, so that we can simplify the



cosmological constant term

$$S_\Lambda = -2 \frac{1}{8\pi G} \int_M d^d x \sqrt{|\det g|} \Lambda = -2\Lambda \sum_{s \in \mathcal{S}} V_s^{(d)},$$

where \mathcal{S} is the collection of maximal simplices. So the complete Regge action is

$$S_{\text{Regge}} = \frac{1}{8\pi G} \left[\sum_{b \in \mathcal{B}} V_b^{(d-2)} \epsilon_b - 2\Lambda \sum_{s \in \mathcal{S}} V_s^{(d)} \right], \quad (5.13)$$

where the first term corresponds to the contribution of the curvature of the bones, and the second term corresponds to the contribution of the cosmological constant (energy density of the vacuum).

As a next step we will use the variational principle on the Regge action (5.13) with $\Lambda = 0$ for calculating the discrete equations of motion, which can be found by maximizing the action by setting $\delta S = 0$. Because for a fixed triangulation the metric of the space is determined completely by the edge lengths, one can treat the edge lengths as the dynamic variables and calculate the variation of the action in terms of the edge lengths by

$$\delta S = \frac{1}{8\pi G} \sum_{b \in \mathcal{B}} (\epsilon_b \delta V_b + V_b \delta \epsilon_b).$$

One can show that the second term vanishes (see Ref. [338] for details), which is the discrete analog to the Palatini identity

$$\sum_{b \in \mathcal{B}} V_b \delta \epsilon_b = 0 \quad \Leftrightarrow \quad \int_{\mathcal{M}} \sqrt{|\det g|} g^{\alpha\beta} \delta R_{\alpha\beta} d^d x = 0,$$

so we have to consider only the first term.

If \mathcal{E} denotes the set of edges (1-simplices) of the triangulation, the $|\mathcal{E}|$ not necessarily independent equations of motions in d dimensions are

$$\sum_{b \in \mathcal{B}} \epsilon_b \frac{\partial V_b}{\partial l_e} = 0 \quad \forall e \in \mathcal{E}. \quad (5.14)$$

So one has to compute the derivative of the $(d-2)$ -volume of the bones with respect to the length of the edges.

Similar to the continuum version of the Einstein equations

$$R_{\mu\nu} - \frac{1}{2} g_{\mu\nu} R = 0,$$



where $R_{\mu\nu}$ is the Ricci curvature tensor, the discrete equations of motion (5.14) do not describe a time-evolution of the (edge lengths) of the triangulation, because the underlying manifold describes space and time at once. The equations of motion (5.14) describe rather conditions that have to be fulfilled for the triangulation so that it can describe a valid spacetime.

Equations of motion in $d = 2$ In two dimensions, the maximal simplices are triangles and the bones are vertices, whose can be assigned a non-vanishing 0-volume c . But this 0-volume does obviously not affect the volume of the triangles, so all Regge equations of motion (5.14) are fulfilled trivially. This means that every valid simplicial 2-manifold is also a valid spacetime, without restrictions on the edge lengths.

Note that also in continuous general relativity a spacetime dimension $d = 2$ is a pathological case, in this situation the energy-momentum tensor has to vanish, which means that there cannot exist any matter in such a dimension (but curvature can exist) [119].

Equations of motion in $d = 3$ In three dimensions the bones are exactly the edges, and $\partial V_b^1 / \partial l_e = \delta_{b,e}$, so the equations of motions become $\epsilon_b = 0 \forall b$, so there is only the flat solution in $d = 3$ dimensions. The result that there are only flat spacetimes is also valid in the continuum theory [119].

Equations of motion in $d = 4$ In four dimensions the bones of the triangulation are the triangles, so one has to calculate the derivative of the area of a triangle with respect to the length of one side. Let A be the area of the triangle with lengths a , b and l , and denote with θ the angle opposite to side l . The derivative of the area with respect to l (leaving a and b fixed) is then

$$\frac{\partial A}{\partial l} = \frac{1}{2} ab \frac{\partial \sin(\theta)}{\partial l} = \frac{1}{2} ab \cos(\theta) \frac{\partial \theta}{\partial l}.$$

One can express θ in terms of l :

$$l^2 = a^2 + b^2 - 2ab \cos(\theta) \quad \rightarrow \quad \theta = \arccos \left[\frac{1}{2ab} (a^2 + b^2 - l^2) \right]$$

Using this formula one can calculate the derivative:

$$\frac{\partial \theta}{\partial l} = \frac{(-1)}{\sqrt{1 - \cos^2(\theta)}} \cdot \frac{-2l}{2ab} = \frac{l}{ab \cdot \sin(\theta)}.$$



So the derivative of the area with respect to the length is,

$$\frac{\partial A}{\partial l} = \frac{1}{2} l \cot(\theta)$$

and the equations of motions become

$$\sum_{b \in \mathcal{B}(e)} \epsilon_b \cot \alpha_{b,e} = 0 \quad \forall e \in \mathcal{E}, \quad (5.15)$$

where $\alpha_{b,e}$ is the angle inside the triangle (bone) b opposite to edge e , and where $\mathcal{B}(e)$ denotes the set of all triangles that are incident with edge e . Note that all derived equations of motions are all for the case of pure gravity.



5.2 Fluctuating geometry - Dynamical triangulations

The basic idea of the dynamical triangulation model is to replace the continuous Euclidean path integral over all possible geometries of a manifold weighted with the Einstein-Hilbert action with a sum over all possible triangulations of a manifold weighted with the Regge action of this triangulation. In contrast to other models quantizing the Regge model, where the edge lengths as dynamical variables are quantized on a fixed triangulation, the dynamical triangulation model fixes all the edge lengths and uses the triangulation itself as dynamical variable.

In this section we first give the definition of the dynamical triangulation model. Afterwards we derive the action of the model which depends only on the number of d - and $(d - 2)$ -simplices in the triangulation and solve the model analytically in two dimensions. Furthermore we present some important results obtained using the model of dynamical triangulations, and give some problems that are related to both the simulational setup used in literature and of the actual definition of the model. The section is concluded by remarks why multicanonical simulations are difficult to perform on dynamical triangulations for $d > 2$.

5.2.1 Definition of the dynamical triangulation model

Roughly speaking there are two different ways to go from a classical theory to a quantum theory. The first possibility is denoted as canonical quantization, going back to Paul Dirac 1925, where one has to find the canonical conjugated variables of the theory, define them as operators and replace the Poisson brackets with the commutator, carefully dealing with constraints (see e.g., Ref. [388] and the references therein for details). The second one is to use a path-integral formulation, which goes back to Richard Feynman in 1948, with precursors going back to Wiener and Dirac. The basic idea is to identify the propagator $\langle x_f | \exp(-iHt) | x_i \rangle$, which is the quantum mechanical probability that a particle initially located at position x_i will be measured after time t at position x_f , as the following functional integral

$$\langle x_f | \exp(-i\hat{H}t) | x_i \rangle = \int_{\mathbf{x}(0)=x_i, \mathbf{x}(t)=x_f} \mathcal{D}\mathbf{x} \exp(iS[\mathbf{x}]),$$

where $\mathbf{x} : \mathbb{R} \rightarrow \mathbb{R}^d$ is the path of a point particle (mapping time to a position in space), and $S[\mathbf{x}]$ is the action evaluated at path \mathbf{x} . The integration takes into account all pathes that agree with the boundary conditions $\mathbf{x}(0) = x_i$



and $\mathbf{x}(t) = x_f$, and weights every path with its action. The considered standard path integral formulation is for Lorentzian signature of the metric. An Euclidean version of the path integral, which is also used in statistical physics, can be obtained by using an imaginary time $\tau = it$, so the path integral becomes

$$\langle x_f | \exp(-\hat{H}\tau) | x_i \rangle = \int_{\mathbf{x}(0)=x_i, \mathbf{x}(t)=x_f} \mathcal{D}\mathbf{x} \exp(-S[\mathbf{x}]),$$

The connection to statistical physics can be made as follows: Suppose that the Hamilton operator \hat{H} has the eigenbasis $|n\rangle$, and denote by E_n the respective eigenvalue. Set $x_i = x_f = x$ and integrate over all x

$$\begin{aligned} \int dx \langle x | \exp(-\hat{H}\tau) | x \rangle &= \int dx \sum_n \langle x | n \rangle \langle n | \exp(-\hat{H}\tau) | x \rangle = \\ &= \sum_n \exp(-\hat{E}_n\tau) \int dx \langle x | n \rangle \langle n | x \rangle = \\ &= \sum_n \exp(-\hat{E}_n\tau) \end{aligned}$$

The last term is exactly the partition function for $\tau = \beta$, so the partition function is given by the path integral

$$Z(\tau) = \int dx \int_{\mathbf{x}(0)=x, \mathbf{x}(\tau)=x} \mathcal{D}\mathbf{x} \exp(-S[\mathbf{x}]),$$

where we only take into account periodic pathes with period τ .

The path integral can formally also be used for quantizing the continuum version of general relativity, which is in the Euclidean formulation given by

$$Z = \int \mathcal{D}_M[g] \exp(-S_{\text{EH}}(g))$$

Here the metric g takes the role of the configuration variable x , and the integration is with respect to all possible equivalence classes $[g]$ of (pseudo Riemannian) metrics on the manifold M . Here two metrics are considered as equivalent if there is a diffeomorphism that maps the first to the second metric, which is a corollary from the diffeomorphism invariance of general relativity (the physical observables do not change if coordinates are transformed by a diffeomorphism). It is also possible to consider all possible metrics and define the partition function as

$$Z = \int \frac{\mathcal{D}_M g}{\text{Vol}(\text{Diff}(M))} \exp(-S_{\text{EH}}(g)),$$



where the measure $\mathcal{D}_M g$ has to be divided through the size $\text{Vol}(\text{Diff}(M))$ of the diffeomorphism group to eliminate the unphysical degrees of freedom of the metric introduced by integrating over all possible metrics, and not over the equivalence classes.

The dynamical triangulation approach is now the following: Integrating over all physical different geometries or equivalence classes of metrics $[g]$ is equivalent to integrating over all triangulations $\mathcal{T}(M)$ of the manifold M , and the Einstein-Hilbert action can then be replaced with the Regge action.

$$\int \frac{\mathcal{D}g}{\text{Vol}(\text{Diff}(M))} \exp(-S_{\text{EH}}(g)) \rightarrow \sum_{\mathcal{T} \in \text{Triang}(M)} \frac{1}{C_{\mathcal{T}}} \exp(-S_{\text{Regge}}(\mathcal{T})) \tag{5.16}$$

The factor $C_{\mathcal{T}}$ is the size of the automorphism group of the triangulation \mathcal{T} , which has the same implication as the volume of the diffeomorphism group. It is a priori not clear which weights to assign to each triangulation $\mathcal{T} \in \text{Triang}(M)$, but the best and reasonable guess is to assign a constant weight to each triangulation. Note that the sum over $\mathcal{T} \in \text{Triang}(M)$ is a sum over triangulations of a fixed piecewise linear structure M (which equals a sum over fixed topology in low dimensions). Including all possible piecewise-linear (or topological) structures is not possible, which will be explained in Sec. 5.2.5.

Different to quantum Regge calculus, where the path integral is evaluated for a fixed triangulation and all possible assignments of the edge lengths, in the dynamical triangulation approach one uses a constant length a for every edge length in the triangulation, but evaluates the path integral over all possible triangulations of the manifold. Using constant edge lengths leads to constant volumes of the vertices, which simplifies the Regge action dramatically. In the next Sec. 5.2.2 it will be presented in detail that the action in d dimensions can be written as

$$S_{\text{DT}}(\mathcal{T}) = \kappa_{d-2} N_{d-2}(\mathcal{T}) - \kappa_d N_d(\mathcal{T}),$$

where N_k is the number of k -simplices of the triangulation, and κ_d and κ_{d-2} are coupling constants (which correspond to inverse temperatures if one uses the statistical interpretation of the Euclidean path integral). The coupling constant $\kappa_{d-2} \propto G^{-1}$ corresponds to the inverse of Newton constant G , the coupling constant $\kappa_d \propto G^{-1}(1 + c\Lambda)$ depends on both the Newton constant and the cosmological constant Λ .

Using this in the path integral leads to the partition function

$$Z_{\text{DT}}(\kappa_{d-2}, \kappa_d) = \sum_{\mathcal{T} \in \text{Triang}(M)} \exp(\kappa_{d-2} N_{d-2}(\mathcal{T}) - \kappa_d N_d(\mathcal{T}))$$



neglecting the symmetry factor $C_{\mathcal{T}}$. This can be seen as a grandcanonical partition function with system size N_4 and energy N_2 , and the canonical part can be split

$$Z_{\text{DT}}(\kappa_{d-2}, \kappa_d) = \sum_{N_d} \exp(-\kappa_d N_d) \sum_{\mathcal{T} \in \text{Triang}(M, N_d)} \exp(\kappa_{d-2} N_{d-2}(\mathcal{T}))$$

where $\text{Triang}(M, N_d)$ is the set of triangulations of manifold M with N_d maximal simplices.

In Secs. 4.2 and 4.3 we found numerical hints that the number of triangulations of the sphere scales exponentially with N_d in leading order. We introduced the notation $\kappa_d^{(c)}$ for the prefactor of the exponential scaling, which is also the entropy density of triangulations. In contrast to our previous calculations, we have now $\kappa_{d-2} \neq 0$, and the second part of the partition function behaves as [41, 111]

$$\sum_{\mathcal{T} \in \text{Triang}(M, N_d)} \exp(\kappa_{d-2} N_{d-2}(\mathcal{T})) \xrightarrow{N_d \rightarrow \infty} \exp\left(\kappa_d^{(c)}(\kappa_{d-2})\right),$$

where $\kappa_d^{(c)}(0)$ equals the previously considered constant $\kappa_d^{(c)}$. In order to get a meaningful continuum limit, the coupling constants κ_d and κ_{d-2} may not be chosen independently, but one has to use $\kappa_d = \kappa_d^{(c)}(\kappa_{d-2})$. For smaller κ_d the partition function is ill-defined, and for larger κ_d one gets a finite $\langle N_d \rangle$, which does not allow for taking the thermodynamic limit.

5.2.2 The action of dynamical triangulations

In this section the action of dynamical triangulations is derived from the Regge action (5.13), and we will show that it does only depend on the total number of simplices. Consider a d -dimensional triangulation with N_k k -simplices, $0 \leq k \leq d$, and let all edges of the triangulation have equal length a . So the k -volume $V(\sigma_i^{(k)})$ of a k -simplex is constant for all simplices and will be denoted by V_k . So the Regge action (5.13) becomes

$$S_{\text{Regge}} = \frac{1}{8\pi G} \left[V_{d-2} \sum_{b=1}^{N_{d-2}} \epsilon_b - 2\Lambda V_d \sum_{s=1}^{N_d} 1 \right],$$

Let c be the number of d -simplices (with all edge lengths equal to a) that have to be placed around a $(d-2)$ -simplex so that the deficient angle is $\epsilon = 0$ ($c = 6$ for $d = 2$, note that $c \notin \mathbb{N}$ for $d > 2$). Then

$$\epsilon_b = \frac{\pi}{c}(c - N_d(b))$$



is the deficient angle at bone b if $N_d(b)$ is the number of incident d -simplices at bone b . Every d -simplex has $\binom{d+1}{d-1} = \binom{d+1}{2}$ incident $(d-2)$ -simplices, so

$$\sum_{b=1}^{N_{d-2}} N_d(b) = \binom{d+1}{2} N_d \Rightarrow \frac{V_{d-2}}{8\pi G} \sum_{b=1}^{N_{d-2}} \epsilon_b = \frac{V_{d-2}}{8G} N_{d-2} - \frac{V_{d-2}}{8cG} \binom{d+1}{2} N_d$$

and the total action becomes:

$$\begin{aligned} S_{\text{DT}} &= \frac{V_{d-2}}{8G} N_{d-2} - \frac{V_{d-2}}{8cG} \binom{d+1}{2} N_d - \frac{N_d V_d \Lambda}{4\pi G} \\ &= \frac{V_{d-2}}{8G} N_{d-2} - \left[\frac{V_{d-2}}{8cG} \binom{d+1}{2} + \frac{V_d \Lambda}{4\pi G} \right] N_d \\ &=: \kappa_{d-2} N_{d-2} - \kappa_d N_d \end{aligned} \quad (5.17)$$

Here κ_{d-2} and κ_d are coupling constants, where κ_{d-2} depends on the value Newton constant G and κ_d depends on both the value of G and on the value of the cosmological constant Λ .

The constant c , which is the number of d -simplices that needs to be incident with an $(d-2)$ -simplex to get a vanishing deficit angle, can be calculated using the dihedral angle $\arccos(d^{-1})$, so that we have

$$c = \frac{2\pi}{\arccos(d^{-1})}.$$

Furthermore the volume V_d of a d -simplex with edge length a is known to be

$$V_d = \frac{\sqrt{d+1}}{d!2^{d/2}} a^d,$$

so the action of dynamical triangulations can be written as

$$\begin{aligned} S_{\text{DT}} &= \frac{\sqrt{d-1} a^{d-2}}{2^{-1+d/2} (d-2)! 4G} N_{d-2} \\ &\quad - \frac{1}{4\pi G} \left[\frac{\sqrt{d-1} \arccos(d^{-1}) d (d+1) a^{d-2}}{2^{1+d/2} (d-2)!} + \frac{\sqrt{d+1} \Lambda a^d}{2^{d/2} d!} \right] N_d \end{aligned}$$

Specializing for low dimensions yields

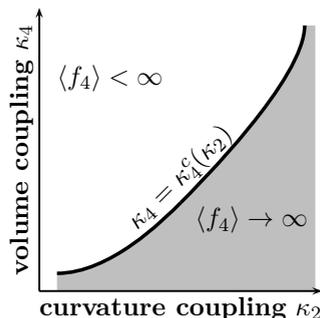
$$d = 2 \quad S_{\text{DT}} = \frac{1}{4G} N_0 - \left[\frac{1}{8G} + \frac{\sqrt{3} a^2 \Lambda}{16\pi G} \right] N_2 \quad (5.18a)$$

$$d = 3 \quad S_{\text{DT}} = \frac{a}{4G} N_1 - \left[\frac{3a \arccos(1/3)}{4\pi G} + \frac{a^3 \Lambda}{24\sqrt{2}\pi G} \right] N_3 \quad (5.18b)$$

$$d = 4 \quad S_{\text{DT}} = \frac{\sqrt{3} a^2}{16G} N_2 - \left[\frac{5\sqrt{3} a^2 \arccos(1/4)}{16\pi G} + \frac{\sqrt{5} a^4 \Lambda}{384\pi G} \right] N_4 \quad (5.18c)$$



Figure 5.5: Fine-tuning in dynamical triangulations



Note that for $d = 2$ in Eq. (5.18a) the number N_0 of vertices and the number N_2 of triangles are not independent, but connected by the Euler characteristic χ of the surface. So there is only one dynamic quantity, and one generalized inverse temperature, as explained in more detail in Sec. 5.2.3.

The action (5.17) will be used in a path integral formulation, and results in the partition function

$$Z_{\text{DT}} = \sum_{\mathcal{T}} e^{S_{\text{DT}}} = \sum_{\mathcal{T}} e^{\kappa_{d-2} N_{d-2}(\mathcal{T}) - \kappa_d N_d(\mathcal{T})} \quad (5.19)$$

Here \mathcal{T} is the set of all possible triangulations of a given underlying manifold. One can calculate this partition function analytically for $d = 2$ (compare Sec. 5.2.3), but one has to use Monte Carlo simulations in higher dimensions, because analytical results are unknown.

5.2.3 Analytical solution for dynamical triangulations in two dimensions

In Eq. (5.18a) we saw that the action of dynamical triangulations in $d = 2$ is given by

$$\frac{1}{8G} N_0 - \left[\frac{1}{16G} + \frac{\sqrt{3}a^2\Lambda}{32\pi G} \right] N_2$$

Note that the number N_0 of vertices and the number N_2 of triangles are not independent, but connected for closed surfaces by the Euler characteristic χ through

$$\left. \begin{aligned} \chi &= N_2 - N_1 + N_0 \\ 3N_2 &= 2N_1 \end{aligned} \right\} \Rightarrow N_0 = \chi + \frac{1}{2}N_2.$$

Remember that the two equations are the Dehn-Sommerville relations (4.6) for two-dimensional triangulations, the second claiming that in a closed



triangulation there are two triangles per edge, and three edges per triangle. So the actual action becomes

$$S_{\text{Regge}} = \frac{\chi}{4G} - \frac{\sqrt{3}a^2\Lambda}{16\pi G}N_2 := \frac{\chi}{4G} - \kappa_2 N_2.$$

This can also be seen more directly: The Gauss-Bonnet theorem tells us that in a two-dimensional closed manifold the deficit angles ϵ_v at vertices v are connected with the Euler characteristic χ of the manifold by

$$\sum_{v \in \mathcal{V}} \epsilon_v = 2\pi\chi,$$

which can be used in Eq. (5.13) for eliminating the sum over deficit angles. This leads to the same result as given before. The coupling constant or generalized inverse temperature κ_2 is also denoted as bare cosmological constant.

Inserting the action into the partition function (5.19) of dynamical triangulations yields

$$Z = \exp\left(\frac{\chi}{4G}\right) \sum_{\mathcal{T}(\mathcal{M})} \exp(-\kappa_2 N_2)$$

In Sec. 4.2 it was shown numerically that the number of triangulations $g(N_2)$ with N_2 maximal simplices scales as

$$g(N_2) \propto e^{\kappa_c N_2} \text{ with } \kappa_c = \log\left(\sqrt{\frac{256}{27}}\right) \approx 1.125$$

for $N_2 \rightarrow \infty$, independent of the genus or the orientability of the surfaces. The result is proven for triangulations of the 2-sphere S^2 with $\chi = 2$ [398]. The partition function then becomes

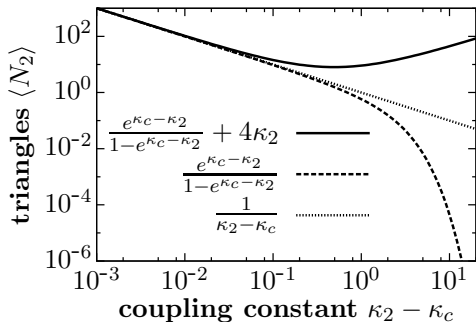
$$Z = \exp\left(\frac{\chi}{4G}\right) \sum_{N_2} g(N_2) \exp(-\kappa_2 N_2) = \exp\left(\frac{\chi}{4G}\right) \sum_{N_2} \exp((\kappa_c - \kappa_2)N_2).$$

Note that for $\kappa_2 \leq \kappa_c$ the partition function diverges. For $\kappa_2 > \kappa_c$ the partition function is a convergent geometric series, which results in

$$\begin{aligned} Z &= \exp\left(\frac{\chi}{4G}\right) \left[\sum_{N_2=0}^{\infty} (\exp(\kappa_c - \kappa_2))^{N_2} - \sum_{N_2=0}^{N_{2,\min}-1} (\exp(\kappa_c - \kappa_2))^{N_2} \right] \\ &= \exp\left(\frac{\chi}{4G}\right) \frac{\exp((\kappa_c - \kappa_2)N_{2,\min})}{1 - \exp(\kappa_2 - \kappa_c)} \end{aligned} \tag{5.20}$$



Figure 5.6: Expectation value $\langle N_2 \rangle$ for two-dimensional dynamical triangulations for different approximations. Full solution (5.21) (solid), neglecting the term $\kappa_2 N_{2,\min} \approx 0$ (dashed) and approximating $\langle N_2 \rangle \approx (\kappa_2 - \kappa_c)$ for $\kappa_2 \approx \kappa_c$ (dotted).



For $\kappa_2 \approx \kappa_c$ the partition function becomes

$$Z = \exp\left(\frac{\chi}{4G}\right) \frac{1}{\kappa_c - \kappa_2}$$

which is also the result if one replaces the infinite series with an integral with respect to dN_2 .

Since the partition function is known explicitly as function of κ_2 , expectation values of observables can easily be calculated as derivatives of the partition function. For the average number of triangles we get e.g.,

$$\langle N_2 \rangle(\kappa_2) = -\frac{\partial}{\partial \kappa_2} \log Z = \frac{\exp(\kappa_c - \kappa_2)}{1 - \exp(\kappa_c - \kappa_2)} + \kappa_2 N_{2,\min} \quad (5.21)$$

This quantity is displayed in Fig. 5.6 together with the approximations $\kappa_2 N_{2,\min} \approx 0$ and $\kappa_2 \approx \kappa_c$, which leads to

$$\langle N_2 \rangle(\kappa_2) \approx \frac{1}{\kappa_2 - \kappa_c} = -\frac{\partial}{\partial \kappa_2} \log\left(\frac{1}{\kappa_2 - \kappa_c}\right)$$

which is also the result if one derives the logarithm of the approximated partition function.

One can also calculate the fluctuations in the number of triangles using derivatives of the partition function by

$$\text{Var } N_2(\kappa_2) = \frac{\partial^2}{\partial \kappa_2^2} \log Z = -\frac{\exp(\kappa_c - \kappa_2)}{[1 - \exp(\kappa_c - \kappa_2)]^2} + N_{2,\min}$$

which is approximately

$$\text{Var } N_2(\kappa_2) \approx -\frac{1}{(\kappa_c - \kappa_2)^2}$$

for $\kappa_2 N_{2,\min} \approx 0$ and $\kappa_2 \approx \kappa_c$.



The discretisation length a , which is the length of all edges in the triangulation, is an unphysical quantity, because it is just the discretisation scale. So the results or expectation values obtained should not depend on a . The only possibility to get this in our statistical setup is to obtain a phase transition, where a statistical system becomes scale free. In this setup the phase transition happens for $\lambda \rightarrow \lambda_c$, one can see that in this limit the discretisation edge length a is not important. Since

$$\kappa_2 = \frac{\sqrt{3}}{4\pi} \frac{1}{8G} \Lambda a^2$$

we can introduce a renormalized coupling constant $K_R = a^{-2}(\kappa_2 - \kappa_c)$ and take a continuum limit such that $a \rightarrow 0$, $\kappa \rightarrow \kappa_c$ with K_R fixed. Intuitively this means that the number of triangles $\langle N_2 \rangle \rightarrow \infty$, but the area of a single triangle becomes arbitrary small, while the area of the universe is kept constant. This area can be calculated by

$$\langle A \rangle \propto a^2 \langle N_2 \rangle = \frac{a^2}{\kappa - \kappa_c} = \frac{1}{K_R},$$

so K_R can be interpreted as the inverse area of the universe. All other physical quantities, e.g., the fluctuation of the area

$$\text{Var } A \propto a^4 \text{Var } N_2 = -\frac{a^4}{(\kappa_2 - \kappa_c)^2} = -\frac{1}{K_R^2}$$

can then also be calculated in terms of the renormalized physical coupling constant K_R .

The model of two-dimensional dynamical triangulation can also be solved if one takes into account the sub-exponential scaling behavior of the number of triangulations of a surface. In Sec. 4.2 we saw that

$$g(N_2) = N_2^\gamma \exp(\kappa_c N_2),$$

with γ being a constant that depends only on the topology (orientability and genus of the surface). Using this in the partition function yields [418]

$$Z := \sum_{N_2=1}^{\infty} N_2^\gamma [\exp(\kappa_c - \kappa_2)]^{N_2} = \text{Li}_{-\gamma}(\kappa_c - \kappa),$$

where $\text{Li}_c(x)$ is the polylogarithm of order c . The derivative of the polylogarithm is $\partial \text{Li}_c(x)/\partial x = \text{Li}_{c-1}(x)/x$ [418], so the expectation value $\langle N_2 \rangle$ for the number of triangles can be calculated as

$$\langle N_2 \rangle = -\frac{\partial}{\partial \kappa} \log Z = \frac{\text{Li}_{-\gamma-1}(\kappa_c - \kappa)}{(\kappa - \kappa_c) \text{Li}_{-\gamma}(\kappa_c - \kappa)} = \frac{1}{\kappa - \kappa_c} - 2^\gamma + \mathcal{O}(\kappa - \kappa_c)$$



So taking into account the sub-exponential scaling decreases the average number of triangles, but if one considers again the physical relevant limit $a \rightarrow 0$, $\kappa \rightarrow \kappa_c$ with K_R fixed, one gets for the area of the universe

$$\langle A \rangle = a^2 \langle N_2 \rangle = \frac{1}{K_R} - a^2 2^\gamma \xrightarrow{a \rightarrow 0} \frac{1}{K_R}.$$

This means that in the physical relevant limit the area does not depend on the actual topology of the considered surface. Further calculations show that this is also valid for the fluctuations of the area.

5.2.4 Results of the dynamical triangulation approach

In this section we present the results that were obtained using the dynamical triangulation approach. Therefor we mainly follow the 1998 review paper of Loll [280], but also include some new results.

Remember that dynamical triangulations have two free parameters, namely κ_{d-2} and κ_d , but that κ_d has to be chosen as the critical value $\kappa_d^c(\kappa_{d-2})$ that depends on κ_{d-2} , in order to get a converging partition function that allows for a thermodynamic limit. So there is only one controllable parameter, the coupling constant κ_2 .

Already early simulations found that there is a critical value $\kappa_2^c(N_4)$ the depends on the number N_4 of maximal simplices that separates a crumpled phase for $\kappa_2 < \kappa_2^c$ and an elongated phase for $\kappa_2 > \kappa_2^c$ [3, 4, 27]. It was first suggested that the critical coupling constant $\kappa_2^c(N_4) \rightarrow \infty$ for $N_4 \rightarrow \infty$ [110, 130], but later simulations for larger values of N_4 showed that $\kappa_2^c(N_4)$ converges towards a constant value for $N_4 \rightarrow \infty$ with a power law $|\kappa_2^c(N_4) - \kappa_2^c(\infty)| \propto N_4^{-\delta}$ with $\delta = 0.47 \pm 0.03$ and $\kappa_2^c(\infty) = 1.336 \pm 0.006$ [30].

An important question about this phase transition is whether it is a continuous (second-order) or discontinuous (first-order) phase transition. A continuous phase transition is feasible because it can lead to a flat ground state [280]. As for the scaling of the critical point $\kappa_2(N_4)$, also for the order of the phase transition has been subject to a major discussion in the literature. The very first calculations in Ref. [4] claimed the phase transition to be first order, because a hysteresis in the average curvature was found. Many successive studies argued for a second-order phase transition using different methods, e.g., considering the Binder cumulant [14, 403], the critical exponent of certain observables [3, 403], or the height of the peak in the susceptibilities [30, 32, 110] (Note that in some of these simulations some modifications were applied that are explained in the next paragraphs). But examining the finite size scaling in all these studies is difficult due to



the critical exponents being hard to determine [280]. So some time later there were other studies with higher system sizes that found again that the phase transition is in fact first-order [90, 129], by calculating the distribution of some observables and showing that there is a two-peak structure that survives for $N_4 \rightarrow \infty$. Recently there has been a further examination of the phase structure in Ref. [345], where the author listed some mistakes that were done in the previous simulations (compare also Sec. 5.2.5). But also with a correct simulational setups, in Ref. [345] the phase transition was found to be first-order.

For examining closer the structure of the two phases a convenient observable is the expected effective dimension in the respective phases. One has several possibilities to define length and dimension. A convenient choice for measuring distance is the *geodesic distance* r between two maximal simplices, which is the shortest path length in the dual graph of the triangulations (the minimal number of hops to neighboring maximal simplices that has to be done in order to go from the one to the other simplex). The geodesic distance can be used for defining the *fractal dimension* of the triangulated space [131], also denoted as *Hausdorff dimension*. If $N_s(r)$ denotes the number of simplices that have geodesic distance r or less from a given maximal simplex s , and $V_s(r) \propto N_s(r)$ is the volume of the r -ball, then we denote by $\langle N(r) \rangle$ and $\langle V(r) \rangle$ the averages over all maximal simplices s of the triangulation. The fractal dimension d_f describes the scaling of $\langle V(r) \rangle$ in the power law

$$\langle V(r) \rangle \propto \langle N(r) \rangle \propto r^{d_f}$$

Another dimensional measure is the *spectral dimension*, which is defined using a random walk on the dual graph of the triangulation [39]. If $p_s(t)$ is the probability that a random walker being initial at maximal simplex s is back again at s after time t , the spectral dimension d_s is the average scaling exponent of this quantity

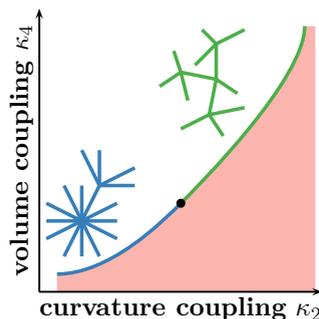
$$\langle p(t) \rangle = \frac{1}{N_d} \sum_{s=1}^{N_d} p_s(t) \propto t^{-d_s/2}$$

In general both dimensional measures do not need to coincide.

The two different phases are commonly described as *crumpled* or *hot phase* for $\kappa_2 < \kappa_2^c(N_4)$ and as *elongated* or *cold phase* $\kappa_2 > \kappa_2^c(N_4)$ [45, 345]. In the crumpled phase there is one highly connected cluster of maximal simplices, and only a few clusters outside that have a size which is way below the size of the main cluster. In the elongated phase there are several clusters of comparable sizes, which are connected among each other only



Figure 5.7: Phase diagram of 4d dynamical triangulations. The coupling constant κ_4 has to be tuned to its critical value $\kappa_4^c(\kappa_2)$ to obtain the infinite-volume limit (compare Fig. 5.5 for a detailed explanation). One observes that there are two different phases: For low κ_2 there is a crumpled phase with one big cluster, for high κ_2 there is an elongated phase with several clusters connected by small structures. At the critical point one finds probably a first-order phase transition according to literature.



through very small structures [345]. The average curvature in the elongated phase is positive in the elongated phase, but very small in the crumpled phase [27]. The fractal dimension of the crumpled phase approaches ∞ , and is approximately 2 in the elongated phase [345]. A qualitative plot of the phase diagram can be found in Fig. 5.7.

For a closer examination, one can use methods of renormalization group theory and calculate the renormalization flows. The standard approach is to apply this to continuous phase transitions to obtain the continuum limit, but it is also possible to consider first order phase transitions. For dynamical triangulations, two different approaches for defining the renormalization step were tried. The first is to cut baby-universes from the whole triangulation [90, 105], but this has the disadvantage that it is not possible to apply several steps successively. The second is a blocking procedure that consists of removing vertices from the triangulation using a generalized removal step [340, 341].

There have also been tries to extend the model by several modifications. One ansatz is to include higher derivative terms (e.g., $\propto R^2$ and $\propto R_{\mu\nu}R^{\mu\nu}$) into the Einstein-Hilbert and therewith the Regge-action, which introduces the term [32]

$$\Delta S = \kappa_{\text{HD}} \cdot c_d \cdot \sum_{b \in \mathcal{B}} \left(\frac{c_d - N_d(b)}{N_d(b)} \right)^2$$

where c_d denotes the (not necessarily integer) number of d -simplices that have to be arranged around a $(d-2)$ -simplex (bone) to have no deficit angle, $N_d(b)$ denotes the actual number of d -simplices incident with the bone b , and κ_{HD} denotes the additional coupling constant. This is comparable with the energy function that we introduced for lattice triangulations in Chap. 3. For the considered parameter ranges in Ref. [32] no qualitative



difference was found compared to the standard case $\kappa_{\text{HD}} = 0$. Another possible modification is not to consider triangulations of the d -sphere, but to use triangulations of other topologies. But again for this modification no qualitative difference was found [91, 93]. It is also possible to consider triangulations with boundaries, introducing an additional boundary coupling constant. In both three and four dimensions one gets additional phases that are dominated by the boundary, but also the transitions between this phase and the other phases are discontinuous [409, 410].

Until now only vacuum solutions of Regge calculus and dynamical triangulations were considered. Of course for a complete theory of quantum gravity there has to be a possibility to couple the gravitational degrees of freedom to some matter fields, and to take into account the back-reaction of the matter fields on the geometry. In the approach of dynamical triangulations, several Ansätze were tried. Coupling dynamical triangulations with Ising spins and Gaussian fields did not induce qualitative differences to vacuum gravity, even if one includes higher derivative terms in the curvature [14, 32]. Also the use of \mathbb{Z}_2 spin variables cannot change the critical region between the two phases [31]. The introduction of coupling to several $U(1)$ -fields in $d = 4$ led to a possible replacement of the branched-polymer phase with a weakly coupling phase with fractal dimension of 4 [92], which also can be understand in mean field theory [49]. But the considered system sizes are too small to get reliable results [280].

5.2.5 Problems of the dynamical triangulation approach

There are also some problems related with the approach of dynamical triangulations, which we will summarize in this section.

In Sec. 5.2.1 it was mentioned that it is not possible to include all triangulations of all piecewise-linear structures (of the considered dimension d) into the partition sum. The problem is that not fixing the piecewise-linear (or, in low dimension equivalently, the topological structure) would imply that more than exponentially many simplicial complexes with N_d maximal simplices have to be taken into account in the sum (compare e.g., Cor. 2.3.2 and Cor. 2.3.5 in Ref. [77] for proof for $d = 2$ and $d = 3$). Formally written this means that there is no constant C such that $g(N_d) \leq \exp(CN_2)$, which induces that the entropy density grows with the system size (and does not converge towards a constant value), so the thermodynamic limit is not well-defined. Intuitively, it is irrelevant on how large the coupling constant κ_d is chosen, the system is always driven to infinite system size due to entropy. Fixing the topology or the piecewise-linear structure means that it



has to be given as an input parameter into the theory or into the simulations, but it would be more desirable if the (perhaps average) topology of the universe would be an outcome of the theory.

As explained in Chap. 4 even if restricting to a certain piecewise linear structure (like a sphere), it is not proven that there not more than exponentially many spheres for $d = 3$ and $d = 4$, so the model may even be ill-defined in the restricted version. In fact one can show that the number of so-called locally constructable spheres (which is an actual subset of all simplicial spheres [77]) grows only exponentially with the number of maximal simplices [147], and one can limit the summation in the partition function only to those locally constructable spheres. However, such a restriction is very arbitrary, and there is no argument in favor for such a restriction. There are simulations arguing for and against exponential bounds in three and in four-dimensions [28, 44, 45, 100, 104, 111, 112], and also in Sec. 4.3 of this thesis, but of course they can only give some clues and hints and no strict mathematical proofs.

Using the Metropolis algorithm in the setup of dynamical triangulations forces the restriction to a quasi-canonical ensemble. Directly restricting to a fixed N_4 is not possible because in general there is no set of canonical ergodic moves. The usual cure to keep the simulation near a given \overline{N}_4 is to introduce an additional potential $\gamma(N_4 - \overline{N}_4)^2$ that penalizes systems near the desired \overline{N}_4 , and to take the measurements only if the system is at $N_4 = \overline{N}_4$. The coupling constant γ is unphysical and has to be chosen large enough that enough systems have $N_4 = \overline{N}_4$, but small enough that ergodicity is not violated. In Ref. [113] the system was forced to lie in the range $\overline{N}_4 \pm \Delta N_4$, and for \overline{N}_4 no dependence of the expectation values of the number of vertices and the average length on ΔN_4 was found for $\overline{N}_4 = 4000$. In Ref. [91] the parabolic penalty was used and a comparison between the distribution of N_0 was performed for an effective $\Delta N_4 = 45$ corresponding to $\gamma = 5 \cdot 10^{-4}$ and $\Delta N_4 = 14$ corresponding to $\gamma = 5 \cdot 10^{-3}$ near the average value $\overline{N}_4 = 3.2 \cdot 10^4$, and no qualitative disagreement was found.² The data obtained by the systematic studies using Wang-Landau simulations in this thesis for three-dimensional topological triangulations (presented in Sec. 4.3) shows that there can be in fact a problem with ergodicity if introducing an additional term. This differs from the two former considerations in literature, because in Ref. [113] only very small triangulations were considered, and in

² In fact, the authors of Ref. [91] claim that they considered both $\gamma = 5 \cdot 10^{-4}$ and $\gamma = 5 \cdot 10^{-3}$, but they did not mention which one they use for the comparison with the large deviation. So one has to conjecture that $\gamma = 5 \cdot 10^{-4}$ was used



Ref. [91] the considered γ is larger than usual choices of γ (e.g., $\gamma = 5 \cdot 10^{-3}$ in Ref. [111]), so ergodicity breaking is weak. But also in the literature there is the concern that the simulational setups of Refs. [93,113] consider too small system sizes [93,280].

Beside the problem of ergodicity, triangulation have to fulfill also the stronger notion of computational ergodicity. Triangulations are computationally ergodic, if they are ergodic and there is a recursive function that bounds the number of Pachner moves that is necessary to go from one to the other triangulations. It was proven that the 4-sphere is not computationally ergodic [308]. This is strongly related with the question whether the d -sphere S^d (or any other topology that is used in the simulation) is recognizable, i.e., whether there exists an algorithm that decides whether the triangulated space of an arbitrary input d -triangulation is homeomorphic to the d -sphere. For $d = 1$ and $d = 2$ this is trivial, in the former case one has to check that for each vertex there are two edges incident with it and vice versa, for the latter one has to calculate the Euler characteristic χ . In three dimension the question was solved only in the 1990s by Rubinstein and Thompson [355,356,389], but it can be shown that this algorithm is in the NP complexity class [359]. For $d \geq 5$ it can be shown that the d -sphere is not recognizable (§10 by S. P. Novikov in Ref. [405]), and for $d = 4$ it is currently unknown whether the S^4 is recognizable or not. There are numerical studies that claim that the 4-sphere is recognizable by performing simulated annealing on triangulated 4-spheres simplifying triangulations to the boundary of the 5-simplex and obtaining that there are no large barriers in N_4 [29]. But on the one hand there are also such studies for the 5-sphere [128], which is known to be non-recognizable, and on the other hand the algorithm used for creating triangulations of the S^4 in [29] is constructing spheres from the boundary of the 5-simplex, so it is not astonishing that they can be simplified easily to the boundary of the 5-simplex again.

In the recent simulational study in Ref. [345] the following three possible sources for errors were listed, especially for the setup of Refs. [3,110]:

- The simulation time was measured not in terms of suggested steps as usual in Monte Carlo simulations, but in terms of accepted steps, which can be problematic because there are different acceptance probabilities at different inverse temperatures.³

³ This can be understood in the following way: Consider a two-state system with energies $E_1 = 0$ and $E_2 = E$. A standard Metropolis simulation with inverse temperature $\beta \gg 0$ will almost always stay in the state E_1 and rejecting steps to E_2 . So the e.g., the average



- The use of a harmonic potential to keep the simulations near the desired value of N_4 can induce errors, as already mentioned in Sec. 4.3. The authors of Ref. [345] suggested to simply cut the available energy range.
- There is no systematic examination of the autocorrelation time.

Until now we listed only problems involving the simulational setup. Beside these there are also some results that make it questionable whether dynamical triangulations are feasible as model for quantum geometry. Since there is successor model called Causal Dynamical Triangulations (presented in the next section) by some of the main contributors to the dynamical triangulation setup, of course several problems of the latter are listed in motivations for constructing the former approach, that may otherwise never be mentioned in any papers of the main contributors.

The main problem associated with four-dimensional dynamical triangulations is that the fractal dimension is $d_f \neq 4$ on large length scales, but $d_f = 2$ or $d_f = \infty$ depending on the considered phase. This is despite the fact that one uses explicitly four-dimensional simplicial building blocks as input parameter for the simulation. It was proposed that an additional non-trivial measure term in the action (which introduces a third coupling constant) can lead to a phase with fractal dimension four on large scales [268], but this additional measure term together with the coupling constant cannot be motivated directly from the Einstein-Hilbert action or its discrete analogue, the Regge action. Furthermore it was shown later on that the additional phase shows features that are not compatible with an expanded universe [124].

An important problem is that the path integral used to define the model of dynamical triangulations is an Euclidean path integral, whereas the physical world we live in is a Lorentzian spacetime, so a Lorentzian path integral should be used. The usual procedure for transforming an Euclidean path integral into a Lorentzian one, the *Wick-rotation*, can only be applied under certain very restrictive conditions (e.g., if the time- and the space-components of the metric tensor do not mix, and the spatial components are independent of time) [42]. The intuitive reason is that in a general four-dimensional manifold there is no preferred direction of time [33]. So it is unlikely that performing an Euclidean path integral as in dynamical triangulations can be used at all to describe a Lorentzian spacetime (in contrast to usual lattice QFT) [42].

energy is $\langle E \rangle = 0$. If one takes only into account accepted steps, one misleadingly calculates the average energy to be $\langle E \rangle = (E_1 + E_2)/2 = E/2$.



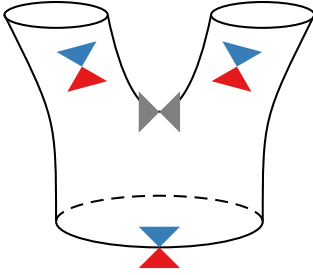


Figure 5.8: Change of the spatial topology in the setup of dynamical triangulations. If one tries to artificially impose a time-direction on a manifold (here S^2 if one includes the lower and the two upper cups), it is possible that the topology changes. If the time direction is assumed to be from bottom to the top, for early times we have the spatial topology S^1 , and for late times we have the topology of two different S^1 . Furthermore there are critical points where one cannot define a causality structure (blue corresponds to future, red to past, and grey to unknown). This figure is adopted from [193, p. 13].

Another problem that is related to the previous is that given an arbitrary triangulation of, e.g., S^3 it can be impossible to choose a time-direction such that the spatial topology remains unchanged. Consider e.g., dynamical triangulations defined on S^2 as depicted in Fig. 5.8. Imposing an artificial time direction can lead to a change in the topology, and there are critical points where one does not have a valid causal structure (i.e., one cannot define past and future).

A minor problem that we list for completeness is that it is argued in Ref. [48] that the expectation value $\langle R \rangle$ of curvature should vanish in the thermodynamic limit. But in the considered setup of dynamical triangulations we have $\langle R \rangle > 0$, also in the cases of the modified action and the modified topology. Sometimes it is argued in literature that the volume and the curvature contributions to the action mix during a renormalization process, so that the curvature in fact vanishes [131].

5.2.6 Multicanonical algorithms for dynamical triangulations

The results for dynamical triangulations presented in Sec. 5.2.4 were mainly obtained using a Metropolis Monte Carlo algorithm. The problems of the dynamical triangulation approach listed in Sec. 5.2.5 are sometimes related with this particular choice of algorithm. One might suggest that using multicanonical algorithms as the Wang-Landau algorithm can be used for the numerical treatment of dynamical triangulations, since we successfully applied it e.g., in Sec. 4.2 for calculating the entropy density



$\kappa_d^{(c)}$ of topological triangulations, a quantity that is of direct importance for the dynamical triangulation approach. In this section we will show some problems that occur if trying to use multicanonical methods on dynamical triangulations in three and higher dimensions.

Using the standard Wang-Landau algorithm for calculating the density of states (DOS) $g(N_d, N_{d-2})$ in terms of N_d and N_{d-2} directly is computationally expensive. To calculate canonical expectation values at $\overline{N_d}$ maximal simplices one has to consider an interval $N_d \in [\overline{N_d} - \Delta N_d, \overline{N_d} + \Delta N_d]$ with high enough ΔN_d to avoid problems with ergodicity as described in Sec. 4.3. For each possible N_d there are a huge number of possible N_{d-2} , and for each pair there is a bin of the DOS to be calculated. As calculated in Sec. 2.3.2 the calculation time for the Wang-Landau algorithm scales as $b \log b$, where b is the number of energy bins. So it is hard to use the Wang-Landau algorithm for calculating $g(N_d, N_{d-2})$ in a reasonable computation time. One possible cure is to use the replica exchange version of the Wang-Landau algorithm [404], because here one can subdivide the density of states without violating the ergodicity, because a certain replica can actually reach every possible value of (N_d, N_{d-2}) through replica exchange steps.

Since the DOS $g(N_d, N_{d-2})$ is not directly accessible numerically, one can try to split the calculations into two parts. Note that the partition function is given by

$$\begin{aligned} Z(\kappa_d, \kappa_{d-2}) &= \sum_{\mathcal{T} \in \text{Triang}(M)} \exp(-\kappa_d N_d(\mathcal{T}) + \kappa_{d-2} N_{d-2}(\mathcal{T})) \\ &= \sum_{N_d} \exp(-\kappa_d N_d) \sum_{\mathcal{T} \in \text{Triang}(M, N_d)} \exp(\kappa_{d-2} N_{d-2}(\mathcal{T})). \end{aligned}$$

The second part of the partition function can be interpreted as canonical partition function $Z(N_d, \kappa_{d-2})$ for fixed N_d . This is used by the usual Metropolis simulations by restricting the simulation to a certain quasi-canonical range around $\overline{N_d}$, but therefore a fine-tuning of the parameter κ_d to its critical values $\kappa_d^c(\kappa_{d-2})$ is necessary as described above. But also a multicanonical approach is possible. First the integrated DOS $g(N_d) = \sum_{N_{d-2}} g(N_d, N_{d-2})$ can be calculated using the Wang-Landau algorithm as described in Chap. 4. Then this DOS can be used for a combined sampling which is flat in N_d and Metropolis-like in N_{d-2} , so that the actual sampling probability becomes

$$P(N_d, N_{d-2}) \propto \frac{1}{g(N_d)} \exp(\kappa_{d-2} N_{d-2}),$$



which can be used for calculating acceptance probabilities (Note that in practice one has to restrict the range of possible N_d to an interval big enough so that the ergodicity holds, and that one only takes measurements for $N_d = \bar{N}_d$. This works for $\kappa_{d-2} \approx 0$, but fails for other values of this coupling constant. The reason is the following: The integrated DOS $g(N_d)$ is the DOS for simple sampling in N_{d-2} . Using a high coupling constant κ_{d-2} drives the system to high or low N_{d-2} , which effectively changes the DOS⁴. This means that in the simulations the system is driven to the boundaries of the interval in N_d , which could be in principle corrected by modifying the coupling constant κ_d , but this corresponds to a fine-tuning procedure one would like to avoid.

The only time a multicanonical algorithm was applied in the setup of dynamical triangulations was in Ref. [220] for $d = 3$. Unfortunately this work was not recognized in the literature about triangulations as spacetime models. The main problem of this paper is that they claim to use a very small interval in N_3 for their calculations. This reduces the number of bins in the DOS and speeds up the calculation, but also the ergodicity of the Pachner moves is probably violated (as shown in Sec. 4.2).

⁴ For the same reason the critical coupling $\kappa_d^c(\kappa_{d-2})$ is not only a function of the system size, but also on the coupling constant κ_{d-2} used



5.3 Fluctuating spacetimes - Causal Dynamical Triangulations

In Sec. 5.2.5 it was presented that several problems occur within the approach of dynamical triangulations. Beside all the problems that are related to the simulational setup, one cannot observe any structures that look like the universe we are living in on large length-scales. Furthermore, there can be severe problems with causality, because there are a lot of triangulations where it is not possible to define a proper time direction. There have been several tries to modify the setup or the action of dynamical triangulations to solve this physical problems, e.g., by including higher derivative or non-trivial measure terms into the action, or by coupling the action to matter (compare Sec. 5.2.4 for details and references), but none of them lead to a real solution of the problems.

The key ingredient to solve some of the problems goes back to an idea of Claudio Teitelboim [385, 386] and was adopted to dynamical triangulations first 1998 in Ref. [42]. The idea is in order to have a properly defined path integral to only include single pathes that obey causality. Transferred to the dynamical triangulation approach this means that only causal triangulations, i.e., triangulations with a valid causal structure, should contribute to the partition function. The implementation of this idea in fact lead to a solution of some of the problems that arise in the dynamical triangulation approach.

In this section we first define a causal triangulation and formulate the partition function of the model called causal dynamical triangulations (CDT). Then we give a short introduction about the existing literature and present the most important results of the CDT approach. To be able to use Markov chain Monte Carlo simulations within this approach we afterwards describe the how to define causality preserving flips and to construct small causal triangulations. The next step is to modify the action of dynamical triangulations to take into account the Lorentzian signature of the metric and the artificial break of symmetry between space-like and time-like links.

Using Wang-Landau simulations it is possible to calculate the density of states of causal triangulations of one slice. We will present how this density of states can be used for calculating a transfer matrix and to directly calculate the limit of infinite time slices. This exact transfer matrix approach will be applied numerically to $(2 + 1)$ -dimensional causal dynamical triangulations, where there is strong evidence for a second order phase transition that is claimed to be needed for defining a valid continuum limit, but only in one phase of the discontinuous phase transition used fro fine-tuning. We



conclude this section by describing some remaining problems of the causal dynamical triangulation approach and presenting a summary and an outlook on work that can be done with our methods in the setup of causal dynamical triangulations.

5.3.1 Causal dynamical triangulation setup

In this section we present how the already considered approach of dynamical triangulations (DT) can be modified to get a causal version thereof. We present the basic ideas of this new causal dynamical triangulation (CDT) approach and list the main differences to the standard approach of DT.

Remember that the model of dynamical triangulations was defined as an (Euclidean) path integral over all possible discretized versions of a given manifold (which are the triangulations), each of them weighted with the Regge action. This definition leads to the partition function (5.16) of dynamical triangulations

$$Z_{\text{DT}}(\kappa_{d-2}, \kappa_d) = \sum_{\mathcal{T} \in \text{Triang}(M)} \frac{1}{C_{\mathcal{T}}} \exp(-S_{\text{DT}}(\mathcal{T}, \kappa_{d-2}, \kappa_d)),$$

where $\mathcal{T} \in \text{triang}(M)$ is an arbitrary triangulation of a given manifold M , and $S_{\text{DT}}(\mathcal{T}, \kappa_{d-2}, \kappa_d)$ is the action (5.17) of dynamical triangulations that depends on topological quantities of the triangulation \mathcal{T} (namely the number N_d of d -dimensional and the number N_{d-2} of $(d-2)$ -dimensional simplices) and on some coupling constants κ_d and κ_{d-2} , and $C_{\mathcal{T}}$ is a symmetry factor that can be set to one in almost all situations. One can use analytical calculations or Monte Carlo simulations to find expectation values with regard to this partition function, in order to draw conclusions about the generated spacetime. But also with some modifications there are several problems (presented in Sec. 5.2.5) in the approach of dynamical triangulations that could not be solved.

Two of the main problems associated with the DT approach are that it is defined purely within Euclidean signature, and that there can occur configurations that violated causality. The latter might not be a problem at all, because one can conjecture that these strange configurations are of measure zero with respect to the other configurations, and do not contribute to the partition function at all. But the Euclidean signature can probably not be turned to a Lorentzian signature of the whole spacetime even if considering the ensemble of all triangulations (at least this cannot be observed in the simulations).



One possible refinement that can cure these problems is commonly known as causal dynamical triangulations (CDT) approach, which considers causal triangulations or equivalently a foliation of the underlying spacetime manifolds. It goes back mainly to the work of Jan Ambjørn, Renate Loll and Jerzy Jurkiewicz starting in 1998 (see e.g., Refs. [35, 42] for some early original papers, and [38, 281] for some reviews), but they claim that their idea goes back to Claudio Teitelboim [385, 386] in 1983. He argues that history as well as causality have to be implemented into the single pathes of a path integral formulation of quantum gravity, which means that for the path integral one considers only such pathes or spacetimes where every spatial geometry is either in the past or in the future of every other spatial geometry.

This led to the idea to replace the Euclidean path integral over all possible triangulations $\mathcal{T} \in \text{triang}(M)$ of an arbitrary manifold M with the Lorentzian path integral over triangulations respecting the causal structure of a manifold $M = \Sigma \times \mathcal{I}$, where Σ is the underlying manifold of a single spatial slice and \mathcal{I} is the manifold describing the topology of the time coordinate, which can be an open interval $\subset \mathbb{R}$ or the closed 1-sphere S^1 :

$$Z_{\text{CDT}}(\vec{\kappa}) = \sum_{\mathcal{T} \in \text{cTriang}(\Sigma \times \mathcal{I})} \exp(iS_{\text{CDT}}(\mathcal{T}, \vec{\kappa}))$$

where $\text{cTriang}(\Sigma \times \mathcal{I})$ is the set of triangulations admitting a proper causal structure, and $S_{\text{CDT}}(\mathcal{T}, \vec{\kappa})$ is the action of the causal triangulation \mathcal{T} (described in details later) that depends furthermore on a set $\vec{\kappa}$ of coupling constants. A common choice for the spatial manifold is the $(d-1)$ -sphere $\Sigma = S^{d-1}$. Since a triangulation consists of a finite number of vertices, there is also only a finite number T of spatial slices that can be indexed by natural numbers $\Sigma_0, \dots, \Sigma_{T-1}$.

Before we give conditions whether a triangulation is a causal one, we first introduce some technical definitions. An edge is called *space-like*, if the constituting two vertices lay in the same spatial slice Σ_t . Otherwise it is called *time-like*, which implies that the constituting vertices lay on different spatial slices. A simplex is called *space-like*, if all of its one-dimensional subsimplices (edges) are all space-like, otherwise it is called *time-like*. We define a 0-simplex to be space-like, although there are no edges as subsimplices, but the previous definition implies that for a space-like simplex all constituting vertices live in the same spatial slice, which is trivially fulfilled for a vertex.

A triangulation is now defined to admit a proper causal structure, if for each vertex one can choose a unique time coordinate (w.l.o.g. $\in \mathbb{Z}$), so that



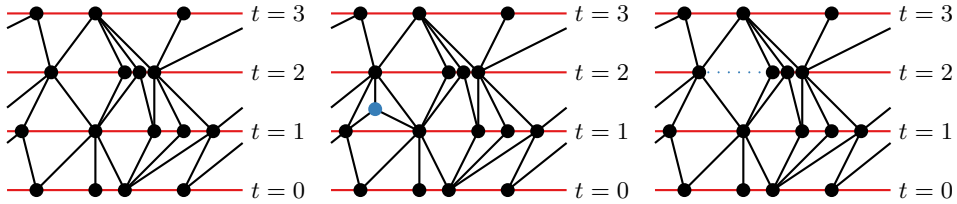


Figure 5.9: Example of valid causal triangulation (left), and examples of triangulations (middle and left) violating the causality structure, both in $(1 + 1)$ dimensions. In the middle triangulation the blue vertex cannot be assigned a valid time coordinate (because it lies between two spatial slices). In the left triangulation the spatial triangulation at time coordinate $t = 2$ is not a triangulation of the spatial manifold S^1 .

each vertex at time coordinate t is only connected with vertices with time coordinates t and $t \pm 1$. (The time coordinate t of a vertex corresponds to the index of the spatial slice Σ_t) Furthermore all space-like simplices consisting of vertices with the same time coordinate form a valid triangulation of Σ . So it is, e.g., not allowed to have simplices that consist of vertices which are located on more than two spatial slices, or on two spatial slices that are no direct neighbors⁵. Examples for valid and non-valid causal triangulations in $(1 + 1)$ dimensions can be found in Fig. 5.9.

Since by this definition simplices contain only vertices from two neighboring spatial slices, a time-like k -simplex can be classified further by specifying how many of its vertices live in the different spatial slices, so we denote by (\underline{k}, \bar{k}) -simplex a k -simplex ($k = \underline{k} + \bar{k} - 1$) with \underline{k} vertices located in the one spatial slice, and \bar{k} vertices located in the other spatial slice. Since the order of the spatial slices is not important, we define that $\underline{k} \geq \bar{k}$. Using this scheme a space-like k -simplex can be denoted as $(k + 1, 0)$ -simplex.

In addition to the structure of the triangulation also the structure of the simplicial building blocks is changed in the CDT approach. Remember that in the DT approach all edge lengths were fixed to a constant value a . Due to the Lorentzian signature of the metric space-like edges must have a positive spacetime interval $\ell_{\text{space}}^2 > 0$, whereas time-like edges must have a negative spacetime interval $\ell_{\text{space}}^2 < 0$. In the CDT approach one also allows different absolute values for the spacetime interval for time-like and space-like edges, which describes an imbalance between space and time direction. Usually

⁵ In this section we denote as *spatial slice* a $(d - 1)$ -dimensional triangulation of the spacetime $(d - 1)$ -manifold Σ , and as *(time) slice* the d -dimensional triangulation of two neighboring spatial slices and the d -dimensional space inbetween



one sets $\ell_{\text{space}}^2 = a^2$ for space-like edges, and $\ell_{\text{time}}^2 = -\alpha a^2$ for time-like edges. The parameter α then becomes important for the Wick rotation.

5.3.2 Important results in causal dynamical triangulations

In this section we give a short overview about the existing literature and results within the causal dynamical triangulation (CDT) approach. For a first impression about CDT there is a popular science review [40] presenting the basic concepts, and scientific review papers [38, 281] for literature review and the basic results.

In 1998 Jan Ambjørn and Renate Loll for the first time introduced causality into the dynamical triangulation (DT) approach and were able to solve causal dynamical triangulations analytically in $(1 + 1)$ dimensions [42]. Later on it was shown that there is a one-to-one correspondence between DT and CDT if one allows for changes in the spatial topology (which is normally excluded to prevent the formation of baby universes) in the latter approach [15, 43]. CDT in $(2 + 1)$ and $(3 + 1)$ dimensions was first treated in Refs. [35] and [36], respectively.

Due to the split of the considered space in one time and several space directions it is easier to find mathematical results about the extensivity of causal triangulations. It was found in Ref. [148] that $(2 + 1)$ -dimensional causal triangulations are extensive in terms of the number of 3-simplices, and that $(3 + 1)$ -dimensional causal triangulations are extensive in terms of the number of 4-simplices if there are exponentially many 3-spheres (which is still an open questions, see Sec. 4.3).

Due to causal dynamical triangulations being solvable analytically in $(1 + 1)$ dimensions, proofs and extensions were performed mainly in this dimensionality. There were, e.g., several tries to include a coupling between matter and geometry into the theory [22–24, 46, 81] (the coupling in $(3 + 1)$ dimensions was examined numerically only in Ref. [246]). Furthermore, in Refs. [282, 283] it was shown that in $(1 + 1)$ -dimensions including a sum over all possible topologies of the manifold into the partition function is possible and does, in contrast to Euclidean dynamical triangulations, not lead to an over-exponential scaling of the number of triangulations in terms of the system size, which seems to be a really good result, because one does not have to artificially input a certain topology from the beginning. But note that there is a fundamental difference between the notion of *summing over all topologies* in the two setups, although they are both two-dimensional: In DT this means summing over all possible 2-manifolds, whereas in CDT this notion means summing over all possible 1-manifolds M_1 and using $\mathcal{I} \times M_1$



as underlying manifold of the causal triangulation⁶. Furthermore, it is definitely not possible to include a sum over the topologies into the partition function of CDT in more than two dimensions, because then already the number of triangulations of the spatial slices grows faster than exponential.

The discovery of the phase structure and the analysis of the transitions between the phases was a big success in $(3+1)$ -dimensional causal dynamical triangulations [25, 26]: It was found that in the two-dimensional parameter space (κ_1, Δ) after fine-tuning $\kappa_3 \rightarrow \kappa_3^{(c)}(\kappa_1, \Delta)$ one can find three different phases. The first is dominated by triangulations where the three-volume $V_3(t) \propto N_3(t)$ of the spatial slices has only a finite value at one time-coordinate t_0 , and all other three-volumes almost vanish. To the second phase there contribute mainly triangulations where the three-volume $V_3(t)$ has peaks at some time-coordinates t_1, \dots, t_k , but the spatial slices with non-vanishing three-volume are separated by spatial slices with vanishing volume. Clearly, on large scales these phases or a transition do not describe the spacetime we live in. But there is a third phase, which is denoted as extended phase, where most or all time slices have a non-vanishing three-volume. The transition between the one-slice and the extended phase is continuous (or second order), the transition between the multiple-slice and the extended phase is discontinuous (or first order).

Furthermore there are hints that between the one-slice and the extended phase there is another phase which is denoted as bifurcation phase [19]. In this phase the spectral dimensions is believed to be greater than four, furthermore one use an effective transfer matrix approach to derive an effective action. In this effective action one can observe from the sign of the kinetic and the potential distribution that the signature of the metric changes from Lorentzian to Euclidean signature [16].

One of the important features of $(3+1)$ -dimensional CDT is that the extended phase has a fractal dimensions four on large scales and fractal dimension two on small scales. Remember that for ordinary dynamical triangulations only phases with Hausdorff dimension two or ∞ were found (compare Sec. 5.2.4 and the references therein), so our actual macroscopic spacetime (which has (at least) four dimensions) could not be described. The first numerical measurements of the Hausdorff dimension were performed in [36, 39]. Note that the measured Hausdorff dimensions depend on the actual value of the coupling constants used [123], and that for most coupling

⁶ Note that the spatial topology in one dimension is given only by the number of components, where every component is a ring and posses only one triangulation with given number of maximal simplices (edges).



constants the spectral dimension at high energy (or short length scales) becomes $3/2$ rather than 2. But $d = 3/2$ is exactly the dimension that one needs to fulfill the asymptotic safety scenario [123].

The asymptotic safety scenario [416] states that there is a possibility for renormalize the in general non-renormalizable theory of general relativity. The standard procedure of perturbative renormalization applied to field theories fails for general relativity in three or more spacetime dimensions, because one needs an infinity number of tunable coupling constants to cancel diverging terms, which implies that the perturbatively quantized theory is not predictive. The asymptotic safety scenario claims that the theory becomes predictive if the renormalization flow of a finite number of coupling constants approaches an ultraviolet fix-point, which is a second-order transition in a lattice theory as DT or CDT. There is one big problem associated with the scenario of asymptotic safety [59, 367]: One can argue that the entropy of a renormalizable theory in regime of high energies scales as $S \propto E^{(d-1)/d}$, whereas in general relativity one expects that the high energy states are dominated by black holes, whose entropy scales as $S \propto E^{(d-2)/(d-3)}$ (d is the dimension of the spacetime). For $d = 4$ these two equations disagree, only for $d = 3/2$ the two entropies scale with the same power law $S \propto E^{1/3}$. Since high energy scales correspond to small length scales, one can argue that the asymptotic safety scenario in fact holds, but that the fractal dimension of the spacetime depends on the length scale, with $d = 3/2$ for $E \rightarrow \infty$.

So one might argue that due to this results causal dynamical triangulations is a theory in which the asymptotic safety scenario holds. Unfortunately the fractal dimensions in [123] were measured inside the extended phase, and not on a second-order phase transition between two phases, which is necessary for a non-trivial fix-point. Also note that a scale-dependent dimension implies very strong consequences like a non-constant speed of light or a broken Lorenz invariance (see Ref. [125] and the references therein).

Another property of the extended phase in the $(3 + 1)$ -dimensional CDT approach is that the extended phase exhibits a de-Sitter-like structure [21, 37]. By de-Sitter space one denotes an elliptic spacetime with Lorentzian signature and constant positive curvature (sphere), but without matter. It has the same relation to the sphere as the Minkowski spacetime to Euclidean space. Note that there are some conceptional problems that are related with the analysis in Ref. [21] that will be presented later. Furthermore, similarities between the phase diagram of Hořava-Lifshitz gravity [221] (which also relies on a broken symmetry between space and time, which is recovered in a continuum limit) and of the phase diagram of CDT have been



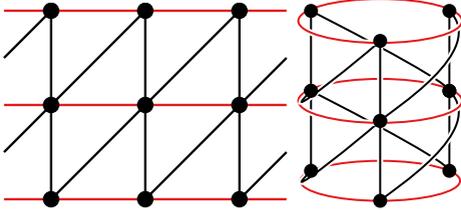


Figure 5.10: Minimal causal triangulation of $S^1 \times S^1$ with two time slices and three spatial slices, composed of two one-slice triangulations (5.23). Embedding into a plane (left), where the edges to the left and to the right are continued to the other side, and onto the boundary of a cylinder (right).

found [20], which can possibly lead to a mutual exchange of ideas between the two theories.

5.3.3 Constructing causal triangulations - small triangulations and flips

To apply Markov chain Monte Carlo simulations also to the model of causal dynamical triangulations, one has to construct at least one valid causal triangulation and to define ergodic moves that transform causal triangulations into each other, as already done before for embedded and topological triangulations. In this section we construct such small causal triangulations for $(1 + 1)$ - and $(2 + 1)$ -dimensional manifolds with spatial manifold $\Sigma = S^1$ and $\Sigma = S^2$. It is enough to construct a triangulation of one time slice (which equals two spatial slices and the spacetime portion inbetween), if the two boundary spatial triangulations are equal, because T -slice triangulations (with open and periodic boundary conditions) can then be constructed by stacking these small triangulations. For $(2 + 1)$ dimensions we explicitly count the number of some small triangulations to have a normalization for our counting algorithm. Furthermore we define a restriction of the Pachner moves defined in Sec. 4.1.2, the so-called *causal Pachner moves*, that allow to transform causal triangulations into causal ones.

Small triangulations in $(1 + 1)$ and $(2 + 1)$ dimensions

We start by constructing the minimal causal triangulation of a time slice in $(1 + 1)$ dimensions. The minimal triangulation of the spatial manifold $\Sigma = S^1$ is given by three vertices and edges between each two of the vertices, so the minimal triangulation of the time slice has at least six vertices. Such



a minimal causal triangulation is given by

$$\mathcal{T} = \{\{0, 1, 3\}, \{1, 2, 4\}, \{0, 2, 5\}, \{1, 3, 4\}, \{2, 4, 5\}, \{0, 3, 5\}\} \cup \text{subsimpllices} \quad (5.22)$$

and is displayed Fig. 5.10. This is up to isomorphism the only triangulation of a time slice with six maximal simplices.

In $(2 + 1)$ -dimensions the construction of a valid small triangulation becomes slightly more involved. The idea is the same as for the $(1 + 1)$ dimensional case, one constructs a triangulations that links two minimal triangulation of the spatial S^2 slices (which are the boundary of a 3-simplex). We index the vertices of the first S^1 -triangulation by $0, \dots, 3$, and the vertices of the second one by $4, \dots, 7$. The two minimal S^2 -triangulations are given by

$$\begin{aligned} \underline{\mathcal{T}} &= \{\{0, 1, 2\}, \{0, 1, 3\}, \{0, 2, 3\}, \{1, 2, 3\}\} \cup \text{subsimpllices} \\ \overline{\mathcal{T}} &= \{\{4, 5, 6\}, \{4, 5, 7\}, \{4, 6, 7\}, \{5, 6, 7\}\} \cup \text{subsimpllices} \end{aligned}$$

To construct the causal triangulation inbetween, we consider first the prisms that are given by the triangles $\{i_1, i_2, i_3\}$ and $\{i_1 + 3, i_2 + 3, i_3 + 3\}$. Such as prism can be triangulated using

- one $(3, 1)$ -simplex consisting of the triangle $\{i_1, i_2, i_3\}$ and a vertex $\bar{j} \in \{i_1 + 3, i_2 + 3, i_3 + 3\}$,
- one $(3, 1)$ -simplex consisting of the triangle $\{i_1 + 3, i_2 + 3, i_3 + 3\}$ and a vertex $\underline{j} \in \{i_1, i_2, i_3\} \setminus \{\bar{j} - 3\}$,
- and the $(2, 2)$ -simplex consisting of the vertices $\{i_1, i_2, i_3\} \setminus \{\bar{j} - 3\}$ and $\{i_1 + 3, i_2 + 3, i_3 + 3\} \setminus \{\underline{j} + 3\}$.

The choice of the triangulation of the prism can perhaps be understood better if one twists the prism as depicted in Fig. 5.11, then the choice of the triangulation corresponds to the choice of one of the three inner diagonals of the twisted prism. Altogether there are four prisms (one for each pair of triangles in the boundary), and one has to choose \underline{j} and \bar{j} such that the triangulations can be matched (this means, if there is an edge between two vertices in the triangulation of one prism, this edge has also to be present in the triangulations of the other prisms containing these two vertices). Using this algorithm, one can, e.g., construct the following minimal triangulation of $S^2 \times \mathcal{I}$ with one time and two spatial slices (see Fig. 5.12).

$$\begin{aligned} \mathcal{T} &= \{\{0125\}, \{0245\}, \{2456\}, \{0135\}, \{0357\}, \{0457\}, \\ &\quad \{1235\}, \{2357\}, \{2567\}, \{0237\}, \{0247\}, \{2467\}\} \cup \text{subsimpllices}. \end{aligned} \quad (5.23)$$



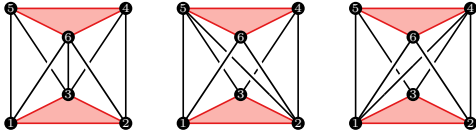


Figure 5.11: Triangulation of a (twisted) prism bounded by two spatial triangulations, which is one of the four building blocks of the smallest triangulation of $S^2 \times \mathcal{I}$ with two spatial slices. The red edges are space-like, the black edges are space-like, the three different triangulations correspond to a choice of the inner diagonal.

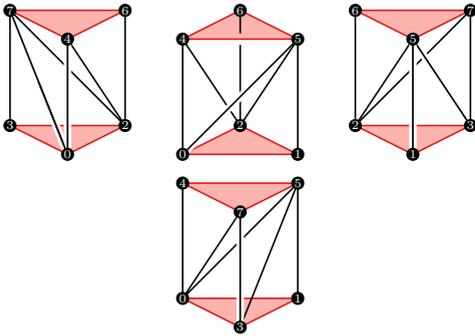


Figure 5.12: Smallest possible $(2 + 1)$ causal triangulation given in Eq. (5.23). The spatial triangulations are split into the four triangles constituting them, also the causal triangulations decomposes in causal triangulations connecting two spatial triangulations. All vertices with the same number have to be considered as equal.

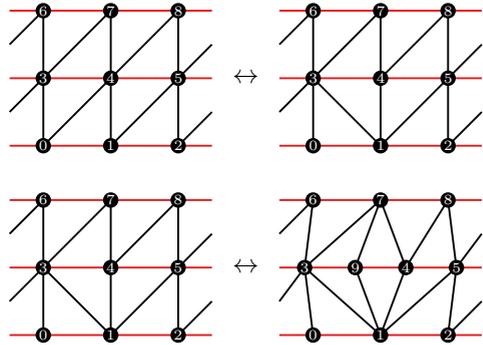
Causal Pachner moves

As for the approach of dynamical triangulations (DT) also causal dynamical triangulations (CDT) use flips to generate all possible triangulations of the manifold $S^1 \times \mathcal{M}$. Since the causal structure of the triangulation must not be violated, only flips which leave the causal structure independent are allowed. This implies that one cannot insert vertices into maximal simplices, because these join two neighboring time slices, and the additional vertex could not be assigned a time slice. Furthermore it is not allowed to perform flips that insert edges between two time slices that are not neighbors. Altogether there are two different types of flips that can be executed, which will be denoted as *causal Pachner moves*, because they are the subset of the Pachner moves that conserve the causality structure of the triangulation.

The first type are flips generated by time-like k -simplices, here both the positive and the negative circuit points must be located on two neighboring time slices. This leads to $(d - k + 1 \rightarrow k + 1)$ -flips with $1 \leq k \leq d - 1$.



Figure 5.13: The possible flips in two-dimensional Causal Dynamical Triangulations (CDT). Top: $(2, 2)$ -flip mediated by a time-like edge. Bottom: $(2, 4)$ -flip and the inverse $(4, 2)$ -flip mediated by a space-like edge. In principle this is an insertion $(1, 2)$ -flip or deletion $(2, 1)$ -flip in the 1-dimensional time slice, extended with two zero points to higher dimensions.



The case $k = d$ is excluded, because this would insert a vertex between two time slices and break the causality structure. The case $k = 0$ is excluded, because there is no time-like 0-simplex since one point can only be located in a single time slice.

The second type are flips generated by space-like k -simplices. These flips are treated as $(d - k \rightarrow k + 1)$ -flips in the $(d - 1)$ -dimensional time slice, and handling the maximal simplices of the generating k -simplex in terms of the notion of a degenerated flip in Def. 3.15. (If there is more than one point in a maximal simplex of the generating k -simplex in a neighboring time slice the flip is not executable). This leads to $(2d - 2k \rightarrow 2k + 2)$ -flips with $0 \leq k \leq d - 1$. The case $k = d$ is trivially excluded because there is no d -simplex fully contained in a single time slice.

In Fig. 5.13 one can see the $(2 \rightarrow 2)$ -flip (generated by a time-like 2-simplex), and the $(2 \rightarrow 4)$ -flip (generated by a space-like 1-simplex) together with its inverse $(4 \rightarrow 2)$ -flip (generated by a space-like 0-simplex) in a $(1 + 1)$ -dimensional causal triangulation.

In Fig. 5.14 one can see the possible flips in $(2 + 1)$ -dimensional CDT. There are three flips that are induced by flips in a spatial slice, the $(2 \rightarrow 6)$ -flip induced by a spatial $(1 \rightarrow 3)$ -flip, its inverse, the $(6 \rightarrow 2)$ -flip induced by a spatial $(3 \rightarrow 1)$ -flip, and the $(4 \rightarrow 4)$ -flip induced by a spatial $(2 \rightarrow 2)$ -flip. Furthermore there are two flips generated by time-like simplices, first the $(2 \rightarrow 3)$ -flip generated by a spatial edge, and its inverse, the $(3 \rightarrow 2)$ -flip generated by a spatial triangle.

An important open question is whether the causal Pachner moves are ergodic, i.e. whether every triangulation of a given spacetime foliation can be transformed into every other triangulation of the same structure by a finite number of causal Pachner moves. Ergodicity is proven for triangula-



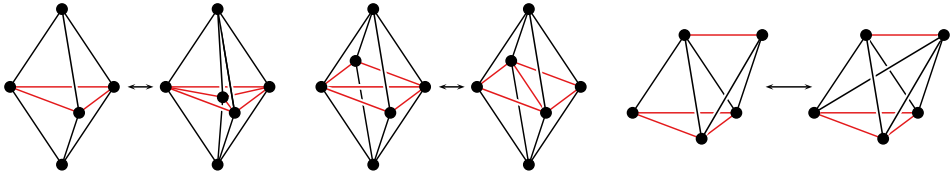


Figure 5.14: All possible flips in $(3+1)$ -dimensional causal dynamical triangulations. From left to right: $(2 \rightarrow 6)$ -flip (induced by a spatial $(1 \rightarrow 3)$ flip), $(4 \rightarrow 4)$ -flip (induced by a spatial $(2 \rightarrow 2)$ -flip) and $(2 \rightarrow 3)$ -flip. The red edges are space-like edges, the black edges are time-like edges.

tions of two- and three-dimensional manifolds, for triangulations of higher dimensional manifolds Pachner moves are only ergodic for manifolds with the same PL structure (compare Sec. 4.1). But it is not clear a priori whether a restriction to causal Pachner moves is ergodic for causal triangulation, because in principle two different causal triangulations could be linked by a third triangulation that is not causal. It was discussed in Sec. 4.3 why the question of ergodicity is difficult to answer for topological triangulations. In Euclidean dynamical triangulation the question of ergodicity has been considered numerically in the literature (compare Refs. [91, 113] and Sec. 5.2.5), but in contrast ergodicity was not addressed in the literature about causal dynamical triangulations until now. So the ergodicity of causal Pachner moves has to be seen as a working hypothesis and must be examined in greater details in future work.

If doing Markov chain Monte Carlo simulations with causal Pachner moves on causal triangulations, for calculating the ratio of selection probabilities one has to take into account that triangulations are defined only up to isomorphy, so two triangulations have to be treated as equal if there is a vertex permutation that maps one onto the other. The problem was described in detail in Sec. 4.1.4 for topological triangulations, and most of the results from this section also apply to causal triangulations. In fact, the situation is a bit simpler in the causal setup, because one has to take into account only permutations that keep the time slice of each vertex invariant.

A bit larger triangulations in $(2 + 1)$ -dimensions

As next step we construct the triangulations of $S^2 \times \mathcal{I}$ that can be constructed from the smallest triangulation (5.23) within one causal Pachner move. These triangulations and their numbers can be used for testing the algorithms for creating and executing flips defined later. The smallest triangulation



(5.23) consists of eight (3, 1)-simplices and four (2, 2)-simplices, and there are two different types of possible moves: The (2 → 3)-move, and the spatial-induced (1 → 3) move (which would be a (2 → 6)-move if the spatial slice would not be the boundary of the triangulation).

For each of the (2, 1)-triangles one can define a (2 → 3)-flip that transforms one (3, 1) and one (2, 2)-simplex into another (3, 1)-simplex and two (2, 2)-simplices:

$$\{0125\}, \{0245\} \rightarrow \{0124\}, \{0145\}, \{1245\} \quad (5.24a)$$

$$\{0245\}, \{2456\} \rightarrow \{0246\}, \{0256\}, \{0456\} \quad (5.24b)$$

$$\{1235\}, \{2357\} \rightarrow \{1237\}, \{1257\}, \{1357\} \quad (5.24c)$$

$$\{2357\}, \{2567\} \rightarrow \{2356\}, \{2367\}, \{3567\} \quad (5.24d)$$

$$\{0357\}, \{0457\} \rightarrow \{0345\}, \{0347\}, \{3457\} \quad (5.24e)$$

$$\{0135\}, \{0357\} \rightarrow \{0137\}, \{0157\}, \{1357\} \quad (5.24f)$$

$$\{0237\}, \{0247\} \rightarrow \{0234\}, \{0347\}, \{2347\} \quad (5.24g)$$

$$\{0247\}, \{2467\} \rightarrow \{0246\}, \{0267\}, \{0467\} \quad (5.24h)$$

By calculating the number of incident edges and tetrahedra at each vertex after these flips, one can check that the flips (5.24a) and (5.24d) lead to different triangulations, whereas (5.24b) and (5.24h) (by interchanging the vertex labels $0 \leftrightarrow 2$ and $4 \leftrightarrow 6$), (5.24c) and (5.24f) (by interchanging the vertex labels $1 \leftrightarrow 3$ and $5 \leftrightarrow 7$), as well as (5.24e) and (5.24g) lead to isomorphic triangulations (by interchanging the vertex labels $0 \leftrightarrow 3$ and $4 \leftrightarrow 7$). This leads to the following non-isomorphic triangulations with eight (3, 1)-simplices and five (2, 2)-simplices:

$$\begin{aligned} \mathcal{T}_1 = \{ & \{0124\}, \{0145\}, \{1245\}, \{2456\}, \{0135\}, \{0357\}, \{0457\}, \\ & \{1235\}, \{2357\}, \{2567\}, \{0237\}, \{0247\}, \{2467\} \} \end{aligned} \quad (5.25a)$$

$$\begin{aligned} \mathcal{T}_2 = \{ & \{0125\}, \{0246\}, \{0256\}, \{0456\}, \{0135\}, \{0357\}, \{0457\}, \\ & \{1235\}, \{2357\}, \{2567\}, \{0237\}, \{0247\}, \{2467\} \} \end{aligned} \quad (5.25b)$$

$$\begin{aligned} \mathcal{T}_3 = \{ & \{0125\}, \{0245\}, \{2456\}, \{0135\}, \{0357\}, \{0457\}, \\ & \{1237\}, \{1257\}, \{1357\}, \{2567\}, \{0237\}, \{0247\}, \{2467\} \} \end{aligned} \quad (5.25c)$$

$$\begin{aligned} \mathcal{T}_4 = \{ & \{0125\}, \{0245\}, \{2456\}, \{0135\}, \{0357\}, \{0457\}, \\ & \{1235\}, \{2356\}, \{2367\}, \{3567\}, \{0237\}, \{0247\}, \{2467\} \} \end{aligned} \quad (5.25d)$$

$$\begin{aligned} \mathcal{T}_5 = \{ & \{0125\}, \{0245\}, \{2456\}, \{0135\}, \{0345\}, \{0347\}, \{3457\}, \\ & \{1235\}, \{2357\}, \{2567\}, \{0237\}, \{0247\}, \{2467\} \} \end{aligned} \quad (5.25e)$$



Due to the fact that every vertex of the boundary triangulations has different incidence numbers, each $(1 \rightarrow 3)$ -insertion move into one of the 8 boundary triangles (4 at each spatial boundary slice) produces a different triangulation, so the number of triangulations with 10 $(3, 1)$ -simplices and 4 $(2, 2)$ -simplices after these steps is 8.

5.3.4 The action of causal dynamical triangulations

In this section we follow closely the approach of [34] to derive the action of three- and four-dimensional causal dynamical triangulations. In Sec. 5.3.1 we introduced an asymmetry between space-like with spacetime interval a^2 and time-like edge lengths with spacetime interval $-\alpha a^2$. This modification implies that the volume of a k -simplex does not only depend on the total number $(k + 1)$ of its generating points, but on the number of points in each of the two neighboring time slices a simplex connects (the causal structure of the simplex). A k -simplex which has a points in the first time slice and b points in the second time slice is denoted as (a, b) -simplex. Since the direction of the time coordinate is arbitrary, we assume w.l.o.g. that $a \geq b$. The volume of a (a, b) -simplex will be denoted by $V_{a,b}$, and the number of (a, b) -simplices in a triangulation will be denoted by $N_{a,b}$, both defined for $a \geq b$. Of course we can related by

$$N_k = \sum_{i=0}^{\lfloor (k+1)/2 \rfloor} N_{k-i+1,i}$$

the number N_k of all k -simplices with the number of k -simplices with specified causal structure.

To derive the action of the CDT model, we start with the usual Regge action (5.13)

$$S_{\text{Regge}} = \frac{1}{8\pi G} \left[\sum_{b \in \mathcal{B}} \sigma_b^{(d-2)} V_b^{(d-2)} \epsilon_b - \Lambda \sum_{s \in \mathcal{S}} V_s^{(d)} \right].$$

Here $b \in \mathcal{B}$ denotes a $(d - 2)$ -simplex in the set \mathcal{B} of all $(d - 2)$ -simplices (bones), and $s \in \mathcal{S}$ denotes a d -simplex in the set \mathcal{S} of all maximal simplices. $V_s^{(d)}$ denotes the d -dimensional volume of the simplex s (by definition we choose all volumes to be real and positive), and ϵ_b denotes the deficit angle associated with the bone b . Note that there is an additional sign factor $\sigma_b^{(d-2)} \in \{1, -1\}$ that arises if we use a Lorentzian metric in the Regge action, compare Ref. [373, B1]. The details of the calculation of $\sigma_b^{(d-2)}$ will



be presented later. Introducing the causal structure and using that the sign and volume of a simplex and the sign do only depend on its causal structure, the action becomes

$$S = \frac{1}{8\pi G} \left[\sum_{i=0}^{\lfloor (d-1)/2 \rfloor} \sigma_{d-i-1,i} V_{d-i-1,i} \sum_{b \in \mathcal{B}_{d-i-1,i}} \epsilon_b - \Lambda \sum_{j=0}^{\lfloor (d+1)/2 \rfloor} N_{d-j+1,j} V_{d-j+1,j} \right],$$

where $\mathcal{B}_{a,b}$ with $a + b = d - 1$ denotes the set of bones with causal structure (a, b) .

Remember that in the derivation of the action of DT the next step was to reexpress the deficit angle ϵ_b at bone b with the number of maximal simplices incident with b . For CDT this is slightly more complicated, because first the deficit angle depends on the number of simplices with a certain causal structure, and second the dihedral angle of the maximal simplices does also depend on their causal structure. So denote by $\theta_{d-i-1,i}^{(d-j+1,j),(d-\alpha,\alpha)(d-\beta,\beta)}$ be the dihedral angle of a $(d-j+1, j)$ -simplex located at an incident $(d-i-1, i)$ -simplex, which is formed by the intersection of a $(d-\alpha, \alpha)$ and a $(d-\beta, \beta)$ simplex. Mind that $\alpha, \beta \in \{i, i+1\}$, otherwise the $(d-i-1, i)$ -simplex cannot be a subsimplex of the $(d-\alpha, \alpha)$ or the $(d-\beta, \beta)$ -simplex. Furthermore the order of the $(d-\alpha, \alpha)$ and $(d-\beta, \beta)$ -simplex is not important, so there are only the following three possibilities for choosing the pair (α, β) ,

$$(\alpha, \beta) = (i, i) \quad (\alpha, \beta) = (i, i+1) \quad (\alpha, \beta) = (i+1, i+1).$$

Furthermore we have the condition $\alpha \leq j$ and $\beta \leq j$, because the simplices must be subsimplices of the maximal $(d-j+1, j)$ -simplex. For example $\theta_{1,0}^{(2,1),(1,1)(2,0)}$ is the angle within a $(2, 1)$ -triangle (consisting of one space-like edge and two space-like edges) at a vertex that is common to a space-like and a time-like edge.

So the deficit angle ϵ_b can be written as sum over the number of simplices of a certain kind times the associated internal angle as

$$\epsilon_b = 2\pi - \sum_{j=0}^{\lfloor (d+1)/2 \rfloor} \sum_{\substack{\alpha, \beta \in \{i, i+1\} \\ \alpha \leq \beta}} N_{d-j+1,j}^{(d-\alpha,\alpha)(d-\beta,\beta)}(b) \cdot \theta_{d-i-1,i}^{(d-j+1,j),(d-\alpha,\alpha)(d-\beta,\beta)}$$

where $N_{d-j+1,j}^{(d-\alpha,\alpha)(d-\beta,\beta)}(b)$ is the number of $(d-j+1, j)$ -simplices incident with the bone b , where b is the common subsimplex of a $(d-\alpha, \alpha)$ and a $(d-\beta, \beta)$ -simplex.



For the next step of the calculation the simplex incidence numbers $n_{d-i-1,i}^{(d-j+1,j),(d-\alpha,\alpha)(d-\beta,\beta)}$ are introduced, which are the number of $(d-i-1, i)$ -subsimplices of an arbitrary maximal $(d-j+1, j)$ -simplex, which are common to a $(d-\alpha, \alpha)$ and a $(d-\beta, \beta)$ -subsimplex of the maximal simplex. To calculate these numbers in full generality is difficult, but for a given dimension d the values can be calculated by constructing a simplicial complex consisting of the considered maximal simplex and all subsimplex and inspecting how many $(d-2)$ -simplices of each type are common to the certain types of $(d-1)$ -simplices. The numbers will be calculated later separately for each considered dimension. More easily one can calculate the values

$$n_{d-i-1,i}^{(d-j+1,j)} := \sum_{\substack{\alpha,\beta \in \{i,i+1\} \\ \alpha \leq \beta}} n_{d-i-1,i}^{(d-j+1,j),(d-\alpha,\alpha)(d-\beta,\beta)},$$

which are the numbers of $(d-i-1, i)$ -simplices that are incident with a $(d-j+1, j)$ -simplex, without considering the types of the $(d-1)$ -simplices that constitute the $(d-2)$ -simplex. If $d-i+1 \neq i$, one can choose $d-i-1$ of the $d-j+1$ points of supersimplex on the one time slice and i of j points on the other time slice, or vice versa. If $d-i+1 = i$, both possibilities equal the same case. So

$$n_{d-i-1,i}^{(d-j+1,j)} = \binom{d-j+1}{d-i-1} \binom{j}{i} + \binom{d-j+1}{i} \binom{j}{d-i-1} (1 - \delta_{d-i-1,i})$$

From this we can deduce that

$$\sum_{\sigma^{(d-i-1,i)}} N_{d-j+1,j} \left(\sigma^{(d-i-1,i)} \right) = n_{d-i-1,i}^{(d-j+1,j)} N_{d-j+1,j}$$

This can be used for cross-checking the calculated numbers in Eqs. (5.51), (5.54) and (5.57).

By using the simplex incidence numbers, the sum over the bones can be eliminated from the action by

$$\sum_{b \in \mathcal{B}_{d-i-1,i}} N_{d-j+1,j}^{(d-\alpha,\alpha)(d-\beta,\beta)}(b) = n_{d-i-1,i}^{(d-j+1,j),(d-\alpha,\alpha)(d-\beta,\beta)} N_{d-j+1,j},$$

where on the left hand of the equation one sums the number of maximal simplices of a certain causality structure incident with a certain bone over all bones, and on the right hand side one multiplies the number of maximal simplices with the number of bones of the correct type incident with such a



maximal simplex. Both numbers are equal, as in the derivation of the DT action. Using this in the action yields

$$\begin{aligned}
 S_{\text{CDT}} &= \frac{2}{8G} \sum_{i=0}^{\lfloor (d-1)/2 \rfloor} \sigma_{d-i-1,i} V_{d-i-1,i} N_{d-i-1,i} \\
 &- \frac{1}{8\pi G} \sum_{i=0}^{\lfloor (d-1)/2 \rfloor} \sigma_{d-i-1,i} V_{d-i-1,i} \sum_{j=0}^{\lfloor (d+1)/2 \rfloor} \sum_{\substack{\alpha, \beta \in \{i, i+1\} \\ \alpha \leq \beta}} [n\theta]_{d-i-1,i}^{(d-j+1,j), (d-\alpha, \alpha)(d-\beta, \beta)} N_{d-j+1,j} \\
 &- \frac{\Lambda}{8\pi G} \sum_{j=0}^{\lfloor (d+1)/2 \rfloor} N_{d-j+1,j} V_{d-j+1,j}
 \end{aligned}$$

where we used the short notation

$$[n\theta]_{d-i-1,i}^{(d-j+1,j), (d-\alpha, \alpha)(d-\beta, \beta)} := n_{d-i-1,i}^{(d-j+1,j), (d-\alpha, \alpha)(d-\beta, \beta)} \theta_{d-i-1,i}^{(d-j+1,j), (d-\alpha, \alpha)(d-\beta, \beta)}$$

Sorting with respect to the $N_{m,n}$ gives

$$\begin{aligned}
 S_{\text{CDT}} &= \frac{1}{4G} \sum_{i=0}^{\lfloor (d-1)/2 \rfloor} \sigma_{d-i-1,i} V_{d-i-1,i} N_{d-i-1,i} - \frac{1}{8\pi G} \sum_{j=0}^{\lfloor (d+1)/2 \rfloor} c_{d,j} N_{d-j+1,j} \\
 c_{d,j} &= \Lambda V_{d-j+1,j} + \sum_{i=0}^{\lfloor (d-1)/2 \rfloor} \sigma_{d-i-1,i} V_{d-i-1,i} \sum_{\substack{\alpha, \beta \in \{i, i+1\} \\ \alpha \leq \beta}} [n\theta]_{d-i-1,i}^{(d-j+1,j), (d-\alpha, \alpha)(d-\beta, \beta)}.
 \end{aligned} \tag{5.26}$$

In order to calculate the correct action of causal dynamical triangulations, two things have to be done:

- The geometric quantities, the volume $V_{d-i\pm 1,i}$ of the different d and $(d-2)$ -simplices, the sign factor $\sigma_{d-i-1,i}$ and the angles $\theta_{d-i-1,i}^{(d-j+1,j), \dots}$ must be calculated.
- The topological quantities, the numbers $N_{d-i\pm 1,i}$ of different d and $(d-2)$ -simplices, can be linearly dependent. These dependencies have to be found, in order to capture only the relevant degrees of freedom in the action.

Both tasks will be performed in the next sections.



Geometric quantities - Volumes, angles and signs

In order to calculate the action we need to calculate the volumes of the different types of simplices and the deficit angles. We assume that space-like edges have a length of $\ell_{\text{space-like}}^2 = a^2$, and time-like edges have a length of $\ell_{\text{time-like}}^2 = -\alpha a^2$. In general calculating volumes and angles in a Lorentzian spacetime can be more subtle than in Euclidean space, here we follow the considerations of Ref. [373, B3], which were also used in Ref. [34].

For a systematic way of calculating we embed the simplices into an $\mathbb{R} \times \mathbb{R}^{d-1}$ with flat Minkowski metric $\eta_{\mu\nu}$, so that the scalar product of two vectors is defined as

$$\langle \bullet, \bullet \rangle : \mathbb{R}^d \times \mathbb{R}^d \rightarrow \mathbb{R}, \langle u, v \rangle = \eta_{\mu\nu} u^\mu v^\nu = -u_0 v_0 + u_1 v_1 + \dots + u_{d-1} v_{d-1}$$

In the Euclidean case one can use the scalar product to calculate the cos of an angle $\theta(u, v)$ between two vectors u and v by

$$\cos(\theta(u, v)) = \frac{\langle u, v \rangle}{\sqrt{\langle u, u \rangle \langle v, v \rangle}},$$

but on the one hand the sign on the right hand side is arbitrary, and on the other hand also the angle $\theta(u, v)$ is determined by $\cos(\theta(u, v))$ only up to a sign [373]. Note that in Lorentzian spacetime angles can even be imaginary.

To resolve the ambiguities, there remains the following possibility [373]: The angle $\theta(u, v)$ between two vectors u and v is determined by

$$\begin{aligned} \cos(\theta(u, v)) &= \frac{\langle u, v \rangle}{\sqrt{\langle u, u \rangle \langle v, v \rangle}} \\ \sin(\theta(u, v)) &= \frac{\sqrt{\langle u, u \rangle \langle v, v \rangle - \langle u, v \rangle^2}}{\sqrt{\langle u, u \rangle \langle v, v \rangle}} \end{aligned} \tag{5.27}$$

and we postulate that $0 \leq \text{Re}(\theta(u, v)) \leq \pi$. The resulting angles are than in fact additive, and reveal the correct contribution to the action [373].

Furthermore we need a generalization of the vector product that assigns $(d - 1)$ vectors in d dimensions a vector that has a vanishing scalar product with all its arguments (this is the generalization of orthogonality). This vector product is defined by the property

$$\langle u, v_1 \times v_2 \times \dots \times v_{d-1} \rangle = \epsilon_{\mu\nu_1\nu_2\dots\nu_{d-1}} u^\mu v_1^{\nu_1} v_2^{\nu_2} \dots v_{d-1}^{\nu_{d-1}},$$

where $\epsilon_{\mu\nu_1\nu_2\dots\nu_{d-1}}$ is the Levi-Civita symbol (which is 1 if $\mu\nu_1 \dots \nu_{d-1}$ is an even permutation, -1 if it is an odd permutation and zero otherwise) and



the i -th coordinate of $v_1 \times v_2 \times \cdots \times v_{d-1}$ can be found by using the basis vector e_i as vector u . In two dimension the vector product takes only one argument, and we have

$$\times : \mathbb{R}^3 \rightarrow \mathbb{R}^3, \times u = \begin{pmatrix} u_2 \\ u_1 \end{pmatrix}, \quad (5.28)$$

which is just an interchange of the coordinates. In three dimensions the vector product has the usual form

$$\times : \mathbb{R}^3 \times \mathbb{R}^3 \rightarrow \mathbb{R}^3, u \times v = \begin{pmatrix} u_2 v_3 - u_3 v_2 \\ u_1 v_3 - u_3 v_1 \\ u_2 v_1 - u_1 v_2 \end{pmatrix}, \quad (5.29)$$

but note that there are some differences to the usual Euclidean form due to the Lorentzian signature. In four dimensions we have $\times : \mathbb{R}^4 \times \mathbb{R}^4 \times \mathbb{R}^4 \rightarrow \mathbb{R}^4$, with the single components given by

$$\begin{aligned} (u \times v \times w)_1 &= u_2(v_3 w_4 - v_4 w_3) + u_3(v_4 w_2 - v_2 w_4) + u_4(v_2 w_3 - v_3 w_2) \\ (u \times v \times w)_2 &= u_1(v_3 w_4 - v_4 w_3) + u_3(v_4 w_1 - v_1 w_4) + u_4(v_1 w_3 - v_3 w_1) \\ (u \times v \times w)_3 &= u_1(v_4 w_2 - v_2 w_4) + u_2(v_1 w_4 - v_4 w_1) + u_4(v_2 w_1 - v_1 w_2) \\ (u \times v \times w)_4 &= u_1(v_2 w_3 - v_3 w_2) + u_2(v_3 w_1 - v_1 w_3) + u_3(v_1 w_2 - v_2 w_1) \end{aligned} \quad (5.30)$$

The vector product can be used for calculating the angle between two hyperplanes ($(d - 1)$ -dimensional linear subspaces), between this angle equals the angle between the two associated normal vectors, which can be calculated using the vector product. Note that for three dimensions also the 2-volume spanned by the two vectors and in four dimensions the 3-volume spanned by the three vectors is encoded in the length of the resulting vector product.

Geometry in Lorentzian spacetime Using Eq. (5.27) for calculating angles between vectors in Lorentzian spacetime can lead to difficulties. Consider e.g., a (1+1)-dimensional spacetime and the vectors

$$v_1 = \begin{pmatrix} 0 \\ 1 \end{pmatrix} \quad v_2 = \begin{pmatrix} \lambda \\ 1 \end{pmatrix} \quad v_3 = \begin{pmatrix} 1 \\ 0 \end{pmatrix}$$

where v_1 is a space-like vector, v_3 is time-like and v_2 is space-like for $|\lambda| < 1$ and time-like for $|\lambda| > 1$. In the following we restrict to the case $\lambda > 0$.



Using Eq. (5.27) for calculating the angles θ_{12} between v_1 and v_2 and θ_{23} between v_2 and v_3 results in

$$\begin{aligned} \cos(\theta_{12}) &= \frac{1}{\sqrt{1-\lambda^2}} & \sin(\theta_{12}) &= \frac{i\lambda}{\sqrt{1-\lambda^2}} \\ \cos(\theta_{23}) &= \frac{-\lambda}{\sqrt{\lambda^2-1}} & \sin(\theta_{23}) &= \frac{i}{\sqrt{\lambda^2-1}} \end{aligned}$$

Calculating the angles θ_{12} or θ_{23} using real analysis is not possible, the arguments of the inverse trigonometric functions are either real but larger than one, or even imaginary. We can solve the issue by using complex analysis, where the inverse trigonometric functions are defined for the whole complex plane and can be written using the (imaginary logarithm) as

$$\begin{aligned} \arcsin(z) &= -i \log(iz + \sqrt{1-z^2}) \\ \arccos(z) &= -i \log(z + i\sqrt{1-z^2}) \end{aligned}$$

So for imaginary arguments we have

$$\begin{aligned} \arcsin(i \cdot x) &= -i \log(-x + \sqrt{1+x^2}) \\ \arccos(i \cdot x) &= -i \log(x + \sqrt{1+x^2}) + \pi(2n + 1/2) \end{aligned}$$

(using $\log(ix) = \log(x) + i\pi(2n + 1/2)$ with $n \in \mathbb{Z}$ chosen arbitrarily), while for real arguments $x > 1$ we get

$$\begin{aligned} \arcsin(x) &= -i \log(x + \sqrt{x^2-1}) + \pi(2n + 1/2) \\ \arccos(x) &= -i \log(x - \sqrt{x^2-1}) \end{aligned}$$

for $x > 1$. In principle it is not important which inverse trigonometric function we use for calculating the actual angle, so we will use the one without the branching ambiguity whenever possible.

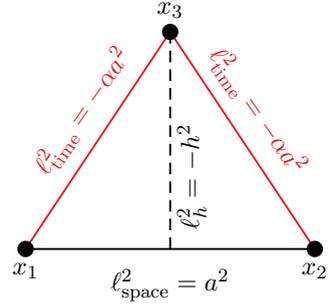
In Lorentzian spacetime one has also pay attention to the sign of a deficit angle that contributes to the action. A space-like deficit angle has to contribute positively to the action, and a time-like deficit angle has to contribute negatively to the action (intuitively this is because a space-like angle corresponds to a rotation, while a time-like angle corresponds to a boost, compare Refs. [34,373] for detailed discussion.) So a space-like defect as well as a time-like excess contribute positively, while a space-like excess as well as a time-like defect contribute negatively.



Figure 5.15: Embedding of a $(2, 1)$ -simplex into the \mathbb{R}^{1+1} with Minkowski metric $\eta_{\mu\nu}$. The coordinates of the points $x_i, i = 1, 2, 3$ can be chosen according to

$$\begin{aligned} x_1 &= (0, -a/2)^t \\ x_2 &= (0, a/2)^t \\ x_3 &= (h, 0)^t \end{aligned}$$

where h can be calculated e.g., from the squared length $-h^2 + a^2/4 = -\alpha a^2$ of the time-like vector $\overrightarrow{x_1x_3}$.



This can be realized by choosing the sign $\sigma_{d-1-i,i}$ of a $(d-1-i, i)$ -bone correctly. In Ref. [373] the following procedure was proposed: Let ω be a tensor associated with the bone (which encodes also the volume), and let θ be the deficit angle at the bone. Then the contribution to the action is $iS = |\omega|\theta$, so $S = -i|\omega|\theta = \sigma_{d-1-i,i}V_{d-1-i,i}\theta$, where $|\omega| = (\langle\omega, \omega\rangle)^{1/2}$ and the scalar product is defined for higher rank tensors as for vectors by e.g., $\langle\omega, \omega\rangle := \omega_{\mu\nu}\omega^{\mu\nu}$ for rank-2 tensors. The actual calculation of the sign factors will be done in the following sections for each relevant type of bone. Note that the sign factors are Lorentz scalars, i.e., they do not depend on the actual choice of the coordinates of the considered bones, but only on their causal type. So it is enough to calculate the sign factor for one example of the respective bone type.

Zero- and one-dimensional simplices The volume of a $(1, 0)$ -simplex (vertex) is set to $V_{1,0} := 1$, volume of the time-like and space-like simplices can easily be deduced from the edge length assignments:

$$V_{2,0} = a \quad V_{1,1} = \sqrt{\alpha}ai$$

Two-dimensional simplices The volume of a $(3, 0)$ -simplex (space-like triangle) is the area of an equilateral triangle with edge length a , so $V_{3,0} = \sqrt{3}a^2/4$, and all angles at all points are $\pi/3$, as in the usual setup of dynamical triangulations.

For the $(2, 1)$ -simplex, which is a triangle with two sides having length $\ell^2_{\text{time}} = -\alpha a^2$ and one side having length $\ell^2_{\text{space}} = a^2$, we can choose the



following coordinates:

$$x_1 = \begin{pmatrix} 0 \\ -a/2 \end{pmatrix} x_2 = \begin{pmatrix} 0 \\ a/2 \end{pmatrix} x_3 = \begin{pmatrix} h \\ 0 \end{pmatrix}$$

The quantity h has to be chosen so that $-h^2 + a^2/4 = \ell_{\text{time}}^2$ since $|\overrightarrow{x_1 x_3}|^2 = -\alpha a^2$, so $h = a\sqrt{4\alpha + 1}/2$, as depicted in Fig. 5.15. The volume of the $(2, 1)$ -simplex can then be calculated using a common formula for the area of a triangle, e.g., by using half the length of the vector product of two adjacent edges extended to the R^3 . The resulting volume is

$$V_{2,1} = \frac{a^2}{4} \sqrt{4\alpha + 1} \quad (5.31)$$

The angle between two time-like edges (e.g., the time-like vectors $\overrightarrow{x_3 x_1} = (-h, a/2)^t$ and $\overrightarrow{x_3 x_2} = (-h, -a/2)^t$) can be calculated using (5.27) by

$$\begin{aligned} \cos \left(\theta_{(1,0)}^{(2,1),(1,1)(1,1)} \right) &= \frac{-h^2 - a^2/4}{-\alpha a^2} = \frac{2\alpha + 1}{2\alpha} \\ \sin \left(\theta_{(1,0)}^{(2,1),(1,1)(1,1)} \right) &= \frac{\sqrt{-\alpha a^4 - a^4/4}}{-\alpha a^2} = -i \frac{4\alpha + 1}{2\alpha} \end{aligned} \quad (5.32)$$

as well as the angle between a time-like and a space-like edge (e.g., the angle between the space-like vector $\overrightarrow{x_1 x_2} = (0, a)^t$ and the time-like vector $\overrightarrow{x_1 x_3} = (h, a/2)^t$), which is given by

$$\begin{aligned} \Rightarrow \cos \left(\theta_{(1,0)}^{(2,1),(2,0)(1,1)} \right) &= \frac{a^2/2}{a \cdot \sqrt{-\alpha a^2}} = \frac{-i}{2\sqrt{\alpha}} \\ \Rightarrow \cos \left(\theta_{(1,0)}^{(2,1),(2,0)(1,1)} \right) &= \frac{\sqrt{-\alpha a^2 - a^2/4}}{a \cdot \sqrt{-\alpha a^2}} = \sqrt{\frac{4\alpha + 1}{4\alpha}} \end{aligned} \quad (5.33)$$

The sign of the contribution of the bone volume cannot be derived with the previously described method, because in $(1 + 1)$ dimensions the bones do not have a well-defined volume. The sign will be derived later in the actual formulation of the action in $(1 + 1)$ dimensions.

Three-dimensional simplices The volume of the space-like $(4, 0)$ simplex can be calculated as in Euclidean signature.

For the $(3, 1)$ simplex that consists of three space-like edges and three time-like edges, we can choose the following coordinates for the vertices:

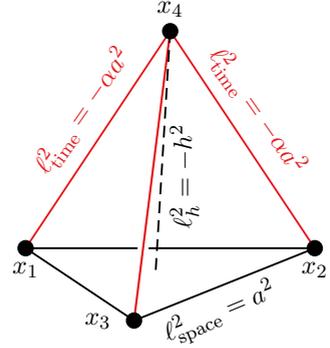
$$x_1 = \begin{pmatrix} 0 \\ -\sqrt{3}a/6 \\ -a/2 \end{pmatrix} x_2 = \begin{pmatrix} 0 \\ -\sqrt{3}a/6 \\ a/2 \end{pmatrix} x_3 = \begin{pmatrix} 0 \\ \sqrt{3}a/3 \\ 0 \end{pmatrix} x_4 = \begin{pmatrix} h \\ 0 \\ 0 \end{pmatrix}$$



Figure 5.16: Embedding of a $(3, 1)$ -simplex into the \mathbb{R}^{1+2} with Minkowski metric $\eta_{\mu\nu}$. The coordinates of the points $x_i, i = 1, 2, 3, 4$ can be chosen according to

$$\begin{aligned} x_1 &= (0, -\sqrt{3}a/6, -a/2)^t \\ x_2 &= (0, -\sqrt{3}a/6, a/2)^t \\ x_3 &= (0, \sqrt{3}a/3, 0)^t \\ x_4 &= (h, 0, 0)^t \end{aligned}$$

where h can be calculated from the squared length $|\vec{x}_3x_4|^2$ of a time-like vector to be $-h^2 + a^2/3 = -\alpha a^2$.



where $h = a\sqrt{(3\alpha + 1)}/3$ can be calculated from the length of a time-like vector Fig. 5.16.

The volume can be calculated using the determinant

$$V_{3,1} = \frac{1}{3!} \begin{vmatrix} -h & -h & -h \\ -\sqrt{3}a/6 & -\sqrt{3}a/6 & \sqrt{3}a/3 \\ -a/2 & a/2 & 0 \end{vmatrix} = \frac{a^3}{12} \sqrt{3\alpha + 1} \quad (5.34)$$

of three vectors spanning the simplex.

The interior angles in a $(3, 1)$ -simplex at space-like and time-like edges can be calculated using (5.27). The angle at the space-like edge x_1x_2 is given by the angles between the planes spanned by the points x_1, x_2 and x_3 and by the points x_1, x_2 and x_4 equals the angle between $\vec{y}x_3$ and $\vec{y}x_4$, where $y = (x_1 + x_2)/2 = (0, -\sqrt{3}a/6, 0)^t$ is the midpoint of x_1 and x_2 , and can be calculated as

$$\begin{aligned} \cos \left(\theta_{(2,0)}^{(3,1),(3,0)(2,1)} \right) &= \frac{a^2/4}{(\sqrt{3}a/2) \cdot (ia\sqrt{4\alpha + 1})} = \frac{-i}{\sqrt{3(4\alpha + 1)}} \\ \sin \left(\theta_{(2,0)}^{(3,1),(3,0)(2,1)} \right) &= \frac{\sqrt{-3a^4(4\alpha + 1)/16 - a^4/16}}{(\sqrt{3}a/2) \cdot (ia\sqrt{4\alpha + 1})} = \frac{2\sqrt{3\alpha + 1}}{\sqrt{3(4\alpha + 1)}} \end{aligned} \quad (5.35)$$

For the angle at a time-like edge, e.g. the edge \vec{x}_3x_4 , it is not possible to use the mid point z between x_3 and x_4 and its vectors to x_1 and x_2 to compute the angle, because in general $\vec{z}x_1$ is not perpendicular to \vec{x}_3x_4 . The exact coordinates of z could be found by stipulating that these two vectors are perpendicular, but we will use the vector product for calculating vectors



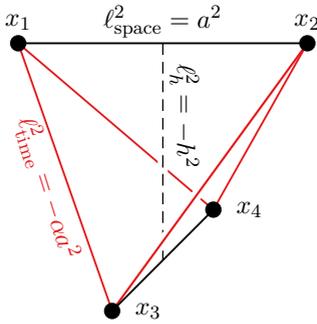


Figure 5.17: Embedding of a $(2, 2)$ -simplex into the \mathbb{R}^{1+2} with Minkowski metric $\eta_{\mu\nu}$. The coordinates of the points $x_i, i = 1, 2, 3, 4$ can be chosen according to

$$\begin{aligned} x_1 &= (h/2, -a/2, 0)^t \\ x_2 &= (h/2, a/2, 0)^t \\ x_3 &= (-h/2, 0, -a/2)^t \\ x_4 &= (-h/2, 0, a/2)^t \end{aligned}$$

where h can be calculated from the length of a time-like vector $-h^2 + a^2/2 = -\alpha a^2$.

that are normal to the planes $x_1x_3x_4$ and $x_2x_3x_4$, so that the angle between these two vectors corresponds to the angle at the time-like edge $\overrightarrow{x_3x_4}$. These vectors are given by

$$\begin{aligned} \overrightarrow{x_3x_2} \times \overrightarrow{x_3x_4} &= \begin{pmatrix} h \\ -\sqrt{3}a/3 \\ 0 \end{pmatrix} \times \begin{pmatrix} 0 \\ -\sqrt{3}a/2 \\ a/2 \end{pmatrix} = \begin{pmatrix} -\sqrt{3}a^2/6 \\ ha/2 \\ \sqrt{3}ha/2 \end{pmatrix} \\ \overrightarrow{x_3x_2} \times \overrightarrow{x_3x_4} &= \begin{pmatrix} h \\ -\sqrt{3}a/3 \\ 0 \end{pmatrix} \times \begin{pmatrix} 0 \\ -\sqrt{3}a/2 \\ -a/2 \end{pmatrix} = \begin{pmatrix} \sqrt{3}a^2/6 \\ -ha/2 \\ \sqrt{3}ha/2 \end{pmatrix} \end{aligned}$$

both have squared length $(3\alpha + 1)a^4/3 - a^4/12$, and the angle between the two vectors can be calculated by

$$\begin{aligned} \cos(\theta_{(1,1)}^{(3,1),(2,1)(2,1)}) &= \frac{(3\alpha + 1)a^4/3 + a^4/12}{(3\alpha + 1)a^4/3 - a^4/12} = \frac{2\alpha + 1}{4\alpha + 1} \\ \sin(\theta_{(1,1)}^{(3,1),(2,1)(2,1)}) &= \frac{\sqrt{(12\alpha + 3)^2 - (6\alpha + 3)^2}}{12\alpha + 3} = \frac{2\sqrt{\alpha}\sqrt{3\alpha + 1}}{4\alpha + 1} \end{aligned} \tag{5.36}$$

For the $(2, 2)$ simplex that consists of two space-like edges and four time-like edges, we can choose the following coordinates for the vertices:

$$x_1 = \begin{pmatrix} h/2 \\ -a/2 \\ 0 \end{pmatrix} \quad x_2 = \begin{pmatrix} h/2 \\ a/2 \\ 0 \end{pmatrix} \quad x_3 = \begin{pmatrix} -h/2 \\ 0 \\ -a/2 \end{pmatrix} \quad x_4 = \begin{pmatrix} -h/2 \\ 0 \\ a/2 \end{pmatrix}$$

where $h = a\sqrt{(2\alpha + 1)/2}$ can be calculated from the length of one of the time-like vectors as displayed in Figure 5.17.



The volume can be calculated using the determinant of the connection vectors of these four points

$$V_{2,2} = \frac{1}{3!} \begin{vmatrix} 0 & -h & -h \\ a & a/2 & a/2 \\ 0 & -a/2 & a/2 \end{vmatrix} = \frac{a^3}{6\sqrt{2}} \sqrt{2\alpha + 1} \quad (5.37)$$

The interior angles at space-like and time-like edges can be calculated using (5.27). For the angle at the space-like edge $\overrightarrow{x_3x_4}$ we have to calculate the angles between the vectors $\overrightarrow{yx_1}$ and $\overrightarrow{yx_2}$, where $y = (x_3 + x_4)/2$ is the mid of the points x_3 and x_4 , which has the coordinates $y = (-h/2, 0, 0)^t$. So the angle can be calculated by

$$\begin{aligned} \cos \left(\theta_{(2,0)}^{(2,2),(2,1)(2,1)} \right) &= \frac{-h^2 - a^2/4}{-h^2 + a^2/4} = \frac{4\alpha + 3}{4\alpha + 1} \\ \sin \left(\theta_{(2,0)}^{(2,2),(2,1)(2,1)} \right) &= \frac{\sqrt{-a^2h^2}}{-h^2 + a^2/4} = \frac{-i2\sqrt{2}\sqrt{2\alpha + 1}}{4\alpha + 1} \end{aligned} \quad (5.38)$$

For the angle at a time-like edge, e.g. the edge $\overrightarrow{x_1x_3}$, we calculate again the normal vectors of the planes $x_1x_2x_3$ and $x_1x_3x_4$, whose angle correspond to the interior angle at the time-like edge. The normal vectors are given by

$$\begin{aligned} \overrightarrow{x_1x_3} \times \overrightarrow{x_1x_2} &= \begin{pmatrix} -h \\ a/2 \\ -a/2 \end{pmatrix} \times \begin{pmatrix} 0 \\ a \\ 0 \end{pmatrix} = \begin{pmatrix} a^2/2 \\ 0 \\ ah \end{pmatrix} \\ \overrightarrow{x_1x_3} \times \overrightarrow{x_1x_4} &= \begin{pmatrix} -h \\ a/2 \\ -a/2 \end{pmatrix} \times \begin{pmatrix} h \\ a/2 \\ -a/2 \end{pmatrix} = \begin{pmatrix} a^2/2 \\ -ah \\ 0 \end{pmatrix} \end{aligned}$$

both have squared length $a^2h^2 - a^4/4$, and the angle between the two vectors can be calculated by

$$\begin{aligned} \cos \left(\theta_{(1,1)}^{(2,2),(2,1)(2,1)} \right) &= \frac{a^4/4}{a^2h^2 - a^4/4} = -\frac{1}{4\alpha + 1} \\ \sin \left(\theta_{(1,1)}^{(2,2),(2,1)(2,1)} \right) &= \frac{\sqrt{a^4h^4 - a^6h^2/2}}{a^2h^2 - a^4/4} = \frac{2\sqrt{2\alpha}\sqrt{2\alpha + 1}}{4\alpha + 1} \end{aligned} \quad (5.39)$$

The last task in this section is to calculate the sign factors σ of the bone volume. For $(2+1)$ -dimensional causal dynamical triangulations there are two different types of bones, space-like $(2,0)$ -edges and time-like $(2,0)$ -edges. For a time-like vector $v = (\sqrt{\alpha}a, 0, 0)^t$ one gets

$$i\sigma_{1,1}V_{1,1} = i\sigma_{1,1}\sqrt{\alpha}a = \sqrt{v^\mu v_\mu} = \sqrt{-v_1v_1} = i\sqrt{\alpha}a \Rightarrow \sigma_{1,1} = 1 \quad (5.40)$$



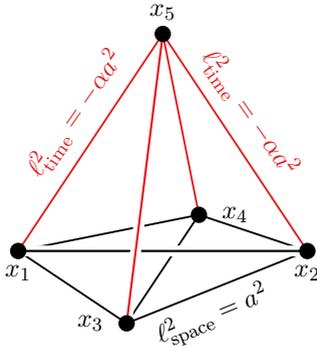


Figure 5.18: Embedding of a $(4, 1)$ -simplex into the \mathbb{R}^{1+3} with Minkowski metric $\eta_{\mu\nu}$. The coordinates of the points $x_i, i = 1, 2, 3, 4, 5$ can be chosen according to

$$\begin{aligned} x_1 &= (0, -\sqrt{3}a/6, -a/2, -\sqrt{6}a/12)^t \\ x_2 &= (0, -\sqrt{3}a/6, a/2, -\sqrt{6}a/12)^t \\ x_3 &= (0, -\sqrt{3}a/3, 0, -\sqrt{6}a/12)^t \\ x_4 &= (0, 0, 0, \sqrt{6}a/4)^t \\ x_5 &= (h, 0, 0, 0)^t \end{aligned}$$

where h can be calculated from the condition $\ell_{x_4x_5} = -h^2 + (\sqrt{6}a/4)^2 = -\alpha a^2$.

For a space-like vector $v = (0, a, 0)^t$ one gets

$$i\sigma_{2,0}V_{2,0} = i\sigma_{2,0}a = \sqrt{v^\mu v_\mu} = \sqrt{v_2 v_2} = a \Rightarrow \sigma_{2,0} = -i \quad (5.41)$$

As mentioned before, the sign factors do only depend on the type of the bone and not on the actual coordinates.

Four-dimensional simplices For the $(4, 1)$ simplex that consists of four space-like edges and four time-like edges, we can choose the following coordinates for the vertices:

$$\begin{aligned} x_1 &= \begin{pmatrix} 0 \\ -\sqrt{3}a/6 \\ -a/2 \\ -\sqrt{6}a/12 \end{pmatrix} & x_2 &= \begin{pmatrix} 0 \\ -\sqrt{3}a/6 \\ a/2 \\ -\sqrt{6}a/12 \end{pmatrix} & x_3 &= \begin{pmatrix} 0 \\ -\sqrt{3}a/3 \\ 0 \\ -\sqrt{6}a/12 \end{pmatrix} \\ x_4 &= \begin{pmatrix} 0 \\ 0 \\ 0 \\ \sqrt{6}a/4 \end{pmatrix} & x_5 &= \begin{pmatrix} h \\ 0 \\ 0 \\ 0 \end{pmatrix}^t \end{aligned}$$

where $h = (a/2) \cdot \sqrt{(8\alpha + 3)/2}$ can be calculated from the condition that the squared distance between x_4 and x_5 is $-\alpha a^2$.

The volume can be calculated using the determinant of the connection



vectors of these five points

$$\begin{aligned}
 V_{4,1} &= \frac{1}{4!} \begin{vmatrix} -h & -h & -h & -h \\ 0 & -\sqrt{3}a/6 & -\sqrt{3}a/6 & \sqrt{3}a/3 \\ 0 & -a/2 & a/2 & 0 \\ \sqrt{6}a/4 & -\sqrt{6}a/12 & -\sqrt{6}a/12 & -\sqrt{6}a/12 \end{vmatrix} = \\
 &= \frac{1}{24} \sqrt{2} h a^3 = \frac{a^4}{96} \sqrt{8\alpha + 3}
 \end{aligned} \tag{5.42}$$

We have to calculate the angles at a space-like (3,0)-triangle and a time-like (2,1)-triangle. The interior angle at a space-like (3,0)-triangles (e.g., the triangle $x_1x_2x_3$) corresponds to the angle between the normal vectors v_1 of the hyperplanes $x_1x_2x_3x_4$ and v_2 of the hyperplane $x_1x_2x_3x_5$. Educated guessing yields $v_1 = (1, 0, 0, 0)^t$, for v_2 we use the vector product

$$\begin{aligned}
 v_2 &= \overrightarrow{x_1x_5} \times \overrightarrow{x_2x_5} \times \overrightarrow{x_3x_5} \\
 &= \begin{pmatrix} h \\ \sqrt{3}a/6 \\ a/2 \\ \sqrt{6}a/12 \end{pmatrix} \times \begin{pmatrix} h \\ \sqrt{3}a/6 \\ -a/2 \\ \sqrt{6}a/12 \end{pmatrix} \times \begin{pmatrix} h \\ \sqrt{3}a/3 \\ 0 \\ \sqrt{6}a/12 \end{pmatrix} = \begin{pmatrix} \sqrt{2}a^3/24 \\ 0 \\ 0 \\ \sqrt{3}a^2h/6 \end{pmatrix}
 \end{aligned}$$

The vectors have the squared length -1 and $-a^6/288 + a^4h^2/12$, which can be used for calculating the angle at triangle $x_1x_2x_3$

$$\begin{aligned}
 \cos \left(\theta_{(3,0)}^{(4,1),(4,0)(3,1)} \right) &= \frac{\sqrt{2}a^3/24}{i\sqrt{-a^6/288 + a^4h^2/12}} = \frac{-i}{2\sqrt{2}\sqrt{3\alpha + 1}} \\
 \sin \left(\theta_{(3,0)}^{(4,1),(4,0)(3,1)} \right) &= \frac{\sqrt{-a^6/288 + a^4h^2/12} - a^6/288}{i\sqrt{-a^6/288 + a^4h^2/12}} = \frac{\sqrt{3(8\alpha + 3)}}{2\sqrt{2}\sqrt{3\alpha + 1}}
 \end{aligned} \tag{5.43}$$

For the angle at the time-like (2,1)-triangle $x_1x_2x_5$ between the simplices $x_1x_2x_3x_5$ and $x_1x_2x_4x_5$ one has to calculate the angle between the normal vectors v_2 and v_3 , with

$$\begin{aligned}
 v_3 &= \overrightarrow{x_1x_5} \times \overrightarrow{x_4x_5} \times \overrightarrow{x_3x_5} \\
 &= \begin{pmatrix} h \\ \sqrt{3}a/6 \\ a/2 \\ \sqrt{6}a/12 \end{pmatrix} \times \begin{pmatrix} h \\ \sqrt{3}a/6 \\ -a/2 \\ \sqrt{6}a/12 \end{pmatrix} \times \begin{pmatrix} h \\ 0 \\ 0 \\ -\sqrt{6}a/4 \end{pmatrix} = \begin{pmatrix} \sqrt{2}a^3/8 \\ \sqrt{6}a^2h/3 \\ 0 \\ -\sqrt{3}a^2h/6 \end{pmatrix}
 \end{aligned}$$



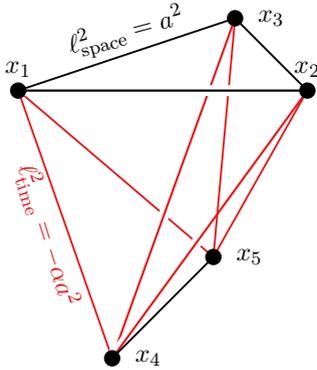


Figure 5.19: Embedding of a $(3, 2)$ -simplex into the \mathbb{R}^{1+4} with Minkowski metric $\eta_{\mu\nu}$. The coordinates of the points $x_i, i = 1, 2, 3, 4, 5$ can be chosen according to

$$\begin{aligned} x_1 &= (h, a/2, -a\sqrt{3}/6, 0)^t \\ x_2 &= (h, -a/2, -a\sqrt{3}/6, 0)^t \\ x_3 &= (h, 0, a\sqrt{3}/3, 0)^t \\ x_4 &= (0, 0, 0, a/2)^t \\ x_5 &= (0, 0, 0, -a/2)^t \end{aligned}$$

where h can be calculated from the condition $\ell_{x_3x_4} = -h^2 + a^2/3 + a^2/4 = -\alpha a^2$.

which has the squared length $-a^6/32 + 3a^4h^2/4$. The angle between the two normal vectors is then

$$\begin{aligned} \cos\left(\theta_{\binom{(4,1)}{(2,1)}, \binom{(3,1)}{(3,1)}}, \binom{(3,1)}{(3,1)}\right) &= \frac{-a^6/96 - a^4h^2/12}{\sqrt{-a^6/288 + a^4h^2/12} \cdot \sqrt{-a^6/32 + 3a^4h^2/4}} = \\ &= \frac{-(2\alpha + 1)}{2(3\alpha + 1)} \\ \sin\left(\theta_{\binom{(4,1)}{(2,1)}, \binom{(3,1)}{(3,1)}}, \binom{(3,1)}{(3,1)}\right) &= \frac{\sqrt{-a^6/288 + a^4h^2/12} - a^6/288}{i\sqrt{-a^6/288 + a^4h^2/12}} = \frac{\sqrt{3(8\alpha + 3)}}{2\sqrt{2}\sqrt{3\alpha + 1}} \end{aligned}$$

For the $(3, 2)$ simplex that consists of four space-like edges and four time-like edges, we can choose the following coordinates for the vertices, as depicted in Fig. 5.19:

$$\begin{aligned} x_1 &= \begin{pmatrix} h \\ a/2 \\ -\sqrt{3}a/6 \\ 0 \end{pmatrix} & x_2 &= \begin{pmatrix} h \\ -a/2 \\ -\sqrt{3}a/6 \\ 0 \end{pmatrix} & x_3 &= \begin{pmatrix} h \\ 0 \\ \sqrt{3}a/3 \\ 0 \end{pmatrix} \\ x_4 &= \begin{pmatrix} 0 \\ 0 \\ 0 \\ a/2 \end{pmatrix} & x_5 &= \begin{pmatrix} 0 \\ 0 \\ 0 \\ -a/2 \end{pmatrix} \end{aligned}$$

where $h = \sqrt{\alpha + 7/12}$ can be calculated from the condition that the squared distance between x_3 and x_4 is $-\alpha a^2$.



The volume can be calculated using the determinant of the connection vectors of these five points

$$V_{3,2} = \frac{1}{4!} \begin{vmatrix} h & h & h & 0 \\ a/2 & -a/2 & 0 & 0 \\ -\sqrt{3}a/6 & -\sqrt{3}a/6 & \sqrt{3}a/3 & 0 \\ -a/2 & -a/2 & -a/2 & -a \end{vmatrix} = \frac{\sqrt{3}ha^3}{2} = \frac{a^4}{96} \sqrt{12\alpha + 7} \quad (5.44)$$

As for the (4, 1)-simplex, one has to calculate the interior angles at a (3, 0) and a (2, 1)-triangle. We start with the (3, 0)-triangle $x_1x_2x_3$, which is formed by the tetrahedra $x_1x_2x_3x_4$ and $x_1x_2x_3x_5$. The normal vectors v_1 and v_2 of this tetrahedra are given by

$$\begin{aligned} v_{1/2} &= \overrightarrow{x_1x_4/5} \times \overrightarrow{x_2x_4/5} \times \overrightarrow{x_3x_4/5} \\ &= \begin{pmatrix} -h \\ -a/2 \\ \sqrt{3}a/6 \\ \pm a/2 \end{pmatrix} \times \begin{pmatrix} -h \\ a/2 \\ \sqrt{3}a/6 \\ \pm a/2 \end{pmatrix} \times \begin{pmatrix} -h \\ 0 \\ -\sqrt{3}a/3 \\ \pm a/2 \end{pmatrix} = \begin{pmatrix} \mp \sqrt{3}a^3/4 \\ 0 \\ 0 \\ \sqrt{3}a^2h/2 \end{pmatrix} \end{aligned}$$

which both have a squared length $-3a^6/16 + 3a^4h^2/4$. For the angle between the both vectors one gets

$$\begin{aligned} \cos \left(\theta_{(3,0)}^{(3,2),(3,1)(3,1)} \right) &= \frac{3a^6/16 + 3a^4h^2/4}{-3a^6/16 + 3a^4h^2/4} = \frac{6\alpha + 5}{2(3\alpha + 1)} \\ \sin \left(\theta_{(3,0)}^{(3,2),(3,1)(3,1)} \right) &= \frac{\sqrt{-9/16a^8h^4}}{-3a^6/16 + 3a^4h^2/4} = \frac{i\sqrt{3(12\alpha + 7)}}{2(3\alpha + 1)} \end{aligned} \quad (5.45)$$

For the (2, 1)-triangle there is the special feature that there are two possibilities how a (2, 1)-triangle can be formed, on the one hand by the intersection of two (2, 2)-tetrahedra, and on the other hand by the intersection of a (2, 2) and a (3, 1)-tetrahedron. We consider first a (2, 1)-triangle $x_3x_4x_5$ formed by the (2, 2)-tetrahedra $x_1x_3x_4x_5$ and $x_2x_3x_4x_5$, whose normal vectors are given by

$$\begin{aligned} v_{1/2} &= \overrightarrow{x_{1/2}x_3} \times \overrightarrow{x_{1/2}x_4} \times \overrightarrow{x_{1/2}x_5} \\ &= \begin{pmatrix} 0 \\ \pm a/2 \\ -\sqrt{3}a/2 \\ 0 \end{pmatrix} \times \begin{pmatrix} h \\ \pm a/2 \\ -\sqrt{3}a/6 \\ -a/2 \end{pmatrix} \times \begin{pmatrix} h \\ \pm a/2 \\ -\sqrt{3}a/6 \\ a/2 \end{pmatrix} = \begin{pmatrix} \pm \sqrt{3}a^3/6 \\ \sqrt{3}a^2h/2 \\ \pm a^2h/2 \\ 0 \end{pmatrix} \end{aligned}$$



The squared length of both vectors is $-a^6/12 + a^4h^2$, and the angle can be calculated using

$$\begin{aligned} \cos \left(\theta_{(2,1)}^{(3,2),(2,2)(2,2)} \right) &= \frac{a^6/12 + a^4h^2/2}{-a^6/12 + a^4h^2} = \frac{4\alpha + 3}{4(2\alpha + 1)} \\ \sin \left(\theta_{(2,1)}^{(3,2),(2,2)(2,2)} \right) &= \frac{\sqrt{-a^{10}h^2/4 + 3a^8h^4/4}}{-a^6/12 + a^4h^2} = \frac{\sqrt{(4\alpha + 1)(12\alpha + 7)}}{4(2\alpha + 1)} \end{aligned} \quad (5.46)$$

For the second possibility we consider the (2, 1)-triangle $x_2x_3x_4$ formed by the (3, 1)-tetrahedron $x_1x_2x_3x_4$ and the (2, 2)-tetrahedron $x_2x_3x_4x_5$, both normal vectors have been calculated previously to be

$$\begin{aligned} v_1 &= \overrightarrow{x_1x_4} \times \overrightarrow{x_2x_4} \times \overrightarrow{x_3x_4} = \begin{pmatrix} -\sqrt{3}a^3/4 \\ 0 \\ 0 \\ \sqrt{3}a^2h/2 \end{pmatrix} \\ v_2 &= \overrightarrow{x_2x_3} \times \overrightarrow{x_2x_4} \times \overrightarrow{x_2x_5} = \begin{pmatrix} -\sqrt{3}a^3/6 \\ \sqrt{3}a^2h/2 \\ -a^2h/2 \\ 0 \end{pmatrix} \end{aligned}$$

The squared length of v_1 is $-3a^6/16 + 3a^4h^2/4$, the squared length of v_2 is $-a^6/12 + a^4h^2$, so the angle between the vectors can be calculated by

$$\begin{aligned} \cos \left(\theta_{(2,1)}^{(3,2),(3,1)(2,2)} \right) &= \frac{-a^6/8}{\sqrt{-3a^6/16 + 3a^4h^2/4}\sqrt{-a^6/12 + a^4h^2}} = \\ &= \frac{-1}{2\sqrt{2(3\alpha + 1)(2\alpha + 1)}} \\ \sin \left(\theta_{(2,1)}^{(3,2),(3,1)(2,2)} \right) &= \frac{\sqrt{-a^{10}h^2/4 + 3a^8h^4/4}}{\sqrt{-3a^6/16 + 3a^4h^2/4}\sqrt{-a^6/12 + a^4h^2}} = \\ &= \frac{\sqrt{(4\alpha + 1)(12\alpha + 7)}}{2\sqrt{2(3\alpha + 1)(2\alpha + 1)}} \end{aligned} \quad (5.47)$$

The sign factors can be calculated analogous as in the (2 + 1)-dimensional case, which results in $\sigma_{3,0} = -i$ and $\sigma_{2,1} = 1$ (compare Ref. [34]).

Topological quantities

If M and N are two manifolds, the Euler characteristic of the product space is given by

$$\chi(M \times N) = \chi(M) \cdot \chi(N)$$



The underlying manifold for d -dimensional causal dynamical triangulation can be written as a product of a $(d - 1)$ -dimensional spatial slices manifold Σ (in almost all situations we use a $(d - 1)$ -sphere \mathbb{S}_{d-1}) and a 1-dimensional time evolution manifold \mathcal{T} (we use either a 1-sphere \mathbb{S}_1 for periodic boundary conditions or an interval \mathcal{I} for open or fixed boundary conditions). So the Euler characteristic of the whole triangulation can be calculated to be

$$\chi(\mathcal{T} \times \Sigma) = \chi(\mathcal{T}) \cdot \chi(\Sigma)$$

Note that $\chi(\mathbb{S}_i) = 0$ for odd i and $\chi(\mathbb{S}_i) = 2$ for even i , so if $\mathcal{T} = \mathbb{S}_1$ the Euler characteristic vanishes for all space-slice topologies. For completeness note that $\chi(\mathcal{I}) = 1$.

In general there are the following relations between the topological variables for closed manifolds (manifolds without border):

- Causal split of the triangulation into $(d - 1)$ -dimensional spatial slices:

$$\begin{aligned} N_{d+1,0} &= 0 \\ N_{d,1} &= 2N_{d,0} \end{aligned} \tag{5.48a}$$

The first equation ensures that the spatial slices are $(d - 1)$ -dimensional, the second equation is due to the fact that each spatial maximal simplex is subsimplex of two simplices of type $(d, 1)$.

- Dehn-Sommerville relations for the whole triangulation:

$$\begin{aligned} N_k &= \sum_{i=k}^d (-1)^{i+d} \binom{i+1}{k+1} N_i \\ \Rightarrow \sum_{j=0}^{\lfloor k/2 \rfloor} N_{k-j+1,j} &= \sum_{i=k}^d \sum_{j=0}^{\lfloor i/2 \rfloor} (-1)^{i+d} \binom{i+1}{k+1} N_{i-j+1,j} \end{aligned} \tag{5.48b}$$

For $k = d - 1$ the Dehn-Sommerville relation include the well-known result that each $(d - 1)$ -simplex is incident with two d -simplices, and each d -simplex is incident with $(d + 1)$ $(d - 1)$ -simplices:

$$2N_{d-1} = (d + 1) \cdot N_d \Rightarrow 2 \cdot \sum_{i=0}^{\lfloor (d-1)/2 \rfloor} N_{d-i,i} = (d + 1) \cdot \sum_{i=1}^{\lfloor d/2 \rfloor} N_{d-i+1,i}$$

- Dehn-Sommerville relations for the spatial slices:

$$N_{k+1,0} = \sum_{i=k}^{d-1} (-1)^{i+d-1} \binom{i+1}{k+1} N_{i+1,0} \tag{5.48c}$$



For $k = d - 2$ the Dehn-Sommerville relations for the spatial slices include that each spatial $(d - 2)$ -simplex is incident with two spatial $(d - 1)$ -simplices, and each spatial $(d - 1)$ simplex is incident with d spatial $(d - 2)$ simplices:

$$2N_{d-1,0} = dN_{d-2,0}$$

- Euler-characteristic of the whole triangulation:

$$\chi(\mathcal{T} \times \Sigma) = \sum_{i=-1}^d \sum_{j=0}^{\lfloor i/2 \rfloor} (-1)^{i+d} N_{i-j+1,j} \quad (5.48d)$$

- Euler-characteristic of the spatial slices:

$$t \cdot \chi(\pm) = \sum_{i=1}^{d+1} (-1)^{i-1} N_{i,0} \quad (5.48e)$$

Here t is the number of spatial slices in the triangulation. Note that for $\chi(\Sigma) = 0$ the topological quantities of the triangulation do not depend on the number t of spatial slices.

Mind that these equations are only valid for causal dynamical triangulations with periodic boundary conditions. It is possible to formulate similar equations for open and fixed boundary conditions that must take into account the number of respective simplices of the two boundary simplices.

(1+1)-dimensional topological quantities In two dimensions the topological constraints (5.48) can be specialized to be

$$N_{2,1} = 2N_{2,0} \quad (5.49a)$$

$$3 \cdot N_{2,1} = 2 \cdot (N_{2,0} + N_{1,1}) \quad (5.49b)$$

$$2N_{1,0} = 2N_{2,0} \quad (5.49c)$$

$$\chi(\mathcal{T})\chi(\Sigma) = N_{1,0} - N_{2,0} - N_{1,1} + N_{2,1} \quad (5.49d)$$

$$t \cdot \chi(\Sigma) = N_{1,0} - N_{2,0} \quad (5.49e)$$

One might conclude that there is a contradiction between Equations (5.49c) and (5.49e). But $\Sigma = \mathbb{S}_1$ is the only possible topology of a closed manifold, and $\chi(\mathbb{S}_1) = 0$, so both equations are equivalent.

There is only one independent topological quantity, because we have three constraints (5.49) (there are five equations, but only three are independent)



for four topological quantities. So all topological quantities can be expressed in terms of a single topological quantity (here the number $N_{2,1}$ of triangles):

$$N_{1,0} = \frac{1}{2}N_{2,1} \quad (5.50a)$$

$$N_{2,0} = \frac{1}{2}N_{2,1} \quad (5.50b)$$

$$N_{1,1} = N_{2,1} \quad (5.50c)$$

The next step is to calculate the simplex incidence numbers $n_{(1,0)}^{(2,1)}$, which is the number of vertices incident with $(2, 1)$ -triangle. For the triangulation to be causal space-like triangles are prohibited, so this is the only simplex incidence number to be calculated. There are two different numbers, because the vertex can be between two time-like edges or between a time-like and a space-like edge. The resulting numbers are

$$\begin{aligned} n_{(1,0)}^{(2,1),(2,0)(1,1)} &= 2 \\ n_{(1,0)}^{(2,1),(1,1)(1,1)} &= 1 \end{aligned} \quad (5.51)$$

All other incidence numbers vanish.

(2+1)-dimensional topological quantities In three dimensions, the topological quantities (5.48) can be specialized to

$$N_{3,1} = 2N_{3,0} \quad (5.52a)$$

$$N_{3,0} + N_{2,1} = 2(N_{3,1} + N_{2,2}) \quad (5.52b)$$

$$2N_{2,0} = 3N_{3,0} \quad (5.52c)$$

$$N_{1,0} - N_{2,0} - N_{1,1} + N_{3,0} + N_{2,1} - N_{3,1} - N_{2,2} = \chi(\mathcal{T})\chi(\Sigma) \quad (5.52d)$$

$$N_{1,0} - N_{2,0} + N_{3,0} = \chi(\Sigma) \cdot t \quad (5.52e)$$

One can simplify these five equations for eight variables and show that the topological quantities of a $(2+1)$ causal dynamical triangulation can completely be written in terms of $N_{3,1}$, $N_{2,2}$ and $N_{1,0}$:

$$N_{1,1} = N_{1,0} + \frac{1}{4}N_{3,1} + N_{2,2} - \chi(\mathcal{T})\chi(\Sigma) \quad (5.53a)$$

$$N_{2,0} = \frac{3}{4}N_{3,1} \quad (5.53b)$$

$$N_{2,1} = \frac{3}{2}N_{3,1} + 2N_{2,2} \quad (5.53c)$$



$$N_{3,0} = \frac{1}{2}N_{3,1} \quad (5.53d)$$

$$t = \frac{1}{\chi(\Sigma)}N_{1,0} - \frac{1}{4\chi(\Sigma)}N_{3,1} \quad (5.53e)$$

Eq. (5.53e) leads to undefined behavior for vanishing Euler characteristic $\chi(\Sigma)$ of the spatial slices Σ . In this case in Eq. (5.52e) and in the whole system of equations there is no dependence on the variable t .

The last step is to calculate the simplex incidence numbers, which are the number of incident bones at the different types of maximal simplices. In $(2+1)$ dimensions one can have a maximal $(3,1)$ -simplex or a maximal $(2,2)$ -simplex, furthermore there are $(2,0)$ -bones and $(1,1)$ -bones. The resulting numbers are

$$\begin{aligned} n_{(2,0)}^{(3,1),(3,0)(2,1)} &= 3 & n_{(2,0)}^{(2,2),(2,1)(2,1)} &= 2 \\ n_{(1,1)}^{(3,1),(2,1)(2,1)} &= 3 & n_{(1,1)}^{(2,2),(2,1)(2,1)} &= 4 \end{aligned} \quad (5.54)$$

All other incidence numbers vanish.

(3+1)-dimensional topological quantities In four dimensions the topological quantities 5.48 can be specialized to

$$2N_{4,0} = N_{4,1} \quad (5.55a)$$

$$2N_{2,2} = 3N_{3,2} \quad (5.55b)$$

$$\begin{aligned} 2(N_{2,0} + N_{1,1}) - 3(N_{3,0} + N_{2,1}) + \\ 4(N_{4,0} + N_{3,1} + N_{2,2}) - 5(N_{4,1} + N_{3,2}) = 0 \end{aligned} \quad (5.55c)$$

$$5(N_{4,1} + N_{3,2}) = 2(N_{4,0} + N_{3,1} + N_{2,2}) \quad (5.55d)$$

$$N_{3,0} = 2N_{4,0} \quad (5.55e)$$

$$\begin{aligned} N_{1,0} - N_{2,0} - N_{1,1} + N_{3,0} + N_{2,1} - \\ N_{4,0} - N_{3,1} - N_{2,2} + N_{4,1} + N_{3,2} = \chi(\mathcal{T})\chi(\Sigma) \end{aligned} \quad (5.55f)$$

$$N_{1,0} - N_{2,0} - N_{3,0} - N_{4,0} = t \cdot \chi(\Sigma) \quad (5.55g)$$

One can simplify these seven constrains for ten variables and show that the topological quantities of a $(3+1)$ causal dynamical triangulation can completely be written in terms of $N_{4,1}$, $N_{3,2}$ and $N_{1,0}$:

$$N_{2,0} = N_{1,0} + \frac{1}{2}N_{4,1} - \chi(\Sigma)t \quad (5.56a)$$

$$N_{1,1} = 2N_{1,0} + \frac{1}{2}N_{3,2} - \chi(\Sigma)(t - 3\chi(\mathcal{T})) \quad (5.56b)$$



$$N_{3,0} = N_{4,1} \quad (5.56c)$$

$$N_{2,1} = 2N_{1,0} + N_{4,1} + 2N_{3,2} - 2\chi(\mathcal{T})\chi(\Sigma) \quad (5.56d)$$

$$N_{4,0} = \frac{1}{2}N_{4,1} \quad (5.56e)$$

$$N_{3,1} = 2N_{4,1} + N_{3,2} \quad (5.56f)$$

$$N_{2,2} = \frac{3}{2}N_{3,2} \quad (5.56g)$$

Here we do not treat t as an important variable, because in almost all cases we use $\Sigma = \mathbb{S}_3$, which has an Euler characteristic $\chi(\mathbb{S}_3) = 0$.

The last step is to calculate the simplex incidence numbers, which are the number of incident bones of a certain type with a maximal simplex of certain type. In $(3+1)$ dimensions one can have a maximal $(4,1)$ -simplex or a maximal $(3,2)$ -simplex, there are $(3,0)$ -bones and $(2,1)$ -bones. The resulting numbers are

$$\begin{aligned} n_{(3,0)}^{(4,1),(4,0)(3,1)} &= 4 & n_{(3,0)}^{(3,2),(3,1)(3,1)} &= 1 \\ n_{(2,1)}^{(4,1),(3,1)(3,1)} &= 6 & n_{(2,1)}^{(3,2),(3,1)(2,2)} &= 6 \\ & & n_{(2,1)}^{(3,2),(2,2)(2,2)} &= 3 \end{aligned} \quad (5.57)$$

All other incidence numbers vanish.

The action of $(1+1)$ -dimensional CDT

In this section we derive the actual form of the action for $(1+1)$ causal dynamical triangulations. We use (5.26), specialize first for $d=2$ and define $k=1/8\pi G$ for convenience, which yields

$$S_{\text{CDT}} = 2\pi k \sigma_{1,0} V_{1,0} N_{1,0} - k c_{2,1} N_{2,1}$$

where the coefficient $c_{2,1}$ is given by

$$c_{2,1} = \Lambda V_{2,1} + \sigma_{1,0} V_{1,0} \left(2\theta_{1,0}^{(2,1),(2,0)(1,1)} + \theta_{1,0}^{(2,1),(1,1)(1,1)} \right)$$

Inserting the geometric quantities $V_{2,1}$ from Eq. (5.31), $\theta_{1,0}^{(2,1)}$ from Eqs. (5.33) and (5.32) and using $V_{1,0} = 1$ gives

$$\begin{aligned} S_{\text{CDT}} &= 2\pi k \sigma_{1,0} V_{1,0} N_{1,0} \\ &\quad - k \left(\frac{\Lambda a^2}{4} \sqrt{4\alpha + 1} + 2\sigma_{1,0} \arccos \left(\frac{-i}{2\sqrt{\alpha}} \right) + \arcsin \left(-i \frac{4\alpha + 1}{2\alpha} \right) \right) N_{2,1} \end{aligned}$$



We use the identities $\arccos(-i \cdot x) = i \operatorname{arsinh}(x) + \pi/2$ and $\arcsin(-i \cdot x) = -i \operatorname{arsinh}(x)$ to rewrite the trigonometric functions and get

$$S_{\text{CDT}} = 2\pi k \sigma_{1,0} V_{1,0} N_{1,0} - k \left(\frac{\Lambda \alpha^2}{4} \sqrt{4\alpha + 1} + \sigma_{1,0} \pi + 2\sigma_{1,0} i \operatorname{arsinh} \left(\frac{i}{2\sqrt{\alpha}} \right) - \sigma_{1,0} i \operatorname{arsinh} \left(\frac{4\alpha + 1}{2\alpha} \right) \right) N_{2,1}$$

Using the topological identity (5.50a), which gives $N_{1,0} = N_{2,1}/2$ for $(1+1)$ causal dynamical triangulations, cancels the first term with the second term of the brackets. For the action to be real for $\alpha > 0$ we conclude that $\sigma_{1,0} = -i$, and we get for the action

$$\begin{aligned} S_{\text{CDT}} &= \kappa_{2,1} N_{2,1} = \\ &= -k \left(\frac{\Lambda \alpha^2}{4} \sqrt{4\alpha + 1} + 2 \operatorname{arsinh} \left(\frac{i}{2\sqrt{\alpha}} \right) - \operatorname{arsinh} \left(\frac{4\alpha + 1}{2\alpha} \right) \right) N_{2,1} \end{aligned} \quad (5.58)$$

The action of $(2+1)$ -dimensional CDT

In this section we derive the actual form of the action for $(2+1)$ causal dynamical triangulations. We use (5.26), and specialize first for $d = 3$ and define $k = 1/8\pi G$ for convenience, which yields

$$S_{\text{CDT}} = 2\pi k V_{2,0} \sigma_{2,0} N_{2,0} + 2\pi k V_{1,1} \sigma_{1,1} N_{1,1} - k c_{3,1} N_{3,1} - k c_{3,2} N_{2,2}$$

Using (5.54) in the definition (5.26) of the coefficients $c_{3,1}$ and $c_{3,2}$ gives

$$\begin{aligned} c_{3,1} &= \Lambda V_{3,1} + 3\theta_{2,0}^{(3,1),(3,0)(2,1)} \sigma_{2,0} V_{2,0} + 3\theta_{1,1}^{(3,1),(2,1)(2,1)} \sigma_{1,1} V_{1,1} \\ c_{3,2} &= \Lambda V_{2,2} + 2\theta_{2,0}^{(2,2),(2,1)(2,1)} \sigma_{2,0} V_{2,0} + 3\theta_{1,1}^{(2,2),(2,1)(2,1)} \sigma_{1,1} V_{1,1} \end{aligned}$$

One can see that one can omit the last two upper indices of the angles, because they do not carry any information. Using Eq. (5.53b) for replacing $N_{2,0}$ with $N_{3,1}$ gives

$$\begin{aligned} S_{\text{CDT}} &= 2\pi k \sigma_{2,0} V_{2,0} \frac{3N_{3,1}}{4} + 2\pi k \sigma_{1,1} V_{1,1} N_{1,1} \\ &\quad - k \left(\Lambda V_{3,1} + 3\theta_{2,0}^{(3,1)} \sigma_{2,0} V_{2,0} + 3\theta_{1,1}^{(3,1)} \sigma_{1,1} V_{1,1} \right) N_{3,1} \\ &\quad - k \left(\Lambda V_{2,2} + 2\theta_{2,0}^{(2,2)} \sigma_{2,0} V_{2,0} + 4\theta_{1,1}^{(2,2)} \sigma_{1,1} V_{1,1} \right) N_{2,2} \end{aligned}$$



which can be sorted with respect to the dynamical quantities $N_{1,1}$, $N_{3,1}$ and $N_{2,2}$, which yields

$$\begin{aligned} S_{\text{CDT}} &= 2\pi k\sigma_{1,1}V_{1,1}N_{1,1} \\ &+ \left(\frac{3\pi k}{2}\sigma_{2,0}V_{2,0} - k\Lambda V_{3,1} - 3k\theta_{2,0}^{(3,1)}\sigma_{2,0}V_{2,0} - 3k\theta_{1,1}^{(3,1)}\sigma_{1,1}V_{1,1} \right) N_{3,1} \\ &+ \left(-k\Lambda V_{2,2} - 2k\theta_{2,0}^{(2,2)}\sigma_{2,0}V_{2,0} - 4k\theta_{1,1}^{(2,2)}\sigma_{1,1}V_{1,1} \right) N_{2,2} \end{aligned}$$

We introduce now effective coupling constants κ by

$$S_{\text{CDT}} = \kappa_{1,1}N_{1,1} + \kappa_{3,1}N_{3,1} + \kappa_{2,2}N_{2,2}.$$

Now use the geometric volumes and angles calculated in Sec. 5.3.4, so for the coupling constant $\kappa_{1,1}$ (which is the generalized inverse temperature with respect to the time-like edges) we have $\kappa_{1,1} = 2\pi\sqrt{\alpha}ka$. For the coupling constant $\kappa_{3,1}$ (which is the generalized inverse temperature for the maximal (3, 1)-simplices) we get

$$\begin{aligned} \frac{\kappa_{3,1}}{ka} &= -i\frac{3\pi}{2} - \frac{\Lambda a^2\sqrt{3\alpha+1}}{12} + i3\arccos\left(\frac{-i}{\sqrt{3(4\alpha+1)}}\right) \\ &- 3\arccos\left(\frac{2\alpha+1}{4\alpha+1}\right)\sqrt{\alpha} \end{aligned}$$

We use the identity $\arccos(-i \cdot x) = i\operatorname{arsinh}(x) + \pi/2$, so that the first term cancels and the coupling constant can be expressed as

$$\frac{\kappa_{3,1}}{ka} = -\frac{\Lambda a^2\sqrt{3\alpha+1}}{12} - 3\operatorname{arsinh}\left(\frac{1}{\sqrt{3(4\alpha+1)}}\right) - 3\sqrt{\alpha}\arccos\left(\frac{2\alpha+1}{4\alpha+1}\right) \quad (5.59)$$

For the coupling constant $\kappa_{2,2}$ (which is the generalized inverse temperature for the maximal (2, 2)-simplices) we get

$$\frac{\kappa_{2,2}}{ka} = -\frac{\Lambda a^2\sqrt{2\alpha+1}}{6\sqrt{2}} + i\arcsin\left(\frac{-2i\sqrt{8(2\alpha+1)}}{4\alpha+1}\right) - 4\arccos\left(\frac{-1}{4\alpha+1}\right)\sqrt{\alpha}$$

We use the identity $\arcsin(-ix) = -i\operatorname{arsinh}(x)$ and rearrange the first term, which yields

$$\frac{\kappa_{2,2}}{ka} = -\frac{\Lambda a^2\sqrt{4\alpha+2}}{12} + 2\operatorname{arsinh}\left(\frac{\sqrt{8(2\alpha+1)}}{4\alpha+1}\right) - 4\sqrt{\alpha}\arccos\left(\frac{-1}{4\alpha+1}\right) \quad (5.60)$$



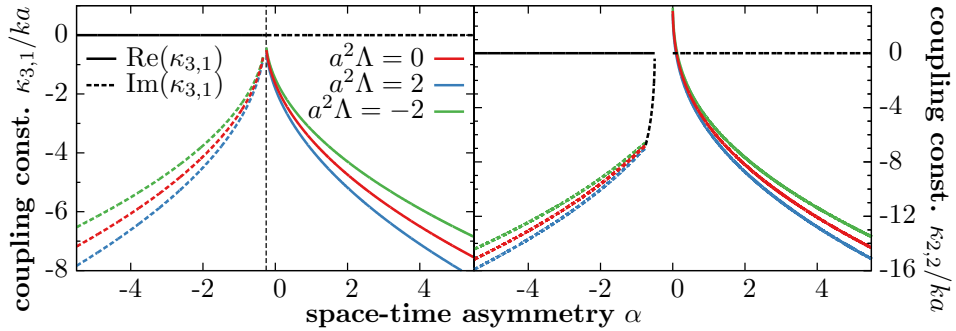


Figure 5.20: Coupling constants $\kappa_{3,1}/ka$ (5.59) and $\kappa_{2,2}/ka$ (5.60) of $(2+1)$ -dimensional causal dynamical triangulations in terms of the spacetime asymmetry factor α for different values of the cosmological constant $a^2\Lambda$ ($a^2\Lambda = 0$, $a^2\Lambda = 2$ and $a^2\Lambda = -2$). The real part of κ is displayed with solid lines, the imaginary part is displayed with dashed lines.

In Fig. 5.20 the values for the two coupling constants $\kappa_{3,1}$ and $\kappa_{2,2}$ are displayed for different values $a^2\Lambda$ of the cosmological constant in terms of the spacetime asymmetry parameter α . For the considered range of $\alpha > 0$ both coupling constants and therewith the action are real, and for $\alpha < -0.5$ both coupling constants are purely imaginary. For $-0.5 < \alpha < 0$ the coupling constant $\kappa_{2,2}$ is a complex number. This means that for $\alpha > 0$ the weight factor $\propto \exp(iS_{CDT})$ is just a phase factor (as one would expect for a Lorentzian path integral), whereas for $\alpha < -0.5$ the weight factor $\propto \exp(iS_{CDT})$ is a real number, which can be used for performing a Wick-rotation to the Euclidean domain.

In the following we will show that for $\alpha = -1$ the action of causal dynamical triangulations equals the action of Euclidean dynamical triangulations, as expected by construction (since for $\alpha = -1$ the length of a time-like edge becomes $\ell_{\text{time}}^2 = -\alpha a^2 = a^2 = \ell_{\text{space}}^2$). For the edge coupling constant we get $\kappa_{1,1} = 2\pi k a i$. The coupling constant $\kappa_{3,1}$ becomes

$$(\kappa_{3,1}/ka)|_{\alpha=-1} = -i\Lambda a^2\sqrt{2}/12 - 3 \operatorname{arsinh}(-i/3) - 3i \arccos(1/3)$$

We use the trigonometric identities $\operatorname{arsinh}(-ix) = -i \arcsin(x)$ and $\arcsin(x) = \pi/2 - \arccos(x)$ to obtain

$$(\kappa_{3,1}/ka)|_{\alpha=-1} = -i\Lambda a^2\sqrt{2}/12 - 6i \arccos(1/3) + \frac{3\pi i}{2}$$

The coupling constant $\kappa_{2,2}$ becomes

$$(\kappa_{2,2}/ka)|_{\alpha=-1} = -i\Lambda a^2\sqrt{2}/12 + 2 \operatorname{arsinh}(-2i\sqrt{2}/3) - 4i \arccos(1/3)$$



$$= -i\Lambda a^2 \sqrt{2}/12 - 2i \arcsin(2\sqrt{2}/3) - 4i \arccos(1/3)$$

By using the identity $\arcsin(x) = \arccos(\sqrt{1-x^2})$ we have

$$(\kappa_{2,2}/ka) = -i\Lambda a^2 \sqrt{2}/12 - 6i \arccos(1/3)$$

So the action for $\alpha = -1$ becomes

$$S_{\text{CDT}} = 2\pi kai \left[N_{1,1} + \frac{3}{4} N_{3,1} \right] - i \left[\frac{\Lambda ka^3 \sqrt{2}}{12} - 6ika \arccos\left(\frac{1}{3}\right) \right] (N_{3,1} + N_{2,2})$$

Using the topological identity $N_{2,0} = 3N_{3,1}/4$ and using the total number $N_1 = N_{2,0} + N_{1,1}$ of edges and the total number $N_3 = N_{3,1} + N_{2,2}$ of maximal simplices, we get

$$S_{\text{CDT}}|_{\alpha=-1} = 2\pi kai N_1 - i \left[\frac{\Lambda ka^3 \sqrt{2}}{12} - 6ika \arccos\left(\frac{1}{3}\right) \right] N_3 = i \cdot S_{\text{DT}},$$

where S_{DT} is the action (5.18b) of the (Euclidean) dynamical triangulation approach.

The action of (3 + 1)-dimensional CDT

In this section we derive the actual form of the action for (3 + 1) causal dynamical triangulations. We use (5.26), and specialize first for $d = 4$ and define $k = 1/8\pi G$ for convenience, which yields

$$S_{\text{CDT}} = 2\pi k V_{3,0} \sigma_{3,0} N_{3,0} + 2\pi k V_{2,1} \sigma_{2,1} N_{2,1} - kc_{4,1} N_{4,1} - kc_{4,2} N_{3,2}$$

Using (5.57) in the definition (5.26) of the coefficients $c_{3,1}$ and $c_{3,2}$ gives

$$\begin{aligned} c_{4,1} &= \Lambda V_{4,1} + 4\theta_{3,0}^{(4,1),(4,0)(3,1)} \sigma_{3,0} V_{3,0} + 6\theta_{2,1}^{(4,1),(3,1)(3,1)} \sigma_{2,1} V_{2,1} \\ c_{4,2} &= \Lambda V_{3,2} + \theta_{3,0}^{(3,2),(3,1)(3,1)} \sigma_{3,0} V_{3,0} + 6\theta_{2,1}^{(3,2),(3,1)(2,2)} \sigma_{2,1} V_{2,1} \\ &\quad + 3\theta_{2,1}^{(3,2),(2,2)(2,2)} \sigma_{2,1} V_{2,1} \end{aligned}$$

For most angles one can omit the second and the third upper index without any loss of information (for the remaining two angles one can omit the third upper index), and we can calculate the action

$$\begin{aligned} S_{\text{CDT}} &= 2\pi k V_{3,0} \sigma_{3,0} N_{3,0} + 2\pi k V_{2,1} \sigma_{2,1} N_{2,1} \\ &\quad - k \left(\Lambda V_{4,1} + 4\theta_{3,0}^{(4,1)} \sigma_{3,0} V_{3,0} + 6\theta_{2,1}^{(4,1)} \sigma_{2,1} V_{2,1} \right) N_{4,1} \end{aligned}$$



$$\begin{aligned}
 & -k \left(\Lambda V_{3,2} + \theta_{3,0}^{(3,2)} \sigma_{3,0} V_{3,0} + 6\theta_{2,1}^{(3,2),(3,1)} \sigma_{2,1} V_{2,1} \right. \\
 & \quad \left. + 3\theta_{2,1}^{(3,2),(2,2)} \sigma_{2,1} V_{2,1} \right) N_{3,2}
 \end{aligned}$$

We can use the topological identity (5.56c), which yields $N_{3,0} = N_{4,1}$, to express the action in the three independent quantities $N_{2,1}$, $N_{4,1}$ and $N_{3,2}$. Furthermore we introduce the generalized inverse temperatures κ with respect to the independent extensive quantities, so that the actual action is

$$S_{\text{CDT}} = \kappa_{2,1} N_{2,1} + \kappa_{4,1} N_{4,1} + \kappa_{3,2} N_{3,2}.$$

The first generalized inverse temperature is given by

$$\frac{\kappa_{2,1}}{ka^2} = \pi \frac{\sqrt{4\alpha + 1}}{2}$$

The second coupling constant $\kappa_{4,1}$, which is the generalized inverse temperature for the extensive quantity $N_{4,1}$, is given by

$$\begin{aligned}
 \frac{\kappa_{4,1}}{ka^2} &= -\pi i \frac{\sqrt{3}}{2} - \Lambda \frac{a^4}{96} \sqrt{8\alpha + 3} + 4i \arccos \left(\frac{-i}{2\sqrt{2}\sqrt{3\alpha + 1}} \right) \frac{\sqrt{3}}{4} \\
 & - 6 \arccos \left(\frac{2\alpha + 1}{2(3\alpha + 1)} \right) \frac{\sqrt{4\alpha + 1}}{4}
 \end{aligned}$$

Note that in the last term we used the positive argument of the arccos function to obtain an angle between 0 and π , and not the complementary angle. We use the identity $\arccos(-i \cdot x) = \pi/2 - i \operatorname{arsinh}(x)$ (where the real part cancels the first term of the coupling constant), and arrive at

$$\begin{aligned}
 \frac{\kappa_{4,1}}{ka^2} &= -\frac{\Lambda a^2}{96} \sqrt{8\alpha + 3} - \sqrt{3} \operatorname{arsinh} \left(\frac{1}{2\sqrt{2}\sqrt{3\alpha + 1}} \right) \\
 & - \frac{3}{2} \sqrt{4\alpha + 1} \arccos \left(\frac{2\alpha + 1}{2(3\alpha + 1)} \right) \tag{5.61}
 \end{aligned}$$

The third coupling constant $\kappa_{3,2}$, which is the generalized inverse temperature for the extensive quantity $N_{3,2}$, is given by

$$\begin{aligned}
 \frac{\kappa_{3,2}}{ka^2} &= -\frac{\Lambda a^2}{96} \sqrt{12\alpha + 7} + i \arcsin \left(\frac{-i\sqrt{3(12\alpha + 7)}}{2(3\alpha + 1)} \right) \frac{\sqrt{3}}{4} \\
 & - 6 \arccos \left(\frac{-1}{2\sqrt{2}(3\alpha + 1)(2\alpha + 1)} \right) \frac{\sqrt{4\alpha + 1}}{4}
 \end{aligned}$$



$$- 3 \arccos \left(\frac{4\alpha + 3}{4(2\alpha + 1)} \right) \frac{\sqrt{4\alpha + 1}}{4}$$

Note that we also interchanged the sign of the argument of the arcsin function to get the right contribution to the action. Using the identity $\arcsin(-i \cdot x) = -i \operatorname{arsinh}(x)$ leads to the final form of the coupling constant

$$\begin{aligned} \frac{\kappa_{3,2}}{ka^2} &= -\frac{\Lambda a^2}{96} \sqrt{12\alpha + 7} + \frac{\sqrt{3}}{4} \operatorname{arsinh} \left(\frac{\sqrt{3(12\alpha + 7)}}{2(3\alpha + 1)} \right) \\ &\quad - \frac{3\sqrt{4\alpha + 1}}{2} \arccos \left(\frac{-1}{2\sqrt{2(3\alpha + 1)(2\alpha + 1)}} \right) \\ &\quad - \frac{3\sqrt{4\alpha + 1}}{4} \arccos \left(\frac{4\alpha + 3}{4(2\alpha + 1)} \right) \end{aligned} \quad (5.62)$$

In Fig. 5.21 the values for the two coupling constants $\kappa_{4,1}$ and $\kappa_{3,2}$ are displayed for different values $a^2\Lambda$ of the cosmological constant in terms of the spacetime asymmetry parameter α . For the considered range of $\alpha > 0$ both coupling constants and therewith the action are real, and for $\alpha < -7/12$ both coupling constants are purely imaginary. This means that for $\alpha > 0$ the weight factor $\propto \exp(iS_{CDT})$ is just a phase factor (as one would expect for a Lorentzian path integral), whereas for $\alpha < -7/12$ the weight factor $\propto \exp(iS_{CDT})$ is a real number, which can be used for performing a Wick-Rotation to the Euclidean domain. Similar to the $(2 + 1)$ -dimensional case, one can then identify the action of Euclidean dynamical triangulations with the action of causal dynamical triangulations for spacetime asymmetry $\alpha = -1$. We omit this calculation here and point the interested reader to Ref. [34], where it was shown numerically that the two actions can be identified.

5.3.5 Grandcanonical one-slice propagator approach to CDT

In this section we derive how the partition function of causal dynamical triangulations can be reduced to the density of states defined for triangulations of one time slice. We will show that if this one-slice DOS can be calculated, e.g., by the Wang-Landau algorithm, the limit $T \rightarrow \infty$ can be implemented at once.



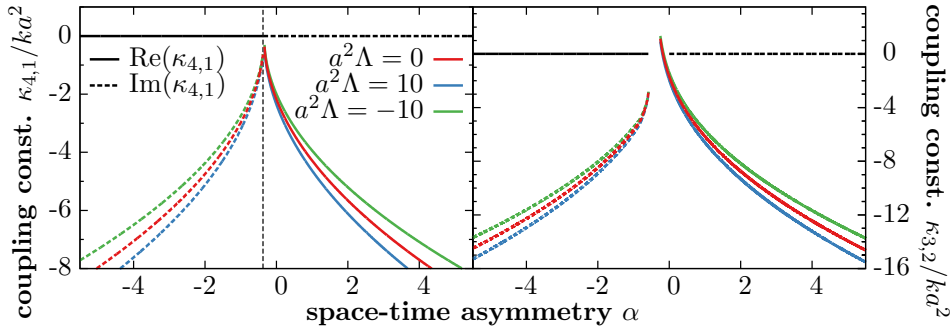


Figure 5.21: Coupling constants $\kappa_{4,1}/ka^2$ (5.61) and $\kappa_{3,2}/ka^2$ (5.62) of $(3 + 1)$ -dimensional causal dynamical triangulations in terms of the spacetime asymmetry factor α for different values of the cosmological constant $a^2\Lambda$ ($a^2\Lambda = 0$, $a^2\Lambda = 10$ and $a^2\Lambda = -10$). The real part of κ is displayed with solid lines, the imaginary part is displayed with dashed lines.

Partition function

In the following we denote by $\Sigma_{d-1} \times \mathcal{I}_T$ the underlying manifold of the causal dynamical triangulations with T time slices, where usually $\Sigma_{d-1} = S^{d-1}$ for the spatial slices and \mathcal{I} is an interval (for open or fixed boundary conditions) or S^1 (for periodic boundary conditions). For $\mathcal{T} \in \text{triang}(\Sigma_{d-1} \times \mathcal{I}_T)$ we denote by $\partial\mathcal{T} \in \text{triang}(\Sigma_{d-1})$ the triangulation which is the lower boundary of \mathcal{T} , and by $\bar{\partial}\mathcal{T} \in \text{triang}(\Sigma_{d-1})$ the triangulation which is the upper boundary of \mathcal{T} (if not using periodic boundary conditions). In general we define $\partial_t\mathcal{T} \in \text{triang}(\Sigma_{d-1})$ as the triangulation at time slice t .

Furthermore, denote by $N(\mathcal{T})$ an independent tuple of topological quantities describing the triangulation $\mathcal{T} \in \Sigma_{d-1} \times \mathcal{I}_T \rightarrow \mathbb{Z}^k$, compare Sec. 5.3.4 for details, e.g., $N(\mathcal{T}) = (N_{1,0}(\mathcal{T}), N_{3,1}(\mathcal{T}), N_{2,2}(\mathcal{T}))^t$ for $(2 + 1)$ -dimensional CDT. The number $N_i(\mathcal{T})$ denotes the topological quantities of the i -th time slice. Denote by $M(\tau)$ an independent tuple of topological quantities describing the spatial triangulation $\tau \in \Sigma_{d-1}$, e.g., $M(\tau) = N_2(\tau)$ for 2-dimensional triangulations with fixed topology, and by $M_i(\mathcal{T})$ the spatial topological quantities of the spatial slice of triangulation \mathcal{T} between the $(i - 1)$ -th and the i -th time slice. Last, we denote by κ the coupling constants which are dual to the independent topological quantities of the respective dimension. Note that in general N , M and κ are vectorial quantities, and that $\kappa \cdot N$ denotes a scalar product between these quantities. We often omit the argument of the quantities if it is clear to which triangulation they belong.



Depending on the choice of boundary conditions, the partition function for causal dynamical triangulations with T time slices can then be written as:

$$\begin{aligned}
 Z_T^{\text{fixed}}(M_0, M_T) &= \sum_{\substack{\mathcal{T} \in \text{triang}(\Sigma_{d-1} \times \mathcal{I}_T) \\ M(\partial\mathcal{T})=M_0, M(\bar{\partial}\mathcal{T})=M_T}} e^{-\kappa \cdot N(\mathcal{T})} = \sum_N g_T(N, M_0, M_T) e^{-\kappa \cdot N} \\
 Z_T^{\text{periodic}} &= \sum_{M_0} Z_T^{\text{fixed}}(M_0, M_0) \\
 Z_T^{\text{open}} &= \sum_{M_0} \sum_{M_T} Z_T^{\text{fixed}}(M_0, M_T)
 \end{aligned}$$

The density of states (DOS) $g_T(N, M_0, M_t)$ is basically the (normalized) number of T -slice triangulations with N simplices and M_0 boundary simplices at the one end and M_T boundary simplices at the other end of the triangulation. In principle this DOS can be calculated with a Wang-Landau simulation, but for large T the algorithm does not converge anymore because of the large number of energy bins.

But it is possible to calculate the T -slice DOS $g_T(N, M_0, M_T)$ in terms of the 1-slice DOS $g_1(N, M_0, M_1)$, as described in the following. Note that the one-slice DOS can be written as

$$g_1(N, M_0, M_1) = \sum_{\tau_0, \bar{\tau} \in \text{triang}(\Sigma_{d-1})} \delta_{M(\tau_0), M_0} \delta_{M(\bar{\tau}), M_1} \sum_{\substack{\mathcal{T} \in \text{triang}(\Sigma_d \times \mathcal{I}_1) \\ \partial\mathcal{T}=\tau_0, \bar{\partial}\mathcal{T}=\bar{\tau}}} \delta_{N(\mathcal{T}), N}$$

We now assume that

$$\sum_{\substack{\mathcal{T} \in \text{triang}(\Sigma_d \times \mathcal{I}_1) \\ \partial\mathcal{T}=\tau_0, \bar{\partial}\mathcal{T}=\tau_1}} \delta_{N(\mathcal{T}), N} \approx h(N, M(\tau_0), M(\tau_1)),$$

where the function $h(N, M_1, M_2)$ is the number of (1-slice) triangulations with topological quantities N that join one⁷ spatial triangulation with topological quantities M_1 with one with topological quantities M_2 . This assumption means that the number of triangulations joining two boundary triangulations $\underline{\tau}$ and $\bar{\tau}$ do not depend on the actual boundary triangulations,

⁷ The difference between the DOS $g(N, M_1, M_2)$ and $h(N, M_1, M_2)$ is that g corresponds to the number of triangulations joining all possible triangulations with boundary topological quantities M_1 and M_2 , and h corresponds to the (average) number of possible triangulations joining two fixed boundary triangulations with topological quantities M_1 and M_2



but only on the topological quantities of the boundary triangulations. Denote by

$$h_{\partial}(M) = \sum_{\tau \in \text{triang}(\Sigma_{d-1})} \delta_{M(\tau), M}$$

the number of boundary triangulations with topological quantities M (which is the density of states for triangulations of the spatial manifold as considered in Secs. 4.2 or Sec. 4.3), so the one-slice density of states can be written as

$$g_1(N, M_0, M_1) = h_{\partial}(M_0)h_{\partial}(M_1)h(N, M_0, M_1)$$

Next, we find a similar expression for the two-slice DOS and try to write it in terms of the one-slice DOS. The 2-slice DOS $g_2(N, M_0, M_2)$ (which is basically the number of two-slice spacetime triangulations with topological quantities N , which have boundaries with topological quantities M_0 and M_2) can be calculated by

$$g_2(N, M_0, M_2) = \sum_{\tau_{0,2} \in \text{triang}(\Sigma_{d-1})} \delta_{M(\tau_0), M_0} \delta_{M(\tau_2), M_2} \sum_{\substack{\mathcal{T} \in \text{triang}(\Sigma_d \times \mathcal{I}_2) \\ \partial T = \tau_0, \bar{\partial} T = \tau_2}} \delta_{N(\mathcal{T}), N}$$

Next we use the fact that the sum over all two-slice triangulations $\mathcal{T} \in \text{triang}(\Sigma_d \times \mathcal{I}_2)$ can be expressed as a sum over all intermediate spatial triangulations τ_1 and all one-slice triangulations $\mathcal{T}_{1,2} \in \text{triang}(\Sigma_d \times \mathcal{I}_1)$ with the correct boundary conditions:

$$g_2(N, M_0, M_2) = \sum_{\tau_{0,1,2} \in \text{triang}(\Sigma_{d-1})} \delta_{M(\tau_0), M_0} \delta_{M(\tau_2), M_2} \sum_{\substack{\mathcal{T}_{0,1} \in \text{triang}(\Sigma_d \times \mathcal{I}_1) \\ \partial T_0 = \tau_0, \bar{\partial} T_0 = \tau_1 \\ \partial T_1 = \tau_1, \bar{\partial} T_1 = \tau_2}} \delta_{N(\mathcal{T}_0) + N(\mathcal{T}_1), N}$$

Now we divide the condition $N(\mathcal{T}_0) + N(\mathcal{T}_1) = N$, which is encoded in the last delta function, into the conditions $N(\mathcal{T}_0) = N_0$ and $N(\mathcal{T}_1) = N - N_0$, summing over all possible N_0 , which results in

$$g_2(N, M_0, M_2) = \sum_{\tau_{0,1,2} \in \text{triang}(\Sigma_{d-1})} \delta_{M(\tau_0), M_0} \delta_{M(\tau_2), M_2} \sum_{N_0} \sum_{\substack{\mathcal{T}_{0,1} \in \text{triang}(\Sigma_d \times \mathcal{I}_1) \\ \partial T_0 = \tau_0, \bar{\partial} T_0 = \tau_1 \\ \partial T_1 = \tau_1, \bar{\partial} T_1 = \tau_2}} \delta_{N(\mathcal{T}_0), N_0} \delta_{N(\mathcal{T}_1), N - N_0}$$

Inserting the functions h and h_{∂} then yields

$$g_2(N, M_0, M_2) = \sum_{M_1} h_{\partial}(M_1)h_{\partial}(M_2)h_{\partial}(M_3) \cdot \sum_{N_0} h(N_0, M_0, M_1)h(N - N_0, M_1, M_2),$$



which means that one can express the two-slice DOS g_2 in terms of the one-slice DOS g_1 by

$$g_2(N, M_0, M_2) = \sum_{M_1} \sum_{N_0} \frac{1}{h_\partial(M_1)} g_1(N_0, M_0, M_1) g_1(N - N_0, M_1, M_2),$$

or, in a way that is more symmetric in the first arguments of the one-slice DOS, by

$$g_2(N, M_0, M_2) = \sum_{M_1} \sum_{N_0, N_1} \frac{1}{h_\partial(M_1)} g_1(N_0, M_0, M_1) g_1(N_1, M_1, M_2) \delta_{N_0+N_1, N} \quad (5.63)$$

This can be generalized for the T -slice DOS by

$$g_T(N, M_0, M_T) = \sum_{M_1, \dots, M_{T-1}} \sum_{N_0, \dots, N_{T-1}} \frac{\prod_{r=1}^T g_1(N_r, M_{r-1}, M_r)}{\prod_{s=1}^{T-1} h_\partial(M_s)} \delta_{\sum_i N_i, N} \quad (5.64)$$

Using the T -slice DOS in the partition function yields

$$Z_T^{\text{fixed}}(M_0, M_T) = \sum_{M_1, \dots, M_{T-1}} \sum_{N_0, \dots, N_{T-1}} \prod_{i=1}^T \frac{g_1(N_i, M_{i-1}, M_i)}{h_\partial(M_i)} h_\partial(M_T) e^{-\kappa \cdot N} \quad (5.65)$$

Note that the factor $h_\partial(M_T)$ is constant if considering fixed M_i , so it is not important for calculating expectation values using this partition function, and will be omitted further on. The partition functions for open and periodic boundary conditions can be calculated from the fixed boundary partition function. In principle one can use this DOS or this partition function for calculations of expectation values directly. But numerically it is a problem to evaluate the nested sums that occur in the formulas and to store the resulting DOS in memory, so in the next section we will derive a transfer-matrix approach for extrapolation expectation values directly from the 1-slice DOS.

Construction of the transfer matrix

The aim of this section is to formulate the partition function using transfer matrices, as already done for the one-dimensional Ising model in Sec. 2.1.7. This is quite easy if the action is slice-additive, i.e., if \mathcal{T}_1 and \mathcal{T}_2 are two one-slice triangulations with matching boundaries $\bar{\partial}\mathcal{T}_1 = \partial\mathcal{T}_2$, and $\mathcal{T} = \mathcal{T}_1 \cup \mathcal{T}_2$ is the two-slice triangulation that consists of the triangulations \mathcal{T}_1 and \mathcal{T}_2 , then

$$N(\mathcal{T}_1 \cup \mathcal{T}_2) = N(\mathcal{T}_1) + N(\mathcal{T}_2)$$



This is true if N consists only of the number of simplices of type $(k - i + 1, i)$ with $1 \leq k \leq d$ and $i \leq 1$, but it fails if N has a component that is the number of a space-like $(k + 1, 0)$ -simplices, because these are shared between the neighbors, and we get

$$N(\mathcal{T}_1 \cup \mathcal{T}_2) = N(\mathcal{T}_1) + N(\mathcal{T}_2) - N(\mathcal{T}_1 \cap \mathcal{T}_2)$$

We will introduce the transfer matrix notation for the partition function in this section first for slice-additive actions. At the end of the section we will present how to generalize this formulation also for non-slice-additive actions.

If the action is slice-additive, the T -slice partition function (5.65) for fixed boundary conditions can be written as

$$Z_T^{\text{fixed}}(M_0, M_T) = \sum_{M_1} \cdots \sum_{M_{T-1}} \prod_{i=1}^T V(\kappa, M_{i-1}, M_i)$$

with $V(\kappa, M_{i-1}, M_i) := \sum_N \frac{g_1(N, M_{i-1}, M_i)}{h_\partial(M_i)} e^{-\kappa \cdot N}$

In the following we identify $V(\kappa, \bullet, \bullet)$ with the components of a symmetric *transfer matrix* $\mathbf{V}(\kappa)$, so that we can identify matrix products in the upper formula and for the other types of partition functions:

$$Z_T^{\text{fixed}}(\kappa, M_0, M_T) = \left(\mathbf{V}(\kappa)^T \right) (M_0, M_T) \tag{5.66a}$$

$$Z_T^{\text{open}}(\kappa) = \sum_{M_0} \sum_{M_T} \left(\mathbf{V}(\kappa)^t \right) (M_0, M_T) \tag{5.66b}$$

$$Z_T^{\text{periodic}}(\kappa) = \text{Tr} \left(\mathbf{V}(\kappa)^t \right) \tag{5.66c}$$

For the fixed boundary conditions, the result is simply the proper entry of the power of the transfer matrix. For open boundary conditions, the result is the grand sum of the power of the matrix, and for periodic boundary conditions, the result is the trace of the power of the transfer matrix.

Since the transfer matrix $\mathbf{V}(\kappa)$ is a symmetric matrix, it has a non-negative eigenbasis

$$\mathbf{V}(\kappa) |a\rangle = \lambda_a(\kappa) |a\rangle \quad \lambda_1 \leq \lambda_2 \leq \lambda_3 \dots \tag{5.67}$$

Note that of course also the eigenvectors $|a\rangle$ depend on the coupling constants κ , which is not reflected in the notation. Furthermore we introduce the notion $|M\rangle$ for the standard-basis of the transfer-matrix, so that

$$\langle M | \mathbf{V}(\kappa) | M' \rangle = V(\kappa, M, M')$$



For distinction, we use upper-case letters for the standard basis and lower-case letters for the eigenbasis. Using this notation the different partition functions can be written as

$$\begin{aligned} Z_T^{\text{fixed}}(\kappa, M_0, M_T) &= \langle M_0 | \mathbf{V}(\kappa)^T | M_T \rangle = \sum_a \langle M_0 | a \rangle \langle a | M_T \rangle \lambda_a(\kappa)^T \\ Z_T^{\text{open}}(\kappa) &= \sum_{ab} \langle a | \mathbf{V}(\kappa)^T | b \rangle = \sum_{M_0, M_T} \sum_a \langle M_0 | a \rangle \langle a | M_T \rangle \lambda_a(\kappa)^T \\ Z_T^{\text{periodic}}(\kappa) &= \sum_a \langle a | \mathbf{V}(\kappa)^T | a \rangle = \sum_a \lambda_a(\kappa)^T \end{aligned}$$

The formulation of the partition functions in the eigenbasis has the advantage that the limit $T \rightarrow \infty$ can be implemented easily, because there only the largest eigenvalue λ_1 contributes to the partition function. This results in

$$\lim_{T \rightarrow \infty} Z_T^{\text{fixed}}(\kappa, M_0, M_T) = \langle M_0 | 1 \rangle \langle 1 | M_T \rangle \lambda_1(\kappa)^T \quad (5.68a)$$

$$\lim_{T \rightarrow \infty} Z_T^{\text{open}}(\kappa) = \sum_{M_0, M_T} \langle M_0 | 1 \rangle \langle 1 | M_T \rangle \lambda_1(\kappa)^T \quad (5.68b)$$

$$\lim_{T \rightarrow \infty} Z_T^{\text{periodic}}(\kappa) = \sum_1 \lambda_1(\kappa)^T \quad (5.68c)$$

So if the dependence of $\lambda_1(\kappa)$ on the coupling constants κ is known analytically, all relevant quantities could be calculated using derivatives of this eigenvalue.

As mentioned before, the action of causal dynamical triangulations can be non-slice-additive, if there are contributions of the number of spatial simplices (which are counted in both neighboring triangulation slices). One can generalize the transfer matrix method by calculating the total topological contribution of the whole triangulation by

$$N = \sum_{i=1}^T N_i + \sum_{i=0}^{T-1} f(M_i) = \sum_{i=1}^T N_i + f\left(\sum_{i=0}^T M_i\right)$$

for periodic boundary conditions with a linear boundary contribution function f . Using this correction the (periodic boundary) partition function



becomes

$$\begin{aligned}
 Z_T &= \sum_{N_1} \cdots \sum_{N_t} \sum_{M_0} \sum_{M_1} \cdots \sum_{M_{t-1}} \prod_{i=1}^T \frac{g_1(N_i, M_{i-1}, M_i)}{h_{\partial}(M_i)} e^{-\kappa \cdot (\sum_i N_i + \sum_i f(M_i))} = \\
 &= \sum_{M_0} \sum_{M_1} \cdots \sum_{M_{T-1}} \prod_{i=1}^T V(\kappa, M_{i-1}, M_i) e^{-\kappa \cdot \sum_i f(M_i)} \\
 &= \sum_{M_0} \sum_{M_1} \cdots \sum_{M_{T-1}} \prod_{i=1}^T \tilde{V}(\kappa, M_{i-1}, M_i)
 \end{aligned}$$

$$\text{with } \tilde{V}(\kappa, M_{i-1}, M_i) := V(\kappa, M_{i-1}, M_i) \exp \left[-\frac{\kappa}{2} \cdot (f(M_{i-1}) + f(M_i)) \right]$$

Using again the matrix representation results in

$$Z_T = \text{Tr} \left(\tilde{\mathbf{V}}(\kappa)^T \right) \rightarrow \tilde{\lambda}_1^T$$

So one can do all the following calculations with the modified transfer matrix $\tilde{\mathbf{V}}$ instead of the standard transfer matrix \mathbf{V} , if there are non-additive topological quantities.

Sometimes it is more convenient to use the matrix notation instead of the bracket notation. In this cases we use the eigenvalue decomposition

$$\mathbf{V}(\kappa) = \mathbf{P} \cdot \text{diag}(\lambda_1, \dots, \lambda_k) \cdot \mathbf{P}^{-1}$$

of the transfer matrix, where \mathbf{P} is the projection operator or matrix on the corresponding eigenvectors.

For simplicity we use only periodic boundary conditions in the following derivations, but give the results for closed and open boundaries if appropriate. If nothing is specified, the partition functions and the expectation values are for periodic boundary conditions. In the following sections, we use the transfer matrix method to calculate expectation values and correlations of slice observables (e.g., number of simplices that connect neighboring time slices), spatial observables (e.g., number of simplices in the same spatial slice, this can be used for calculating the spatial volume of the universe, or its correlations) and world observables (e.g., density of simplices).

Slice observables

The first task is to calculate the expectation value of functions of the independent topological quantities N within a given spacetime slice. We denote by N_j the topological quantities of the j -th spacetime slice.



We start by calculating the linear expectation value $\langle N_j \rangle_T$ for T time slices by modifying Eq. (5.65) for the partition function:

$$\begin{aligned}
 \langle N_j \rangle_T &= \frac{1}{Z_T(\kappa)} \sum_{N_1} \cdots \sum_{N_T} \sum_{M_0} \cdots \sum_{M_{T-1}} N_j \prod_{i=1}^T \frac{g_1(N_i, M_{i-1}, M_i)}{h_{\partial}(M_i)} e^{-\kappa \cdot N} = \\
 &= \frac{1}{Z_T(\kappa)} \sum_{M_0} \cdots \sum_{\substack{M_{T-1} \\ i \neq j}} \prod_{i=1}^T V(\kappa, M_{i-1}, M_i) \sum_{N_j} N_j \frac{g_1(N_j, M_{j-1}, M_j)}{h_{\partial}(M_j)} e^{-\kappa \cdot N_j} \\
 &= \frac{1}{Z_T(\kappa)} \text{Tr} \left(\mathbf{V}(\kappa)^j \mathbf{S}^{(1)}(\kappa) \mathbf{V}(\kappa)^{t-j-1} \right) \\
 &\quad \text{with } S^{(1)}(\kappa, M_{j-1}, M_j) := \sum_{N_j} N_j \frac{g_1(N_j, M_{j-1}, M_j)}{h_{\partial}(M_j)} e^{-\kappa \cdot N_j}.
 \end{aligned}$$

Using the commutativity of the trace results, and evaluation the trace in the eigenbasis of the transfer matrix results in

$$\begin{aligned}
 \langle N \rangle_T = \langle N_j \rangle_T &= \frac{1}{Z_T(\kappa)} \sum_{ab} \langle a | S^{(1)}(\kappa) | b \rangle \langle b | V(\kappa)^{T-1} | a \rangle = \\
 &= \frac{1}{Z_T(\kappa)} \sum_a \langle a | S^{(1)}(\kappa) | a \rangle \lambda_a^{T-1},
 \end{aligned} \tag{5.69}$$

which of course does not depend on the index j if using periodic boundary conditions. We can calculate the limit $T \rightarrow \infty$ for Eq. (5.69) as for the partition function, where only the largest eigenvalue λ_1 did contribute to the sum. The result is

$$\begin{aligned}
 \langle N \rangle &= \lim_{T \rightarrow \infty} \frac{1}{Z_T(\kappa)} \sum_a \langle a | S^{(1)}(\kappa) | a \rangle \lambda_a^{T-1} = \\
 &= \lim_{T \rightarrow \infty} \frac{1}{\lambda_1^T} \langle 1 | S^{(1)}(\kappa) | 1 \rangle \lambda_1^{T-1} = \frac{\langle 1 | S^{(1)}(\kappa) | 1 \rangle}{\lambda_1}
 \end{aligned} \tag{5.70}$$

Using the same method one can also calculate the expectation values $\langle N^k \rangle$ of powers of the topological quantities N by

$$\begin{aligned}
 \langle N_j^k \rangle_t &= \frac{1}{Z_t(\kappa)} \sum_{N_1} \cdots \sum_{N_t} \sum_{M_0} \sum_{M_1} \cdots \sum_{M_{t-1}} N_j^k \prod_{i=1}^t \frac{g_1(N_i, M_{i-1}, M_i)}{h_{\partial}(M_i)} e^{-\kappa \cdot N} = \\
 &= \frac{1}{Z_t(\kappa)} \sum_{M_0} \cdots \sum_{\substack{M_{t-1} \\ i \neq j}} \prod_{i=1}^t V(\kappa, M_{i-1}, M_i) \sum_{N_j} N_j^k \frac{g_1(N_j, M_{j-1}, M_j)}{h_{\partial}(M_j)} e^{-\kappa \cdot N_j}
 \end{aligned}$$



$$= \frac{1}{Z_t(\kappa)} \text{Tr} \left(\mathbf{V}(\kappa)^j \mathbf{S}^{(k)}(\kappa) \mathbf{V}(\kappa)^{t-j-1} \right)$$

$$\text{with } S^{(k)}(\kappa, M_{j-1}, M_j) := \sum_{N_j} N_j^k \frac{g_1(N_j, M_{j-1}, M_j)}{h_\partial(M_j)} e^{-\kappa \cdot N_j}$$

Using again the commutativity of the trace and going to the eigenbasis of the transfer matrix results in

$$\begin{aligned} \langle N^k \rangle_T &= \langle N_j^k \rangle_T = \frac{1}{Z_T(\kappa)} \sum_{ab} \langle a | S^{(k)}(\kappa) | b \rangle \langle b | V(\kappa)^{T-1} | a \rangle = \\ &= \frac{1}{Z_T(\kappa)} \sum_a \langle a | S^{(k)}(\kappa) | a \rangle \lambda_a^{T-1} \end{aligned} \quad (5.71)$$

which again does not depend on the index j due to the periodic boundary conditions. The continuum limit can be calculated as before by

$$\begin{aligned} \langle N^k \rangle &= \lim_{T \rightarrow \infty} \frac{1}{Z_T(\kappa)} \sum_a \langle a | S^{(k)}(\kappa) | a \rangle \lambda_a^{T-1} = \\ &= \lim_{T \rightarrow \infty} \frac{1}{\lambda_1^T} \langle 1 | S^{(k)}(\kappa) | 1 \rangle \lambda_1^{T-1} = \frac{\langle 1 | S^{(k)}(\kappa) | 1 \rangle}{\lambda_1} \end{aligned} \quad (5.72)$$

This enables us to calculate the variance of slice observables by

$$\text{Var}(N) = \langle N^2 \rangle - \langle N \rangle^2 = \frac{1}{\lambda_1} \langle 1 | S^{(2)}(\kappa) | 1 \rangle - \frac{1}{\lambda_1^2} \langle 1 | S^{(1)}(\kappa) | 1 \rangle^2, \quad (5.73)$$

as well as all other continuous functions $f(N)$ of the topological quantities N by using a Taylor expansion.

To calculate correlations in the topological quantities N across several slices, one has to calculate mixed expectation values. The covariance $\text{Cov}(N_t, N_{t+\Delta t})$ equals the covariance $\text{Cov}(N_0, N_{\Delta t})$ for periodic boundary conditions and can be calculated using

$$\text{Cov}(N_0, N_{\Delta t}) = \langle N_0 N_{\Delta t} \rangle - \langle N_0 \rangle \langle N_{\Delta t} \rangle = \langle N_0 N_{\Delta t} \rangle - \langle N \rangle^2. \quad (5.74)$$

The second part has been calculated before, and the mixed expectation values can be calculated by

$$\begin{aligned} \langle N_0 N_{\Delta t} \rangle_T &= \frac{1}{Z(\kappa)} \sum_a \langle a | S^{(1)} V^{\Delta t-1} S^{(1)} V^{T-\Delta t-1} | a \rangle = \\ &= \frac{1}{Z(\kappa)} \sum_{abcd} \langle a | S^{(1)} | b \rangle \langle b | V^{\Delta t-1} | c \rangle \langle c | S^{(1)} | d \rangle \langle d | V^{T-\Delta t-1} | a \rangle = \end{aligned}$$



$$\begin{aligned}
 &= \frac{1}{Z(\kappa)} \sum_{abcd} \langle a | S^{(1)} | b \rangle \lambda_b^{\Delta t - 1} \delta_{bc} \langle c | S^{(1)} | d \rangle \lambda_a^{T - \Delta t - 1} \delta_{ad} = \\
 &= \frac{1}{Z(\kappa)} \sum_{ab} \lambda_a^{T - \Delta - 1} \lambda_b^{\Delta - 1} \left| \langle a | S^{(1)} | b \rangle \right|^2.
 \end{aligned}$$

For $T \rightarrow \infty$ only the largest eigenvalue $\lambda_a = \lambda_1$ does contribute, and we use $Z(\kappa)_T = \lambda_1^T$ for the partition function. Furthermore we split the sum over b into the part $b = 1$ and $b \neq 1$:

$$\langle N_0 N_{\Delta t} \rangle_T = \frac{1}{\lambda_1^2} \left| \langle 1 | S^{(1)} | 1 \rangle \right|^2 + \frac{1}{\lambda_1^{\Delta t + 1}} \sum_{b \neq 1} \lambda_b^{\Delta t - 1} \left| \langle 1 | S^{(1)} | b \rangle \right|^2. \quad (5.75)$$

The first term can be recognized to be the second moment of the slice observable $\langle N^2 \rangle$, so the covariance (5.74) of two slice variables becomes

$$\text{Cov}(N_0, N_{\Delta t}) = \frac{1}{\lambda_1^2} \sum_{b \neq 1} \left(\frac{\lambda_b}{\lambda_1} \right)^{\Delta t - 1} \left| \langle 1 | S^{(1)} | b \rangle \right|^2 \quad (5.76)$$

Eq. (5.76) can be simplified further in the limit of large Δt . Here only the second-largest eigenvalue $\lambda_b = \lambda_2$ does contribute in the sum, and we can approximate

$$\begin{aligned}
 \text{Cov}(N_0, N_{\Delta t})|_{\Delta t \gg 1} &\approx \frac{1}{\lambda_1^2} \left(\frac{\lambda_2}{\lambda_1} \right)^{\Delta t - 1} \left| \langle 1 | S^{(1)} | 2 \rangle \right|^2 = \\
 &= \frac{\left| \langle 1 | S^{(1)} | 2 \rangle \right|^2}{\lambda_1 \lambda_2} \left(\frac{\lambda_2}{\lambda_1} \right)^{\Delta t}
 \end{aligned}$$

The last term can be written as an exponential function, resulting in

$$\text{Cov}(N_0, N_{\Delta t})|_{\Delta t \gg 1} \approx \frac{\left| \langle 1 | S^{(1)} | 2 \rangle \right|^2}{\lambda_1 \lambda_2} \exp \left[\log \left(\frac{\lambda_2}{\lambda_1} \right) \cdot \Delta t \right] \quad (5.77)$$

So one can read off the relation for a correlation time τ

$$\tau = -\frac{1}{\log(\lambda_2/\lambda_1)} = \frac{1}{\log(\lambda_1) - \log(\lambda_2)}, \quad (5.78)$$

which is independent of the considered observable. Note that the ordering of the eigenvalues is by their absolute value, so that the exponential approximation is only valid for $\lambda_2 > 0$. The case $\lambda_2 < 0$ means that the covariance alternates between positive and negative values, and one can approximate the absolute values of the covariance by an exponential function.



Spatial observables

In the previous section we calculated expectation values and correlations of slice observables. In this section we will calculate both for spatial observables, i.e., the number of spatial $(k+1, 0)$ -simplices. They can be calculated analogous to the slice observables by

$$\begin{aligned} \langle M_j^k \rangle_t &= \frac{1}{Z_t(\kappa)} \sum_{N_1} \cdots \sum_{N_t} \sum_{M_0} \sum_{M_1} \cdots \sum_{M_{t-1}} M_j \prod_{i=1}^t g_1(N_i, M_{i-1}, M_i) e^{-\kappa \cdot N} = \\ &= \frac{1}{Z_t(\kappa)} \sum_{M_0} \sum_{M_1} \cdots \sum_{M_{t-1}} M_j \prod_{i=1}^t V(\kappa, M_{i-1}, M_i) \\ &= \frac{1}{Z_t(\kappa)} \text{Tr} \left(\mathbf{V}(\kappa)^j \mathbf{R}^{(k)}(\kappa) \mathbf{V}(\kappa)^{t-j-1} \right) = \frac{1}{Z_t(\kappa)} \text{Tr} \left(\mathbf{V}(\kappa)^{t-1} \mathbf{R}^{(k)}(\kappa) \right) \end{aligned}$$

with $R^{(k)}(\kappa, M_{j-1}, M_j) := M_{j-1}^k V(M_{j-1}, M_j)$

Due to the periodic boundary conditions these results also do not depend on the index j . Using the approximations for $T \rightarrow \infty$ as in the previous section yields

$$\langle M^k \rangle = \frac{1}{\lambda_1} \langle 1 | \mathbf{R}^{(k)}(\kappa) | 1 \rangle \quad (5.79)$$

The correlation of spatial observables can also be calculated as in the section before as

$$\begin{aligned} \langle M_0 M_\tau \rangle &= \frac{1}{Z_t(\kappa)} \text{Tr} \left(\mathbf{R}(\kappa) \mathbf{V}(\kappa)^{\tau-1} \mathbf{R}(\kappa) \mathbf{V}(\kappa)^{t-\tau-1} \right) \\ &= \frac{1}{\lambda^{\tau+1}} \text{Tr} \left(\mathbf{R}(\kappa) \mathbf{V}(\kappa)^{\tau-1} \mathbf{R}(\kappa) \mathbf{P}_\lambda \right), \end{aligned}$$

and with this also the covariance function as in Eq. (5.76).

World observables

Until now we calculated expectation values only for observables defined for single slices, e.g. the average number of 3-simplices $\langle N_3 \rangle$ or their variance $\text{Var}(N_3) = \langle N_3^2 \rangle - \langle N_3 \rangle^2$. In this subsection expectation values of quantities of the whole triangulation are considered. To discriminate between slice and triangulation observables, we denote the latter by bold letters. In general we are interested in calculating expectation values of the observable

$$\mathbf{N} := \sum_{t=0}^{T-1} N_t, \quad (5.80)$$



which is finite only for finite T and where N_t denotes the slices observable at the t -th slice, or the density

$$\mathbf{n} := \frac{1}{T} \sum_{t=0}^{T-1} N_t, \tag{5.81}$$

which has a finite value also in the limit $T \rightarrow \infty$.

The first moments can be simply calculated in terms of the slice expectation values

$$\langle \mathbf{N} \rangle = \left\langle \sum_{t=0}^{T-1} N_t \right\rangle = \sum_{t=0}^{T-1} \langle N_t \rangle = T \cdot \langle N \rangle \tag{5.82}$$

$$\langle \mathbf{n} \rangle = \frac{1}{T} \left\langle \sum_{t=0}^{T-1} N_t \right\rangle = \langle N \rangle, \tag{5.83}$$

where we used $\langle N_t \rangle = \langle N \rangle$ independent of t for periodic boundary conditions.

For higher moments the calculation becomes more involved due to the correlations between different slices, which we one see for calculating e.g., the second moment

$$\begin{aligned} \langle \mathbf{N}^2 \rangle &= \left\langle \left(\sum_{t=0}^{T-1} N_t \right) \cdot \left(\sum_{t'=0}^{T-1} N_{t'} \right) \right\rangle = \sum_{t=0}^{T-1} \sum_{t'=0}^{T-1} \langle N_t N_{t'} \rangle = \\ &= \sum_{t=0}^{T-1} \langle N_t^2 \rangle + \sum_{t=0}^{T-1} \sum_{t'=0, t' \neq t}^{T-1} \langle N_t N_{t'} \rangle = \\ &= T \langle N^2 \rangle + T \sum_{t=1}^{T-1} \langle N_t N_{t'} \rangle = T \cdot \left[\langle N^2 \rangle + \sum_{t=1}^{T-1} \langle N_t N_{t'} \rangle \right] \end{aligned}$$

This can be used for calculating the variance of triangulation observables by

$$\text{Var}(\mathbf{N}) = \langle \mathbf{N}^2 \rangle - \langle \mathbf{N} \rangle^2 = T \cdot \left(\text{Var}(N) + \sum_{t=1}^{T-1} \text{Cov}(N(0), N_t) \right). \tag{5.84}$$

So the variance of the triangulation observable is not just the sum of the single time slice variables, also the summed covariance of the observables has to be taken into account.

Using Eq. (5.76) for the covariance of the slice observables one gets

$$\frac{\text{Var}(\mathbf{N})}{T} = \text{Var}(N) + \sum_{t=1}^{T-1} \sum_{b \neq 1} \left(\frac{|\langle 1 | S^{(1)} | b \rangle|}{\lambda_1} \right)^2 \cdot \left(\frac{\lambda_b}{\lambda_1} \right)^{t-1} =$$



$$\begin{aligned}
 &= \text{Var}(N) + \sum_{b \neq 1} \left(\frac{|\langle 1 | S^{(1)} | b \rangle|}{\lambda_1} \right)^2 \sum_{t=0}^{T-2} \left(\frac{\lambda_b}{\lambda_1} \right)^t = \\
 &= \text{Var}(N) + \sum_{b \neq 1} \left(\frac{|\langle 1 | S^{(1)} | b \rangle|}{\lambda_1} \right)^2 \frac{1 - (\lambda_b/\lambda_1)^{T-1}}{1 - \lambda_b/\lambda_1}
 \end{aligned}$$

where we used that the sum over t is a geometric series. Note that we cannot use the approximation for large t because due to the sum also small values of t are always present. In the limit $T \rightarrow \infty$ we get

$$\lim_{T \rightarrow \infty} \frac{\text{Var}(\mathbf{N})}{T} = \text{Var}(N) + \sum_{b \neq 1} \frac{|\langle 1 | S^{(1)} | b \rangle|^2}{\lambda_1(\lambda_1 - \lambda_b)} \quad (5.85)$$

for the variance of the total number of simplices in the triangulation.

5.3.6 Numerical results of $(2 + 1)$ -dimensional CDT

In this section we use the developed one-slice propagator approach to calculate observables in $(2+1)$ -dimensional causal dynamical triangulations.

Calculating the 1-slice DOS

The first task is to calculate the density of states of a single slice causal dynamical triangulations in terms of the numbers $N_{3,1}$ and $N_{2,2}$ of maximal simplices and the number \underline{N}_2 and \overline{N}_2 of maximal boundary simplices using the Wang-Landau algorithm [406, 407]. For an efficient calculation the number of energy bins has to be reduced as far as possible by symmetry considerations.

We denote by $g(N_{3,1}; N_{2,2}; \underline{N}_2; \overline{N}_2)$ the (normalized) number of triangulations with these topological quantities. Note that the number of triangulations does not depend on $N_{1,0}$ (the number of vertices), because $N_{1,0}$ is determined by \underline{N}_2 and \overline{N}_2 and the Euler characteristic of the boundary triangulations by

$$N_{1,0} = 2 \cdot \chi(\Sigma) + \frac{1}{2} (\underline{N}_2 + \overline{N}_2),$$

where $\chi(\Sigma)$ is the Euler-characteristic of the spatial slices.

Because the labeling of one boundary as lower boundary and the other boundary as upper boundary is not important, the density of states is



symmetric in the last two arguments:

$$g(N_{3,1}; N_{2,2}; \underline{N}_2; \overline{N}_2) = g(N_{3,1}; N_{2,2}; \overline{N}_2; \underline{N}_2)$$

So it is enough to calculate only the density of states with $\underline{N}_2 \leq \overline{N}_2$. Furthermore the following relation is true

$$\underline{N}_2 + \overline{N}_2 = N_{3,1}$$

since each maximal spatial simplex is the face to exactly one $(3, 1)$ -simplex and vice versa. So the density of states only depend on the (absolute value of the) difference of the boundary simplex numbers:

$$g(N_{3,1}; N_{2,2}; \underline{N}_2; \overline{N}_2) = g(N_{3,1}; N_{2,2}; |\underline{N}_2 - \overline{N}_2|) =: g(N_{3,1}; N_{2,2}; |\Delta N_2|)$$

Since spatial slices have the topology of spheres, $N_{3,1}$ is always even, because it is for the minimal configuration and all flips alter the number by 0 or 2.

Bounds on simplex numbers In this section we numerically estimate and proof bounds on the number of simplices allowed in one slice of a $(2 + 1)$ causal dynamical triangulation. This can be used for estimating the number of bins of the 1-slice DOS to calculate with the Wang-Landau algorithm.

We first consider the number of maximal simplices of type $(3, 1)$ and $(2, 2)$. The lower bounds for this number is

$$N_{3,1} \geq 8 \quad N_{2,2} \geq 4$$

because the smallest spatial triangulation of S^2 has 4 maximal simplices, so $\underline{N}_2 + \overline{N}_2 = N_{3,1} \geq 8$. The lower bound for $N_{2,2}$ can be verified numerically.

For the difference of the boundary simplices there are the following possible values.

$$|\Delta N_2| \in \begin{cases} \{0, 4, 8, \dots, N_{3,1} - 8\} & \text{for } N_{3,1}/2 \text{ even} \\ \{2, 6, 10, \dots, N_{3,1} - 8\} & \text{for } N_{3,1}/2 \text{ odd} \end{cases}$$

This can be proven in the following way: We have that \underline{N}_2 and \overline{N}_2 are even (all possible Pachner flips alter these numbers either by 0 or by 2), so also $N_{3,1} = \underline{N}_2 + \overline{N}_2$ is even. For the difference of the boundary simplices we have

$$|\Delta N_2| = |\underline{N}_2 - \overline{N}_2| = |2\underline{N}_2 - N_{3,1}|,$$

and $|\Delta N_2|/2$ is even if and only if $N_{3,1}/2$ is even. The upper bound for $|\Delta N_2|$ is due to the lower bounds $\underline{N}_2, \overline{N}_2 \geq 4$ for the spatial slices.



Table 5.1: Table showing the numerically calculated upper bounds for $N_{2,2}$ in terms of $N_{3,1}$, \underline{N}_2 and \overline{N}_2

N_{3_1}	\underline{N}_2	\overline{N}_2	up. bound	N_{3_1}	\underline{N}_2	\overline{N}_2	up. bound
8	4	4	$N_{2,2} \leq 10$	26	4	22	$N_{2,2} \leq 37$
10	4	6	$N_{2,2} \leq 13$	26	6	20	$N_{2,2} \leq 45$
12	4	8	$N_{2,2} \leq 16$	26	8	18	$N_{2,2} \leq 51$
12	6	6	$N_{2,2} \leq 17$	26	10	16	$N_{2,2} \leq 55$
14	4	10	$N_{2,2} \leq 19$	26	12	14	$N_{2,2} \leq 57$
14	6	8	$N_{2,2} \leq 21$	28	4	24	$N_{2,2} \leq 40$
16	4	12	$N_{2,2} \leq 22$	28	6	22	$N_{2,2} \leq 49$
16	6	10	$N_{2,2} \leq 25$	28	8	20	$N_{2,2} \leq 56$
16	8	8	$N_{2,2} \leq 26$	28	10	18	$N_{2,2} \leq 61$
18	4	14	$N_{2,2} \leq 25$	28	12	16	$N_{2,2} \leq 64$
18	6	12	$N_{2,2} \leq 29$	28	14	14	$N_{2,2} \leq 65$
18	8	10	$N_{2,2} \leq 31$	30	4	26	$N_{2,2} \leq 43$
20	4	16	$N_{2,2} \leq 28$	30	6	24	$N_{2,2} \leq 53$
20	6	14	$N_{2,2} \leq 33$	30	8	22	$N_{2,2} \leq 61$
20	8	12	$N_{2,2} \leq 36$	30	10	20	$N_{2,2} \leq 67$
20	10	10	$N_{2,2} \leq 37$	30	12	18	$N_{2,2} \leq 71$
22	4	18	$N_{2,2} \leq 31$	30	14	16	$N_{2,2} \leq 73$
22	6	16	$N_{2,2} \leq 37$	32	4	28	$N_{2,2} \leq 46$
22	8	14	$N_{2,2} \leq 41$	32	6	26	$N_{2,2} \leq 57$
22	10	12	$N_{2,2} \leq 43$	32	8	24	$N_{2,2} \leq 66$
24	4	20	$N_{2,2} \leq 34$	32	10	22	$N_{2,2} \leq 73$
24	6	18	$N_{2,2} \leq 41$	32	12	20	$N_{2,2} \leq 78$
24	8	16	$N_{2,2} \leq 46$	32	14	18	$N_{2,2} \leq 81$
24	10	14	$N_{2,2} \leq 49$	32	16	16	$N_{2,2} \leq 82$
24	12	12	$N_{2,2} \leq 50$				



The next step is to derive an upper bound for $N_{2,2}$ in terms of $N_{3,1}$ and the number of boundary maximal simplices. In Tab. 5.1 such upper bounds for $N_{2,2}$ that can be found numerically are displayed.

Neglecting the influence of the upper and lower boundary simplices one can conjecture that the upper boundary $N_{2,2}^{\max}(N_{3,1})$ is given by the following recursion relation:

$$\begin{aligned} N_{2,2}^{\max}(8) &= 10 \\ N_{2,2}^{\max}(N_{3,1}) &= N_{2,2}^{\max}(N_{3,1} - 2) + 1 + \left\lfloor \frac{N_{3,1}}{4} \right\rfloor \end{aligned} \quad (5.86)$$

Since the number $N_{3,1}$ is always even, a recursion relation for $\tilde{N}_{2,2}^{\max}(N_{3,1}/2) := N_{2,2}^{\max}(N_{3,1})$ can be written in terms of $N_{3,1}/2$ as

$$\begin{aligned} \tilde{N}_{2,2}^{\max}(4) &= 10 \\ \tilde{N}_{2,2}^{\max}\left(\frac{N_{3,1}}{2}\right) &= \tilde{N}_{2,2}^{\max}\left(\frac{N_{3,1}}{2} - 1\right) + 1 + \left\lfloor \frac{N_{3,1}}{4} \right\rfloor \\ &= \begin{cases} \tilde{N}_{2,2}^{\max}\left(\frac{N_{3,1}}{2} - 1\right) + \frac{N_{3,1}}{4} + 1 & \frac{N_{3,1}}{2} \text{ even} \\ \tilde{N}_{2,2}^{\max}\left(\frac{N_{3,1}}{2} - 1\right) + \frac{N_{3,1}}{4} + \frac{1}{2} & \frac{N_{3,1}}{2} \text{ odd} \end{cases} \end{aligned}$$

The case by case analysis can be written in terms of two recursion relations, one for even $M = N_{3,1}/2$ and one for odd $M = N_{3,1}/2$.

$$\begin{aligned} \tilde{N}_{2,2}^{\max}(4) &= 10 & \tilde{N}_{2,2}^{\max}(2M) &= \tilde{N}_{2,2}^{\max}(2M - 2) + 2M + 1 \\ \tilde{N}_{2,2}^{\max\text{odd}}(5) &= 13 & \tilde{N}_{2,2}^{\max\text{odd}}(2M + 1) &= \tilde{N}_{2,2}^{\max\text{odd}}(2M - 1) + 2M + 2 \end{aligned}$$

Using the standard procedure for solving such recursive relations⁸ leads to the following proposition:

Proposition 5.1 (Rough upper bound for single slice $N_{2,2}$). *Consider a $(2+1)$ -dimensional causal triangulation of $\mathbb{S}^2 \times \mathcal{I}$ with $T = 2$ time slices, $N_{3,1}$ $(3, 1)$ -simplices and $N_{2,2}$ $(2, 2)$ -simplices. Then there is the following upper bound for $N_{2,2}$ in terms of $N_{3,1}$*

$$N_{2,2} \leq \begin{cases} \frac{1}{4}N_{3,1}^2 + N_{3,1} + 2 & \text{for } N_{3,1}/2 \text{ even} \\ \frac{1}{4}N_{3,1}^2 + \frac{3}{2}N_{3,1} + 3 & \text{for } N_{3,1}/2 \text{ odd} \end{cases} \quad (5.87)$$

⁸ Make the ansatz $N_{2,2}^{\max}(x) = ax^2 + bx + c$, calculate $N_{2,2}^{\max}(2M) - N_{2,2}^{\max}(2M - 2)$ for both the recursion relation and the ansatz and compare the coefficients to calculate a and b . Then use the single known value to calculate the constant offset c



We do not prove this proposition here (the only thing that needs to be proven is the recursion relation (5.86)), but derive and prove a more general one that includes this proposition as a special case.

This proposition can even be made better if one includes also the number \underline{N}_2 of maximal simplices of the lower boundary, or equivalently the difference ΔN_2 into account. Let $N_{2,2}^{\max}(N_{3,1}; \underline{N}_2)$ be the upper boundary for the number of $(2, 2)$ -simplices in terms of these two quantities. Looking at the entries of Table 5.1 with $\underline{N}_2 = 4$ one sees that there is the following functional dependency in terms of $N_{3,1}$:

$$N_{2,2}^{\max}(N_{3,1}; 4) = \frac{3}{2}N_{3,1} - 2$$

Looking at the entries with fixed $N_{3,1}$ one can conjecture the following relation:

$$\begin{aligned} N_{2,2}^{\max}(N_{3,1}; 4 + 2n) &= N_{2,2}^{\max}(N_{3,1}; 4 + 2(n - 1)) + (\delta - 2(n - 1)) \\ \delta &= \frac{1}{2}(N_{3,1} - 10) \end{aligned}$$

Solving these recursion relation for constant $N_{3,1}$ leads to the following proposition:

Proposition 5.2 (Fine upper bound for single slice $N_{2,2}$). *Consider a causal triangulation as in conjecture 5.1, and let \underline{N}_2 and \overline{N}_2 be the number of 2-simplices of the lower and the upper boundary sphere triangulation. Assume without loss of generality $\underline{N}_2 \leq \overline{N}_2$ and denote $\Delta N_2 := \overline{N}_2 - \underline{N}_2 \geq 0$. Then there is the following upper bound for $N_{2,2}$ in terms of $N_{3,1}$ and \underline{N}_2 or ΔN_2 :*

$$\begin{aligned} N_{2,2} &\leq -\frac{1}{4}\underline{N}_2^2 + \frac{1}{4}N_{3,1}(\underline{N}_2 + 2) + 2 \\ &= \frac{1}{16}\left(N_{3,1}^2 - (\Delta N_2)^2\right) + \frac{1}{2}N_{3,1} + 2 \end{aligned} \tag{5.88}$$

Note that if one uses $\Delta N_2 \geq 0$ for even $N_{3,1}/2$ and $\Delta N_2 \geq 2$ for odd $N_{3,1}/2$ in Equation (5.88), this is the same as the rough bound (5.87)

Proof. We show that this upper bound is given by the maximal number of $N_{1,1}$ -simplices in the triangulation. The maximal number is given by

$$N_{1,1} \leq \underline{N}_0 \overline{N}_0$$



because every vertex of the lower boundary can be connected at most with every vertex of the upper boundary. Using $N_0 = \chi + N_2/2 = 2 + N_2/2$ for the two spatial slices gives

$$N_{1,1} \leq 4 + \underline{N}_2 + \overline{N}_2 + \frac{1}{4}\underline{N}_2\overline{N}_2.$$

Now we need to write the number of diagonals $N_{1,1}$ in terms of $N_{3,1}$ and $N_{2,2}$. Therefor we use the ansatz

$$N_{1,1}(N_{3,1}; N_{2,2}) = aN_{3,1} + bN_{2,2} + c$$

and the change of the numbers $N_{1,1}$, $N_{3,1}$ and $N_{2,2}$ in the possible causal Pachner flips to determine a and b , as well as these numbers in the ground state to determine c . Using $\underline{N}_2 + \overline{N}_2 = N_{3,1}$ this results in

$$\begin{aligned} \frac{1}{2}N_{3,1} + N_{2,2} + 2 &\leq 4 + \underline{N}_2 + \overline{N}_2 + \frac{1}{4}\underline{N}_2\overline{N}_2 \\ N_{2,2} &\leq -\frac{1}{4}\underline{N}_2^2 + \frac{1}{4}N_{3,1}(\underline{N}_2 + 2) + 2. \end{aligned}$$

□

The remaining questions is whether these bounds are tight, i.e., whether there is a triangulation so that the equality is valid:

Conjecture 5.3 (Tightness of fine upper bound for single slice $N_{2,2}$). *The upper bound given in Proposition 5.2 is tight, i.e. there is a single slice triangulation with*

$$N_{2,2} = -\frac{1}{4}\underline{N}_2^2 + \frac{1}{4}N_{3,1}(\underline{N}_2 + 2) + 2$$

We did not find an analytical proof for this conjecture, but our numerical data shows that one can construct such triangulations for all considered values of the topological parameters.

Splitting of the configuration space In the previous section we saw that using $(N_{3,1}, N_{2,2}, \underline{N}_2)$ as energy leads to a huge grow of the number of energy levels. Since the convergence of the Wang-Landau algorithm is determined mainly by the number of energy bins (the time for becoming flat scales approximately as $b \log b$ if b is the number of bins, as shown in Sec. 2.3.2), the space of possible energies must be cut into small suitable pieces, so that the system is ergodic within the sub-ranges.



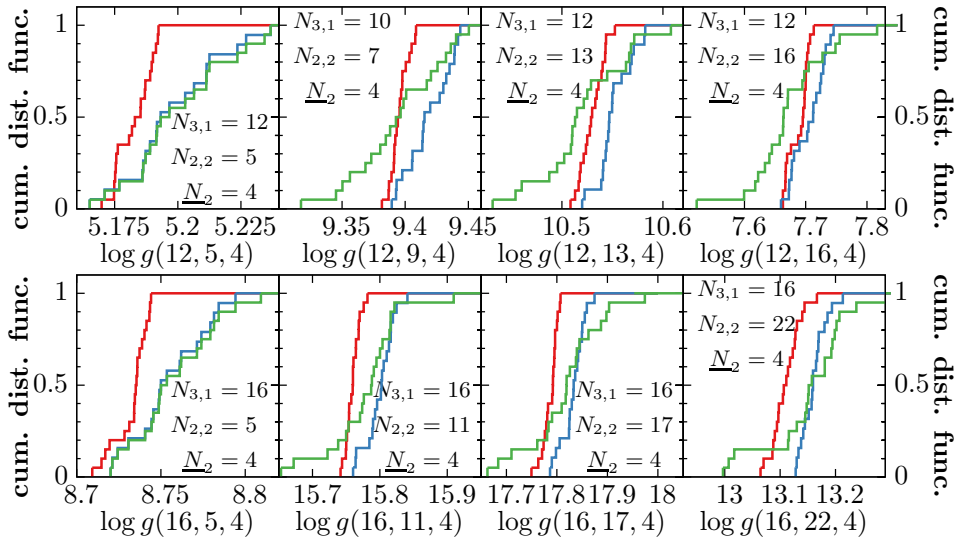


Figure 5.22: Comparison of the cumulative distribution function of the density of states $g(N_{3,1}, N_{2,2}, \underline{N}_2)$ calculated using the Wang-Landau algorithm with unrestricted DOS (red) with $N_{3,1} \leq 16$ (blue) and with DOS restricted to constant $N_{3,1}$ and constant \underline{N}_2 (green). The upper row shows a comparison for $N_{3,1} = 12$, the lower row for $N_{3,1} = 16$, both for $\underline{N}_2 = 4$ and different values of $N_{2,2}$.

Restricting the considered DOS to constant $N_{3,1}$ and constant \underline{N}_2 (and therewith constant \overline{N}_2) probably does not violate the ergodicity, because diagonal edge flips are ergodic for the two-dimensional boundary triangulations (for the sphere and for large enough triangulations with genus $g \neq 0$, compare Sec. 4.2). Furthermore, also the full-dimensional ($2 \rightarrow 3$) and ($3 \rightarrow 2$) flips do flip one $(3, 1)$ and one $(2, 2)$ -simplex into another $(3, 1)$ -simplex and two $(2, 2)$ -simplex, so they keep $N_{3,1}$ constant.

Since there is no analytical proof for this ergodicity conjecture, one has to perform suitable simulations that strengthen this conjecture. Therefore we compare calculations of the full DOS for $N_{3,1} \leq 16$ and all possible values of $N_{2,2}$ and \underline{N}_2 (and therewith \overline{N}_2) and compare with DOSs obtained for fixed $N_{3,1}$ and fixed \underline{N}_2 in this interval. In Fig. 5.22 the cumulative distribution function of the DOS obtained by several independent Wang-Landau simulations are displayed for the full DOS and the restricted DOS for $N_{3,1} = 12$ and $N_{3,1} = 16$. One sees a good qualitative agreement between the different methods of calculating the density of states, which is better for $N_{3,1} = 16$ than for $N_{3,1} = 12$. The calculations were performed using the exact ratio of selection probabilities.



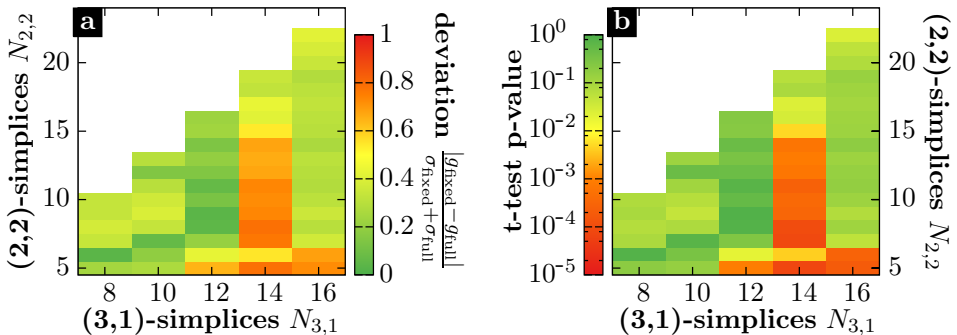


Figure 5.23: Deviation of the DOS calculated for fixed $N_{3,1}$ and $N_{2,2}$ from the actual DOS calculated over the full range of energy bins, in terms of the number $N_{3,1}$ and $N_{2,2}$ of maximal simplices. (a) Absolute difference $|g_{\text{full}} - g_{\text{restricted}}|$ of the DOS in units of $\sigma_{\text{full}} + \sigma_{\text{restricted}}$, which is the sum of the standard deviations of the respective DOS. (b) p -value of a t -test, where a high p -value corresponds to a good agreement. Usually one rejects the hypothesis that the two distributions are equal for $p > 0.01$.

For a quantitative comparison of the two calculation methods, we use two different methods. First, we measure the distance between the means of the two distributions in units of the standard deviation of the calculations for the full DOS. Second, we apply a t -test which tests whether two data sets of a normal distribution have the same mean [378], in this case we use the p -value of the test as a measure for the comparison. The results of the calculations are displayed in Fig. 5.23. One sees that the results fit quite well qualitatively, except for a small number $N_{2,2}$ of (2,2)-triangulations.

From the qualitative and the quantitative comparison we can conclude that it is in fact possible to calculate the DOS only for fixed $N_{3,1}$ and $N_{2,2}$. Note that this makes it necessary to perform a simulation for the whole range of $N_{3,1}$ and $N_{2,2}$ with restricted $N_{2,2}$ for normalizing the different density of states, because intrinsically they have no common energy bin that can be used for normalization. Using these DOS for normalization makes it possible to cure the deviations from the overall DOS for small $N_{2,2}$, because one can use the values of the normalization DOS for this range.

A further reduction of the number of bins can be applied by cutting the considered interval of $N_{2,2}$ for fixed $N_{3,1}$ and $N_{2,2}$. The ergodicity of these cuts has to be tested numerically by the same methods presented above, with similar results. Since a cut of $N_{2,2}$ was not applied for the results in the section, these numerical tests are not displayed here.



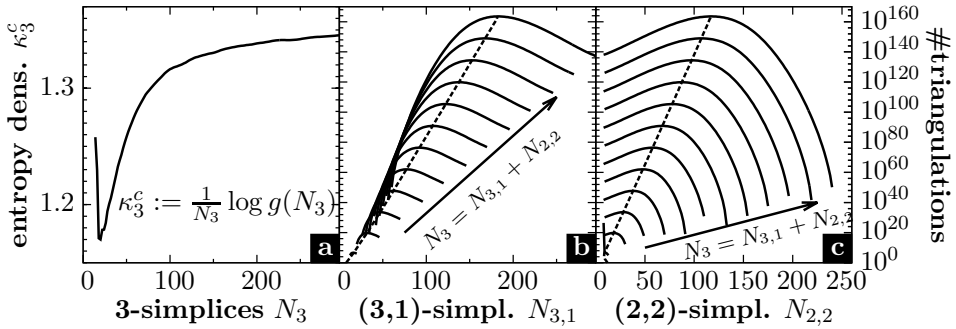


Figure 5.24: Number of $(2 + 1)$ -dimensional causal dynamical triangulations of one time slice in terms of the number of maximal simplices. (a) Entropy density (5.89) in terms of the number $N_3 = N_{3,1} + N_{2,2}$ of maximal simplices. (b) Number of triangulations in terms of $N_{3,1}$ for fixed $N_3 = 25, 50, \dots, 275, 300$. The dashed line shows the location of the maxima of the DOS. (c) Number of triangulations in terms of $N_{2,2}$ for fixed $N_3 = 25, 50, \dots, 275, 300$.

Number of causal dynamical triangulations

As for lattice and topological triangulations, the number of causal dynamical triangulation of a single slice is an important quantity for the convergence of the partition function and is accessible with our Wang-Landau simulations. We study the number of $(2 + 1)$ -dimensional one-slice triangulations in terms of the total number $N_3 = N_{3,1} + N_{2,2}$ of maximal simplices, and in terms of the number $N_{3,1}$ and $N_{2,2}$ with fixed N_3 , the results are displayed in Figs. 5.24 and 5.25.

For the entropy density

$$\kappa_3^c(N_3) := \frac{1}{N_3} \log g(N_3), \quad (5.89)$$

(which at the same time determines the phase transition necessary to obtain a valid thermodynamical limit in the causal dynamical triangulation model for $\kappa_0 = 0$) we obtain that $\kappa_3^c(N_3) \approx 1.35$ for large $N_3 = 300$ (the largest number of maximal simplices we considered), which is below the entropy density for three-dimensional topological triangulations calculated in Sec. 4.3. This is intuitively clear because in the setup of causal dynamical triangulations one restricts the set of possible triangulations by imposing causality conditions. Similar to topology triangulation with our code it would be possible to access much higher numbers N_3 of maximal simplices if altering the energy function. The presented results are obtained by summing over the full DOS $g(N_{3,1}, N_{2,2}, \underline{N}_2, \overline{N}_2)$, using only the number of maximal simplices as energy



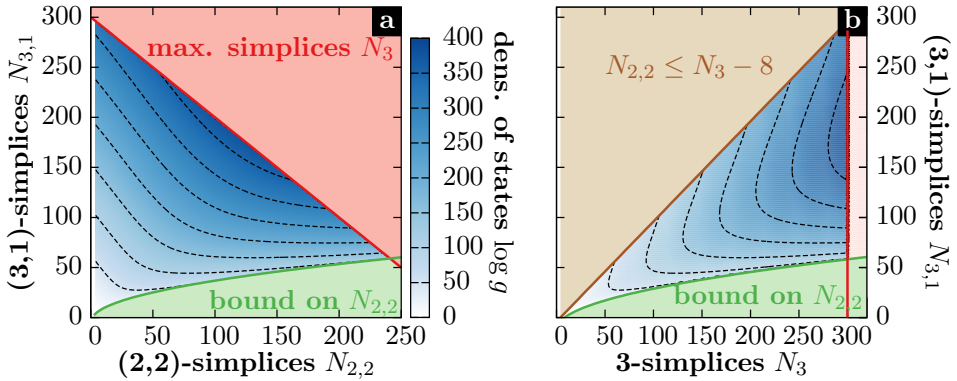


Figure 5.25: Number of $(2 + 1)$ -dimensional causal dynamical triangulations of one time slice in terms of the number of maximal simplices in terms of $N_{2,2}$ and $N_{3,1}$ (a) or N_3 (b). Contour lines are drawn for the values 50, 100, \dots , 350. The red region of the DOS is excluded because we calculated the DOS only up to $N_3 \leq 300$. The brown region is excluded because $N_{2,2} < N_3 - 8$, and the green region is excluded due the bound (5.87).

function directly in the calculations would lead to a large speed up and to a larger range of accessible N_3 , because the number of energy bins decreases.

The number of triangulations $g(N_{3,1})|_{N_3}$ in terms of $N_{3,1}$ for fixed N_3 (which is basically the integrated density of states) shows a steep rise for the first possible values of $N_{3,1}$. Due to the resulting small acceptance probabilities in the Wang-Landau simulations this drastically slows down simulations and explains why it is better to calculate for fixed $N_{3,1}$.

One can also examine the location of the maximum $g_{\max}(N_{3,1}, N_{2,2})$ of the DOS in more detail. Using a linear fit we find that

$$\log g_{\max}(N_3) \approx 1.3255(7) \cdot N_3 - 22.4(1),$$

where the prefactor is approximately the value $\kappa_3^{(c)}$ of the critical entropy density. Furthermore we have $N_{3,1}/N_3 \approx 0.6129(6)$ for the location of the maximum, which implies that typical triangulations have twice as much $(3, 1)$ -simplices as $(2, 2)$ -simplices, independent of the total number N_3 of maximal simplices. Both results imply that the functional dependency of the DOS does not change qualitatively for growing system size N_3 , which can then be used for giving initial estimates for the DOS of Wang-Landau simulations for higher system sizes.



Validity of the one-slice extrapolation

In this section we mainly test two assumptions that are done for actually calculating expectation values with the transfer matrix method. The first assumption is that one can in fact extrapolate the two-slice density of states (DOS) in terms of the one-slice DOS using Eq. (5.63), which then implies also the possibility for extrapolating a T -slice DOS using Eq. (5.64). The second assumption is that one can use a simplified version of the selection probability factor for large enough triangulations, similar to topological triangulations (compare Sec. 4.1.4 and Fig. 4.10).

For testing Eq. (5.63) we explicitly compute the two-slice DOS $g_2(N_{3,1}, N_{2,2}, \bar{N}_2, \bar{N}_2)$ for $N_{3,1} \leq 24$ using the Wang-Landau algorithm and compare the results with the two-slice DOS that was extrapolated from the one-slice DOS and the spatial DOS $h_\partial(N_2)$ (that equals the DOS of topological triangulations of the 2-sphere). The comparison was done for exact and simple ratios of the selection probability, and the results are displayed in Fig. 5.26.

One sees that in both cases the relative error is below 0.02, and that the error becomes smaller for larger $N_{3,1}$. The largest errors occur at the boundaries of the allowed range of $N_{2,2}$. Furthermore the error in the exact calculations is larger than in the simple calculations, which can be explained by noting that using the exact ratio of selection probabilities takes into account the isomorphy of the considered triangulation, but these are completely neglected in the approximation (5.63) (there a triangulation is simply represented by its topological quantities). One can conclude that the extrapolation of the T -slice DOS is in fact approximately correct and can be used for calculating expectation values.

For verifying that it is possible to use the simple ratio of selection probabilities for large triangulations, in Fig. 5.27 a comparison of the entropy $\log g(N_{3,1}, N_{2,2})$ in terms of $N_{2,2}$ for different values of $N_{3,1}$ calculated with both simple and exact ratio of selection probabilities can be found. For small system sizes the errors are quite large (more than 0.1), but for $N_{3,1} = 14$ and $N_{3,1} = 16$ the errors are lower than 0.05 in almost all cases. So one can conclude that using simple selection probability ratios is approximately valid for high enough system sizes.

Fine-tuning in $(2 + 1)$ -CDT

As for the approach of dynamical triangulations also in the causal version one has to fine-tune a coupling constant in order to get a thermodynamical



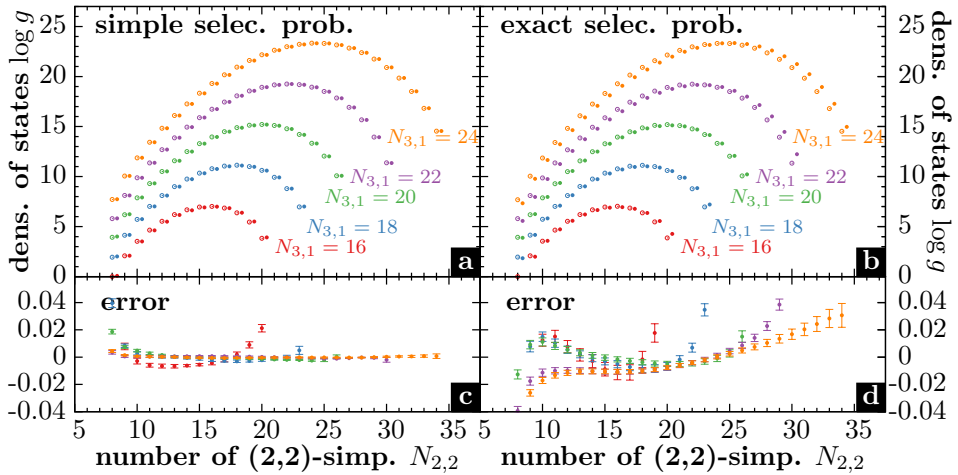
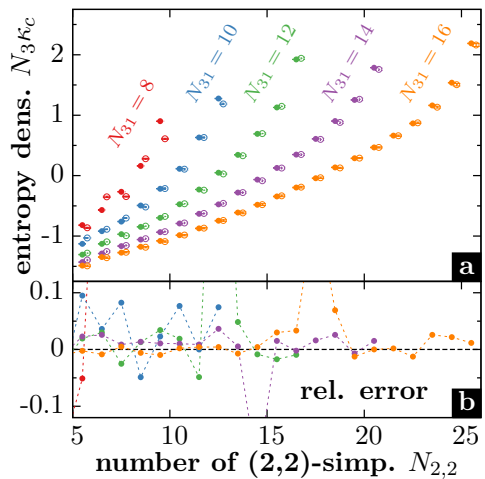


Figure 5.26: Extrapolation of the 1-slice DOS.

Comparison of the density of states (DOS) of causal dynamical triangulations (CDT) with two time slices directly calculated using Wang-Landau simulations (\circ , slightly shifted) and indirectly calculated by multiplying the DOS of two combined one-slice DOSs according to Eq. (5.63) (\bullet). Plots (a) and (b) shows the logarithmic DOS $\log g(N_{3,1}, N_{2,2})$ in terms of the number of (2,2)-simplices $N_{2,2}$ for different numbers of (3,1)-simplices $N_{3,1} = 16$, $N_{3,1} = 18$, $N_{3,1} = 20$, $N_{3,1} = 22$ and $N_{3,1} = 24$. The other degrees of freedom are traced out. Plots (c) and (d) show the relative error of the extrapolated two-slice DOS with respect to the directly calculated two-slice DOS. Plots (a) and (c) are done using the simple selection probability ratio, (b) and (d) with exact selection probability ratio. Note that the extrapolated density of states are not normalized with respect to the first bin, but with respect to the sum of all bins.

Figure 5.27: Comparison of the CDT slice DOS obtained with the simple and the exact selection probability ratio for different values of $N_{3,1}$ ($N_{3,1} = 8$, $N_{3,1} = 10$, $N_{3,1} = 12$, $N_{3,1} = 14$ and $N_{3,1} = 16$) in terms of $N_{2,2}$. (a) Comparison of the entropy $S(N_{3,1}, N_{2,2})$ obtained by using exact (\circ) and simple (\bullet) selection probability ratios. (b) Relative error of using simple selection probability.



limit independent of the discretization scale. It is convenient to replace the dynamical variables N_0 , $N_{3,1}$ and $N_{2,2}$ with the corresponding coupling constants κ_0 , $\kappa_{3,1}$ and $\kappa_{2,2}$ by rewriting

$$\begin{aligned} S &= \kappa_0 N_0 + \kappa_{3,1} N_{3,1} + \kappa_{2,2} N_{2,2} = \\ &= \kappa_0 N_0 + \kappa_{3,1} N_{3,1} + \kappa_{2,2} (N_3 - N_{2,2}) = \\ &= \kappa_0 N_0 + \kappa_{2,2} N_3 + (\kappa_{3,1} - \kappa_{2,2}) N_{3,1} = \\ &=: \kappa_0 N_0 + \kappa_3 N_3 + \Delta N_{3,1}, \end{aligned}$$

where we use the total number $N_3 = N_{3,1} + N_{2,2}$ of 3-simplices and the new coupling constants⁹ $\kappa_3 := \kappa_{2,2}$ and $\Delta = \kappa_{3,1} - \kappa_{2,2}$. The coupling constant κ_3 (which can be interpreted as the chemical potential of the triangulations with system size N_3) will be fine-tuned to its critical value $\kappa_3^{(c)}(\kappa_0, \Delta)$ (which corresponds to the entropy density), where the new coupling constant Δ weights the difference of the two types of 3-simplices. Remember that the thermodynamical limit is only defined for $\kappa_3 \geq \kappa_3^{(c)}$, for $\kappa_3 < \kappa_3^{(c)}$ the partition function does not converge.

The conjugated, extrinsic variable to the (intrinsic) fine-tuned coupling constant κ_3 is the number N_3 of maximal simplices. In Fig. 5.28 the probability distribution of N_3 is displayed for a fixed value of κ_0 and Δ in terms of κ_3 , with κ_3 located near the conjectured location of the phase transition. Although the considered system size is small, one can already see that for $\kappa_3 < \kappa_3^{(c)}$ the partition function is dominated by triangulations with $N_3 \approx N_3^{\max}$, whereas for $\kappa_3 > \kappa_3^{(c)}$ it is dominated by triangulations with $N_3 \approx N_3^{\min} = 12$. Triangulations with N_3 between these two extremal values do almost not contribute at all to the partition function. Furthermore, the transition between $\langle N_3 \rangle \approx 12$ to $\langle N_3 \rangle \approx N_3^{\max}$ is located sharply in a small interval around $\kappa_3^{(c)}$.

There are several possibilities to locate the fine-tuned coupling constant $\kappa_3^{(c)}$, which will be described in detail in the following paragraphs. Furthermore we consider the finite-size-scaling of the fine-tuned coupling constant, and the structure of the phase transition that is used for fine-tuning. All methods of calculating $\kappa_3^{(c)}(N_3^{\max})$ have the problem that for large enough $N_3^{\max} \approx 200$ for $T \rightarrow \infty$ the transition happens in an interval in κ_3 that is smaller than the usual machine precision of around 10^{-15} . We avoid this problem by not using the limit $T \rightarrow \infty$, but a finite, large T , and will show that the considered expectation values do not depend anymore on T . Using

⁹ Note that in the usual CDT literature slightly different notations are used for the coupling constants, but the results can be matched by using a linear transformation.



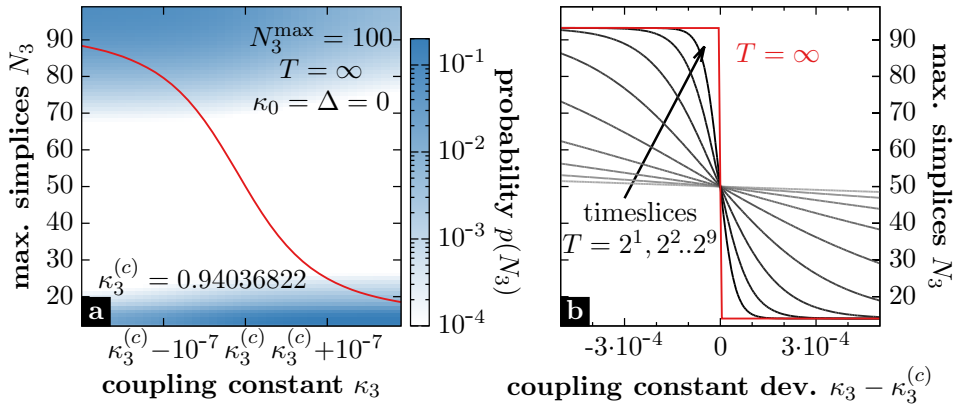


Figure 5.28: Fine-tuning transition in terms of κ_3 and $\langle N_3 \rangle$.

Influence of the coupling constant κ_3 on the number of maximal simplices N_3 in the triangulation. (a) The (logarithmic) colorscale shows the probability distribution of N_3 of the coupling constant κ_3 around the quasi-critical value $\kappa_3^{(c)}$ for $N_3^{\max} = 100$ and the two other coupling constants κ_0 and Δ chosen to be 0. The red, solid line is the average number $\langle N_3 \rangle$ in terms of κ_3 . The data was calculated using the transfer matrix method for periodic boundary conditions in the limit $T \rightarrow \infty$ of infinite time slices. (b) Average number $\langle N_3 \rangle$ of maximal simplices in terms of $\kappa_3 - \kappa_3^{(c)}(T)$ for different number $T = 2, 4, \dots, 512$ of time slices (black, solid lines) and for $T \rightarrow \infty$ (red, solid line). Note that the scale of the x-axis is much larger than in sub-figure (a), in fact the two red curves are the same.



a finite T significantly broadens the interval where the fine-tune transition takes place, as can be seen in Fig. 5.28b.

Fine-tuning κ_3 using the variance $\text{Var}(N_3)$ From the probability distribution of N_3 displayed in Fig. 5.28 one can formulate the conjecture that the phase transition used for fine-tuning κ_3 is a discontinuous or first-order phase transition. In the limit of infinite system sizes, the expectation value $\langle N_3 \rangle$ is then given by a step function, and its derivative (which is connected with the variance) has a pole at the critical point. For finite systems the step function is not exact, and its derivative does not possess a pole, but a maximum. The location of this maximum is a good estimation for the critical coupling constant $\kappa_3^{(c)}$.

In principle one can use Eq. (5.73) for calculating the variance directly from $\langle N_3^2 \rangle$, but this leads to numerical instabilities (which can be possibly cured by defining an observable matrix directly of the variance, and not of the second power of an observable). So we used the fact that in the limit of $T \rightarrow \infty$ of infinitely many time slices, the variance

$$\text{Var}(N_3)(\kappa_0, \kappa_3, \Delta) := \frac{\partial^2}{\partial \kappa_3^2} \log Z(\kappa_0, \kappa_3, \Delta) = T \frac{\partial^2}{\partial \kappa_3^2} \log \lambda_1(\kappa_0, \kappa_3, \Delta)$$

of the number of 3-simplices can be calculated by a derivative of the logarithm of the partition function, which is given by the largest eigenvalue λ_1 of the transfer matrix. The derivative has to be calculated numerically by using the method of finite differences, it is given by

$$\frac{\partial^2}{\partial \kappa^2} \log \lambda(\kappa) \approx \frac{1}{\delta \kappa^2} [\log \lambda(\kappa - \delta \kappa) - 2 \cdot \log \lambda(\kappa) + \log \lambda(\kappa + \delta \kappa)], \quad (5.90)$$

where $\delta \kappa$ is the (small) difference that is used for the coupling constants. For $\delta \kappa \rightarrow 0$ the method becomes exact. In practice we use the following algorithm to locate the maximum of the respective variance:

- Calculate $\text{Var}(N)$ at n points of support κ_i , with $0 \leq i \leq n - 1$ and $\kappa_{i+1} - \kappa_i = \text{const.}$, using the finite difference $\delta \kappa = 0.1 \cdot (\kappa_{i+1} - \kappa_i)$.
- Find the point of support κ_j where $\text{Var}(N)$ is maximal.
- Start again with n points of support between κ_{j-1} and κ_{j+1} .

Additionally, reducing $\delta \kappa$ gradually is necessary because the maximum in $\text{Var}(N)$ can be extremely sharp, so using a small $\delta \kappa$ in the beginning



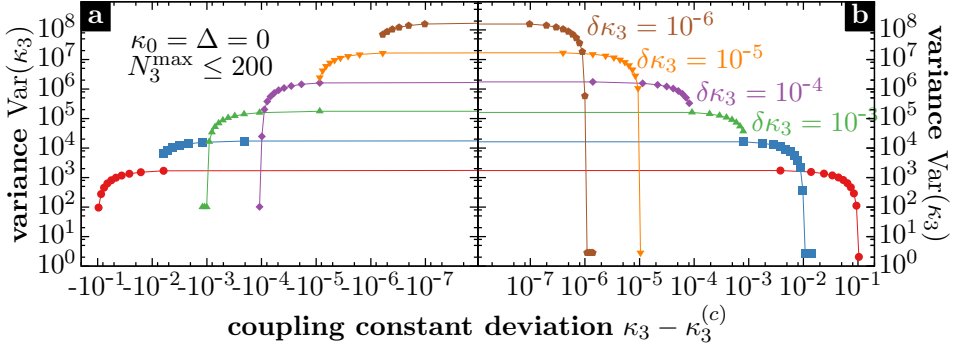


Figure 5.29: Fine-tuning using $\text{Var}(N_3)$.

Algorithm used for fine-tuning the coupling constant $\kappa_3^{(c)}$ for $\kappa_0 = \Delta = 0$. The variance $\text{Var}(N_3)$ is displayed in terms of the deviation $\kappa_3 - \kappa_3^{(c)}$ for $\kappa_3 < \kappa_3^{(c)}$ (a) and $\kappa_3 > \kappa_3^{(c)}$ (b) for different value $\delta\kappa_3$ of the finite difference used in Eq. (5.90): $\delta\kappa_3 = 10^{-1}$ (\bullet), $\delta\kappa_3 = 10^{-2}$ (\blacksquare), $\delta\kappa_3 = 10^{-3}$ (\blacktriangle), $\delta\kappa_3 = 10^{-4}$ (\blacklozenge), $\delta\kappa_3 = 10^{-5}$ (\blacktriangledown), $\delta\kappa_3 = 10^{-6}$ (\bullet). The difference $\kappa_{3,i+1} - \kappa_{3,i}$ equals the respective finite difference $\delta\kappa_3$ used for calculating the variance. Note that $\delta\kappa_3$ is chosen 10 times higher than in production runs for the single coupling constants to be able to display its influence better.

can lead to a miss of the maximum in the scan. Eventually it can be possible to reduce the considered intervals by inspecting $\text{Var}(N)(\kappa_{j-1})$ and $\text{Var}(N)(\kappa_{j+1})$ around the maximal value and to conjecture that the actual maximum lies between κ_j and κ_{j+1} if $\text{Var}(N)(\kappa_{j+1}) > \text{Var}(N)(\kappa_{j-1})$, but this can be influenced by small errors in the transfer matrix especially in the cases where the two variances are approximately equal, so we did not apply this optimization.

The algorithm for calculating the fine-tuned value of κ_3 is displayed in Fig. 5.29. Here one can see that for fixed $\delta\kappa_3$ the variance $\text{Var}(\kappa_3)$ saturates for $\kappa_c \rightarrow \kappa_3^{(c)}$, which makes it difficult to extract the maximal value without further reducing $\delta\kappa_3$. Contrary, choosing $\delta\kappa_3$ to small from the beginning could lead to a miss of the maximum of the variance due to small resolution.

In Fig. 5.30 the value of the fine tuned coupling constant $\kappa_3^{(c)}(\kappa_0, N_3^{\max})$ in terms of the other two coupling constants κ_0 and Δ is displayed. It is remarkable that for large κ_0 and Δ there is an area where $\kappa_3^{(c)}$ is negative, which means that energy dominates over entropy in this region and the probability for large systems has to be increased by the fine tuning. Furthermore the contour lines of constant $\kappa_3^{(c)}$ are approximately parallel lines in κ_0 and Δ with slope $-1/4$.



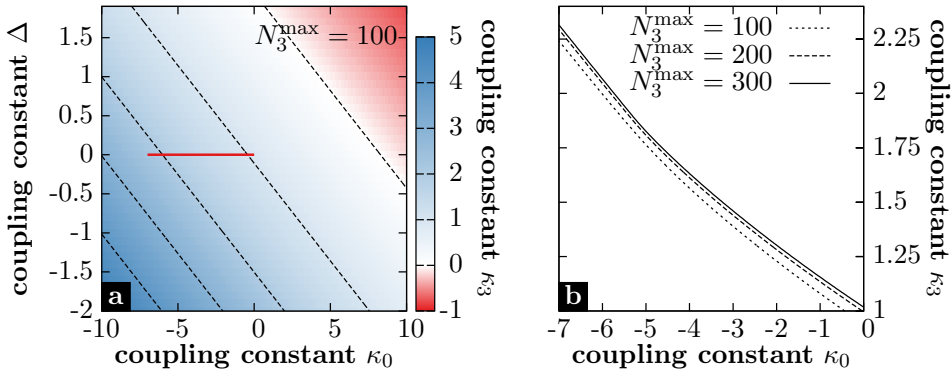
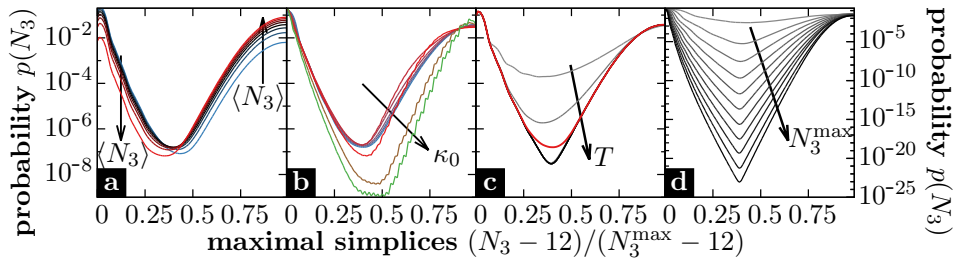


Figure 5.30: Fine-tuned coupling constant $\kappa_3^{(c)}$ in terms of κ_0 and Δ . (a) Colorplot as function of both independent coupling constants, the contour lines are at the integers 0 to 4. The red line is the parameter range shown on the right side. (b) Dependency of $\kappa_3^{(c)}$ on the coupling constant for $\Delta = 0$ for $N_3^{\max} = 100$ (dotted), $N_3^{\max} = 200$ (dashed) and $N_3^{\max} = 300$ (solid). The red line in (a) corresponds to the parameters shown in plot (b).

Fine-tuning κ_3 using the expectation value $\langle N_3 \rangle$ As seen in the previous section, locating the phase transition using variances can lead to problems due to the numerical derivative. A much simpler procedure is to tune the value of κ_3 such that one gets a given expectation value $\langle N_3 \rangle$ for the number of maximal simplices. This procedure is much easier than finding the maximum of a derivative, because calculating the expectation value does not involve calculating a variance or a numerical derivative, which can lead to numerical instabilities. Furthermore, due to statistical errors in the density of states the variance can have multiple maxima, so algorithms for finding a maximum can run into one of the local minima. In contrast, the expectation value $\langle N_3 \rangle$ is decreasing monotonically with increasing κ_3 , so there is a unique solution for $\kappa_3^{(c)}$.

Fine-tuning using the expectation value $\langle N_3 \rangle$ introduces the ambiguity which value in the range $[N_3^{\min}, N_3^{\max}]$ is chosen for $\langle N_3 \rangle$, and it is not a priori clear which value corresponds to the maximum in the variance. We conjecture that $\langle N_3 \rangle = N_3^{\max}/2$ is a good choice, because this is approximately the mid between the two phases in the phase diagram, so it should be the point where the variance is maximal, and use it in the calculations within this section. Furthermore, in Fig. 5.31 it will be shown that the probability distribution of $p(N_3)$ is not altered qualitatively, if one alters $\langle N_3 \rangle$, only the height of the peaks change. So the concrete choice of $\langle N_3 \rangle$





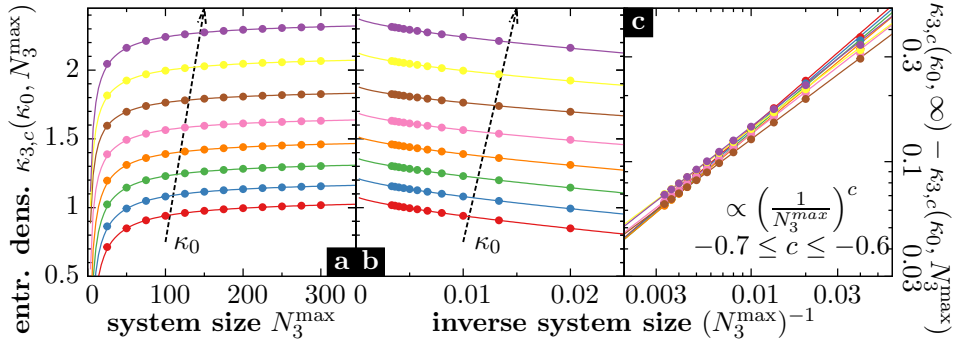


Figure 5.32: Finite size scaling of the fine-tuned $\kappa_3^{(c)}$.

The fine-tuned coupling constant (entropy density) $\kappa_3^{(c)}$ is displayed in terms of the system size N_3^{\max} (a) and in terms of the inverse system size (b) for different values of the coupling constant κ_0 ($\kappa_0 = 0.0$, $\kappa_0 = 1.0$, $\kappa_0 = 2.0$, $\kappa_0 = 3.0$, $\kappa_0 = 4.0$, $\kappa_0 = 5.0$, $\kappa_0 = 6.0$ and $\kappa_0 = 7.0$). The solid lines are fits to the power law (5.91). (c) Double-logarithmic plot of the deviation $\kappa_3^{(c)}(\kappa_0, \infty) - \kappa_3^{(c)}(\kappa_0, N_3^{\max})$ in terms of the inverse system size. In all plots $\Delta = 0$ is used.

the minimum is slightly shifted. One can also see that using a finite number T of time slices also has no influence on the result for $T \geq 8$, but that the height of the minimum is lower than in the calculation for $T \rightarrow \infty$ (compare Fig. 5.28c). This is probably due to the limited numerical precision that has to be taken into account for finite T , because one has to calculate powers λ^T of eigenvalues.

An important result is displayed in Fig. 5.28d, where the dependency of the probability distribution $p(N_3)$ is plotted for increasing system size N_3^{\max} . The location of the two maxima and the minimum does almost not depend on the system size, if one uses the normalization $(N_3 - N_3^{\max}) / (N_3^{\min} - N_3^{\max})$ for the number of 3-simplices. But the height of the minimum decreases with system size, which is a clear indication that the transition used for fine-tuning is first-order phase transition with two distinct phases.

In Fig. 5.32 the finite size scaling of the fine tuned coupling constant $\kappa_3^{(c)}(\kappa_0, N_3^{\max})$ in terms of the system size N_3^{\max} is displayed. Using a fit with respect to the power law

$$\kappa_3^{(c)}(\kappa_0, N_3^{\max}) = \kappa_3^{(c)}(\kappa_0, \infty) - a \cdot (N_3^{\max})^c \quad (5.91)$$

the value of the entropy density at infinite system size can be extrapolated. The fits show that $0.6 \leq c \leq 0.7$ and $2.5 \leq a \leq 3.9$ depend only weakly on the value of the coupling constant κ_0 . The dependence on the other



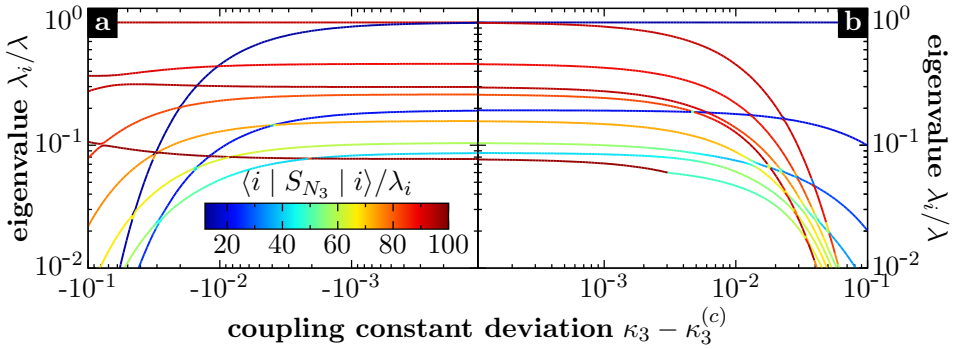


Figure 5.33: Relative eigenvalues λ_i/λ ($\lambda_1 \geq \lambda_2 \dots$) of the transfer matrix near the fine-tune transition in terms of $\kappa_3 - \kappa_3^{(c)}$ for $N_3^{\max} = 100$ and $\kappa_0 = \Delta = 0$. The eigenvalue $\lambda = \lambda_1$ used for scaling is the maximal eigenvalue of the transfer matrix. The colorcode corresponds to $\langle i | S_{N_3} | i \rangle / \lambda_i$, which is the expectation value $\langle N_3 \rangle$ considering only the contribution of the respective eigenvalue.

coupling constant Δ was not examined, we chose $\Delta = 0$ (no asymmetry) for our calculations.

Fine-tuning κ_3 using the eigenvalues of the transfer matrix The third and last possibility to find the fine-tuned value $\kappa_3^{(c)}$ of the coupling constant κ_3 is by inspecting the eigenvalues λ_i of the transfer matrix $V(\kappa)$. Directly at the phase transition the two largest eigenvalues $\lambda_1(\kappa)$ and $\lambda_2(\kappa)$ become equal. Intuitively this can be understood in the following way: The fine-tuning is done using the described first-order transition, where (for fixed N_3^{\max}) there are two coexisting phases, one with N_3 being near the minimal number of 3-simplices, and one with N_3 being near N_3^{\max} . Near the critical point $\kappa_3^{(c)}$ there are then two eigenvalues that dominate over the other eigenvalues (remember that $Z = \sum_i \lambda_i^T$, and we usually consider T being large or even $T \rightarrow \infty$), one with an eigenvector that is located mainly in the first phase, one located mainly in the second phase. In order to get a true phase-transition in the limit $T \rightarrow \infty$, the two eigenvalues must be exactly equal, otherwise one of the phases would be suppressed.

In Fig. 5.33 the 10 largest eigenvalues are plotted for $\kappa_0 = \Delta = 0$ and $N_3^{\max} = 100$ near the critical point $\kappa_3^{(c)}$. Furthermore in this Figure the reduced expectation value

$$\langle N_3 \rangle_{|\lambda_i} := \frac{1}{\lambda_i} \langle i | S_{N_3} | i \rangle, \quad (5.92)$$



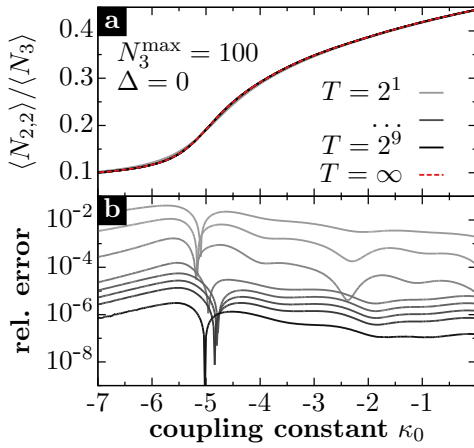


Figure 5.34: Convergence of the slice observables in $(2 + 1)$ -dimensional CDT for increasing number T of time slices (for $N_3^{\max} = 100$, $\langle N_3 \rangle = 50$ and $\Delta = 0$). (a) Relative number $\langle N_{2,2} \rangle / \langle N_3 \rangle$ of $(2, 2)$ -simplices in terms of the coupling constant κ_0 for different values $T = 2^1, \dots, 2^9$ of the number of time slices. The red, dashed line is the result for $T \rightarrow \infty$ time slices. (b) Relative error $\langle N_{2,2} \rangle(T) / \langle N_{2,2} \rangle(\infty) - 1$ of the number of $(2, 2)$ simplices with respect to the results for $T \rightarrow \infty$ time slices.

which is the observable matrix S_{N_3} projected onto one eigenspace of the transfer matrix. This corresponds to the expectation value (5.70) if one assumes that λ_i is the maximal eigenvalue of the transfer matrix. In Fig. 5.33 one sees that the phase transition occurs exactly where the two eigenvalues corresponding to the two phases are equal.

Expectation values and phase transition of $(2 + 1)$ -CDT

In this section we calculate expectation values in $(2+1)$ -dimensional causal dynamical triangulations using the fine-tuned coupling constant $\kappa_3(\kappa_0, \Delta)$ from the previous section. We will see that there are two-phases separated by a second-order phase transition which we will examine in more detail. In all calculations we fine-tune $\langle N_3 \rangle$ to $N_3^{\max}/2$, due to difficulties in the fine-tuning within large systems for $T = \infty$, we use $T = 64$ within all following calculations.

Order parameter and critical point In Fig. 5.34 the dependence of the relative number $\langle N_{2,2} \rangle / \langle N_3 \rangle$ of $(2, 2)$ -simplices on the number of time slices T is displayed in terms of the coupling constant κ_0 . One finds that even if using only four time slices, the error compared to using $T \rightarrow \infty$ time slices is below 1 percent. So the choice $T = 64$ yields negligible errors, especially if one takes into account that there are also statistical errors from the calculation of the density of states.



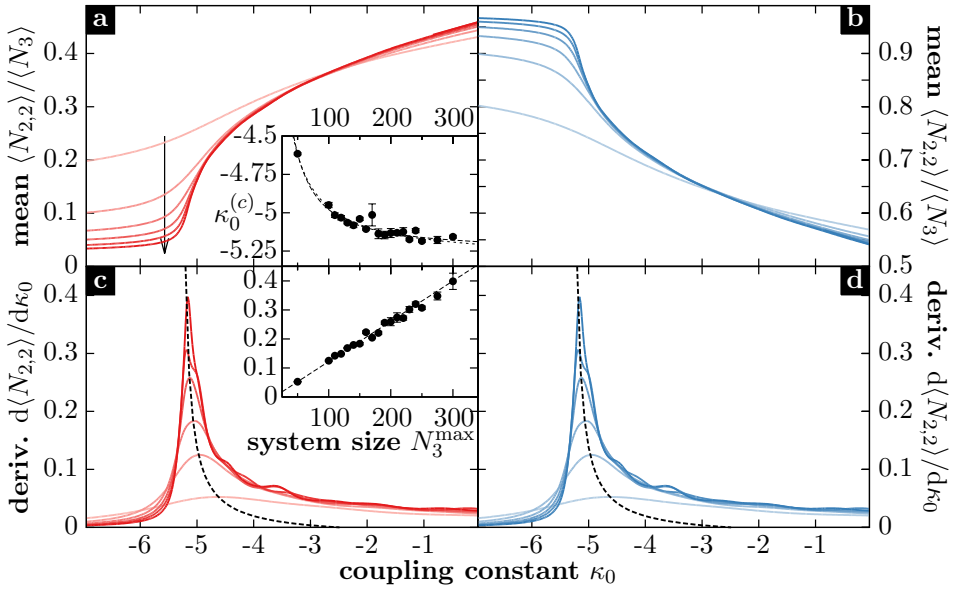


Figure 5.35: Order parameter and critical point in $(2 + 1)$ -dimensional CDT.

Slice expectation values for $(2 + 1)$ -dimensional causal dynamical triangulations in terms of the coupling constant κ_0 for $\Delta = 0.0$ and $T = 64$ for different values of N_3^{\max} . $\langle N_3 \rangle$ is fine-tuned to $N_3^{\max}/2$. (a) Expected ratio $\langle N_{2,2} \rangle / \langle N_3 \rangle$ of $(2, 2)$ -simplices. (b) Expected ratio $\langle N_{3,1} \rangle / \langle N_3 \rangle$ of $(3, 1)$ -simplices, which is of course equal to $1 - \langle N_{2,2} \rangle / \langle N_3 \rangle$. (c, d) Total derivative $|d(\langle N_{2,2/3,1} \rangle / \langle N_3 \rangle) / d\kappa_0|$ of the simplex number ratios, which coincide for both types of simplices. The dashed lines are a combination of Eqs. (5.93b) and (5.94) for the quasi-critical coupling constant. (a, inset) Dependence of the location of the quasi-critical coupling constant $\kappa_0^{(c)}(N_3^{\max})$ on the system size N_3^{\max} . The dashed line is the power law fit Eq. (5.93b), the dotted line is the power law fit Eq. (5.93a). The location of the quasi-critical temperature was located using the maximum of the displayed total derivatives. (b, inset) Dependence on the value of the total derivative at the quasi-critical temperature in terms of the system size. The dashed line is the linear fit Eq. (5.94).



In Fig. 5.35 the expectation values of the relative number of (2, 2)- and (3, 1)-simplices are displayed for different system sizes N_3^{\max} in terms of the coupling constant κ_0 for $\Delta = 0$. Remember that $N_3 = N_{3,1} + N_{2,2}$ for every triangulation, so that

$$\frac{\langle N_{3,1} \rangle}{\langle N_3 \rangle} = 1 - \frac{\langle N_{2,2} \rangle}{\langle N_3 \rangle}$$

Also the expectation values of the other slice and spatial slice quantities can be calculated in terms of $\langle N_{3,1} \rangle$, e.g., the number of maximal spatial simplices is given by $\langle N_2 \rangle = \langle N_{3,1} \rangle / 2$, and the number of vertices can be calculated from it.

One observes that there are two different phases in terms of κ_0 . For $\kappa_0 \lesssim -5.0$ the ratio of (2, 2)-simplices vanishes, whereas for $\kappa_0 \gtrsim -5.0$ the ratio is finite, which implies that this ratio can be used as an order parameter (as also suggested in [34]). The remaining task is to examine whether this phase transition is a continuous or a discontinuous phase transition. Since the fine-tuning phase transition is clearly a first-order phase transition, as discussed in the previous section, which does not lead to a scale-invariant continuum limit, only in the case of a discontinuous phase transition one can define a sensible continuum limit of the theory.

In order to do finite size scaling and to extract critical exponents, one first needs to extract the quasi-critical coupling constants $\kappa_0^{(c)}(N_3^{\max})$ for each system size. In principle there are several possibilities for doing so (e.g. using the Binder cumulant), we locate the maximum of the total derivative of the order parameter $\langle N_{2,2} \rangle / \langle N_3 \rangle$ (which are displayed in Figs. 5.35c and Figs. 5.35d). The results are displayed in Fig. 5.35a (inset). We use a power law fit to determine the critical coupling constant $\kappa_0^{(c)} = \lim_{N_3^{\max} \rightarrow \infty} \kappa_0^{(c)}(N_3^{\max})$ and the exponent of the scaling. Including the exponent as a fit parameter yields

$$\kappa_0^{(c)}(N_3^{\max}) = -5.25 \pm 0.03 + (80 \pm 45) \cdot (N_3^{\max})^{-1.24 \pm 0.16}, \quad (5.93a)$$

whereas fixing the exponent to -1 and using only two fit parameters yields

$$\kappa_0^{(c)}(N_3^{\max}) = -5.306 \pm 0.010 + \frac{34 \pm 1}{N_3^{\max}}. \quad (5.93b)$$

For the maximal value of the total derivative $d(\langle N_{2,2} \rangle / \langle N_2 \rangle) / d\kappa_0$ one finds the linear dependency

$$\frac{d\langle N_{2,2} \rangle}{\langle N_3 \rangle d\kappa_0} \left(\kappa_0^{(c)}(N_3^{\max}) \right) = (1.39 \pm 0.02) \cdot 10^{-3} \cdot N_3^{\max} - 0.017 \pm 0.001 \quad (5.94)$$



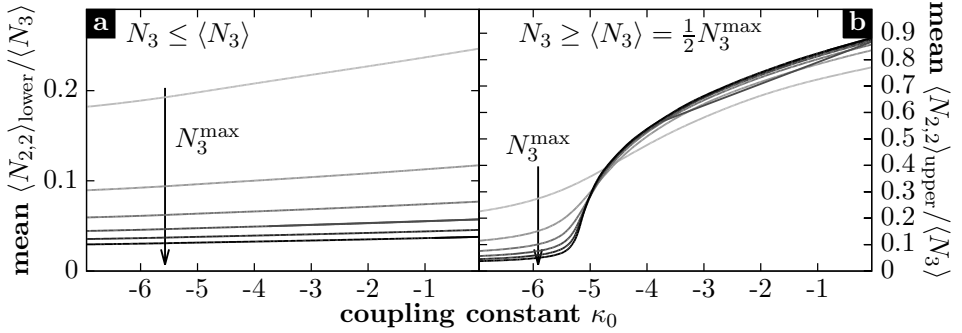


Figure 5.36: Order parameter in the coexisting phases.

Order parameter within the two coexisting phases of the fine-tune transition in terms of the coupling constant κ_0 for $\Delta = 0.0$ and $T = 64$ for different values of N_3^{max} . $\langle N_3 \rangle$ is fine-tuned to $N_3^{\text{max}}/2$. (a) Expected ratio $(\langle N_{2,2} \rangle / \langle N_3 \rangle)_{\text{lower}}$ of $(2, 2)$ -simplices for the phase with $N_3 \leq \langle N_3 \rangle$. (b) Expected ratio $(\langle N_{2,2} \rangle / \langle N_3 \rangle)_{\text{upper}}$ of $(2, 2)$ -simplices for the phase with $N_3 \leq \langle N_3 \rangle$.

In the previous section we saw that the phase-transition used to fine-tune the coupling constant κ_3 is a discontinuous phase transition, so using the fine-tuned value of κ_3 we are in a coexistence of two phases. We can now consider the two different phases separately by considering only triangulations with $N_3 \leq \langle N_3 \rangle$ and with $N_3 \geq \langle N_3 \rangle$, which was done in Fig. 5.36 for the order parameter $\langle N_{2,2} \rangle_{\text{lower,upper}} / \langle N_3 \rangle_{\text{lower,upper}}$. Note that we have $\langle N_3 \rangle_{\text{lower}} < \langle N_3 \rangle$ and $\langle N_3 \rangle_{\text{upper}} > \langle N_3 \rangle$, and both expectation values have to be calculated. One can clearly see that the phase transition does only occur in the large- N_3 phase, whereas in the small- N_3 phase the order parameters converges to zero for the whole considered range of κ_0 , so there is no continuous phase transition in this phase.

For the large- N_3 phase plotting with respect to $(\kappa_0 - \kappa_0^{(c)})$ (where $\kappa_0^{(c)}$ is the extrapolated temperature at infinite volume taken from Eq. (5.93b) or Eq. (5.93a)) yields that there is a power law behavior

$$\frac{\langle N_{2,2} \rangle}{\langle N_3 \rangle} = (0.056 \pm 0.008) \cdot (\kappa_0 - \kappa_0^{(c)})^{0.428 \pm 0.002} \quad \kappa_0 > \kappa_0^{(c)} \quad (5.95)$$

of the order parameter on one side of the critical coupling constant, which is depicted in Fig. 5.37. For $\kappa_0 < \kappa_0^{(c)}$ the order parameter vanishes.

Correlation time The phase transition can also be examined in terms of the correlation time. Remember that the covariance $\text{Cov}_N(t)$ of an



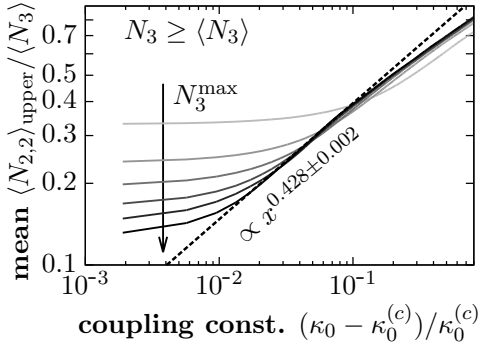


Figure 5.37: Scaling of the order parameter in (2 + 1)-dimensional causal dynamical triangulations. The order parameter $\langle N_{2,2} \rangle / \langle N_3 \rangle$ is plotted in terms of $(\kappa_0 - \kappa_0^{(c)}) / \kappa_0^{(c)}$, where $\kappa_0^{(c)}$ is the limit for N_3^{max} from (5.93a), for different values of N_3^{max} . For the plot only configurations with $N_3 \geq \langle N_3 \rangle$ are taken into account. The black, dashed line corresponds to the power law fit (5.95).

observables usually scales exponentially

$$\text{Cov}_N(t) := \langle N(0)N(t) \rangle - \langle N \rangle^2 \propto \exp\left(-\frac{t}{\tau}\right),$$

where the timescale τ is denoted as correlation time. The correlation time can only be calculated using Eq. (5.78) if the largest eigenvalue is not degenerated, but in the phase transition used for fine-tuning the two smallest eigenvalues are equal. If one denotes the value of the two largest eigenvalues as $\lambda = \lambda_1 = \lambda_2$, the covariance has to be calculated using

$$\begin{aligned} \text{Cov}_N(t) &= \frac{1}{2\lambda^2} \sum_{a,b} |\langle a|S|b \rangle|^2 \left(\frac{\lambda_a}{\lambda}\right)^{T-t-1} \left(\frac{\lambda_b}{\lambda}\right)^{t-1} \\ &\quad - \frac{1}{4\lambda^2} \left(\sum_a \langle a|S|a \rangle \left(\frac{\lambda_a}{\lambda}\right)^{T-1} \right)^2. \end{aligned}$$

Note that the 2 in the denominator of the first term and the 4 in the denominator are the value of the partition function if divided by λ^T in the limit $T \rightarrow \infty$. In this limit also all relative eigenvalues with exponent $T - t - 1$, except those with $a = 1, 2$ vanish, so the covariance is

$$\begin{aligned} \text{Cov}_N(t) &= \frac{1}{2\lambda^2} \sum_b \left(|\langle 1|S|b \rangle|^2 + |\langle 2|S|b \rangle|^2 \right) \left(\frac{\lambda_b}{\lambda}\right)^{t-1} \\ &\quad - \frac{1}{4\lambda^2} \left(\langle 1|S|1 \rangle^2 + \langle 2|S|2 \rangle^2 + 2 \langle 1|S|1 \rangle \langle 2|S|2 \rangle \right). \end{aligned}$$



For large times t also the other relative eigenvalues can be neglected if not $b = 1, 2$, so the covariance can be simplified further to be

$$\begin{aligned} \text{Cov}_N(t) &= \frac{1}{2\lambda^2} \sum_b \left(|\langle 1|S|1\rangle|^2 + |\langle 2|S|2\rangle|^2 + 2|\langle 1|S|2\rangle|^2 \right) \\ &\quad - \frac{1}{4\lambda^2} \left(\langle 1|S|1\rangle^2 + \langle 2|S|2\rangle^2 + 2\langle 1|S|1\rangle\langle 2|S|2\rangle \right) \end{aligned}$$

in the leading order, independent of t . (Note that for the previous calculation that lead to Eq. (5.76) the terms independent of t canceled, so that the leading order depends on t). Since the two eigenvalues and the corresponding eigenvectors correspond to the two different phases, one can use

$$\langle 1|S|1\rangle/\lambda = \langle N\rangle_{\text{lower}} \quad \text{and} \quad \langle 2|S|2\rangle/\lambda = \langle N\rangle_{\text{upper}}$$

or vice versa, where $\langle N\rangle_{\text{lower}}$ is the expectation value of N if restricting to the phase $N_3 \leq \langle N_3\rangle$. Furthermore the overlap $\langle 1|S|2\rangle$ vanishes approximately because the phases are separated. So the leading term of the covariance becomes

$$\text{Cov}_N(t) = \frac{1}{4} (\langle N\rangle_{\text{lower}} - \langle N\rangle_{\text{upper}})^2. \quad (5.96)$$

Since $\langle N\rangle_{\text{lower}} \neq \langle N\rangle_{\text{upper}}$, the t -independent part of the covariance does not vanish, and there is no exponential decay of the covariance function that can lead to the definition of a correlation time.

The situation is different if one considers only a subsystem consisting of one of the two separate phases. In this case the above calculation is altered in two details: First, instead of the partition function $Z = 2\lambda^T$ of the whole system, one has to consider the partition function $Z_{\text{lower,upper}} = \lambda^T$, because in a simplified picture the transfer matrix is in block-diagonal form with two blocks corresponding to each phase (each of which has an eigenvalue λ), and considering only one phase is equivalent to considering only one block in the transfer matrix. Second, if considering the phase that is connected with the eigenvector $|1\rangle$, the expectation values $\langle 2|S|2\rangle$ do vanish. If one uses these modifications, the covariance can be calculated according to Eqs. (5.76) and (5.78), and we get two different correlation times

$$\begin{aligned} \tau_{\text{lower}} &= [\log(\lambda) - \log(\lambda_{\text{lower}})]^{-1} \\ \tau_{\text{upper}} &= [\log(\lambda) - \log(\lambda_{\text{upper}})]^{-1}, \end{aligned} \quad (5.97)$$

where λ_{lower} and λ_{upper} are the second-largest eigenvalues which corresponding eigenvectors located in one of the two phases. For the numerical



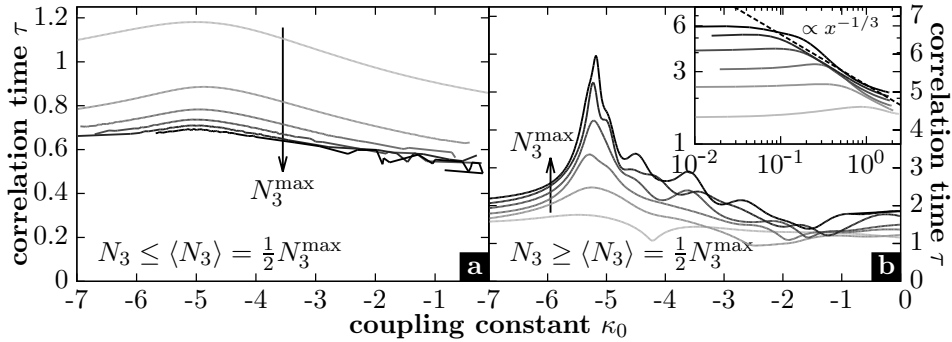


Figure 5.38: Correlation time τ of the covariance $\langle N_{2,2}(0)N_{2,2}(t) \rangle - \langle N_{2,2} \rangle^2 \propto \exp(-t/\tau)$ for the two coexisting phases of the κ_3 -transition in terms of the coupling constant κ_0 for $\Delta = 0.0$ and $T = 64$ for different values of N_3^{\max} . $\langle N_3 \rangle$ is fine-tuned to $N_3^{\max}/2$. (a) Expected ratio $(\langle N_{2,2} \rangle / \langle N_3 \rangle)_{\text{lower}}$ of $(2, 2)$ -simplices for the phase with $N_3 \leq \langle N_3 \rangle$. (b) Expected ratio $(\langle N_{2,2} \rangle / \langle N_3 \rangle)_{\text{upper}}$ of $(2, 2)$ -simplices for the phase with $N_3 \geq \langle N_3 \rangle$. The inset shows the dependence of the correlation time on $|\kappa_0 - \kappa_0^{(c)}|$ for $\kappa_0 \leq \kappa_0^{(c)}$ in a double-logarithmic plot, the dashed black line corresponds to the power law (5.98) with exponent $-1/3$.

calculation of the correlation time, we do not calculate directly Eq. (5.97), because it can be difficult to know which eigenvalue does correspond to which phase. We rather cut the possible values of N_3 into $N_3 \leq \langle N_3 \rangle$ and $N_3 \geq \langle N_3 \rangle$, calculate the covariance function and use a linear fit to obtain the correlation time. The results of these calculations are displayed in Fig. 5.38 for the observable $N_{2,2}$.

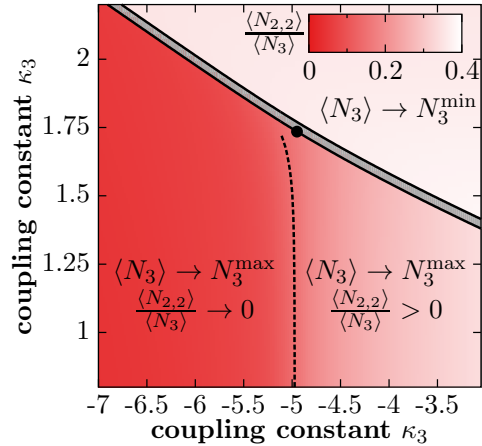
As for the values of the observables, also from the divergence of the correlation time one can conjecture a phase transition at $\kappa_0 \approx -5.2$ for the high- N_3 phase, whereas in the low- N_3 phase no signs for a divergent correlation time can be found. Plotting the correlation time for $\kappa_0 < \kappa_0^{(c)}$ with respect to $|\kappa_0 - \kappa_0^{(c)}|$, where $\kappa_c^{(c)}$ was extracted from the maximum of the derivative of $N_{2,2}$ as described before, yields a power law behavior of approximately

$$\tau_{N_{2,2}, \text{upper}} \propto |\kappa_0 - \kappa_0^{(c)}|^{-1/3}, \quad (5.98)$$

where the critical exponent was not determined by fitting, but is an educated guess which agrees quite well with the data. In the region $\kappa_0 > \kappa_0^{(c)}$ there are structures that are probably numerical artifacts that make it difficult to find the critical exponent.



Figure 5.39: Phase-diagram of (2+1)-dimensional causal dynamical triangulations. The order parameter $\langle N_{2,2} \rangle / \langle N_3 \rangle$ is displayed as colorcode in terms of the coupling constants κ_0 and κ_3 for $N_3^{\max} = 100$. The solid black double line is the location of the fine-tuning transition between separating a phase with small slices ($\langle N_3 \rangle \rightarrow N_3^{\min} = 12$, above the transition line) and large slices ($\langle N_3 \rangle \rightarrow N_3^{\max}$, above the transition line). The dot on one of the solid black line corresponds to the location of the second-order phase transition on the fine-tuned line in one component of the fine-tune transition. The dashed black lines lives in the phase of large slices and separates a phase with vanishing order parameter and with non-vanishing order parameter.



Phase diagram In Fig. 5.39 one can see the resulting phase-diagram of (2+1)-dimensional causal dynamical triangulations. Neglecting the necessity for fine-tuning, one finds three different phases in the phase diagram: First we have a first-order transition between the phases of small slices ($\langle N_3 \rangle \rightarrow N_3^{\min} = 12$) and of large slices ($\langle N_3 \rangle \rightarrow N_3^{\max}$). Within the phase of large slices there is a (probably) second-order transition between a sub-phase with vanishing order parameter $\langle N_{2,2} \rangle / \langle N_3 \rangle$ for κ_0 below a certain critical value, and a sub-phase with finite order parameter for κ_0 above this value.

As argued above, a physical relevant system has to live on the first-order transition where small and large slices coexist. In fact there is a second-order phase transition on this line (compare Figs. 5.35 and 5.38), which can indicate the possibility of a scale-invariant continuum limit of the theory. One needs the scale-invariance because the discretization length a introduced by regulating the action is not a physical length, but only introduced for the discretization procedure, and the results should be independent of the actual choice of the discretization length a .

5.3.7 Problems of the causal dynamical triangulation approach

In this last section we list some of the problems that come with the approach of causal dynamical triangulations (CDT). Many problems have already be addressed in Sec. 5.2.5 for dynamical triangulations (DT) and are also present within the causal version of this approach. As in DT, one has to fix the topology of the underlying manifold also in CDT, where one usually considers the manifold $\mathbb{S} \times \mathbb{S}^{d-1}$, otherwise there would be more then exponentially many triangulations and the partition function would not converge. This means that one has to fix the topology of space and time as an input parameter, where it would be feasible to get the topology as a result from the calculations.

It was already mentioned before that it is crucial for DT and CDT that the number of triangulations of this fixed manifold does grow only exponentially with the number of maximal simplices, and not faster than exponential, because otherwise the partition function would break. The usage of the causal version effectively reduces the problem by one dimension, because intuitively it should be true that if there are only exponentially many $(d-1)$ -spheres, there should also be only exponentially triangulations of $\mathbb{S} \times \mathbb{S}^{d-1}$, which was proven for $d-1=2$ and $d-1=3$ in Ref. [148]. Since there are only exponentially many 2-spheres (or in general triangulations of a given surface), there are also only exponentially many triangulations of $\mathbb{S} \times \mathbb{S}^2$,



but the situation is still unclear for 3-spheres, despite of many numerical hints for their extensivity.

As in the DT approach also in CDT almost nothing is known about the (computational) ergodicity of the Pachner moves, which is needed for the Markov chain Monte Carlo simulations to get the right results. Though causal Pachner moves for $(3 + 1)$ dimensions are probably ergodic, there is still a problem with computational ergodicity if introducing a cutoff in the range of accessible triangulations, either by using a strict cutoff as we do for our Wang-Landau simulations, or by using an additional potential as done for Metropolis simulations in the literature.

Our results on the continuous phase transition for $(2 + 1)$ -dimensional triangulations show that there is also a fundamental problem if one using an additional potential for having a quasi-canonical Metropolis simulation. In the literature, if one wants the system to stay near a certain value \overline{N}_d of maximal simplices, an additional potential term $\propto \gamma \cdot (\overline{N}_d - N_d)$ is inserted into the action that penalizes states far away from \overline{N}_d . In Fig. 5.31 one can see that the probability distribution $p(N_3)$ of the number of simplices per slices has two-peaks, one near the minimal number of simplices N_3^{\min} , and one near the maximal number N_3^{\max} . The expectation value $\langle N_3 \rangle$ for the number of maximal simplices is due to the fine-tuning given by

$$\langle N_3 \rangle \approx \frac{1}{2} \left(N_3^{\min} + N_3^{\max} \right),$$

where there is a minimum of the probability distribution $p(N_3)$. If one introduces now the additional potential to have $N_3 \approx \langle N_3 \rangle$, one selects the states with the lowest probability for the calculation of the partition function, which could be a big source of systematic errors.

These considerations show that a Metropolis-like simulation which is used throughout the whole literature of DT and CDT is actually not suited due to the necessary introduction of an artificial potential term. Furthermore we showed that the fine-tuning transition is actually a discontinuous phase transition, which is the situation where Metropolis-like simulations usually fail due to an effective break of computational ergodicity. This can also be made clear by considering again Fig. 5.31, where one can see that the probability for going from one phase to the other phase of the fine-tuning transition is almost zero if using the Metropolis algorithm. The only possible solution is using an algorithm which samples according to the entropy, and not the energy, as we did using the Wang-Landau algorithm.

Although the approach of CDT found some remarking results, especially if compared to DT, e.g., the running and asymptotically correct Hausdorff



dimensions [36, 39, 123] or the existence of continuous phase transitions [25, 26], these results should be reviewed in the context of the obtained results of this thesis. Furthermore, for the coupling of matter to the CDT approach there are only few results [246] outside of the $(1 + 1)$ -dimensional case, where analytical calculations are possible.



6 Concluding remarks

In this last section we summarize the work about triangulations done within the thesis and review its most important results, with the focus being on possible applications of the methods developed and possible new research direction that arise from the results obtained. Afterwards we give an extended outlook to two discrete space time models that were considered during this thesis besides triangulations, namely finite projective geometry and spin foam models.

Counting like a physicist The main method presented and partially developed within this thesis is the possibility to use Markov chain Monte Carlo simulations, precisely the Wang-Landau simulations, to count the number of all states or states with certain properties of any arbitrary system. The basic idea that was presented in Sec. 2.3.3 is to normalize the density of states, which is the output of a Wang-Landau simulation, with a prior knowledge of the system, or if this is not available, to modify the energy or quantitation function so that this knowledge is created. Using the approximate counting algorithm it is possible to estimate counts that differ by several hundred orders of magnitudes, but always with an errorbar originating from the random nature of the underlying algorithm.

This algorithm was applied already onto several diverse system within this thesis. In Secs. 3.2 and 3.3 it was applied for counting the number of triangulations of two- and three-dimensional integer lattices. These systems show the power of the described counting algorithm, e.g., for two-dimensional lattice triangulations one is able to calculate the state counts from 2 for the smallest lattice to $\approx 10^{370}$ for the largest considered lattice.

The modification of the energy or quantitation function had to be applied to estimate the number of topological triangulations of closed (oriented and non-oriented) surfaces in Sec. 4.2, because the number of minimal triangulations is not known a prior. This example also demonstrates that one can use almost every function that maps the complex structure of the state to a simple number or small vector can be used as energy function, and that this function does not have to be related at all with the physical



notion of energy. For topological triangulation we used either the number of vertices in the triangulation or the number of maximal simplices.

There are several possible applications for this algorithm in the near future. Even if restricting to the topics considered in this thesis, there are a lot of open research questions that can possibly be answered with the proposed approximate counting algorithm in the future. Mathematicians are e.g., interested in counting (especially topological triangulations) where the minimal (maximal) degree of the vertices is bounded from below (above), furthermore there are certain types of triangulations that can be counted, e.g.,

- *q-equivelar* triangulations [287, 310] (which are regular graphs, i.e., every vertex has the same degree q)
- *q-covered* triangulations [287] (where at least one of the two vertices of every edge has the degree q)
- *cyclic* triangulations [285] (where every cycle is a simplex of the triangulation, i.e., for every three edges $\{ab\}$, $\{ac\}$ and $\{bc\}$ also the triangle $\{abc\}$ is contained in the triangulation. A possible counterexample is the minimal triangulation of a torus.)

This could be easily done using our algorithm, either by cutting the range of triangulations in the simulation, or by introducing another component of the energy functional that measures binary whether the considered triangulation has the desired properties.

However, the approximate counting algorithm can also be applied to other counting problems of discrete mathematics (graph or game theory) and computer science. One possible application is the counting of k -connected graphs, which can be done exactly only for small graphs (e.g., Ref. [377] for $k = 2$), where the case $k = 2$ can be utilized for a calculation scheme of virial coefficients in statistical physics [212]. Another problem from graph theory (that is somehow related to q -equivelar triangulations) is the number of non-isomorphic q -regular graphs with n vertices, where actual counts are only known for $n \leq 22$ for suitable q [290], our method can provide the asymptotics, and where our method could possibly provide the asymptotic behavior in n and q .

There are also more esoteric problems that can be addressed: Consider e.g., a quadratic $n \times n$ chess board and place n queens on it, so that no two queens can attack each other. How many possible placings are there? Until now this question is only answered for $n \leq 26$ [288] and can possibly be



answered asymptotically using our algorithm. A multitude of such problems arising in mathematics can be found in the *On-Line Encyclopedia of Integer Sequences* [225]. Remember that for applying the algorithm one needs elementary steps that ergodically link the different states of the system, and a suitable quantitation function.

Tessellating space We presented within this thesis that triangulations are a clever way for tessellating or discretizing space, mainly because within a triangulation everything is fixed in terms of the length of the edges, and does not need to consider certain angles (like it would be necessary if one considered quadrangulations). They are especially useful if objects with curvature need to be discretized (e.g., surfaces embedded into the three-dimensional space).

Triangulations are not only interesting inherently, but can often be used as a tool in physics. The simplest applications would be a description of boundaries in some finite-element methods, e.g., in flow simulations. Here one has to carefully choose the needed fineness of the triangulation, because using too small triangles increases the simulation time (e.g., for testing for boundary collisions), but using too coarse triangles possibly hides important features of the objects to be discretized.

Another reason why triangulations can be used as a tool is that the dual of a certain triangulation, the so-called Delaunay triangulation, is the Voronoi tessellation, which divides the space into regions that are nearest to a certain of the given points, it can be used for studying properties of the underlying (possibly random) system, e.g., in terms of integral geometry. Furthermore, the Voronoi tessellation can be used a starting point for studying foams, and triangulations can be used for understanding better the topological properties of or topological changes within foams and granular matter.

Another important property of triangulations that was widely used within this thesis is that they are maximal planar graphs. This means that one cannot include a new edge between two nodes without intersecting an existing one and violating the planarity. So every planar graph can be considered as a subgraph of a triangulation, so the graph properties that were examined in Sec. 3.4 are of special interest. Since every planar graph can be realized with rational coordinates (by choosing first real coordinates and then slightly wiggling the coordinates so that they become rational, which is possible because the rational numbers are dense in the real ones), by scaling every planar graph can also be realized with integer coordinates. So it is in fact no severe restriction to consider only triangulations of integer



lattices. Nevertheless in future research one could consider first the number and second the graph properties of triangulations of random two-dimensional point sets, but note that this leads to an increase in computation time by a factor that equals the number of systems that is used to average over the randomness. Furthermore, triangulations of real point sets can be studied to examine properties of planar graphs on this point sets (e.g., the location of power plants in a country for planing electricity networks).

Another important application of triangulations can be found in topology, where they can be used as a discretized version of manifolds. It seems to be a restriction to consider triangulations and no other discretizations, but one can expect that the fundamental results obtained from triangulations are also valid for other discretization methods. For example one often considers CW complexes (which are a generalization of triangulations), where every cell is homeomorphic to a closed ball, but triangulations are accommodating because everything is specified by giving the edge lengths.

We used our approximate counting algorithm on triangulations of surfaces in Sec. 3.2 to estimate the number of small triangulations and extend the existing numbers, and to furthermore find the asymptotics of the number in terms of the genus of the surface and the number of simplices used. For three dimensions we considered in Sec. 3.3 the two basic questions about triangulations using the same methods, the ergodicity (of the Pachner moves) and the extensivity of the topological triangulations. Understanding better Adiprasito's obstruction about the simulational recognizability of non-extensivity using numerical simulations one can hope to modify the simulations in order to be able to make statements about extensivity. Then, our numerical calculations can be extended to four dimensions to answer the very two very fundamental questions, whether Pachner moves are ergodic for different 4-manifolds, and whether there are more than exponentially many triangulations. For these tasks one has to be careful about the numerical ergodicity, because some tests already showed that it is possible that two triangulations with the same number of maximal simplices can be reached only by using detours to triangulations with much higher number of maximal simplices, and these detours have to be included into the numerical algorithm. Our algorithm could also be applied to other discretizations of manifolds in arbitrary dimensions to extract the facts about (discrete) topology itself from results that depend on the discretization scheme.

Our methods can also help to consider other fundamental open problems in discrete topology. E.g., although it is known that the topological d -sphere has a unique PL structure for dimension $d \neq 4$ [304, 370], there is neither a



proof or a counterexample in $d = 4$. Monte Carlo algorithms as simulated annealing or Wang-Landau simulations can help to test whether proposed exotic 4-spheres are bistellar equivalent to the boundary of the 5-simplex, which means to obstruct possible counterexamples (for details compare Ref. [395]).

Similar algorithms can also be used to examine the flip graph of topological triangulations in more detail. The nodes of this graph correspond to the different triangulation of the manifold, and there is an edge present between two nodes if there is a Pachner move that transforms the respective pair of triangulation into each other. There are only very few facts that can be proven rigorously about the flip graph, e.g., its connectedness, which corresponds to the ergodicity of Pachner moves. Similar to considering triangulations of graphs, one could calculate various observables of the flip graph, for example

- the average shortest path length, which is the minimal number of Pachner moves that one has to apply to go from one to another triangulation, averaged over all triangulations,
- the distribution of shortest path length, which can be used to learn something about computational ergodicity of triangulations,
- the clustering coefficient, which is a measure for the locality of Pachner moves, because it gives the probability that two triangulations that are neighbors of a common triangulation are also connected by a Pachner move,
- or the degree distribution, which can be used to measure how diverse the single triangulations are in terms of the number of Pachner moves originating from them.

Each of the quantities can be measured in terms of the size of the triangulation, or only for a certain subset of triangulations, to study also the local structure of the flip graph.

Another very interesting application of random surface triangulations is given by the KPZ formula [146,184,254]. Consider a statistical model defined on a two-dimensional regular lattice (quadratic, triangular, hexagonal etc.) near a critical point. The same model can sometimes be easier to solve on a random (or quantum) surface, which can be described by a triangulation, and the KPZ-formula relates the critical exponents on the regular lattice and on the quantum surface.



Discrete analogs of curvature In addition to being a tessellation of curved space, triangulations additionally provide an elegant way for studying the curvature of the underlying space itself. This goes back to the work of Tullio Regge, which we summarized in Sec. 5.1, who showed that the curvature of a triangulation of a d -manifold is a distribution taking only values on the $(d - 2)$ -simplices. This observation can be used to find the Regge action, which is a triangulation equivalent of the Einstein-Hilbert action, and to derive the analogs of the Einstein equations, the equations of motions corresponding to this action, where the dynamical variables are given by the edge lengths of the triangulation, which fix the geometry.

The Regge formalism then provides two possibilities to obtain a quantum theory. The first is to fix the underlying triangulation and to canonically quantize the edge length degrees of freedom. The other one is to fix the edge lengths to a cutoff length and to use a path-integral like sum over all possible triangulations of the manifold, weighted with the respective Regge action. The latter possibility has the advantage that the Regge action is completely determined by the f -vector of the triangulation, i.e., the number of k -dimensional simplices for some $k \leq d$, and the respective coupling constants can be read off. Since the path-integral quantization procedure can be interpreted in terms of the usual formalism of statistical physics, we used the Wang-Landau algorithm to calculate the density of states with respect to the relevant simplex numbers.

We presented that there are some problems with the approach of dynamical triangulations, and how some of the problems can be solved by using causal dynamical triangulations, where a causality condition is imposed on every triangulation contributing to the path integral. But even within this setup some conceptual problems remain, especially if one uses traditional Markov chain Monte Carlo algorithms as in the literature. It was explicitly demonstrated for $(2 + 1)$ -dimensional causal dynamical triangulations the continuous phase transition that is claimed to exist does take place only in one component of the system, which has been tuned to a first-order phase transition to allow for a valid thermodynamic limit.

If the computational ergodicity of 3-spheres or in general 3-manifolds can be understood better, our approach can be used for calculating phase diagrams for $(3 + 1)$ -dimensional causal triangulations. The problem with the current lack of knowledge is that one cannot split the energy range (here the range of simplex numbers) as nicely as in $(2 + 1)$ -dimensional case without violating ergodicity, so one has to perform Wang-Landau simulations of large energy ranges, which are known to slowly converge



(compare Sec. 2.3.2). If it is not possible to take gain more understanding about the ergodicity, one has to rely on massively parallel replica exchange Wang-Landau simulations for calculating the one-slice propagator to have small enough number of energy bins in each replica for fast convergence, but also guaranteed ergodicity.

6.1 Outlook: Equidistance in finite projective geometries through biquadratics

Many mathematical descriptions of the physical reality relies on or postulates a continuous spacetime equipped with a metric (Riemannian or Pseudo-Riemannian manifold). For special or general relativity these continuous manifolds are the objects that are described by the theory, but also for other topics the existence of a continuous space with a metric is assumed, e.g., in Maxwell theory, which can be formulated using differential equations.

Despite the fact that a continuous spacetime and the existence of a metric is used everywhere throughout physics, some kind of discreteness has to be inserted into the theories to take into account the quantum properties of nature. Usual quantum mechanics or quantum field theory keep the continuous and metrizable spacetime and quantize only the objects that live thereon (particles or matter). If one speculates about the quantum nature of space and time itself, its discreteness is introduced *a posteriori* e.g., by quantization (as in loop quantum gravity [388]) or regularization (as in (causal) dynamical triangulations¹, see Sec. 5) a continuous spacetime. There are only few possible counterexamples that postulate discreteness *a priori*, e.g., causal set theory [141].

But not only the continuity and the metrizable of the underlying geometry is used tacitly, but also the demand that space(-time) is at least locally an affine geometry to use coordinates that can be identified with elements of a vectors space. However, in mathematics geometry can be considered in a much more abstract way, by just considering the objects of the geometry and their incidence relation, i.e., which objects are contained in or intersect with other objects. Based on this elementary notions, in mathematics two certain types of geometries are considered: on the one hand

¹ Remember that Regge calculus or the (causal) dynamical triangulation approach do not postulate the triangles or simplices as building blocks of the spacetime, but as a regularization or discretization scheme. Inside of the simplices spacetime is considered as flat, and only the curvature is located on discrete objects (inside of a simplex the geometry is considered as flat).



the already mentioned affine geometry, which is the prototype of Euclidean or Lorentzian geometry, and on the other hand projective geometry, which is often considered to be a more valuable object of study in mathematics, because it possesses several nice symmetries which simplify many notions and theorems ².

Breaking with the two usual design principles (affinity and continuity) for the underlying geometry of space(-time), one naturally arrives at *finite projective geometries*, which are widely studied in the mathematical literature [89]. Furthermore, due to the inherent discreteness such geometries are well-suited to be considered using a computer, because theorems for small geometries can be proven by simply verifying all of the finitely many possibilities. We want to test whether finite projective geometries are suited for describing the geometry of space and time. Since in this approach discreteness is postulated *a priori*, an important question is whether one can recover the usual continuous metrizable as well as affine geometry in a limiting procedure.

Therefore one has to answer a fundamental open question: How to define distance between two points in a finite projective geometry, so that this distance is invariant under certain transformations? The question that should be addressed in this section is whether it is possible to define places of equal distance from a given point, similar to standard Euclidean geometry (where these places are given by a circle around a given point) or Lorentzian geometry (where these places are given by a hyperbola centered at the given point). In these standard setups, the places of equidistance are given by different quadrics, which can be seen as cone intersections. These quadrics can also be defined consistently within finite projective geometries.

We will show that it is not sufficient for defining equidistance in finite projective geometries to consider only one quadric, but to use two quadrics with certain properties, because there are not enough points on one quadric to have an intersection into each direction originating from a point.

This section is based mainly on the master's thesis

[271] ———, *Biquadric fields: Equipping finite projective spaces with metric structure*, (2014), master's thesis

as well as partly on the bachelor theses and project reports

[62] W. Barfuss, *Quadrics in finite projective planes*, (2012), short term research project

² e.g., the Erlangen program of Felix Klein is formulated using projective geometry.



- [10] N. Alex, *Quadriken in endlichen projektiven Ebenen*, (2012), bachelor's thesis
- [425] F. Winterhalter, *Monte-Carlo-Simulationen mit Quadriken in endlichen projektiven Ebenen*, (2013), bachelor's thesis

which were supervised jointly by me and Klaus Mecke.

In our following consideration we suppose that the necessary mathematical basics are known, especially (finite) group theory. Details about the mathematical setup can be found in great details in Ref. [271].

6.1.1 Affine and projective geometries

We start by giving the basic definition of the term *geometry*, which encodes that there is a set of objects (points, lines, planes, circles etc.) and their respective relation of incidence (Is a point contained in a line? Do two lines intersect?):

Definition 6.1 (geometry [89, p. 1]):

Let Ω be a set and let $I \subset \Omega \times \Omega$ be a relation on Ω . The pair $G = (\Omega, I)$ is called a *geometry*, if

- I is symmetric, i.e. $(x, y) \in I \Rightarrow (y, x) \in I$ for $x, y \in \Omega$
- I is reflexive, i.e. $\forall x \in \Omega: (x, x) \in I$.

The relation I is called *incidence relation*.

The symmetry requirement means that for an object x that is incident with an object y also the object y is incident with the object x , and the reflexivity requirement means that an object is incident with itself. We consider only geometries where there is a set \mathcal{P} of points, and all other objects are composed of points (i.e., we identify a line with the set of the constituting points), so two objects x and y can be considered as incident if $x \cap y \neq \emptyset$ (*set-incidence relation*).

Formally the set Ω can be split into subsets $\Omega = \Omega_1 \cup \Omega_2 \cup \dots \cup \Omega_r$, where r is denoted as *rank* of the geometry, so that the subsets fulfill certain properties (e.g., they are disjoint and no two elements of the same subset are incident, compare [89, Sec. 1.1]). Intuitively the set Ω_1 consist of the points, Ω_2 of the lines and Ω_3 of the planes of the geometry. It can be shown that it is enough to describe a geometry only by the sets of Ω_1 and Ω_2 , which will be denoted by points \mathcal{P} and lines \mathcal{L} [89, Sec. 1.1].



6. Concluding remarks

As next step we define axiomatically the two geometries that are the starting point of our further considerations, and that are the most considered types of geometry considered in mathematics.

Definition 6.2 (projective and affine geometry [89, Sec. 1.2] and [82, Sec. 6.1]):

Let $G = (\mathcal{P}, \mathcal{L}, I)$ be a geometry consisting of points \mathcal{P} , lines \mathcal{L} and an incidence relation I . The geometry is called *projective*, if

PG1 For all pairs $p_1, p_2 \in \mathcal{P}$ of distinct points there is a unique line $\overline{p_1 p_2} \in \mathcal{L}$ that is incident with these two points (line through two points).

PG2 For all quadruples $p_1, p_2, p_3, p_4 \in \mathcal{P}$ of distinct points with $\overline{p_1 p_2} \cap \overline{p_3 p_4} = q_1 \in \mathcal{P}$, also the lines $\overline{p_1 p_3}$ and $\overline{p_1 p_4}$ intersect in a unique point (Veblen-Young-Paschen axiom).

PG3 There are at least two lines and three points per line.

The geometry is called *affine*, if PG1 and PG3 and the following axiom holds

AG2 For every line $\ell \in \mathcal{L}$ and every point $p \in \mathcal{P}$ there is a unique line $\ell' \in \mathcal{L}$ so that $p \in \ell'$ and $\ell' \parallel \ell$, so that \parallel is a equivalence relation.

If $\ell \parallel \ell'$, one calls ℓ *parallel* to ℓ' and vice versa.

Note that the affine geometry is a generalization of the usual Euclidean or Lorentzian spacetime.

We denote by a *hyperplane* h an object with maximal rank (compare [89, Sec. 1.1] (intuitively this is an object with dimensionality one less than the dimensionality of the space, which we did not yet introduce), and use these objects to find an interesting relationship between affine and projective geometries:

Theorem 6.3 (relation of affine and projective geometry [89, Sec. 1.6]). *Let $G = (\mathcal{P}, \mathcal{L}, I)$ be a projective geometry, and let h_∞ be a hyperplane of G . The triple $G' = (\mathcal{P}', \mathcal{L}', I)$ with \mathcal{P}' being the set of points not contained in h_∞ and \mathcal{L}' being the set of lines not lying in h_∞ is then an affine geometry.*

This means that one can construct affine from projective geometries by slicing (leaving out) one hyperplane, and projective from affine geometries by suitably adding one hyperplane. This special hyperplane is often denoted



as *hyperplane at infinity* and can be considered as the place where all parallel lines from an affine geometry intersect.

An important special case of a projective geometry is its two-dimensional specialization, the projective plane, which can be defined independently as

Definition 6.4 (projective plane):

Let $G = (\mathcal{P}, \mathcal{L}, I)$ be a geometry consisting of point \mathcal{P} , lines \mathcal{L} and an incidence relation I . The geometry is called *projective plane*, if PG1 and PG3 hold, and if

PP2 for all pairs $\ell_1, \ell_2 \in \mathcal{L}$ of distinct lines there is a unique point $p = \ell_1 \cap \ell_2$, which is incident with both lines (intersection of two lines).

In this definition one can see clearly the inherent symmetry: The usage of the terms lines and planes can be interchanged without changing the definition. So from first principles it does not matter which objects to denote as points, and which as lines.

Until now projective and affine geometries were defined *synthetically* in terms of axioms for the incidence of the basic objects. For doing actual calculations or for physical applications one has to consider *analytical* geometry in terms of coordinates. While for affine geometries one uses normal vector spaces over fields as coordinates, for projective geometries one needs

Definition 6.5 (homogeneous coordinates, [344, p. 47 and p. 48]):

Let \mathbb{F} be an arbitrary field³ and \mathbb{F}^{d+1} the $(d + 1)$ -dimensional vector space over \mathbb{F} . The *homogeneity equivalence* relation for $x_1, x_2 \in \mathbb{F}^{d+1} \setminus \{0\}$ is defined by

$$x_1 \sim x_2 \quad :\Leftrightarrow \quad \exists \lambda \in \mathbb{F} \setminus \{0\} : x_1 = \lambda \cdot x_2$$

By *homogeneous coordinates* one denotes the equivalence classes with respect to the homogeneity equivalence.

One can now prove that these coordinates in fact give the points of a projective geometry⁴:

³ Note that one has to coordinatize some projective geometries with R-modules over skew fields (these are Desarguanian, but not Papposian geometries). But since we consider only finite fields, and a finite skew field is already a field due to a theorem by Wedderburn, we can restrict the following considerations to vector spaces and fields. See Ref. [271, p. 20 and p. 21] for details.

⁴ Note that there are two-dimensional non-Desarguanian geometries, which cannot be coordinatized in this way. For $d \geq 3$ and finite projective spaces every geometry can be coordinatized in this way. See Ref. [271, p. 20 and p. 21] for details.



Theorem 6.6 (projective geometries over fields \mathbb{F} , [89, Thm. 2.1.1]). *Let \mathbb{F} be an arbitrary field and \mathbb{F}^{d+1} the $(d + 1)$ -dimensional vector space over \mathbb{F} . Let $\mathcal{P} = \mathbb{F}^{d+1} / \sim$ be the set of 1-dimensional subspaces of \mathbb{F}^{d+1} , and let \mathcal{L} be the 1-dimensional subspaces of \mathbb{F}^{d+1} , then $\mathbb{P}^d \mathbb{F} := (\mathcal{P}, \mathcal{L}, \subset)$ with \subset being the set-incidence relation is a projective space.*

Intuitively this means that points in a d -dimensional projective space are given by $(d + 1)$ -homogeneous vectors, e.g., for $\mathbb{P}^3 \mathbb{F}$

$$\mathcal{P} = \left\{ \left\{ \begin{pmatrix} x_1 \\ x_2 \\ x_3 \\ 1 \end{pmatrix}, x_{1/2/3} \in \mathbb{F} \right\} \cup \left\{ \begin{pmatrix} x_1 \\ x_2 \\ 1 \\ 0 \end{pmatrix}, x_{1/2} \in \mathbb{F} \right\} \right. \\ \left. \cup \left\{ \begin{pmatrix} x_1 \\ 1 \\ 0 \\ 0 \end{pmatrix}, x_1 \in \mathbb{F} \right\} \cup \left\{ \begin{pmatrix} 1 \\ 0 \\ 0 \\ 0 \end{pmatrix} \right\} \right\}.$$

Another important quantity will be the hyperplanes \mathcal{H} , which are the $(d - 1)$ -dimensional objects in the geometry, that can be coordinatised using dual homogeneous vectors, e.g., for $\mathbb{P}^3 \mathbb{F}$

$$\mathcal{H} = \left\{ (x_1, x_2, x_3, 1), x_{1/2/3} \in \mathbb{F} \right\} \cup \left\{ (x_1, x_2, 1, 0), x_{1/2} \in \mathbb{F} \right\} \\ \cup \left\{ (x_1, 1, 0, 0), x_1 \in \mathbb{F} \right\} \cup \left\{ (1, 0, 0, 0) \right\}$$

It can be shown that a point lies on a hyperplane if the (scalar) product of its coordinates vanishes, and that the (generalized) vector product can be used for calculating the hyperplane spanned by d points in general position or the common intersection point of d hyperplanes in general position [271, Sec. 2.2].

Note that we introduced the dimension of a projective geometry using the dimension of the vector space used for its coordinatization. It is also possible to define the dimension of a projective geometry synthetically without using coordinates (compare Ref. [89, Sec. 1.3]).

From now on we will restrict ourselves to finite projective geometries, which means that we use the finite field \mathbb{F}_q as underlying field of the projective geometry, where q is a prime or a power of a prime. For prime p the field \mathbb{F} can be identified with defining addition and multiplication modulo p (which is the remainder if dividing by p), for prime powers the situation is more complicated (one has then to consider the Galois extensions of the additive and multiplicative group). Working with finite fields has the



advantage that the objects of the projective geometry space can be counted, e.g., for a projective geometry $\mathbb{P}^d\mathbb{F}_q$ there are [89, Thm. 1.5.3, Thm. 1.5.4]

- $\sum_{i=0}^d q^i = q^d + \dots + q + 1$ points and hyperplanes in the geometry,
- $\sum_{i=0}^{d-1} q^i = q^{d-1} + \dots + q + 1$ points incident with every hyperplanes and vice versa,
- $\sum_{i=0}^{d-1} q^i = q^{d-1} + \dots + q + 1$ lines incident with every point, and
- $p + 1$ points on every line

6.1.2 Quadrics and Biquadratics

Commonly the fundamental objects for defining distance and therewith metric in spaces used in physics are quadrics (roots of quadratic polynomials in the coordinates, which correspond to cone intersections), which give the places of equal distance from an observer. E.g., in the standard three-dimensional Euclidean space, all points that have unit distance from the origin fulfill

$$x_1^2 + x_2^2 + x_3^2 = 1,$$

which defines a sphere in space, whereas in the (1+3)-dimensional Lorentzian spacetime, all points that have a unit distance from the origin fulfill

$$-x_0^2 + x_1^2 + x_2^2 + x_3^2 = 1,$$

which defines a hyperbola in space, and where x_0 is identified as time-direction (if using $c = 1$). So one can conclude that quadrics should also play an important role in projective geometries for defining equidistance or a metric.

Quadrics can also be defined for projective geometries in the following way:

Definition 6.7 (quadric):

Let $\mathbb{P}^d\mathbb{F}_q$ be a projective space over the field \mathbb{F}_q , and let M be a $(d + 1) \times (d + 1)$ matrix. The point set

$$Q_M := \{x \in \mathcal{P} \mid x^t M x = 0\} \tag{6.1}$$

is called *quadric*⁵ associated with the matrix M . A quadric Q_M is

⁵ Mathematically one first defines a *quadratic form* $f(x)$ by imposing that $B(x, y) := f(x + y) - f(x) - f(y)$ is symmetric and bilinear, and then shows that this quadratic form can be written using a matrix (see Ref. [89, Sec. 4.7] for details). It is also possible to define a quadratic set, which is a generalization of a quadric, synthetically (see Ref. [89, Sec. 4.1] for details).



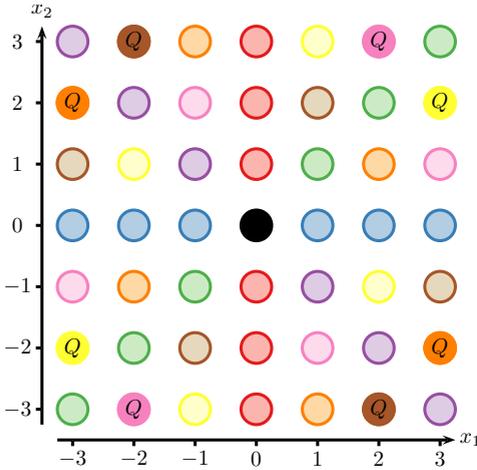


Figure 6.1: Single quadric in a finite projective plane.

(Affine) points of the quadric $Q_1 : x_1^2 + x_2^2 + x_3^2 = 0$ (i.e., $x_3 = 1$) in the affine part of the finite projective plane $P^2\mathbb{F}_7$. The center black point has coordinates $p_c = (0, 0, 1)^t$, the color of the other points encodes the different lines through the centering points they lie on. Dark colors correspond to points of the quadric Q_1 .

called *(non)-degenerated*, if the matrix M is (non)-degenerated. For an arbitrary point $x \in \mathcal{P}$, the hyperplane given by $h = x^t M$ is called *polar* of the quadric Q_M with respect to the point x .

Note that only the symmetric part $(M + M^t)/2$ of the matrix is relevant for the quadric, because the antisymmetric part cancels in the calculation. Furthermore, in projective geometries there is no distinction of (non-degenerated) quadrics into hyperbolas, parabolas and ellipsis as in the usual affine geometry, which also shows that projective geometries can be considered as more symmetric⁶.

Normally in physical used geometries, the positional relationship between a line and a (non-degenerated) quadric can be characterized by the number of intersections. For a given quadric Q and a line ℓ the line is called a *secant* of Q if both have two common points, the line is called *tangent* of Q if both have one common point, and the line is called *passant* if both have no common point. Note that for $d \geq 3$ there is also the possibility that a line is completely contained in a quadric.

As for Euclidean or Lorentzian space, we want to use quadrics for defining equidistant points in finite projective geometries. The aim is to find for every point p_c a suitable quadric so that we have an intersection into every direction originating from this point⁷, or equivalently two intersections

⁶ The usual notion of quadric types can be considered by marking a hyperplane at infinity and considering the positional relationship between the quadric and this hyperplane at infinity.

⁷ We consider first the Euclidean or elliptical case. For a Lorentzian or hyperbolic case there are two lines in a plane (in higher dimensions a degenerated quadric) where one



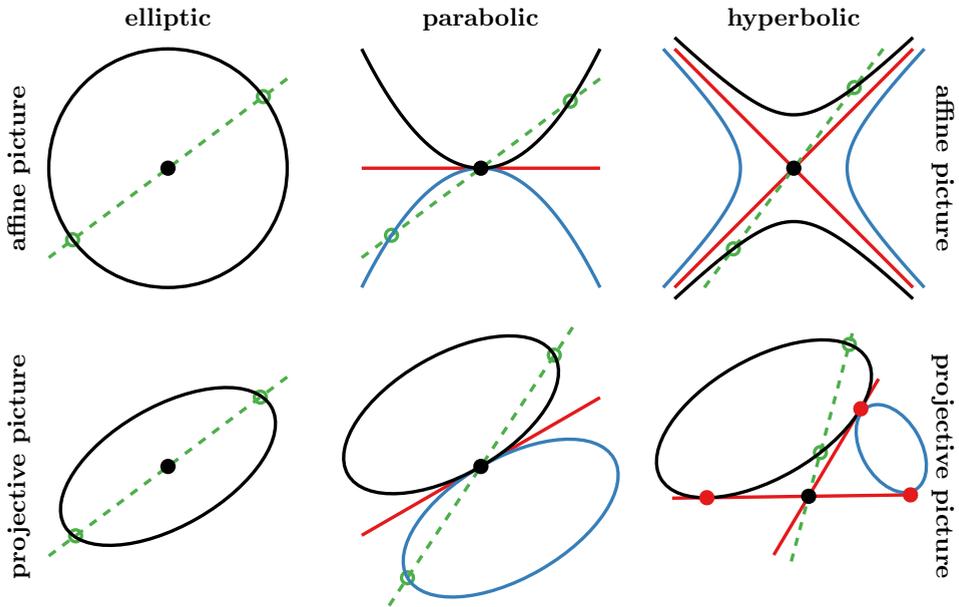


Figure 6.2: Types of metrics and their embedding into the projective space.

In the top row the possible types of metrics in a (continuous) affine plane are displayed: Elliptic (positive signature, as in the Euclidean case), parabolic (vanishing signature) and hyperbolic (negative signature, as in the Lorentzian case). In the bottom row the projective counterparts are displayed. The red solid lines are the tangents from the center point to the quadrics (the number of tangents defines the type of the metric), the dashed, green lines are lines through the center that needed to be intersected twice. The blue quadrics needs to be included so that every line through the center that is not a tangent is intersected twice. Note that if one uses finite projective geometries, one also would need an additional quadric in the elliptic case (because intuitively the quadric is not dense enough).

for every line through p_c (because one needs two intersection per line to define forward and backward direction). If we consider the simplest possible case of a projective plane, there are $(p + 1)$ points through every line, so one needs $2(p + 1)$ different intersection points with the quadric. But a non-degenerated quadric in the plane has only $p + 1$ points, so one needs in fact two quadrics. This situation is displayed in Figs.6.1 (with one quadric) for P^2F_7 . In higher dimensions one can find similar counting arguments that one quadric is not enough for defining equidistance in every direction.

A similar phenomenon can also be found in Lorentzian spacetime, where

has no intersections, these correspond to the light-like directions



the usual choice $\eta_{\mu\nu}x_\mu x_\nu = 1$ only leads to intersections into time-like directions, and one needs a second quadric $\eta_{\mu\nu}x_\mu x_\nu = -1$ to get intersections also in the space-like directions. The situation for different types of geometries is displayed in Fig. 6.2.

Surely one cannot choose two arbitrary quadrics for defining equidistance, but one needs two quadrics in a certain relation, which leads to the proposition of the following definition:

Definition 6.8 (biquadric [10, 271]):

Let Q_1 and Q_2 be two quadrics with matrices M_1 and M_2 , let $p_c \in \mathcal{P}$ be a point and $h_\infty \in \mathcal{H}$ be a hyperplane so that $p_c \notin h_\infty$. Then (Q_1, Q_2) is called biquadric with center p_c and hyperplane h_∞ at infinity if

- h_∞ is the polar of p_c with respect to both Q_1 and Q_2 .
- Every line through p_c except the lines in at most two hyperplanes intersects either Q_1 or Q_2 in exactly two points.

If the second condition is true for every line through p_c , the biquadric is called *elliptic*, if it is true for every line except the lines in one hyperplane, the biquadric is called *parabolic*, otherwise the quadric is called *hyperbolic*.

The first question one has to answer is whether one can construct such a biquadric. In fact it is possible to find the matrices M_1 and M_2 easily if p_c and h_∞ have some special coordinates:

Proposition 6.9 (Coordinate description of biquadrics, special case [10, 271]). *Let $\mathbb{P}^d \mathbb{F}_q$ the projective geometry over the field \mathbb{F}_q , and let m be a non-degenerated $d \times d$ matrix, and let M_1 and M_2 be the $(d+1) \times (d+1)$ matrices*

$$M_1 := \begin{pmatrix} m & \vec{0} \\ \vec{0}^t & 1 \end{pmatrix} \quad M_2 := \begin{pmatrix} \bar{r} \cdot m & \vec{0} \\ \vec{0}^t & 1 \end{pmatrix}, \quad (6.2)$$

where $\bar{r} \in \mathbb{F}_q$ is a number that does not possess a square root. Then the quadrics Q_1 and Q_2 associated with M_1 and M_2 are biquadrics with center p_c and hyperplane at infinity h_∞ , where

$$p_c = \begin{pmatrix} \vec{0} \\ 1 \end{pmatrix} \quad h_\infty = \left(\vec{0}^t \quad 1 \right)$$



Proof. (Sketch) Consider an arbitrary line through p_c , whose affine points are all $a \cdot p$ with $p \in \mathcal{P} \setminus h_\infty$ (i.e., $p = (\vec{p}, 1)$) and $a \in F_q$. We calculate the value of a so that $a \cdot p \in Q_{1,2}$:

$$\begin{aligned} p \in Q_1 & \quad a^2 \vec{p}^t m \vec{p} + 1 = 0 & \Rightarrow & \quad a^2 = \frac{-1}{\vec{p}^t m \vec{p}} \\ p \in Q_2 & \quad \bar{r} \cdot a^2 \vec{p}^t m \vec{p} + 1 = 0 & \Rightarrow & \quad a^2 = \frac{1}{\bar{r}} \frac{-1}{\vec{p}^t m \vec{p}} \end{aligned}$$

Suppose that w.l.o.g. the first equation has a solution $a = \pm(-\vec{p}^t m \vec{p})^{1/2}$. This means that $-\vec{p}^t m \vec{p}$ possesses a square root, then the second equation does not have a solution, since $-\bar{r} \vec{p}^t m \vec{p}$ does not have a square root, and vice versa. This implies that lines that are secant for Q_1 are passants for Q_2 and vice versa, and similar one can show that tangents for Q_1 are also tangents for Q_2 . \square

Of course having coordinates only for special p_c and h_∞ is not satisfying. But one can derive actual coordinates for the general case. The idea is to consider maps that transform affine to projective coordinates or vice versa in general, which are denoted as *homogenizations* and *dehomogenizations* (note that these are not given simply in terms of a matrix, because one has to consider that vectors for points and covectors for hyperplanes transform differently, see Ref. [271] for details), and apply them to matrices that define affine quadrics. The result is the following theorem:

Theorem 6.10 (Coordinate description of biquadratics, general case [270]). *Let $P^d F_q$ the projective geometry over the field F_q , and let m be a non-degenerated $d \times d$ matrix, let $p_c \in \mathcal{P}$ be an arbitrary point and let $h_\infty \in \mathcal{H}$ be an arbitrary hyperplane so that $p_c \notin h_\infty$. Choose d points $p_i^\infty \in h_\infty$ in general position, and define the matrix H by*

$$\begin{pmatrix} H \\ h_\infty \end{pmatrix} := (\hat{P}^{-1})^t \quad \text{with} \quad \hat{P} := (p_1^\infty, p_2^\infty, \dots, p_d^\infty, p_c)$$

Then the quadrics Q_1 and Q_2 associated with

$$\begin{aligned} M_1 & := H^t m H + h_\infty h_\infty^t \\ M_2 & := r \cdot H^t m H + h_\infty h_\infty^t, \end{aligned} \tag{6.3}$$

where $r \in F_q$ is a number that does not possess a square root, are biquadratics with center p_c and hyperplane h_∞ at infinity. Note that one must use the same representative of the homogeneous equivalence class in Eq. (6.3) as in $(\hat{P}^{-1})^t$.



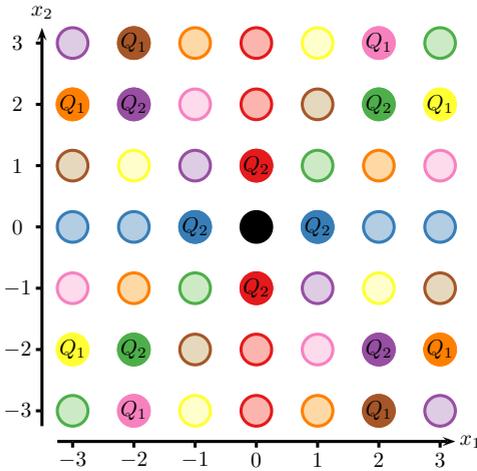


Figure 6.3: Biquadric in a finite projective plane.

(Affine) points of the biquadric $Q_{1,2} : \pm x_1^2 \pm x_2^2 + x_3^2 = 0$ (i.e., $x_3 = 1$) in the affine part of the finite projective plane P^2F_7 . The center black point has coordinates $p_c = (0, 0, 1)^t$, the color of the other points encodes the different lines through the centering points they lie on. Dark colors correspond to points of the quadrics Q_1 and Q_2 . Note that every line through the center has two common points with the quadric.

Note that this theorem is only proven in one direction, i.e., that two matrices calculated as in (6.3) are biquadrics. The other direction is not proven until now, but is only a conjecture:

Conjecture 6.11 (Inverse coordinate description of biquadrics). *The inverse of Theorem 6.10 is true, i.e., for every biquadric (Q_1, Q_2) as defined in Def. 6.8 one can find a suitable p_c and h_∞ as well as a matrix H so that matrices M_1 and M_2 associated with the two quadrics can be calculated as in (6.3).*

Since we are dealing with finite geometries, for small q and d one can explicitly check this conjecture by testing all possible combinations of quadrics.

Proposition 6.12 (Inverse coordinate description of biquadrics, [270]). *Conjecture 6.11 is true for $d = 2$ and $q = 2, q = 3$ and $q = 5$.*

6.1.3 Open questions and research directions

The presented considerations about finite projective geometries are just a small step towards an actual formulation as a possible spacetime model. Although it is possible to introduce an object denoted as *biquadric* which allows to define places of constant distance from a center, there are still major open questions and need to be addressed in future research.



A major open question is whether the Definition 6.8 and the coordinatization (6.3) are equivalent. Until now it is only known that two matrices as in (6.3) describe a biquadric. For an equivalency Conjecture 6.11, which is basically the inverse statement, has to be proven.

The introduced biquadrics also induces only places of constant distance to a given center p_c . Until now it is not clear in general how to define distance between to points in the strict sense of a metric, so that e.g., the triangle inequality is fulfilled and so that the distance is invariant with respect to at least some projectivities. It is thinkable that it is impossible to define a metric on finite projective space, but that something like an effective metric arises from a superposition of several biquadrics (in a path-integral sense). A last major open question that is related with the previous ones is how to define a meaningful limit to get a continuous spacetime, which is what we can observe at normal length-scales.

6.2 Outlook: Efficient calculations of $3nj$ -symbols for spin foam amplitudes

Spin networks, which were originally introduced by R. Penrose [326, 327] for describing classical spacetime combinatorially, can be used as a description of the states of the Loop quantum gravity (LQG) Hilbert space. Since LQG uses a foliation of spacetime to use the canonical quantization method, the states or the spin-networks describe space at fixed time, and the time-dependence does enter the theory only by a constraint. Spin foams are an extension of spin networks that try to describe space and time simultaneously in a path-integral like quantization formalism. While a spin network is a graph where each edge is colored with a representation of an underlying group, e.g., $SU(2)$ or $SL(\mathbb{R}, 2)$, and each vertex⁸ is labeled with an intertwiner, a spin foam is a complex with vertices, edges and faces where the faces are colored with a representation of the underlying group, and edges are labeled with intertwiners. So every intersection of a plane and a spin foam is again a spin network, and one can interpret spin foams as the time-evolution of spin networks and use them to calculate transition amplitudes between different spin networks. In Fig. 6.4 a simple spin foam with boundary spin networks

⁸ Note that the term *vertex* in this section and in the spin network and spin foam literature is used differently than in the previous sections of this thesis. While in the latter case *vertex* refers to a 0-simplex of a triangulation, here *vertex* refers to a node of the graph dual to the possibly underlying triangulation, so it corresponds to a d -simplex of the triangulation.



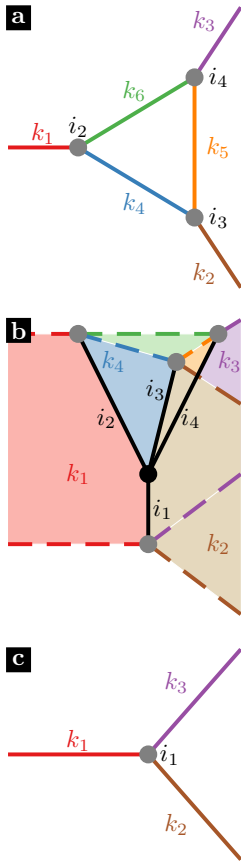


Figure 6.4: Spin networks and spin foam.

(b) Spin foam with group representations k_a associated with the six displayed faces and intertwiners i_b associated with the four displayed edges (black, solid lines). On the top (a) and on the bottom (c) the spin networks that arise if one cuts the spin foam with two horizontal planes are displayed. Due to the cut, the group representations k_a live on the edges, and the intertwiners i_b live on the vertices of the spin networks. Note that the dashed lines in (b) are no edges of the spin foam, but arise only from the cut with the planes, so they have no associated group representation, and also the gray points are no actual vertices of the spin foam.

If one defines the time direction upwards parallel to the i_1 edge, one can interpret the spin foam as transition between the initial lower spin network (c) and the final upper spin network (a), where the vertex i_1 of the network is split into the three vertices i_2 , i_3 and i_4 inbetween.

The displayed spin foam is dual to a 3-triangulation consisting of only one tetrahedron, the group representations can then be identified with the six 1-simplices, and the intertwiners can be identified with the four 2-simplices of the triangulation.

can be found, for a general review about spin foams see Refs. [55,56].

For a path-integral-like formulation of spin foams there are several possibilities for choosing the contributing 2-complexes and their weight. One can e.g., consider all possible 2-complexes that can be constructed, even those that cannot be embedded into any manifold. Alternatively one can consider only those 2-complexes which can be embedded into a manifold. Using these options one has to be careful to not overcount the 2-complexes. A possible regularization scheme is to consider only 2-complexes which are dual to a given triangulation of a manifold [55,56], which connects spin foams with the previous sections of this thesis. So one can assign to every $(d - 2)$ -simplex (which is dual to a face of the spin foam) of the triangulation an irreducible representation of the associated group, and to every $(d - 1)$ -simplex (which is dual to an edge of the spin foam) an intertwiner.



In this section we consider a certain model of spin foams, the so-called EPRL-model [155]. Our work is entirely on numerical calculations within this spin foam model, we are not concerned about its actual derivation or interpretation of the obtained result. We rather want to show that it is possible to calculate transition or vertex amplitudes numerically for small quantum numbers, we therefor calculate amplitudes for simple examples and discuss a coarsening step. Previous calculations considered mostly the asymptotic limit of large quantum numbers, consider e.g., Refs. [8, 67, 121, 245].

This section is based on the numerical simulations and conceptual thoughts of the following two theses supervised by me

[144] M. Düll, *Effiziente Berechnung von Wigner $3nj$ -Symbolen*, (2013), short term research project

[145] ———, *Numerische Berechnung von Vertex-Amplituden im EPRL-Modell*, (2013), bachelor's thesis

6.2.1 Spin foam models and amplitudes

In this section we present different spin foam models and describe the spin foam amplitude of the considered EPRL model. The most general form of the amplitude for single spin foam is

$$A = \sum_{k_f, i_e} \left(\prod_{\text{faces } f} \mathcal{A}_f(k_f) \right) \cdot \left(\prod_{\text{edges } e} \mathcal{A}_e(k_f, i_e) \right) \cdot \left(\prod_{\text{vertices } v} \mathcal{A}_v(k_f, i_e) \right), \quad (6.4)$$

where k_f are the group representations associated with the faces and i_e are the intertwiners associated with the edges. The products go over all faces f , edges e and vertices v of the dual 2-complex (bones, $(d - 1)$ -simplices and maximal simplices of the triangulation). The different models then have to define the face, edge and vertex amplitudes A_f , A_e and A_v .

An early and successful spin-foam model is denoted as *Barrett-Crane* model [65, 66]. Despite its success, there are several problems with this model, e.g., its boundary states are not equivalent with the LQG spin networks, and the volume operator within the model is ill-defined [9, 57]. An alternative model (denotes as *EPR-model*) that can resolve these problems was proposed by J. Engle, R. Pereira and C. Rovelli [156, 157], where the vertex amplitude is defined as a square of a Wigner $15j$ symbol, and one can show that its kinematics match those of LQG. But this model is still defined only for the Euclidean case and for vanishing Barbero-Immirzi parameter γ .



The Barbero-Immirzi parameter γ is a parameter not relevant in the classical theory, it appears in front of a total derivative term in the Lagrangian and does not contribute to the classical equations of motion. But it is important in the quantum theory, because it influences eigenvalues of certain operators (e.g. the area and the volume operator) [61, 138, 224]. One can fix the Barbero-Immirzi parameter (to a non-vanishing value) if one compares the entropy of a black hole calculated by Bekenstein and Hawking with the according value calculated in LQG [50]. It can be concluded that spin-foam models must implement a Barbero-Immirzi parameter $\gamma \neq 0$ to produce the correct results.

A new model originating from the EPR model and taking into account a finite Barbero-Immirzi parameter γ was proposed by J. Engle, E. Livine, R. Pereira and C. Rovelli [155] and is denoted as *EPRL-model* according to the names of this authors. Furthermore this model can be used in Euclidean and Lorentzian spacetimes. A similar model was proposed in Ref. [176]. In the Euclidean case, which is the case we use in the following, the underlying group of the spin foam is $\text{Spin}(4) = \text{SU}(2) \times \text{SU}(2)$, the double cover of $\text{SO}(4)$, where the different unitary representations can be labeled by two half integers k^+ and k^- . In the Lorentzian case the underlying group is $\text{Spin}(3, 1) = \text{SL}(2, \mathbb{C})$, where the unitary representations can be labeled by a positive integer and a real number.

Consider a vertex which is dual to a four-simplex, and denote by i_a the intertwiners assigned to the five 3-simplices dual to the edges, and by k_{ab} the ten group representations assigned to the 2-simplices dual to the faces, where k_{ab} is incident with the intertwiners i_a and i_b . In the EPRL model the amplitude of this vertex is given by⁹

$$A_{v,\gamma}(\vec{k}, \vec{i}) = \sum_{i_1^+, \dots, i_5^+} \sum_{i_1^-, \dots, i_5^-} 15j(\vec{k}^-; \vec{i}^-) 15j(\vec{k}^+; \vec{i}^+) \prod_a \int_{i_a^- i_a^+}^{i_a}(\vec{k}) \quad (6.5)$$

Here $k_{ab}^\pm := |1 \pm \gamma| k_{ab} / 2$ with Barbero-Immirzi parameter γ , and i^\pm are summation indices. For the Wigner $15j$ symbol one has to use the combination

$$15j(\vec{k}^\pm; \vec{i}^\pm) = 15j(k_{12}^\pm, k_{13}^\pm, k_{14}^\pm, k_{15}^\pm, k_{23}^\pm, k_{24}^\pm, k_{25}^\pm, k_{34}^\pm, k_{35}^\pm, k_{45}^\pm; i_1^\pm, i_2^\pm, i_3^\pm, i_4^\pm, i_5^\pm) \quad (6.6)$$

Note that a non-vanishing Barbero-Immirzi parameter γ imposes some selection rules on the k_{ab} . Since $k_{ab}^\pm \in \mathbb{Z}/2$ it follows that $(1 \pm \gamma)k_{ab} \in \mathbb{Z}$.

⁹ For simplicity reasons here and in the course of this section we do not give the boundaries of the sums. In all cases these are given by certain selection rules for the quantum numbers used as summation index that can be easily implemented.



This implies that for a rational $\gamma = \gamma_n/\gamma_d$ with γ_n and γ_d prime one can only choose $k_{ab} \in \gamma_d \cdot \mathbb{Z}$. The fusion coefficients $f_{i^+i^-}^i$ are defined as [8]

$$f_{i^+i^-}^i(k_1, k_2, k_3, k_4) := (-1)^{k_1 - k_2 + k_3 - k_4} \sqrt{(2i+1)(2i^+ + 1)(2i^- + 1)} \prod_{a=1}^4 \sqrt{2k_a + 1} \left\{ \begin{matrix} k_1^- & i^- & k_2^- \\ k_1^+ & i^+ & k_2^+ \\ k_1 & i & k_2 \end{matrix} \right\} \left\{ \begin{matrix} k_3^- & i^- & k_4^- \\ k_3^+ & i^+ & k_4^+ \\ k_3 & i & k_4 \end{matrix} \right\}, \tag{6.7}$$

where one has to use the four spins k_{ab} or k_{ba} as arguments for the fusion coefficient f of the intertwiner i_a , and $\{\bullet\}$ are Wigner $9j$ symbols. Details about the Wigner $15j$ and $9j$ symbol can be found in Sec. 6.2.2.

The amplitudes Eq. (6.5) are defined for one vertex of the spin foam, which corresponds to one 4-simplex of the dual triangulation. For a whole spin foam, the amplitude is given as a specialization of the general amplitude (6.4) by

$$A_\gamma = \sum_{k_f i_e} \prod_{\text{faces } f} (2k_f + 1) \prod_{\text{vertices } v} A_{v,\gamma}(k_f, i_e), \tag{6.8}$$

where the sum runs over all internal group representations k_f associated with the faces f , and all internal intertwiners associated with the edges e .

One of the aims of this project is to calculate the change of the amplitude if one considers a coarsening step of the triangulation. For the four-dimensional spacetime this is a $(5 \rightarrow 1)$ -Pachner move that removes a 0-simplex and transform five 4-simplices into one 4-simplex. We state here exactly how to calculate the amplitude according to Eq. (6.8). Therefor we consider as an example the move of the 4-simplices

$$\{01235, 01245, 01345, 02345, 12345\} \rightarrow \{01234\},$$

which induces the replacement

$$\left(\begin{matrix} \underbrace{0123}_{i_1}, \underbrace{0124}_{i_2}, \underbrace{0134}_{i_3}, \underbrace{0234}_{i_4}, \underbrace{1234}_{i_5} \\ \underbrace{0125}_{j_0}, \underbrace{0135}_{j_1}, \underbrace{0145}_{j_2}, \underbrace{0235}_{j_3}, \underbrace{0245}_{j_4} \\ \underbrace{0345}_{j_5}, \underbrace{1235}_{j_6}, \underbrace{1245}_{j_7}, \underbrace{1345}_{j_8}, \underbrace{2345}_{j_9} \end{matrix} \right) \rightarrow \left\{ \underbrace{0123}_{i_1}, \underbrace{0124}_{i_2}, \underbrace{0134}_{i_3}, \underbrace{0234}_{i_4}, \underbrace{1234}_{i_5} \right\}$$

for the 3-simplices (tetrahedra), where i_a are the fixed external intertwiners and j_b are the internal intertwiners that are summed associated with the



tetrahedra, and the replacement

$$\left\{ \begin{array}{c} \underbrace{012}_{k_{12}}, \underbrace{013}_{k_{13}}, \underbrace{014}_{k_{23}}, \underbrace{023}_{k_{14}}, \underbrace{024}_{k_{24}} \\ \underbrace{034}_{k_{34}}, \underbrace{123}_{k_{15}}, \underbrace{124}_{k_{25}}, \underbrace{134}_{k_{35}}, \underbrace{234}_{k_{45}} \\ \underbrace{015}_{l_{012}}, \underbrace{025}_{l_{034}}, \underbrace{035}_{l_{135}}, \underbrace{045}_{l_{245}}, \underbrace{125}_{l_{067}} \\ \underbrace{135}_{l_{168}}, \underbrace{145}_{l_{278}}, \underbrace{235}_{l_{369}}, \underbrace{245}_{l_{479}}, \underbrace{345}_{l_{589}} \end{array} \right\} \rightarrow \left\{ \begin{array}{c} \underbrace{012}_{k_{12}}, \underbrace{013}_{k_{13}}, \underbrace{014}_{k_{23}}, \underbrace{023}_{k_{14}}, \underbrace{024}_{k_{24}} \\ \underbrace{034}_{k_{34}}, \underbrace{123}_{k_{15}}, \underbrace{124}_{k_{25}}, \underbrace{134}_{k_{35}}, \underbrace{234}_{k_{45}} \end{array} \right\}$$

for the 2-simplices (triangles), where k_{ab} are the external spins and l_{cde} are the internal spins that are traced out associated with the triangles. Note that l_{cde} indicates that this spin (triangle) is incident with the intertwiners (tetrahedra) j_c , j_d and j_e , where k_{ab} indicates that this spin is incident with the intertwiners i_a and i_b and another intertwiner j_e that is not specified in the indices. The resulting amplitudes for five maximal simplices (vertices of the dual graph) are then

$$A_{v,\gamma}^{01235}(k_{12}, k_{13}, k_{14}, k_{15}, l_{012}, l_{034}, l_{067}, l_{135}, l_{168}, l_{369}; i_1, j_0, j_1, j_3, j_6) \quad (6.9a)$$

$$A_{v,\gamma}^{01245}(k_{12}, k_{23}, k_{24}, k_{25}, l_{012}, l_{034}, l_{067}, l_{245}, l_{278}, l_{479}; i_2, j_0, j_2, j_4, j_7) \quad (6.9b)$$

$$A_{v,\gamma}^{01345}(k_{13}, k_{23}, k_{34}, k_{35}, l_{012}, l_{135}, l_{168}, l_{245}, l_{278}, l_{589}; i_3, j_1, j_2, j_5, j_8) \quad (6.9c)$$

$$A_{v,\gamma}^{02345}(k_{14}, k_{24}, k_{34}, k_{45}, l_{025}, l_{035}, l_{235}, l_{045}, l_{245}, l_{589}; i_4, j_3, j_4, j_5, j_9) \quad (6.9d)$$

$$A_{v,\gamma}^{12345}(k_{15}, k_{25}, k_{35}, k_{45}, l_{067}, l_{168}, l_{369}, l_{278}, l_{479}, l_{589}; i_5, j_6, j_7, j_8, j_9) \quad (6.9e)$$

We want to calculate the amplitude A_γ

$$A_\gamma(\vec{k}, \vec{i}) = \sum_{\vec{l}, \vec{j}} \prod_f (2l_f + 1) \prod_v A_\gamma^{(v)}(\vec{k}, \vec{l}; \vec{i}, \vec{j}) \quad (6.10)$$

of the spin foam consisting of the dual objects of the five simplices in order to compare with the single vertex amplitude $A_{v,\gamma}(\vec{k}, \vec{i})$ as defined in Eq. (6.5) to later be able to quantify the effect of coarsening on the model.

6.2.2 Clebsch-Gordan coefficients and 3nj-symbols

In the previous section we saw that the spin foam amplitudes in the EPRL model are closely related with Wigner 3nj-symbols. In this section we state the definition of the necessary symbols based on the notions of the coupling of quantized angular momenta.



Clebsch-Gordan coefficients describe how to couple two angular momenta together to a third angular momentum. They are the matrix elements of the unitary transformation from the product basis of the two angular momenta to the eigenbasis of the total angular momentum

$$\underbrace{|j, m, j_1, j_2\rangle}_{\text{eigenbasis}} = \sum_{m_1, m_2} \underbrace{|j_1, m_1; j_2, m_2\rangle}_{\text{product basis}} \underbrace{\langle j_1, m_1; j_2, m_2 | j, m, j_1, j_2\rangle}_{\text{Clebsch-Gordan coeff.}}$$

The $3j$ -symbols can be viewed as a more symmetric version of the Clebsch-Gordan coefficients, they describe a coupling of three angular momenta j_1 , j_2 and j_3 to a vanishing angular momentum. They are defined in terms of the Clebsch-Gordan coefficients as

$$\begin{pmatrix} j_1 & j_2 & j_3 \\ m_1 & m_2 & m_3 \end{pmatrix} := \frac{(-1)^{j_1-j_2+m_3}}{\sqrt{2j_3+1}} \langle j_1, m_1; j_2, m_2 | j_3, -m_3, j_1, j_2 \rangle$$

Wigner $6j$ -symbols relate the three different possibilities to couple three spins. One couples first two of the three spins, and the joint spin is coupled with the remaining spin. The $6j$ -symbols mediate between the three different coupling possibilities. The important fact is that they can be defined directly or as sum of $3j$ symbols.

$$\begin{Bmatrix} j_1 & j_2 & j_3 \\ j_4 & j_5 & j_6 \end{Bmatrix} := \sum_{\text{all } m} (-1)^S \begin{pmatrix} j_1 & j_2 & j_3 \\ m_1 & m_2 & -m_3 \end{pmatrix} \begin{pmatrix} j_1 & j_5 & j_6 \\ -m_1 & m_5 & m_6 \end{pmatrix} \begin{pmatrix} j_4 & j_2 & j_6 \\ -m_4 & -m_2 & -m_6 \end{pmatrix} \begin{pmatrix} j_4 & j_5 & j_3 \\ m_4 & -m_5 & m_3 \end{pmatrix}$$

Of the 6 angular momenta in the symbol three are the total quantum numbers for the original momenta, one is the resulting total angular momentum, and two are the two different coupled intermediate angular momenta from the different schemes. Due to the selection rules of the underlying $3j$ -symbols the summation of the six dependent m can be reduced to a summation of three independent m .

Similar to the $6j$ -symbol, one can also calculate $3nj$ -symbols which correspond to coupling schemes of a higher number of angular momenta. All of these symbols can be reduced to symbols of smaller kind, so a recursive calculation is possible. For the EPRL model the $15j$ and the $9j$ symbol are important, because these two are used in the definition of the vertex amplitude (the latter one in the fusion constants). The $9j$ symbol can be



expressed in terms of $6j$ symbols

$$\left\{ \begin{matrix} j_1 & j_2 & j_3 \\ j_4 & j_5 & j_6 \\ j_7 & j_8 & j_9 \end{matrix} \right\} = \sum_i (2i+1)(-1)^{2i} \left\{ \begin{matrix} j_1 & j_2 & j_3 \\ j_6 & j_9 & i \end{matrix} \right\} \left\{ \begin{matrix} j_4 & j_5 & j_6 \\ j_2 & i & j_8 \end{matrix} \right\} \left\{ \begin{matrix} j_7 & j_8 & j_9 \\ i & j_1 & j_4 \end{matrix} \right\} \quad (6.11)$$

but it is also possible to express it directly in terms of binomial coefficients [414, 415]. Also the higher and thus the $15j$ -symbol can be expressed in terms of $3j$ -symbols [431],

$$\begin{aligned} & 15j(k_{12}, k_{13}, k_{14}, k_{15}, k_{23}, k_{24}, k_{25}, k_{34}, k_{35}, k_{45}; i_1, i_2, i_3, i_4, i_5) = \\ & = \sum_{a_i=-k_i}^{k_i} (-1)^m \sum (k_m - a_m) \begin{bmatrix} k_{15} & k_{14} & k_{13} & k_{12} \\ a_{15} & a_{14} & a_{13} & a_{12} \end{bmatrix}_{i_1} \begin{bmatrix} k_{12} & k_{25} & k_{24} & k_{23} \\ -a_{12} & a_{25} & a_{24} & a_{23} \end{bmatrix}_{i_2} \\ & \cdot \begin{bmatrix} k_{23} & k_{13} & k_{35} & k_{34} \\ -a_{23} & -a_{13} & a_{35} & a_{34} \end{bmatrix}_{i_3} \begin{bmatrix} k_{34} & k_{24} & k_{14} & k_{45} \\ -a_{34} & -a_{24} & -a_{14} & a_{45} \end{bmatrix}_{i_4} \\ & \cdot \begin{bmatrix} k_{45} & k_{35} & k_{25} & k_{15} \\ -a_{45} & -a_{35} & -a_{25} & -a_{15} \end{bmatrix}_{i_5} \end{aligned}$$

with $[\bullet]$ being defined as

$$\begin{aligned} \begin{bmatrix} k_1 & k_2 & k_3 & k_4 \\ a_1 & a_2 & a_3 & a_4 \end{bmatrix}_i & := \sqrt{2i+1}(-1)^{i-a_1-a_2} \\ & \cdot \begin{pmatrix} k_1 & k_2 & i \\ a_1 & a_2 & -a_1 - a_2 \end{pmatrix} \cdot \begin{pmatrix} i & k_3 & k_4 \\ a_1 + a_2 & a_3 & a_4 \end{pmatrix}, \end{aligned}$$

but a representation in terms of binomial coefficients is not known in general.

6.2.3 Calculation time of $3nj$ -symbols

The amplitude of a single vertex $A_{v,\gamma}$ within the EPRL-model is given by a summation over $15j$ -symbols and fusion coefficients f , which are basically $9j$ -symbols. The previous section explained that all of these higher order symbols can be expressed in terms of the elementary $3j$ -symbols. So for an efficient calculation of the vertex amplitudes it is necessary to calculate $3j$ -symbols fast.

In principle there are two options for a fast calculation: One can pre-calculate and store all necessary $3j$ -symbols, or one can calculate them directly whenever they are needed in the calculation. Which option is faster depends on how often a single $3j$ -symbol is used in the calculation, as a



rule of thumb one should use the pre-calculation if every symbol is needed on average more than once in the calculations.

For an efficient storage scheme one has to take into account the symmetries of the $3j$ -symbol to avoid calculating and storing the same symbol twice. The $3j$ -symbol is e.g., invariant up to a sign under permutations of the rows

$$\begin{pmatrix} j_{\pi(1)} & j_{\pi(2)} & j_{\pi(3)} \\ m_{\pi(1)} & m_{\pi(1)} & m_{\pi(3)} \end{pmatrix} = \text{sgn}[\pi]^{j_1+j_2+j_3} \cdot \begin{pmatrix} j_1 & j_2 & j_3 \\ m_1 & m_2 & m_3 \end{pmatrix},$$

where π is a permutation. Furthermore it is invariant under the change of the sign of the lower row up to a sign

$$\begin{pmatrix} j_1 & j_2 & j_3 \\ -m_1 & -m_2 & -m_3 \end{pmatrix} = (-1)^{j_1+j_2+j_3} \cdot \begin{pmatrix} j_1 & j_2 & j_3 \\ m_1 & m_2 & m_3 \end{pmatrix}.$$

Note that due to selection rules of the angular momentum coupling always $m_1+m_2+m_3 = 0$, otherwise the $3j$ -symbol is 0. These three facts can be used for storing only symbols with $j_1 \geq j_2 \geq j_3$, $m_1 \geq 0$ and $m_3 = -m_1 - m_2$.

Several calculation schemes for $3j$ -symbols were tested for their speed for the range of desired quantum numbers. It turns out that using the representation of the $3j$ -symbols in terms of binomial coefficients [181] is the fastest method for calculating the $3j$ -symbols. Therefore it is necessary that the binomial coefficients can be calculated efficiently. One can use tabulated binomial coefficients as in the GNU Scientific Library (GSL) [181], which stores and uses all binomial coefficients for $n \leq 25$, larger coefficients have to be calculated using the definition. Another possibility is to use a recursion formula [414] for the binomial coefficients, which allows to calculate $3j$ -symbols at high quantum numbers much faster than the standard GSL-function (for $j_{\max} = 250$ there is a speedup of approximately one magnitude).

Tests calculating a huge number ($\approx 10^{10}$) of $3j$ -symbols and comparing the calculation time of the direct calculation with a look-up table showed that the initialization time

$$t_{\text{init}}[\text{s}] \approx (2.45 \pm 0.42) \cdot j_{\max}^{6.49 \pm 0.05} \quad (6.12)$$

for calculating the look-up table scales with a power law, but that the look-up time per symbol is slightly smaller than the direct calculation time (compare Fig. 6.5). This means that the look-up method is more efficient for small maximal angular momenta j_{\max} or for a large number of calculated $3j$ -symbols. In our example calculations for $j_{\max} \leq 20$ the look-up method is always faster if one calculates more than 10^{10} $3j$ -symbols. Since we are



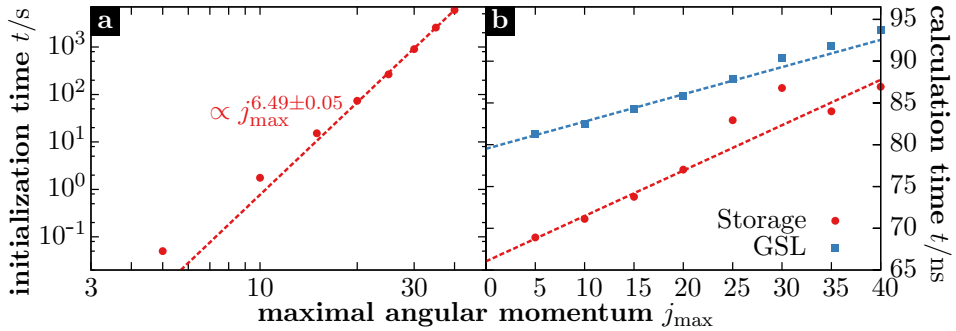


Figure 6.5: Calculation time of Wigner- $3j$ symbols.

(a) Initialization time (in seconds) of the necessary $3j$ -symbols in a storage scheme in terms of the maximal angular momentum j_{\max} . The initialization time scales approximately with a power law $\propto j_{\max}^{6.49 \pm 0.05}$. (b) Comparison for the calculation time per symbol for using a **storage scheme** and the **direct calculation using GSL** in terms of the maximal angular momentum j_{\max} . Both methods show approximately a linear increase with j_{\max} and a large offset.

interested mainly in the limit of small quantum numbers, we use the look-up method for the $3j$ -symbols. Note that for the calculations we explicitly used only those $3j$ -symbols that fulfill certain selection rules (e.g., that the sum $m_1 + m_2 + m_3$ vanishes, and that the triangle inequality for the j 's is fulfilled). If one would use random numbers for all entries, the calculation time would decrease drastically, because the match of the selection rules can be checked fast.

For calculations of the EPRL vertex amplitude $A_{v,\gamma}$ according to Eq. (6.5) the relevant Wigner symbols are the $15j$ -symbol and the $9j$ -symbol, where the latter is needed for the calculation of the fusion coefficients (6.7). There are two relevant methods for calculation the $9j$ -symbol: On the one hand one can express the $9j$ -symbol in terms of sums of $6j$ -symbols and hence in terms of sums of $3j$ -symbols. The other possibility is to use a formulation of the $9j$ -symbol in terms of binomial coefficients [414]. In both cases the underlying basic objects, the binomial coefficient and the $3j$ -symbol, can be calculated in advance and be stored in a look-up table. For the limit of low angular momenta our calculations show that the second method, using binomial coefficients, is more efficient than the usage of the $3j$ -symbols.

For the $15j$ -symbol one has to use the calculation method in terms of lower order Wigner symbols, because no direct calculation in term of binomial coefficients is known. In Fig. 6.6 the calculation time of random $15j$ -symbols is displayed in terms of the number of calculated symbols. As expected one



Figure 6.6: Calculation time of Wigner-15j symbols.

Time (in hours) for the calculation of random 15j symbols in terms of the number of calculated symbols. The colors encode different maximal values of the angular momenta used in the symbols. Inset: Calculation time per symbol (in seconds) in terms of the maximal angular momentum used.

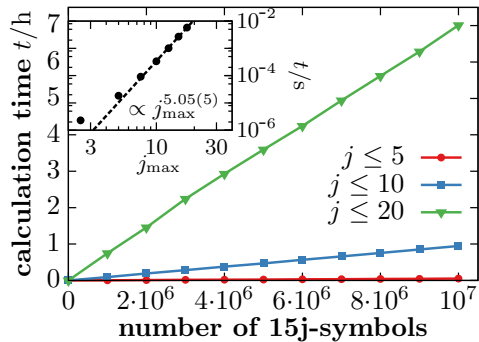
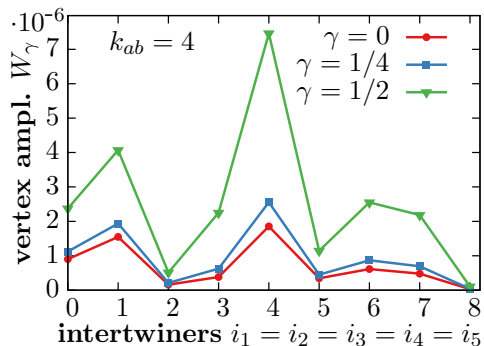


Figure 6.7: Vertex amplitude $A_{v,\gamma}$ of the EPRL-model for fixed spins $k_{ab} = 4$ in terms of the intertwiners i for different Immirzi parameters γ . Note that we chose equal values $i_a = i$ for all intertwiners.



finds a linear behavior, where the slope determines the calculation time per symbol. This calculation time per symbol scales as

$$t \propto j_{\max}^{5.05 \pm 0.05} \quad (6.13)$$

in terms of the maximal angular momentum used, which shows that direct calculations are really only feasible for small quantum numbers.

6.2.4 Small angular momentum vertex amplitudes in the EPRL-model

The numerical tests of the previous section allowed us to identify efficient calculation schemes for $15j$ and $9j$ -symbols, which are the building blocks of the vertex amplitude (6.5) of the EPRL model. In this section we apply these results to actually calculate vertex amplitudes of certain spin configurations, and finally consider convergence in the renormalization step of the EPRL model.

We first consider the amplitude of an EPRL vertex, where all angular momenta are equal to $k_{ab} = 4$ and where all quantum numbers of the



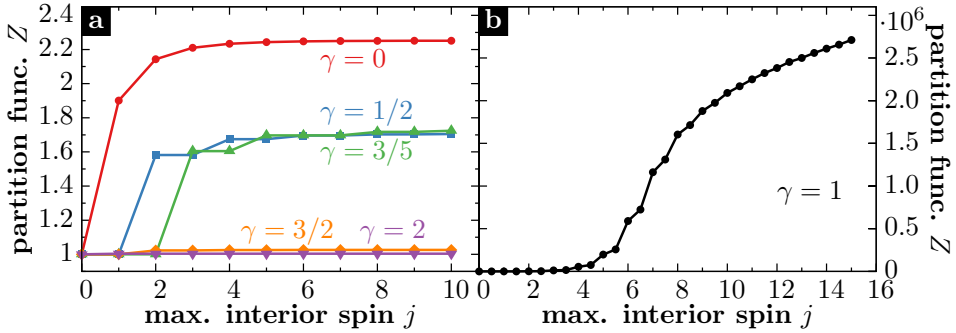


Figure 6.8: Partition function of coarsening step.

Partition function Z of the EPRL-model for a refinement step (summing over all interior degrees of freedom), in terms of the maximal quantum number j used for the interior degrees of freedom. (a) Convergent behavior for Immirzi parameter $\gamma \neq 1$. (b) Divergent behavior for Immirzi parameter $\gamma = 1$.

intertwiners are equal, in terms of these intertwiner quantum numbers for different values of the Barbero-Immirzi parameter γ . The results of our calculations are shown in Fig. 6.7. For all γ the amplitude A_γ has its maximal value if $i_c = k_{ab}$, and the absolute value of the amplitude grows for all values of the intertwiner spin with increasing Barbero-Immirzi parameter. In the underlying bachelor's thesis [145] several other spin configurations were considered.

The last step is to calculate the amplitude of the renormalization steps and ask for their convergence. We consider here only the simplest case where all external spin degrees of freedom are set to 0, and we sum over the internal spins or degrees of freedom and divide the resulting amplitude by the amplitude $A_{v,\gamma}(\vec{0}; \vec{0}) = 1$ of the single vertex. The results of our calculations are shown in Fig. 6.8a for Immirzi parameter $\gamma \neq 1$ and in Fig. 6.8b for $\gamma = 1$. In both cases the total amplitude A_γ is plotted in terms of the maximal values of the interior spins, which are a necessary cutoff due to limited computation time. In all considered cases where $\gamma \neq 1$ the total amplitude converges already for small cutoffs, whereas for $\gamma = 1$ no convergence can be seen in the considered interval, and the partition function is quantitatively much larger than for the other γ at equal cutoffs (by six orders of magnitude). This is in agreement with Ref. [155] and can be understood intuitively by considering the vertex amplitude (6.7), for $\gamma = 1$ all spins k_{ab}^- are degenerated and equal to 0, which probably leads to a break down of the model. Results for other external spins and the necessary calculation time for the partition functions can be found in [145].



Our research about spin foam amplitudes is surely only one step towards numerically calculating spin foam amplitudes for small quantum numbers, but it is promising to extend the research into this direction. First one has to optimize the calculation of the single vertex amplitudes $A_{v,\gamma}$ as defined in Eq. (6.5). Therefor some importance sampling method can be suited, where one calculates only the summands in Eq. (6.5) which contribute most to the amplitude $A_{v,\gamma}$. Alternatively one has to examine some heuristics about the contribution of the single summands to the actual amplitude to be able to neglect unimportant summands. With this improved calculation technique one can then try to calculate perturbative expansions (similar to Feynman diagrams) by considering more and more complicated spin foams mediating between two boundary spin networks. The considered coarsening step would be something like a first order correction to the spin foam displayed in Fig. 6.4. Furthermore it can be promising to use the considered coarsening step to calculate renormalization group flows in order to find the continuum limit of spin foam models, but note that it is highly non-trivial to even find a set of Pachner moves that transform a 4-triangulation into the simplest triangulation of the given manifold, perhaps even impossible (consider the general remarks about ergodicity of triangulations in Sec. 4).



6.3 Software developed within this thesis

In this short section we give an overview of the software that was developed for this thesis and that was used for doing the numerical simulations that lead to the data presented. This section should not be an exhaustive technical documentation of the usage of the software, but rather a short overview about the concepts that were used and how they relate to the properties of the underlying physical structures. For the technical details we refer to the documentation of the respective software.

The section will consist of the description of the following two parts:

- **mocasinn**s: Generic template library for Markov chain Monte Carlo simulations on arbitrary, user-defined systems
- **mocatrin**d: Library for representing different types of triangulations on the computer, to be used together with the **mocasinn**s template library

Two other smaller packages that were developed during this thesis are **resampling**¹⁰, which is a python scripts that can be used for doing Jackknife and Bootstrap resampling for arbitrary data sets, and **gnuplot_utils**¹¹, which provides a compilation of scripts for using with gnuplot.

6.3.1 The generic MCMC library **mocasinn**s

To use the various Monte Carlo algorithms that were introduced in Sec. 2.2 within several applications, in principle there needs to be one program for every combination of a system and an algorithm. This approach is of course unsuitable, because it leads to code duplication for both the code modeling the system and the Monte Carlo algorithms. Changes in the system properties must be managed and provided to all different programs. Additionally each user interested in the properties of a certain system must write the code for the Monte Carlo simulation on its own, being perhaps only an expert in the system he wants to study numerically, and not an expert in Monte Carlo simulations. He wastes his time writing code that actually exists, but is hidden in and interwoven with code describing other systems.

A common solution to such problems is using an available program or library. There are several projects for doing Markov chain Monte Carlo

¹⁰<https://github.com/bkrueger/resampling>

¹¹https://github.com/bkrueger/gnuplot_utilities



(MCMC) simulations on different systems: The **ALPS** (Algorithms and Libraries for Physics Simulations) library [68] contains code for classical Metropolis simulation of Ising, Heisenberg, XY and Potts spin systems as well as several implementations of Quantum Monte Carlo algorithms. The **GSL** (GNU scientific library) [181] contains algorithms for Monte-Carlo integration of multidimensional functions and cannot be used for usual problems in statistical physics. The **SMCTC** (Sequential Monte Carlo Template Class) library [231] is a template library applicable for sequential Monte Carlo that is used mainly in particle tracking and signal processing, there are also the projects **PyMC** [324] and **BUGS/WinBUGS** [284] that are special packages for Bayesian data analysis. All considered libraries or programs are designed only for simulating only one or at best a few similar systems.

It is not possible to write a standard pre-compiled library for doing Markov chain Monte Carlo (MCMC) simulations on arbitrary systems, because the MCMC code and the system code must interact at various places. The generic template library **mocasinns** we will present in this section addresses the described problems for MCMC simulations. We made the observation that a lot of physical systems can be described in terms of a common interface, and that most MCMC simulations just need the data provided by this interface. By writing a generic library that demands just this simple common interface, but provides a rich choice of simulation algorithms, analysis tools and data management, we give the user a *one-fits-all* solution for applying modern MCMC algorithms on his problem without the need to write Monte Carlo code on its own..

The **mocasinns** library is also designed for an an easy expandability, it is possible for the user to write own MCMC algorithms, random number generators or utility classes and use them within the **mocasinns** framework. So **mocasinns** can also be used as a test and benchmark for new algorithms. The **mocasinns** library has very little dependencies, the only foreign library that is needed is the well-known and commonly used **boost** library (and the unit-testing framework **CPPUnit**, which is only used for testing **mocasinns** and not needed by the user). The whole code is clean and well-documented and can be used as a reference implementation of the presented MCMC algorithms.

Examples for every algorithm and utility class are provided as well as an extensive tutorial to make the learning process easy. The code is documented using the Doxygen documentation tool to create an online version of the manual. Nevertheless should users of the library at least be partially familiar with the concept of template programming in C++.



Common features of systems treated with Markov chain Monte Carlo algorithms

In this section we extract similarities of systems which can be treated numerically using Markov chain Monte Carlo algorithms. Based on this similarities we develop the interface of two classes representing states of these systems and steps between the states for use in `mocasimns`. Therefore we consider three different examples for physical systems that can be treated with Monte Carlo simulations

1. Ising-like spin systems with nearest neighbor interaction:
2. Canonical simulations of particles interacting according to a Lennard-Jones potential
3. Grand-canonical simulations of hard spheres in a confinement

We consider additionally the traveling salesman problem, where a shortest path can be found by a simulated annealing procedure, to show that the introduced notions are not limited to physics. Now the question arises: What are the common features of this systems?

States and steps between states The considered systems all exhibit a notion of *state*, which is natural since we are mainly interested in problems of statistical physics. In the Ising system a state is the set of the directions of all spins. For the Lennard-Jones fluid and the grand-canonical hard spheres the state is the tuple of the coordinates of the single particles or spheres. For the traveling salesman problem a state is a permutation of the cities which gives the order of the visits. We will denote a single state as ω and the set of all states as Ω .

Since we consider Markov chain Monte Carlo algorithms, for each system there is the notation of a *step* that connects two different system states. These steps must be ergodic, i.e. that every state can be reached from every other state by a finite number of steps. In the example of the Ising lattice a step is changing the direction of a single spin (spin flip), in the Lennard-Jones case a step is a small move of the coordinates of one single particle, for the grand-canonical hard spheres a step is given by the insertion or the removal of a certain hard sphere, and for the traveling salesman problem a step is an interchange of two cities in the visiting sequence. We will denote a step that leads from state ω_1 to ω_2 as $\omega_1 \rightarrow \omega_2$.



Energy (difference) of states and steps Each system defines something like a (generalized) energy and a (generalized) inverse temperature that will be used for calculating average values

1. For the Ising-like spin-systems the energy is given by:

$$E = -J \sum_{\langle i,j \rangle} \sigma_i \sigma_j$$

where $\langle i, j \rangle$ indicates the summation over pairs of next neighbor spins σ_i and σ_j , and where J is the coupling constant. For the standard Ising system one chooses $\sigma = \pm 1$.

2. For the Lennard-Jones fluid the energy is given by

$$E = \sum_{i < j} \phi(|\vec{x}_i - \vec{x}_j|) \quad \phi(x) = 4\epsilon \left[\left(\frac{\sigma}{x} \right)^6 - \left(\frac{\sigma}{x} \right)^{12} \right]$$

where $\phi(x)$ is the Lennard-Jones potential with parameters σ and ϵ that depends on the distance $|\vec{x}_i - \vec{x}_j|$ of the particles i and j .

3. For the grand-canonical hard sphere system the actual energy of the system is either 0 (if all spheres are separate) or ∞ (if there are overlapping spheres), so it makes no sense to use the actual energy as energy for the Monte Carlo simulations. Instead one can choose the number N of particles as the energy, the generalized inverse temperature is here the chemical potential μ .
4. For the traveling salesman problem the energy is the total length of the path, which is the sum of the distances between cities that are neighbors in the visiting sequence.

Since a step changes the state of the systems, it changes its energy, too. So one can associate with each step a change in the energy with we will denote by ΔE . For performance reasons it is desirable that ΔE can be calculated locally, so that the energy of the system does not need to be recalculated. Suppose in the Ising-like spin system a step $\omega_1 \rightarrow \omega_2$ consists of a change in the spin i from σ_i to σ'_i . The energy difference induced by this flip is then given by

$$\Delta E(\omega_1 \rightarrow \omega_2) = E(\omega_2) - E(\omega_1) = J (\sigma_i - \sigma'_i) \sum_{j \in \text{NN}(i)} \sigma_j$$



The change of the energy in a Lennard-Jones fluid induced by a step moving a particle $\vec{x}_i \rightarrow \vec{x}_i + \Delta\vec{x}_i$ can be calculated as

$$\Delta E = \sum_{j \neq i} [\phi(|\vec{x}_i + \Delta\vec{x}_i - \vec{x}_j|) - \phi(|\vec{x}_i - \vec{x}_j|)]$$

For the grand-canonical hard sphere system the calculation of the energy difference is simple. Since we interpret the total number of spheres as energy, the change is $\Delta N = \pm 1$ depending on whether the step inserts or deletes a sphere. For the traveling salesman the change in the travel distance can be calculated by only considering the distances between the cities interchanged in the steps and their precursors and successors.

Step selection probability There are two further common properties of Monte Carlo steps that do not appear in every system setup. In Markov chain Monte Carlo simulations one usually splits the probability $P(\omega_1 \rightarrow \omega_2)$ for doing a step $\omega_1 \rightarrow \omega_2$ into the probability $S(\omega_1 \rightarrow \omega_2)$ for selecting this step and the probability $A(\omega_1 \rightarrow \omega_2)$ for accepting the step, so that the detailed balance condition becomes:

$$\frac{P(\omega_1 \rightarrow \omega_2)}{P(\omega_2 \rightarrow \omega_1)} = \frac{S(\omega_1 \rightarrow \omega_2) \cdot A(\omega_1 \rightarrow \omega_2)}{S(\omega_2 \rightarrow \omega_1) \cdot A(\omega_2 \rightarrow \omega_1)} = P_{\text{MC}}(\omega_1, \omega_2)$$

where $P_{\text{MC}}(\omega_1, \omega_2)$ is a probability that depends on the two states ω_1 and ω_2 and that is given by the Monte Carlo algorithm used. One then has to choose the acceptance probability such that the detailed balance condition is fulfilled:

$$\frac{A(\omega_1 \rightarrow \omega_2)}{A(\omega_2 \rightarrow \omega_1)} = P_{\text{MC}}(\omega_1, \omega_2) \left(\frac{S(\omega_1 \rightarrow \omega_2)}{S(\omega_2 \rightarrow \omega_1)} \right)^{-1}$$

where the right hand side is a common choice for the acceptance probability to fulfill the detailed balance condition.

For the Ising system the selection probability for each step is $S(\omega_1 \rightarrow \omega_2) = 1/N$, where N is the total number of spins, so the ratio of the selection probabilities is always 1. For other systems this is not necessarily the case. The selection probability for the grandcanonical spheres is $S(N \rightarrow N + 1) = V/(N + 1)$ for the insertion of a sphere and $S(N + 1 \rightarrow N) = 1/2(N + 1)$ for the removal of a sphere [1].

Executability of steps There are also systems where not every proposed step leads to a valid state. Consider, e.g., the system of grand-canonical



hard spheres with radius r . The algorithm can propose an insertion of a sphere at coordinates \vec{x} , so that $|\vec{x}_i - \vec{x}| < r$ for the coordinates \vec{x}_i of an already present sphere, but an actual insertion would lead to overlapping hard spheres, which is an invalid state. Not proposing this steps is difficult, because for getting a simple selection probability one has to sample uniformly the volume where a sphere can be inserted. So there should be the possibility for the user to provide a function to test whether a step is executable, which is in most cases easier to decide than to correct for this issue in the step selection. Since for a lot of systems every state is executable, the user should not be forced to provide such a function.

Serialization of the configuration Especially for long running simulations so-called checkpointing is convenient. This means that in regular intervals the status of the simulation is permanently stored to be able to continue the simulation if it stops expected or unexpected. Additionally, it is convenient to react directly on the signal input of the user or the operating system and store the current simulation state if the simulation ought to stop. The complete status of a simulation consists of both the current values of the simulation parameters and the current state of the simulated systems. So it should be possible for a user-defined system to store the actual state, but only as an optional feature.

Complete list of all steps For almost all Markov chain Monte Carlo simulations a rejection-free version can be defined to avoid situations where the system is in a certain, preferred state for a lot of steps. In the rejection-free versions one needs the acceptance probabilities of all possible steps to calculate the average time the system is trapped in a state and to decide which step will be executed after this average time. As a consequence, in order to do rejection-free simulations within `mocasimns` the user defined configuration needs a possibility to propose not one random, but all possible steps.

Requirements for user-defined systems and steps Based on the common properties of systems used in Monte Carlo simulations, we demand that a class representing the current state of a system to expose the following interface for using it in `mocasimns`:

- `EnergyType energy()`: Calculates the current energy of the system



- `StepType propose_step(RNG* rnd)`: Creates a step originating from the actual state of the system into another state. Gets a random number generator as parameter to create random and not deterministic steps.
- `std::vector<StepType> all_steps()` (optional): Returns list with all steps that are possible from the current state of the system. This functions needs to be implemented if rejection-free algorithms should be used.
- `vector<StepType> all_steps()` (optional): Returns all possible steps originating from the actual state of the system. This function is only needed if using rejection-free versions of the algorithms.
- `void serialize()` (optional): Method for serializing the system using boost serialization.

The class representing a step between two states of the system should expose the following interface

- `EnergyType delta_E()`: Function that calculates the energy difference induced by the step.
- `void execute()`: Executes the step and changes the current state of the system.
- `double selection_probability_factor()` (optional): Calculates the ratio of the selection probabilities

$$S(\omega_1 \rightarrow \omega_2)/S(\omega_2 \rightarrow \omega_1)$$

- `bool is_executable()` (optional): Decides whether the step $\omega_1 \rightarrow \omega_2$ leads to a valid state ω_2 .

Design of the library

Based on the observation of the previous section, we concluded that for writing a template library that can be used for MCMC simulations on arbitrary systems, this library may only interact with the system trough the few well-defined functions. We also examined the structure of the various types of MCMC simulations and found that each can be mapped on one of the following procedures for doing steps. For standard MCMC simulations one step can be described as



1. Being at state ω_i , propose a certain step $\omega_i \rightarrow \omega_j$ and test whether the step is executable. If the step is not executable, handle the step as a rejected step (e.g., increment the histograms in a Wang-Landau simulation) and propose another step.
2. If the step is executable, calculate the ratio of selection probabilities S_{ij} , with

$$S_{ij} := \frac{S(\omega_i \rightarrow \omega_j)}{S(\omega_j \rightarrow \omega_i)}$$

3. Calculate the ratio of acceptance probabilities P_{ij} , which is given by the ratio $P(\omega_j)/P(\omega_i)$ of the sampled probability distributions at the respective states
4. Accept the step with probability

$$A_{ij} = \min \left(1, \frac{P_{ij}}{S_{ij}} \right).$$

Depending on the acceptance, handle the step as an accepted or rejected step.

For rejection free MCMC simulation, one step can be described as

1. Being at state ω_i , calculate the ratio of selection probabilities S_{ij} and the ratio of sampled probability distributions P_{ij} for each (executable) step $\omega_i \rightarrow \omega_j$ originating from the state ω_i .
2. Calculate the accumulated acceptance probability

$$A_i := \sum_{\omega_i \rightarrow \omega_j \text{ executable}} \min \left(1, \frac{P_{ij}}{S_{ij}} \right).$$

3. Calculate a random number p between 0 and A_i , and execute the step $\omega_i \rightarrow \omega_k$, where

$$\sum_{\substack{j < k \\ \omega_i \rightarrow \omega_j \text{ executable}}} \min \left(1, \frac{P_{ij}}{S_{ij}} \right) \leq p < \sum_{\substack{j < k+1 \\ \omega_i \rightarrow \omega_j \text{ executable}}} \min \left(1, \frac{P_{ij}}{S_{ij}} \right)$$

4. Handle the step as if one would have stayed A_i^{-1} times in the state i and then stepped to state k .



This means we can use a `Simulation` class that defines these two procedures for doing steps (and certain other helping features that are common to all simulations, e.g., the management of the random number generator), and to provide several algorithm classes that use these methods of simulations for doing steps. The algorithms then have to provide methods for calculating the ratio of the sampled probability distribution, and the methods for handling accepted and rejected steps. For example, the class for Metropolis simulations does only need to store the temperature and the times when to do measurements. In contrast, the class for Wang-Landau simulations has to store the density of states, the incidence histogram and the procedure how to decrease the modification factor.

These algorithm classes inherit from the class `Simulation` in order to provide the common functionality of all simulations, so to be able to access the methods of the different algorithms from the `Simulation` class one has to use the CRTP (curiously recurring template pattern). This implies that the `Simulation` class has the template signature

```
Simulation<Configuration, Step, RNG, Derived>
```

where `Configuration` and `Step` are the user-provided classes that represent a state of a system and the elementary steps between this states, and `RNG` is one of the random number generators provided by `mocasinnns`. The template parameter `Derived` corresponds then to the actual algorithm. As an example, the class for doing Metropolis simulations then has the template signature

```
Metropolis<Configuration, Step, RNG>  
: Simulation<Configuration, Step, RNG, Metropolis<...> >
```

and the class for Wang-Landau simulations has the template signature

```
WangLandau<Configuration, Step, EnergyType, Histogram, RNG>  
: Simulation<Configuration, Step, RNG, WangLandau<...> >
```

where the template parameters `Energy` and `Histogram` are needed for the additional stored histograms (e.g., to realize different binning procedures).

Some further design aspects

In this section we list some of the design patterns that are used in the `mocasinnns` library.



Providing parameters for the different algorithms Each of the implemented Monte-Carlo algorithms needs a different set of parameters. These parameters are gathered in a class `Parameters` that is a subclass of the respective algorithm class and that contains the parameters as public members. In the default constructor of this class reasonable values of the parameters are predefined. The meaning of the single parameter members is explained in the documentation of the class.

Exchange of information between algorithms and user code There are a lot of situations where a possible interaction between the template library and the user defined code is suitable to take place. E.g., one could desire to write a short output to the terminal at every measurement of a Metropolis Monte Carlo simulation. Additionally, the library code should be able to react on signals sent by the operating systems and for example save the actual simulation status if the simulation is terminated.

For those interactions between the template library and the user code `mocasinn`s uses the concept of signals from the boost signal library [195]. There are two kinds of signals used: Signals that are called by the simulation if certain checkpoints are reached, and signals that are called if a signal from the operating system was caught (these are the POSIX signals `SIGTERM`, `SIGUSR1` and `SIGUSR2`). For each of this signals the user can provide one or several functions that are executed if the signal is called. If the signal `SIGTERM` is recorded, the simulation terminates after executing the code linked to the handler. It is recommended to store all necessary data to continue the simulation later on. The two signals `SIGUSR1` and `SIGUSR2` can be used for example to output some information of the simulation on demand (e.g. simulation progress or actual value of some parameters or observables).

Checking the compliance of user provided classes As a generic template library that uses user-provided classes, `mocasinn`s relies on the them providing the correct interface. Template libraries are known to show cryptic compiler errors if the user provided template parameters do not fulfill the requirements for correct interface. To get human readable error messages for incorrect interfaces, the boost concept check library [368] is used for checking the user defined types. These concept checks are done at compile time so that the performance of the program is not influenced.

Beside the errors in the user code that can be detected at compile time (e.g., wrong return types, missing functions) there are logical requirements



that the user code has to fulfill. For example the result of `delta_E()` for a step must match the difference between the energies of the system after and before the step. These logical requirements can be tested using the class `Mocasinns::ConfigurationTest` that contains several test functions.

Checkpointing, storing intermediate and final results To be able to store the current state of the simulation (in case of planned or system induced breaks of the algorithm) the library uses the concepts of `boost serialization` [336]. So the current state of the library can be stored, e.g., reacting to a POSIX signal as described in 6.3.1 and reimplemented later on.

If the user defined configuration class is serializable, too (see 6.3.1 for the optional member functions), the serialization of the algorithm classes also includes the serialization of the actual configuration, so the simulation can be continued almost without further user input.

Optional function in user-provided code As stated before there are functions that can be provided by the user code, but are not required by the `mocasinns` library. These functions cannot be used in the algorithms of the library directly, because this would lead to a compilation error if there are no such functions in the user provided classes. So `mocasinns` has to inspect the user provided classes on whether they contain the functions and use a default value if this is not the case. The inspection of the classes is done with the boost type traits introspection library `boost::tti` [135], and wrapper functions returning a default value or the value of the function are defined using the SFINAE (substitution failure is not an error, [401]) construct `enable_if` [229] based on the results of `boost::tti`. Since the inspection of the classes is done at compile time, the runtime of the algorithms is not affected by this construction.

For the serialization this construction is not possible, since the boost serialization functionality can be provided as a free function outside of the class or as a private function, which would both not be recognized by `boost::tti`. Additionally the serialization function must be a template member function to deal with the different possible output formats (e.g., binary and text output), but `boost::tti` does not support the detection of template member functions. So if the user wants to enable the serialization functionality he has to define a static member function `is_serializable()`. Note that the return value of this function can determine whether to serialize the configuration space, but the existence of this function must imply the



existence of the serialization functionality, otherwise a compilation error will occur.

6.3.2 Triangulations on the computer with `mocatrind`

To use the generic library `mocasimns` with triangulation, another software library for doing MCMC simulations on triangulation implementing the necessary interface was developed within this thesis. This library is denoted as `mocatrind` (**M**onte-**C**arlo **t**riangulations in **n** dimensions), it tries to extract the common properties of the different types of triangulations and their flips considered in this thesis (embedded triangulations, topological triangulations, causal triangulations) into two common triangulation and flip classes to remove code duplication and increase the maintainability of the code. The functionality which is special to the certain types of triangulations and flips is included in certain classes that inherit from the two base classes and that later are used in the simulations.

There are already some existing libraries that can be used for working on triangulations. A widely used library is `CGAL` (**C**omputational **G**eometry **A**lgorithms Library, [114]), which can describe triangulations of point sets in arbitrary dimensions and provides a large set of algorithms for constructing triangulations of given point sets and calculating some related properties (Voronoi diagrams or convex hulls). This library is designed mainly for use in computational geometry, so there is no built-in support for topological triangulations, furthermore there is no concept of flips within this library. Another library that can be used for approximately the same purposes as `CGAL` is `GTS` (**G**NU **T**riangulated **S**urface library, [331]), but it is designed only for two-dimensional surfaces. Due to the shortcomings of these two libraries with respect to the necessary structures and algorithms for doing Monte Carlo simulations, they cannot be used for our purposes, and we had to develop an own triangulation library.

All the code is optimized and profiled for doing fast MCMC simulations, this means that fast computation time is preferred to small memory consumption. For example, we store for every one of the vertices the simplices that it is contained in, although this could in principle be determined by inspecting the set of all simplices and leads to the same information stored twice, which then also has to be updated twice if the adjacency changes. But having this information in place leads to a remarkable increase in computation time if creating and executing flips.

We give here a short overview, which functionality is common for all triangulations and flips, and what has to be included into specialized subclasses.



Common and non-common functionality for flips In the introductory sections about embedded and topological triangulations we saw that each flip in a triangulation is associated with a certain simplex and can be selected by choosing this simplex, this is also true for causal triangulations. The vertices of this simplex that induces the flip basically set the negative circuit vertices. So it is possible to store the simplex that is defining the flip in the common flip class.

Furthermore, every considered flip can be described by a set of positive, negative and zero circuit vertices. For embedded triangulations those were introduced in Def. 3.15, for topological triangulations it was proven in Thm. 4.22 that the Pachner moves can be formulated in positive and negative circuit vertices, and also the steps for causal triangulations can be described in this way (trivially for full-dimensional flips, and also for flips in the single spatial slices if one includes the adjacent vertices of the neighboring time slices defined by the maximal simplices of the flip as zero circuit vertices). So the base class of the flips can include the containers for the positive, negative and zero circuit vertices.

Additionally, it can contain containers for the simplices that will be removed and inserted by the respective flip, also the method for calculating these from the circuit vertices is the same for all types of considered flips and is basically given by Eq. (3.8).

A last functionality that can be implemented in the common base class is for undoing the present step (which is needed for calculating the exact ratio of selection probabilities for topological and causal triangulations, where every step of the triangulation is executed test-wise, and one has to check the results for isomorphy, and undo the steps afterwards). This function can be implemented by simply executing a step where the positive and the negative circuit vertices are interchanged.

There is also some functionality that differs for the considered types of flips. The first important point is that determining whether a given flip is executable, differs for the different considered types of triangulations. For topological triangulations one has to check that none of the simplices that should be included by a flip is already included in the triangulation, for causal triangulations one additionally must check that the causal structure of the triangulation is not violated by the flip. In contrast to this, for embedded triangulations one has to check that only convex structures are flipped.

The second important difference is the calculation of the positive, negative and zero circuit vertices. For topological flips, the negative vertices are the



vertices of the simplex that induces the flip, and the positive vertices are all other vertices of the maximal simplices that contain the flip inducing simplex. The same principle can be applied for causal triangulations, but one has to discriminate between full-dimensional flips and flips in one spatial slice. In the latter case one to find additionally the zero circuit vertices.

The last major difference between the three flip classes is the calculation of the ratio of selection probabilities. While for embedded triangulations the ratio can be calculated solely in terms of the change of the number of simplices introduced by flip, for topological and causal triangulations isomorphism checks have to be performed to calculate the exact ratio.

Common and non-common functionality for triangulations For triangulations one can implement the storage of the underlying set of vertices and the set of simplices within the common base class. In fact there are different classes for the underlying vertices for each triangulation (for causal triangulations, a vertex stores its time coordinate, and for embedded triangulations, a vertex stores all its coordinates), this can be solved by using the type of the vertex as template parameter. Furthermore, the code for proposing and applying a certain step to the triangulation can be common to all triangulations, because in the former case it consists of randomly selecting one of the simplices of the triangulation that is associated with the flips, and in the latter case the simplices that have to be deleted or inserted are provided by the respective flips.

The construction of triangulations that are used as initial points of the simulations has to be done in the different triangulation classes, e.g., by the boundary of a $(d + 1)$ -simplex for topological triangulations or by the small triangulations presented in Sec. 5.3.3 for causal triangulations.

Including flexibility for energy and isomorphism calculations While for causal dynamical triangulations the energy or the action of a triangulation has a physical meaning, for the approximative counting of triangulations one can choose an arbitrary energy function. The runtime or even the convergence of the counting algorithm can differ by magnitudes depending on the chosen energy function, so one would like to have the freedom to test different energy functions. For the design of the library it should be possible to use all triangulations with different energy functions. In *mocatrind* this is realized using the design pattern of a *concept class*, which means that every triangulation class takes an additional class as template parameter that implements the calculation of the energy of the triangulation. Simulta-



neously every flip class takes a template parameter to calculate the energy difference that is induced by a flip. Using concepts it is possible to use different energy functions without changing the code for the triangulation and flip classes.

The same design pattern is used for enabling the user to switch between different calculation methods for the isomorphy of topological and causal triangulations for calculating the exact ratio of selection probabilities.



Bibliography

- [1] D. J. Adams, *Chemical potential of hard-sphere fluids by Monte Carlo methods*, Mol. Phys. **28**(5), 1241–1252 (1974).
- [2] K. Adiprasito and B. Benedetti, *Metric geometry, convexity and collapsibility*, (2011), arXiv:1107.5789.
- [3] M. E. Agishtein and A. A. Migdal, *Critical behavior of dynamically triangulated quantum gravity in four dimensions*, Nucl. Phys. B **385**(1-2), 395–412 (1992).
- [4] ———, *Simulations of four-dimensional simplicial quantum gravity as dynamical triangulation*, Mod. Phys. Lett. A **07**(12), 1039–1061 (1992).
- [5] O. Aichholzer, *The path of a triangulation*, Proceedings of the Fifteenth Annual Symposium on Computational Geometry (New York, NY, USA), SCG '99, ACM, 1999, pp. 14–23.
- [6] ———, *Counting triangulations – Olympics*, (2006), <http://www.ist.tugraz.at/aichholzer/research/rp/triangulations/counting/>.
- [7] R. Albert and A.-L. Barabási, *Statistical mechanics of complex networks*, Rev. Mod. Phys. **74**, 47–97 (2002).
- [8] E. Alesci, E. Bianchi, E. Magliaro, and C. Perini, *Asymptotics of loop quantum gravity fusion coefficients*, Class. Quantum Grav., **27**(9), 095016 (2010).
- [9] E. Alesci and C. Rovelli, *Complete LQG propagator: Difficulties with the Barrett-Crane vertex*, Phys. Rev. D **76**, 104012 (2007).
- [10] N. Alex, *Quadriken in endlichen projektiven Ebenen*, (2012), bachelor's thesis.
- [11] J. W. Alexander, *The combinatorial theory of complexes*, Ann. Math. **31**, 292–320 (1930).



- [12] J. A. Almendral and A. Díaz-Guilera, *Dynamical and spectral properties of complex networks*, New J. Phys. **9**(6), 187 (2007).
- [13] J. Ambjørn, *Quantum gravity represented as dynamical triangulations*, Class. Quantum Grav. **12**(9), 2079 (1995).
- [14] J. Ambjørn, Z. Burda, J. Jurkiewicz, and C. F. Kristjansen, *Four-dimensional dynamically triangulated gravity coupled to matter*, Phys. Rev. D **48**, 3695–3703 (1993).
- [15] J. Ambjørn, J. Correia, C. Kristjansen, and R. Loll, *The relation between Euclidean and Lorentzian 2d quantum gravity*, Phys. Lett. B **475**(1-2), 24–32 (2000).
- [16] J. Ambjørn, D. Coumbe, J. Gizbert-Studnicki, and J. Jurkiewicz, *Signature change of the metric in CDT quantum gravity?*, J. High Energy Phys. **2015**(8), 33 (2015).
- [17] J. Ambjørn, B. Durhuus, and J. Fröhlich, *Diseases of triangulated random surface models, and possible cures*, Nucl. Phys. B **257**, 433–449 (1985).
- [18] J. Ambjørn, B. Durhuus, and T. Jonsson, *Three-dimensional simplicial quantum gravity and generalized matrix models*, Mod. Phys. Lett. A **06**(12), 1133–1146 (1991).
- [19] J. Ambjørn, J. Gizbert-Studnicki, A. Görlich, and J. Jurkiewicz, *The effective action in 4-dim CDT. The transfer matrix approach*, J. High Energy Phys. **2014**(6), 34 (2014).
- [20] J. Ambjørn, A. Görlich, S. Jordan, J. Jurkiewicz, and R. Loll, *CDT meets Hořava-Lifshitz gravity*, Phys. Lett. B **690**(4), 413–419 (2010).
- [21] J. Ambjørn, A. Görlich, J. Jurkiewicz, and R. Loll, *Nonperturbative quantum de Sitter universe*, Phys. Rev. D **78**, 063544 (2008).
- [22] J. Ambjørn, A. Görlich, J. Jurkiewicz, and H. Zhang, *The microscopic structure of 2d CDT coupled to matter*, Phys. Lett. B **746**, 359–364 (2015).
- [23] ———, *The spectral dimension in 2d CDT gravity coupled to scalar fields*, Mod. Phys. Lett. A **30**(13), 1550077 (2015).



- [24] J. Ambjørn and A. Ipsen, *Two-dimensional causal dynamical triangulations with gauge fields*, Phys. Rev. D **88**, 067502 (2013).
- [25] J. Ambjørn, S. Jordan, J. Jurkiewicz, and R. Loll, *Second-order phase transition in causal dynamical triangulations*, Phys. Rev. Lett. **107**, 211303 (2011).
- [26] ———, *Second- and first-order phase transitions in causal dynamical triangulations*, Phys. Rev. D **85**, 124044 (2012).
- [27] J. Ambjørn and J. Jurkiewicz, *Four-dimensional simplicial quantum gravity*, Phys. Lett. B **278**(1-2), 42–50 (1992).
- [28] ———, *On the exponential bound in four dimensional simplicial gravity*, Phys. Lett. B **335**(3-4), 355–358 (1994).
- [29] ———, *Computational ergodicity of S^4* , Phys. Lett. B **345**(4), 435–440 (1995).
- [30] ———, *Scaling in four-dimensional quantum gravity*, Nucl. Phys. B **451**(3), 643–676 (1995).
- [31] J. Ambjørn, J. Jurkiewicz, S. Bilke, Z. Burda, and B. Petersson, *Z_2 gauge matter coupled to 4-d simplicial quantum gravity*, Mod. Phys. Lett. A **09**(27), 2527–2541 (1994).
- [32] J. Ambjørn, J. Jurkiewicz, and C. F. Kristjansen, *Quantum gravity, dynamical triangulations and higher-derivative regularization*, Nucl. Phys. B **393**(3), 601–629 (1993).
- [33] J. Ambjørn, J. Jurkiewicz, and R. Loll, *Nonperturbative Lorentzian path integral for gravity*, Phys. Rev. Lett. **85**, 924–927 (2000).
- [34] ———, *Dynamically triangulating Lorentzian quantum gravity*, Nucl. Phys. B **610**(1-2), 347–382 (2001).
- [35] ———, *Nonperturbative 3d lorentzian quantum gravity*, Phys. Rev. D **64**, 044011 (2001).
- [36] ———, *Emergence of a 4d world from causal quantum gravity*, Phys. Rev. Lett. **93**, 131301 (2004).
- [37] ———, *Semiclassical universe from first principles*, Phys. Lett. B **607**(3-4), 205–213 (2005).



- [38] ———, *Reconstructing the universe*, Phys. Rev. D **72**, 064014 (2005).
- [39] ———, *The spectral dimension of the universe is scale dependent*, Phys. Rev. Lett. **95**, 171301 (2005).
- [40] ———, *The universe from scratch*, Contemp. Phys. **47**(2), 103–117 (2006).
- [41] J. Ambjørn, J. Jurkiewicz, and Y. Watabiki, *Dynamical triangulations, a gateway to quantum gravity?*, J. Math. Phys. **36**, 6299 (1995).
- [42] J. Ambjørn and R. Loll, *Non-perturbative Lorentzian quantum gravity, causality and topology change*, Nucl. Phys. B **536**(1-2), 407–434 (1998).
- [43] J. Ambjørn, R. Loll, J. L. Nielsen, and J. Rolf, *Euclidean and Lorentzian quantum gravity - lessons from two dimensions*, Chaos Solitons Fractals **10**(2-3), 177–195 (1999).
- [44] J. Ambjørn and S. Varsted, *Entropy estimate in three-dimensional simplicial quantum gravity*, Phys. Lett. B **266**(3-4), 285–290 (1991).
- [45] ———, *Three-dimensional simplicial quantum gravity*, Nucl. Phys. B **373**(2), 557–577 (1992).
- [46] J. A. Ambjørn, K. N. Anagnostopoulos, R. Loll, and I. Pushkina, *Shaken, but not stirred - Potts model coupled to quantum gravity*, Nucl. Phys. B **807**(1-2), 251–264 (2009).
- [47] J. S. Andrade Jr., H. J. Herrmann, R. F. S. Andrade, and L. R. da Silva, *Apollonian networks: Simultaneously scale-free, small world, Euclidean, space filling, and with matching graphs*, Phys. Rev. Lett. **94**, 018702 (2005).
- [48] I. Antoniadis, P. O. Mazur, and E. Mottola, *Scaling behavior of quantum four-geometries*, Phys. Lett. B **323**(3-4), 284–291 (1994).
- [49] ———, *Criticality and scaling in 4d quantum gravity*, Phys. Lett. B **394**(1-2), 49–56 (1997).
- [50] A. Ashtekar, J. Baez, A. Corichi, and K. Krasnov, *Quantum geometry and black hole entropy*, Phys. Rev. Lett. **80**, 904–907 (1998).
- [51] A. Ashtekar and J. Lewandowski, *Quantum theory of geometry: I. Area operators*, Class. Quantum Grav. **14**(1A), A55 (1997).



- [52] T. Aste, R. Gramatica, and T. Di Matteo, *Exploring complex networks via topological embedding on surfaces*, Phys. Rev. E **86**, 036109 (2012).
- [53] T. Aste and N. Rivier, *Random cellular froths in spaces of any dimension and curvature*, J. Phys. A **28**(5), 1381 (1995).
- [54] T. Aste and D. Sherrington, *Glass transition in self-organizing cellular patterns*, J. Phys. A **32**, 7049–7056 (1999).
- [55] J. C. Baez, *Spin foam models*, Class. Quantum Grav. **15**(7), 1827 (1998).
- [56] ———, *An introduction to spin foam models of BF theory and quantum gravity*, Geometry and Quantum Physics. Proceeding of the 38. Internationale Universitätswochen für Kern- und Teilchenphysik (H. G. H. Gausterer, L. Pittner, ed.), Lect. Notes Phys., vol. 543, 1999.
- [57] J. C. Baez, J. D. Christensen, T. R. Halford, and D. C. Tsang, *Spin foam models of Riemannian quantum gravity*, Class. Quantum Grav. **19**(18), 4627 (2002).
- [58] A. Banerjee and J. Jost, *Graph spectra as a systematic tool in computational biology*, Discrete Appl. Math. **157**(10), 2425–2431 (2009).
- [59] T. Banks, *TASI lectures on holographic space-time, SUSY and gravitational effective field theory*, (2010), arXiv:1007.4001.
- [60] A.-L. Barabási and R. Albert, *Emergence of scaling in random networks*, Science **286**(5439), 509–512 (1999).
- [61] J. F. Barbero, *Real Ashtekar variables for Lorentzian signature space-times*, Phys. Rev. D **51**, 5507–5510 (1995).
- [62] W. Barfuss, *Quadrics in finite projective planes*, (2012), short term research project.
- [63] D. Barnette and A. Edelson, *All 2-manifolds have finitely many minimal triangulations*, Isr. J. Math. **67**(1), 123–128 (1989).
- [64] A. Barrat and M. Weigt, *On the properties of small-world network models*, Eur. Phys. J. B **13**(3), 547–560 (2000).
- [65] J. W. Barrett and L. Crane, *Relativistic spin networks and quantum gravity*, J. Math. Phys. **39**(6), 3296–3302 (1998).



- [66] ———, *A Lorentzian signature model for quantum general relativity*, *Class. Quantum Grav.* **17**(16), 3101 (2000).
- [67] J. W. Barrett, R. J. Dowdall, W. J. Fairbairn, H. Gomes, F. Hellmann, and R. Pereira, *Asymptotics of 4d spin foam models*, *Gen. Rel. Gravit.* **43**(9), 2421–2436 (2010).
- [68] B. Bauer, L. D. Carr, H. G. Evertz, A. Feiguin, J. Freire, S. Fuchs, L. Gamper, J. Gukelberger, E. Gull, S. Guertler, A. Hehn, R. Igarashi, S. V. Isakov, D. Koop, P. N. Ma, P. Mates, H. Matsuo, O. Parcollet, G. Pawłowski, J. D. Picon, L. Pollet, E. Santos, V. W. Scarola, U. Schollwöck, C. Silva, B. Surer, S. Todo, S. Trebst, M. Troyer, M. L. Wall, P. Werner, and S. Wessel, *The ALPS project release 2.0: Open source software for strongly correlated systems*, *J. Stat. Mech.* **2011**(05), P05001 (2011).
- [69] M. Bauer and O. Golinelli, *Random incidence matrices: Moments of the spectral density*, *J. Stat. Phys.* **103**(1-2), 301–337 (2001).
- [70] R. J. Baxter, *Exactly solved models in statistical mechanics*, Academic Press, 1982.
- [71] K. Becker, M. Becker, and J. H. Schwarz, *String-theory and M-theory. A modern introduction*, Cambridge University Press, 2007.
- [72] R. E. Belardinelli and V. D. Pereyra, *Wang-Landau algorithm: A theoretical analysis of the saturation of the error*, *J. Chem. Phys.* **127**, 184105 (2007).
- [73] ———, *Fast algorithm to calculate density of states*, *Phys. Rev. E* **75**, 046701 (2007).
- [74] D. ben Avraham, A. F. Rozenfeld, R. Cohen, and S. Havlin, *Geographical embedding of scale-free networks*, *Phys. A* **330**(1-2), 107–116 (2003).
- [75] E. A. Bender and E. R. Canfield, *The asymptotic number of rooted maps on a surface*, *J. Comb. Theory A* **43**(2), 244–257 (1986).
- [76] E. A. Bender, Z. Gao, and L. B. Richmond, *The map asymptotics constant t_g* , *Electron. J. Combin.* **15**, #R51 (2008).
- [77] B. Benedetti, *On locally constructible manifolds*, Ph.D. thesis, Technischen Universität Berlin, 2009.



- [78] ———, *Smoothing discrete Morse theory*, (2012), arXiv:1212.0885.
- [79] ———, *Discrete Morse theory for manifolds with boundary*, Trans. Amer. Math. Soc. **364**, 6631–6670 (2012).
- [80] B. Benedetti and G. M. Ziegler, *On locally constructible spheres and balls*, Acta Math. **206**, 205–243 (2011).
- [81] D. Benedetti and R. Loll, *Quantum gravity and matter: Counting graphs on causal dynamical triangulations*, Gen. Rel. Gravit. **39**(6), 863–898 (2007).
- [82] M. K. Bennett, *Affine and projective geometry*, Wiley, 1995.
- [83] B. A. Berg, *Exploratory numerical study of discrete quantum gravity*, Phys. Rev. Lett. **55**, 904–907 (1985).
- [84] ———, *Multicanonical simulations step by step*, Comput. Phys. Comm. **153**(3), 397–406 (2003).
- [85] ———, *Markov chain Monte Carlo simulations and their statistical analysis*, World Scientific, 2004.
- [86] ———, *Introduction to Markov chain Monte Carlo simulations and their statistical analysis*, Markov Chain Monte Carlo (W. Kendall, ed.), Lecture Notes Series, vol. 7, World Scientific, 2005, p. 1ff.
- [87] B. A. Berg, C. Muguruma, and Y. Okamoto, *Residual entropy of ordinary ice from multicanonical simulations*, Phys. Rev. B **75**, 092202 (2007).
- [88] B. A. Berg and T. Neuhaus, *Multicanonical ensemble: A new approach to simulate first-order phase transitions*, Phys. Rev. Lett. **68**, 9–12 (1992).
- [89] A. Beutelspacher and U. Rosenbaum, *Projective geometry: From foundations to applications*, Cambridge University Press, 1998.
- [90] P. Bialas, Z. Burda, A. Krzywicki, and B. Petersson, *Focusing on the fixed point of 4d simplicial gravity*, Nucl. Phys. B **472**(1-2), 293–308 (1996).
- [91] S. Bilke, Z. Burda, A. Krzywicki, and B. Petersson, *Phase transition and topology in 4d simplicial gravity*, Nucl. Phys. B (Proc. Suppl.) **53**(1-3), 743–745 (1997).



- [92] S. Bilke, Z. Burda, A. Krzywicki, B. Petersson, J. Tabaczek, and G. Thorleifsson, *4d simplicial quantum gravity interacting with gauge matter fields*, Phys. Lett. B **418**(3-4), 266–272 (1998).
- [93] S. Bilke, Z. Burda, and B. Petersson, *Topology in 4d simplicial quantum gravity*, Phys. Lett. B **395**(1-2), 4–9 (1997).
- [94] W. Billenstein, *Monte Carlo simulations of the Ising model on triangulations*, (2013), bachelor’s thesis.
- [95] K. Binder, *Finite size scaling analysis of ising model block distribution functions*, Z. Phys. B. **43**(2), 119–140 (1981).
- [96] G. Biroli and R. Monasson, *A single defect approximation for localized states on random lattices*, J. Phys. A **32**(24), L255 (1999).
- [97] A. Björner and F. H. Lutz, *Simplicial manifolds, bistellar flips and a 16-vertex triangulation of the Poincaré homology 3-sphere*, Exp. Math. **9**(2), 275–289 (2000).
- [98] C. Borgs and R. Kotecký, *A rigorous theory of finite-size scaling at first-order phase transitions*, J. Stat. Phys. **61**(1), 79–119 (1990).
- [99] A. B. Bortz, M. H. Kalos, and J. L. Lebowitz, *A new algorithm for Monte Carlo simulation of Ising spin systems*, J. Comput. Phys. **17**(1), 10–18 (1975).
- [100] D. V. Boulatov and A. Krzywicki, *On the phase diagram of three-dimensional simplicial quantum gravity*, Mod. Phys. Lett. A **06**(32), 3005–3014 (1991).
- [101] H. R. Brahana, *Systems of circuits on two-dimensional manifolds*, Ann. Math. **23**(2), 144–168 (1921).
- [102] A. J. Bray and G. J. Rodgers, *Diffusion in a sparsely connected space: A model for glassy relaxation*, Phys. Rev. B **38**, 11461–11470 (1988).
- [103] G. Brinkmann and B. D. McKay, *Fast generation of planar graphs*, Commun. Math. Comput. Chem. **58**(2), 323–357 (2007).
- [104] B. Brüggemann, *Nonuniform measure in four-dimensional simplicial quantum gravity*, Phys. Rev. D **47**, 3330–3338 (1993).



- [105] Z. Burda, J. P. Kownacki, and A. Krzywicki, *Towards a non-perturbative renormalization of euclidean quantum gravity*, Phys. Lett. B **356**(4), 466–471 (1995).
- [106] B. A. Burton, *The Pachner graph and the simplification of 3-sphere triangulations*, Proceedings of the twenty-seventh annual symposium on Computational geometry (New York, NY, USA), SoCG '11, ACM, 2011, pp. 153–162.
- [107] S. S. Cairns, *Triangulation of the manifold of class one*, Bull. Amer. Math. Soc. **41**(8), 549–552 (1935).
- [108] P. Caputo, F. Martinelli, A. Sinclair, and A. Stauffer, *Random lattice triangulations: Structure and algorithms*, Proceedings of the Forty-fifth Annual ACM Symposium on Theory of Computing (New York, NY, USA), STOC '13, ACM, 2013, pp. 615–624.
- [109] ———, *Random lattice triangulations: Structure and algorithms*, Ann. Appl. Probab. **25**(3), 1650–1685 (2015).
- [110] S. Catterall, J. Kogut, and R. Renken, *Phase structure of four dimensional simplicial quantum gravity*, Phys. Lett. B **328**(3), 277–283 (1994).
- [111] ———, *Is there an exponential bound in four-dimensional simplicial gravity?*, Phys. Rev. Lett. **72**, 4062–4065 (1994).
- [112] ———, *Entropy and the approach to the thermodynamic limit in three-dimensional simplicial gravity*, Phys. Lett. B **342**(1-4), 53–57 (1995).
- [113] S. Catterall, G. Thorleifsson, J. Kogut, and R. Renken, *Singular vertices and the triangulation space of the d -sphere*, Nucl. Phys. B **468**(1-2), 263–276 (1996).
- [114] CGAL Project, *CGAL user and reference manual*, 4.7 ed., CGAL Editorial Board, 2015.
- [115] J. Cheeger, W. Müller, and R. Schrader, *On the curvature of piecewise flat spaces*, Comm. Math. Phys. **92**(3), 405–454 (1984).
- [116] Y. Chow and F. Y. Wu, *Residual entropy and validity of the third law of thermodynamics in discrete spin systems*, Phys. Rev. B **36**, 285–288 (1987).



- [117] F. Chung and L. Lu, *Complex graphs and networks*, CBMS Regional Conference Series in Mathematics, no. 107, American Mathematical Society, 2006.
- [118] B. Collaboration, *Detection of B-mode polarization at degree angular scales by BICEP2*, Phys. Rev. Lett. **112**, 241101 (2014).
- [119] P. Collas, *General relativity in two- and three-dimensional space-times*, Amer. J. Phys. **45**(9), 833–837 (1977).
- [120] P. Collet, J.-P. Eckmann, and M. Younan, *Trees of nuclei and bounds on the number of triangulations of the 3-ball*, Commun. Math. Phys. **325**(1), 259–289 (2014).
- [121] F. Conrady and L. Freidel, *Semiclassical limit of 4-dimensional spin foam models*, Phys. Rev. D **78**, 104023 (2008).
- [122] L. d. F. Costa, O. N. Oliveira, G. Travieso, F. A. Rodrigues, P. R. Villas Boas, L. Antiqueira, M. P. Viana, and L. E. Correa Rocha, *Analyzing and modeling real-world phenomena with complex networks: a survey of applications*, Adv. Phys. **60**(3), 329–412 (2011).
- [123] D. Coumbe and J. Jurkiewicz, *Evidence for asymptotic safety from dimensional reduction in causal dynamical triangulations*, J. High Energy Phys. **2015**(3), 151 (2015).
- [124] D. Coumbe and J. Laiho, *Exploring Euclidean dynamical triangulations with a non-trivial measure term*, J. High Energy Phys. **2015**(4), 28 (2015).
- [125] D. N. Coumbe, *Hypothesis on the nature of time*, Phys. Rev. D **91**, 124040 (2015).
- [126] D. M. Cvetković, P. Rowlinson, and S. Simić, *An introduction to the theory of graph spectra*, Cambridge University Press, Cambridge, 2010.
- [127] N. M. M. de Abreu, *Old and new results on algebraic connectivity of graphs*, Linear Algebra Appl. **423**(1), 53–73 (2007).
- [128] B. V. de Bakker, *Absence of barriers in dynamical triangulation*, Phys. Lett. B **348**(1-2), 35–38 (1995).



- [129] ———, *Further evidence that the transition of 4d dynamical triangulation is 1st order*, Phys. Lett. B **389**(2), 238–242 (1996).
- [130] B. V. de Bakker and J. Smit, *Volume dependence of the phase boundary in 4d dynamical triangulation*, Phys. Lett. B **334**(3), 304–308 (1994).
- [131] ———, *Curvature and scaling in 4d dynamical triangulation*, Nucl. Phys. B **439**(1-2), 239–258 (1995).
- [132] J. A. De Loera, J. Rambau, and F. Santos, *Triangulations. structures for algorithms and applications*, Springer, 2010.
- [133] D. S. Dean, *An approximation scheme for the density of states of the Laplacian on random graphs*, J. Phys. A **35**(12), L153 (2002).
- [134] M. Dehn, *Über den Inhalt sphärischer Dreiecke*, Math. Ann. **60**, 166–174 (1905).
- [135] E. Diener, *Boost type traits inspection (TTI) library*.
- [136] X. Ding and T. Jiang, *Spectral distributions of adjacency and Laplacian matrices of random graphs*, Ann. Appl. Probab. **20**(6), 2086–2117 (2010).
- [137] P. A. M. Dirac, *Generalized Hamiltonian dynamics*, Canad. J. Math. **2**, 129–148 (1950).
- [138] B. Dittrich and J. P. Ryan, *On the role of the Barbero-Immirzi parameter in discrete quantum gravity*, Class. Quantum Grav. **30**(9), 095015 (2013).
- [139] S. N. Dorogovtsev, A. V. Goltsev, and J. F. F. Mendes, *Ising model on networks with an arbitrary distribution of connections*, Phys. Rev. E **66**, 016104 (2002).
- [140] S. N. Dorogovtsev, J. F. F. Mendes, and A. N. Samukhin, *Structure of growing networks with preferential linking*, Phys. Rev. Lett. **85**, 4633–4636 (2000).
- [141] F. Dowker, *Introduction to causal sets and their phenomenology*, Gen. Rel. Gravit. **45**(9), 1651–1667 (2013).
- [142] Z. Du and Z. Liu, *On the Estrada and Laplacian Estrada indices of graphs*, Linear Algebra Appl. **435**(8), 2065–2076 (2011).



- [143] B. Dubertret, N. Rivier, and M. A. Peshkin, *Long-range geometrical correlations in two-dimensional foams*, J. Phys. A. **31**(3), 879 (1998).
- [144] M. Düll, *Effiziente Berechnung von Wigner 3nj-Symbolen*, (2013), short term research project.
- [145] ———, *Numerische Berechnung von Vertex-Amplituden im EPRL-Modell*, (2013), bachelor's thesis.
- [146] B. Duplantier and S. Sheffield, *Liouville quantum gravity and KPZ*, Invent. Math. **185**(2), 333–393 (2011).
- [147] B. Durhuus and T. Jonsson, *Remarks on the entropy of 3-manifolds*, Nucl. Phys. B **445**(1), 182–192 (1995).
- [148] ———, *Exponential bounds on the number of causal triangulations*, Comm. Math. Phys. **340**(1), 105–124 (2015).
- [149] D. J. Earl and M. W. Deem, *Markov chains of infinite order and asymptotic satisfaction of balance: application to the adaptive integration method*, J. Phys. Chem. B **109**(14), 6701–6704 (2005).
- [150] ———, *Parallel tempering: Theory, applications, and new perspectives*, Phys. Chem. Chem. Phys. **7**, 3910–3916 (2005).
- [151] H. Edelsbrunner, *Triangulations and meshes in computational geometry*, Acta Numer. **9**, 133–213 (2000).
- [152] B. Efron, *Bootstrap methods: Another look at the jackknife*, Ann. Stat. **7**, 1–26 (1979).
- [153] ———, *Nonparametric estimates of standard error: The jackknife, the bootstrap and other methods*, Biometrika **68**(3), 589–599 (1981).
- [154] T. P. Eggarter, *Cayley trees, the Ising problem, and the thermodynamic limit*, Phys. Rev. B **9**, 2989–2992 (1974).
- [155] J. Engle, E. Livine, R. Pereira, and C. Rovelli, *LQG vertex with finite Immirzi parameter*, Nucl. Phys. B **799**(1-2), 136–149 (2008).
- [156] J. Engle, R. Pereira, and C. Rovelli, *Loop-quantum-gravity vertex amplitude*, Phys. Rev. Lett. **99**, 161301 (2007).
- [157] ———, *Flipped spinfoam vertex and loop gravity*, Nucl. Phys. B **798**(1-2), 251–290 (2008).



- [158] P. Erdős and A. Rényi, *On random graphs*, Publ. Math. Debrecen **6**, 290–297 (1959).
- [159] ———, *On the evolution of random graphs*, Publication of the Mathematical Institute of the Hungarian Academy of Sciences, 1960, pp. 17–61.
- [160] ———, *On the strength of connectedness of a random graph*, Acta Math. Acad. Sci. H. **12**(1-2), 261–267 (1964).
- [161] S. Ermon, C. Gomes, and S. Bart, *Computing the density of states of boolean formulas*, Principles and Practice of Constraint Programming - CP 2010 (D. Cohen, ed.), Lecture Notes in Computer Science, vol. 6308, Springer Berlin Heidelberg, 2010, pp. 38–52.
- [162] ———, *A flat histogram method for computing the density of states of combinatorial problems*, Proceedings of the Twenty-Second international joint conference on Artificial Intelligence - Volume Volume Three, IJCAI'11, AAAI Press, 2011, pp. 2608–2613.
- [163] E. Estrada, *Characterization of 3d molecular structure*, Chem. Phys. Lett. **319**(5-6), 713–718 (2000).
- [164] E. Estrada and J. A. Rodríguez-Velázquez, *Spectral measures of bipartivity in complex networks*, Phys. Rev. E **72**, 046105 (2005).
- [165] S. N. Evangelou, *Quantum percolation and the Anderson transition in dilute systems*, Phys. Rev. B **27**, 1397–1400 (1983).
- [166] ———, *A numerical study of sparse random matrices*, J. Stat. Phys. **69**(1-2), 361–383 (1992).
- [167] S. N. Evangelou and E. N. Economou, *Spectral density singularities, level statistics, and localization in a sparse random matrix ensemble*, Phys. Rev. Lett. **68**, 361–364 (1992).
- [168] I. Farkas, I. Derenyi, G. Palla, and T. Vicsek, *Equilibrium statistical mechanics of network structures*, Complex Networks (E. Ben-Naim, H. Frauenfelder, and Z. Toroczkai, eds.), Lecture Notes in Physics, vol. 650, Springer, 2004, pp. 163–187.
- [169] I. J. Farkas, I. Derényi, A.-L. Barabási, and T. Vicsek, *Spectra of real-world graphs: Beyond the semicircle law*, Phys. Rev. E **64**, 026704 (2001).



- [170] M. Fiedler, *Algebraic connectivity of graphs*, Czechoslovak Math. J. **23**(2), 298–305 (1973).
- [171] M. E. Fisher, *Quantum corrections to critical-point behavior*, Phys. Rev. Lett. **16**, 11–14 (1966).
- [172] ———, *The renormalization group in the theory of critical behavior*, Rev. Mod. Phys. **46**, 597–616 (1974).
- [173] ———, *Renormalization group theory: Its basis and formulation in statistical physics*, Rev. Mod. Phys. **70**, 653–681 (1998).
- [174] C. Forbes, M. Evans, N. Hastings, and B. Peacock, *Statistical distributions*, 4 ed., Wiley, 2011.
- [175] M. H. Freedman, *The topology of four-dimensional manifolds*, J. Differential Geom. **17**(3), 357–453 (1982).
- [176] L. Freidel and K. Krasnov, *A new spin foam model for 4d gravity*, Class. Quantum Grav. **25**(12), 125018 (2008).
- [177] R. Friedberg and T. D. Lee, *Derivation of Regge’s action from Einstein’s theory of general relativity*, Nucl. Phys. B **242**(1), 145–166 (1984).
- [178] J. Fröhlich, *The statistical mechanics of surfaces*, Applications of Field Theory to Statistical Mechanics (L. Garrido, ed.), Lecture Notes in Physics, vol. 216, Springer Berlin Heidelberg, 1985, pp. 31–57.
- [179] A. Fronczak, P. Fronczak, and J. A. Holyst, *Mean-field theory for clustering coefficients in Barabási-Albert networks*, Phys. Rev. E **68**, 046126 (2003).
- [180] ———, *Average path length in random networks*, Phys. Rev. E **70**, 056110 (2004).
- [181] M. Galassi, J. Davies, J. Theiler, B. Gough, G. Jungman, P. Alken, M. Booth, F. Rossi, and R. Uleric, *GNU scientific library: Reference manual*, Network Theory, Bristol, 2009.
- [182] Z. Gao, *A pattern for the asymptotic number of rooted maps on surfaces*, J. Comb. Theory A **64**(2), 246–264 (1993).
- [183] Z.-C. Gao, *The number of rooted triangular maps on a surface*, J. Comb. Theory B **52**(2), 236–249 (1991).



-
- [184] C. Garban, *Quantum gravity and the KPZ formula*, Astérisque **352**, 1052 (2013).
- [185] A. E. Gelfand and A. F. M. Smith, *Sampling-based approaches to calculating marginal densities*, J. Amer. Statist. Assoc. **85**(410), 398–409 (1990).
- [186] S. Geman and D. Geman, *Stochastic relaxation, Gibbs distributions, and the Bayesian restoration of images*, IEEE Trans. Pattern Anal. Mach. Intell. **6**(6), 721–741 (1984).
- [187] A. P. Gentle, *Regge calculus: A unique tool for numerical relativity*, Gen. Rel. Gravit. **34**(10), 1701–1718 (2002).
- [188] R. J. Glauber, *Time-dependent statistics of the Ising model*, J. Math. Phys. **4**(2), 294–307 (1963).
- [189] R. E. Gompf, *An exotic menagerie*, J. Differential Geom. **37**(1), 199–223 (1993).
- [190] G. Gompper and D. M. Kroll, *Phase diagram and scaling behavior of fluid vesicles*, Phys. Rev. E **51**, 514–525 (1995).
- [191] ———, *Network models of fluid, hexatic and polymerized membranes*, J. Phys.: Condens. Matter **9**(42), 8795 (1997).
- [192] D. Göring, M. A. Klatt, C. Stegmann, and K. Mecke, *Morphometric analysis in gamma-ray astronomy using Minkowski functionals*, Astron. Astrophys. **555**, A38 (2013).
- [193] A. Görlich, *Causal dynamical triangulations in four dimensions*, (2010), arXiv:1111.6938.
- [194] I. P. Goulden and D. M. Jackson, *The KP hierarchy, branched covers, and triangulations*, Adv. Math. **219**(3), 932–951 (2008).
- [195] D. Gregor, *Boost signal library*.
- [196] R. B. Griffiths, *Dependence of critical indices on a parameter*, Phys. Rev. Lett. **24**, 1479–1482 (1970).
- [197] M. Gromov, *Spaces and questions*, Visions in Mathematics (N. Alon, J. Bourgain, A. Connes, M. Gromov, and V. Milman, eds.), Modern Birkhäuser Classics, Birkhäuser Basel, 2010, pp. 118–161.



- [198] R. D. Grone, *Eigenvalues and the degree sequences of graphs*, Linear Multilinear Algebra **39**, 133–136 (1995).
- [199] T. Guhr, A. Müller-Groeling, and H. A. Weidenmüller, *Random-matrix theories in quantum physics: Common concepts*, Phys. Lett. B **299**(4-6), 189–425 (1998).
- [200] R. Gurau and J. P. Ryan, *Colored tensor models - a review*, SIGMA **8**, 020 (2012).
- [201] A. A. Hagberg, D. A. Schult, and P. J. Swart, *Exploring network structure, dynamics, and function using NetworkX*, Proceedings of the 7th Python in Science Conference (Pasadena, CA USA) (G. Varoquaux, T. Vaught, and J. Millman, eds.), 2008, pp. 11–15.
- [202] H. W. Hamber, *Critical behavior in simplicial quantum gravity*, Nucl. Phys. B (Proc. Suppl.) **20**, 728–732 (1991).
- [203] ———, *Phases of four-dimensional simplicial quantum gravity*, Phys. Rev. D **45**, 507–512 (1992).
- [204] ———, *Quantum gravitation. The Feynman path integral approach*, Springer, 2009.
- [205] H. W. Hamber, R. Toriumi, and R. M. Williams, *Wheeler-dewitt equation in 3 + 1 dimensions*, Phys. Rev. D **88**, 084012 (2013).
- [206] H. W. Hamber and R. M. Williams, *Higher derivative quantum gravity on a simplicial lattice*, Nucl. Phys. B **248**(2), 392–414 (1984).
- [207] ———, *Two-dimensional simplicial quantum gravity*, Nucl. Phys. B **267**(2), 482–496 (1986).
- [208] ———, *Simplicial gravity coupled to scalar matter*, Nucl. Phys. B **415**(2), 463–496 (1994).
- [209] ———, *Gauge invariance in simplicial gravity*, Nucl. Phys. B **487**(1-2), 345–408 (1997).
- [210] ———, *On the measure in simplicial gravity*, Phys. Rev. D **59**, 064014 (1999).
- [211] ———, *Gravitational Wilson loop in discrete quantum gravity*, Phys. Rev. D **81**, 084048 (2010).



- [212] J.-P. Hansen and I. R. McDonald, *Theory of simple liquids*, 3rd ed., Academic Press, 2006.
- [213] E. Hartmann, *A marching method for the triangulation of surfaces*, Vis. Comput. **14**(3), 95–108 (1998).
- [214] W. K. Hastings, *Monte Carlo sampling methods using Markov chains and their applications*, Biometrika **57**(1), 97–109 (1970).
- [215] P. J. Heawood, *Map colour theorem*, Quart. J. Pure Appl. Math. **24**, 332–338 (1890).
- [216] D. B. Hitchcock, *A history of the Metropolis-Hastings algorithm*, Am. Stat. **57**(4), 254–257 (2003).
- [217] R. Hocken and M. R. Moldover, *Ising critical exponents in real fluids: An experiment*, Phys. Rev. Lett. **37**, 29–32 (1976).
- [218] P. Holme and B. J. Kim, *Growing scale-free networks with tunable clustering*, Phys. Rev. E **65**, 026107 (2002).
- [219] S. Hossenfelder, *Experimental search for quantum gravity*, Classical and Quantum Gravity: Theory, Analysis and Applications (V. R. Frignanni, ed.), Nova Science Publishers, 2012.
- [220] T. Hotta, T. Izubuchi, and J. Nishimura, *Multicanonical simulation of 3d dynamical triangulation model and a new phase structure*, Nucl. Phys. B **531**(1-3), 446–458 (1998).
- [221] P. Hořava, *Quantum gravity at a lifshitz point*, Phys. Rev. D **79**, 084008 (2009).
- [222] J. F. P. Hudson, *Piecewise linear topology*, W. A. Benjamin Inc., New York, 1969.
- [223] K. Hukushima and K. Nemoto, *Exchange Monte Carlo method and application to spin glass simulations*, J. Phys. Soc. Japan **65**(6), 1604–1608 (1996).
- [224] G. Immirzi, *Real and complex connections for canonical gravity*, Class. Quantum Grav. **14**(10), L177 (1997).
- [225] O. F. Inc., *The on-line encyclopedia of integer sequences*, (2011), <http://oeis.org>.



- [226] E. Ising, *Beitrag zur Theorie des Ferromagnetismus*, Z. Phys. **31**(1), 253–258 (1925).
- [227] G. Jaeger, *The Ehrenfest classification of phase transitions: Introduction and evolution*, Arch. Hist. Exact Sci. **53**(1), 51–81 (1998).
- [228] M. Jansen, H. Choi, S. Lavu, and R. Baraniuk, *Multiscale image processing using normal triangulated meshes*, Proceedings 2001 International Conference on Image Processing, vol. 2, Oct 2001, pp. 229–232.
- [229] J. Järvi, J. Willcock, A. Lumsdaine, and M. Calabrese, *Boost enable if utility*.
- [230] M. Jerrum and A. Sinclair, *The Markov chain Monte Carlo method an approach to approximate counting and integration*, Approximation Algorithms for NP-hard Problems (D. Hochbaum, ed.), PWS, 1996.
- [231] A. M. Johansen, `smctc: sequential monte carlo in c++`, J. Stat. Soft. **30**(6), 1 (2009).
- [232] F. Johansson et al., *mpmath: a Python library for arbitrary-precision floating-point arithmetic*, <http://mpmath.org>.
- [233] F. Juhász, *On the spectrum of a random graph*, Algebraic Methods in Graph Theory (L. Lovasz and V. T. Sos, eds.), Colloquia Mathematica Societatis Janos Bolyai, vol. 25, 1981.
- [234] M. Jungerman and G. Ringel, *Minimal triangulations on orientable surfaces*, Acta Math. **145**(1), 121–154 (1980).
- [235] M. Juvan and B. Mohar, *Laplace eigenvalues and bandwidth-type invariants of graphs*, J. Graph Theory **17**(3), 393–407 (1993).
- [236] L. Kadanoff, *Scaling laws for Ising models near t_c* , Physics **2**, 263–272 (1966).
- [237] ———, *Critical behavior. universality and scaling*, Proceedings of the Int. School of Physics, "Enrico Fermi", Course LI (New York) (M. S. Green, ed.), Academic Press, 1971, p. 101.
- [238] V. Kaibel and G. M. Ziegler, *Counting lattice triangulations*, Surveys in Combinatorics 2003, number 307 in Lond. Math. Soc. Lect. Note Ser, Cambridge University Press, 2003, pp. 277–308.



- [239] G. Kalai, *Many triangulated spheres*, Discrete Comput. Geom. **3**(1), 1–14 (1988).
- [240] R. M. Karp, M. Luby, and N. Madras, *Monte-Carlo approximation algorithms for enumeration problems*, J. Algorithms **10**(3), 429–448 (1989).
- [241] H. G. Katzgraber, S. Trebst, D. A. Huse, and M. Troyer, *Feedback-optimized parallel tempering Monte Carlo*, J. Stat. Mech. **3**, P03018 (2006).
- [242] C. Kenyon, D. Randall, and A. Sinclair, *Approximating the number of monomer-dimer coverings of a lattice*, J. Stat. Phys. **83**, 637–659 (1996).
- [243] M. A. Kervaire, *A manifold which does not admit any differentiable structure*, Comm. Math. Helvetici **34**(1), 257–270 (1960).
- [244] B. Kessler, *The significance of word lists*, CSLI Press, Stanford, 2001.
- [245] I. Khavkine, *Evaluation of new spin foam vertex amplitudes*, Class. Quantum Grav. **26**(12), 125012 (2009).
- [246] I. Khavkine, R. Loll, and P. Reska, *Coupling a point-like mass to quantum gravity with causal dynamical triangulations*, Class. Quantum Grav. **27**(18), 185025 (2010).
- [247] S. A. King, *Regular flip equivalence of surface triangulations*, Topol. Appl. **127**(1-2), 169–173 (2003).
- [248] R. C. Kirby and L. C. Siebenmann, *Foundational essays on topological manifolds, smoothings, and triangulations*, Princeton Univ. Press, Princeton, 1977.
- [249] G. Kirchhoff, *Über die Auflösung der Gleichungen, auf welche man bei der Untersuchung der linearen Verteilung galvanischer Ströme geführt wird*, Ann. Phys. Chem. **72**, 497–508 (1847).
- [250] S. Kirkpatrick, C. D. Gelatt, and M. P. Vecchi, *Optimization by simulated annealing*, Science **220**(4598), 671–680 (1983).
- [251] D. A. Klain, *Dehn-Sommerville relations for triangulated manifolds*, (n.y.), <http://faculty.uml.edu/dklain/ds.pdf>.



- [252] K. Klemm and V. M. Eguíluz, *Highly clustered scale-free networks*, Phys. Rev. E **65**, 036123 (2002).
- [253] J. F. Knauf, B. Krüger, and K. Mecke, *Entropy of unimodular lattice triangulations*, EPL **109**(4), 40011 (2015).
- [254] V. Knizhnik, A. Polyakov, and A. Zamolodchikov, *Fractal structure of 2d-quantum gravity*, Mod. Phys. Lett. A **03**(08), 819–826 (1988).
- [255] H. Koibuchi, *Flat histogram Monte Carlo simulations of triangulated fixed-connectivity surface models*, J. Stat. Phys. **140**(4), 676–687 (2010).
- [256] H. Koibuchi, N. Kusano, A. Nidaira, K. Suzuki, and M. Yamada, *Grand canonical Monte Carlo simulations of elastic membranes with fluidity*, Phys. Lett. A **319**(1-2), 44–52 (2003).
- [257] I. Kolingerová, *On triangulations*, Computational Science and Its Applications - ICCSA 2004 (A. Laganá, M. Gavrilova, V. Kumar, Y. Mun, C. Tan, and O. Gervasi, eds.), Lecture Notes in Computer Science, vol. 3044, Springer Berlin Heidelberg, 2004, pp. 544–553.
- [258] I. Kolingerová and A. Ferko, *Multicriteria-optimized triangulations*, Visual Comput. **17**(6), 380–395 (2001).
- [259] J.-P. Kownacki, *Freezing of triangulations*, Eur. Phys. J. B **38**(3), 485–494 (2004).
- [260] D. Kozlov, *Combinatorial algebraic topology*, Springer, 2008.
- [261] N. Krahnstoever and C. Lorenz, *Computing curvature-adaptive surface triangulations of three-dimensional image data*, Visual Comput. **20**(1), 17–36 (2004).
- [262] P. L. Krapivsky, S. Redner, and F. Leyvraz, *Connectivity of growing random networks*, Phys. Rev. Lett. **85**, 4629–4632 (2000).
- [263] D. M. Kroll and G. Gompper, *The conformation of fluid membranes: Monte Carlo simulations*, Science **255**(5047), 968–971 (1992).
- [264] B. Krüger and K. Mecke, *Genus dependence of the number of (non-)orientable surface triangulations*, Phys. Rev. D **93**, 085018 (2016).



- [265] B. Krüger, E. M. Schmidt, and K. Mecke, *Unimodular lattice triangulations as small-world and scale-free random graphs*, New J. Phys. **17**(2), 023013 (2015).
- [266] ———, *Spectral properties of unimodular lattice triangulations*, J. Stat. Phys. **163**(3), 514–543 (2016).
- [267] S. Kumar, *Random matrix ensembles: Wang-Landau algorithm for spectral densities*, EPL **101**(2), 20002 (2013).
- [268] J. Laiho and D. Coumbe, *Evidence for asymptotic safety from lattice quantum gravity*, Phys. Rev. Lett. **107**, 161301 (2011).
- [269] D. Landau and K. Binder, *A guide to Monte Carlo simulations in statistical physics*, 2nd ed., Cambridge University Press, 2005.
- [270] A. Laska, 2014, personal communication.
- [271] ———, *Biquadric fields: Equipping finite projective spaces with metric structure*, (2014), master’s thesis.
- [272] C. L. Lawson, *Transforming triangulations*, Discrete Math. **3**(4), 365–372 (1972).
- [273] H. K. Lee, Y. Okabe, and D. P. Landau, *Convergence and refinement of the Wang-Landau algorithm*, Comput. Phys. Comm. **175**(1), 36–40 (2006).
- [274] J. Lee, *New Monte Carlo algorithm: Entropic sampling*, Phys. Rev. Lett. **71**, 211–214 (1993).
- [275] J. M. Lee, *Introduction to topological manifolds*, 2 ed., Graduate Texts in Mathematics, Springer, New York, 2000.
- [276] ———, *Introduction to smooth manifolds*, 2 ed., Graduate Texts in Mathematics, Springer, New York, 2012.
- [277] M. Leone, A. Vázquez, A. Vespignani, and R. Zecchina, *Ferromagnetic ordering in graphs with arbitrary degree distribution*, Eur. Phys. J. B **28**(2), 191–197 (2002).
- [278] B. Levin, *A representation for multinomial cumulative distribution functions*, Ann. Stat. **9**(5), 1123–1126 (1981).



- [279] D. A. Levin, Y. Peres, and E. L. Wilmer, *Markov chains and mixing times*, American Mathematical Society, 2008.
- [280] R. Loll, *Discrete approaches to quantum gravity in four dimensions*, Living Rev. Relativity **1**, 13 (1998).
- [281] ———, *The emergence of spacetime or quantum gravity on your desktop*, Class. Quantum Grav. **25**(11), 114006 (2008).
- [282] R. Loll and W. Westra, *Sum over topologies and double-scaling limit in 2d Lorentzian quantum gravity*, Class. Quantum Grav. **23**(2), 465 (2006).
- [283] R. Loll, W. Westra, and S. Zohren, *Taming the cosmological constant in 2d causal quantum gravity with topology change*, Nucl. Phys. B **751**(3), 419–435 (2006).
- [284] D. Lunn, A. Thomas, N. Best, and D. Spiegelhalter, *WinBUGS - a Bayesian modelling framework: Concepts, structure, and extensibility*, Statist. Comp. **10**(4), 325–337 (2000).
- [285] F. H. Lutz, *Equivelar and d-covered triangulations of surfaces. II. Cyclic triangulations and tessellations*, (2010), arXiv:1001.2779.
- [286] ———, 2016, personal communication.
- [287] F. H. Lutz, T. Sulanke, A. K. Tiwari, and A. K. Upadhyay, *Equivelar and d-covered triangulations of surfaces. I*, (2010), arXiv:1001.2777.
- [288] E. Masehian, H. Akbaripour, and N. Mohabbati-Kalejahi, *Landscape analysis and efficient metaheuristics for solving the n-queens problem*, Comput. Optim. Appl. **56**(3), 735–764 (2013).
- [289] J. L. McWhirter, H. Noguchi, and G. Gompper, *Flow-induced clustering and alignment of vesicles and red blood cells in microcapillaries*, Proc. Natl. Acad. Sci. **106**(15), 6039–6043 (2009).
- [290] M. Meringer, *Fast generation of regular graphs and construction of cages*, J. Graph Theory **30**(2), 137–146 (1999).
- [291] N. Metropolis, A. W. Rosenbluth, M. N. Rosenbluth, A. H. Teller, and E. Teller, *Equation of state calculations by fast computing machines*, J. Chem. Phys. **21**, 1087 (1953).



- [292] N. Metropolis and S. Ulam, *The Monte Carlo method*, J. Amer. Statist. Assoc. **44**(247), 335–341 (1949).
- [293] A. Mijatović, *Simplifying triangulations of S^3* , Pacific J. Math. **208**, 291–324 (2003).
- [294] J. Milnor, *On manifolds homeomorphic to the 7-sphere*, Ann. Math. **64**(2), 399–405 (1956).
- [295] ———, *Two complexes which are homeomorphic but combinatorially distinct*, Ann. Math. **74**(3), 575–590 (1961).
- [296] ———, *Differential topology forty-six years later*, Notices Amer. Math. Soc. **58**(6), 804–809 (2011).
- [297] A. D. Mirlin and Y. V. Fyodorov, *Universality of level correlation function of sparse random matrices*, J. Phys. A **24**(10), 2273 (1991).
- [298] C. J. Mode (ed.), *Applications of Monte Carlo methods in biology, medicine and other fields of science*, InTech, 2011.
- [299] B. Mohar, *Isoperimetric numbers of graphs*, J. Comb. Theory B **47**(3), 274–291 (1989).
- [300] ———, *The Laplacian spectrum of graphs*, Graph Theory, Combinatorics, and Applications (Y. Alavi, G. Chartrand, O. R. Oellermann, and A. J. Schwenk, eds.), vol. 2, Wiley, 1991, pp. 871–898.
- [301] ———, *Laplace eigenvalues of graphs – a survey*, Discrete Math. **109**(1-3), 171–183 (1992).
- [302] B. Mohar and S. Poljak, *Eigenvalues in combinatorial optimization*, Combinatorial and Graph-Theoretical Problems in Linear Algebra (R. Brualdi, S. Friedland, and V. Klee, eds.), The IMA Volumes in Mathematics and its Applications, vol. 50, Springer New York, 1993, pp. 107–151.
- [303] E. E. Moise, *Affine structures in 3-manifolds: V. The triangulation theorem and hauptvermutung*, Ann. Math. **56**(1), 96–114 (1952).
- [304] ———, *Geometric topology in dimensions 2 and 3*, Springer, 1977.
- [305] R. Monasson, *Diffusion, localization and dispersion relations on "small-world" lattices*, Eur. Phys. J. B **12**(4), 555–567 (1999).



- [306] A. N. Morozov and S. H. Lin, *Accuracy and convergence of the Wang-Landau sampling algorithm*, Phys. Rev. E **76**, 026701 (2007).
- [307] O. Mülken and A. Blumen, *Continuous-time quantum walks: Models for coherent transport on complex networks*, Phys. Rep. **502**(2-3), 37–87 (2011).
- [308] A. Nabutovsky and R. Ben-Av, *Noncomputability arising in dynamical triangulation model of four-dimensional quantum gravity*, Commun. Math. Phys. **156**, 93–98 (1993).
- [309] S. Negami, *Diagonal flips in triangulations of surfaces*, Discrete Math. **135**(1-3), 225–232 (1994).
- [310] S. Negami and A. Nakamoto, *Triangulations on closed surfaces covered by vertices of given degree*, Graph. Combinator. **17**(3), 529–537 (2001).
- [311] J. Nerbonne and W. Wiersma, *A measure of aggregate syntactic distance*, Proceedings of the Workshop on Linguistic Distances (Stroudsburg, PA, USA), LD '06, Association for Computational Linguistics, 2006, pp. 82–90.
- [312] E. Nevo, F. Santos, and S. Wilson, *Many triangulated odd-spheres*, Math. Ann. **364**(3), 737–762 (2016).
- [313] D. J. Newman and L. Shepp, *The double dixie cup problem*, Amer. Math. Monthly **67**(1), 58–61 (1960).
- [314] M. E. J. Newman, *Networks. an introduction*, Oxford University Press, 2010.
- [315] M. E. J. Newman and G. Barkema, *Monte Carlo methods in statistical physics*, Oxford University Press, 1999.
- [316] M. E. J. Newman and D. J. Watts, *Renormalization group analysis of the small-world network model*, Phys. Lett. A **263**(4-6), 341–346 (1999).
- [317] W. Nolting, *Grundkurs Theoretische Physik 6. Statistische Physik*, 6 ed., Springer, 2007.
- [318] R. Oeckl, *Discrete gauge theory*, Imperial College Press, 2005.
- [319] C. Oguey, N. Rivier, and T. Aste, *Stratifications of cellular patterns: Hysteresis and convergence*, Eur. Phys. J. B **33**(4), 447–455 (2003).



- [320] L. Onsager, *Crystal statistics. I. A two-dimensional model with an order-disorder transition*, Phys. Rev. **65**, 117–149 (1944).
- [321] ———, *Statistical hydrodynamics*, Nuovo Cim. (Suppl.) **6**, 261 (1949), cited from C. Longuet-Higgins, M. F. Fisher: Lars Onsager. A Biographical Memoir. National Academy of Science, Washington D.C., 1991.
- [322] U. Pachner, *Konstruktionsmethoden und das kombinatorische Homöomorphieproblem für Triangulationen kompakter semilinearer Mannigfaltigkeiten*, Abh. Math. Sem. Univ. Hamburg **57**, 69–85 (1986).
- [323] E. Parzen, *On estimation of a probability density function and mode*, Ann. Math. Stat. **33**, 1065 (1962).
- [324] A. Patil, D. Huard, and C. J. Fonnesbeck, *PyMC: Bayesian stochastic modelling in python*, J. Stat. Soft. **35**(4), 1–81 (2010).
- [325] L. Pauling, *The structure and entropy of ice and of other crystals with some randomness of atomic arrangement*, J. Amer. Chem. Soc. **57**(12), 2680–2684 (1935).
- [326] R. Penrose, *Angular momentum. an approach to combinatorial space-time*, Quantum Theory and Beyond (T. Bastin, ed.), Cambridge University Press, 1971, pp. 147–150.
- [327] ———, *On the nature of quantum geometry*, Magic without Magic (J. Klauder, ed.), Freeman, 1972, pp. 333–354.
- [328] A. Perez, *The spin-foam approach to quantum gravity*, Living Rev. Relativity **16**, 3 (2013).
- [329] J. Pfeifle and G. M. Ziegler, *Many triangulated 3-spheres*, Math. Ann. **330**(4), 829–873 (2004).
- [330] G. Ponzano and T. Regge, *On Racah coefficients as coupling coefficients for the vector space of Wigner operators*, Spectroscopic and Group Theoretical Methods in Physics (F. Bloch, S. G. Cohen, A. de Shalit, S. Sambursky, and I. Talmi, eds.), North-Holland Publishing Co., 1968, p. 1.
- [331] S. Popinet, *GNU Triangulated Surface Library*.



- [332] A. Poutsma, *Applying Monte Carlo techniques to language identification*, Proceedings of Computational Linguistics in the Netherlands (CLIN), Rodopi, 2001, pp. 179–189.
- [333] M. H. Quenouille, *Notes on bias in estimation*, *Biometrika* **43**(3–4), 353–360 (1956).
- [334] T. Radó, *Über den Begriff der Riemannschen Fläche*, *Acta Sci. Math. (Szeged)* **2**, 101–121 (1925).
- [335] J. Rambau, *TOPCOM: Triangulations of point configurations and oriented matroids*, Mathematical Software—ICMS 2002 (A. M. Cohen, X.-S. Gao, and N. Takayama, eds.), World Scientific, 2002, pp. 330–340.
- [336] R. Ramey, *Boost serialization library*.
- [337] A. A. Ranicki, *On the hauptvermutung*, The Hauptvermutung Book. A Collection of Papers on the Topology of Manifolds (A. A. Ranicki, ed.), Springer, 1996.
- [338] T. Regge, *General relativity without coordinates*, *Nuovo Cim.* **19**, 558–571 (1961).
- [339] T. Regge and R. M. Williams, *Discrete structures in gravity*, *J. Math. Phys.* **41**(6), 3964–3984 (2000).
- [340] R. L. Renken, *A renormalization group for dynamical triangulations in arbitrary dimensions*, *Nucl. Phys. B* **485**(1-2), 503–514 (1997).
- [341] ———, *The renormalization group and dynamical triangulations*, *Nucl. Phys. B (Proc. Suppl.)* **53**(1-3), 783–785 (1997).
- [342] M. Richey, *The evolution of Markov chain Monte Carlo methods*, *Amer. Math. Monthly* **117**(5), 383–413 (2010).
- [343] L. B. Richmond and N. C. Wormald, *Almost all maps are asymmetric*, *J. Comb. Theory B* **63**(1), 1–7 (1995).
- [344] J. Richter-Gebert, *Perspectives on projective geometry. A guided tour through real and complex geometry*, Springer, 2011.
- [345] T. Rindlisbacher and P. de Forcrand, *Euclidean dynamical triangulation revisited: Is the phase transition really 1st order?*, *J. High Energy Phys.* **2015**(5), 138 (2015).



- [346] G. Ringel, *Wie man die geschlossenen nichtorientierbaren Flächen in möglichst wenig Dreiecke zerlegen kann*, Math. Ann. **130**(4), 317–326 (1955).
- [347] V. Rivasseau, *Spheres are rare*, EPL **102**(6), 61001 (2013).
- [348] C. Robert and G. Casella, *A short history of Markov chain Monte Carlo: Subjective recollections from incomplete data*, Statist. Sci. **26**(1), 102–115 (2011).
- [349] H. Römer and M. Zähringer, *Functional integration and the diffeomorphism group in euclidean lattice quantum gravity*, Class. Quantum Grav. **3**(5), 897 (1986).
- [350] M. Rosenblatt, *Remarks on some nonparametric estimates of a density function*, Ann. Math. Stat. **27**(3), 832–837 (1956).
- [351] C. P. Rourke and B. J. Sanderson, *Introduction to piecewise-linear topology*, Springer, New York, 1982.
- [352] C. Rovelli, *Quantum gravity*, Cambridge Monographs on Mathematical Physics, Cambridge University Press, 2007.
- [353] C. Rovelli and L. Smolin, *Discreteness of area and volume in quantum gravity*, Nucl. Phys. B **442**(3), 593–619 (1995).
- [354] A. F. Rozenfeld, R. Cohen, D. ben Avraham, and S. Havlin, *Scale-free networks on lattices*, Phys. Rev. Lett. **89**, 218701 (2002).
- [355] J. H. Rubinstein, *An algorithm to recognize the 3-sphere*, Proceedings of the International Congress of Mathematicians 1994, Zürich (Basel) (S. D. Chatterji, ed.), vol. 1, Birkhäuser, 1995, pp. 601–611.
- [356] ———, *Polyhedral minimal surfaces, heegaard splittings and decision problems for 3-dimensional manifolds*, Geometric topology 1993, Georgia International Topology Conference (Providence, R.I) (W. Kazez, ed.), American Mathematical Society International Press, 1997, pp. 1–20.
- [357] F. Santos, *A point set whose space of triangulations is disconnected*, J. Amer. Math. Soc. **13**, 611–637 (2000).
- [358] ———, *Non-connected toric Hilbert schemes*, Math. Ann. **332**(3), 645–665 (2005).



- [359] S. Schleimer, *Sphere recognition lies in NP*, (2004), arXiv:math/0407047.
- [360] E. M. Schmidt, *Spectrum of the discrete Laplace operator on two-dimensional lattice triangulations*, (2013), short term research project.
- [361] M. F. W. Schmidt, *Cutting cubes — visualizing implicit surfaces by adaptive polygonization*, Vis. Comput. **10**(2), 101–115 (1993).
- [362] G. E. Schröder-Turk, W. Mickel, S. C. Kapfer, F. M. Schaller, B. Breidenbach, D. Hug, and K. Mecke, *Minkowski tensors of anisotropic spatial structure*, New J. Phys. **15**(8), 083028 (2013).
- [363] B. Schuetrumpf, M. A. Klatt, K. Iida, J. A. Maruhn, K. Mecke, and P.-G. Reinhard, *Time-dependent Hartree-Fock approach to nuclear “pasta” at finite temperature*, Phys. Rev. C **87**, 055805 (2013).
- [364] B. J. Schulz, K. Binder, and M. Müller, *Flat histogram method of Wang-Landau and N-fold way*, Int. J. Mod. Phys. C **13**(04), 477–494 (2002).
- [365] B. J. Schulz, K. Binder, M. Müller, and D. P. Landau, *Avoiding boundary effects in Wang-Landau sampling*, Phys. Rev. E **67**, 067102 (2003).
- [366] P. Scott, *The geometries of 3-manifolds*, Bulletin of the London Mathematical Society **15**(5), 401–487 (1983).
- [367] A. Shomer, *A pedagogical explanation for the non-renormalizability of gravity*, (2007), arXiv:0709.3555.
- [368] J. Siek, *Boost concept check library*.
- [369] B. W. Silverman, *Density estimation for statistics and data analysis*, Monographs on Statistics & Applied Probability, Chapman & Hall/CRC, 1986.
- [370] S. Smale, *On the structure of manifolds*, Amer. J. Math. **84**(3), 387–399 (1962).
- [371] D. M. Y. Sommerville, *The relations connecting the angle-sums and volume of a polytope in space of n dimensions*, Proc. R. Soc. A **115**(770), 103–119 (1927).



- [372] W.-M. Song, T. Di Matteo, and T. Aste, *Building complex networks with Platonic solids*, Phys. Rev. E **85**, 046115 (2012).
- [373] R. Sorkin, *Time-evolution problem in Regge calculus*, Phys. Rev. D **12**, 385–396 (1975).
- [374] A. Stauffer, *A Lyapunov function for Glauber dynamics on lattice triangulations*, (2015), arxiv:1504.07980v1.
- [375] J. Steiner, *Über parallele Flächen*, Bericht über die zur Bekanntmachung geeigneten Verhandlungen der Königl. Preuß. Akademie der Wissenschaften zu Berlin, Druckerei der Königlichen Akademie der Wissenschaften zu Berlin, 1840, pp. 114–118.
- [376] E. Steinitz, *Beitraege zur Analysis situs*, Sitz.-Ber. Berl. Math. Ges. **7**, 29–49 (1908).
- [377] D. Stolee, *Isomorph-free generation of 2-connected graphs with applications*, (2011), arXiv:1104.5261.
- [378] Student, *The probable error of a mean*, Biometrika **6**(1), 1–25 (1908).
- [379] T. Sulanke, *Counts of triangulations of surfaces*, (2005), <http://hep.physics.indiana.edu/~tsulanke/graphs/surftri/counts.txt>.
- [380] T. Sulanke and F. H. Lutz, *Isomorphism-free lexicographic enumeration of triangulated surfaces and 3-manifolds*, Eur. J. Comb. **30**(8), 1965–1979 (2009).
- [381] J. M. Sullivan, *The geometry of bubbles and foams*, Foams and Emulsions (J. Sadoc and N. Rivier, eds.), NATO Science Series E, vol. 354, Springer, 1999, pp. 379–402.
- [382] R. H. Swendsen and J.-S. Wang, *Replica Monte Carlo simulation of spin-glasses*, Phys. Rev. Lett. **57**, 2607–2609 (1986).
- [383] G. Szabó, M. Alava, and J. Kertész, *Structural transitions in scale-free networks*, Phys. Rev. E **67**, 056102 (2003).
- [384] M. A. Tanner and H. Wong, *The calculation of posterior distributions by data augmentation.*, J. Amer. Statist. Assoc. **82**(398), 528–550 (1987).
- [385] C. Teitelboim, *Proper-time gauge in the quantum theory of gravitation*, Phys. Rev. D **28**, 297–309 (1983).



- [386] ———, *Causality versus gauge invariance in quantum gravity and supergravity*, Phys. Rev. Lett. **50**, 705–708 (1983).
- [387] T. Thiemann, *Closed formula for the matrix elements of the volume operator in canonical quantum gravity*, J. Math. Phys. **39**(6), 3347–3371 (1998).
- [388] ———, *Introduction to modern canonical quantum general relativity*, (2001), arXiv:gr-qc/0110034.
- [389] A. Thompson, *Thin position and the recognition problem for S^3* , Math. Res. Lett. **1**(5), 613–630 (1994).
- [390] W. P. Thurston, *Three-dimensional geometry and topology. vol. 1.*, Princeton Mathematical Series, vol. 35, Princeton University Press, 1997.
- [391] H. Tietze, *Über die topologischen Invarianten mehrdimensionaler Mannigfaltigkeiten*, Monatshefte fuer Math. und Phys. **19**, 1–118 (1908).
- [392] S. Trebst, D. A. Huse, E. Gull, H. G. Katzgraber, U. H. E. Hansmann, and M. Troyer, *Ensemble optimization techniques for the simulation of slowly equilibrating systems*, Computer Simulation Studies in Condensed-Matter Physics XIX: Proceedings of the Nineteenth Workshop Athens, GA, USA, February 20–24, 2006 (D. P. Landau, S. P. Lewis, and H.-B. Schüttler, eds.), Springer Proceedings in Physics, vol. 123, Springer, 2007.
- [393] S. Trebst, D. A. Huse, and M. Troyer, *Optimizing the ensemble for equilibration in broad-histogram Monte Carlo simulations*, Phys. Rev. E **70**, 046701 (2004).
- [394] N. Trinajstić, *Graph theory and molecular orbitals*, Chemical Graph Theory: Introduction and Fundamentals (D. Bonchev and D. Rouvray, eds.), Mathematical Chemistry Series, Abacus Press, 1991, pp. 235–275.
- [395] M. Tsuruga and F. H. Lutz, *Constructing complicated spheres*, (2013), arXiv:1302.6856.
- [396] J. W. Tukey, *Bias and confidence in not quite large samples*, Ann. Math. Stat. **29**(2), 614 (1958).



- [397] V. G. Turaev and O. Y. Viro, *State sum invariants of 3-manifolds and quantum 6j-symbols*, *Topology* **31**(4), 865–902 (1992).
- [398] W. T. Tutte, *A census of planar triangulations*, *Canad. J. Math.* **14**, 21–38 (1962).
- [399] ———, *On the enumeration of convex polyhedra*, *J. Comb. Theory B* **28**(2), 105–126 (1980).
- [400] J. van den Heuvel and S. Pejić, *Using Laplacian eigenvalues and eigenvectors in the analysis of frequency assignment problems*, *Ann. Oper. Res.* **107**(1-4), 349–368 (2001).
- [401] D. Vandevoorde and M. Josuttis, *C++ templates: The complete guide*, Addison-Wesley Professional, 2002.
- [402] L. Varshney, *The wiring economy principle for designing inference networks*, *IEEE J. Sel. Areas Commun.* **31**(6), 1095–1104 (2013).
- [403] S. Varsted, *Four-dimensional quantum gravity by dynamical triangulations*, *Nucl. Phys. B* **412**(1-2), 406–414 (1994).
- [404] T. Vogel, Y. W. Li, T. Wüst, and D. P. Landau, *Scalable replica-exchange framework for Wang-Landau sampling*, *Phys. Rev. E* **90**, 023302 (2014).
- [405] I. A. Volodin, V. E. Kuznetsov, and A. T. Fomenko, *The problem of discriminating algorithmically the standard three-dimensional sphere*, *Russian Math. Surveys* **29**(5), 71 (1974).
- [406] F. Wang and D. P. Landau, *Determining the density of states for classical statistical models: a random walk algorithm to produce a flat histogram*, *Phys. Rev. E* **64**, 056101 (2001).
- [407] ———, *Efficient, multiple-range random walk algorithm to calculate the density of states*, *Phys. Rev. Lett.* **86**, 2050–2053 (2001).
- [408] J.-S. Wang and R. H. Swendsen, *Transition matrix Monte Carlo method*, *J. Stat. Phys.* **106**(1-2), 245–285 (2002).
- [409] S. Warner and S. Catterall, *Phase diagram of four-dimensional dynamical triangulations with a boundary*, *Phys. Lett. B* **493**(3-4), 389–394 (2000).



- [410] S. Warner, S. Catterall, and R. Renken, *Phase diagram of three-dimensional dynamical triangulations with a boundary*, Phys. Lett. B **442**(1-4), 266–272 (1998).
- [411] T. Wasserka, *Critical phenomena of the Ising model on triangulations*, (2016), master’s thesis.
- [412] D. J. Watts and S. H. Strogatz, *Collective dynamics of ‘small-world’ networks*, Nature **393**(6684), 440–442 (1998).
- [413] J. Wechs, *Lattice Laplacian on triangulations*, (2013), short term research project.
- [414] L. Wei, *New formula for 9-j symbols and their direct calculation*, Comput. Phys. **12**(6), 632–634 (1998).
- [415] ———, *Unified approach for exact calculation of angular momentum coupling and recoupling coefficients*, Comput. Phys. Comm. **120**(2-3), 222–230 (1999), Withdrawn in 2013, doi:10.1016/j.cpc.2013.05.004.
- [416] S. Weinberg, *Ultraviolet divergences in quantum theories of gravitation*, General relativity: Einstein centenary survey (S. W. Hawking and W. Israel, eds.), Cambridge University Press, Cambridge, UK, 1979, pp. 790–831.
- [417] D. Weingarten, *Euclidean quantum gravity on a lattice*, Nucl. Phys. B **210**(2), 229–245 (1982).
- [418] E. W. Weisstein, *Polylogarithm*.
- [419] J. H. C. Whitehead, *On C^1 -complexes*, Ann. Math. **41**(4), 809–824 (1940).
- [420] E. P. Wigner, *Characteristic vectors of bordered matrices with infinite dimensions*, Ann. Math. **62**(3), 548–564 (1955).
- [421] ———, *On the distribution of the roots of certain symmetric matrices*, Ann. Math. **67**(2), 325–327 (1958).
- [422] R. M. Williams and P. A. Tuckey, *Regge calculus: A brief review and bibliography*, Class. Quantum Grav. **9**(5), 1409 (1992).
- [423] K. G. Wilson, *Renormalization group and critical phenomena. I. Renormalization group and the Kadanoff scaling picture*, Phys. Rev. B **4**, 3174–3183 (1971).



- [424] ———, *The renormalization group: Critical phenomena and the Kondo problem*, Rev. Mod. Phys. **47**, 773–840 (1975).
- [425] F. Winterhalter, *Monte-Carlo-Simulationen mit Quadriken in endlichen projektiven Ebenen*, (2013), bachelor’s thesis.
- [426] F. Y. Wu, *The Potts model*, Rev. Mod. Phys. **54**, 235–268 (1982).
- [427] T. Wüst and D. P. Landau, *Versatile approach to access the low temperature thermodynamics of lattice polymers and proteins*, Phys. Rev. Lett. **102**, 178101 (2009).
- [428] X.-J. Xu, Z.-X. Wu, and G. Chen, *Epidemic spreading in lattice-embedded scale-free networks*, Phys. A **377**(1), 125–130 (2007).
- [429] C. N. Yang, *The spontaneous magnetization of a two-dimensional Ising model*, Phys. Rev. **85**, 808–816 (1952).
- [430] A. Yu, M. Lu, and F. Tian, *On the spectral radius of graphs*, Linear Algebra Appl. **387**, 41–49 (2004).
- [431] A. P. Yutsis, I. B. Levinson, and V. V. Vanagas, *Mathematical apparatus of the theory of angular momentum*, Israel Program for Scientific Translations, 1962.
- [432] C. Zhou and R. N. Bhatt, *Understanding and improving the Wang-Landau algorithm*, Phys. Rev. E **72**, 025701 (2005).
- [433] T. Zhou, G. Yan, and B.-H. Wang, *Maximal planar networks with large clustering coefficient and power-law degree distribution*, Phys. Rev. E **71**, 046141 (2005).
- [434] B. Zwiebach, *A first course in string theory*, Cambridge University Press, 2004.





Acknowledgments

First of all I want to thank *Prof. Klaus Mecke* for giving me the opportunity to write this thesis in his group and under his supervision, as well as for many valuable discussions about methods used and results found in this thesis as well as the concept and style of my published manuscripts and this thesis. Furthermore, he gave me the responsibility for the supervision of several students and some tutorials, which I think was very valuable for my personal development.

Another big “thank you” goes to *Johannes Knauf*, who introduced me to the world of triangulations, gave me the possibility to collaborate on the counting of lattice triangulations and provided some very valuable experience about programming in general. Even after leaving university he gave some important hints and discussions about my work. Beside physics and programming we had some very interesting and fruitful discussions about politics, society and raising children.

Some major work was done by students that were supervised by me during their theses. I want to emphasize the contribution of *Ella Schmidt*, who worked on the Laplacian spectrum of lattice triangulations which resulted in two publications, *Alexander Laska*, who delivered a remarkable master’s thesis concluding much of the work done on finite projective geometries, *Maximilian Düll*, who worked on numerical simulations within the EPRL model, and *Tony Wasserka*, who simulated the Ising model on lattice and topological triangulations. Some parts of this thesis are directly based on their results.

I want to thank *Bruno Benedetti*, *Frank Lutz*, *Sebastian Kapfer* and *Andreas Döring* for very useful discussions about parts of my work. Some of the proofreading was done by *Frank Lutz* (Sec. 4.1 and the introduction of Chap. 4), *Thomas Zilker* (Sec. 6.2 and the introduction of Chap. 5), *Alexander Laska* (Sec. 6.1), and my father *Robert Krüger* (references), many thanks for their work.

Concluding this part, I want to thank the whole chair *Theorie 1* for the friendly welcome at the beginning of my thesis, the nice time I had during my thesis and the funny projects we did together.





Danksagung

Ein großer Dank gilt meiner gesamten Familie für ihre tatkräftige Unterstützung während meiner Promotion. Zu allererst möchte ich mich bei meiner Frau Katharina bedanken. Durch ihre immerwährende und starke Unterstützung, neben ihrer eigenen Berufstätigkeit und vielen sonstigen Verpflichtungen, war es mir erst möglich, die nötige Zeit und Kraft zu finden, die hier vorliegende Arbeit zu erstellen.

Weiterhin möchte ich meinem Sohn Jonathan Danke sagen. Durch seine stets gute Laune und sein Lachen hat er mich einige Frustrationen vergessen lassen. Zwar ist er heute gerade erst zwei Jahre alt, ich hoffe aber, dass er in einigen Jahren einmal diese Arbeit zur Hand nehmen und lesen wird. Ich würde mir wünschen, dass er dann nachvollziehen kann, dass ich viele Stunden, die eigentlich ihm als gemeinsame Zeit zugestanden hätten, mit dieser Arbeit verbracht habe.

Herzlich bedanken möchte ich mich an dieser Stelle auch bei meinen Eltern, die mich schon während meines Studiums, aber auch in der Promotionsphase immer unterstützt haben, und die bedingungslos hinter allen meinen Entscheidungen standen. Sie haben mich zu dem Menschen gemacht, der ich heute bin.

Danke sagen möchte ich auch meiner Schwiegermutter und meinen Schwiegergroßeltern, die Katharina und mich außerordentlich bei der Betreuung von Jonathan unterstützt haben, Sie haben es erst ermöglicht, dass Jonathan trotz unserer beider Berufstätigkeit in einem familiären Umfeld aufwachsen kann.



Triangulations, which can intuitively be described as a tessellation of space into simplicial building blocks, are structures that arise in various different branches of physics: They can be used for describing complicated and curved objects in a discretized way, e.g., in foams, gels or porous media, or for discretizing curved boundaries for fluid simulations or dissipative systems. Interpreting triangulations as (maximal planar) graphs makes it possible to use them in graph theory or statistical physics, e.g., as small-world networks, as networks of spins or in biological physics as actin networks. Since one can find an analogue of the Einstein-Hilbert action on triangulations, they can even be used for formulating theories of quantum gravity. Triangulations have also important applications in mathematics, especially in discrete topology.

Despite their wide occurrence in different branches of physics and mathematics, there are still some fundamental open questions about triangulations in general. It is a priori unknown how many triangulations there are for a given set of points or a given manifold, or even whether there are exponentially many triangulations or more, a question that relates to a well-defined behavior of certain quantum geometry models. Another major unknown question is whether elementary steps transforming triangulations into each other, which are used in computer simulations, are ergodic. Using triangulations as model for spacetime, it is not clear whether there is a meaningful continuum limit that can be identified with the usual and well-tested theory of general relativity.

Within this thesis some of these fundamental questions about triangulations are answered by the use of Markov chain Monte Carlo simulations, which are a probabilistic method for calculating statistical expectation values, or more generally a tool for calculating high-dimensional integrals. Additionally, some details about the Wang-Landau algorithm, which is the primary used numerical method in this thesis, are examined in detail.

